Metti⁸

Advanced Autumn School - **8th** Edition -

Thermal Measurements & Inverse Techniques

Sept. 24th – Sept. 29th, 2023 - *Ile d'Oléron, France*

VOLUME **2** : **TUTORIALS**

Metti⁸

Advanced Autumn School

Thermal Measurements

&

Inverse Techniques

- **8th** Edition -

Sept. 24th – Sept. 29th, 2023
Ile d'Oléron – France

https://metti8.sciencesconf.org/

Supported by :

https://metti8.sciencesconf.org/

Scientific coordination of METTI 8:

Denis Maillet
LEMTA, Nancy
Denis.Maillet@univ-lorraine.fr

Jean-Luc Battaglia
I2M, Bordeaux
jean-luc.battaglia@u-bordeaux.fr

Organisation of METTI 8

Yassine Rouizi
LMEE, Evry
Tel.: (33) 1 69 47 79 31
yassine.rouizi@univ-evry.fr

Olivier Quéméner
LMEE, Evry
Tel.: (33) 1 69 47 79 38
o.quemener@iut.univ-evry.fr

(Secretary) Olivia Viardot
LMEE, Evry
Tel.: (33) 1 69 47 75 51
olivia.viardot@univ-evry.fr

METTI 8 Commitee

J. C. Batsale, J. L. Battaglia, J. G. Bauzin, J. Berger, S. Demeyer, T. Duvaut, Y. Favennec, J.-L. Gardarein, B. Garnier, J. Gaspar, N. Horny, L. Ibos, J. C. Krapez, F. Lanzetta, N. Laraqi, P. Le Masson, C. Le Niliot, D. Maillet, J. Meulemans, H. Orlande, L. Pérez, T. Pierre, O. Quéméner, B. Rémy, F. Rigollet, C. Rodiet, S. Rouchier, Y. Rouizi, P. Salagnac

METTI 8 Location

CNRS Center "La Vieille Perrotine village", Oléron Island, (France)

https://metti8.sciencesconf.org/

FOREWORD

The 8th edition of the Advanced Autumn school 'Thermal Measurement and Inverse Techniques' is run by the METTI Group (**ME**sures en **T**hermique et **T**echniques **I**nverses) that constitutes a division of the Société Française de Thermique (SFT, French Heat Transfer Society).

* * *

Finding 'causes' from measured 'consequences' using a mathematical model linking the two is an inverse problem. This is met in different areas of physical sciences, especially in Heat Transfer. Techniques for solving inverse problems as well as their applications may seem quite obscure for newcomers to the field. Experimentalists desiring to go beyond traditional data processing techniques for estimating the parameters of a model with the maximum accuracy feel often ill prepared in front of inverse techniques. In order to avoid biases at different levels of this kind of involved task, it seems compulsory that specialists of measurement inversion techniques, modelling techniques and experimental techniques share a wide common culture and language. These exchanges are necessary to take into account the difficulties associated to all these fields. It is in this state of mind that this school is proposed. The METTI Group (Thermal Measurements and Inverse Techniques), which is a division of the French Heat Transfer Society (SFT), has already run or co- organized seven similar schools, in the Alps (Aussois, 1995 and 2005), in the Pyrenees (Bolquère-Odeillo, 1999), in Brasil (Rio de Janeiro, 2009), in Bretagne (Roscoff, 2011), in Pays Basque (Biarritz, 2015) and in Porquerolles island (Porquerolles 2019). For this eighth edition the school is again open to participants from the European Community with the support of the Eurotherm Committee.

* * *

Two books are distributed at the beginning of the school. Volume 1 contains the texts used as supports for the lectures and Volume 2 contains the texts used as supports for the tutorials.

https://metti8.sciencesconf.org/

TUTORIALS - TABLE OF CONTENTS

ID	Tutorial Title, Teachers	page
T1	Multispectral pyrometry, *N. Horny, T. Duvaut, T. Pierre*	1 - 14
T2	Thermal characterization by hot-plates, *T. Pierre, P. Le Masson, Y. Jannot,* A. Kusiak, E. Geslain	15 - 41
T3	Temperature and heat Flux measurements, F. Lanzetta, B. Garnier	43 - 51
T4	InfraRed Thermography : Materials & buildings, *L. Ibos, J. Meulemans*	53 - 96
T5	Periodic Heating methods for materials thermal characterisation, *L. Pérez, L. Autrique*	97 - 121
T6	Model Reduction by Modal Analysis, *F. Joly, Y. Rouizi, B. Gaume, O. Quéméner*	123 - 145
T7	Identification of Transfer Functions and of Boundary conditions, B. Rémy, D. Maillet, A. Barthélémy	147 - 188
T8	Heat Flux identification, *J.L. Gardarein, J.L. Battaglia, J. Gaspar*	189 - 198
T9	Bayesian approach for Inversion, *S. Demeyer*	199 - 209
T10	ThermoMechanical inversion, *J.G. Bauzin, M.N. Nguyen, N. Laraqi*	211 - 229
T11	Thermal imaging in semi-transparent media, *S. Chevalier, C. Bourgès, J. Maire, A. Sommier, C. Pradère, S. Dilhaire*	231 - 248
T12	Optimal Wavelengths Selection Criteria for Multispectral Pyrometry, *C. Rodiet*	249 - 265
T13	Optimal Experiment Design for inverse heat conduction problem, *J. Berger, S. Gasparin, A. Jumabekova*	267 - 288
T14	On the use of the Approximation Error Model Approach in Inverse Problems, *C. C. Pacheco, H. R. B. Orlande*	289 - 320
T15	Experimental identification of mobile heat sources , *M.B Cherikh, J. G. Bauzin, A. Hocine, N. Laraqi*	321 - 339

Tutorial 1: Multispectral pyrometry

N. Horny[1], T. Duvaut[1], T. Pierre[2]

[1] ITheMM (EA 7548), Univ. de Reims Champagne-Ardenne, 51100 Reims, France.
E-mail: nicolas.horny@univ-reims.fr; thierry.duvaut@univ-reims.fr
[2] Univ. Bretagne Sud, UMR CNRS 6027, IRDL, F-56100, Lorient, France.
E-mail : thomas.pierre@univ-ubs.fr

Abstract. This tutorial deals with the multispectral pyrometry for the temperature and emissivity estimation. This is a contactless technique where the surface radiative emission is recorded by an appropriate sensor, which delivers a signal proportional to the radiation. The latter, measured within a certain wavelength bandwidth, depends on the surface temperature. A spectral treatment of the signal offers the possibility to select one or more narrow ranges to estimate the temperature and/or the emissivity. This tutorial is divided in three parts: the first one presents briefly generalities about radiative transfer, emissivity and its dependencies, and the mono-, bi-, and multispectral pyrometry principles with the algorithms used to perform the estimation; the second part concerns the detailed presentation of a pyrometer and its calibration; and the third part is dedicated to the multispectral pyrometry, that is to say with more than two signals.

Nomenclature

Latine letters

c	light speed, $m{\cdot}s^{-1}$
h	Planck constant, J·s
H	constant
k	Boltzmann constant, $J{\cdot}K^{-1}$
K	amplification factor
L	radiance, $W{\cdot}m^{-2}{\cdot}\mu m^{-1}{\cdot}sr^{-1}$
p	*parameter*
S	signal, arbitrary unit
T	temperature, K
X	sensitivity
n	Flux density, $W.m^{-2}$
C_1	Constant Planck's law, $W.m^2$
C_2	Constant Planck's law, $m.K$

Greek letters

ε	emissivity
λ	wavelength, µm or m
ρ	reflectivity
σ	Stefan-Boltzmann constant, $W{\cdot}m^{-2}{\cdot}K^{-4}$
σ	noise or standard deviation
τ	transmittivity

Indices and subscripts

T	temperature
noise	noise
λ	wavelength
atm	atmosphere
eff	effective
env	environment
i	index
s	sensor
0	blackbody
‘	directional

Introduction

This tutorial concerns the contactless *pyrometry*, whose basics are the following: an appropriate sensor aims at a surface, records a radiative flux coming from its direction, and delivers a signal (a current for example) proportional to this flux. Among other parameters, the latter depends on the surface temperature and is defined in a certain wavelenght range. As previously mentioned, the pyrometry can be used for two different aspects. The first aspect is practically to perform *absolute flux, temperature and/or emissivity measurements itselves*. It

only implies the use of the basic radiometric equations [1] and the Planck law [2]. The second aspect is different from the first one since it is based on variation of the measured signal. It concerns the *material intrinsic properties characterisation* by combining the previous relations with the heat equation for example. Those two aspects can be associated, but, in most applications, both the sensor calibration with a blackbody and the Planck law are necessary.

The principal issue is the surface changing emission feature, namely the *emissivity*, which can vary versus the wavelength [3], the direction [4], the temperature [5], or the surface state [6] to name the major. Unfortunately, the experience shows that combination of two or more dependencies is possible [3]. And what happens to the emissivity is even true for the other radiative properties, the reflectivity, the absorptivity, and the transmittivity [1]. The emissivity variation problem is present whatever the pyrometric measurement technique. During radiative measurement with a broadband pyrometer, such as short wave (SW), middle wave (MW) or long wave (LW) infrared camera, the collected flux is not spectric, it is integrated along the whole spectral bandwidth. And the software usually requires an *effective emissivity* input to get the temperature, meaning a *greybody assumption*, which is a strong assumption. If it is not the case and the radiative properties changes with respect to the wavelength, the error would be difficult to evaluate. Unfortunately, post-treatment with a spectral emissivity model neither can be considered. The bispectral pyrometry manages the emissivity problem but leads to other questions.

The principle of the bispectral pyrometry is to perform radiative measurements at two different wavelengths *strictly monochromatic* as close as possible to each other in order to approve the greybody assumption, but not to close not to increase the temperature theoretical uncertainty [7,8]. This methodology is subjective since a compromise must be found. Therefore, several studies deal between this compromise and the definition of a more objective methodology [9]. The wavelengths choice points out also the signals ratio criterion [7,8]. If the greybody assumption is valid, a two equations two unknowns system is solved to calculate simultaneously both the temperature and the emissivity or to estimate them through a least-square method.

Numerous authors work on the multispectral pyrometry [10], that is to say with more than two wavelengths. Increase the spectral bandwidth tends to make the greybody assumption less and less applicable. The system to solve is always a n equations n+1 unknowns system, namely the n emissivities and the temperature, which is impossible to solve. One possibility is to use a mathematical function (polynomial, exponential) or a physical function to represent the behaviour of the emissivity with respect to the wavelength. Litterature presents numbers of physical functions (Maxwell, Hagen-Rubens, *e.g.*) [1]. Some emissivity models exist also for temperature dependency [11] or combine both the spectral and temperature dependencies.

The previous discussions are mainly true when the environment and the atmosphere (*i.e.* the space between the material and the sensor) contributions regarding the measured signal by the sensor is negligible. It is true for two reasons: the material temperature makes their temperature negligible, and when the material emissivity tends to unity. On the contrary, when the material emissivity tends to zero (aluminum, copper *e.g.*), the part of the received flux by the sensor coming from the environment and the atmosphere and reflected by the material cannot be negligible. Surface emissivity of the material can also change due to chemical reactions that can occur during high temperature measurements, such as oxidation [12],

requiring sometimes important experimental condition modifications and the use of vacuum or transparent inert gas (argon, helium).

This tutorial presents the basics of the multispectral pyrometry for the temperature and emissivity determination in the case of high and constant temperature measurements of surfaces of various surface state. During experiments, the environment and the atmosphere are assumed transparent and their influences negligible. The present text is composed of three parts. The first one deals with generalities about the mono-, the bi-, and the multipectral pyrometry: the equations are presented and the influence of the radiative properties and of the surrounding is discussed. The second part describes the experimental apparatus composed of a high temperature element with different samples, a spectrometer and a blackbody for the calibration. Finally and to go further, the third part presents the multispectral pyrometry, the methodology of the wavelengths selection, some emissivity models, and the limitations of the methods.

Several termonologies exist in pyrometry. The literature mentions indifferently bispectral or bi-coulour pyrometry for the temperature/emissivity estimation with the help of two signals, or multiwavelength or multi-colour pyrometry with more than two signals. In this tutorial, the terms spectral or wavelength will be prefered.

1. Generalities on multispectral pyrometry

The radiation that leaves a surface of temperature T and emissivity $\varepsilon'(\lambda,T)$ is the sum of two terms: the part emitted from the surface itself and the part coming from the environment at temperature T_{env} reflected by the surface of bidirectional reflectance $\rho''(\lambda,T)$. Considering the radiation received by the sensor, these two contributions are weighted by the atmosphere transmittivity $\tau(\lambda,T_{atm})$ and one must also consider the atmosphere self-emission of temperature T_{atm} (see J.-C. Krapez/ T. Pierre lecture for more information or [8]).

In the case of an opaque and isotropic surface and of a transparent atmosphere, the general thermometry equation is commonly written:

$$L_s(\lambda,T_{eff}) = \varepsilon'(\lambda,T)L^0(\lambda,T) + [1-\varepsilon'(\lambda,T)]L^0(\lambda,T_{env}) \quad (1.1)$$

where L^0 is the blackbody radiance given by the Planck law (1.2) in which h = 6.62 × 10^{-34} J·s, k = 1.38 × 10^{-23} J·K^{-1}, and c = 3 × 10^8 m·s^{-1} are the Planck constant, the Boltzmann constant, and the light speed, respectively.

$$L^0(\lambda,T) = \frac{2hc^2\lambda^{-5}}{e^{\frac{hc}{k\lambda T}}-1} \quad (1.2)$$

In relation (1.1), T_{eff} is an effective temperature obtained from the total radiation. An effective emissivity can also be introduced by:

$$L_s(\lambda,T_{eff}) = \varepsilon'_{eff}(\lambda,T_{eff})L^0_s(\lambda,T_{eff}) \quad (1.3)$$

An example is given in Figure 1 representing the theoretical radiations calculated with equation 1.1 considering a radiation emitted from a surface at temperature T = 423.15 K (150 °C) and

constant emissivity ε' = 0.5 and an environment at temperature T_{env} = 298.15 K (25 °C) in the spectral range λ_1 = 8 µm – λ_2 = 12 µm. The quantities theoretically measured by the sensor are the areas beneath the curves in Figure 1 (down to the horizontal abscissa), which are the integration of equation (1.1) with respect to the wavelength (1.4). In relation (1.4), the surface and the environment radiations are represented by the grid and the right-slanted lines area in Figure 1, the total radiation being the sum.

$$\underbrace{\int_{\lambda_1}^{\lambda_2} L_s(\lambda, T_{eff})d\lambda}_{total} = \underbrace{\int_{\lambda_1}^{\lambda_2} \varepsilon'(\lambda,T)L^0(\lambda,T)d\lambda}_{surface} + \underbrace{\int_{\lambda_1}^{\lambda_2} [1-\varepsilon'(\lambda,T)]L^0(\lambda,T_{env})d\lambda}_{environment} \quad (1.4)$$

The plot shows that 81.5 % of the radiation is the surface proper emission the complement coming from the environment. The effective temperature, or the blackbody temperature, of the total radiation is T_{eff} = 372 K (100 °C), which is obtained by solving:

$$L_s(T_{eff}) = \int_{\lambda_1}^{\lambda_2} L_s(\lambda, T_{eff})d\lambda \quad (1.5)$$

This effective temperature have no meaning, but allows quantifying the influence of both the emissivity and the environment temperature regarding the surface temperature. In this example, there is a difference of about 12 % between the real surface temperature and the effective one. This difference changes with the surface emissivity and the environment temperature.

As an example, Figures 2 and 3 plot the evolutions of the total radiance $L(T_{eff})$ and of the effective temperature T_{eff} of equation (1.4) versus surface temperature T and for different surface emissivities. The chosen values are the following:

- T = 373 K to 1 073 K
- ε' = 0.2 to 1.
- T_{env} = 298 K.

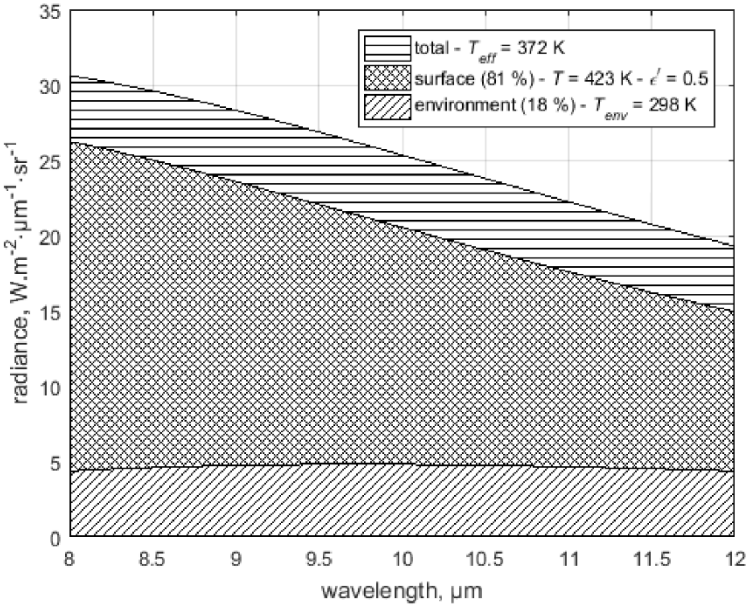

Figure 1. Surface, environment, and total radiations.

These plots really present the importance and the influence of these two parameters and the errors that could be involved. Considering the total radiation measured by the sensor, it can happen that the major part belongs to the environment due to the weak emissivity value. The principal issue is that it is not possible to separate both contributions in equation (1.4). However, among all the existing commercial pyrometers, in the case of spectral broadband sensors, different possibilities of tuning are available functions of the applications.

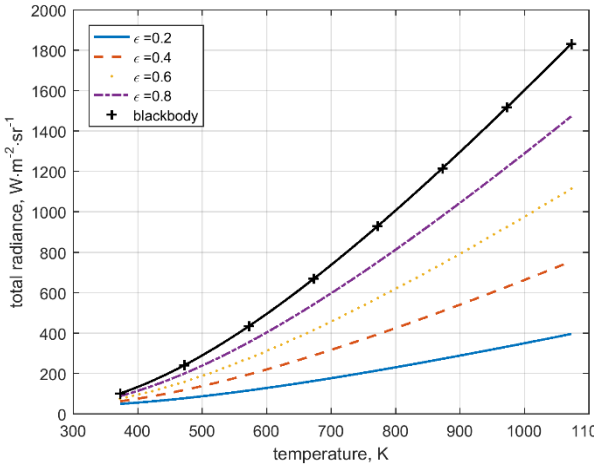

Figure 2. Evolution of the total radiance versus surface temperature for different surface emissivities.

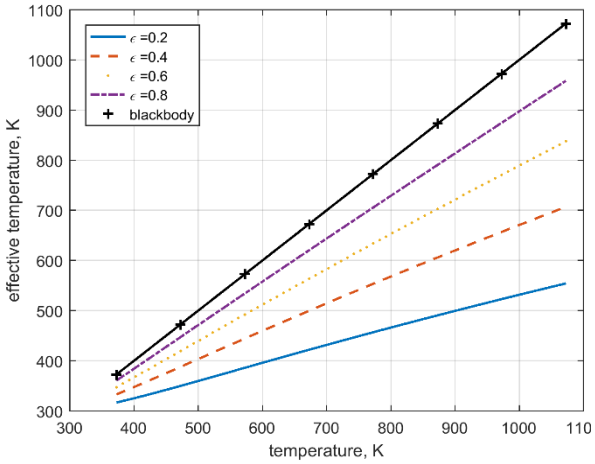

Figure 3. Evolution of the effective temperature versus surface temperature for different surface emissivities.

Some pyrometers (infrared, thermal guns) only offer the possibility to set the emissivity, which is the effective ε'_{eff} (1.3) since it is not possible to separate the surface from the environment radiations (1.3). These pyrometers aim an area, collect the radiation from it and typically, an effective temperature is put up functions of the set emissivity. If both the surface and the

environment temperatures are known, a first approximation commonly used allows to consider that the surface emissivity is given by:

$$\varepsilon' \cong \frac{\varepsilon'_{eff} T_{eff}^4 - T_{env}^4}{T^4 - T_{env}^4} \tag{1.6}$$

assuming:

$$L^0(T) = \frac{\sigma T^4}{\pi} \tag{1.7}$$

where σ = 5.67 × 10^{-8} W·m^{-2}·K^{-4} is the Stefan-Boltzmann constant.

Other pyrometers, such as the bolometric thermal imaging guns, have the possibility to set an emissivity and the environment temperature T_{env}. In this case, it is the real surface emissivity ε' since it is possible to separate the surface from the environment radiations. The temperature indicated by the gun is the real surface one. These imaging guns usually put up a temperature field image of the screen. However, it is possible to get from a software the signal proportional to the radiation collected by the sensor.

For efficient pyrometers, such as the infrared camera equipped with a cooled sensor with the emissivity and the environment temperature, user has the possibility to set the temperature of the atmosphere, and, if the latter is participating, its distance from the sensor and its transmittivity such as needed in equation (1.1). The signal is given in digital level unit (DL) or in temperature if the calibration has been performed.

The great drawback of these spectral broadband pyrometers is that they require a beforehand approximate knowledge of the emissivity of the surface. The radiative properties tuned in these pyrometers are constant values. Therefore, it is a major error source since these properties are liable to change along the whole spectral range (we have already mentioned in the introduction the other possible dependencies of the radiative properties). This error source is all the more important that the emissivity is weak and the environment temperature is close to the surface temperature. Numerous applications such as in building domain encountered this type of issue. The problem can be lower during high temperature measurements, namely when the environment temperature becomes negligible compared with the surface one, but still exists. The bispectral pyrometry proposes some possibilities to get rid of these multiple unwanted effects.

1.1. Simulation of radiometric signal (T1 - Exercise 1)

In this part, simulations of radiometric signals (RS) are built and used to test the three mentioned pyrometry technics (see Figure 4). Two spectral ranges are chosen: the shortwave (SW) between 0.9 µm and 1.7 µm representing small commercial spectrometers and the middle wave (MW) between 3 µm and 4 µm simulating MW infrared camera. Two temperatures of 800 K and 1 300 K are also chosen to represent different configurations. It gives four sets of experimental data, which can be noised or not.
In this example, a linear model of emissivity is chosen to simulate a variation of emissivity. It allows to quantify the influence of emissivity uncertainties on temperature.

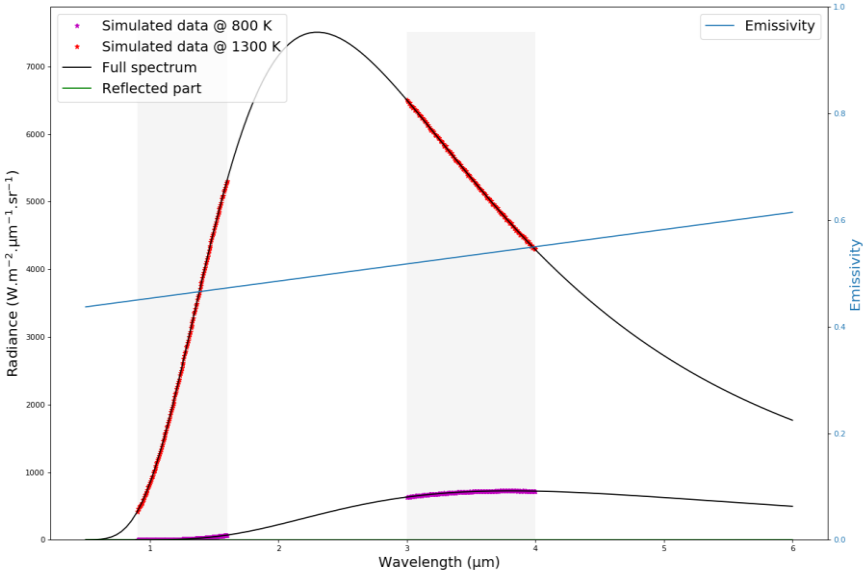

Figure 4. Experimental data simulations.

On these examples, the RS reflected part could be neglected contrary to the cases of small temperature of the sample and for higher wavelengths. Sensitivities are numerically calculated and plotted with different definitions (1.8)-(1.10) in Figure 5.

Sensitivity: $$X_p = \frac{\partial L}{\partial p} \quad (1.8)$$

Relative sensitivity: $$X_{p_R} = p\frac{\partial L}{\partial p} \quad (1.9)$$

Normalized sensitivity: $$X_{p_N} = \frac{p}{L}\frac{\partial L}{\partial p} \quad (1.10)$$

These sensitivities are used in the next parts to identify temperature and emissivity. One notes that the first sensitivity (1.8) is used in minimisation algorithm. A strong difference of order of magnitude could pose a problem such as bad condition number of $(X^TX)^{-1}$ matrix, but it can be solved easily by using normalised parameters (i.e. $p_1 = T/T_0$ and $p_2 = \varepsilon/\varepsilon_0$).

These sensitivities are very useful to check the validity of estimation. It allows to estimate the radiance error propagation to the parameters (variance amplification factor):

$$\sigma_p = diag[(X^TX)^{-1}]\sigma_{noise} \quad (1.11)$$

where X is the sensitivity matrix of the chosen fitting parameters and σ_{noise} is the variance of the observable. It is also possible to estimate the total uncertainty including the uncertainty of the supposed known parameter $\sigma_{supp\ known}$ of the experience [13] (wavelength, ambient temperature, calibration factors…):

$$\sigma_{supp\ known} = -(X^TX)^{-1}X^TX_c\ e_{\beta_c} \quad (1.12)$$

where X_c is the sensitivity matrix to the parameters supposed known and e_{β_c} is the absolute uncertainty vector of the supposed known parameters.

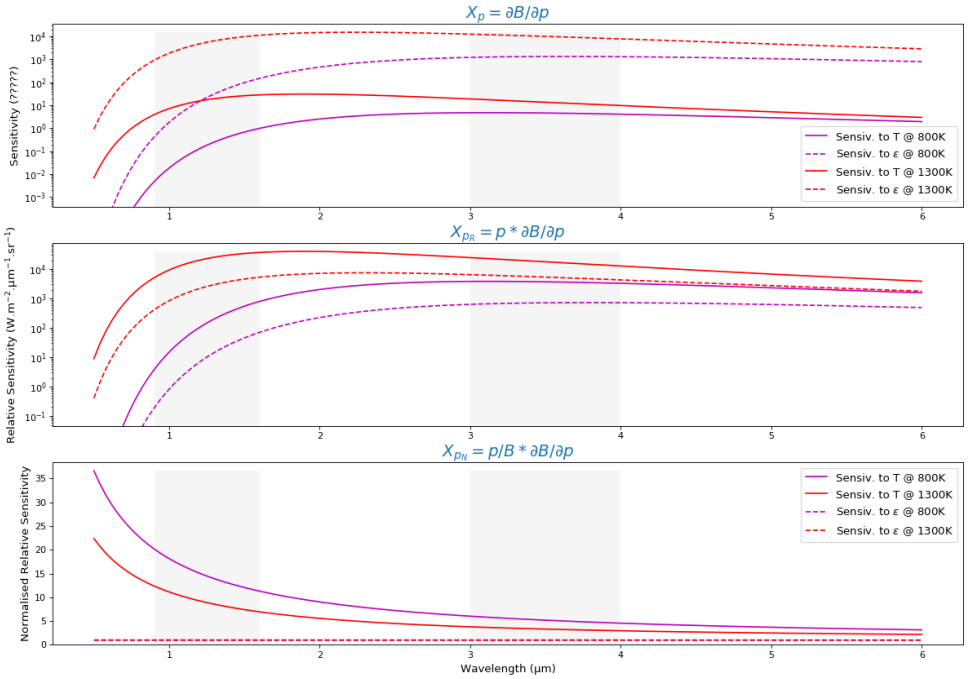

Figure 5 Sensitivities to temperature and emissivity.

In Figure 5, the normalised sensitivity to emissivity is 1 because the model is directly proportional to emissivity (it is not the case when the reflected part is not negligible).
In mono and bispectral pyrometry, the amplification factor, which evaluates the temperature sensitivity to an error on emissivity, could be calculated, it corresponds to the term $(X^T X)^{-1} X^T X_c$ in the equation (1.12).

For multispectral pyrometry, an estimation of uncertainties is made assuming the noise corresponds to the residuals (in simulations, noise is 0.5 % of the maximum signal). Another parameter useful to check the validity of measurement is the correlation matrix which non-diagonal terms represent the angle between sensitivity vectors.

1.2. Monospectral pyrometry (T1 - Exercise 2)

The previous simulated data are integrated over the SW or MW ranges and a minimisation with temperature as parameter is achieved with Nelder-Mead (NM) (fminsearch Matlab function) and Gauss-Newton (GN) algorithms for comparison [14]. Temperature identifications are tested with different initial values. The relative amplification factor *K* (1.13) is used to estimate temperature uncertainties (1.14) [13].

$$K = \frac{\varepsilon}{T}(X^T X)^{-1} X^T X_c \tag{1.13}$$

$$\frac{\Delta T}{T} = K \frac{\Delta \varepsilon}{\varepsilon} \tag{1.14}$$

In the examples, the amplification factor is between 0.08 and 0.3. As an example, an amplification factor of 0.2 gives an error of 16 K for an uncertainty of 10 % on the emissivity at 800 K and of 26 K at 1 300 K.

The comparison between NM and GN algorithms allows to see the importance of initial parameters on final value (see temperature value at first iteration in Figure 6).

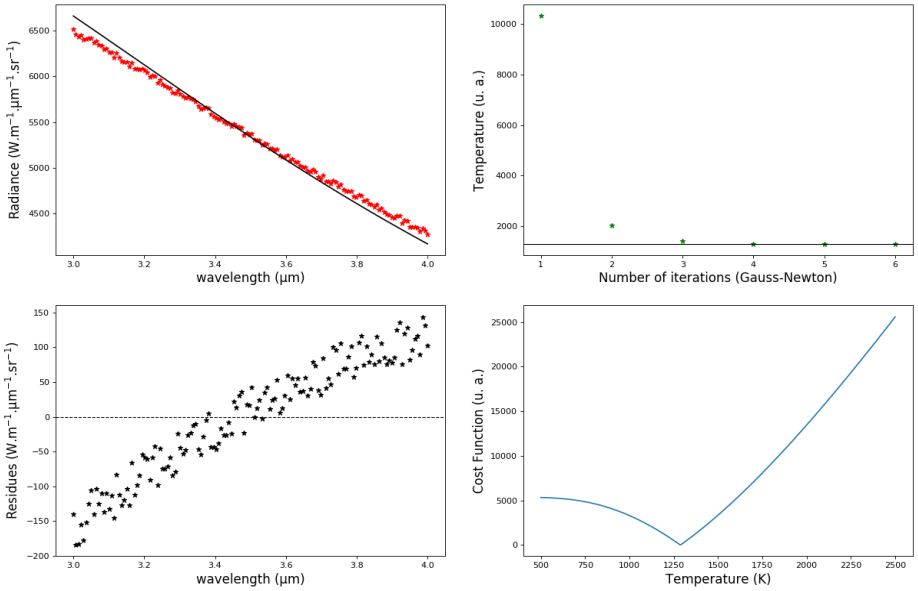

Figure 6. Result of monospectral pyrometry with simulated data. A bias is clearly identified but not detectable.

On the example in Figure 6, the two figures on the left present the influence of a bias in hypothesis, even though these curves are not available in monospectral pyrometry. With the GN algorithm, due to the flat cost function, a started point at low temperature gives a first correction temperature at a value higher than 10 000 K, which could be fatal in some cases.

1.3. Bispectral pyrometry (T1 - Exercise 3)

For the bispectral pyrometry, the surface temperature is determined from radiations measured by a sensor at two different wavelengths, especially as monochromatic and as close as possible. The wavelengths vicinity condition lays on the same emissivity assumption for both measurements. Theoretically, the two measured signals have the following expression (1.15) where i = 1, 2.

$$S_i^{th} = \int_0^{\infty} [\varepsilon_i'(\lambda_i, T) L^0(\lambda_i, T) + [1 - \varepsilon_i'(\lambda_i, T)] L^0(\lambda_i, T_{env})] f_i(\lambda) d\lambda \qquad (1.15)$$

where $f_i(\lambda)$ is a spectral function estimated by calibration, which depends on the transmittivity of the optical elements (filters, mirrors, gratings, optical fibre, *e.g.*) and on geometric factors (view factors, surfaces, mainly). This function can be a constant (1.16) when using a spectrometer or have a Gaussian shape (1.17), which is usually the case when using monochromatic optical filters.

$$f_i(\lambda) = H_i \tag{1.16}$$

$$f_i(\lambda) = H_i e^{-\frac{1}{2}\left(\frac{\lambda-\bar{\lambda}_i}{\sigma_i}\right)^2} \tag{1.17}$$

As an example, Figures 7 and 8 present the radiations measured by a bispectral sensor considering the same input data as previously. According to relation (1.17), the filters are characterized by a central wavelength $\bar{\lambda}$, a standard-deviation σ_i, and a amplitude coefficient H_i. In the case of Figure 7 and 8, the values are the following:

- $\bar{\lambda}_1$ = 1.80 µm, σ_1 = 0.0037 µm, H_1 = 0.45
- $\bar{\lambda}_2$ = 1.85 µm, σ_2 = 0.0028 µm, H_2 = 0.52

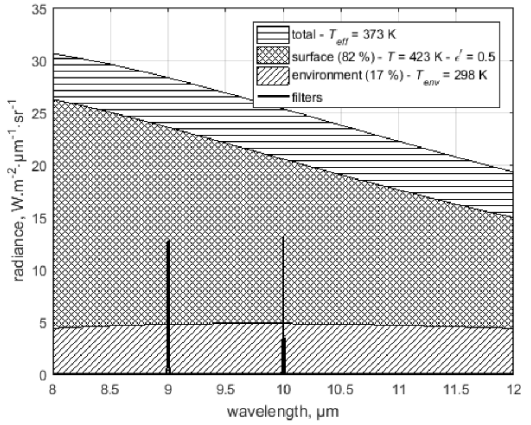

Figure 7. Comparison between the radiations measured by the sensor with and without the two filters.

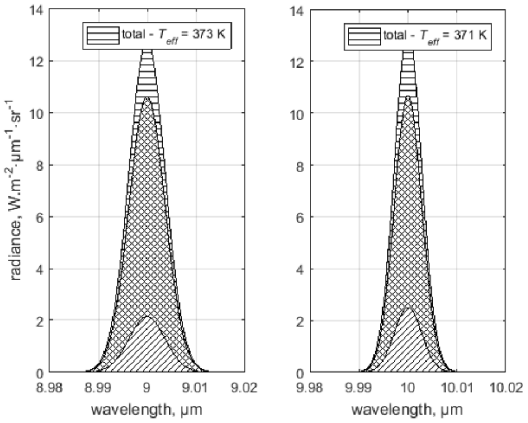

Figure 8. Focus of the different radiations measured by the sensor for each wavelength.

Figure 7 shows the significant difference between the radiation collected by the sensor with and without the two filters. The ratio between the total area collected without and with the filter is about 1 000. Nevertheless, Figure 8 shows that the proportion does not change between the surface and the environment radiations, and so is the effective temperature (about 373 K).

The principle of the bispectral pyrometry is to get at first the temperature from an experimental signals ratio $\xi_{12}^{\exp} = \frac{S_1^{\exp}}{S_2^{\exp}}$, if the following assumptions are made:

- environment influence negligible;
- constant emissivity.

In this case, equation (1.15) becomes:

$$S_i^{th} = \varepsilon_i' \int_0^{\infty} L^0(\lambda_i, T) f_i(\lambda) d\lambda \tag{1.18}$$

If the filters are assumed strictly monochromatic and the Wien approximation valid (λT << 14 000 µm·K), they are defined by a simple amplitude H_i determined by calibration, and relation (1.18) becomes:

$$S_i^{th} = \varepsilon_i' H_i C_1 \lambda_i^{-5} e^{-\frac{C_2}{\lambda_2 T}} \tag{1.19}$$

Thus, the temperature can explicitly be expressed by equation (1.20). Once the temperature obtained, the emissivity is easily calculated.

$$T = \frac{C_2\left(\lambda_2^{-1} - \lambda_1^{-1}\right)}{\ln\left[\xi_{12}^{\exp} \frac{H_2}{H_1}\left(\frac{\lambda_2}{\lambda_1}\right)^{-5}\right]} \tag{1.20}$$

If the filters behave like in relation (1.17) or if one considers the Planck law in place of the Wien approximation, the estimation of the temperature and the emissivity is possible by solving the criteria (1.21), whatever the Wien approximation is considered or not.

$$\left|\xi_{12}^{\exp} - \frac{S_1^{th}}{S_2^{th}}(\varepsilon', T)\right| = 0 \tag{1.21}$$

With the same data used in section 1.1, the identification of temperature is done with the determination of amplification factor. The use of the two wavelengths ratio implies a great influence of the noise. However, either the spectral range of a spectrometer is used and a scan in wavelength could smooth the noise [15], or the bandwidth of the filters reduces the influence of noise. Figure 9 presents results on SW spectral band data at 800 K for λ_1 = 1.4 µm and λ_2 = 1.5 µm. In this case, the amplification factor (relative to emissivity ratio) is about 1.2.

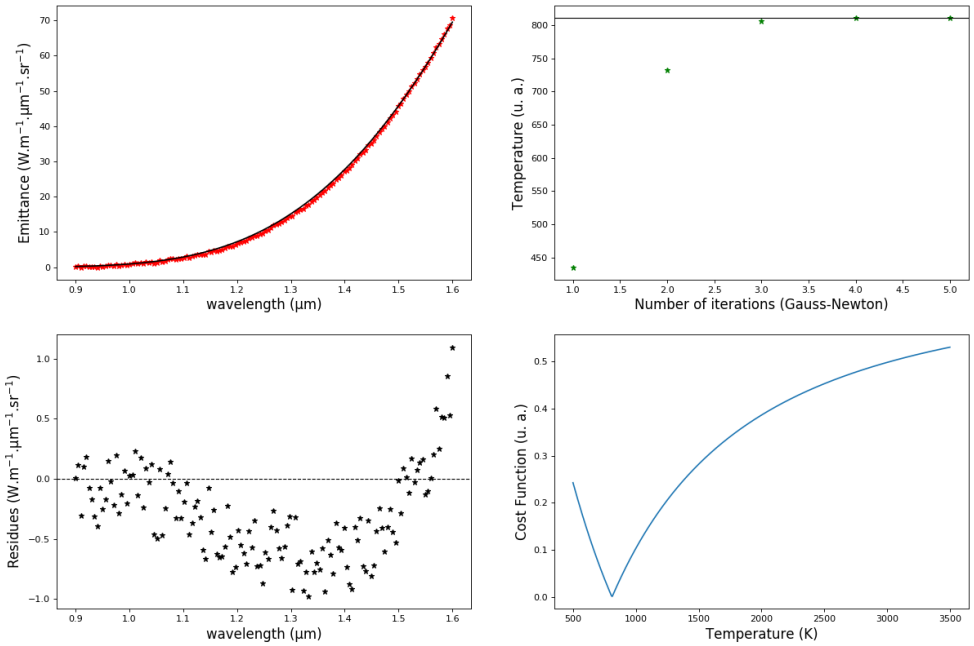

Figure 9. Result of bispectral pyrometry with simulated data. A bias is clearly identified but not detectable.

1.4. The multispectral (MSP) pyrometry (T1 – Exercise 4)

In this part, the multispectral pyrometry (MSP) is tested with a constant emissivity [16] and with a linear wavelength dependency emissivity $\varepsilon = a\lambda + b$. The emissivity and temperature are deduced by using non-linear least-squares based method in order to minimize of the chi-squared (χ^2) criterion, solved by the GN algorithm:

$$\chi^2 = \sum_{i=1}^{N_f} \left| n_{\lambda_i}^{\exp}(T) - n_{\lambda_i}^{th}(T) \right|^2 \qquad (1.22)$$

where $n_{\lambda_i}^{\exp}$ is the radiometric signal measured on the sample. In order to study the quality of the minimization, the residuals of minimization are shown. The dispersion of the residuals around zero reveals the quality of the MSP estimation.

With MSP, it is possible to retrieved the input parameters (*T*, *a*, *b*). However, the real problem is ill-conditioned, it exists a lot of minima, as shown by the valley in Figure 10 (bottom right) and so it exits several solutions to the inverse problem. Only a good knowledge of the physical problem allowing real assumptions or regularisation with *a priori* input will gives confident results.

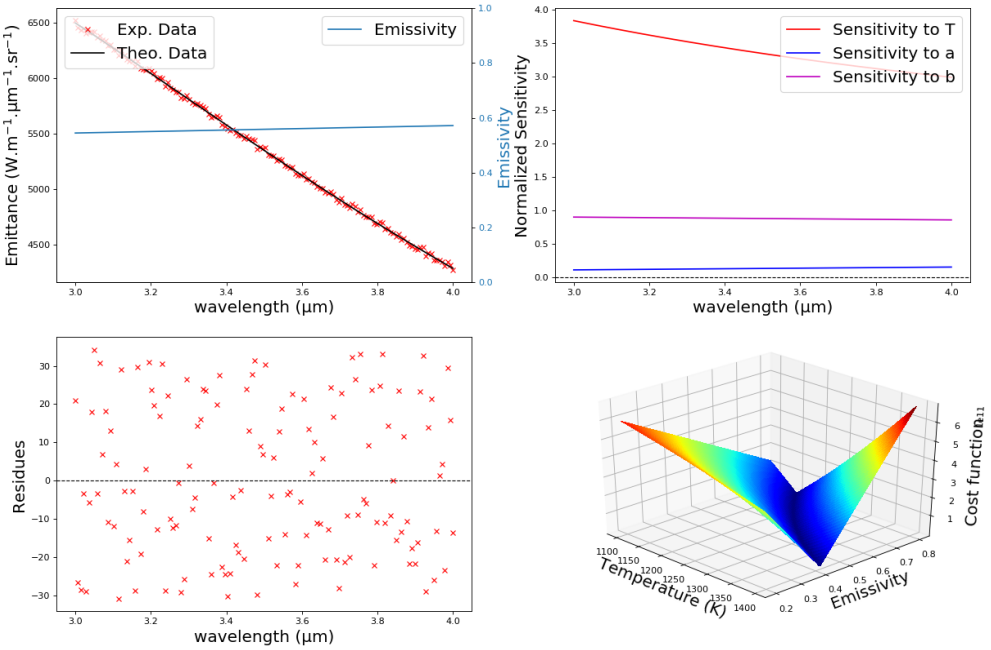

Figure 10. Result of MSP with simulated data. There is no bias in residues.

2. Real experimental data (T2)

In this second part of the tutorial, data from real measurements of radiance coming from different samples at different temperatures are blind tested in order to find the temperature. The principle of the measurement is showed in Figure 9. This multispectral pyrometry method is based on the comparison between the radiance emitted by the sample and by a heat source

with known temperature and emissivity ε, generally a blackbody ($\varepsilon \sim 1$), used as reference, in the same spectral range. Our reference thermal source is a cylindrical blackbody furnace of reference HGH RCN900.

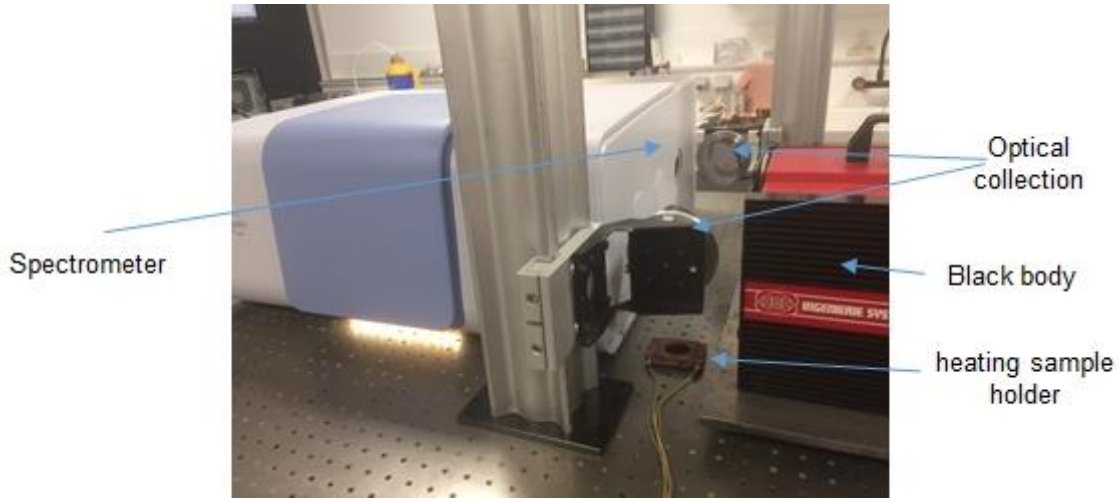

Figure 9. Experimental device.

An enclosure allows to heat the metallic samples (small circular plates of 25 mm diameter and 3 mm thickness) from ambient temperature up to more than 1 073 K (900 °C). Static measurement (P.I.D. regulation) are applied. A hole drilled radially into the centre of each sample plate contains a type K thermocouple to allow reference measurement of the plate temperature. We observe a good homogeneity of the surface temperature lower than 3 K. We test different metallic samples (steel, copper, aluminum) with different surface conditions (raw, polished, and blackened with a known emissivity paint).

The radiation emitted by the sample or the blackbody is focused on the spectrometer input slit by means of two similar out-of-axis parabolic mirrors. The spectra acquisition is successively made, and the change of the radiation source is made by rotation of the first mirror. We used an infrared Fourier transform spectrometer (Brucker, Invenio R) that allows measurement in a spectral range from about 1.25 µm to 25 µm with a resolution of about 2 nm.

The spectrometer does not give directly radiance and a calibration step is needed. The calibration process consists in converting the spectrometer DL in experimental radiance by collecting the signal from the blackbody at different temperatures. It is performed for different blackbody temperatures chosen to obtain emitted powers similar to those of the heated sample surface. For example, the power is measured for ten different temperatures of the blackbody furnace, from 400 K to 800 K every 10 K. The power from the blackbody furnace is measured by the infrared spectrometer. For each wavelength, the result is plotted as function of the radiance deduced from the Planck law. The linear regression obtained is the transfer function. Each wavelength has its own transfer function. The transfer function is used to convert the energy flux from sample, measured by the spectrometer, into radiance.

The aim of this tutorial T2 is to test algorithms of first tutorial T1 with experimental spectrum in order to retrieved the temperature.

References

[1] R. Siegel, J. Howell, Thermal radiation heat transfer, 4th edition, Taylor & Francis Editions, New-York, 2002.

[2] Max Planck, *Ueber das Gesetz der Energieverteilung im Normalspectrum*, *Annalen der Physik*, vol. 4, 1901, p. 553.

[3] Y.S. Touloukian, *Thermal radiative properties*, Plenum, New York (1970).

[4] J.-F. Sacadura, *Initiation aux transferts thermiques*, Ed. Tec&Doc, Paris, 2000.

[5] F. P. Incropera, D. P. DeWitt, *Fundamentals of heat and mass transfer*, Fifth Ed., Wiley, New-York, 2002.

[6] J.-F. Sacadura, *Les méthodes de mesure des propriétés radiatives,* colloque SFT, ISITEM Nantes, 1990.

[7] T. Pierre, B. Rémy, and A. Degiovanni, *Microscale temperature measurement by the multispectral and statistic method in the ultraviolet-visible wavelengths*, J. Appl. Phys., 103, 034904, 2008.

[8] J.-C. Krapez, H. Pron, *Lecture 5: Measurements without contact in heat transfer: principles, implementation and pitfalls*, Metti 6 Advanced School: Thermal Measurements and Inverse Techniques, volume 1, Biarritz, March 1-6, 2014.

[9] C. Rodiet, B. Remy, A. Degiovanni, F. Deumerie, *Optimisation of wavelengths selection used for the multi-spectral temperature measurement by ordinary least squares method of surfaces exhibiting non-uniform emissivity*, *Quantitative InfraRed Thermography Journal*, 2013, vol. 10, n°2, pp. 222-236.

[10] T. Duvaut, Comparison between multiwavelength infrared and visible pyrometry: Application to metals. Infrared Physics & Technology, 51(4), 292-299.

[11] M.F. Modest, *Radiative heat transfer*, Academic Press, Ney-York, 2003.

[12] L. Dejaeghere, T. Pierre, M. Carin, P. Le Masson, M. Courtois, *Development and validation of a high temperature inductive furnace dedicated to molten metals characterization*, High Temperatures High Pressure, 2018.

[13] Y. Jarny, D. Maillet, *Problèmes inverses et estimation de grandeurs en thermique, Métrologie thermique et techniques inverses*, Cours C1A, Ecole d'Hiver METTI '99, Presses Universitaires de Perpignan, 1999.

[14] J. V. Beck, K. J. Arnold. *Parameter estimation in engineering and science*. James Beck, 1977.

[15] B. Bouvry, L. Ramiandrisoa, G. Cheymol, N. Horny, T. Duvaut, C. Gallou, H. Maskrot, C. Destouches, L. Ferry, C. Gonnier, *Optical pyrometry measurement on oxidized Zircaloy-4 cladding*. Journal of Physics: Conference Series, Vol. 745, No. 3, p. 032103, 2016.

[16] B. Bouvry, G. Cheymol, L. Ramiandrisoa, B. Javaudin, C. Gallou, H. Maskrot, N. Horny, T. Duvaut, C. Destouches, L. Ferry & C. Gonnier, *Multispectral pyrometry for surface temperature measurement of oxidized Zircaloy claddings*. Infrared Physics & Technology, 83, 78-87, 2017.

Tutorial 2: Thermal characterization by hot-plates

T. Pierre[1], P. Le Masson[1], Y. Jannot[2], A. Kusiak[3], E. Geslain[1]

[1] Univ. Bretagne Sud, UMR CNRS 6027, IRDL, F-56100, Lorient, France.
E-mail: thomas.pierre@univ-ubs.fr; philippe-le-masson@univ-ubs.fr
[2] Université de Lorraine, CNRS, LEMTA, F-54000, Vandœuvre-lès-Nancy, France.
E-mail: yves.jannot@univ-lorraine.fr
[3] I2M, UMR CNRS 5295, Université de Bordeaux, F-33405 Talence Cedex, France.
E-mail: andrzej.kusiak@u-bordeaux.fr

Abstract. This tutorial presents the well-known hot-plate technique dedicated to the thermal characterization of materials. The experiments are transient, the input data and the observable are, respectively, a heat flux, that thermally excites the material, and a local temperature. Both data are recorded at the material heated face. The principle of the technique is detailed and the corresponding theoretical models are presented with appropriate assumptions. The experimental part of this tutorial is divided in three parts: first, the calibration with a known material, then the tests and the parameters estimation with materials of different natures. The theoretical models are developed thanks to the quadrupole formalism and the Laplace integral transform, and the parameters estimation is performed according to the determinist (Levenberg-Marquardt) fashion.

Nomenclature

Latine letters

c_p^m	thermal capacity, J·kg^{-1}·K^{-1}
C_{he}	half heating element heat capacity, J·m^{-2}·K^{-1}
e	thickness, m
E	thermal effusivity, J·m^{-2}·K^{-1}·s$^{-1/2}$
I	current, A
N	series terms number
k	thermal conductivity, W·m^{-1}·K^{-1}
r_c	contact resistance, m^2·K·W^{-1}
res	residuals
R	electrical resistance, Ω
s	Laplace parameter, s^{-1}
t	time, s
T	temperature, K
U	voltage, V
V_n	Stehfest series terms
X	sensitivity coefficient, K
z	Cartesian position, m

Greek letters

α	thermal diffusivity, m^2·s^{-1}
β	parameter to estimate
δt	sampling time, s
λ	sigmoidal function coefficient
ρ	density, kg·m^{-3}
σ	standard deviation, K
ϕ	heat flux, W·m^{-2}
Φ	Laplace transform of the heat flux
Ψ	digamma function
θ	Laplace transform of the temperature rise
ω	pulsation, s^{-1}

Indices and subscripts

est	estimation
exp	experimental
ext	room
he	heating element
m	per mass unit
p	constant pressure
0	initial
*	reduced

Introduction

Generally speaking, the characterization of the physical properties of materials is of great importance for evident reasons. Among many examples, let cite the multiphysics numerical simulations, which need to be fed by the concerned materials properties in order to predict the behavior of an industrial process or a building in use.

In the thermal characterization field, three aspects of the material must be considered at first sight: i) if it is a conductor or at the opposite an insulating material; ii) both the temperature amplitude and level during its use; and iii) its composition: pure, stratified, composite, porous, semi-transparent... Having an *a priori* answer on these considerations will help to choose a type of characterization technique and consequently a theoretical model, which preferencially would be purely conductive.

For example, the combination of the classifications proposed by Degiovanni and Jannot in [1] and [2] allows the reader to choose an appropriate technique to estimate one or more specific parameters for a geometry, a sensor, and a heat stress given, knowing approximately beforehand the thermal conductivity range of the material. Both (temperature or heat flux) sensor and heat stress can be with or without contact and measurements performed in steady-state or in transient regimes.

The second mentioned point concerns the temperature application and the temperature level reached during the use of materials. It becomes difficult to characterize materials at high temperature, as a consequence the physical properties litterature becomes more and more scarce when the temperature increases. The problems are not only physical but also technical. Let mention some of them: the properties varying strongly with temperature, the phase changes, the non-linear radiative exchanges with the environment, the chemical diffusion between the tested sample and its holder, the thermocouples operating limits, the surface emissivity variation due to oxidation during pyrometry measurements…

If the materials are heterogeneous or porous, chances are that the problem would not be only purely conductive but combines convection, radiative transfers, or also becomes a multiphysics problem. For example, the radiative and eventually the convective heat transfers must be taken into account in the case of aerogels [3]. Let now consider the hemp concrete. It is a porous heterogeneous material composed of lime binder, hemp shiv, and also air and water when it is not dry. At first sight, when the material is dry, only conduction could be sufficient to study its thermal. On the contrary, if the material is not dry anymore, the mass transfer equations must be taken into account and consequently a global understanding of its thermal behavior requires the knowledge of each component properties [4].

In this tutorial, we propose to approach the parameter estimation of common materials using the hot-plate technique at room temperature. The thermal conductivity range (in S.I. units) is set between 10^{-2} and 10^{0}. It is a transient method using a heating element and a thermocouple both in contact with the sample. Experimentally, the temperature, named the *observable*, is recorded versus time, which is the *variable*. The heat flux as *input data* is also recorded. At the same time a purely conductive theoretical model is developed, which gives the evolution of the temperature versus time at the same location as the thermocouple. The parameter estimation is perfomed by minimization of the sum of the quadratic gaps between the experimental and the theoretical temperatures.

The first part of this tutorial describes the hot-plate apparatus itself. The theoretical models and the possible parameters to estimate are presented in detail in the second part. The third part concerns the sensitivity studies and the correlation between the parameters. Experiments are presented in the fourth part: first the calibration with a known material (polycarbonate), then tests with other materials (cork, cellular concrete, rubber). The parameter estimation using the Levenberg-Marquardt algorithm is not explained.

1. Presentation of the hot-plate apparatus

There is a huge quantity of works dealing with the hot-plate technique. Figure 1 shows a global sketch of a hot-plate with a heating element of electrical resistance R and surface S stuck between two identical samples (materials) of thickness e. The heating element is a square heating electrical resistance of side 101.6 ± 0.1 mm^2 (Minco HK5178R42.9L12A). Insulating polyurethane foams and aluminium plates of similar section are placed at the rear face of the sample, and then the whole stack is kept hold with four butterfly screws (Figure 2). The clamp of the latter is not controlled. To assure strictly the parallelism, some authors used two identical heating elements [5], this is not the case in this tutorial.

The heating element delivers a Heaviside type heat flux even if others are possible, this is discussed in Appendix 1. Two type K thermocouples are placed at the centre of the cross section at the positions $z = 0$ and $z = e$ and measure the temperatures $T^{exp}(0,t)$ et $T^{exp}(e,t)$, respectively. The thermocouples characteristics are the following: 125 µm diameter for the wires and 300 µm for the hot junction. At a given time $t = t_0$, a current I flows in the heating element, which delivers in each sample a heat flux density $\phi_0(t)$ by Joule effect. During experiments, the rate of heat flow and the temperatures are recorded every 250 ms. The temperature $T^{exp}(e,t)$ is only used to evaluate the time validity of the semi-infinite model (see section 2.3).

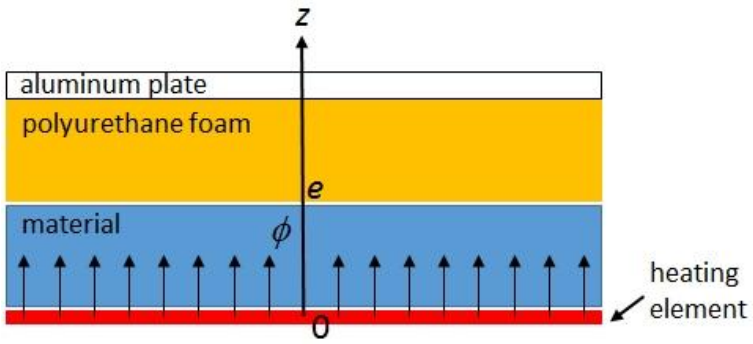

Figure 1. Sketch of the half of the hot-plate apparatus including the heating element, the sample (material), and a polyurethane foam on the rear side (as samples arrangement is symmetrical, only one side is represented).

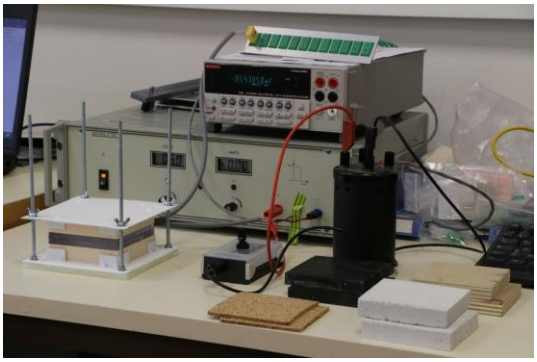

Figure 2. Photo of the complete apparatus and of some samples.

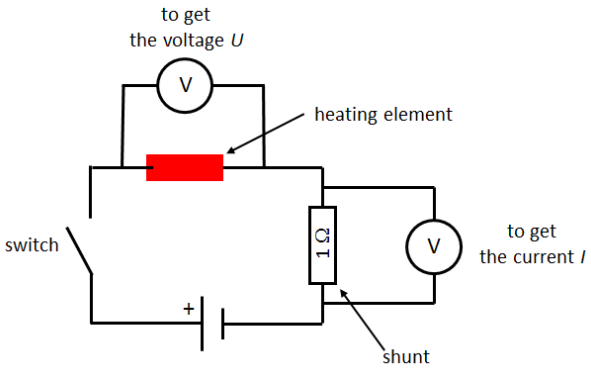

Figure 3. Sketch of the electrical circuit of the apparatus.

Four materials are available: polycarbonate, cellular concrete, rubber, and cork. Table 1 gathers their dimensions, weight, and density.

Table 1. Properties of the tested materials. The weight and dimension uncertainties are 40 mg and 5 µm.

material	weight (g)	thickness (mm)	surface ($mm^2 \times 10^3$)	density ($kg \cdot m^{-3}$)
polycarbonate	91.63	7.73	10.02 ± 0.01	1 183 ± 20
cellular concrete	122.69	19.96	9.98 ± 0.01	615 ± 6
rubber	207.10	14.22	10.25 ± 0.01	1 421 ± 14
cork	10.35	4.08	9.95 ± 0.01	255 ± 2

2. Hot-plate theoretical models

This part presents the theoretical models considered as the most faithful as possible with the experimental conditions and used for the parameter estimation. These models are developped with the help of the quadrupole formalism in the Laplace domain, as the time integral transform [6]. The quadrupole formalism is very practical in the case of multilayer experiments, where lumped bodies, thermal resistance, semi-infinite medium, or even internal source are encountered. Two models with their asymptotic behavior are detailed:

- a finite 1D model with the heating element and contact resistance;
- a semi-infinite 1D model with and without the heating element and contact resistance.

These models are compared with a 3D one developed with the help of space integral transforms, which is not detailled here. For further information about these methods, the reader should refer to references [6,7].

2.1 Assumptions and heat equation in the material

The heat transfers in the tested materials are assumed 1D along the *z*-direction, transient, and purely conductive. The tested materials are assumed dry and homogeneous, and their physical properties are constant in the experiment temperature range. The problem with models of higher dimensions is that they must consider new uncertain parameters, such as heat exchange coefficients due to the radiative and convective exchanges between the sample and

its environment since they have also the possibility to be correlated to the sought parameters during parameter estimation.

The heating element is considered purely capacitive of heat capacity $C_{he} = \rho_{he} c_{p,he}^{m} e_{he}$ where ρ_{he} is its density, e_{he} is its half thickness and $c_{p,he}^{m}$ its thermal capacity. The thermal losses through the heating element wires are negligeable. The contact resistance r_c between the heating element and the material is considered.

The heat equation in the tested material with the boundary conditions can be written as:

$$\frac{\partial^2 T(z,t)}{\partial z^2} = \frac{1}{\alpha}\frac{\partial T(z,t)}{\partial t} \tag{2.1}$$

$$-k\frac{\partial T(0,t)}{\partial z} = \phi(t) \tag{2.2}$$

$$\frac{\partial T(e,t)}{\partial z} = 0 \tag{2.3}$$

$$T(z,0) = T_{ext} \tag{2.4}$$

where α is the thermal diffusivity, k is the thermal conductivity, and T_{ext} is the room temperature, which is also the initial one. Two boundary conditions are possible in $z = e$: imposed temperature or adiabatic. The first one would be possible if a strong capacitive material such as an aluminum block [8] is placed instead of the polyurethane foam, and thus imposes a constant temperature during the experiment. The experiment shows that the adiabatic condition is more appropriate regarding the insulating properties of the polyurethane foam. The convective heat exchange boundary condition is excluded in the case of this experiment, it would add an additional coefficient to estimate. The system (2.1)-(2.4) is now expressed in the Laplace domain knowing that the Laplace transform F of a function f is defined as:

$$F(z,s) = L[f(z,t)] = \int_0^{\infty} f(z,t)e^{-st}dt \tag{2.5}$$

where s is the Laplace parameter, $f(z,t)$ can be either the temperature difference $T(z,t) - T_{ext}$ or the heat flux density $\phi(t)$. The new system is:

$$\frac{d^2\theta(z,s)}{dz^2} = \frac{s}{\alpha}\theta(z,s) \tag{2.6}$$

$$-k\frac{d\theta(0,s)}{dz} = \Phi(s) \tag{2.7}$$

$$\frac{d\theta(e,s)}{dz} = 0 \tag{2.8}$$

with $\theta(z,s) = L[T(z,t) - T_{ext}]$ and $\Phi(s) = L[\phi(t)]$.

2.2. Finite 1D model

The solution of the differential equation (2.6) is:

$$\theta(z,s) = \theta_1 e^{-qz} + \theta_2 e^{qz} \tag{2.9}$$

where θ_1 and θ_2 are two constants defined thanks to the boundary conditions and $q^2 = s/\alpha$. However, considering only the material is not sufficient, the heating element must be taken into account and eventually the thermal contact resistance between them. Therefore, the quadrupole formalism is a good tool to work with multilayer stack. The system heating element /material in the global case where a contact resistance cannot be negligible can be written as equation (2.10).

$$\begin{bmatrix}\theta(0,s)\\ \Phi(0,s)\end{bmatrix} = \underbrace{\begin{bmatrix}1 & 0\\ C_{he}s & 1\end{bmatrix}}_{heating\ element} \underbrace{\begin{bmatrix}1 & r_c\\ 0 & 1\end{bmatrix}}_{contact\ resistance} \underbrace{\begin{bmatrix}A & B\\ C & D\end{bmatrix}}_{material} \begin{bmatrix}\theta(e,s)\\ \Phi(e,s)\end{bmatrix} \tag{2.10}$$

$$A = D = cosh(qe) \tag{2.11}$$

$$B = \frac{sinh(qe)}{kq} \tag{2.12}$$

$$C = kq\, sinh(qe) \tag{2.13}$$

where $\theta(0,s)$, $\Phi(0,s)$, $\theta(e,s)$, and $\Phi(e,s)$ are, respectively the Laplace transforms of temperatures and heat fluxes at the location $z = 0$ and $z = e$. The first 2 × 2 matrix represents the purely capacitive heating element where C_{he} is the half of the heat capacity of the heating element divided by its area (the setup is symmetrical with respect to the plane $z = 0$). The second 2 × 2 matrix corresponds to the thermal contact resistance (on a unit area basis) between heating element and material sample, and the third 2 × 2 matrix is associated to the material sample. The equation (2.10) is an approximation, which works for materials of thermal conductivity greater than the polyurethane one. Indeed, in this case, the adiabatic condition would not be that relevant, thus a more appropriate quadrupole model would be the following:

$$\begin{bmatrix}\theta(0,s)\\ \Phi(0,s)\end{bmatrix} = \underbrace{\begin{bmatrix}1 & 0\\ C_{he}s & 1\end{bmatrix}}_{heating\ element} \underbrace{\begin{bmatrix}1 & r_c\\ 0 & 1\end{bmatrix}}_{contact\ resistance} \underbrace{\begin{bmatrix}A & B\\ C & D\end{bmatrix}}_{material} \underbrace{\begin{bmatrix}A_i & B_i\\ C_i & D_i\end{bmatrix}}_{insulating\ mat} \begin{bmatrix}0\\ \Phi(e+e_i,s)\end{bmatrix} \tag{2.14}$$

With the boundary condition (2.8), equation (2.10) becomes:

$$\theta(0,s) = \frac{1 + tanh(qe)\, kq}{C_{he}s + tanh(qe)\,(r_c C_{he}s + 1)kq}\Phi(0,s) \tag{2.15}$$

In equation (2.15), the thermal excitation $\Phi(0,s) = \Phi_0/s$, where Φ_0 is the level of the power step dissipated by the half heating element on a unit area basis, can be expressed in different ways (see Appendix 1). The asymptotic behavior of equation (2.15) for the long times ($t \to \infty$ and $s \to 0$) is given (see Appendix 2) by:

$$\theta(0,s) = \Phi_0 \left[\frac{1}{s^2\left(C_{he} + \rho c_p^m e\right)} + \frac{\rho c_p^m e r_c}{s\left(C_{he} + \rho c_p^m e\right)} \right] \tag{2.16}$$

And in the time domain, equation (2.16) becomes, for a zero contact resistance:

$$\underset{t\to\infty}{T(0,t)} = \frac{\phi_0}{C_{he} + \rho c_p^m e} t + cte \tag{2.17}$$

This expression shows a linear behavior of the temperature versus time until the influence of the other directions (2D and/or 3D) becomes non-negligible. The slope is inversely proportional to the heat capacity of both the heating element and of the material. Therefore, it is important to know as good as possible C_{he} through a calibration procedure.

To compare the theoretical temperature (2.15) with the experimental one, a Laplace to time inversion is necessary:

$$T(z,t) = L^{-1}[\theta(z,s)] + T_{ext} \tag{2.18}$$

Tables of conversion are available [9] to get back to the time domain for some relations. However, numerical inversion programs are also available. This is discussed in Appendix 1.

2.3. Semi-infinite 1D model

When the material is considered semi-infinite, the last two matrices 2 × 2 of equation (2.10) change and the whole system becomes:

$$\begin{bmatrix} \theta(0,s) \\ \Phi(0,s) \end{bmatrix} = \begin{bmatrix} 1 & 0 \\ C_{he}s & 1 \end{bmatrix} \begin{bmatrix} 1 & r_c \\ 0 & 1 \end{bmatrix} \underbrace{\begin{bmatrix} \theta(e,s) \\ E\sqrt{s}\theta(e,s) \end{bmatrix}}_{semi-infinite\ material} \tag{2.19}$$

where E is the material *thermal effusivity* ($kq = E\sqrt{s}$):

$$E = \sqrt{k\rho c_p^m} \tag{2.20}$$

The temperature solution at $z = 0$ is given by equation (2.19).

$$\theta(0,s) = \frac{1 + r_c E\sqrt{s}}{C_{he}s + (C_{he}r_c s + 1)E\sqrt{s}} \Phi(0,s) \tag{2.21}$$

The asymptotic behavior of equation (2.21) for the long times ($t \to \infty$ and $s \to 0$) yields (see Appendix 3):

$$\underset{s\to 0}{\theta(0,s)} \approx \frac{\Phi_0}{Es^{3/2}} + \frac{\Phi_0}{s}\left(r_c - \frac{C_{he}}{E^2}\right) \tag{2.22}$$

where Φ_0 is the power dissipated by the half of the heating element divided by its area.

Once expressed in the time domain, equation (2.22) gives a linear evolution of the temperature $T(0,t)$ versus the time square root as presented in equation (2.23). This expression is very convenient since it allows to calculate the thermal effusivity thanks to the estimation of the slope of $T(0,t) = f(\sqrt{t})$ between the moment when the inertial effects of the heating element heat capacity are null and until the end of the semi-infinite model validity.

$$T(0,t) = \frac{2\phi_0}{E\sqrt{\pi}}\sqrt{t} + cte \tag{2.23}$$

Both equations (2.17) and (2.23) are useful since they allow to estimate the material heat capacity and effusivity, respectively. Therefore, the *thermal diffusivity* α and the *thermal conductivity* k are available knowing equation (2.20) and that:

$$\alpha = \frac{k}{\rho c_p^m} \tag{2.24}$$

2.4. Comparison and analysis with the 3D model

The four temperature expressions (2.15), (2.16), (2.21), and (2.23) are now compared with a 3D model. For this model, let consider the cross-section $S = 4\,\ell\,L$, where ℓ is the width along the *x*-direction and L the length along the *y*-direction. The boundary conditions are the following:

$$\frac{\partial T(0,y,z,t)}{\partial x} = 0 \tag{2.25}$$

$$-k\frac{\partial T(l,y,z,t)}{\partial x} = hT(l,y,z,t) \tag{2.26}$$

$$\frac{\partial T(x,0,z,t)}{\partial y} = 0 \tag{2.27}$$

$$-k\frac{\partial T(x,L,z,t)}{\partial y} = hT(x,L,z,t) \tag{2.28}$$

The initial data are the following:

- Material:
  - k = 0.25 W·m^{-1}·K^{-1}
  - ρ = 1 500 kg·m^{-3}
  - c_p^m = 1 000 J·kg^{-1}·K^{-1}
  - E = 612 J·m^{-2}·K^{-1}·s$^{-1/2}$.
  - e = 10 mm
- heating element:
  - C_{he} = 1 000 J·m^{-2}·K^{-1}
- contact resistance:
  - r_c = 10^{-2} m^2·K·W^{-1}

- 3D model considerations:
  - h = 10 W·m^{-2}·K^{-1}
  - Fourier series terms number: 100 [6]

Figures 4 and 5 are the comparison between the temperature evolutions for the 3D (✶) and the different 1D models versus time and time square root, respectively. The material thickness e is chosen in order to observe the effect of the boundary conditions at $z = e$ during a reasonable experiment time ($t_{end} = t_N$ = 600 s), and to observe the absence of unwanted multidimensional effects comparing the finite 3D and 1D models (Figure 5). The limit of the semi-infinite 1D model happens when its temperature still increases while the 1D/3D models temperatures begin to increase slowly. The dashed plot is the semi-infinite model where the heating element is influenceless. Its temperature is parallel to the semi-infinite 1D model for a null heating element influence. Finally, the asymptotic linear finite model (2.17) fits well with the 1D/3D models once the semi-infinite model does not fit anymore (Figure 4).

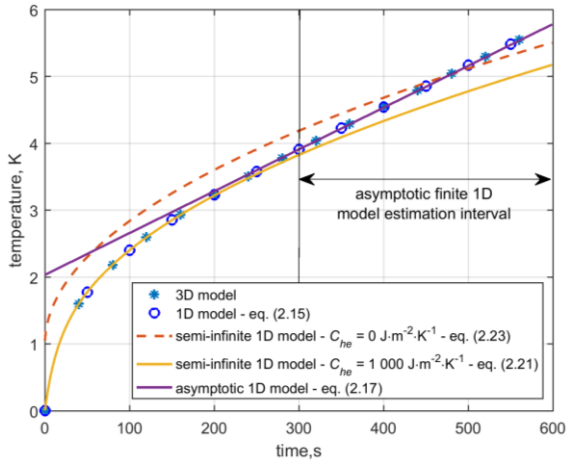

Figure 4. Comparison between the 3D and 1D models versus time.

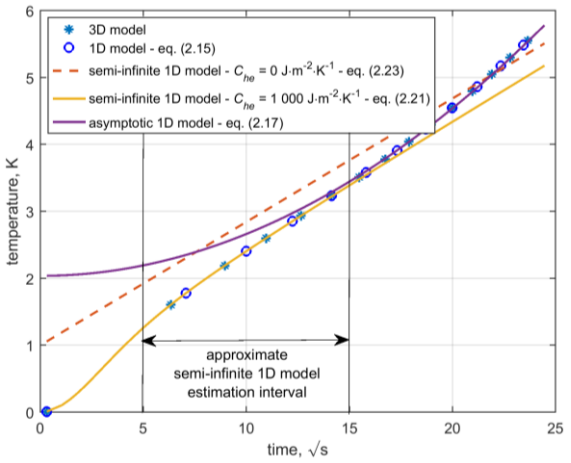

Figure 5. Comparison between the 3D and 1D models versus time square root.

Two simple parametric analysis concerning the heating element heat capacity C_{he} and the contact resistance r_c are presented in Figures 6 and 7, respectively. Figure 6 shows the temperature inertia increasing and is caused by the heat capacity C_{he} augmentation. Fortunately, the experience shows that the heating element has a low heat capacity value of about several hundred (in J·m^{-2}·K^{-1}) (see section 4). Figure 7 plots the possible influence of various contact resistances. These resistances are compared with the material one (**x**), in order to see whether it is possible to neglect them or not. This resistance is even more weak with materials of weaker roughness, such as polycarbonate than cellular concrete for example. However, experimentally, the thermocouple presence between two rigid materials (polycarbonate, cellular concrete) can create an important contact resistance, compared with non-rigid materials (cork, rubber), which can deform themselves and diminish it.

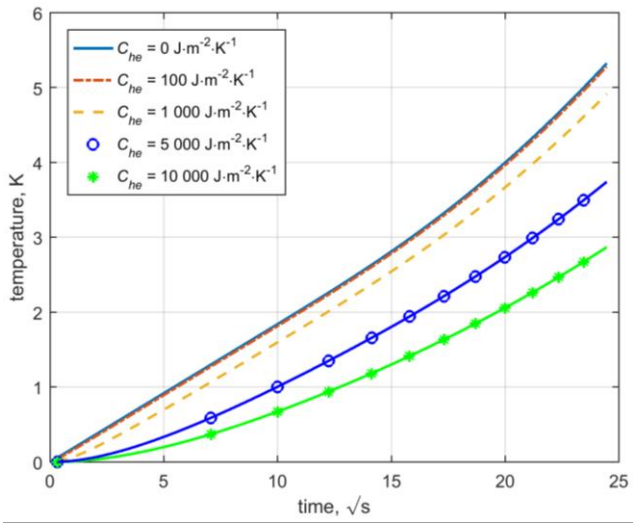

Figure 6. Influence of the heat capacity of the heating element on the temperature evolution for the finite 1D model (2.15) versus the time square root.

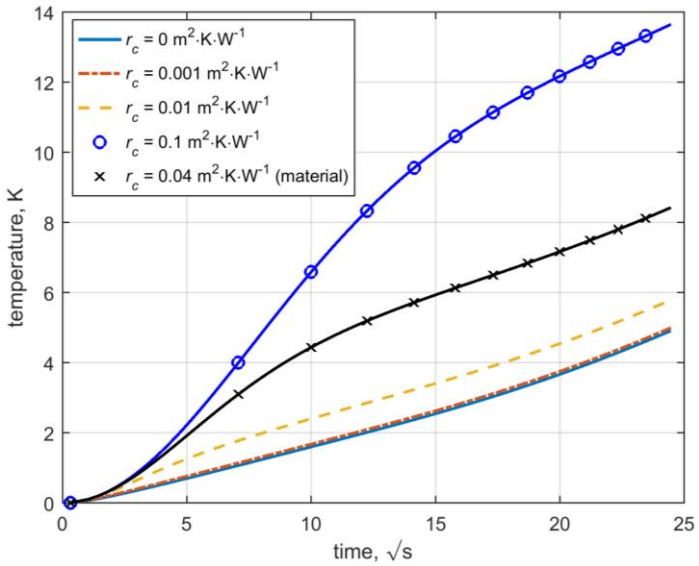

Figure 7. Influence of the contact resistance between the heating element and the material on the temperature evolution for the finite 1D model (2.15) versus the time square root.

Now let consider the equations (2.21) and (2.23) expressing, respectively, the temperatures for the semi-infinite 1D models with (dashed line in Figures 4 and 5) and without (solid line) the heating element. The former depends on three parameters: the heating element heat capacity, the contact resistance, and the effusivity, and the latter on the effusivity only. Since the heat capacity does not belong to the material, it is not a parameter of interest but it must be absolutely known and estimated by *calibration*, since it appears in equation (2.17) for the estimation of the material heat capacity. It is possible to determine it progressively with the help of a benchmark material of well-known properties by estimating the slope of equation (2.23), then with equation (2.21) the heat capacity and the contact resistance. Nevertheless a problem lays on the possible correlation between the latter. This point is discussed in section 3.

To sum up, it is theoretically possible to estimate all the physical parameters of the material with the hot-plate technique combining three 1D models, in semi-infinite and finite conditions. The use of a benchmark material is of prior importance for the estimation of the heating element heat capacity.

Before the proper parameter estimation with experimental data (section 4), the next section presents the sensitivity studies of the recorded temperature, namely the observable to the parameters to estimate.

3. Sensitivity study and correlation between parameters

The actors of the sensitivity study are the parameters and the observable. In the case of the hot-plate technique, the observable is the temperature recorded at the location $z = 0$, $T^{exp}(0,t)$, versus time, the variable. The location of the observable is of great importance since it must correspond to a place where the variation of a parameter implies a maximum influence on the observable itself. If the estimation of multiple parameters is at stake, there is a possibility that the variation of one parameter influences the other ones. Thus, they are correlated and their estimation could be difficult, even impossible, depending on the correlation level between them. If no correlation is obvious, the estimation is possible.

The sensitivity coefficients $\boldsymbol{X}_\beta$ (3.1) and more specifically the reduced sensitivity coefficients $\boldsymbol{X}_\beta^*$ (3.3) of parameters $\boldsymbol{\beta}$ are usually used and are given by the equations (3-1)-(3.3) where M is the number of parameters and N the number of measurements:

$$\mathbf{X}_\beta(t) = \frac{\partial \mathbf{T}(0,t)}{\partial \boldsymbol{\beta}} \tag{3.1}$$

$$\boldsymbol{X}_\beta(t) = \begin{bmatrix} \frac{\partial T(0,t_0)}{\partial \beta_1} & \cdots & \frac{\partial T(0,t_0)}{\partial \beta_M} \\ \vdots & \vdots & \vdots \\ \frac{\partial T(0,t_N)}{\partial \beta_1} & \cdots & \frac{\partial T(0,t_N)}{\partial \beta_M} \end{bmatrix} \tag{3.2}$$

$$\boldsymbol{X}_\beta^*(t) = \boldsymbol{\beta} \frac{\partial \boldsymbol{T}(0,t)}{\partial \boldsymbol{\beta}} \tag{3.3}$$

$\mathbf{X}_{\boldsymbol{\beta}}^*$ is expressed in the same units as the observable (here in kelvin). This is very suitable to compare a $\mathbf{X}_{\boldsymbol{\beta}}^*$ given with the measurement noise level, for instance. In our case, the total parameters to estimate are $\boldsymbol{\beta} = [r_c, C_{he}, \alpha, k, E, \rho c_p^m]^\mathsf{T}$. Knowing the fact that two parameters estimated are enough to have them all, let consider directly the series of parameters $\boldsymbol{\beta} = [E, \rho c_p^m, C_{he}, r_c]^\mathsf{T}$.

The same initial parameters presented in section 2.4 are considered and simulations are made with the help of the 1D model (2.15). Figure 8 plots the reduced sensitivities for the series $\boldsymbol{\beta}$. These plots show that the temperature is first sensitive to the heat capacity of heater, which

reaches a maximum at 20 s then becomes stable after 100 s. Then the temperature seems sensitive to the contact resistance, which also increase until 100 s and then stands still. The temperature is also sensitive to the material properties, first the effusivity then the heat capacity: X_E^* decreases then becomes constant once the semi-infinite assumption is not validate anymore, then $X_{\rho c_p^m}^*$ decreases once the asymptotic finite 1D model is validate when the temperature increases linearly with the time (sensitivity to the material thermal conductivity).

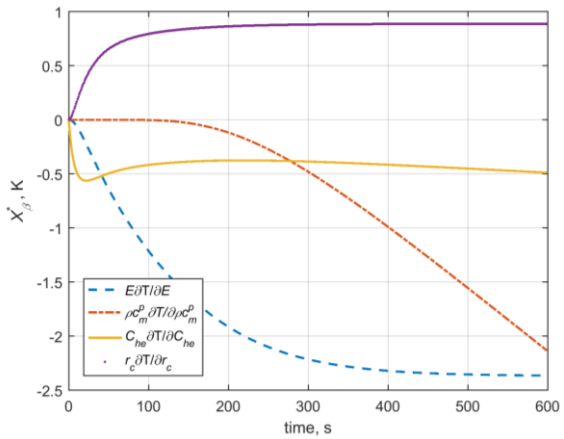

Figure 8. Reduced sensitivities for the first parameters series β for a 0.01 m²·K·W⁻¹ contact resistance.

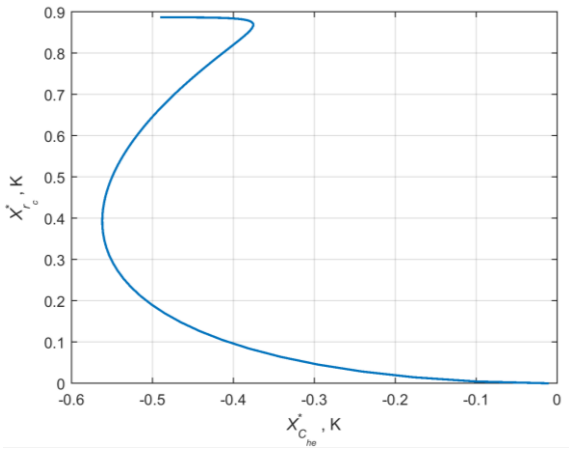

Figure 9. $X_{r_c}^*$ versus $X_{C_{he}}^*$ for a 0.01 m²·K·W⁻¹ contact resistance.

Globaly, after 100 s, the material effusivity and the heat capacity could be estimated since the temperature is not sensitive to C_{he} and r_c anymore. The estimation of C_{he} and r_c could be possible regarding both curves $X_{r_c}^*$ and $X_{C_{he}}^*$, which do not present the same curvatures in Figure 9. Indeed the evolution of $X_{r_c}^*$ versus $X_{C_{he}}^*$, shows no linear evolution between them.

Figures 10 and 11 have been plotted for a contact resistance r_c = 0.001 m²·K⁻¹·W⁻¹, ten times weaker than before. They show that the sentivity to this parameter is less important meaning that it could be difficult to estimate it and thus must be neglected. Even if a linearity is obvious in Figure 11 meaning a correlation between C_{he} and r_c, the estimation of the latter would be difficult since the amplitude of its sensitivity is weak.

It is important to notice that the amplitudes of the reduced sensitivities in Figures 8 to 11 are function of the level of the excitation. For example, a multiplication by 10 of the heat flux ϕ_0 will multiply also by 10 the amplitude of the reduced sensivitities. It increases the signal to noise ratio and would be helpful for the estimation, but a stronger heat excitation increases the temperature rise and can make the properties thermally dependant.

Let express the sensitivity matrix (3.2) in a more simplified way by (3.4), which is a N × M matrix where N is still the number of measurements and M is the number of parameters. Thus *i* is the time increment and *j* the parameter increment.

$$X_\beta(t) = \begin{bmatrix} X_{11} & \cdots & X_{1M} \\ \vdots & \ddots & \vdots \\ X_{N1} & \cdots & X_{NM} \end{bmatrix} \quad \text{with} \quad X_{ij} = \left.\frac{\partial T(t_i;\beta)}{\partial \beta_j}\right|_{\beta_k, \text{for} k \neq j} \tag{3.4}$$

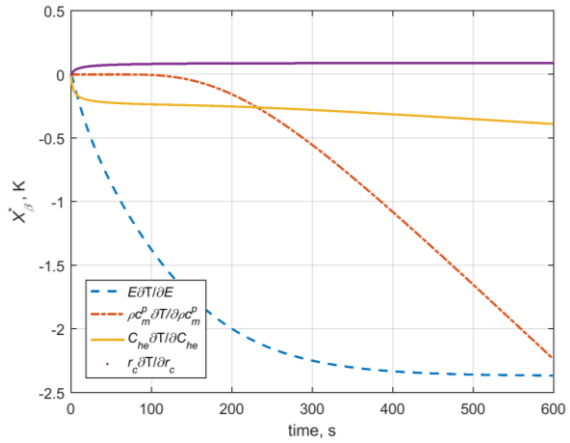

Figure 10. Reduced sensitivities for the first parameters series **β** for a 0.001 m²·K·W⁻¹ contact resistance.

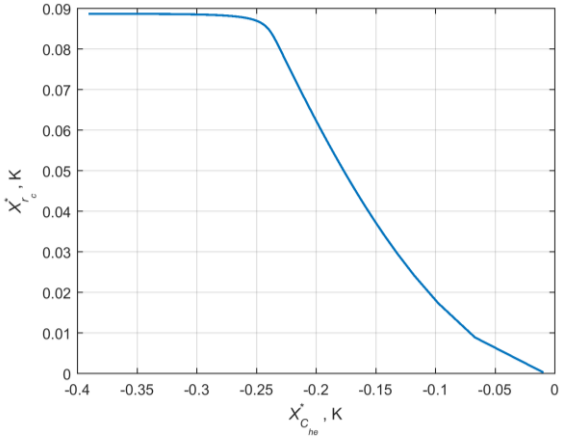

Figure 11. $X^*_{r_c}$ versus $X^*_{C_{he}}$ for a 0.001 m²·K·W⁻¹ constact resistance.

So in equation (3.4), the (square) variance-covariance M x M matrix and the standard deviation $\sigma_{\hat{\beta}_j}$ of the estimated parameters by the ordinary least squares method are defined by:

$$\boldsymbol{C} \equiv \text{cov}(\hat{\boldsymbol{\beta}}) \text{ with } C_{ij} = \text{cov}(\hat{\beta}_i, \hat{\beta}_j) \quad \text{and } \sigma_{\hat{\beta}_j} = \sqrt{C_{jj}} \tag{3.5}$$

They characterize the stochastic behaviour of the presence of an independent identically distributed noise, of standard deviation σ in the signal. They are given by:

$$\text{cov}(\hat{\boldsymbol{\beta}}) \equiv \sigma^2 \mathbf{A} \text{ with } \mathbf{A} = (\mathbf{X}^T \boldsymbol{X})^{-1} \text{ and } \sigma_{\hat{\beta}_j} = \sigma\sqrt{A_{jj}} \tag{3.6}$$

Large relative standard deviations $\sigma_{\hat{\beta}_j}/\beta_j$ may stem from a proportionality between 2 columns of the sensitivity matrix. So, it is interesting to check the level of their correlation coefficient:

$$\rho_{ij} = \frac{\text{cov}(\hat{\beta}_i, \hat{\beta}_j)}{\sigma_{\hat{\beta}_i}\sigma_{\hat{\beta}_j}} = \frac{A_{ij}}{\sqrt{A_{ii}}\sqrt{A_{jj}}} \tag{3.7}$$

The correlation coefficient (3.7) varies between -1 and 1. Parameters tend not to be correlated when ρ_{ij} tends to 0, and on the contrary become more and more correlated when ρ tends to ± 1. This coefficient should not be confused with the Pearson correlation coefficient whose level characterizes the *degree of linearity* of the output of a model to possible explanatory variables X_j that have random properties, while here the sensitivity coefficients are deterministic. The interested reader can find more information about this subject in Lecture L5 on Non linear parameter estimation in this series.

These coefficients depend on the estimation time $t_{est} = N \times \delta t$ (δt being the experimental sampling time time for example here 250 ms). All the correlation coefficients ρ^2 are plotted in Figure 12 for an estimation time varying from 100 s to 1 000 s. It must be helpful to have a first idea of a pertinent estimation time. For example, the estimation of both C_{he} and r_c seems difficult along the whole experiment, since Figure 12 shows that $\rho^2_{C_{he}r_c}$ has a value stated between 0.8 and 0.9 and even $\rho^2_{EC_{he}}$ decreases with time, but $\rho^2_{Er_c}$ is very high, which demonstrates a strong correlation between the contact resistance and the effusivity.This remark shows the importance of a calibration.

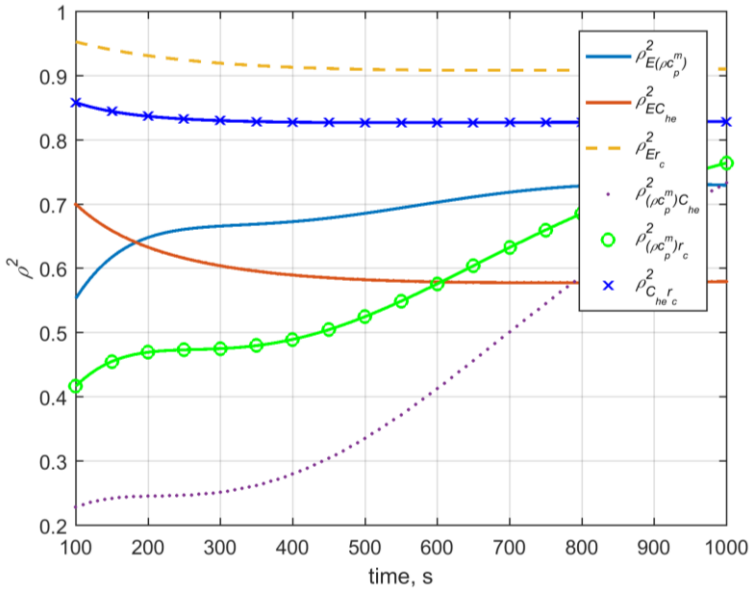

Figure 12. Evolution of the different correlation coefficients ρ^2 versus the estimation time.

4. Parameter estimations, measurements and results

First tests with synthetic data are performed to test the estimation procedure. They are created from the finite 1D model (2.15) presented in section 2.2, then noised. The noise level is adjusted regarding the experimental one. The parameter estimation is performed through the determinist fashion using the Levenberg-Marquadt (LM) algorithm. The procedure is repeated in the second part with real experimental data.

4.1. Tests with synthetic data

The principle is to create synthetic data from the complete model with the expected parameters to estimate and an additive noise representative of the experimental one. This noise is assumed null-averaged and normally distributed. Then the procedure is launched with initial parameters different from the expected ones.

Figures 13 and 14 represent synthetic data obtained with a 0.07 °C noise added to the theoretical model. They are plotted both versus time and the time square root.

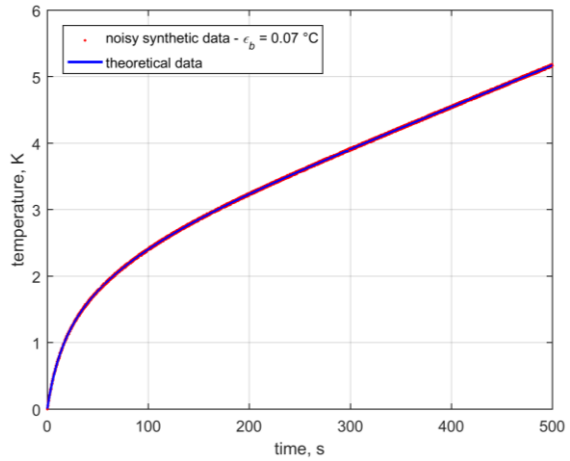

Figure 13. Simulation of synthetic data from the finite 1D model versus time (2.15).

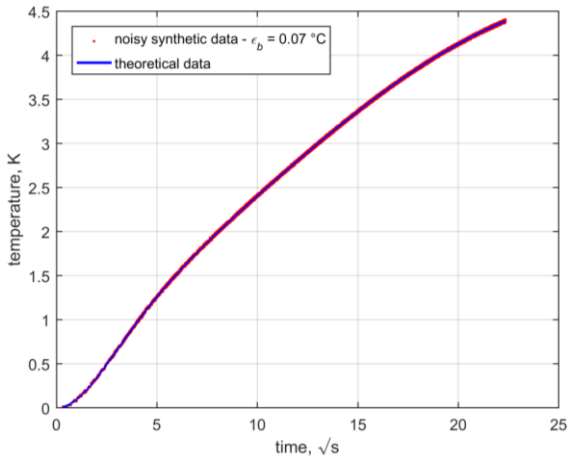

Figure 14. Simulation of synthetic data from the finite 1D model versus the time square root (2.15).

The first step consists in using the semi-infinite model (2.23) in order to estimate the sample thermal effusivity E, giving a linear evolution of the temperature $T(0,t)$ versus the time square root with an initial temperature $T(0,0) = 0$. Regarding the synthetic data (theoretical data corrupted by a simulated additive random noise) in Figures 13 and 14, the temperature linear evolution does not begin at $t = 0$, but later, that is why a constant is added in equation (2.23). Consequently, the estimation of the effusivity must be time-bounded. The estimation time interval has been chosen arbitrarily between 100 and 200 s approximately when the semi-infinite assumption is validated (10 and 14.14 $s^{1/2}$ in Figures 13 and 14). The initial values are E_0 = 200 $J{\cdot}m^{-2}{\cdot}K^{-1}{\cdot}s^{-1/2}$ (and cte = 1) knowing that the expected value is 612 $J{\cdot}m^{-2}{\cdot}K^{-1}{\cdot}s^{-1/2}$. Using the LM algorithm, the estimated effusivity is E = 564 $J{\cdot}m^{-2}{\cdot}K^{-1}{\cdot}s^{-1/2}$, representing a 7.9 % error with the expected value, the number of iteration is 1. Figures 15 and 16 show also the residuals, they highlight the good fitting of the semi-infinite model on the synthetic data during the estimation time interval, what happens before and after this domain is without consideration. Let us note also that the inferior time boundary is sooner when the heat capacity of the material increases and the contact resistance decreases. An asymmetrical device with a flexible insulator on one side allows to diminish the contact resistance [1].

The purpose now is to use the complete semi-infinite model (2.21) to estimate this time the heating element heat capacity, the contact resistance, and the effusivity again in a larger estimation time interval (Figures 17 and 18). This time interval has been chosen between 0 and 200 s. The initial values of the parameters are: C_{he0} = 100 $J{\cdot}m^{-2}{\cdot}K^{-1}$, r_{c0} = 10^{-4} $m^2{\cdot}K{\cdot}W^{-1}$, E_0 = 564 $J{\cdot}m^{-2}{\cdot}K^{-1}{\cdot}s^{-1/2}$. Finally, with the help of the LM algorithm, the estimation gives, for a number of iteration still equals to 1 the following results: C_{he} = 989 $J{\cdot}m^{-2}{\cdot}K^{-1}$, r_c = 0.009 8 $m^2{\cdot}K{\cdot}W^{-1}$, E = 606 $J{\cdot}m^{-2}{\cdot}K^{-1}{\cdot}s^{-1/2}$, thus the errors are 1.1 %, 2.0 %, and 1.0 %, respectively, with the expected values. Note that r_{c0} is in fact the sum of the contact resistance and of the resistance of the Kapton sheet covering the resistive wire of the heating element (about 0.000 5 $m^2{\cdot}K{\cdot}W^{-1}$).

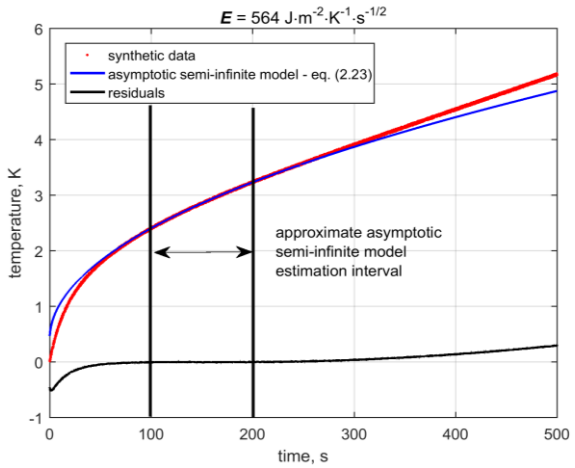

Figure 15. Synthetic and theoretical temperature curves versus time square root for the estimation of the effusivity *E*.

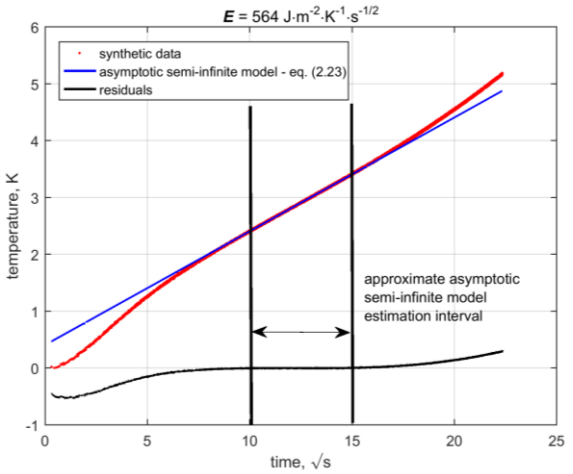

Figure 16. Synthetic and theoretical temperature curves versus time for the estimation of the effusivity *E*.

In Figure 19, the use of the asymptotic model (2.17) for the estimation of the sample heat capacity $\left(\rho c_p^m\right)$ finishes the procedure. The initial value of the heat capacity is $\rho c_{p,0}^m$ = 10 J·m^{-3}·K^{-1}. The estimated value is ρc_p^m= 1.46 × 10^6 J·m^{-3}·K^{-1}, that is to say with a 2.7 % error from the initial value (1.5 × 10^6 J·m^{-3}·K^{-1}). Figures 20 and 21 plot both the synthetic data with the finite 1D model with all the estimated parameters.

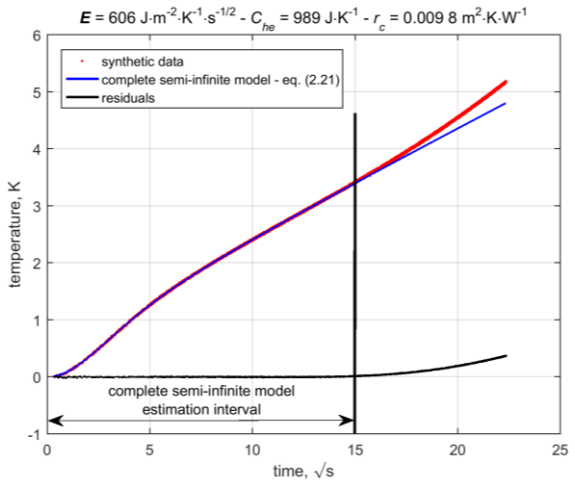

Figure 17. Synthetic and theoretical temperature curves versus time for the estimation of the effusivity *E*, the heating element heat capacity C_{he}, and of the contact resistance r_c in a larger estimation time interval representing the semi-infinite medium assumption.

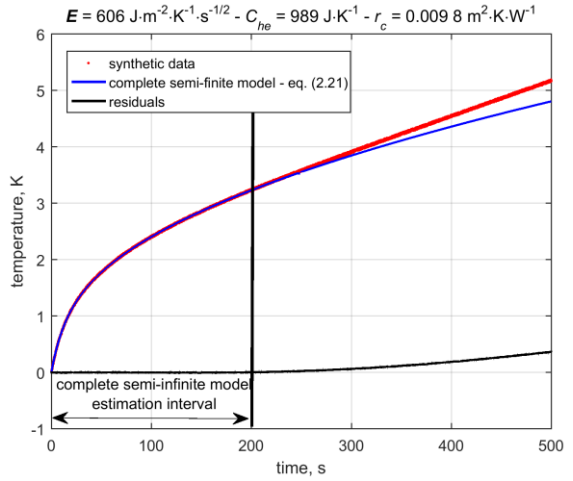

Figure 18. Synthetic and theoretical temperature curves versus time square root for the estimation of the effusivity *E*, the heating element heat capacity C_{he}, and of the contact resistance r_c in a larger estimation time interval representing the semi-infinite medium assumption.

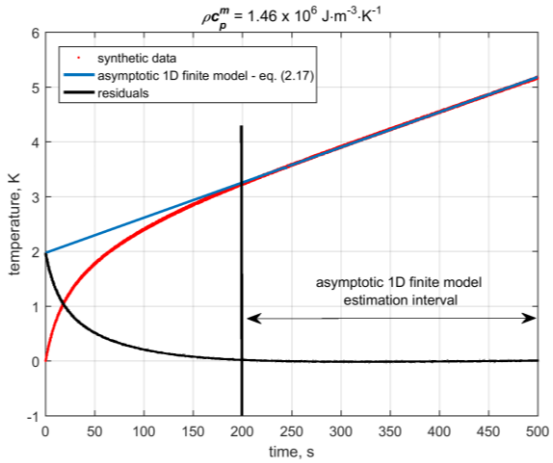

Figure 19. Synthetic and theoretical temperature curves versus time for the estimation of the sample heat capacity ρc_p^m using the asymptotic 1D finite model (2.17).

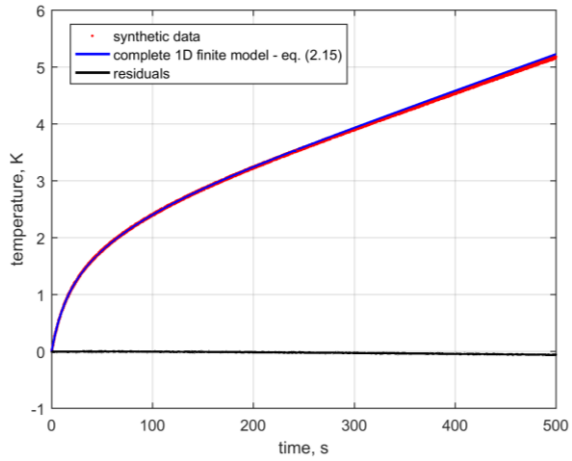

Figure 20. Synthetic and theoretical temperature curves with all the estimated parameters versus time.

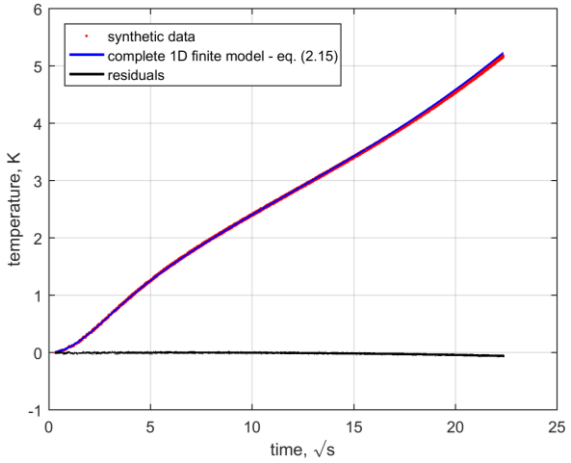

Figure 21. Synthetic and theoretical temperature curves with all the estimated parameters versus time square root.

4.2. Tests with experimental data

Contrary to the previous section 4.1, estimation from experimental data requiers a reference material dedicated to the calibration. The latter allows to determine both a corrected cross section *S* and the heating capacity of heating element. Indeed the flux depends on a surface which may be different from the measured one initially (see section 1). The second parameter is supposed to be constant whatever the tested material.

4.2.1. Heating element calibration

Two thermal properties of the materials presented in Table 1 have been beforehand measured: the thermal conductivity *k* through the guarded hot plate (between 18 °C and

28 °C) and the thermal capacity c_p^m with by calorimetry (between 20 °C and 30 °C). Table 2 gathers all results. The calibration has been performed with the polycarbonate samples.

Table 2. Thermal properties of the tested materials obtained from guarded hot plate technique.

material	thermal conductivity ($W{\cdot}m^{-1}{\cdot}K^{-1}$)	thermal capacity ($J{\cdot}kg^{-1}{\cdot}K^{-1}$)	Effusivity ($J{\cdot}m^{-2}{\cdot}K^{-1}{\cdot}s^{-1/2}$)
polycarbonate	0.196	1 233	534
cellular concrete	0.164	915	304
rubber	0.380	1 258	824
cork	0.047	1 604	139

Figure 22 presents the evolution of the temperature (red dots) versus time square root with the polycarbonate sample. During experiment, the flux is calculated knowing that:

$$\phi_0 = \frac{RI^2}{2S} \tag{4.1}$$

In equation (4.1), S is the cross section, whose value could differ from the simple product of the length per the width of the heating element. It is possible to correct it with the estimation of ϕ_0 using equation (2.23) representing the temperature asymptotic behavior, the slope being proportionnal to S^{-1}. Figure 22 shows the results between the initial and the corrected cross section, since the flux $RI^2/2$ (see Figure 3) and the polycarbonate effusivity are known.

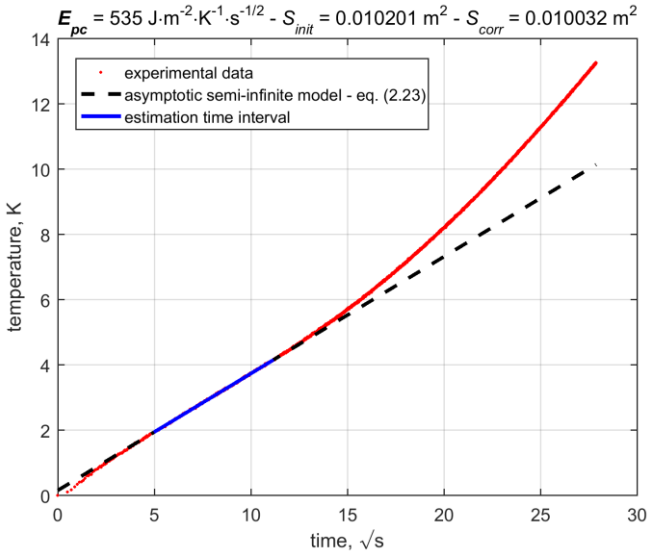

Figure 22. Estimation of the corrected cross section during the calibration with polycarbonate.

The second part of the calibration concerns the heating element heat capacity estimation. This time, the complete semi-infinite model (2.21) is used between 0 and 600 s. Figure 25 and 26 are two cases where the estimation is correct or not, that is to say during and after the asymptotic semi-infinite time interval validity, respectively, approximately fixed at 140 s. During the valid time interval, the mean and the standard deviation of the heat capacity of the heating element is (343 ± 26) $J{\cdot}m^{-2}{\cdot}K^{-1}$, this average value corresponds approximately to the moment when the residuals are the weakest. This value is retained for the next experiments.

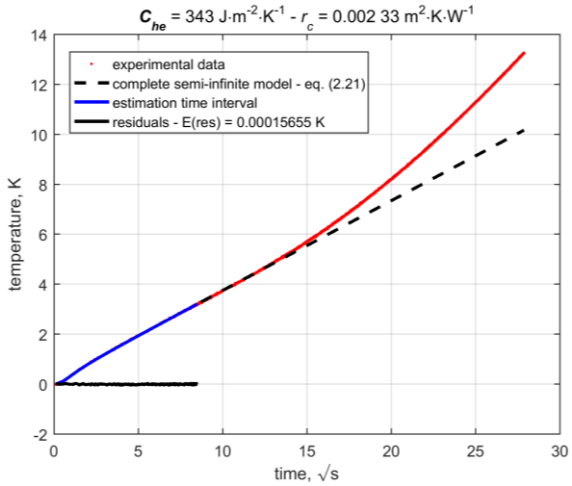

Figure 23. Heating element heat capacity estimation at 60 s.

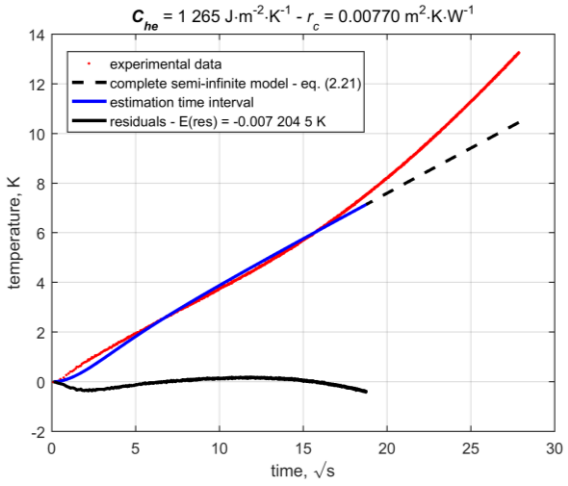

Figure 24. Heating element heat capacity estimation at 350 s.

4.2.2. Estimation with other materials

Such estimations are presented in Tables 1 and 2, where the four same materials have been tested. Table 3 gathers the estimation results concerning the effusivity and the heat capacity. The thermal conductivity and diffusivity are then calculated and compared with the values obtained through the guarded hot plate technique (Table 2).

Table 3. Thermal properties estimation and calculation results.

material	polycarbonate	cellular concrete	rubber	cork
E (J·m^{-2}·K^{-1}·s$^{-1/2}$)	544	316	839	177
r_c, (10^{-3} m^2·K·W^{-1})	2.64	4.13	0.10	10
ρc_p^m (10^5 J·m^{-3}·K^{-1})	15.35	6.62	21.58	7.52
k (W·m^{-1}·K^{-1})	0.191	0.158	0.326	0.042
α (mm^2·s^{-1})	0.124	0.250	0.151	0.056

Figures 25 to 29 present results for the tests with the polycarbonate. Figure 25 shows the first estimation of the effusivity using equation (2.23). This estimation works rather well for every material. The selection of the estimation interval depends on the thickness of the sample and of the acquisition frequency, but even with the cork sample of 4 mm, estimation results are satisfying. The difficulty increases with the estimation of both C_{he} and r_c even if the former is already known. It happens that it does not work every time during tests with rubber and polycarbonate samples.

Figure 26 shows the evolution versus time of the correlation coefficients (3.7). It shows a persistent important correlation between the heating element and the contact resistance but satisfying decreasing correlations versus time between the effusivity and both the heating element and the contact resistance. This observation makes difficult the estimation and shows the importance of the previous calibration.

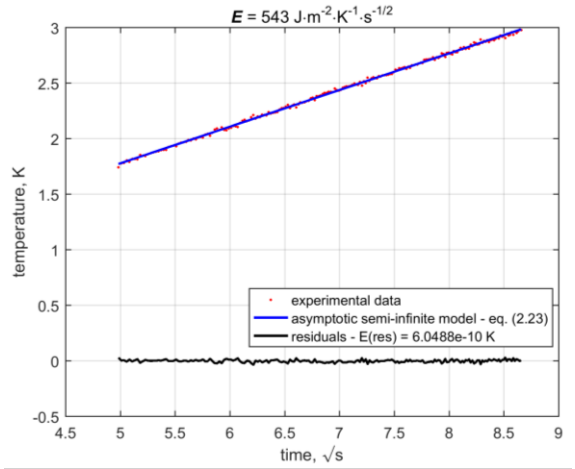

Figure 25. First estimation of the effusivity.

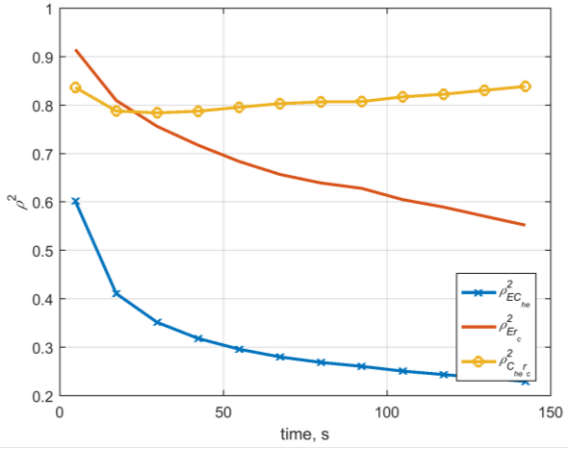

Figure 26. Correlation coefficients of the parameters versus time.

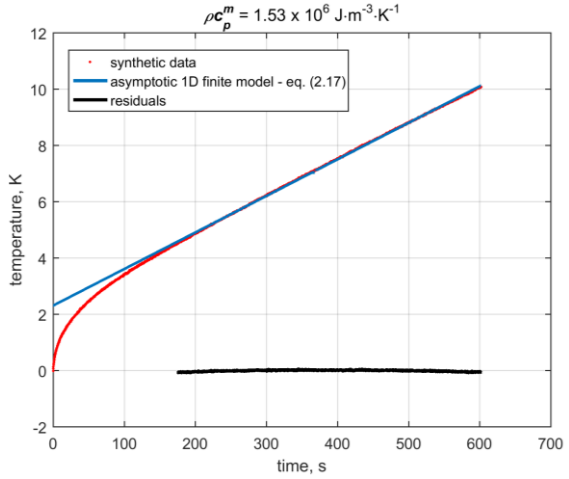

Figure 27. Estimation of the material heat capacity.

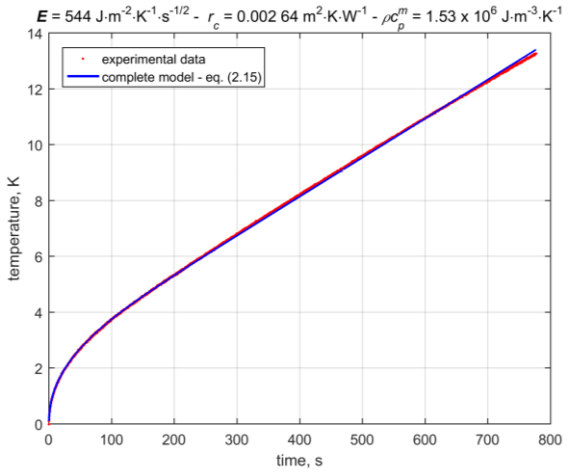

Figure 28. Evolution of the finite 1D model with the estimated parameters and comparison with the experimental data.

Since C_{he} is known, it is now possible to estimate the material heat capacity using equation (2.17). Figure 27 shows an example of its estimation for long times. Finally, once all parameters are estimated, they are used in equation (2.15) for a global comparison with the experimental data (Figure 28).

Conclusion

This tutorial deals with the estimation of thermal properties of low conductivity materials through the hot-plate technique. Once the experimental apparatus and the materials presented during the first part, the theoretical models and the estimation procedure are developped : three finite, semi-infinite, asymptotic models are used to calibrate the heating element and then to estimate the thermal effusivity and the heat capacitiy of the tested material. The chosen

calibration material is the polycarbonate, and the other materials are cellular concrete, rubber, and cork.

A part dedicated to the sensitivity study was presented in order to discuss possible correlations between parameters and thus the possibility to estimate one or more with only one experiment. Anyhow, the calibration of the heating element heat capacity is performed. Tests with different materials have mainly pointed out the importance of the choice of the estimation interval, either for the effusivity or for the heat capacity estimation. Indeed, it is not always easy to determine the beginning or the end of an asymptotic model. However, the residuals signature and the correlation coefficients between the estimated parameter yield supplementary information.

It is important to know that the proposed methodology has limitations. Indeed, for instance, the experimental flux must stay constant and has to be controled during the whole experiment. If it is not constant, its variation should be taken into account. One other point concerns porous materials, such as the cellular concrete or the cork. If their relative humidity is too large, purely conductive heat transfer are not unique anymore and the initial theoretical model is inapropriate. Degiovanni and Jannot discuss this point in [1].

The estimation procedure presented in this tutorial is only perfomed by ordinary least-squares coupled with a Levenberg-Marquadt optimization algorithm. This minimization procedure is deterministic, which means that the uncertainty of the estimated parameter is not calculated but it must be evaluated from other observations, such as the residuals, the covariance matrix. Other heuristic methods exist, such as the Bayesian inference which gives estimation results with an average and a standard deviation. But in any way, the systematic error must evaluated too.

Appendix 1: The Numerical inversion methods of the Laplace transform

The theoretical models (2.15) and (2.21) are transient and expressed in the Laplace domain where the Laplace variable s substitutes the time variable t. To get back to the time domain t, several possibilities exist, such as tables [9] or with the help of numerical algorithms. Three of those are presented in this section, the algorithms of De Hoog [11], Fourier [6], and Stehfest [12,13], and their efficiency depend on the type of the heat excitation. Experimentally, an electrical supply delivers at a given time $t = t_0$ a constant current I in the heating element dissipated by Joule effect. This power $\phi(t)$ can be expressed according to three different ways:

- A Heaviside function:

$t < t_0$ $$\phi(t) = 0 \quad \text{(A1.1)}$$

$t \geq t_0$ $$\phi(t) = \phi_i \quad \text{(A1.2)}$$

- An exponential function:

$t < t_0$ $$\phi(t) = 0 \quad \text{(A1.3)}$$

$t \geq t_0$ $$\phi(t) = \phi_i \left(1 - e^{-\frac{t-t_0}{\tau}}\right) \quad \text{(A1.4)}$$

- A sigmoidal function:

$$\forall t \qquad \phi(t) = \phi_i \frac{1}{1 + e^{-\lambda(t-t_0)}} \tag{A1.5}$$

Experimentally, the power delivery is not strictly abrupt and discontinuous at time t_0 but presents a continuity, and the presence of transitional points between 0 and ϕ_i testifies this consideration. Consequently, the Heaviside function can be sufficient but is a simplified view. The exponential function remains discontinuous at time t_0. The sigmoidal function presents the advantage to be continuous versus time compared with the Heaviside and the exponential ones. In the relations (A1.4) and (A1.5), the coefficients τ and λ must be estimated by ordinary least squares method with experimental data. According to equation (2.5), the thermal stimulation expressions transformed in the Laplace domain are given by (A1.6), (A1.7), and (A1.8) [14] where $\Psi(s)$ are the digamma functions [9].

$$\Phi(0,s) = \phi_i \frac{e^{-st_0}}{s} \tag{A1.6}$$

$$\Phi(0,s) = \phi_i \left[\frac{e^{-st_0}}{s} - \frac{e^{-\left(\frac{1}{\tau}+s\right)t_0}}{\frac{1}{\tau}+s} \right] \tag{A1.7}$$

$$\Phi(0,s) = \frac{\Psi\left(\frac{\lambda+s}{2\lambda}\right) - \Psi\left(\frac{s}{2\lambda}\right)}{2\lambda} \tag{A1.8}$$

The inversion equation for the *Fourier algorithm* is proposed with relations (A1.9) and (A1.10). The readers should consult [6] for more information.

$$f(t) = \frac{exp(ct)}{t_{max}} \left\{ F(c)/2 + \sum_{n=1}^{\infty} \left(Re[F(c+j\omega_n)]\, cos(\omega_n t) + Im[F(c+j\omega_n)]\, sin(\omega_n t) \right) \right\} \tag{A1.9}$$

$$\omega_n = \frac{n\pi}{t_{max}} \tag{A1.10}$$

An infinite series discretizes the equation (A1.9). Naturally, an infinite number of terms is not possible and a choice of a finite number must be done with care. This choice is conditioned also by the terms c and t_{max}. The accuracy of the inversion depends on this triplet. Anyhow, one must verify that the condition (A1.11) is respected.

$$exp(-2ct_{max})\, f(2t_{max}) \cong 0 \tag{A1.11}$$

De *Hoog algorithm* [11], which is not presented here but given during the tutorial, is based on accelerating the convergence of the Fourier series obtained from the inversion integral using the trapezoidal rule. In a worry of both inversion quality and of time consumption where a

compromise can have its importance, the user has the possibility to modify the terms number of the series.

The inversion with *Stehfest algorithm* is given by the relation:

$$f(t) \cong \frac{ln(2)}{t} \sum_{n=1}^{N} V_n F\left[\frac{n\, ln(2)}{t}\right] \qquad \text{(A1.12)}$$

where:

V_1 = 1/12
V_2 = -385/12
V_3 = 1 279
V_4 = -46 871/3
V_5 = 505 465/6
V_6 = -473 915/2
V_7 = 1 127 735/3
V_8 = -1 020 215/3
V_9 = 328 125/2
V_{10} = -65 625/2

Figures A1 to A3 could present examples of inversion results for the three stimulation types and for the three algorithms if t_0 is not 0 like it is commonly done during hot-plate measurement. The initial time is t_0 = 10 s, the response time in relation (A1.4) is τ = 0.1 s and the coefficient λ = 10 in relation (A1.5). Figure A1 concerns the crenel function, which shows that the best results are for De Hoog algorithm. Fourier presents small oscillations around t_0 but fits correctly for a value of c = 0.05. Finally, Stehfest fits rather well away from t_0 but presents instability around; nevertheless, if t_0 = 0, Stehfest works well at t = 0. Figures 4 and 5 present similar results as for Figure A3.

The average residuals <*res*> have been calculated between the results obtained with the relation (A1.13) where the first term is the function in the *t* time domain and the second term is the inversion from the Laplace domain. In every case, the average residuals are all estimated less than ± 10^{-3}.

$$< res >= \frac{1}{N} \sum_{i=1}^{N} \{\phi(t_i) - L^{-1}[\Phi(s_i)]\} \qquad \text{(A1.13)}$$

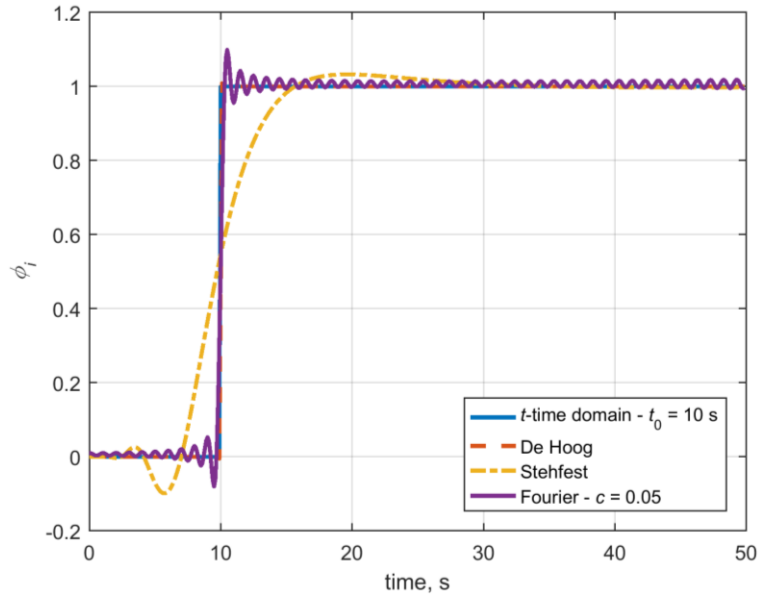

Figure A1. Example of comparison between the different inversion programs from the Laplace to the time domain for a heat excitation initial time t_0 = 10 s in the case of a Heaviside increase.

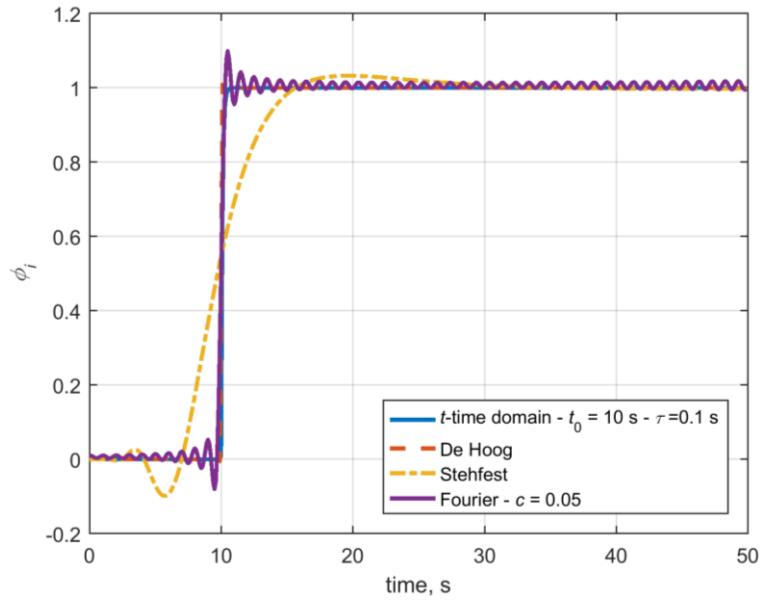

Figure A2. Example of comparison between the different inversion programs from the Laplace to the time domain for a heat excitation initial time t_0 = 10 s in the case of an exponential increase.

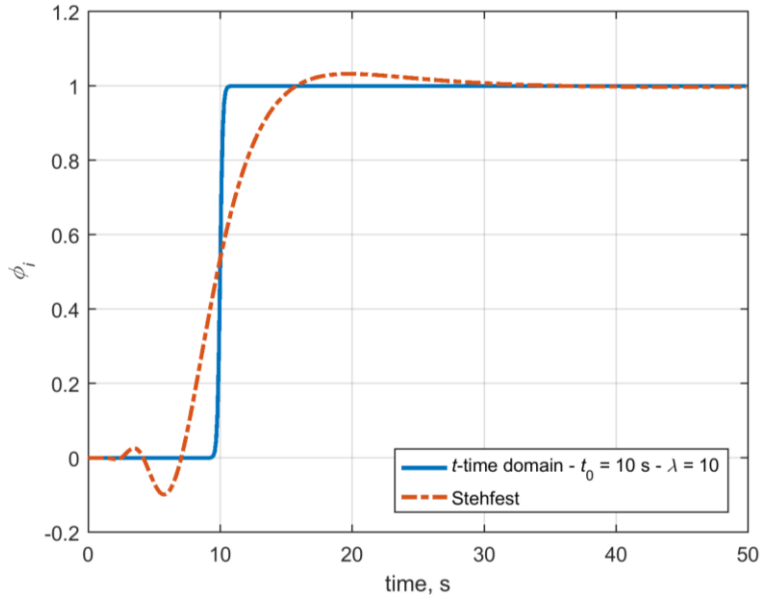

Figure A3. Comparison between the Stehfest inversion program from the Laplace to the time domains for a heat excitation initial time t_0 = 10 s in the case of a sigmoidal signal.

Figures A1-A3 show that it is necessary to verify the good accuracy of the inversion algorithm, since some are more relevant than others. Obviously, in the case of the hot-plate experiments, the Heaviside function is enough to simulate the heat stress and so is the De Hoog algorithm for the inversion, and both are now used for the rest of this tutorial. Indeed, for instance, the residuals study presents results where the average is around zero. Of course, in the case of other characterization techniques, this choice must be again examined.

Appendix 2: finite 1D model asymptotic behavior

Consider again equation (2.15) in section 2.2:

$$\theta(0,s) = \frac{1 + tanh(qe)\, kq}{C_{he}s + tanh(qe)\,(r_c C_{he}s + 1)kq}\Phi(0,s) \tag{A2.1}$$

When $t \to \infty$, $s \to 0$, it comes that:

$$\theta(0,s) = \frac{1 + kq^2 e}{C_{he}s + kq^2 e C_{he} r_c s + kq^2 e}\Phi(0,s) \tag{A2.2}$$

As $kq^2 = \rho c_p^m s$, it comes that:

$$\theta(0,s) = \frac{1 + \rho c_p^m e s}{\rho c_p^m e C_{he} r_c s^2 + \left(C_{he} + \rho c_p^m e\right)s}\Phi(0,s) \tag{A2.3}$$

As s^2 << s, one gets, for a step excitation $\mathrm{F}(0,s) = \mathrm{F}_0 / s$:

$$\theta(0,s)=\frac{\Phi_0}{\left(C_{he}+\rho c_p^m e\right)s^2}+\frac{\rho c_p^m e\Phi_0}{\left(C_{he}+\rho c_p^m e\right)s} \tag{A2.4}$$

Once expressed in the time domain, relation (A2.4) becomes:

$$T(0,t)=\frac{\phi_0}{\left(C_{he}+\rho c_p^m e\right)}t+\frac{\rho c_p^m e\phi_0}{\left(C_{he}+\rho c_p^m e\right)s}+T_{ext} \tag{A2.5}$$

which is the expression of "semi-permanent regime" as proposed by [14], that is to say until the 2D/3D effects appear. Indeed, the slope in relation (A2.5) can be easily obtained considering the lumped body assumption:

$$\phi_0=\left(\rho c_p^m e+C_{he}\right)\frac{dT}{dt} \tag{A2.6}$$

Appendix 3: semi-infinite 1D model asymptotic behavior

Consider equation (2.21) in section 2.3:

$$\theta(0,s)=\frac{\Phi_0}{s}\frac{1+r_cE\sqrt{s}}{C_{he}s+(1+r_cC_{he}s)E\sqrt{s}} \tag{A3.1}$$

Let express the limit development of equation (A3.1) for $t\to\infty$ and $s\to 0$ [1] in the case of a power step excitation with $\Phi(0,\ s)=\Phi_0/s$:

$$\underset{s\to0}{\theta(0,s)}\approx\frac{\Phi_0}{Es^{3/2}}\frac{1+r_cE\sqrt{s}}{1+\frac{C_{he}}{E}\sqrt{s}} \tag{A3.2}$$

$$\underset{s\to0}{\theta(0,s)}\approx\frac{\Phi_0}{Es^{3/2}}\left(1+r_cE\sqrt{s}\right)\left(1-\frac{C_{he}}{E}\sqrt{s}\right) \tag{A3.3}$$

$$\underset{s\to0}{\theta(0,s)}\approx\frac{\Phi_0}{Es^{3/2}}\left[1+\left(r_cE-\frac{C_{he}}{E}\sqrt{s}\right)\right] \tag{A3.4}$$

$$\underset{s\to0}{\theta(0,s)}\approx\frac{\Phi_0}{Es^{3/2}}+\frac{\Phi_0}{s}\left(r_c-\frac{C_{he}}{E^2}\right) \tag{A3.5}$$

Once expressed in the time domain, relation (A3.5) becomes:

$$T(0,t)\underset{t\to\infty}{\approx}\frac{\Phi_0}{E\sqrt{\pi}}\sqrt{t}+\Phi_0\left(r_c-\frac{C_{he}}{E^2}\right) \tag{A3.6}$$

The evolution of the temperature is thus function of the time square root. The heating element inertia and the contact resistance do not influence the temperature when the time tends to infinity. The slope of relation (A3.6) is inversely proportional to the material effusivity.

References

[1] Y. Jannot, A. Degiovanni, *Thermal Properies Measurement of Materials*, ISTE Editions Ltd., London, 2018.
[2] A. Degiovanni, *Conductivité et diffusivité thermique des solides*, Techniques de l'ingénieur, R 2 850, 1994.
[3] T. Pierre, C. Jimenez-Saelices, B. Seantier, Y. Grohens, *Transient pulsed technique to characterize the radiative and conductive properties of bio aerogels*, International Journal of Thermal Science, 116, p. 63-72, 2017.
[4] T. Pierre, T. Colinart, P. Glouannec, *Measurement of thermal properties of biosourced building materials,* Int J Thermophys (2014) 35:1832–1852.
[5] X. X. Zhang, A. Degiovanni, *Mesure de l'effusivité thermique de matériaux solides et homogènes par une méthode de "sonde" plane*, J. Phys. III France 3 (1993), 1243-1265.
[6] D. Maillet, S. André, J.-C. Batsale, A. Degiovanni, C. Moyne, *Thermal quadrupoles, Solving the heat equation through integral transforms*, John Wiley & Sons, Ltd., New-York, 2000.
[7] N. Ozisik, *Heat conduction*, 2nd ed., John Wiley & Sons, Ltd., New-York, 1993.
[8] Y. Jannot, V. Félix, A. Degiovanni, A centered hot plate method for measurement of thermal properties of thin insulating materials, Meas. Sci. Technol. 21 (2010) 035106 (8 pp).
[9] M. Abramowitz, I. A. Stegun, *Handbook of mathematical functions*, 9th edn Dover, New-York, 1970.
[10] F. Rigollet, O. Fudym, D. Maillet, *Lecture 3: Basics for linear estimation, the white boxe case*, Metti 6 Advanced School: Thermal Measurements and Inverse Techniques, volume 1, Biarritz, March 1-6, 2014.
[11] F. R. De Hoog, J. H. Knight, A. N. Stockes, *An improved method for numerical inversion of the Laplace transform*, SIAM J. Sci. Stat. Comput., Vol. 3, No. 3, 1982.
[12] H. Stehfest, *Algorithm 368, Numerical inversion and Laplace transforms*, Commun. ACM, 13, 47-49, 1970.
[13] H. Stehfest, *Remarks on algorithm 368, Numerical inversion and Laplace transforms*, Commun. ACM, 13, 624, 1970.
[14] J. Park, R. VanZee, W. Lal, D. Welter, J. Obeysekera, *Sigmoidal activation of proportional integral control applied to water management*, Journal of water resources, ASCE, 131(4), p. 292-298, 2005.
[15] H. Bal, Y. Jannot, N. Quenette, A. Chenu, S. Gaye, *Water content dependence of the porosity, density and thermal capacity of laterite based bricks with millet additive*, Construction and Building Materials 31 (2012) 144-150.

Tutorial 3: Temperature and heat flux measurements

F Lanzetta[1], B Garnier[2]

[1] FEMTO-ST, Energy Department, Univ. of Franche-Comté, CNRS, Belfort, France
E-mail: francois.lanzetta@univ-fcomte.fr

[2] Laboratoire de Thermique et Energie de Nantes, UMR CNRS 6607, Univ. Nantes, France
E-mail: bertrand.garnier@univ-nantes.fr

Abstract. This tutorial is about temperature and heat flux measurement with thermocouples and can be seen as complementary information to lecture L2. Time constants and errors due to heat leakage through the connection wire of the thermocouples will be illustrated with experiments. Some rules will be explained to implement thermocouples in metallic samples in order to realize accurate and sensitive 1D heat flux sensors. Thin film heat flux sensors will also be discussed.

1. Introduction

One will expect a temperature sensor to be 1) sensitive to temperature, 2) accurate, and 3) with low inertia. The sensitivity is provided by the thermometric phenomena (see lecture L2 for sensitivity values). The accuracy comes on the one hand from the calibration and measurement of the thermometric phenomena and on the other hand, from the correct implementation of the sensors. The first is rather well known, the latter being often ignored. The inertia of a thermocouple is usually characterized by its time constant which depends also on the medium in which it is mounted.

In this tutorial, experiments will be performed in order to illustrate sensor time constants, errors due to incorrect implementation of thermocouples. Then the design of accurate 1D heat flux sensors will be presented.

2. Time constants of various thermocouples

The behavior of a sensor is characterized by its response to a disturbance in its surroundings. The response time of a temperature sensor depends on the physical properties (density, specific heat, thermal conductivity), the transport properties of the fluid (turbulence, pressure, velocity, and physical properties), and the thermal exchanges (radiation, convection, conduction) between the sensor and the surroundings [1-3]. A considerable amount of work has been carried out on the transient behavior of thermocouples and hot/cold wires (standard size, small and micro sizes) in flowing gases and liquids [4, 5].

Different dynamic characterization methods have been used to estimate response times:

- Standard immersion-plunge tests in liquids or gases [6],
- Current injection with sinusoidal, square-wave, 3w methods [3],
- Optical and chopped laser beam methods [7-10],
- Pulsed wire methods [11],
- Rocket plume method [12],
- Convection method with fluid flows [10],

The thermometric device must show characteristics in order that interaction between sensor and medium reaches the equilibrium temperature in a sufficiently small time so that the temperature variations of the medium, during this same time, are negligible.

The thermal inertia is usually quantified by a characteristic time t_x which can be the time constant τ or time response t_r.

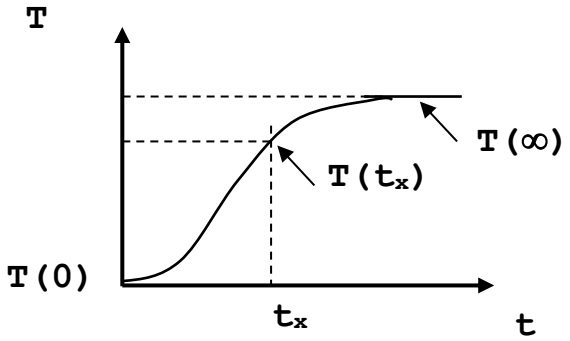

Figure 1: Typical temperature sensor response

Most of these works neglected the effects of conduction along the wires and radiation between the sensor external surface and the surroundings. Investigations have been devoted to the determination of the classical wire time constant τ considering convection heat transfer only:

$$\tau = \frac{\rho_w c_w d^2}{4 \lambda_g Nu} \quad (1)$$

Where d is the diameter of the sensor, ρ_w and c_w are the density and the specific heat of the sensor material, λ is the thermal conductivity of the fluid and Nu the Nusselt number.

If $T(0)$ is the initial temperature and $T(\infty)$ the equilibrium temperature, the time response t_x is defined such that :

$$\frac{T(\infty) - T(t_x)}{T(\infty) - T(0)} = x \quad (2)$$

- The time constant τ, is defined with $x = 1/e \approx 0{,}368$ $(e = 2{,}718...)$
- The $k.10^{-n}$ time response, t_r, is defined with $x = k.10^{-n}$.

The quantities τ or t_r depend not only on the sensor but also on how it is mounted in or on the medium and how it is connected to the measurement device. So talking about the time response of a sensor does not make sense if we don't consider the medium in or on it is mounted.

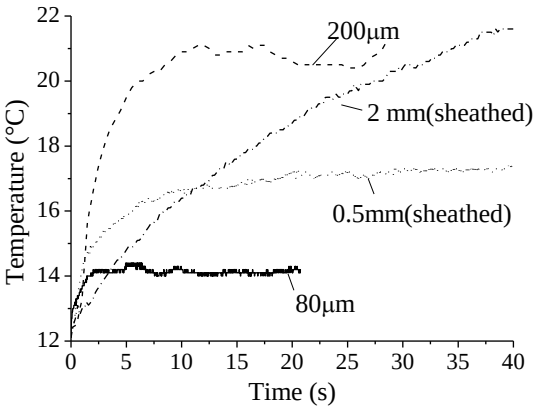

Figure 2: Temperature recording in quiet air

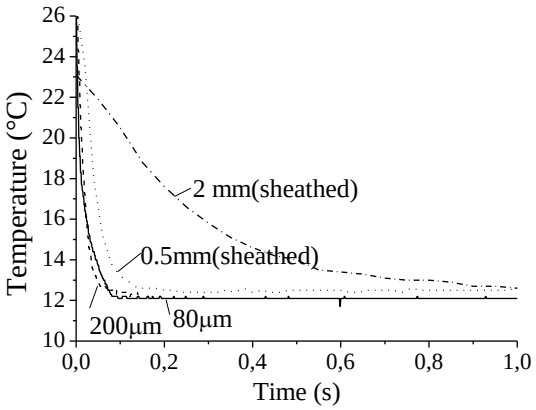

Figure 3: Temperature recording in stirred water (12°C)

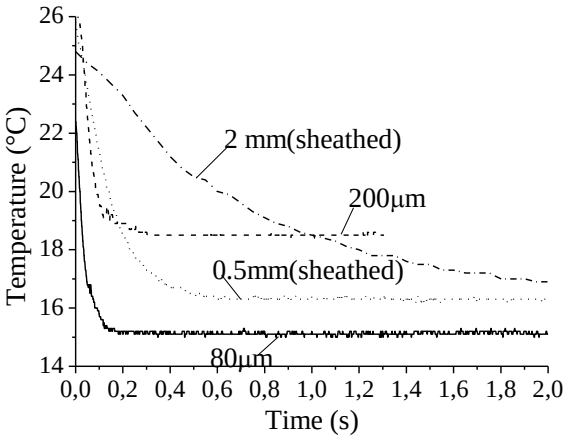

Figure 4 : Temperature recording in mercury (12°C)

In this tutorial, we investigate the time constants of thermocouples since this type of sensor is very common due to their easy implementation, fast response, and low cost. Four type K thermocouples are considered with two diameters (80 and 200 µm) and with or without stainless steel sheath. They were plunged successively into three different mediums. Stirred water was provided by a built-in circulating pump of a temperature-controlled water bath (at 12°C). A $5cm^3$ mercury beaker was maintained also at 12°C. The quiet air was the room air (at about 20°C). Figures 2 to 4 show the measured transient temperatures for the 4 thermocouples plunged in the three different mediums. The transient measurements are performed using a low-voltage recorder (Yokogawa, 16 channels, 100 kHz).

Table 1: Time constants (ms) of common type K thermocouples with various diameters, with and without sheath, and mounted in various mediums.

Thermocouple→ Medium↓	No sheathed		Sheathed*	
	Φ = 0,08 mm	Φ = 0,2mm	Φ = 0,5 mm	Φ = 2,0 mm
quiet air	595	2330	30980	42720
mercury**	45.2	38.3	129.3	1208.5
stirred water	16.4	14.0	28.5	698.1

* : stainless steel sheathed thermocouple with junction welded at the extremity of the sheath
**: mercury k=8.3 $W.m^{-1}.K^{-1}$; c_p= 140 $J.kg^{-1}.K^{-1}$, ρ=13600$kg.m^{-3}$ (a= 4,36 $10^{-6}m^2.s^{-1}$); water (a= 1,68 $10^{-7}m^2.s^{-1}$)

The measurements clearly show the influence of the medium on the time constant of thermocouples. The time constants range from a few ms to several seconds. In addition, one can observe several features:

- As obtained with lumped capacitance model ($\tau=\rho c_p L/h$), the time constant decreases for increasing heat transfer coefficient. This can be observed when switching from quiet air to mercury and then to stirred water.
- The higher the diameter of the sensors, the higher the time constants are

Table 2 shows some additional values of the time constant measured with various temperature sensors [13].

Table 2: Time constants from literature for various temperature sensors [13]

Sensor	Medium	Time constant (s)
mercury-in-glass thermometer ϕ=9mm	quiet air	450
mercury-in-glass thermometer ϕ=9mm	quiet water	4,8
metallic thermoresistances in a ceramic sheath ϕ=2mm	stirred water	0,5
sheathed thermocouples (ϕ =0.5mm) - thermocouple junction inside the insulation-	hot water	0,035
sheathed thermocouples (ϕ =0.5mm) – thermocouple junction welded on the sheath	hot water	0,015
Metallic thin film (a few μm thick) deposited on a substrate (thermocouple or thermoresistance)	-	a few tens of μs

3. Discussion about the time constant

Dahl and Fiock [14] and Alford and Heising [15] have discussed the problem of lead conduction from a spherical bead along the wires for a thermocouple cooled in a static gas from a temperature T_1 to a temperature T_2. The time constant τ includes the effect of convection and conduction:

$$\tau = \left(\frac{3\, h_{cv}}{\rho_w\, c_w\, d} + K_{cd} \right)^{-1} \qquad (3)$$

Melvin [9] adopted a similar point of view in the precedent work and developed a simple approximate solution of the heat conduction equations integrating the heat transfer coefficient as the ratio between the thermal conductivity of the gas and the radius of the thermocouple junction. For gases of relatively low thermal conductivity the time constant of the thermocouple was expressed as:

$$\tau = \left(\frac{3\,\lambda_g}{\rho_w\, c_w\, d^2} \right)^{-1} \tag{4}$$

Benedict [16] established an expression of the time constant accounting convection, conduction and radiation:

$$\tau = \tau_C \frac{(1-\psi_w)}{1+\dfrac{4\beta\,\varepsilon_w}{T_g}} \tag{5}$$

Where ψ_w is a conduction correction factor [5, 17], β a radiation error factor [5], ε_w the thermocouple emissivity and T_g the gas temperature.

If the thermal environment includes effects of convection, conduction and radiation, the response of the sensor is not a first-order. Pandey [2] and Dantzig [18] suggested that a simple time constant can be expressed as:

$$\tau = C_1 + C_1\, h_{cv}^{-1} \tag{6}$$

where C_1 and C_2 are correlation constants dependent on the properties of the thermocouple and h_{cv} is the average heat transfer coefficient between the thermocouple external surface and the air flow.

Actually, the fact that different kinds of heat transfers are involved should lead to a global time-constant in which the different phenomena contributions are included [19, 20]. As a consequence, the ability of a thermocouple to follow any modification of its thermal equilibrium is resulting from a multi-ordered time response which more accessible experimental parameter remains the global time constant.

The multi-ordered temperature response of a thermocouple can be represented by the general relation [1]:

$$\frac{T_g - T}{T_g - T_i} = K_1\, exp\left[-\frac{t}{\tau_1} \right] - K_2\, exp\left[-\frac{t}{\tau_2} \right] - \cdots - K_n\, exp\left[-\frac{t}{\tau_n} \right] \tag{7}$$

Where T_i is the initial temperature, T_g is the fluid temperature. The value of the constants K_1, K_2, …, K_n as well as the time constants τ_1, τ_2, …, τ_n, depending on the heat flow pattern within the thermocouple and the surrounding fluid. Kerlin et al. [21] showed that the time constants τ_1 and τ_2 are the most important. Cimermam [6] used the same result for real Pt-resistance temperature-sensor in dynamic measurement relative to natural and petroleum gas processes.

4. Errors due to heat losses through the connection wires of the thermocouples

To avoid temperature bias due heat loss along the thermocouples wires, one usually considers that a thermocouple has to be mounted along an isothermal line started from the junction and on a length equal to 100 times the metallic wire diameter ϕ of the thermocouple. If it is not the case, one may obtained heat loss which will change locally the temperature of thermocouple junction. In lecture L5 section 2.3, a thermal

model was designed to study the effect of various parameters on this systematic error. In this section, an experiment will be used to quantify this temperature measurement error.
A PMMA sample of 76.8 mm diameter and 20mm thickness is instrumented with 7 type K thermocouples of diameter 0,2 mm as shown on fig. 5. Three thermocouples #1, #2 and# 3 are correctly mounted: starting from the junction, the thermocouples are along isothermal lines at least on a length of 20 mm. On the contrary, thermocouple #7 is perpendicular to the isothermal lines and thermocouples #4, #5 and #6 are close to the edge. Two temperature controlled thermal baths are used to prescribe a constant temperature difference (40°C) between each two sample faces

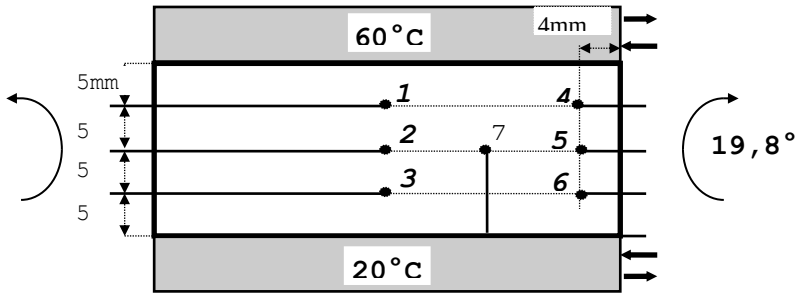

Figure 5: experimental setup with an instrumented PMMA sample

Table 3 : steady state temperature measurements from experimental setup of fig.5

δ*, mm	#	T , °C	#	T , °C	#	T , °C
5	*1*	49,9	*4*	43,5		
10	*2*	**40,5**	*5*	35,4	*7*	**34,8**
15	*3*	31,5	*6*	27,7		

δ: distance between thermocouple and the heated face*

From the measurement obtained with steady state, one can observe that:

- The temperature discrepancy between thermocouple perpendicular (#7) and parallel (#2) to the isothermal lines is very important (5,7°C !), this result from the heat losses through the metallic wire of thermocouple #7 inducing a local temperature decrease at its hot junction. This happens for a 0.2 mm thermocouple, one would have got much more error for metallic sheathed thermocouple where the metallic cross-section of the complete thermocouple is typically 6 times higher than the one of the bare thermocouples (thickness of metallic wall: *10 %ϕ* and metallic wire diameter *18 %ϕ* [22])

- Thermocouples #4, #5 and #6 are closed to the edge (4 mm only) , the connection wires being in the thermal boundary layer therefore they show lower temperature measurement, from 3.3 to 6.4°C less compared to the correct ones (#1, #2 and #3). As illustrated on fig. 6 , thermocouples #4, #5 and #6 show however a linear distribution. So, one should remind that the fact that the temperature distribution is linear is not a criterion to say that temperature measurements are without bias. In fig.6, the temperature shift between the two sets of thermocouples is important, the slopes being slightly different.

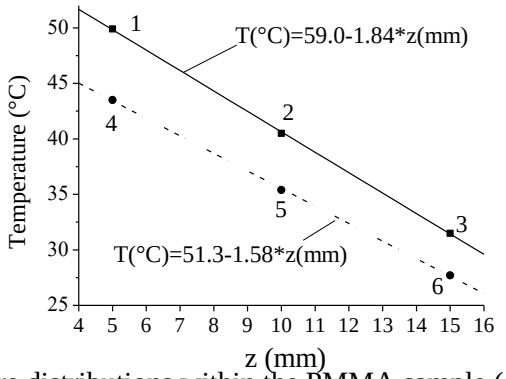

Figure 6: Temperature distributions within the PMMA sample (data from tab.2)

5. Heat flux sensor with wire thermocouples and thin film

Heat flux sensors (HFS) are very useful for the understanding and the control of the thermal phenomena coupled or not with other physical, chemical or mechanical processes. HFS should be judiciously designed to reduce source of bias in heat flux measurement while ensuring the highest sensitivity. The heat flux can be measured by direct methods (see lecture L5). However very often these sensors are mounted directly on the surface to characterize and the sensors create disturbance in the surface/environment heat exchange. There exists one type of HFS which was designed to limit this perturbation [23] especially for 1D transient measurement. As shown on fig.7, a set of microthermocouples is mounted inside the medium at different locations [23]. Practically there are welded on one of the two half shells (fig. 8 [24]).

The discussion in this section will be about the location of the implemented thermocouples. The HFS should have at least 1 thermocouple if the 2nd boundary condition is well known otherwise at least 2 thermocouples are needed. Bourouga [25] has found that the first thermocouple should be located taking into account the following inequality:

$$10\,r \leq x_1 \leq 66\,r \qquad (8)$$

with r the radius of the hole where the thermocouple is mounted.

The first inequality ($10\,r \leq x_1$) comes from the fact that 96% of the temperature drop due to macroconstriction is within an hemisphere of radius $10\,r$ [26]. With this condition, the heat flux ϕ or temperature at the front face will not be affected by the presence of the first thermocouple.

The second inequality ($x_1 \leq 66\,r$) comes from inverse methods consideration. The computation time step Δt (supposed here equal to the experimental one) should not be too small to avoid too much sensitivity to measurement errors. Typically, the condition $a\Delta t/x_1^2 \geq 0.01$ should be respected [26], where a is the thermal diffusivity of the HFS material.
Therefore, one obtains:

$$x_1^2 \leq 100 a \Delta t \qquad (9)$$

The smallest possible Δt value which can be defined as the response time of a thermocouple which is also the characteristic time of the already described $10r$ hemisphere. As shown by Cassagne [27], this

characteristic time is defined by $\Delta t = 44r^2/a$ for a 95% development of the thermal constriction within the $10r$ hemisphere. Using this Δt value in (9), one can obtained: $x_1 \leq 66\ r$
One should notice that for sensitivity enhancement during heat flux estimation, the first thermocouple should be as close as possible to the front face ($x_1 \approx 10\ r$).

For the second location (x_2) corresponding to the 2nd thermocouple or the 2nd boundary condition, its value should be as large as possible also for sensitivity concerns [5].

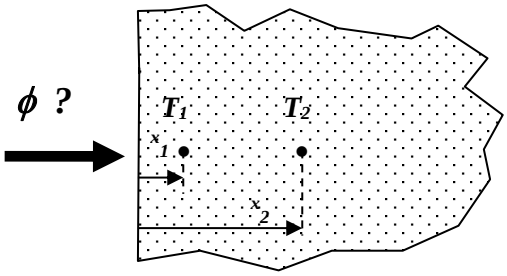

Figure 7: Heat flux sensor [23]

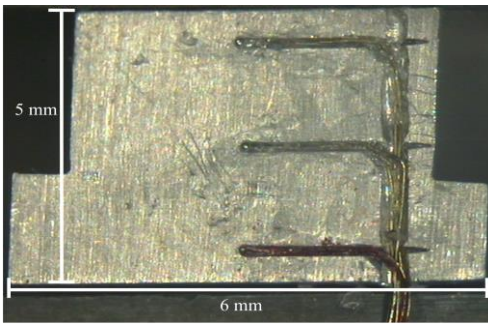

Figure 8: Heat flux sensor [24]

Recent developments in heat flux measurement concern thin film HFS with some advantages such as very accurate locations of the temperature sensors (fig. 9 [28] and fig.10 [29]).

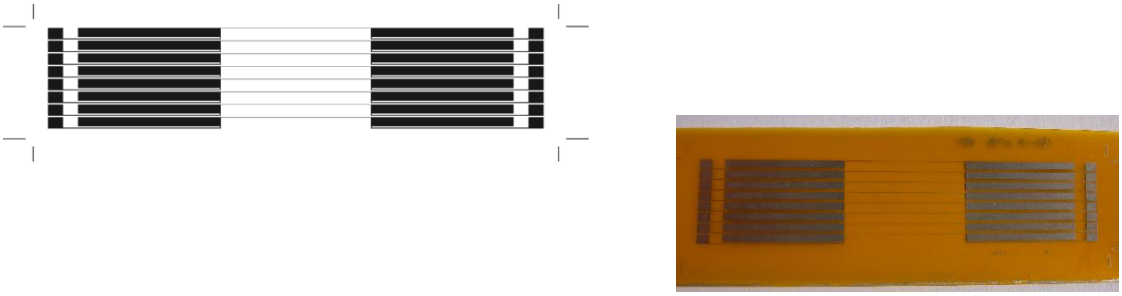

Figure 9: New HFS with thin film technology (wire thickness 30μm) [28]

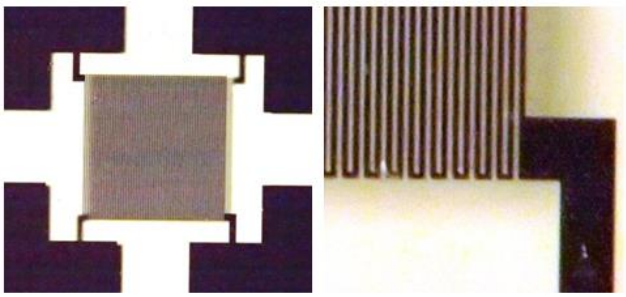

Figure 10: Thin film heat flux sensor (wire thickness 12μm) [29]

5. Conclusion

In this tutorial, we have illustrated the role of the medium in the temperature sensor time constants and also the errors due to the sensor implementation. Temperature and heat flux sensors should be designed and implemented in order to minimize the various sources of systematic errors and also to increase the sensitivity for the estimation of thermal properties, heat transfer coefficient, heat flux ... Some insights on the most favorable thermocouples location were also presented.

References

[1] Manual on the use of thermocouples in temperature measurement, American Society for Testing and Materials, ASTM, Fourth Edition, 1993.
[2] D.K. Pandey *Journal Phys. E:Sci. Instrum.*, 18 (1985) 712–713
[3] J. Lemay, A. Benaissa, R.A. Antonia, *Experim. Thermal and Fluid Science*, 27 (2003) 133-143
[4] N.P. Bailey, *Mech. Engng*., 53 (1931) 797-804.
[5] M.D. Scadron, I. Warshawski, NACA, T.N., 2599 (1952)
[6] F. Cimerman, B. Blagojevic, I. Bajsic, *Sensors and Actuators A*, 96 (2002) 1-13
[7] P. Castellini P., G.L. Rossi, *Rev. Sci. Instrum.*, 67 (7), 1 (1996), 2595-2601.
[8] N.G. Kokodi, V.A. Timanjuk, *LFNM'2001*, 22-24 May, Kharkiv, Ukraine, (2001)
[9] A. Melvin, *Brit. J. Appl. Phys.* (J. Phys. D.), 2 (1969) 1339-1343.
[10] F. Lanzetta, Etude des transferts de chaleur instationnaires au sein d'une machine frigorifique de Stirling, Ph. D. thesis, University of Franche-Comté, France, (1997).
[11] Grignon M., Mathioulakis E., Ngae P., Poloniecki J.G. *Int. J. Heat Mass Transfer* 41 (1998) 3121-3129.
[12] X. Qiang, *Meas. Sci. Technol*., 14 (2003) 1381-1386.
[13] Techniques de l'Ingénieur, traité Mesures et Contrôle R 2 515 1-43
[14] A.I. Dahl, E.F. Fiock, J. Res. Natn. Bur. Stand. 45 (1950) 292-298.
[15] J.S. Alford, C.R. Heising Trans. *Am. Soc. Mech. Engrs*., 75 (1953) 7-14.
[16] R.P. Benedict R.P., *Fundamentals of Temperature, Pressure, and Flow Measurements,* 3d ed. Wiley, New-York, 1984.
[17] K. Farahmand, J.W. Kaufman, *Experimental Heat Transfer*, 14, (2001), 107-118.
[18] J.A. Dantzig, *Rev. Sci. Instrum*., 56 (5) (1985) 723-725.
[19] L. Paranthoen, J.C. Lecordier, *Rev. Gén. Therm.* 35 (1996) 283-308.
[20] H. Sbaibi, Modélisation et étude expérimentale de capteurs thermiques, Ph. D. Thesis, University of Rouen, France, (1987).
[21] T.W. Kerlin, L.F. Miller, H.M. Hashemian, ISA Trans., 17, 4 (1980) 71-88.
[22] Thermocoax, Documentation Products www.thermocoax.com 2011
[23] J.P. Bardon, Y. Jarny, "Procédé et dispositif de mesure en régime transitoire de température et flux surfacique" Patent n° 94.01996, Feb. 22nd1994
[24] A. Sorin; F. Bouloc; B. Bourouga ; P. Anthoine, *Int. J. Thermal Sci.* 47 12 (2008) 1665-1675
[25] B. Bourouga, V. Goizet, J.P. Bardon, *Int. J. Therm. Sci.* 39(2000) 96-109.
[26] J.P. Bardon, M. Raynaud, Y. Scudeller, *Rev. Gen. Therm.* (HS95) 34 (1995) 15-35
[27] B.Cassagne , J.P. Bardon and J.V.Beck 1986 8th *Int. Heat Transfer Conf.*, San Fransisco, Vol.2 pp.483-488.
[28] B. Azerou, B.Garnier, J. Launay, A. Lahmar, Congrès SFT, Perpignan, France, 25-27mai 2011
[29] A. Zribi, F. Lanzetta, M. Barthes, S. Bégot, 3ème Congrès Tunisien de Mécanique, COTUME'2014, 24-26 mars 2014, Sousse, Tunisie.

Tutorial 4: Infrared thermography: materials & buildings

L. Ibos[1], J. Meulemans[2]

[1] CERTES, Université Paris-Est Créteil Val de Marne, IUT de Sénart-Fontainebleau, 240 rue de la Motte, 77550 Moissy-Cramayel, France

[2] Saint-Gobain Research Paris, 39 Quai Lucien Lefranc, 93300 Aubervilliers, France

E-mail: ibos@u-pec.fr
Johann.Meulemans@saint-gobain.com

Abstract. This training session is devoted to the use of infrared thermography for building applications. This session will be divided into two parts. The first part will concern metrological aspects of infrared thermography and more precisely the determination of surface temperature, and its associated uncertainty, using an infrared camera. Uncertainty sources due to the technical characteristics of the camera (measurement noise, non-uniformity, thermal drift) and to the physical properties of opaque surfaces (emissivity, roughness) will be considered. Surfaces of different emissivities will be characterized (spectral emissivity curves will be provided). A particular attention will be paid to the determination of the mean radiant temperature. The work proposed in this first part will be based on theoretical aspects presented in the L4 lecture ("Measurements without contact in heat transfer"). The second part of this training session will be devoted to the study of heat transfers in a building wall using infrared thermography. A reduced scale model of a building wall including thermal irregularities will be used. The work proposed will concern (i) the detection of thermal irregularities such as thermal bridges (or lack of insulation) and (ii) the estimation of multi-layer wall heat losses (including thermal irregularities). Practical work will be done using several infrared cameras equipped with cooled detectors or micro-bolometers arrays.

List of acronyms:

- **EOF:** Empirical Orthogonal Function
- **FOV:** Field Of View
- **FPA** Focal Plane Array
- **IFOV:** Instantaneous Field Of View
- **IR:** InfraRed
- **IWI:** Internal Wall Insulation
- **HFM:** Heat Flow Meters
- **LWIR:** Long Wave InfraRed domain
- **MWIR:** Medium Wave InfraRed domain
- **NDT**: Non-Destructive Testing
- **NETD**: Noise Equivalent Temperature Difference
- **NUC**: Non-Uniformity Correction

- **PC**: Principal Component
- **ROI**: Region Of Interest
- **SNR**: Signal-to-Noise Ratio
- **SVD**: Singular Value Decomposition
- **SWIR:** Short Wave InfraRed domain

Nomenclature:

T	temperature, K
λ	wavelength, µm
ε	emissivity
σ	Stefan-Boltzmann constant, 5.67 x 10^{-8} $W.m^{-2}.K^{-4}$
D, d	distance, m
ϕ	heat flux, W
φ	heat flux density, $W.m^{-2}$
L	intensity, $W.m^{-2}.sr^{-1}$
R	thermal resistance, $m^2.K.W^{-1}$
k	thermal conductivity, $W.m^{-1}.K^{-1}$
a	thermal diffusivity, $m^2.s^{-1}$
C_p	specific heat, $J.kg^{-1}.K^{-1}$
ρ	density, $kg.m^{-3}$
h	heat exchange coefficient, $W.m^{-2}.K^{-1}$
U	wall thermal transmission coefficient, $W.m^{-2}.K^{-1}$
ψ	linear thermal bridge thermal transmission coefficient, $W.m^{-1}.K^{-1}$
χ	punctual thermal bridge thermal transmission coefficient, $W.K^{-1}$

Sub-scripts and upper-scripts

1D	sound region (1D transfers)	*mir*	mirror
app	apparent	*rad*	radiative
env	radiative environment	*ref*	reference
i, e	indoor, outdoor	*S*	surface
mes	measured	*tb*	thermal bridge

Scope

1. Introduction 5
2. Metrological aspects concerning the use of IR cameras for the measurement of surface temperatures 5
2.1 Infrared cameras properties 5
2.1.1 Detectors and Spectral bandwidth 5
2.1.2 NUC 7
2.1.3 NETD 8
2.1.4 FOV and IFOV 9
2.1.5 Technical data of camera used in this tutorial 10
2.2 Emissivity measurements 10
2.2.1 Parameters influencing the emissivity of materials 10
2.2.2 Short review of existing methods for the measurement of emissivity 13
2.3 Mean radiant temperature 15
2.3.1 Principle 15
2.3.2 Practical estimation method 15
2.3.3 Importance of the knowledge of the mean radiant temperature and emissivity 15
3. Infrared thermography for the diagnosis of buildings thermal insulation 17
3.1 Generalities concerning heat transfers inside building walls 17
3.1.1 Thermal resistance and thermal transmittance 17
3.1.2 Thermal bridges 18
3.2 Different ways to investigate heat losses using infrared thermography 19
3.2.1 Passive method 20
3.2.2 Active method 24
4. Tutorial first part : Determination of surface temperature and its associated uncertainty using an IR camera 28
4.1 Description of the test bench 28
4.1.1 Structure and operating conditions 28
4.1.2 Emissivity of materials used in the test-bench of this tutorial 29
4.2 Temperature correction 31
4.2.1 Recall of the method used 31
4.2.2 Determination of the surface emissivities to consider 32
4.2.3 Determination of apparent temperature 32

4.2.4 Determination of mean radiant temperature 33
4.2.5 Performing the temperature correction 33
4.2.6 Uncertainty analysis 34
4.2.7 Analysis of results 35
5. Tutorial Second part : Detection and characterization of thermal bridges inside a building wall 35
5.1 Description of the test bench 36
5.1.1 Structure and operating conditions 36
5.1.2 Thermophysical properties of materials used in the test-bench 37
5.2 Measurement in static regime 37
5.3 Measurement in dynamic regime 39
5.3.1 Using the heating film included in the test-bench 39
5.3.2 Using an external thermal excitation 41
6. Conclusion 41

1. Introduction

Infrared thermography is nowadays extensively used for the inspection of buildings [Balaras 2002, Kylili 2014, Grinzato 1998, Pajani 2012]. This technique allows detecting the presence of thermal irregularities, of moisture, or of air leakage [NF 13187]. Thermal irregularities can come from the local absence or lack of thermal insulation, or from the presence of thermal bridges. The presence of thermal bridges can be due to the structure of the building (for instance to the link between a floor and a façade), or to the presence of the thermal insulation mechanical fixing system, so-called "integrated thermal bridges" [Farkh 2009]. For practical reasons, the work proposed in the second part of this training session will concern only the observation and characterization of integrated thermal bridges. The work will be based on the use of a reduced scale model of a building wall.

The work proposed in this training session will be based on theoretical aspects presented in the L4 lecture ("Measurements without contact in heat transfer"). As seen during this lecture, an infrared camera does not directly measure the surface temperature of an object. The temperature is computed on the basis of the measured intensity on one hand and on the knowledge of influencing parameters: surface emissivity, mean radiant temperature, transmittance and temperature of the surrounding atmosphere. In the first part of this training session, we will discuss about the importance of the surface temperature correction by considering measurements on surfaces of variable emissivity, and by evaluating the associated uncertainty.

Before the extensive presentation of the work proposed in this training session in sections 4 (Tutorial first part : Determination of surface temperature and its associated uncertainty using an IR camera) and 5 (Tutorial Second part : Detection and characterization of thermal bridges inside a building wall), some theoretical supplements and additional information not included in to the L4 lecture are presented in section 2, (for metrological aspects) and in section 3 (for building applications). These information have to be read before starting the training session.

2. Metrological aspects concerning the use of IR cameras for the measurement of surface temperatures

2.1 Infrared cameras properties

The aim of this section is to provide additional information on the technical properties of commonly used IR cameras and most particularly on cameras that will be used in this tutorial. As said before, some aspects already presented in L4 lecture will not be commented anymore in this text.

2.1.1 Detectors and Spectral bandwidth

First of all, we have to recall that historically, infrared cameras can be classified into two families:

- cameras using a unique IR detector coupled to a mechanical scanning system to form an image of the thermal scene (IR scanning cameras);

- cameras using an array of detectors (FPA cameras): in that case, the thermal image is obtained by concatenating the individual responses of each elementary detector in a 2D matrix.

At this time, the most frequently used cameras are the FPA ones. The spectral response of a camera depends mainly on the material used for the detector and on the material used for the optics. Some examples of typical spectral response curves are plotted in Figure 2.1.

Some detectors are sensitive in the wavelength domain comprised between 2 and 5 µm (InSb detectors for instance), so-called Band II domain or MWIR domain. Some other detectors (QWIP or microbolometers for instance) are sensitive in the wavelength domain between 7 and 14 µm (so-called Band III domain or LWIR domain). Microbolometers are thermal detectors, which means that the thermal response of each individual detector is due to the variation of its temperature depending on the absorbed flux. These detectors are not cooled, but an internal system integrated to the camera allows compensating the temperature drift of the detector. QWIP detectors are quantum detectors, *i.e.* based on a conversion of absorbed photons in electrical carriers. These detectors have to be cooled to a low temperature (typically around the liquid nitrogen temperature, 77K) to obtain a high SNR. In most cases, this cooling is ensured using a Stirling engine.

LWIR and MWIR domains correspond to spectral bandwidths of high transparency of the atmosphere as seen in Figure 2.2. According to the Wien's law, LWIR detectors are well adapted to temperature measurements around ambient temperature (300K), whereas MWIR detectors are better suited for higher temperature applications. However, due to the higher sensitivity of MWIR detectors, some of them can be used also for ambient temperature measurements. Other wavelength domains can also be used for higher temperature applications (SWIR or visible domains), as illustrated in Figure 2.3.

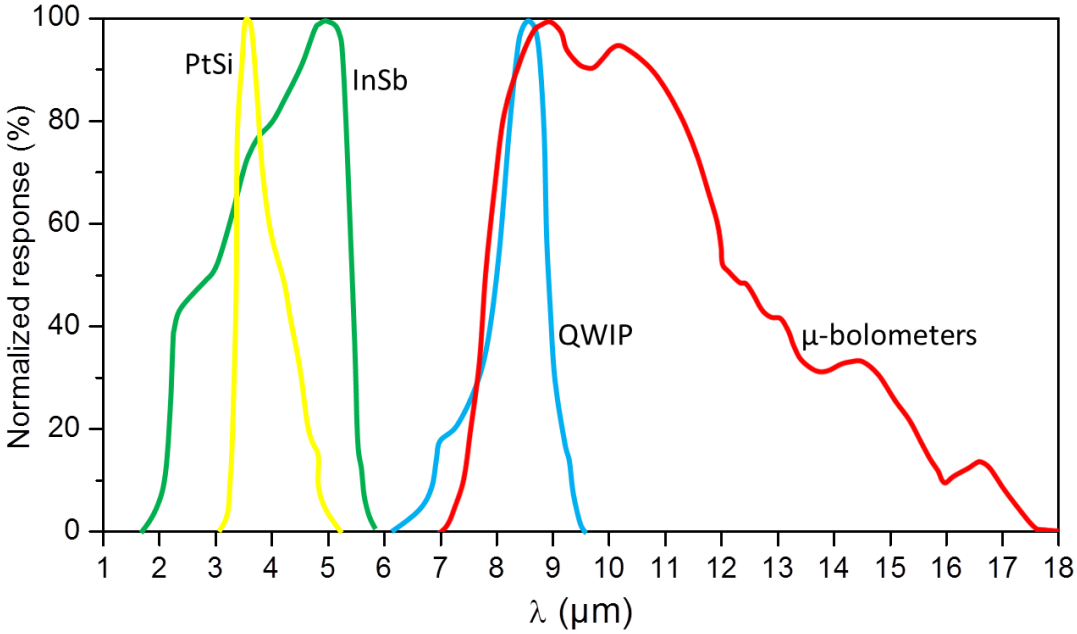

Figure 2.1 *Typical response curves of some IR detectors*

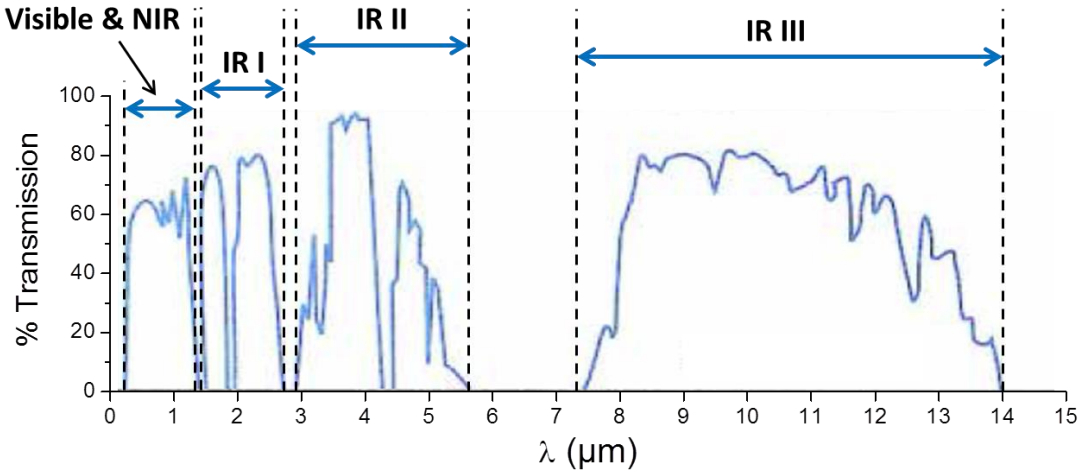

Figure 2.2: *Transmittance of the atmosphere; Adapted from [Cojan 1995]*

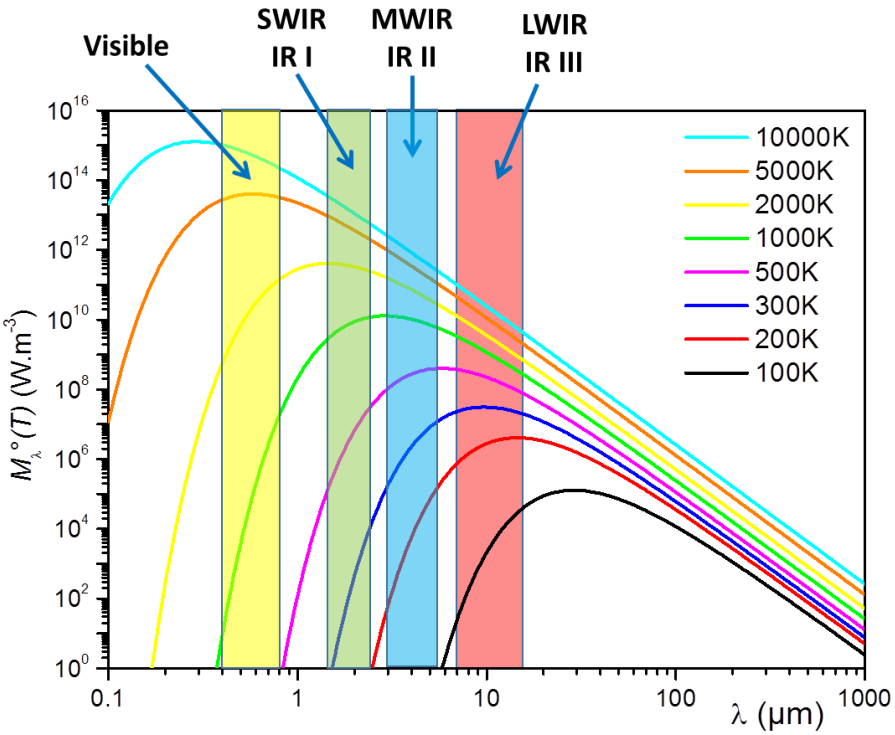

Figure 2.3: *Planck's law and spectral bandwidths of IR cameras*

2.1.2 NUC

The non-unifomity correction (NUC) has to be performed in FPA cameras in order to correct the fact that all individual detectors have not exactly the same response. The effect of NUC is illustrated in Figure 2.4. We compare in this figure two thermal images recorded before and after a NUC. The thermal scene observed is a blackbody plate intended to be at uniform temperature. Images were recorded using an uncooled microbolometer FPA camera. We consider data in the ROI (black rectangle part) drawn on both images. After correction, we

observe a small variation of the mean temperature (21.5°C versus 21.0°C), and a slight decrease of standard deviation on the ROI (0.7°C versus 1.1°C).

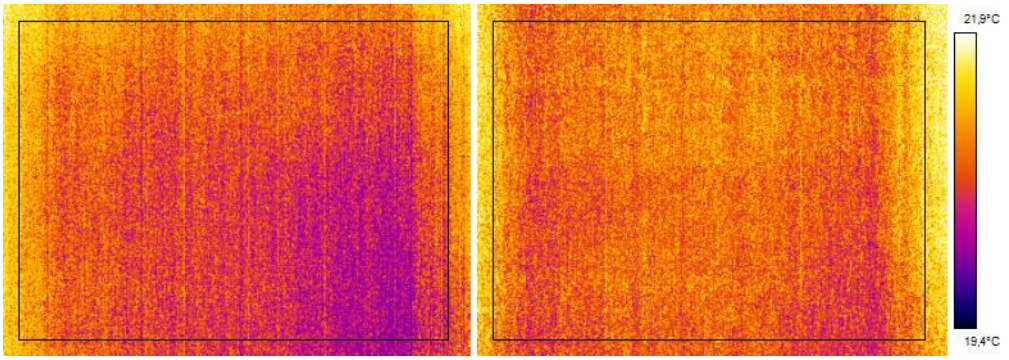

Figure 2.4: *Comparison of two thermal images recorded before (left) and after (right) NUC; uncooled µ-bolometer FPA camera*

2.1.3 NETD

As seen in the previous section, non-uniformity correction allows reducing differences between responses of elementary detectors of a FPA matrix. However, it still exists a measurable difference between individual detectors, although a unique response is expected (for instance when observing an extended plane blackbody for instance). These differences also come from the electronic circuitry and can be assimilated to a random noise. Figure 2.5 presents an example of the response histogram of the pixels of a FPA camera. The standard deviation of this distribution (plotted in digital levels in Figure 2.5), can be converted in a temperature difference, called NETD. Thus, this parameter represents the spatial noise in a thermal image. A temperature difference lower than the NETD cannot thus be detected. NETD values depend on the detector and on the optic used. The lowest NETD values are generally obtained using cameras equipped with cooled IR detectors.

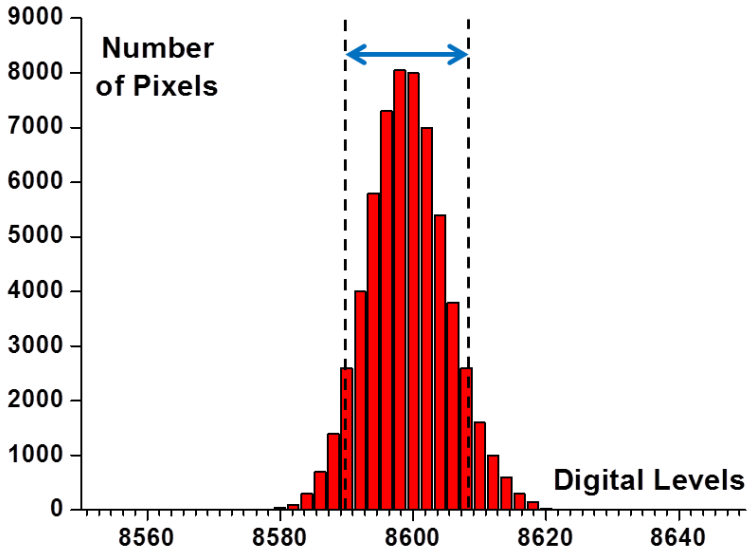

Figure 2.5: *Example of the computation of an IR camera NETD*

2.1.4 FOV and IFOV

The Field Of View (FOV) of an infrared camera represents the Horizontal and Vertical angles, namely HFOV and VFOV respectively, which can be viewed through the IR lens used. The Instantaneous Field Of View (IFOV) represents the view angle corresponding to only one pixel. The IFOV is generally expressed in milliradians (mrad), and allows computing the size *d* (in millimeters) of the smallest element that can be seen in a thermal scene, according to the simple following relationship:

$$d(mm) = \mathrm{IFOV}(mrad) \times \mathrm{D}(m) \quad (1)$$

where *D* is the distance (in meters) between the thermal scene and the lens of the camera (see Figure 2.6).

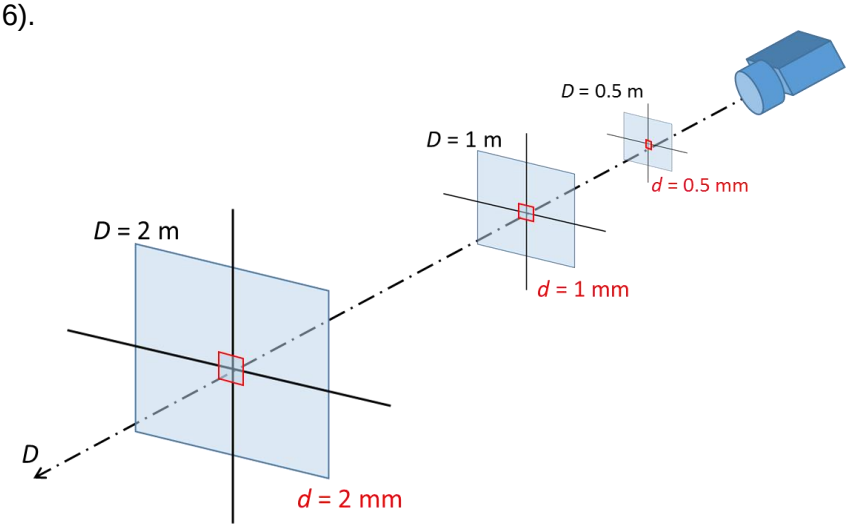

Figure 2.6: *FOV and IFOV of a camera; incidence on the size of smallest object that can be seen on a thermal scene; example for IFOV = 1 mrad.*

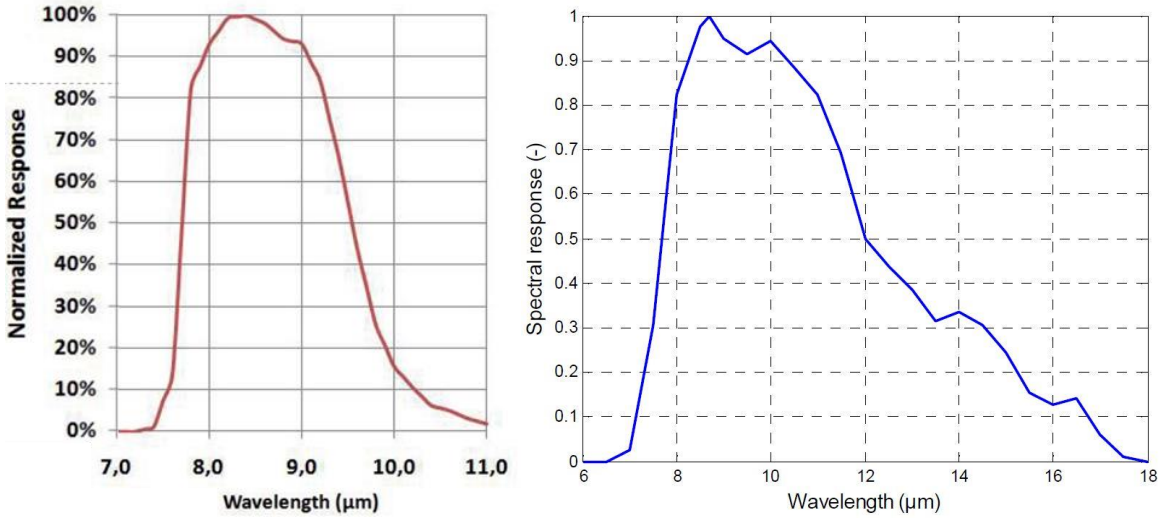

Figure 2.7: *Spectral response curve of FLIR SC7300L; FLIR Data (Left); Spectral response curve of FLIR A325 camera with 25° HFOV; FLIR Data, from [Krapez 2012] (Right)*

2.1.5 Technical data of camera used in this tutorial

In this tutorial, we will use three infrared cameras: FLIR SC7300L, FLIR A325, FLUKE TI32: spectral response curves of two of these cameras are plotted in Figure 2.7. For the Fluke TI32 camera, we will consider a curve response close to the FLIR A325 has both detectors are micro-bolometers arrays. Two of these cameras, are provided with two optics of different FOV. Technical characteristics of these devices are provided in Table 1.

Table 1: *Technical characteristics of IR cameras used in this tutorial*

Camera	FLIR SC 7300L		FLIR A325	FLUKE TI32	
Optics	Normal	Wide angle	Normal	Normal	Wide angle
FOV	22° × 17°	44° × 36°	25° × 18.8°	23° × 17°	46° × 34
IFOV	1.2 mrad	2.4 mrad	1.36 mrad	1.25 mrad	2.5 mrad
Number of pixels	320 x 256	320 x 256	320 x 240	320 x 240	320 x 240
NETD	< 20 mK	< 20 mK	< 50 mK	50 mK	50 mK
Minimum distance	60 cm	30 cm	40 cm	15 cm	7.5 cm
Spectral bandwidth	7.7 – 9.3 µm	7.7 – 9.3 µm	7.5 – 13 µm	8- 14 µm	8 – 14 µm

2.2 Emissivity measurements

As seen in lecture L4, the emissivity of a surface is the ratio between the radiance of the considered surface and the radiance of a blackbody at the same temperature. We will give in this section some additional information concerning the key factors influencing the emissivity and the ways to measure it. Finally, we will illustrate the importance of the knowledge of this parameter for the determination of the temperature of a surface using an IR camera. We will consider in the following that all materials considered are opaque in the wavelength domain considered for the observation.

2.2.1 Parameters influencing the emissivity of materials

Many parameters may have an influence on the emissivity of a material surface. First of all, conducting materials such as metals have generally a low emissivity at ambient temperature and in the infrared domain, thus these materials are good reflectors. On the contrary, dielectric materials exhibit generally a high emissivity in the same conditions.

2.2.1.1 Radiation wavelength

Materials presenting a constant emissivity value upon wavelength are called gray-bodies or gray surfaces. Real gray surfaces do not exist but some materials have an emissivity presenting only small variations versus wavelength at least in a waveband larger than the bandwidth of the camera. In such situation, we can consider valid the gray-body assumption for a given camera and a limited temperature domain. Three examples of variation of normal emissivity upon wavelength at room temperature are presented in Figure 2.8. In the $\Delta\lambda$ band corresponding to the sensitivity of the FLIR SC7300 camera, PVC and Aluminum emissivity remains quite constant, whereas emissivity of glass is varying between 0.7 and 1. For the PVC case, we can consider a constant emissivity on a wide range of wavelength (3 to 16 µm). Thus, we can consider a same emissivity value using a MWIR or LWIR infrared camera, whereas distinct emissivity values have to be considered for glass (We must recall here that glass can be considered as an opaque material only for $\lambda > 5$ µm).

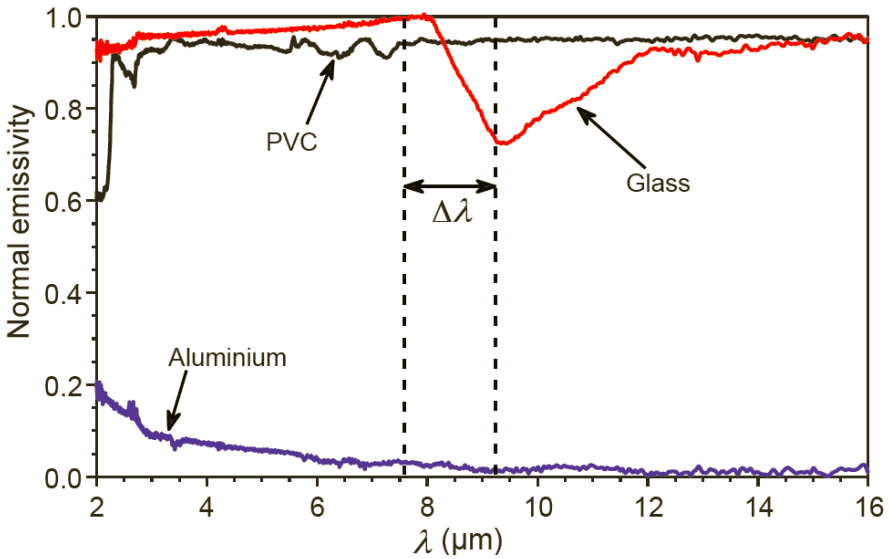

Figure 2.8: *Example of normal spectral emissivity at room temperature for three smooth surface of PVC, Glass and Aluminum [Ibos 2016].*

2.2.1.2 Temperature

The temperature can modify the spectral emissivity of a surface, especially when a phase transition of the material occurs. However, in the case of building applications, temperature variations of materials are small. Thus, the influence of temperature on spectral emissivity is generally neglected.

Nevertheless, in the case of non-gray surfaces, the apparent emissivity computed in a limited wavelength band corresponding to the sensitivity bandwidth of the camera may vary with the temperature. This is due to the displacement of the Planck's law curve as a function of temperature. This phenomenon is illustrated in Figure 2.9 for the case of Alumina. A non-negligible variation of emissivity is observed versus temperature. Moreover, as said before, total emissivity (range 1-50 µm) is different from apparent emissivity computed in the LWIR domain (Band III).

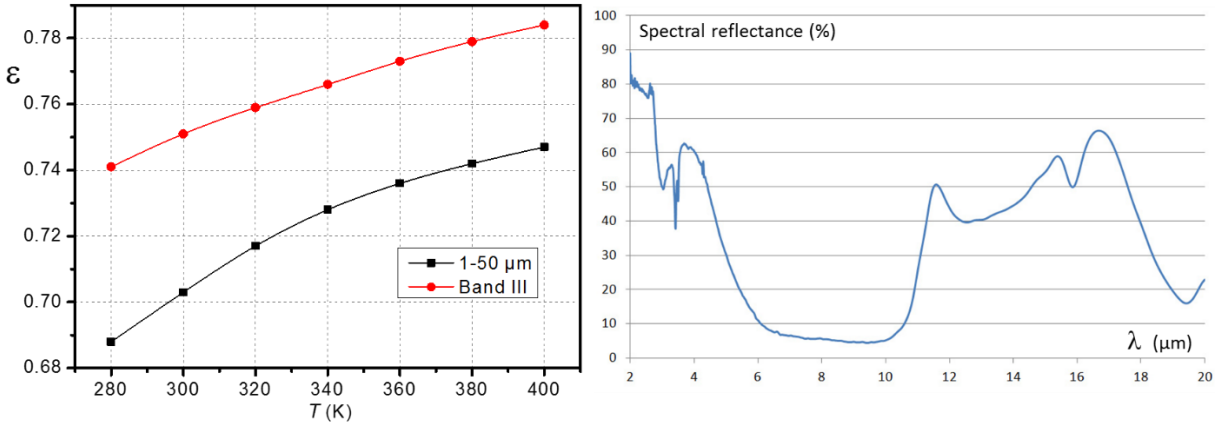

Figure 2.9: *Example of variation of emissivity versus temperature for a non-gray surface of Alumina (Left); spectral reflectance of Alumina (Right); data from [Monchau 2013].*

2.2.1.3 Direction of emission

For smooth and homogeneous materials, directional emissivity can be determined from theoretical relationships and the complex refractive index $n = n_0 + j\chi$ [Lorrain 1979, Kauder 2005]. In the case of a planar diopter plane, emissivity for two polarizations ε// and ε⊥ is defined in Figure 2.10. The directional emissivity is the arithmetic mean of ε// and ε⊥ without polarization.

Directional emissivity of smooth surfaces of PVC, Glass and Aluminum (materials presented in Figure 2.8) is presented in Figure 2.11. Theoretical relationships are compared to measurement performed using the SPIDER instrument [Ibos 2016]. Emissivity values are obtained directly using a FLIR SC7300 camera. For both dielectric materials, emissivity value is maximum at normal angle. This emissivity remains quite constant for angles lower than 45°. Then, the emissivity value drops down to zero for grazing angles. This behavior is typical for dielectrics. Thus, it is commonly recommended to perform measurements with an IR camera for viewing angles comprised between ±45°. For Aluminum surface, emissivity increases with viewing angle and then vanishes for angles close to the grazing incidence. This behavior is typical for metals.

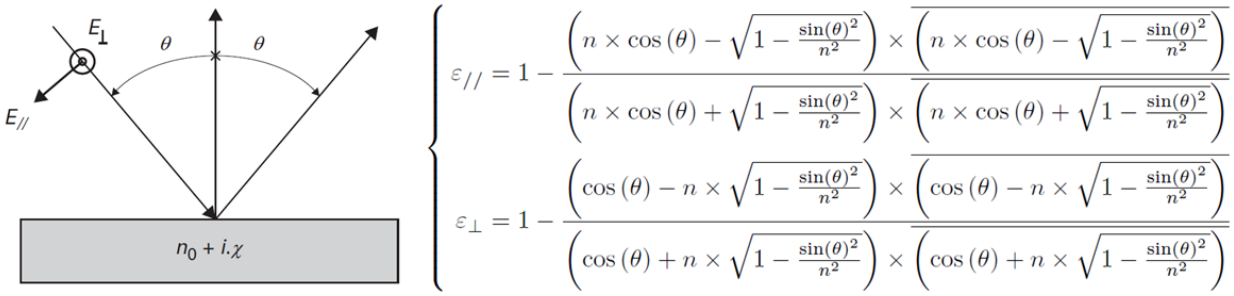

Figure 2.10: *Definition of directional emissivity for a planar diopter; adapted from Refs [Monchau 2013] [Monchau 2018]*

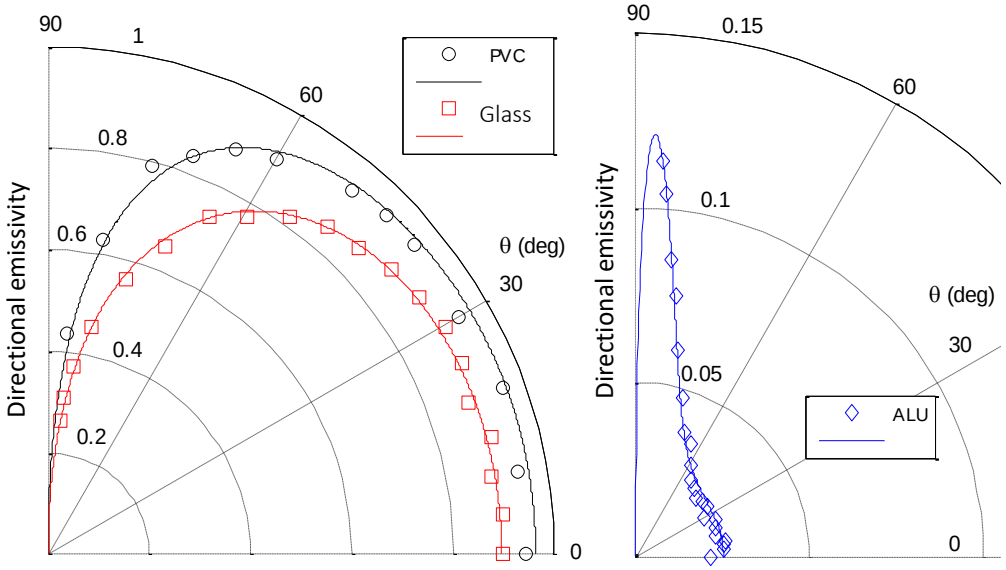

Figure 2.11: *Directional emissivity of three smooth surfaces of PVC, Glass and Aluminum [Ibos 2016]*

2.2.1.4 Surface roughness and oxidation

The emissivity of a material depends on the roughness of its surface. The increase of the surface roughness tends to increase the surface emissivity. This point has to be considered especially for metals that exhibit a very low emissivity when their surface is smooth. Moreover, the increase of surface roughness induces a change of reflection. Smooth surfaces are specular, whereas rough surfaces are diffuse. An example of variation of emissivity of Aluminum versus roughness is presented in Table 2. It is noticeable that the surface emissivity is increased tenfold, due to the fact that the surface roughness is close to the wavelength of the maximum of emission given by the Wien's law at 300K.

Oxidation of metallic surface tends to increase the emissivity. However, the increase is not constant whatever the wavelength. For instance, we have previously seen the difference between emissivity of Aluminum (see Figure 2.8) and of Alumina (see Figure 2.9).

Table 2: *Example of variation of the emissivity of Aluminum surfaces due to roughness; values taken from Ref [Monchau 2013]*

Surface	Roughness R_q (µm)	Total hemispherical emissivity	Total normal Emissivity
Polished Aluminum	0.18	0.057	0.050
Sand-blasted Aluminum	8.9	0.44	0.52

2.2.2 Short review of existing methods for the measurement of emissivity

There are a lot of existing methods for the measurement of the emissivity of materials. These methods can be divided into two families: calorimetric methods on one hand and radiative methods on the other hand. We will consider in this section measurement methods applicable for opaque materials. A complete survey of existing methods, standards and commercial portable devices was proposed recently in [Monchau 2018].

Calorimetric methods can be used in static (constant temperature) or transient regime. Calorimetric methods allow measuring the total hemispherical emissivity of a material as all flux coming from the sample at all wavelengths and directions is considered in the thermal balance. In static regime, the sample surface temperature and the heating power provided to the sample must be measured to compute the emissivity. In transient regime, the thermal capacity of the sample has also to be known.

Radiative methods can also be divided into two families: direct or indirect methods. For direct radiative methods, the flux emitted by the surface is directly measured by an IR detector. These methods require generally a second measurement onto a blackbody or a reference surface (of known emissivity) at the same temperature than the sample. The use of a modulated source allows measuring the emissivity without use of an absolute reference. Spectral measurements can be performed if the detector used is an IR spectrometer. Measurements in a spectral band can be performed by using thermopile or other IR detectors.

For indirect radiative methods, the emissivity is computed from the directional-hemispherical or the hemispherical-directional reflectance of the sample. Then, the directional emissivity is computed using the Kirchhoff's law for opaque materials:

$$\varepsilon' = 1 - \rho'^{\cap} \quad \text{or} \quad \varepsilon' = 1 - \rho^{\cap\prime} \tag{2}$$

In that case, the general principle is to illuminate the sample with an IR source and to measure the reflected flux with an IR detector. The most common method consists in using an IR spectrophotometer equipped with an integrating sphere (see Figure 2.12). This method allows performing spectral measurements. An alternative method consists in using a source with a modulated temperature. In that case, measurements are performed in a spectral band, for instance using thermopile detectors. In both cases, additional measurements on reference samples of known emissivity have to be done. All portable devices allowing to perform in-situ emissivity measurements are using an indirect radiative method.

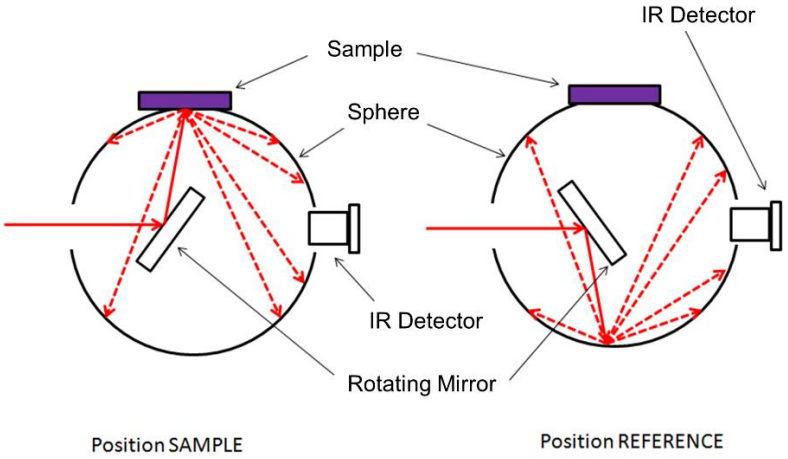

Figure 2.12: *Principle of measurement of normal-hemispherical reflectance using an integrating sphere and a rotating mirror to perform a correction of the sphere factor; Adapted from [Monchau 2013]*

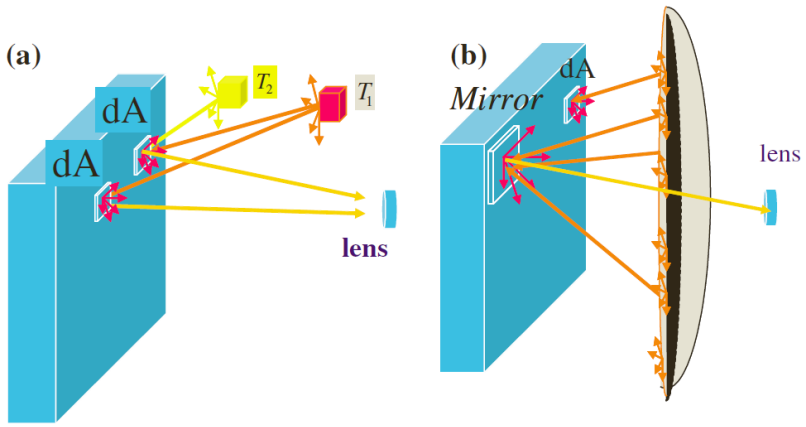

Figure 2.13: *Principle of the determination of the mean radiant temperature. Surrounding radiation: (a) heterogeneous medium, (b) uniform, isotropic medium (approximation of the real surrounding). Illustration from Ref [Datcu 2005]*

2.3 Mean radiant temperature

As the emissivity of real surfaces is not equal to unity, a part of the intensity emitted by surrounding surfaces is reflected by the observed surface and collected by the IR detector. The part of this reflected flux increases as soon as the emissivity of the surface decreases. It is thus important to quantify this surrounding flux in order to compute the surface temperature.

2.3.1 Principle

In practice, the simplest way to quantify the flux coming from the surroundings of a thermal scene consists in placing an infrared mirror directly in the FOV of the camera. This mirror has to be highly reflective and as diffuse as possible in order to reflect the flux coming from all directions. The surrounding of the thermal scene is considered as a blackbody at a particular temperature so-called mean radiant temperature. This principle is illustrated in Figure 2.13.

2.3.2 Practical estimation method

The ASTM E1862-97 standard proposes to use a rough aluminum foil to collect the flux coming from the surroundings. In that case, the mean radiant temperature is directly equal to the apparent temperature on the mirror surface. This method was tested for the determination of building façade temperature (indoor and outdoor conditions) in ref [Datcu 2005]. This method is applicable for building applications because the emissivity of building materials is generally high and the difference between mean radiant temperature and surrounding temperature is generally lower than 20K. For other situations where surface emissivity is low and/or mean radiant temperature is far from surface temperature, this method is no longer applicable. This will be illustrated in the following section.

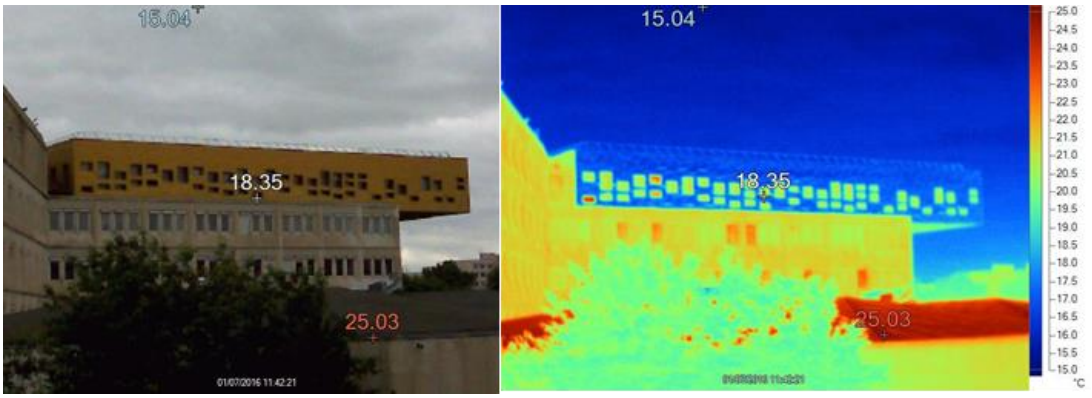

Figure 2.14: *Visible and thermal image of a building façade with a low emissivity cladding*

2.3.3 Importance of the knowledge of the mean radiant temperature and emissivity

Figure 2.14 represents a photograph and a thermal image of a building façade of the Paris-Est Créteil University. The upper floor of the building was recently restored and a low emissivity cladding was used, whereas the rest of the building surface is made of concrete. We can see on the thermal image that the apparent temperature on the restored part is

roughly equal to the sky temperature, because the main flux coming from this surface is reflected flux.

In order to illustrate quantitatively the importance of the surface temperature correction, we have plotted in Figure 2.15 the difference between the apparent temperature and the true temperature of a surface (in °C) as a function of the surface emissivity and of the difference between mean radiant temperature and surface temperature. As said before, we obtain small temperature corrections only for high values of emissivity and/or small differences between mean radiant and surface temperature.

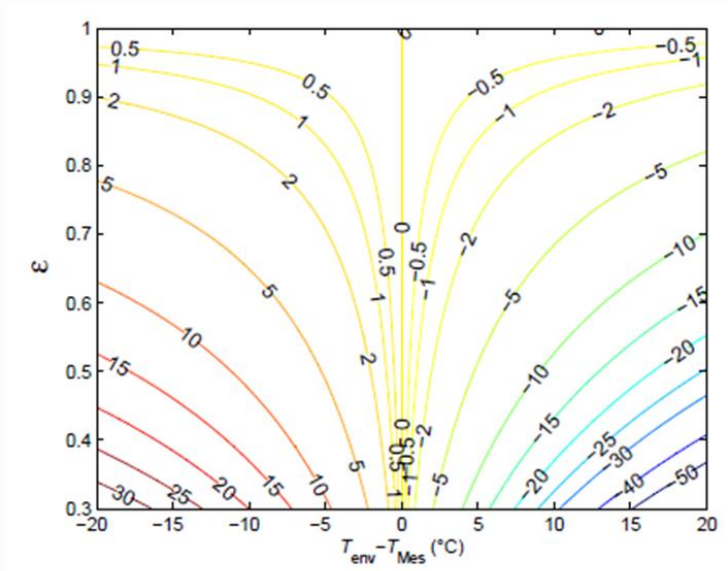

Figure 2.15: *Difference between apparent and true temperature of a surface (in °C) as a function of surface emissivity and of difference between mean radiant and surface temperatures*

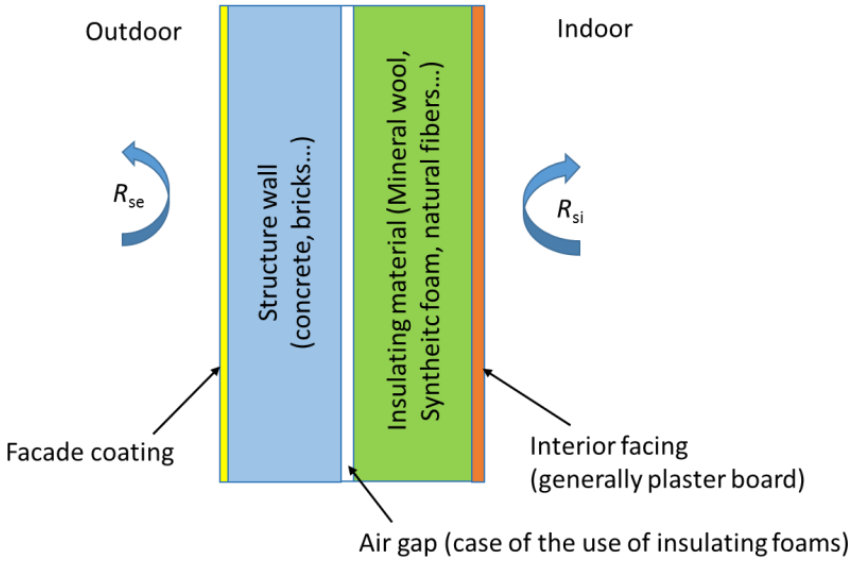

Figure 2.16: *Example of IWI typology*

3. Infrared thermography for the diagnosis of buildings thermal insulation

3.1 Generalities concerning heat transfers inside building walls

3.1.1 Thermal resistance and thermal transmittance

A building wall is generally constituted of a stack of *n* different layers. Each layer *i* has a thermal resistance R_i depending on its thickness e_i and on the thermal conductivity k_i of the material used:

$$R_i = \frac{e_i}{k_i} \tag{3}$$

The total resistance of the wall R_{wall} (expressed in $m^2.K.W^{-1}$) is the sum of the thermal resistances of the *n* layers:

$$R_{wall} = \sum_{i=1}^{n} \frac{e_i}{k_i} \tag{4}$$

Materials used in building walls depend on the typology of the wall and on the expected value of the thermal resistance. We will focus in this tutorial on the IWI typology which is the most frequently used in France, whose structure is presented in Figure 2.16.

The thermal transmission coefficient *U* of a building wall represents the power lost by a wall for an area of 1 m^2 and a temperature difference of 1 K between the indoor and the outdoor ambiances (in steady-state conditions). *U* coefficient is defined by:

$$U = \frac{1}{R_{si} + R_{wall} + R_{se}} \tag{5}$$

where R_{si} and R_{se} are the internal and the external superficial thermal resistances respectively. For the computation of *U* coefficient, R_{si} and R_{se} values are defined by [ISO 6946] standard: R_{si} = 0.13 $m^2.K.W^{-1}$ and R_{se} = 0.04 $m^2.K.W^{-1}$.

An example of typical values of thermal resistances of layers of a wall for a IWI structure in accordance with the actual french thermal regulation [RT 2012] are given in Table 3. According to Equations (4) and (5), this example leads to a wall thermal resistance R_{wall} = 4.012 $m^2.K.W^{-1}$, and consequently a thermal transmission coefficient *U* = 0.239 $W.m^{-2}.K^{-1}$.

Table 3: *Example of values of thermal resistances of a building wall (IWI structure)*

Layer	Material	Thickness (m)	Thermal conductivity ($W.m^{-1}.K^{-1}$)	Thermal resistance ($m^2.K.W^{-1}$)
Interior facing	Plaster board	0.013	0.25	0.052
Insulating material	Glass wool	0.12	0.032	3.75
Structure material	Concrete	0.2	1.0	0.2
Exterior facing	Façade coating	0.01	1.0	0.01

3.1.2 Thermal bridges

The insulation of building walls cannot be continuous due to the necessary presence of doors and windows, of junctions between walls and floors or to the insulating layer fixing system, for instance. All of these irregularities are called "Thermal bridges", as they lead to a local increase of heat losses and consequently to the *U*-coefficient value. An increase of the energy demand due to thermal bridges up to 30% can be sometimes observed [Theodosiou 2008].

3.1.2.1 Junction and Integrated thermal bridges

It is of common use to distinguish between two kinds of thermal bridges: junction or integrated thermal bridges. Junction thermal bridges (*PTL* in French) are mainly due to the junctions between the façade and interior walls or floors, and also to the junction between doors and windows with the façade. These junctions induce a discontinuity in the insulating layer. The impact of junction thermal bridges on the insulation of a wall is strongly dependent on the typology of the building [Farkh 2009]. Integrated Thermal bridges (*PTI* in French) are due to the mechanical system used to fix the insulating material onto a façade wall. This includes for instance the presence of wood stud, metallic rails, metallic or plastic pins… Two examples of visualization of additional losses due to thermal bridges by IR thermography are provided in Figure 3.1.

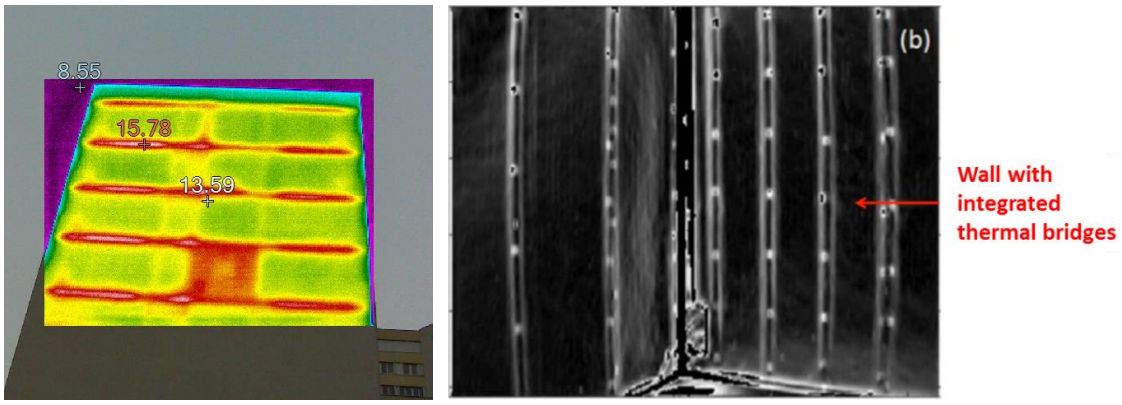

Figure 3.1: *Two examples of visualization of additional losses due to thermal bridges by IR thermography: junction floors/façade wall (left image), integrated thermal bridges due to metallic rails and screws (right image, from [Douguet 2018])*

3.1.2.2 Heat losses in thermal bridges

In order to quantify the importance of a thermal bridge in the global heat losses of a wall or a building, two thermal bridges transmission coefficients are used: ψ and χ coefficients. ψ coefficient quantifies additional thermal losses due to linear thermal bridges, whereas χ coefficient quantifies additional thermal losses due to punctual thermal bridges [ISO 14683]. As illustrated in Figure 3.2 for the case of a linear thermal bridge, the total heat flux ϕ_{tot} through a building wall can be separated into a 1D heat flux (ϕ_{1D}, flux without any thermal bridge) and an additional flux due to the presence of the thermal bridge, labeled ϕ_{tb}.

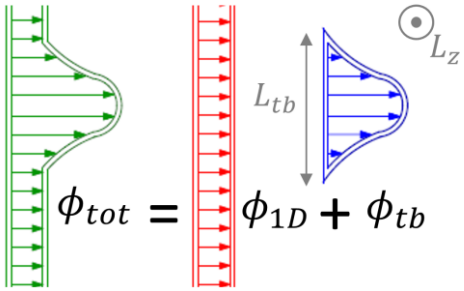

Figure 3.2: *Scheme of additional heat flux (from [François 2019])*

The ψ coefficient is defined by [François 2019]:

$$\psi = L_{tb} \times (U_{tb} - U_{1D}) \tag{6}$$

where U_{tb} is the transmission coefficient of the entire wall (*i.e.* including the contribution of thermal bridges), U_{1D} is the transmission coefficient without thermal bridges and L_{tb} is the width of the thermal bridge impact zone (heat transfers are supposed to be 1D outside this zone). Introducing the heat flux due to the thermal bridge as defined in Figure 3.2, definition of ψ coefficient can be written as follows:

$$\psi = \frac{\phi_{tb}}{L_z \times \Delta T_{ie}} \tag{7}$$

where L_z is the thermal bridge length and ΔT_{ie}, the temperature difference between indoor and outdoor ambiances. In the same way, the χ coefficient is defined by:

$$\chi = S_{tb} \times (U_{tb} - U_{1D}) \tag{8}$$

where S_{tb} is the area of the thermal bridge impact zone (heat transfers are supposed to be 1D outside this zone). Recently, Asdrubali et al proposed to define an impact factor I_{tb} to quantify the importance of a thermal bridge [Asdrubali 2012]:

$$I_{tb} = \frac{U_{tb}}{U_{1D}} \quad \xrightarrow{in\ static\ conditions} \quad I_{tb} \cong \frac{\varphi_{tb}}{\varphi_{1D}} \tag{9}$$

Hence, linear and punctual transmission coefficients can be expressed as a function of this impact factor :

$$\psi = L_{tb} \times U_{1D} \times (I_{tb} - 1) \tag{10}$$
$$\chi = S_{tb} \times U_{1D} \times (I_{tb} - 1) \tag{11}$$

3.2 Different ways to investigate heat losses using infrared thermography

There are two ways to investigate heat losses through a building envelope using IR thermography: the passive method and the active method. The passive method consists in observing a part of a building (façade wall, roof, window…) from inside or outside of the building with an IR camera, during the "normal" use of the building. The observation is generally punctual, but it can sometimes also be monitored during a given period of time. In the active method, an additional thermal load is applied to a part of a building wall or to the

indoor air in order to create a controlled heat flux inside the investigated part of the envelope. In that case, the IR observation is monitored during a given period of time.

3.2.1 Passive method

3.2.1.1 Requirements

In the case of the passive method, heat losses throughout a building envelope can be observed by IR thermography only if there existing a temperature gradient between the inside and the outside of the building. Thus, this method can be used only if the building is in its "normal" use. Moreover, the passive method is strongly dependent on the conditions of observation: indoor air temperature, local weather conditions, orientation of the investigated facade… Thus, the most suitable period for passive observation is the winter period, *i.e.* when there exists an important difference between interior and exterior air temperatures. Moreover, to cancel the possible influence of solar radiation on a façade (especially for southern facades), observations have to be done preferably in the early morning. An illustration of the dependence to weather conditions of a passive IR observation on a southern building façade is presented in Figure 3.3.

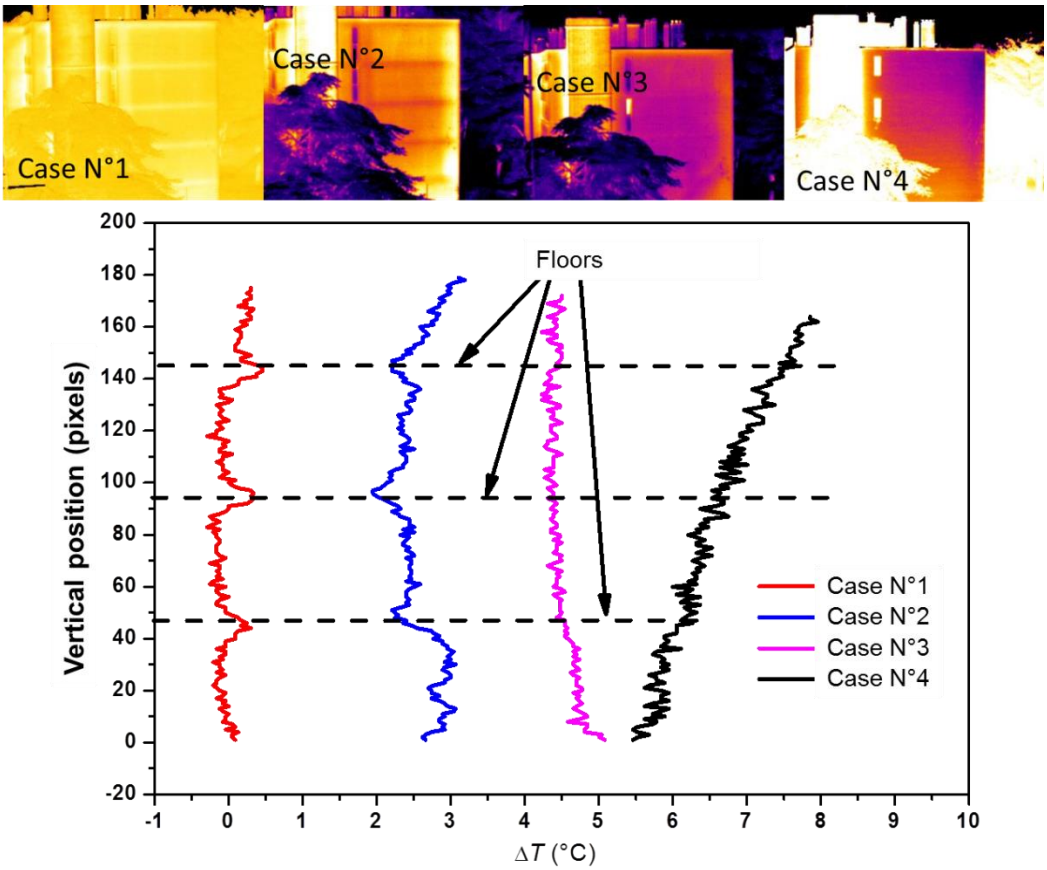

Figure 3.3: *Illustration of the dependence to weather conditions of a passive IR observation on a southern building façade; top: four IR images of the same façade; bottom: plot of temperature vertical profiles along the façade corresponding to each IR image; see text for details*

In case N°1, the apparent temperature is higher on each floor/external wall junction as expected when the indoor temperature is higher than outdoor temperature (observation was done in the early morning). In case N°2, an opposite effect is noted, because the observation was done in the evening of a sunny summer day. In case N°3, it is not possible to visualize any thermal bridge as the observation was done during the inversion of the heat flux inside the wall (*i.e.* during the night). In case N°4, no thermal bridges are visible due to the fact that an outdoor insulation of the building was done. This example illustrates that in passive mode, conclusions on the insulation of a building wall cannot be done if we do not pay attention to observation conditions.

3.2.1.2 R or U measurements using passive IR thermography

An international standard was proposed recently to evaluate the *U* transmission coefficient of building walls using IR thermography [ISO 9869-2]. This method is based on the work of Kato *et al* [Kato 2007] and is a variation of a preceding standard [ISO 9869-1] using only contact temperature sensors and Heat Flow Meters (HFM). The principle of the method is presented in Figure 3.4. The computation of the *U* coefficient is based on the measurement of the indoor surface temperature T_{si} of the wall using an IR camera. The knowledge of the heat exchange coefficient *h* and the indoor and outdoor "environment" temperature, T_{ni} and T_{ne}, require the use of additional devices as seen in Figure 3.4. *U* coefficient is then computed as follows:

$$U = h \times \frac{T_{ni} - T_{si}}{T_{ni} - T_{ne}} \tag{12}$$

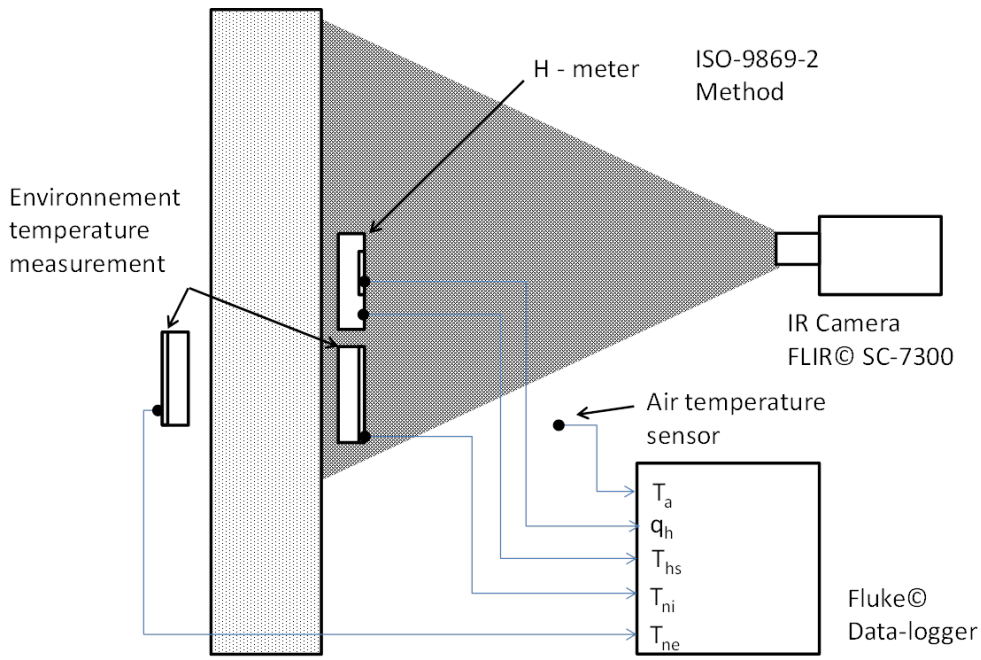

Figure 3.4: *Principle of the measurement of U transmission coefficient of a building wall according to ISO 9869-2 standard*

As this relationship is valid only in static conditions, it is proposed in the standard to average measurements during a period between 3 to 6 days, depending on weather conditions. It is seen from Equation 12 that the accuracy of the method is directly dependent on the evaluation of the heat exchange coefficient.

Another method (named SEID method) was proposed by D. Pajani to evaluate in-situ the *U* coefficient of a building wall [Pajani 2011]. The method consist in placing an additional insulating material (Extruded Polystyrene for instance) of known thermal resistance R_{Ref} on a part of the wall to characterize (see Figure 3.5). After equilibrium is reached, an IR camera is used to monitor surface temperatures of the wall surface T_{si} and of the additional insulating material T_{sRef}. The method requires also the knowledge of the mean radiant temperature T_{mri}. This method has the advantage to be simple and that only apparent surface temperatures are required. Then, the thermal resistance of the wall is computed as follows:

$$R = R_{Ref} \times \frac{T_{mri} - T_{sRef,app}}{T_{sRef,app} - T_{si,app}} \tag{13}$$

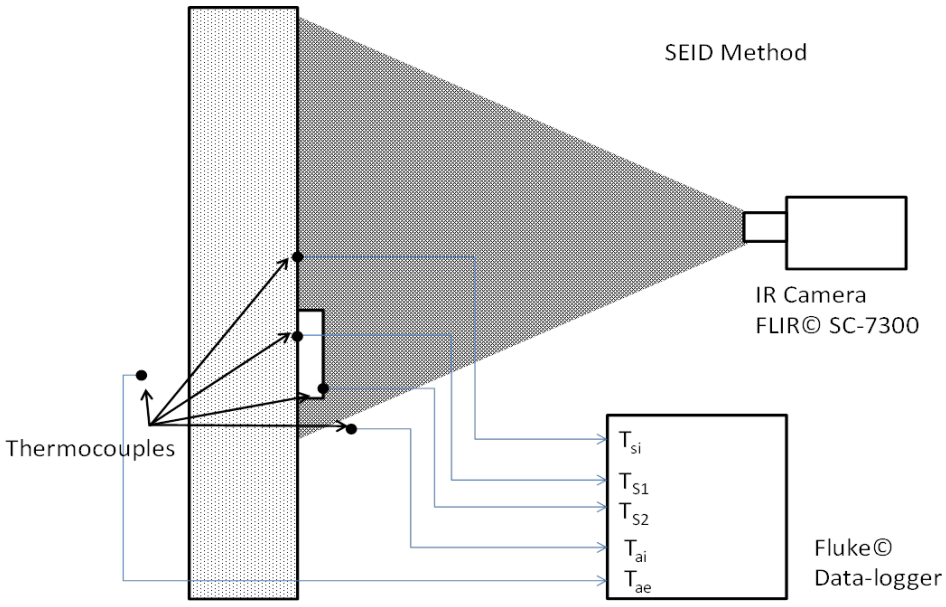

Figure 3.5: *Principle of the SEID method*

Another possibility, proposed by to estimate thermal resistance of a building wall is to record the surface temperature of a façade using an IR camera during a period of about 7 days and to measure simultaneously additional parameters such as indoor and outdoor air temperature and absorbed solar heat flux. Then, a simplified 1D heat transfer model is used and the thermal conductivity and capacity of an equivalent homogeneous wall are identified using an inverse method. Wall thickness has to be known and R_{si} and R_{se} are fixed to conventional values [ISO 6946]. An illustration of the method is proposed in Figure 3.6.

A comparison of the applicability of these methods in the case of the characterization of façade wall of an occupied house was proposed in [Ibos 2015]. Estimated thermal resistances were varying from 2.1 to 4.5 $m^2.K.W^{-1}$ depending on the method used, whereas the expected value was equal to 3.8 $m^2.K.W^{-1}$. Uncertainties were about 1 $m^2.K.W^{-1}$. The

most accurate method was the one using an inverse method for the estimation of the thermal resistance. However, this method requires the longest measurement duration.

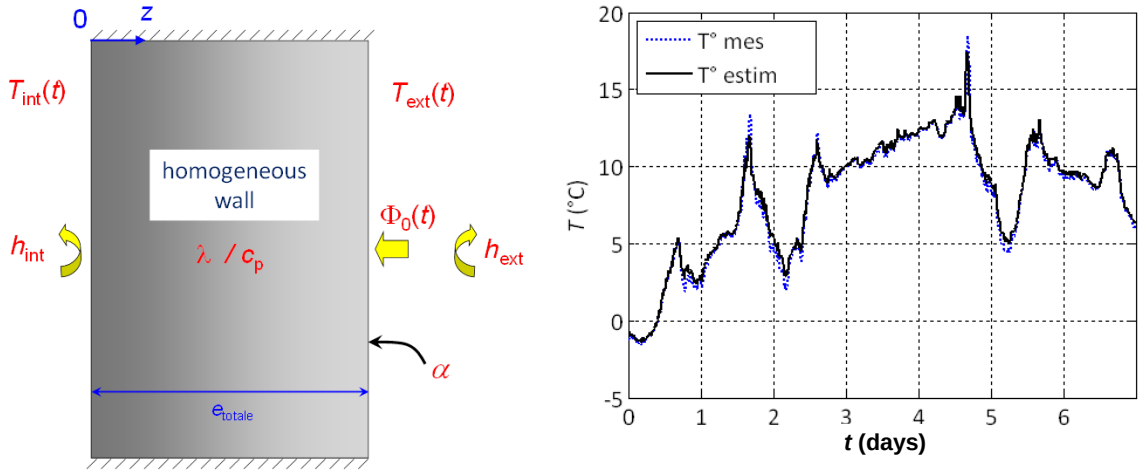

Figure 3.6: *Principle of the estimation of the thermal resistance of a building wall by IR thermography and an inverse method; left: simplified 1D model; right: estimated and measured temperature after estimation; from [Ibos 2015].*

3.2.1.3 Thermal bridges characterization

As presented in section 3.1.2.2, the I_{tb} incidence factor can be used to quantify the local increase of the thermal transmittance of a wall due to a thermal bridge. Using an IR image, it is possible to compute this factor as proposed in [Asdrubali 2012]:

$$I_{tb} = \frac{\sum_{p=1}^{N}(T_i - T_{s,p})}{N \times (T_i - T_{s,1D})} \tag{14}$$

where T_i is the air temperature, N is the number of pixels in the considered area, $T_{s,1D}$ the wall surface temperature in the undisturbed zone and $T_{s,p}$ the surface temperature of pixel p. The main drawback of this method is that it requires the computation of the absolute temperature which is dependent on many factors, particularly the surface emissivity and the mean radiant temperature. Recently, it was proposed to simplify the evaluation of I_{tb}, making the following assumption [François 2019]:

$$I_{tb} \cong \frac{\varphi_{tb}^{rad}}{\varphi_{1D}^{rad}} \tag{15}$$

which consists in considering only radiative fluxes. This assumption is true if the air temperature is close to the mean radiant temperature (which is realistic indoor) and if the radiative and convective heat exchange coefficients can be considered as uniform on the portion of the wall studied (also realistic given the small surface temperature difference between thermal bridges and sound areas). The surface emissivity must be uniform as well in the considered area, but its value is not required as it is possible to work only with surface and mean radiant apparent temperatures:

$$\varphi^{rad} = \sigma \left(T_{s,app}^4 - T_{env,app}^4\right) \tag{16}$$

$T_{env,app}$ can be easily estimated according to the procedure described in section 2.3. Finally, it comes [François 2019]:

$$I_{tb} = \sum_{pixels} \frac{T_{S,tb,app} - T_{env,app}}{T_{S,1D,app} - T_{env,app}} \quad (17)$$

The method was recently tested in laboratory conditions in an experimental building wall with known integrated thermal bridges, as seen in Figure 3.7.

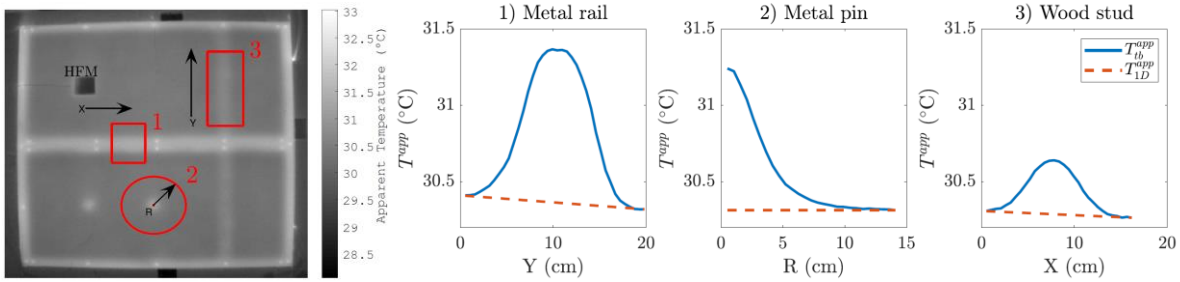

Figure 3.7*: left: IR image of en experimental wall including known integrated thermal bridges; right: averaged apparent temperature profiles used for the computation of Itb factor [François 2019]*

3.2.2 Active method

3.2.2.1 General principles

Active IR thermography consists in recording the variation of temperature of a surface when it is submitted to an artificial thermal excitation. This approach belongs to the family of Non-Destructive Testing (NDT) techniques [Balageas 2016, Maldague 2001]. Active IR has many advantages compared to passive thermography in the case of the inspection of buildings:

- There is no need for existing thermal gradient between the interior and the exterior of a building, thus this method is less sensitive to weather conditions.
- It is sometimes possible to work only with variations of temperatures that are less affected by uncertainties on influencing parameters, particularly on the surface emissivity and mean-radiant temperature.
- The applied thermal power or energy density can be controlled precisely and adapted to the experimental situation to obtain a significant Signal to Noise Ratio and to prevent any damage to the investigated structure.

However, active thermography has also some drawbacks:

- It is required to use additional devices to perform the thermal excitation.
- It is required to record and analyze a sequence of thermal images.

Thermal excitations can have different shapes summarized in Table 4. For in-situ building applications, the use of "flash" excitation is limited to applications devoted to the characterization of the surface of a wall. For instance, it was applied to analyze the presence of coatings, of non-emergent cracks or even to reveal the presence of moisture or salt in walls of historical monuments [Mouhoubi 2016]. Sine wave or random excitations are at this time used mainly for the characterization of materials, but not applied with IR thermography for in-situ building application.

Hence, the most frequently used excitation for building inspection is the square-pulse excitation, mainly for its simplicity to realize in in-situ conditions. For instance, it was used to determine the thermal resistance of building walls in laboratory or in in-situ conditions. In works of Refs [Larbi Youcef 2011] and [Yang 2017], the thermal excitation was provided using halogen or IR lamps to heat a limited part of a wall. The use of an optical excitation allows observing simultaneously the surface temperature variation with an IR camera (front face measurement). In [Chaffar 2012], the outside side of a wall was heated with an instrumented heating plate while the IR camera was used to record the temperature variation onto the opposite face (rear face measurement). Another possibility is to use heating devices to increase the air of a room and to visualize heat losses using an IR camera. This principle was used for instance in [Douguet 2018] to detect integrated thermal bridges in building walls independently of weather conditions.

Table 4: *Classical thermal excitations used in active IR thermography*

Method Name	Excitation shape	Advantages / Drawbacks
Flash	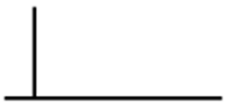	○ Rapid ○ Important temperature increase ○ Expensive devices ○ Limited to the wall surface
Square-pulse		○ Most simple to use ○ Low SNR ○ High power density and excitation duration to be adapted to limit temperature increase ○ Possibility to use only the heating phase (Edge excitation)
Sine wave		○ Most accurate ○ Low power densities ○ Long measurement durations
Random Sequence		Intermediate between square-pulse and sine wave

3.2.2.1 NDT Analysis methods

To analyze the thermal images sequences recorded an active IR thermography experiment on a building wall, it is possible to use common NDT analysis methods. When a thermal irregularity is present inside a building wall, a temperature difference is observed on the surface during or after the thermal excitation as illustrated in Figure 3.8. The interest of active thermography is to increase artificially the temperature contrast on the surface and to observe it whatever the atmospheric conditions. A non-exhaustive list of these methods is presented in Table 5. These methods are useful to detect defects inside a material. Their

application to the detection of thermal irregularities inside a building wall is possible and allows sometimes obtaining quantitative information on the properties of these irregularities. However, at this time, these methods are not very often used for building applications.

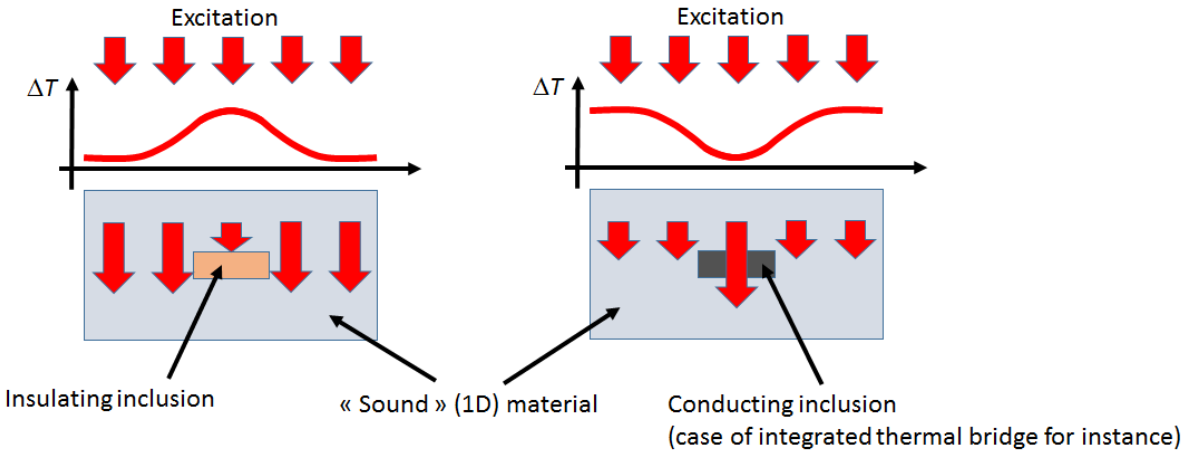

Figure 3.8: *Illustration of the principle of detection of a thermal irregularity inside a material or a building wall*

Table 5: *non-exhaustive list of NDT analysis methods*

Method name	General Principle	Some References
High-order statistics	Computation of a mean, variance, skewness or kurtosis image of the sequence	[Madruga 2010] [Vrabie 2012]
Contrast methods	Computation of absolute, relative or running contrast (temperature difference) between irregularity and "sound" areas Take into account only temperature variation since the beginning of excitation	[Krapez 1994] [Maldague 2001]
PPT (Pulse-Phase Thermography)	Perform a FFT of the temperature evolution of each pixel Obtain Modulus and contrast phases images at each excitation frequency Contrast phase images are low sensitive to surface emissivity variations Requires a spread frequency thermal excitation	[Maldague 1996] [Maldague 2001] [Dumoulin 2011]
TSR (Thermographic Signal Reconstruction)	Logarithmic polynomial interpolation of temperature evolution of each pixel Obtain polynomial coefficients maps	[Shepard 2003] [Balageas 2015] [Dumoulin 2011]
SVD (Singular Value Decomposition)	Acts like a data compression method Thermal images sequence information is compacted in a few images (Empirical Orthogonal Functions) and associated Principal Components	[Rajic 2002] [Marinetti 2004] [Dumoulin 2010] [Douguet 2018] [Mouhoubi 2016]

3.2.2.2 Focus on SVD

One of the most interesting method for building application is the Singular-Value Decomposition method. Indeed, SVD allows the extraction of the spatial and temporal information from a thermographic sequence in a compact and simplified manner. The SVD of an *m*×*n* pixels matrix ***X*** is a linear algebraic factorization which can be calculated as follows [Rajic 2002]:

$$\boldsymbol{X} = \boldsymbol{U} \times \boldsymbol{S} \times \boldsymbol{V}^t \tag{18}$$

where ***U*** is an *m*×*n* orthogonal matrix, ***S*** is a *n*×*n* diagonal matrix (with the singular values of ***X*** in the diagonal, sorted in descending order) and $\boldsymbol{V}^t$ is the transpose of an *n*×*n* orthogonal matrix:

$$\underset{\boldsymbol{X}}{\begin{pmatrix} x_{11} & \cdots & x_{1n} \\ \vdots & \ddots & \vdots \\ x_{m1} & \cdots & x_{mn} \end{pmatrix}} = \underset{\boldsymbol{U}}{\begin{pmatrix} u_{11} & \cdots & u_{1n} \\ \vdots & \ddots & \vdots \\ u_{m1} & \cdots & u_{mn} \end{pmatrix}} \underset{\boldsymbol{S}}{\begin{pmatrix} s_{11} & 0 & \cdots \\ 0 & \ddots & \\ \vdots & & s_{nn} \end{pmatrix}} \underset{\boldsymbol{V}^t}{\begin{pmatrix} v_{11} & \cdots & v_{1n} \\ \vdots & \ddots & \vdots \\ v_{n1} & \cdots & v_{nn} \end{pmatrix}} \tag{19}$$

The thermographic sequence must be rearranged so that the columns of matrix ***X*** correspond to the thermograms at each time (see Figure 3.9):

After applying the SVD on matrix ***X***, the columns of ***U*** represent a set of orthogonal statistical modes known as Empirical Orthogonal Functions (EOF), which describe spatial variations of data. On the other hand, the Principal Components (PC), which represent time variations, are arranged row-wise in matrix $\boldsymbol{V}^t$. The first EOF will represent the most characteristic variability of the data, the second EOF (denoted further as EOF n°2) will contain the second most important variability, and so on. Usually, original data can be adequately represented with only a few EOFs.

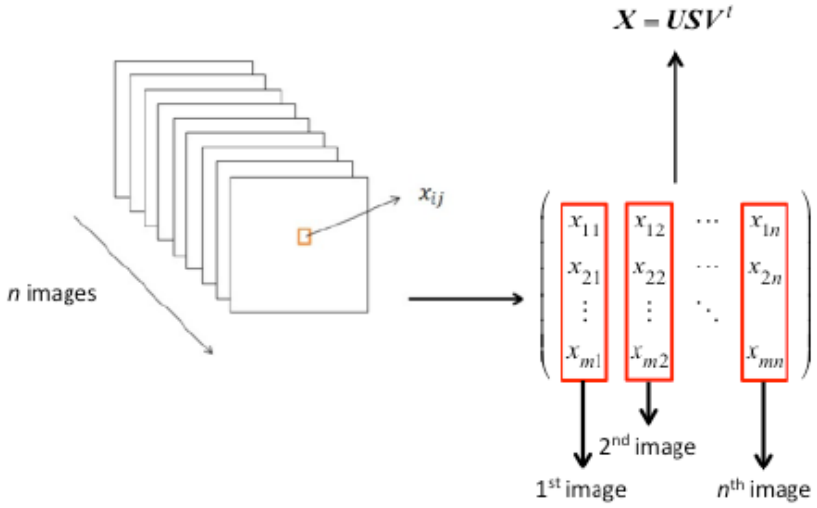

Figure 3.9: *Rearrangement of the thermographic sequence before application of the SVD treatment [Douguet 2018]*

This method was for instance applied recently to the detection of integrated thermal bridges inside building walls as presented in Figure 3.10 [Douguet 2018]. The other advantage of

SVD is that it can reduce noise from original sequence by removing high orders of singular vectors. Superior orders contain less important information, so if some vectors belong to high enough orders, they can be considered as noise. A reconstruction of the thermographic sequence (inverse SVD) from the truncated SVD matrices leads to a filtered sequence. Moreover, the increase of signal to noise ratio induced by an SVD processing allows then to use classical image segmentation methods (such as gradient for instance) to extract edges of thermal irregularities and to use micro-bolometers arrays IR cameras instead of cameras with cooled detectors.

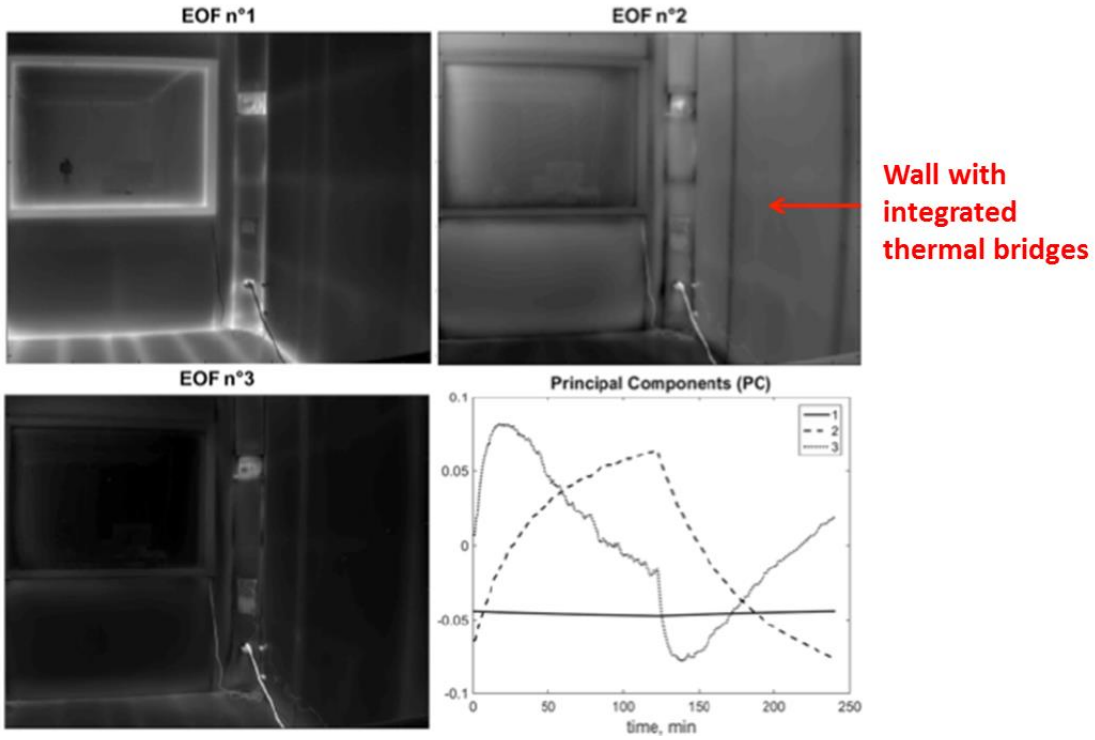

Figure 3.10: *Example of SVD analysis of a thermal images sequence allowing the detection of integrated thermal bridges [Douguet 2018].*

4. Tutorial first part : Determination of surface temperature and its associated uncertainty using an IR camera

As mentioned in the introduction of this article, the first part of this training session will be devoted to the determination of the temperature of a surface using an IR camera. We will particularly discuss about the importance of the surface temperature correction by considering measurements on surfaces of variable emissivity, and by evaluating the associated uncertainty.

4.1 Description of the test bench

4.1.1 Structure and operating conditions

The structure of the test bench used in the first part of this tutorial is presented in Figure 4.1. An image of this test bench with the measurement devices is also presented in Figure 4.2.

The test bench is composed of a metallic plate covered with four coating of different emissivity. This front surface will be observed with an IR camera.

A heating film will allow heating the surface of the test bench to a given temperature. A heat flow meter was placed between the heating film and the metallic plate. A T-type thermocouple is inserted inside this HFM. This allows obtaining the heat flux through the front surface metallic plate and its temperature. In fact, the temperature of the front surface will be different than the one measured by the thermocouple because of the thermal resistance of the metallic plate and the presence of thermal contact resistances between each element. Conducting thermal grease is applied between each element in order to reduce thermal contact resistances.

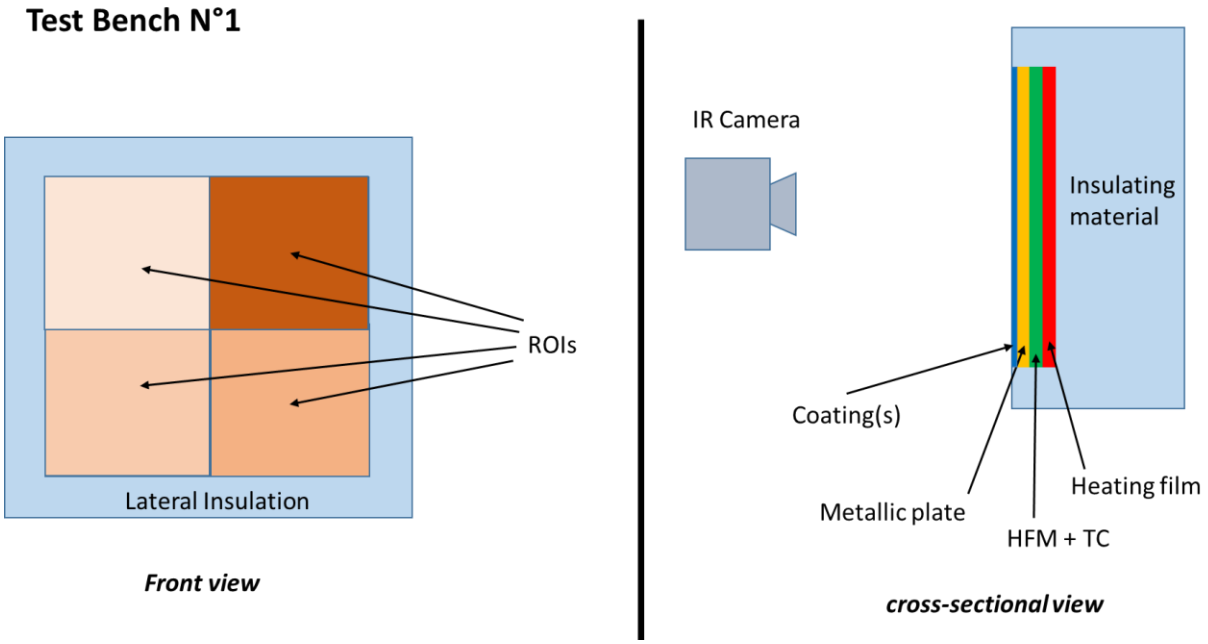

Figure 4.1: *Schematic view of the test bench N°1*

4.1.2 Emissivity of materials used in the test-bench of this tutorial

The normal spectral emissivity of each coating covering the front face of the test bench was measured using an IR spectrometer equipped with an integrating sphere. This measurement method was briefly presented in section 0 and Figure 2.12. Spectral emissivity curves obtained are presented in Figure 4.3. Measurements were performed in laboratory at room temperature (23 ± 2 °C). We will consider in this tutorial that the spectral emissivity is not depending on the temperature. This assumption is acceptable since the surface temperature will remain close to room temperature during the measurements.

The four coatings considered are:

- a black paint (Ref RAL 9005);
- a white paint (Ref RAL 9016);
- a copper finish paint;
- a chrome finish paint.

It can be seen from Figure 4.3, that spectral emissivity if black and white coatings in the IR domain are quite high and close one the other despite their color difference in the visible domain. The presence of metallic particles in chrome and copper coatings, tends to decrease their emissivity.

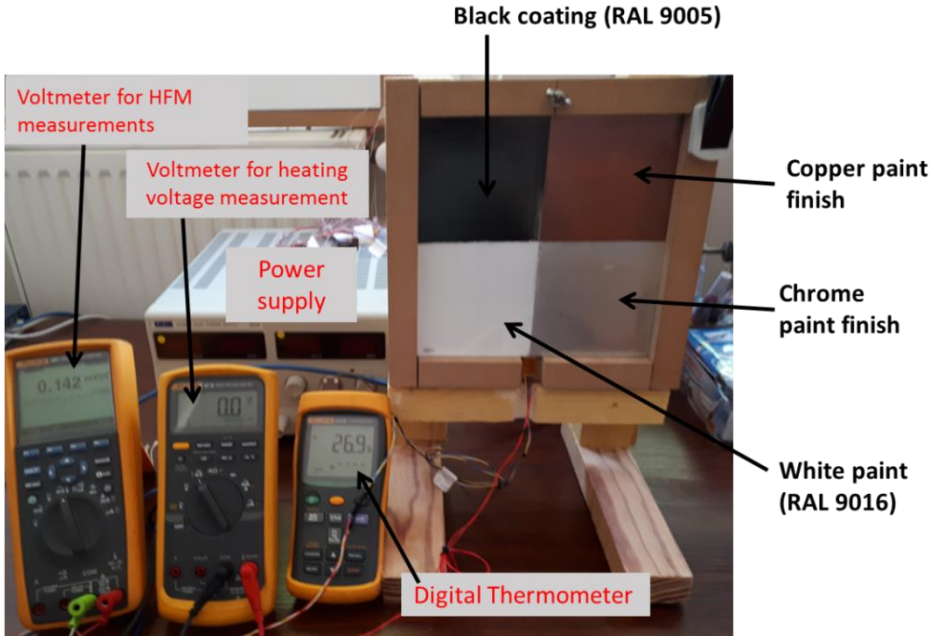

Figure 4.2: *Image of the test bench N°1 with measurement devices*

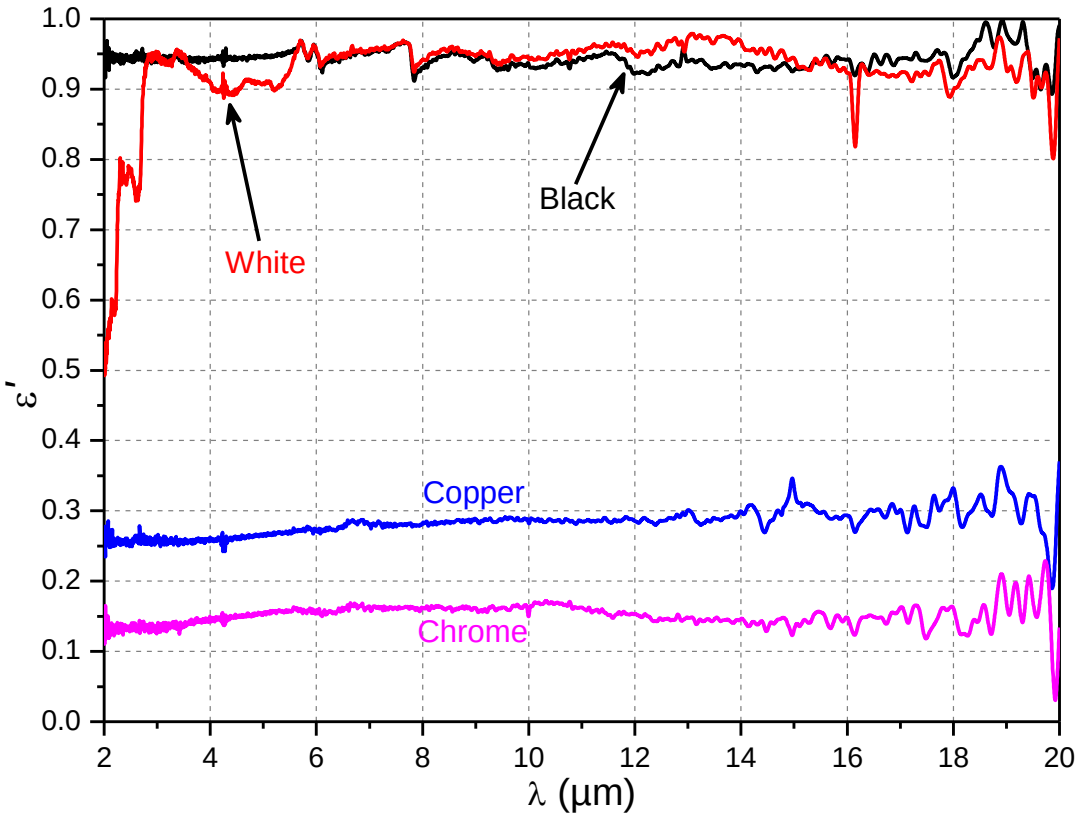

Figure 4.3: *Normal spectral emissivity of the four coatings used in the test bench N°1*

Variations of the spectral emissivity as a function of the wavelength are noted, particularly for the white paint. However, most important variations observed remain outside of the sensitivity domain of the IR cameras used in this tutorial, *i.e.* LWIR cameras.

4.2 Temperature correction

4.2.1 Recall of the method used

In the L4 lecture, it was shown that the intensity measured by the IR camera is the sum of three contributions:

- the self-emission of the target surface;
- the reflection on the target surface coming from the environment;
- the self-emission of the atmosphere between the camera lens and the target surface.

This general principle is illustrated in Figure 4.4. This leads to the general equation of the measured intensity L_{mes}:

$$L_{mes} = \tau_{atm}.\varepsilon.L^o(T_s) + \tau_{atm}.(1-\varepsilon).L^o(T_{env}) + (1-\tau_{atm}).L^o(T_{atm}) \quad (20)$$

As measurements are here done in an indoor environment and at a short distance, we will consider that the transmittance of the atmosphere τ_{atm} is equal to unity and consequently that its contribution to the measured intensity is negligible. Thus, we obtain the simplified equation:

$$L_{mes} = \varepsilon.L^o(T_s) + (1-\varepsilon).L^o(T_{env}) \quad (21)$$

Hence, in such conditions, to obtain the surface temperature T_s, we have to know the surface emissivity ε and the mean-radiant temperature of the environment T_{env}. At this stage, it has to be recalled that the measured intensity can be directly converted into an apparent temperature T_{app} by using the camera calibration curve.

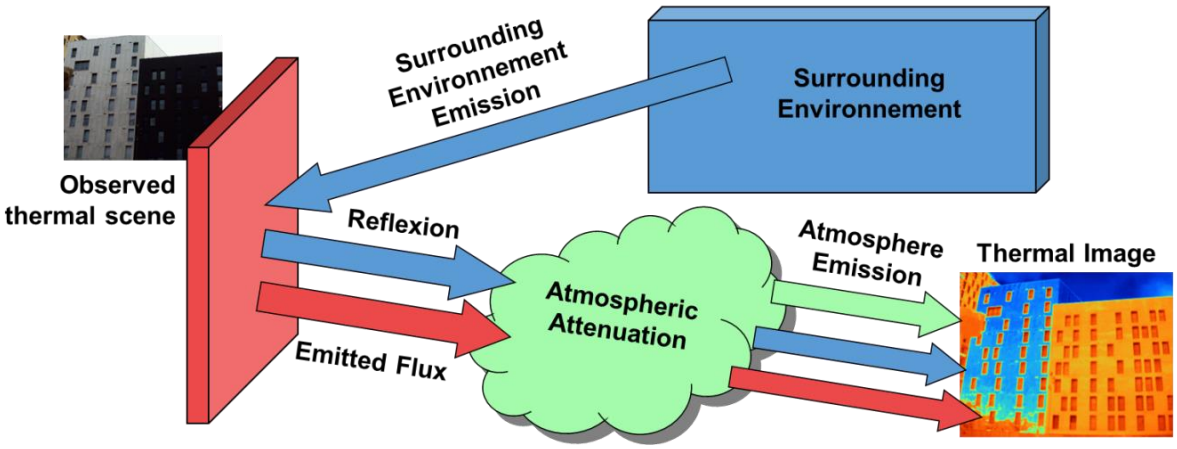

Figure 4.4: *Principle of an IR thermography measurement*

4.2.2 Determination of the surface emissivities to consider

The first step of the temperature correction to perform is the computation of an apparent emissivity of the considered surface. For this operation, we have to consider the spectral emissivity curves presented in Figure 4.3. To obtain the apparent emissivity of the surface, we have to integrate this curve in the sensitivity domain of the camera by weighting it by the Plank's curve response. For that purpose, the surface temperature is required! In the framework of this tutorial, we have a first evaluation of the surface temperature using the thermocouple inserted in the HFM. If there is no prior knowledge of the surface temperature, it is possible to consider in a first step, a "flat" blackbody response, and then to iteratively refine the emissivity correction.

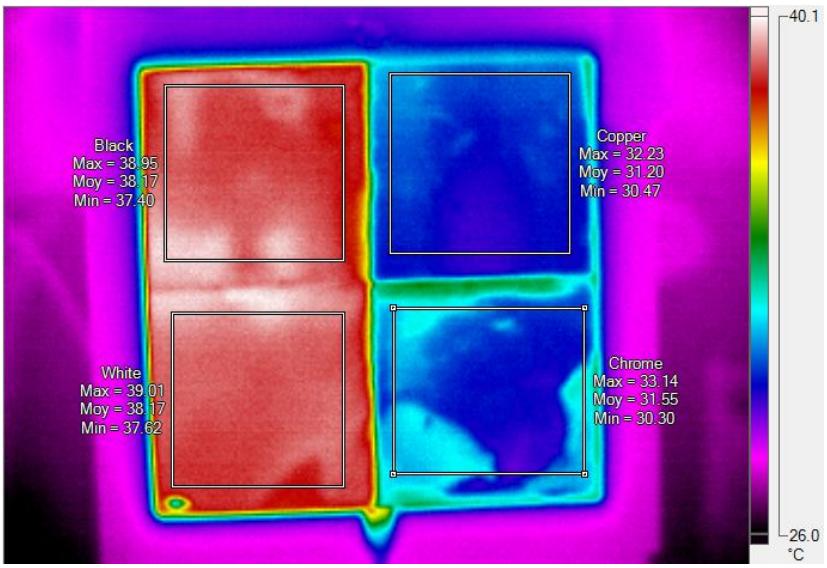

Figure 4.5: *Example of Raw thermal image obtained on the front surface of test-bench N°1 (apparent temperature data in °C)*

4.2.3 Determination of apparent temperature

Work to be done is the following:

- Check that the emissivity value is fixed to unity in the camera software. In that case, thermal images are presented in apparent temperature.
- Record a thermal image of the surface and note the temperature given by the thermocouple inserted in HFM (see example in Figure 4.5).
- Open the recorded image and identify the different ROIs to consider.
- For each ROI, compute a mean apparent temperature and a standard deviation in each ROI area.

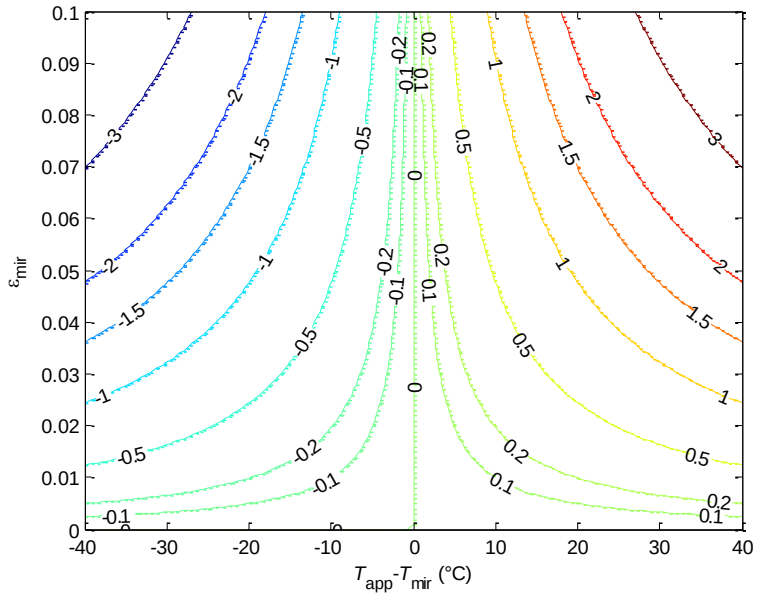

Figure 4.6: *Error made (expressed in °C) on the evaluation of the mean-radiant temperature as a function of mirror emissivity and difference between apparent and mirror temperatures.*

4.2.4 Determination of mean radiant temperature

For the evaluation of the mean radiant temperature, we will use the method proposed in the [ASTM E1862-97] standard and briefly described in section 2.3.2. For that purpose, place the diffusive mirror in front of the test bench surface and take one thermal image of it. Compute the mean apparent temperature on the mirror surface and the associated standard deviation. If the mirror emissivity is approximated to be near 0 (perfect reflector), then the mean apparent temperature obtained on its surface is equal to the mean radiant temperature T_{env}.

In the case where the mirror emissivity cannot be considered equal to 0, it is necessary to know its temperature and its emissivity, respectively T_{mir} and ε_{mir}. Its temperature can be for instance measured with a contact sensor (thermocouple or resistive sensor) and its emissivity have to be characterized with an additional device (by spectrometry for instance). In such a case, we obtain on the mirror surface, the following relationship (atmosphere influence is again neglected) [Datcu 2005]:

$$L^o(T_{env}) = \frac{L_{mir} - \varepsilon_{mir}.L^o(T_{mir})}{1 - \varepsilon_{mir}} \tag{22}$$

where L_{mir} is the intensity measured with the IR camera on the mirror surface. The error on the evaluation of the mean-radiant temperature is plotted in Figure 4.6 for mirror emissivity lower than 0.1 and a difference between apparent and mirror temperatures ranging between -40 and 40°C.

4.2.5 Performing the temperature correction

Once surface emissivity, surface apparent temperature (or surface intensity) and mean radiant temperature are known, it is possible to perform the temperature correction for each

coating, according to equation 21. An example of temperature correction is presented in Table 6. Raw thermal image considered is the one presented in Figure 4.5. We considered a mean-radiant temperature value T_{env} = 28°C and coatings emissivities plotted in Figure 4.3.

After correction, we observed that temperatures on three first coatings (Black, white and copper paint) are close. Due to their high emissivity and a relative small difference (about 10°C) between the mean-radiant temperature and the apparent temperature, the temperature correction on black and white coatings is small (less than 1°C). Due to its lower emissivity, the temperature correction on the copper paint is more important (about 8°C).

The Thermocouple inserted in the HFM was indicating a temperature of 41°C during the experiment. It is thus expected to obtain a surface temperature slightly lower than this value. However, to conclude on the accuracy of this correction, it is required to compute uncertainty on the corrected surface temperature.

Finally, we can notice that the temperature correction on the chrome paint coating gives a value 8°C higher than the one of the thermocouple. As shown in Figure 4.3, this coating is the most reflective of the four used in this experiment. For such low emissivity surfaces, the correction is strongly dependent on the mean-radiant temperature and emissivity value used. For instance, in the present case, the use of mean-radiant temperature of 30°C instead of 28°C leads to a corrected surface temperature of 39.6°C, thus close to the expected one. Moreover, apparent temperature obtained in highly reflective surfaces can also be influenced by non-uniformities of the radiative surrounding environment: we can observe such apparent temperature variations on the chrome coating surface in Figure 4.5.

Table 6: *Example of comparison of apparent and corrected surface temperatures obtained on the four coatings of test bench N°1 using IR image of Figure 4.5.*

Coating	Black paint	White paint	Copper paint	Chrome paint
T_{app} (°C)	38.2	38.2	31.2	31.5
T_S (°C)	38.7	38.8	39.3	49.1

4.2.6 Uncertainty analysis

As the surface temperature T_s is not directly evaluated by a measurement device, but computed from other quantities, its uncertainty $u(T_s)$ has to be computed by considering standard uncertainties on each parameter of equation (21), namely ε, T_{env} and T_S. If we consider that these parameters are not correlated, the combined standard uncertainty on T_s , namely $u_c(T_s)$ is given by [GUM 1995]:

$$u_c^2(T_S) = \left(\frac{\partial T_S}{\partial \varepsilon}\right)^2 \times u^2(\varepsilon) + \left(\frac{\partial T_S}{\partial T_{env}}\right)^2 \times u^2(T_{env}) + \left(\frac{\partial T_S}{\partial T_{app}}\right)^2 \times u^2(T_{app}) \quad (23)$$

Then, the expanded uncertainty $U(T_s)$ is obtained by multiplying the combined standard uncertainty by a coverage factor k:

$$U(T_S) = k \times u_c(T_S) \quad (24)$$

The value of the coverage factor determines the level of confidence on the measured or computed quantity. For many practical measurements, particularly if the objective quantity

can be described by a normal distribution, it can be assumed that a value of k = 2 defines an interval having a level of confidence of approximately 95% (or 99% for k = 3). The validity of this assumption has to be checked by referring to Annex G of the [GUM 1995] reference.

4.2.7 Analysis of results

After evaluation of uncertainties, it is now possible to express the surface temperature result for each coating:

$$T_s = \hat{T}_s \pm U(T_s) \tag{25}$$

where $\hat{T}_s$ is the estimated value of the surface temperature. Surface temperatures evaluated by IR thermography can be compared to the temperature value given by the contact sensor inserted in the test bench. This evaluation can now be also repeated by "disturbing" the thermal scene; this can be done by placing a hot object in the environment, whose emission will be seen by reflection of the surface of the test-bench.

5. Tutorial Second part : Detection and characterization of thermal bridges inside a building wall

As mentioned in the introduction of this article, the second part of this training session will be devoted to the detection and characterization of thermal bridges inside a building wall. We will investigate the case of integrated thermal bridges by using two different materials simulating the presence of a wood stud or of a metallic rail. To reduce the measurement duration, the experiments will be done using a reduced-scale wall.

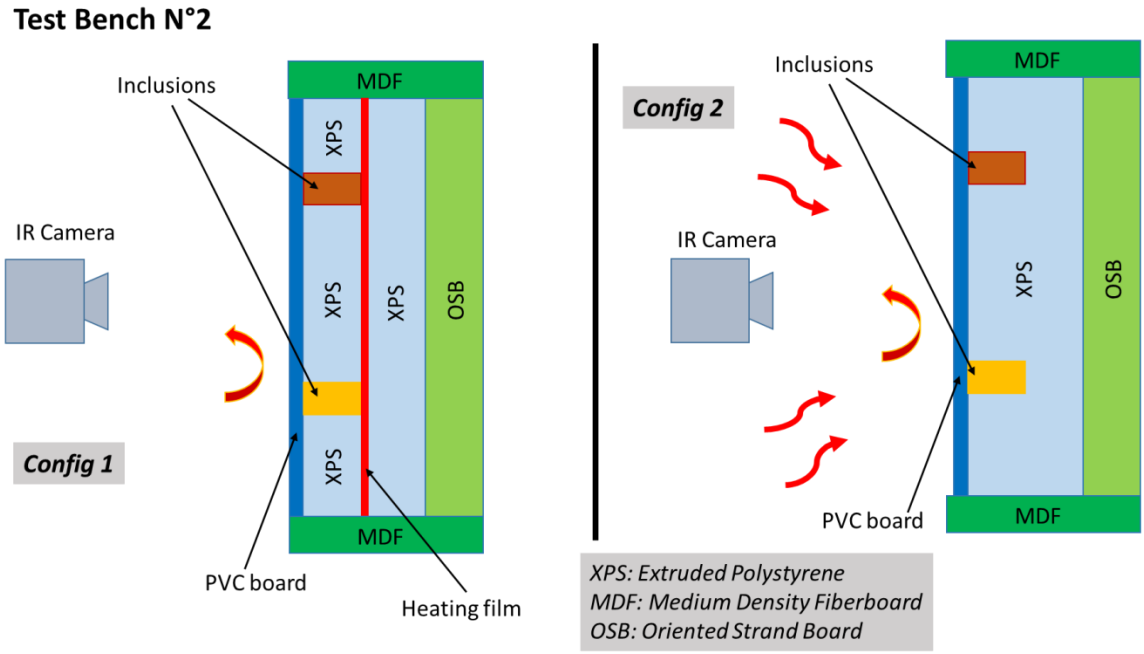

Figure 5.1: *Schematic view of the test bench N°2 and of the two measurement configurations*

5.1 Description of the test bench

5.1.1 Structure and operating conditions

The structure of the test bench used in this second part of the training is presented in 5.1. The front face, observed using an IR camera, will be constituted by a PVC foam plate. The dimensions of this plate are 60 cm x 60 cm.

Behind this first layer, an insulating material (XPS) was placed. Inclusions can be placed inside this layer to simulate the presence of an integrated thermal bridge. These inclusions are either a pine wood rod or a hollow aluminum tube (inclusions have a square section). Both inclusions can also be used simultaneously can be placed vertically or horizontally in the insulating layer. As pine wood and aluminum have a higher thermal conductivity than XPS, heat flow through the wall will be enhanced. Different possible experimental configurations are presented in Figure 5.2.

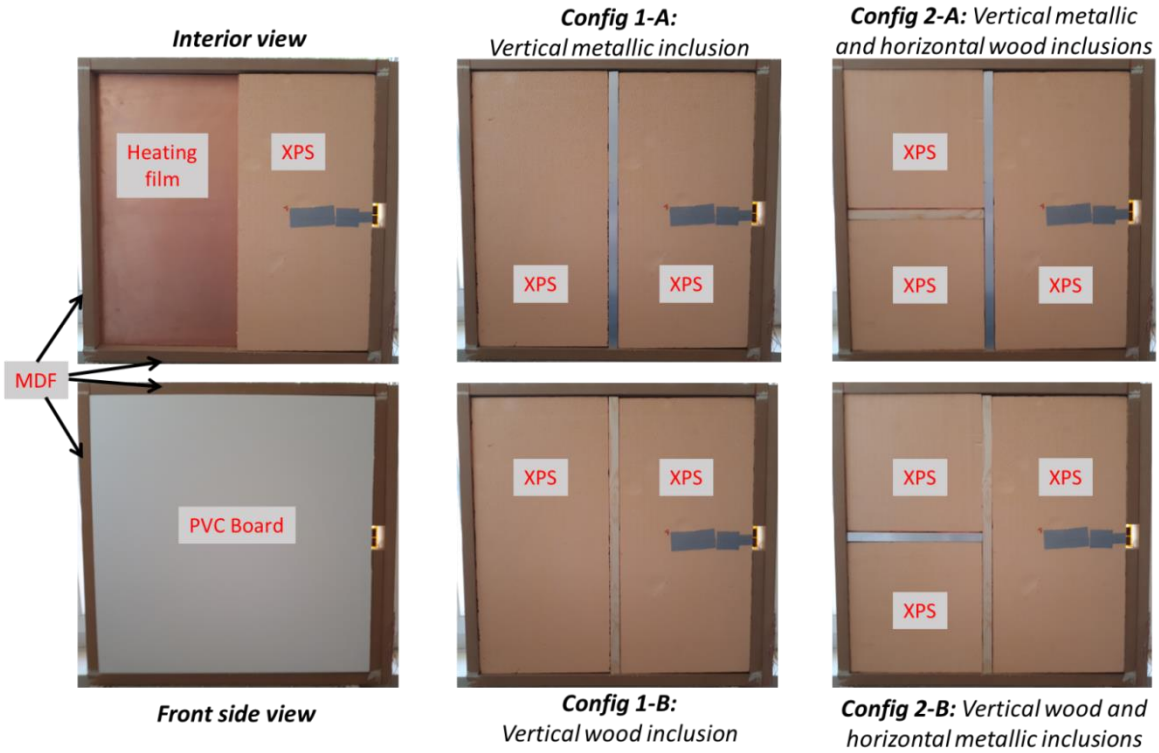

Figure 5.2: *Images of the test bench N°2 with different configurations; wood inclusions are pine wood rods; metallic inclusions are aluminum hollow tubes; all inclusions have a square section of 20 mm x 20 mm*

A heating film was placed behind the insulating layer, to artificially create a constant and homogeneous heat flux inside the insulating layer. This case study corresponds to the configuration N°1 described in Figure 5.1. Finally, another XPS layer is placed behind the heating film and finally an OSB plate is used to ensure the mechanical structure of the wall. In the configuration N°2 presented in Figure 5.1, we will not use the heating film, but we will heat the wall surface either with lamps or heating fans. The edges of the test bench are not

insulated. MDF studs are used to maintain all elements in an adequate position during the experiments. Several T-type thermocouples are also inserted between each layer of the wall.

5.1.2 Thermophysical properties of materials used in the test-bench

Physical properties of the materials used in the test bench N°2 are reported in Table 7. These materials were characterized using the Hot-Disk method. This method allows obtaining the thermal conductivity k and the thermal diffusivity a (or the $\rho.C_p$ product). Materials density ρ was estimated by weighting a known volume of each material. From these values, it is possible to compute the thermal resistance of each layer.

Thermal resistance of the entire wall and of the front part of the wall, *i.e.* between the heating film and the front surface, are reported in Table 8, along with the corresponding U thermal transmission coefficient values (refer to section 3.1.1 for computation details). These values are given without any thermal bridge included inside the first insulating layer.

Table 7: *Thermophysical properties of materials used in the test bench N°2*

Material	e (mm)	k ($mW.m^{-1}.K^{-1}$)	R ($\times 10^{-3}$ $m^2.K.W^{-1}$)	a ($mm^2.s^{-1}$)	ρC_p ($MJ.m^{-3}.K^{-1}$)	ρ ($kg.m^{-3}$)
PVC board	5	69 ± 2	72 ± 3	0.165 ± 0.005	0.423 ± 0.18	443 ± 10
XPS	20	35 ± 1	571 ± 17	0.79 ± 0.12	0.044 ± 0.006	32 ± 1
Pine wood	20	202 ± 19	99 ± 9	0.259 ± 0.026	0.78 ± 0.11	633 ± 6
Aluminum hollow tube	20	(38 ± 3) × 10^3 (*)	0.46 ± 0.03	-	0.685 ± 0.035 (**)	761 ± 6
OSB	15	184 ± 16	82 ± 7	0.234 ± 0.060	0.79 ± 0.13	635 ± 7

(*) Effective thermal conductivity and thermal resistance of the Aluminum hollow tube was computed from measured value for the Aluminum (214 ± 5 $W.m^{-1}.K^{-1}$) and by considering a simplified heat transfer model taking into account the presence of air inside the tube volume and its geometry.

(**) ρC_p value of the Aluminum hollow tube was computed from measured density and conventional C_P value for Aluminum (905 $J.kg^{-1}.K^{-1}$ [Sacadura 2015]).

Table 8: *Thermal resistance and thermal transmission of the wall of the test bench N°2*

Configuration	R ($m^2.K.W^{-1}$)	U ($W.m^{-2}.K^{-1}$)
Entire wall	0.64	1.3
Front part of the wall (from heating film and front surface)	1.3	0.70

5.2 Measurement in static regime

Measurements in static regime are performed using the heating film included in the test bench. An example of thermal image obtained (plotted in apparent temperature) is presented in Figure 5.3, for the configuration 2-A. In that configuration the vertical thermal bridge (metallic tube) and the horizontal thermal bridge (pine wood rod) can be seen in the thermal image. As expected, apparent temperature on the metallic thermal bridge is higher than on the wood thermal bridge, due to the lower its lower thermal resistance.

Once static regime is reached, work to be done is the following:

- Record one of several thermal images of the front surface of the wall; if several images are acquired, only an average image is required for further computations.

- Compute the I_{tb} value for each thermal bridge (refer to sections 3.1.2.2 and 3.2.1.3 for details) and the corresponding ψ value. These computations can be done using either absolute temperature or apparent temperature.

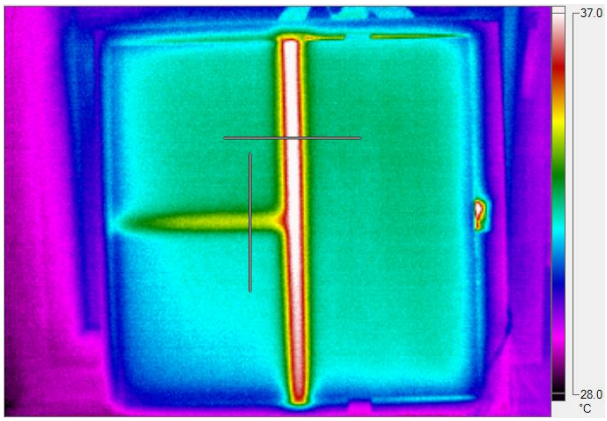

Figure 5.3: *Example of raw thermal image plotted in apparent temperature obtained in static regime for the configuration2-A presented in Figure 5.2*

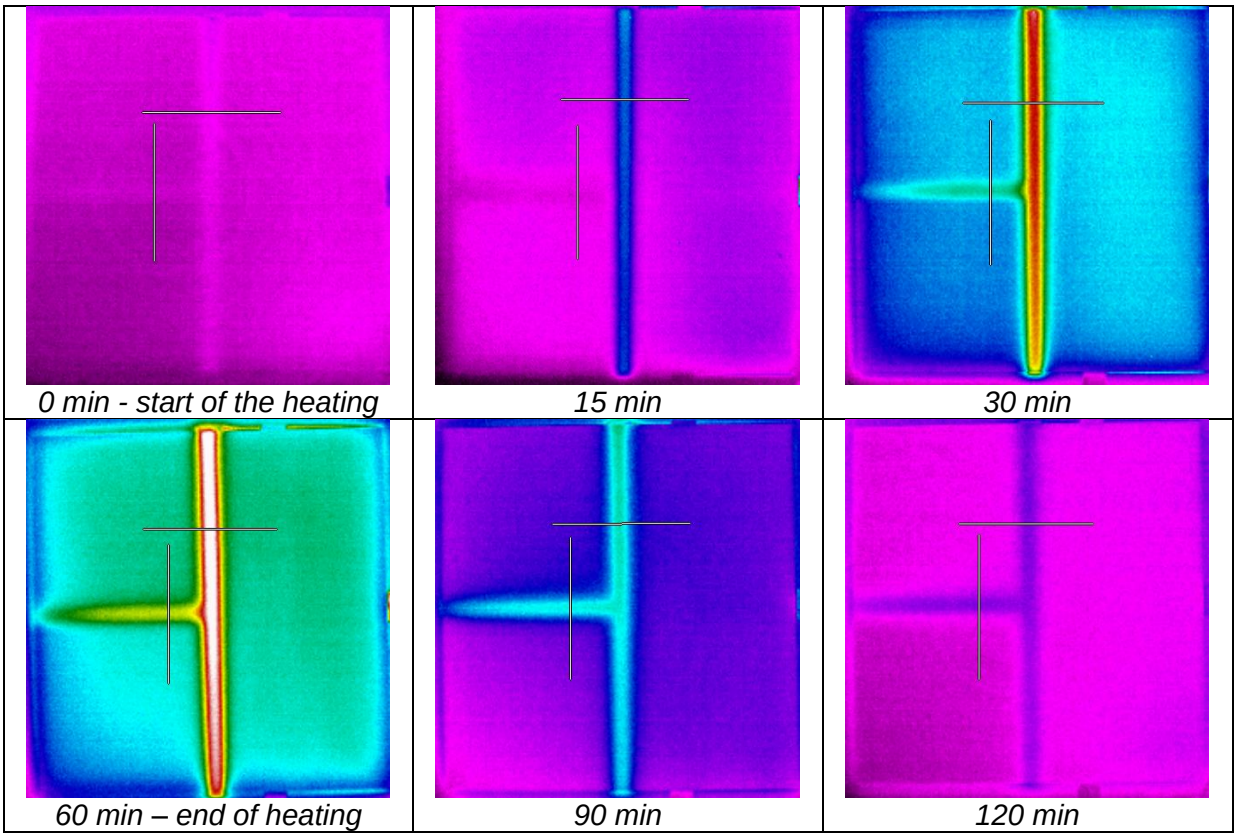

Figure 5.4: *Example of raw thermal images plotted in apparent temperature obtained in dynamic regime for the configuration2-A, after increasing experiment durations*

5.3 Measurement in dynamic regime

5.3.1 Using the heating film included in the test-bench

To illustrate the possible visualization of thermal bridges in dynamic regime, we will first start using the heating film included in the wall. In this experiment, the film is heated with a constant power during one hour. Then, the heating is stopped (relaxation phase). Several images are acquired during a total duration of 2 hours.

In Figure 5.4, we have reported six thermal images recorded at different heating and relaxation durations. These images are plotted using apparent temperature and using the same colormap and thermal range than in Figure 5.3 (from 28.0 to 37.0°C). Again, these images were recorded using the configuration 2-A of the test bench. In each image, lines indicate the position of linear temperature profiles across both thermal bridges plotted in Figure 5.5 for the same experiment durations.

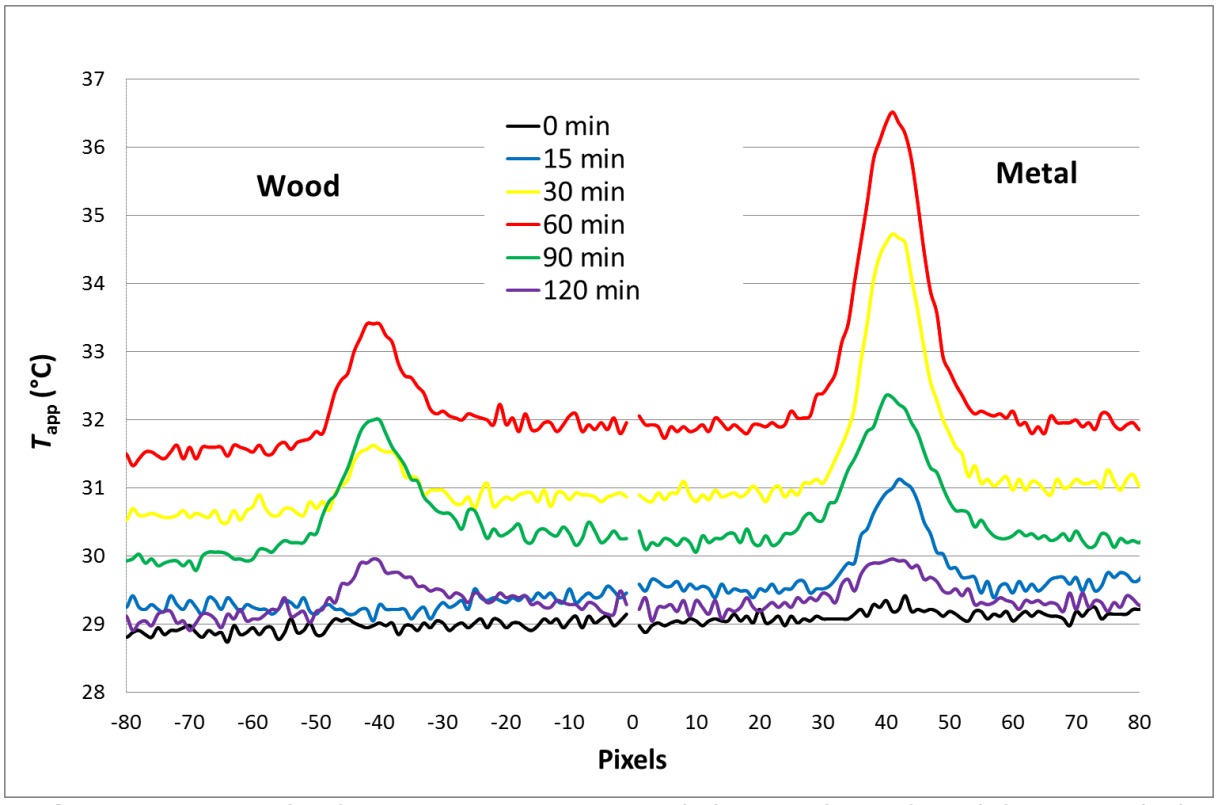

Figure 5.5: *Example of apparent temperature variations on the surface; left part: vertical profile corresponding to the wood rod; right part: horizontal profile corresponding to the metal tube*

Just before heating, thermal bridges are not visible, because the wall is in thermal equilibrium with a stable ambiance, so its temperature is uniform. The vertical metallic thermal bridge appears first due its lower thermal inertia. Moreover, its lower thermal resistance allows observing rapidly a temperature contrast much greater than the NETD of the IR camera. Then, the second thermal bridge (horizontal pine wood rod) appears, due its higher thermal inertia, and with a much lower thermal contrast magnitude. After one hour of heating, a

quasi-stable regime is reached and we observe a temperature contrast three times higher for the metallic thermal bridge (about 4.5K versus 1.5K).

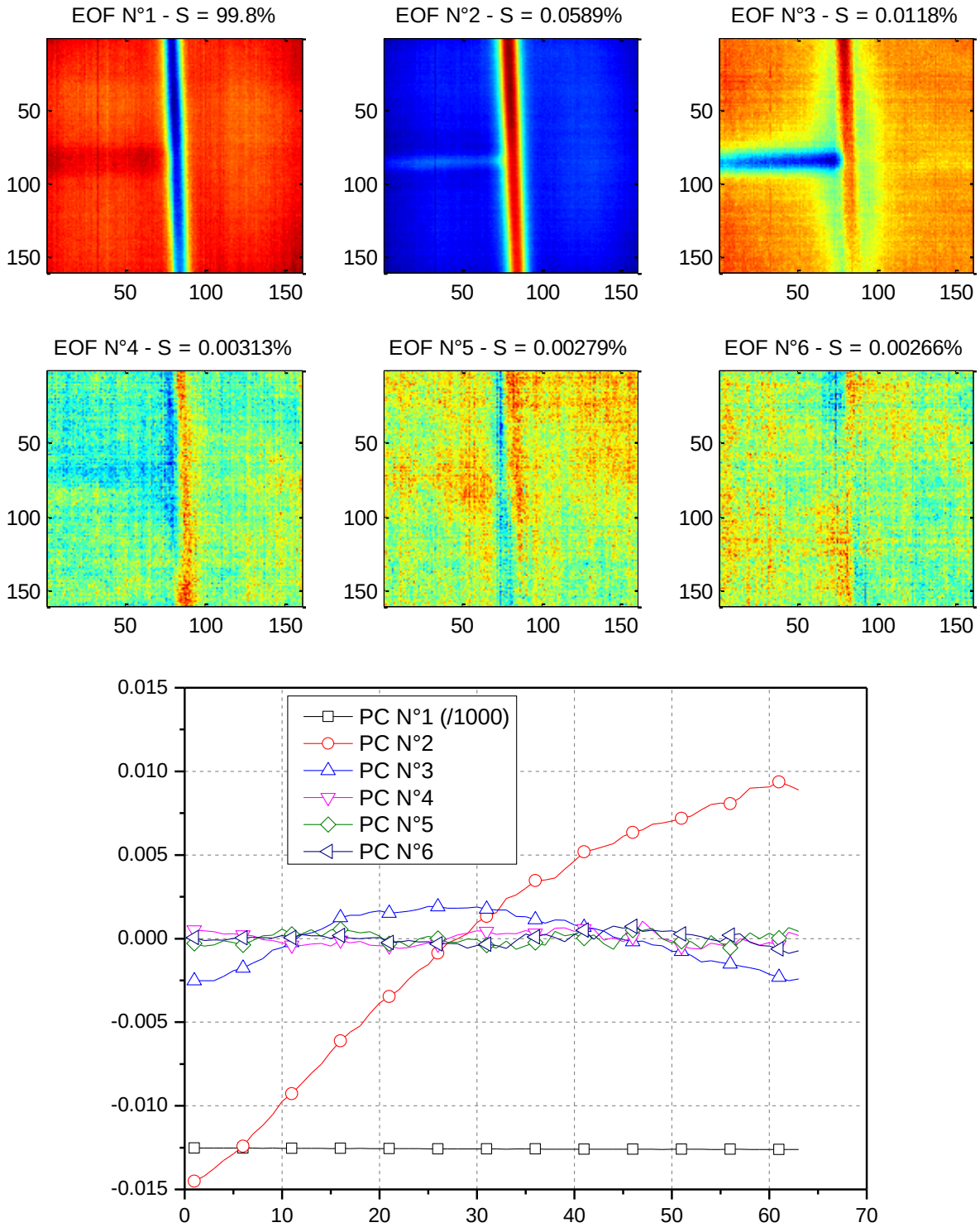

Figure 5.6: *Example of EOFs (top figure) and PCs (bottom figure) obtained after SVD analysis (amplitude of PC 1 was divided by 1000)*

During the subsequent relaxation phase, we observe a rapid decrease of thermal contrast for the metallic thermal bridge, again due to its lower thermal inertia. After that, thermal signatures of both thermal bridges decrease slowly and remain almost identical one to the other. At this stage, the thermal inertia of the whole structure predominates.

In this experiment, as the heating source is placed behind the insulating layer including thermal bridges, we are very sensitive to the transmission coefficient of the thermal bridge and also its thermal inertia.

5.3.2 Using an external thermal excitation

Another way to detect thermal bridges inside a wall is to use an external thermal excitation that can be for instance heating lamps or fans. The experimental conditions remain identical as the ones described in the preceding section. At a given time, the heating source is switched on and thermal images of the wall surface are acquired at a given sampling frequency.

As mentioned before in section 3.2.2, it is possible to use one of the analysis techniques commonly used in NDT to identify the presence of thermal bridges. For instance the SVD analysis (principle was detailed in section 3.2.2.2) was applied to a sequence of thermal images corresponding to configuration 2-A. The result is presented in Figure 5.6. As observed, the first three Orthogonal Empirical Functions contain the main interesting information of the thermal images sequence. This is confirmed by the associated singular values and Principal Components whose amplitude is lower and lower. EOF N°1 can generally be assimilated to a mean thermal image that would be computed from the whole image sequence. In this experiment, we can see that the contributions of vertical and horizontal thermal bridges are seen separately in EOFs N°2 and 3 respectively.

Moreover, with this technique, it is possible:

- to store only the first EOFs and principal components (data compression);
- to rebuild thermal images sequence using the first EOFs (filtering).

6. Conclusion

In the first part of this tutorial, we have illustrated a methodology to estimate the temperature of a surface from the intensity map (or apparent temperature map) obtained using an IR camera. It was shown that this evaluation is sensitive to several parameters, particularly surface emissivity and mean-radiant temperature. For surfaces with high emissivity and for small differences between surface temperature and mean-radiant temperature, a surface temperature can be estimated accurately. However, for low-emissivity surfaces, the result is strongly dependent on the knowledge of the mean-radiant temperature and thus estimation of a surface temperature becomes difficult. In the second part of this tutorial, we have seen that IR thermography is an interesting tool for the characterization of a building wall thermal insulation. At this time, quantitative data such thermal transmittance coefficient of a wall or of thermal bridges can be estimated in static conditions. Active thermography is interesting to detect the presence of thermal irregularities whatever weather conditions. It was shown that the use of NDT analysis techniques allows increasing the SNR ratio and make possible to use micro-bolometers cameras for such inspections.

References

[Asdrubali 2012] F. Asdrubali, G. Baldinelli, F. Bianchi. A quantitative methodology to evaluate thermal bridges in buildings. Applied Energy, 97, pp: 365-373, 2012

[ASTM E1862-97] Standard Test Methods for Measuring and Compensating for Reflected Temperature Using Infrared Imaging Radiometers, ASTM E 1862 – 97 Standard, 1997

[Balageas 2015] D.L. Balageas, J-M. Roche, F. Leroy, W. Liu, A.M. Gorbach, The thermographic signal reconstruction method: a powerful tool for the enhancement of transient thermographic images. Biocybernetics and biomedical engineering, 35, pp. 1-9, 2015

[Balageas 2016] D. Balageas, X. Maldague, D. Burleigh, V-P. Vavilov, B. Oswald-Tranta, J.-M. Roche, C. Pradere, G. M. Carlomagno, Thermal (IR) and Other NDT Techniques for Improved Material Inspection, Journal of Nondestructive Evaluation, 35:18, 2016, DOI 10.1007/s10921-015-0331-7

[Balaras 2002] C-A. Balaras, A-A. Argiriou. Infrared thermography for building diagnostics. Energy and Buildings, 34(2) :171–83, 2002.

[Chaffar 2012] K. Chaffar, Thermographie active appliquée à la caractérisation in-situ de parois de bâtiment, PhD Thesis, Université d'Artois, 2012 (in french)

[Cojan 1995] Y. Cojan, Propagation du rayonnement dans l'atmosphère, Techniques de l'ingénieur, Réf. : E4030 V2, 1995 (in french)

[Datcu 2005] S. Datcu, L. Ibos, Y. Candau, S. Matteï, Improvement of building wall surface temperature measurements by infrared thermography, Infrared Physics & Technology 46, pp. 451–467, 2005

[Douguet 2018] R. Douguet, T-T. Ha, V. Feuillet, J. Meulemans, L. Ibos, A novel experimental method for the in situ detection of thermal bridges in building envelopes based on active infrared thermography and singular value decomposition analysis, 14th QIRT Conference, Berlin, July 2018

[Dumoulin 2010] J. Dumoulin, L. Ibos, C. Ibarra-Castanedo, A. Mazioud, M. Marchetti, X. Maldague, A. Bendada, Active infrared thermography applied to defect detection and characterization on asphalt pavement samples: comparison between experiments and numerical simulations, Journal of Modern Optics, 57, pp. 1759-1769, 2010

[Dumoulin 2011] J. Dumoulin, L. Ibos, M. Marchetti, A. Mazioud. Detection of non-emergent defects in asphalt pavements samples by long pulse and pulse phase infrared thermography. European Journal of Environmental and Civil Engineering, 15, pp 557-574, 2011

[Farkh 2009] S. Farkh, T. Bel, Les ponts thermiques dans le bâtiment – mieux les connaître pour mieux les traiter, Ed. CSTB, November 2009 (in french)

[François 2019] A. François, L. Ibos, V. Feuillet, J. Meulemans, Building thermal bridge heat losses quantification by infrared thermography. Steady-state evaluation and uncertainty calculation, CISBAT Conference, Lausanne, September 2019

[Grinzato 1998] E. Grinzato, V. Vavilov, T. Kauppinen, Quantitative infrared thermography in buildings, Energy and Buildings, 29, pp. 1–9, 1998

[GUM 1995] Evaluation of measurement data – Guide to the expression of uncertainty in measurement, Doc. BIPM, JCGM 100:2008

[Ibos 2015] L. Ibos, J-P. Monchau, V. Feuillet, Y. Candau, A comparative study of in-situ measurement methods of a building wall thermal resistance using infrared thermography, Twelfth International Conference on Quality Control by Artificial Vision 2015; Le Creusot, France, in Proc. SPIE; 9534; 95341I; 2015

[Ibos 2016] L. Ibos, J-P. Monchau, V. Feuillet, J. Dumoulin, P. Ausset, J. Hameury, B. Hay, Investigation of the directional emissivity of materials using infrared thermography coupled with a periodic excitation, 13th QIRT Conference, Gdansk, July 2016

[ISO 14683] Ponts thermiques dans les bâtiments - Coefficient linéique de transmission thermique- Méthodes simplifiées et valeurs par défaut, ISO 14683:2007

[ISO 6946] Building components and building elements — Thermal resistance and thermal transmittance — Calculation method, ISO 6946:2007(E)

[ISO 9869-1] Thermal insulation — Building elements — In-situ measurement of thermal resistance and thermal transmittance —Part1:Heat flow meter method, ISO 9869-1: 2014

[ISO 9869-2] Thermal insulation — Building elements — In-situ measurement of thermal resistance and thermal transmittance —Part 2: Infrared method for frame structure dwelling, ISO 9869-2: 2018

[Kato 2007] S. Kato, K. Kuroki, S. Hagihara, Method of in-situ measurement of thermal insulation performance of building elements using infrared camera, 6th International Conference on Indoor Air Quality, Ventilation & Energy Conservation in Buildings (IAQVEC), Sendai, Japan, October 2007.

[Krapez 1994] J.-C. Krapez, F. Lepoutre, D. Balageas. Early detection of thermal contrast in pulsed stimulated ther-mography. Journal de Physique IV Colloque, 1994, 04 (C7), pp.C7-47-C7-50. 10.1051/jp4:1994712. jpa-00253173

[Krapez 2012] J.-C. Krapez, C. Chatelard, J.-F. Nouvel, P. Déliot, Combined airborne thermography and visible-to-near infrared reflectance measurement for soil moisture mapping, 11th QIRT Conference, Naples, June 2012

[Kauder 2005] L. Kauder, Spacecraft Thermal Control Coatings References. NASA-TP-2005-212792, 2005.

[Kylili 2014] A. Kylili, P-A. Fokaides, P. Christou, S-A. Kalogirou, Infrared thermography (IRT) applications for building diagnostics: A review, Applied Energy, 134, pp. 531–49, 2014

[Larbi Youcef 2011] M-H-A. Larbi Youcef, V. Feuillet, L. Ibos, Y. Candau, P. Balcon, A. Filloux, Quantitative diagnosis of insulated building walls of restored old constructions using active infrared thermography, Quantitative InfraRed Thermography Journal, 8, pp. 65-87, 2011

[Lorrain 1979] P. Lorrain, D-R. Corson, Champs et ondes électromagnétiques, Ed. Armand Collin, Paris, 1979 (in french)

[Madruga 2010] F-J. Madruga, C. Ibarra-Castanedo, O-M. Conde, J-M. López-Higuera, X. Maldague, Infrared thermography processing based on higher-order statistics. NDT&E International. 43, pp. 661–666, 2010

[Maldague 1996] X. Maldague, S. Marinetti, Pulse phase infrared thermography. Journal of Applied Physics, 79, pp. 2694–2698, 1996

[Maldague 2001] X. Maldague, Theory and practice of infrared technology for non-destructive testing, , Ed. John Wiley & Sons, 2001

[Marinetti 2004] S. Marinetti, E. Grinzato, P-G. Bison, E. Bozzi, M. Chimenti, G. Pieri, O. Salvetti O. Statistical analysis of IR thermographic sequences by PCA. Infrared Physics & Technology. 46, pp. 85–91, 2004

[Monchau 2013] J-P. Monchau, Mesure d'émissivité pour la thermographie infrarouge appliquée au diagnostic quantitatif des structures, PhD Thesis, Université Paris-Est, 2013 (in french)

[Monchau 2018] J-P. Monchau, J. Hameury, Mesure de l'émissivité thermique, Techniques de l'Ingénieur, R2747 V1, June 2018 (in french)

[Mouhoubi 2016] K. Mouhoubi, Thermographie infrarouge stimulée appliquée à la détection et à la caractérisation d'altérations structurales de peintures murales du patrimoine, PhD Thesis, Université de Reims Champagne-Ardennes, 2016 (in french)

[NF 13187] Performance thermique des bâtiments – Détection qualitative des irrégularités thermiques sur les enveloppes de bâtiments – Méthode infrarouge, NF EN 13187:1999

[Pajani 2011] D. Pajani, Surface équivalente d'irrégularité ou de défaut (Seid) et mesure du "U" par la méthode du Seid, Thermogram'2011 Conference, Châlons en Champagne, France, 2011 (in french)

[Pajani 2012] D. Pajani, La thermographie du bâtiment – Principes et applications du diagnostic thermographique. Ed. Eyrolles, Paris, 2012 (in french)

[Rajic 2002] N. Rajic N, Principal component thermography for flaw contrast enhancement and flaw depth characterisation in composite structures, Composite Structures, 58, pp. 521–528, 2002

[RT 2012] Réglementation thermique, Ed. CSTB, 2012 (in French)

[Sacadura 2015] J-F Sacadura, Transferts thermiques, Ed Lavoisier Tec & Doc, Paris, 2015 (in french)

[Shepard 2003] S-M. Shepard, J-R. Lhota, B-A. Rubadeux, D. Wang, T. Ahmed, Reconstruction and enhancement of active thermographic image sequences, Optical Engineering, 42, pp. 1337-1342, 2003.

[Theodosiou 2008] T-G. Theodosiou, A-M. Papadopoulos, The impact of thermal bridges on the energy demand of buildings with double brick wall constructions, Energy and Buildings, 40, pp. 2083-2089, 2008

[Vrabie 2012] V. Vrabie, E. Perrin, J-L. Bodnar, K. Mouhoubi, V. Detalle, Active IR thermography processing based on higher order statistics for nondestructive evaluation, 20th European Signal Processing Conference (EUSIPCO), Bucharest, August 2012

[Yang 2017] Y. Yang, Innovative non-destructive methodology for energy diagnosis of building envelope, PhD Thesis, Université de Bordeaux, 2017

Tutorial 5: Periodic heating methods for materials thermal characterisation

Laetitia PEREZ[1], Laurent AUTRIQUE[1]

[1] Laboratoire Angevin de Recherche en Ingénierie des Systèmes, Angers, France

E-mail: laetitia.perez@univ-angers.fr
laurent.autrique@univ-angers.fr

Abstract – Periodic heating methods for materials thermal characterization are commonly used when observable signal/noise ratio or sample thermo stability are low. This workshop is intended to illustrate the ways of analysing the sample thermal behaviour in order to estimate thermal properties. The experimental apparatus is based on cheap heating device and temperature measurement system so as to make it adaptable for educational purpose. The thermal modelling is based on complex temperature approach (amplitude and phase lag of temperature evolution). The parameter estimation procedure is developed (sensitivity analysis, errors sources analysis with a particular attention on noise effects, optimal conception of experiment ...). Two estimation strategies (complex temperature space distribution or frequency evolution) are described, illustrated and compared. Additional information on derived methods usable on problems with increased geometrical complexity with both analytical and finite elements modelling is detailed.

Nomenclature

x	space variable , m	t	time variable, s
e	metallic sample height, m	f	frequency, Hz
α	diffusivity, $m^2.s^{-1}$	ω	period, s^{-1}
μ	diffusion length, m	Q	heating flux, $W.m^{-2}$
ρ	mass density, $kg.m^{-3}$	C	specific heat, $J.kg^{-1}.K^{-1}$
k	conductivity, $W.m^{-1}.K^{-1}$	φ	phase lag $rad\ or\ °$

1. Introduction

Dynamic methods of measuring solid materials thermal properties are based on the observation of the samples behaviour when submitted to a thermal excitation of known characteristics. These dynamic methods are usually classified according to the type of thermal excitation, the more usual being the step function, the Dirac pulse, the sine-wave modulation and more recently the pseudo-random sequences. Each of these methods categories includes advantages and inconveniences that make that either can be more applicable in a given configuration. We will only develop here the methods based on a periodic excitation, the other categories being illustrated in other workshops of this school.

Introduction of periodic methods for determining the thermal parameters of homogeneous solid materials is due to Ångström (1863) [1]. The sample is a long thin rod (length >> diameter) of which an extremity is submitted to a temperature sinusoidal modulation. The thermal parameters are deducted from the evolution of temperature oscillations attenuation and phase lag along the bar. Nearly one century later, Cowan (1961) [2] extended this type of method to the case of disk-shaped samples (diameter >> thickness) submitted to a sinusoidal modulation of flux on one face. Since, the principle has been applied to the characterization of multi-layered materials (coating, gluing), orthotropic materials (long fibre, woven composites) this from macroscopic scale to microscopic scale [3] and to detect default in composites' materials [4].

2. Concepts for periodic heating method

We are now going to introduce specific tools for the use of this kind of periodic methods. The complex temperatures method will be used for ease modelling of the heat transfer within the sample. The lock-in detection will allow extracting the attenuation and phase lag of temperature oscillations from a sensor output.

2.1 Complex Temperatures

When a solid media submitted to a sinusoidal excitation reached a steady-state, if the heat transfer equations are linear (temperature independent parameters), the temperature in all point is the sum of a steady component and a sinusoidal component of same period that excitation.

$$T(\mathbf{r},t) = T_c(\mathbf{r}) + T_s(\mathbf{r},t) \quad \text{with } T_s(\mathbf{r}) = A(\mathbf{r})\cos\left(\omega t + \varphi(\mathbf{r})\right)$$

where $A(\mathbf{r})$ represents the amplitude and $\varphi(\mathbf{r})$ the phase lag with respect to the excitation, of temperature oscillations at location $(\mathbf{r})$ (**Figure 1**). The sinusoidal component can be written as:

$$T_s(\mathbf{r}) = \mathrm{Re}\left(A(\mathbf{r})\exp\left(j\varphi(\mathbf{r})\right)\exp\left(j\omega t\right)\right) = \mathrm{Re}\left(\tilde{T}(\mathbf{r})\exp\left(j\omega t\right)\right)$$

One will call complex temperature the variable $\tilde{T}(\mathbf{r}) = A(\mathbf{r})\exp\left(j\varphi(\mathbf{r})\right)$ that contains the information on amplitude and phase of the temperature oscillations. It results from the same equations that $T(\mathbf{r},t)$ adapted to the sinusoidal steady state.

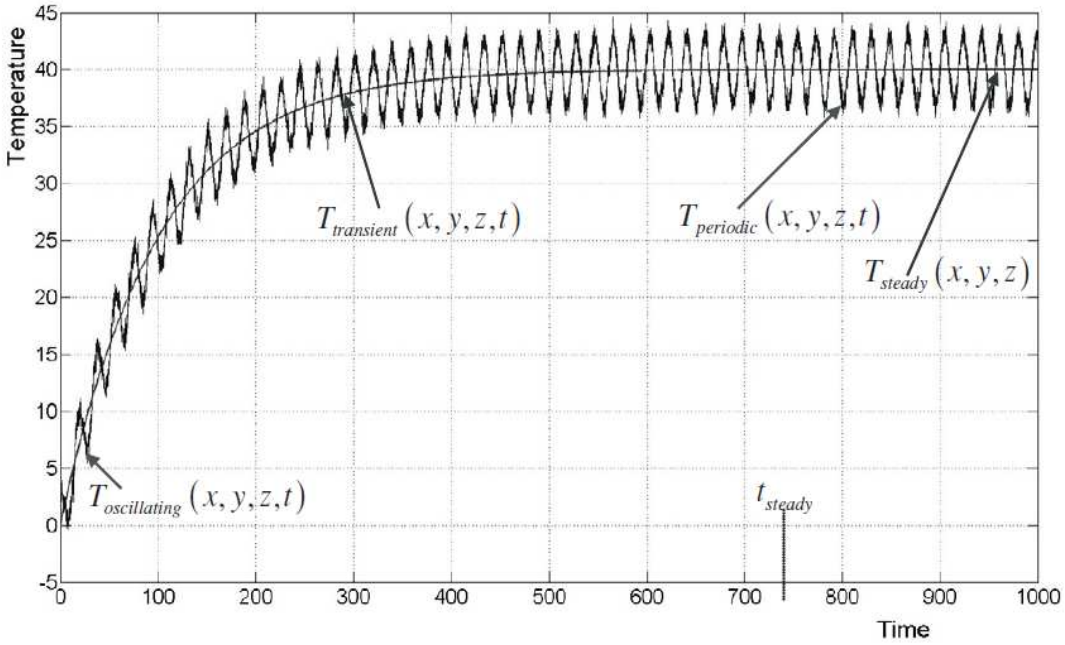

Figure 1: *Phase lag and modulus definition*

Thus,

- the heat transfer equation within the solid $\Delta T = \frac{1}{a}\frac{\partial T}{\partial t}$ becomes $\Delta \tilde{T} = j\frac{\omega}{a}\tilde{T}$
- the Neumann condition equation $-\lambda\frac{\partial T}{\partial x} = \Phi\cos(\omega t)$ becomes $\lambda\frac{\partial \tilde{T}}{\partial x} = \tilde{\Phi}$

The resolution of the problem is brought back to the one of a stationary problem involving stationary limit conditions as well. One will find some examples illustrating the complex temperatures methods in [5].

2.2 Lock-in detection

In a general manner, the periodic methods present some advantages when the signal/noise ratio on observable output is low. This is linked to the processing of the signal coming from the sensor that allows extracting the amplitude and phase of it, even when the noise level is high. The implemented technique is the lock-in detection that will be achieved by a device or software.

2.2.1 Lock-in Amplifier (LIA) [6]

A LIA is a device capable, from any electric input signal and a periodic reference, to select the sinusoidal component of same period that the reference contained in the input signal, and to calculate both module and phase of this component. In addition to this basic function, the LIA significantly decreases the signal band pass and therefore the measurement noise band pass. Its functioning is achieved by several stages that are described in **Figure 2**.

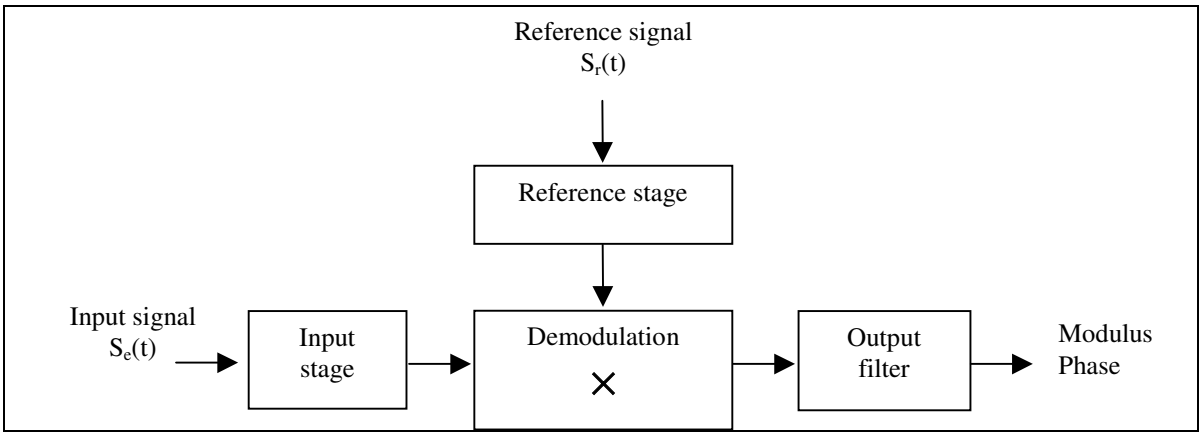

Figure 2*: Functioning principle of a lock-in amplifier*

2.2.1.1 input signal

This input will be the electric signal coming from the sensor: its temporal evolution is unknown but it contains a sinusoidal component of same frequency that the reference signal. This signal can contain a continuous infinity of other frequencies or a discrete series of frequencies.

2.2.1.2 reference signal

This signal is a periodic voltage used as a reference: it represents the temporal evolutions of excitation (mechanical chopper, acousto-optic modulator...). The LIA will extract the sinusoidal component of same frequency that the signal of reference. The fundamental harmonic of this signal allows defining an origin for the phase lag.

2.2.1.3 input stage

This stage is a stage for filtering and formatting the input signal. The operator who decides the nature of the filters used adjusts input analogical filters and amplification gains, acting here as device calibre selection.

2.2.1.4 reference stage

This stage synthesizes two sinusoidal signals of same frequency that the reference, one being in phase with its fundamental harmonic and the second being out of phase of 90 degrees. These signals are $R(t)$ and $R_{90}(t)$ defined by $R(t)=\cos(2\pi f_r t)$ and $R_{90}(t)=\sin(2\pi f_r t)$.

2.2.1.5 demodulator

This stage makes the synchronous demodulation by achieving the multiplication of the input signal by $R(t)$ and $R_{90}(t)$ and provides two signals, $X(t)$ and $Y(t)$ defined by $X(t)=S_e(t)R(t)$ and $Y(t)=S_e(t)R_{90}(t)$.

To illustrate the functioning of the LIA, let us consider an input signal composed of a sine wave of same frequency that the reference (f_r) and a disturbing second one of frequency f_p.

$$S_e(t) = A_r \cos(2\pi f_r t + \varphi_r) + A_p \cos(2\pi f_p t + \varphi_p)$$

Let us write X(t) and Y(t) for $S_e(t)$.

$$X(t) = S_e(t)\cos(2\pi f_r t) = (A_r \cos(2\pi f_r t + \varphi_r) + A_p \cos(2\pi f_p t + \varphi_p))\cos(2\pi f_r t)$$

$$= A_r \cos(2\pi f_r t + \varphi_r)\cos(2\pi f_r t) + A_p \cos(2\pi f_p t + \varphi_p)\cos(2\pi f_r t)$$

$$= \frac{A_r}{2}\cos(\varphi_r) + \frac{A_r}{2}\cos(4\pi f_r t + \varphi_r) + \frac{A_p}{2}\cos(2\pi(f_p + f_r)t + \varphi_p) + \frac{A_p}{2}\cos(2\pi(f_p - f_r)t + \varphi_p)$$

$$Y(t) = S_e(t)\sin(2\pi f_r t) = (A_r \cos(2\pi f_r t + \varphi_r) + A_p \cos(2\pi f_p t + \varphi_p))\sin(2\pi f_r t)$$

$$= A_r \cos(2\pi f_r t + \varphi_r)\sin(2\pi f_r t) + A_p \sin(2\pi f_p t + \varphi_p)\cos(2\pi f_r t)$$

$$= -\frac{A_r}{2}\sin(\varphi_r) + \frac{A_r}{2}\sin(4\pi f_r t + \varphi_r) + \frac{A_p}{2}\sin(2\pi(f_p + f_r)t + \varphi_p) - \frac{A_p}{2}\sin(2\pi(f_p - f_r)t + \varphi_p)$$

Both signals, *X(t)* and *Y(t)*, are the sum of a steady-state component containing the information on modulus and phase, and of periodic components at disturbing frequencies $2f_r$, f_p-f_r and f_p+f_r.

2.2.1.6 output filter

This stage is constituted of a programmable low pass filter applied to *X(t)* and *Y(t)* in order to eliminate the disturbing periodic components and to select the steady-state component only. Proximity between the disturbing frequency f_p and f_r determines the band pass to be used for the low pass filter. Therefore, the LIA takes into account for the output only the part of the input signal belonging to the frequency domain centered on f_r and of same width that the output filter band pass. One finally gets two quantities $M = A_r/2\cos(\varphi_r)$ and $N = -A_r/2\sin(\varphi_r)$ that allows modulus and phase calculation according to:

$$A_r = \sqrt{M^2 + N^2} \text{ and } \varphi_r = -tan^{-1}\left(\frac{N}{M}\right)$$

To recapitulate, the LIA functioning comprises two steps:

- the input signal of whatever shape is multiplied by a sinusoidal signal at the reference frequency. The spectrum of the resulting signal is that of the input signal shifted by the quantity - f_r and $+f_r$
- a low pass filter is then applied to this signal. The output signal is slowly variable and centred on $M/2\cos(\varphi)$ if the component at f_r of the entry signal $M\cos(2\pi f_r \times t + \phi)$.

The LIA extracts, from a signal of whatever shape, the sinusoidal component at a reference frequency.

2.2.2 Lock-in algorithm

In some cases, it can be impossible to incorporate a LIA in the measurement chain. It is the case, for example, when one wants to get a complex temperature mapping (module and

phase) from a thermography recording. For every pixel *(i,j)* of the picture, the aim is to calculate its phase and amplitude from the recorded thermogram. It is possible to simulate by software the functioning of a LIA. Considering a sequence of 512 temperature values noted *T(ndt)*, *n∈{0,.. ,511}* where *dt* is the sampling time, the algorithm is the following one:

1. Calculation of *X(ndt) n∈{0,..,511}* and *Y(ndt) n∈{0,..,511}* according to

$$X(n) = T(ndt)\cos(2\pi f_r ndt) \text{ and } Y(n) = T(ndt)\sin(2\pi f_r ndt)$$

where f_r is the heating frequency (reference)

2. Calculation of *M* and *N* according to

$$M = \frac{1}{512}\sum_{k=0}^{511} X(k) \text{ et } N = \frac{1}{512}\sum_{k=0}^{511} Y(k)$$

These formulas are valid if the record covers an integer number of heating periods.

Calculation of temperature modulus and phase according to

$$M = \sqrt{M^2 + N^2} \text{ et } \varphi = -\tan^{-1}(\frac{N}{M})$$

This educational workshop is based on a cheap heating device in order to illustrate periodic methods for thermal diffusivity characterization.

3. Periodic method for thermal diffusivity identification

3.1. Aims

In this paragraph, periodic method principle is presented. Heat transfers in a thin metallic sample exposed to a periodic excitation are considered. Analytical solution is developed and numerical results have to be compared to experimental results obtained for reference materials. Early knowledge is thermal system science and numerical analysis.

3.2. Mathematical modelling

Let us consider a thin plane metallic sample. Diffusion length is defined by $\mu = \sqrt{\frac{2\alpha}{\omega}} = \sqrt{\frac{\alpha}{\pi f}}$ and for sample height e such as $e \ll \mu$, temperature gradients can be neglected in the sample thickness. Periodic excitation is $Q(x,t) = \begin{cases} Q(t) & \text{if} \quad x < 0 \\ 0 & \text{if} \quad x \geq 0 \end{cases}$ and a moving mask leads to the control of origin position $O(x=0)$. Heat transfers are 1D (see **Figure 3**).

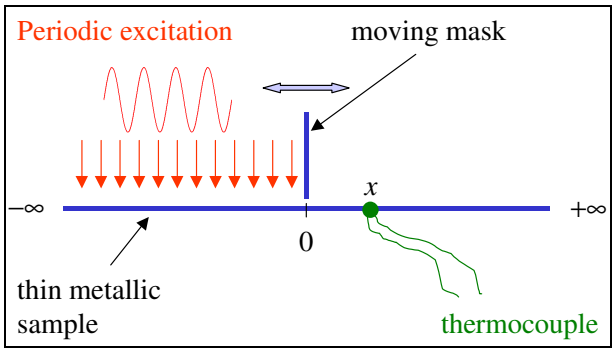

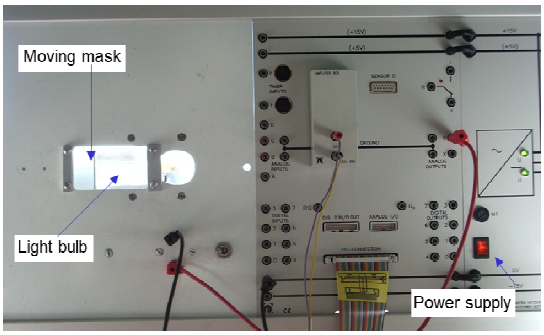

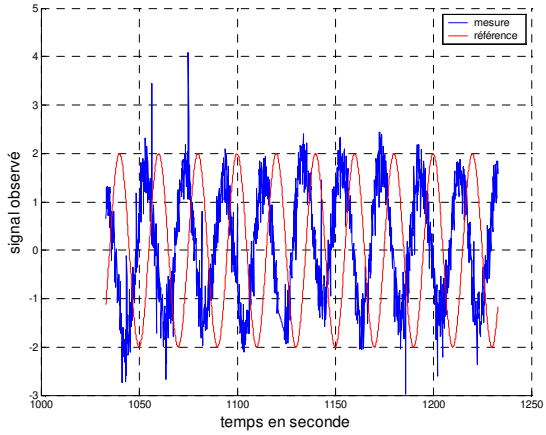

Distance $x = \delta$ from moving mask

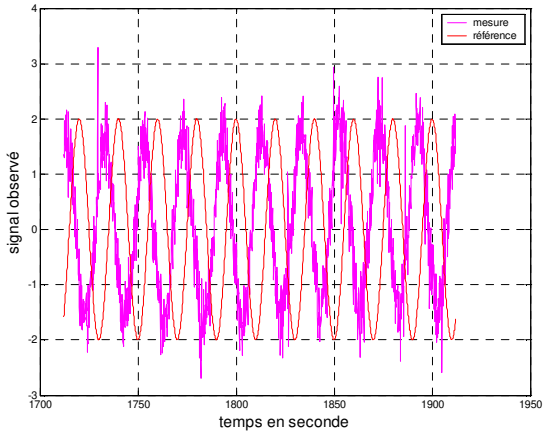

Distance $\delta - 1mm$ from moving mask

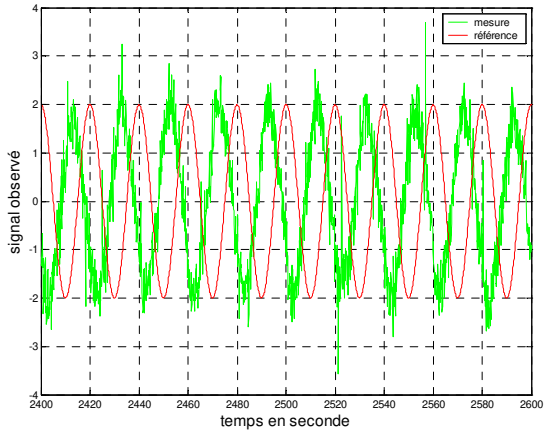

Distance $\delta - 2mm$ from moving mask

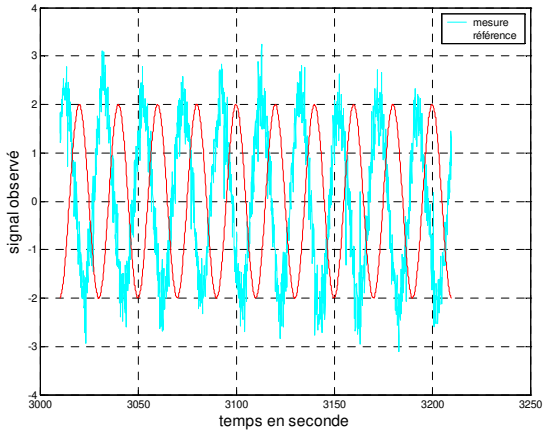

Distance $\delta - 3mm$ from moving mask

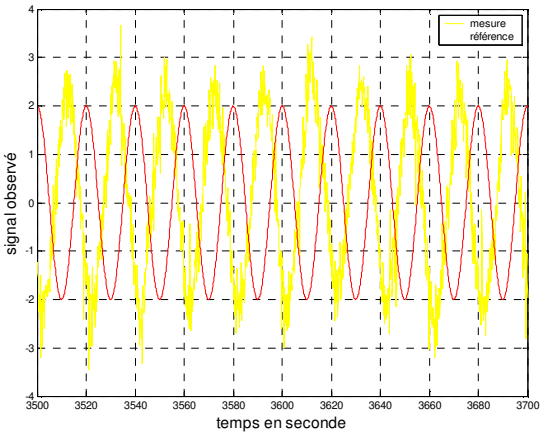

Distance $\delta - 4mm$ from moving mask

Figure 3*: Studied configuration and some experimental results*

Temperature distributions from the initial temperature (assumed to be equal to ambient temperature) are described by the following equation:

$$\rho Ce\frac{\partial T(x,t)}{\partial t} + hT(x,t) - ke\frac{\partial^2 T(x,t)}{\partial x^2} = Q(x,t) \tag{1}$$

Let us consider the quite general following formulation for the periodic heating flux $Q(x,t) = \begin{cases} Qe^{j\omega t} & \text{if} \quad x < 0 \\ 0 & \text{if} \quad x \geq 0 \end{cases}$, then complex temperature is: $T(x,t) = T(x,\varphi)e^{j\omega t}$ where φ is the temperature phase lag relating to the input excitation. Then previous equation reads as follows:

$$j\omega\rho CeT(x,\varphi) + hT(x,\varphi) - ke\frac{\partial^2 T(x,\varphi)}{\partial x^2} = \begin{cases} Q & if \quad x < 0 \\ 0 & if \quad x \geq 0 \end{cases} \tag{2}$$

Introducing $c_1 = j\omega\rho Ce + h$, several situations are encountered:

- for $x > 0$: $c_1 T(x,\varphi) - ke\frac{\partial^2 T(x,\varphi)}{\partial x^2} = 0$. Solution is $T(x,\varphi) = K_1 exp\left(\pm\sqrt{\frac{c_1}{ke}}x\right)$. Since temperature evolution is finite ($\left|T(\infty,\varphi)\right| = 0$) then $T(x,\varphi) = K_1 exp\left(-\sqrt{\frac{c_1}{ke}}x\right)$.
- for $x < 0$: $c_1 T(x,\varphi) - ke\frac{\partial^2 T(x,\varphi)}{\partial x^2} = Q$. Solution is $T(x,\varphi) = K_2 exp\left(\pm\sqrt{\frac{c_1}{ke}}x\right) + \frac{Q}{c_1}$. Since $\left(T(-\infty,\varphi) < \infty\right)$ then $T(x,\varphi) = K_2 exp\left(+\sqrt{\frac{c_1}{ke}}x\right) + \frac{Q}{c_1}$,

- for $x=0$, temperature continuity $\left(K_1 = K_2 + \frac{Q}{c_1}\right)$ and temperature gradient continuity $\left(-K_1 = K_2\right)$ leads to: $K_1 = \frac{Q}{2c_1}$ et $K_2 = -\frac{Q}{2c_1}$.

Thus solution of equation (2) is:

$$T(x,\varphi) = \begin{cases} \frac{Q}{c_1} - \frac{Q}{2c_1} exp\left(+\sqrt{\frac{c_1}{ke}}x\right) & if \quad x<0 \\ \frac{Q}{2c_1} exp\left(-\sqrt{\frac{c_1}{ke}}x\right) & if \quad x\geq 0 \end{cases}$$

A thermal system time characteristic is $\tau = \frac{\rho Ce}{h}$, then:

$$T(x,\varphi) = \frac{Q}{2\omega\rho Ce\left(j+\frac{1}{\omega\tau}\right)} exp\left(-\sqrt{\frac{\omega}{\alpha}\left(j+\frac{1}{\omega\tau}\right)}x\right) \qquad if \quad x\geq 0$$

and for $z = \frac{1}{\omega\tau} + j$; $|z| = \frac{1}{\omega\tau}\sqrt{1+\omega^2\tau^2}$ and $\sqrt{z} = \sqrt{\frac{|z|+\frac{1}{\omega\tau}}{2}} + j\sqrt{\frac{|z|-\frac{1}{\omega\tau}}{2}}$, one obtains:

$$T(x,\varphi) = \frac{Q(1-\omega\tau j)}{2\omega\rho Ce\sqrt{1+\omega^2\tau^2}} exp\left(-\frac{x}{\mu}\left(\sqrt{|z|+\frac{1}{\omega\tau}} + j\sqrt{|z|-\frac{1}{\omega\tau}}\right)\right) \qquad if \quad x\geq 0$$

Thus, the following formulation is proposed $\left(\theta = Arg\left(1-\omega\tau j\right)\right)$:

$$T(x,\varphi) = \frac{Q}{2\omega\rho Ce} exp\left(-\frac{x}{\mu}\sqrt{|z|+\frac{1}{\omega\tau}}\right) exp\left(-j\left(\frac{x}{\mu}\sqrt{|z|-\frac{1}{\omega\tau}} - \theta\right)\right) \qquad if \quad x\geq 0$$

For $\omega\tau << 1$, $|z| \approx 1$ and temperature modulus for $x\geq 0$ is:

$$\left|T(x,\varphi)\right| \approx \frac{Q}{2\omega\rho Ce} exp\left(-\frac{x}{\mu}\right) \qquad if \quad x\geq 0 \qquad (3)$$

Moreover for $\omega\tau << 1$, then $\theta \approx -\frac{\pi}{2}$ and for $x \geq 0$:

$$Arg\left(T\left(x,\varphi\right)\right) = \varphi \approx -\frac{x}{\mu} - \frac{\pi}{2} \qquad if \quad x \geq 0 \tag{4}$$

3.3. Analysis

In the previous paragraph, it has been shown that temperature modulus and phase lag induced by a periodic excitation depend on thermal diffusivity of the studied material. Then two approaches are proposed (**Figure 4**).

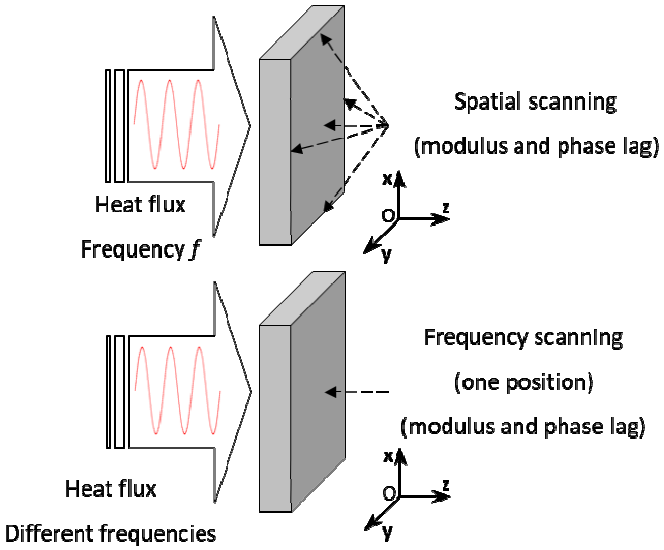

Figure 4*: 2 configurations*

3.3.1. Spatial scanning

- Measurements of temperature modulus at point x for several mask positions are performed and equation (3) is written as:

$$log\left|T\left(x,\varphi\right)\right| \approx log\left(\frac{Q}{2\omega\rho Ce}\right) - \frac{x}{\mu} \tag{5}$$

Drawing $log\left|T\left(x,\varphi\right)\right|$ versus x, gives a straight line and coefficient is equal to $-\frac{1}{\mu} = -\sqrt{\frac{\pi f}{\alpha}}$ (see **Figure 5** for an illustration).

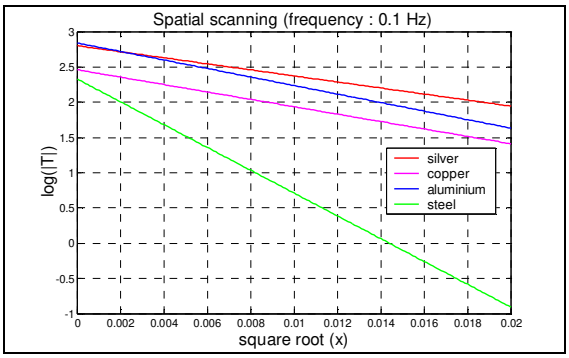

Figure 5: *Temperature modulus for spatial scanning*

- Measurements of temperature phase lag at point x for several mask position are performed. Equation (4) leads to a straight line; coefficient is $-\frac{1}{\mu}=-\sqrt{\frac{\pi f}{\alpha}}$ (see **Figure 6** for an illustration).

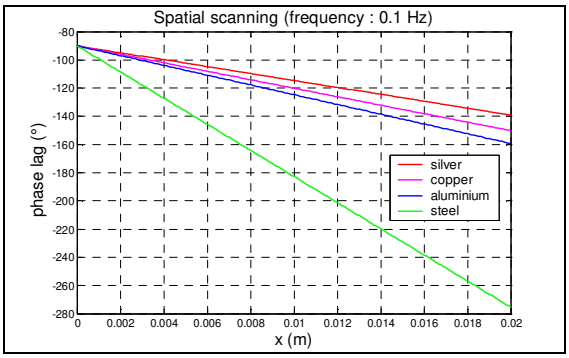

Figure 6: *Phase lag for spatial scanning*

Results are obtained with the following data:

Table 1:

	ρ	C	α
	$kg.m^{-3}$	$J.kg^{-1}.K^{-1}$	$m^2.s^{-1}$
silver	10500	230	$171\ 10^{-6}$
copper	8940	380	$114\ 10^{-6}$
aluminium	2700	860	$86\ 10^{-6}$
steel	7850	490	$12\ 10^{-6}$

Q	e	h
$W.m^{-2}$	m	$W.m^{-2}.K^{-1}$
$5\ 10^{3}$	10^{-4}	10

Table 1: *Parameters*

According to the previous data, it is obvious to verify that for the studied materials, $\tau > 23s$. If $f \geq 0.1Hz$ then $\omega\tau > 14$ and it is verified that $\omega\tau \gg 1$ and solutions given in equations (3) and (4) are assumed to be correct.

3.3.2. Frequency scanning

- Temperature modulus measurements at point x for a fixed mask position are performed for a frequency scanning and equation (3) is written as:

$$log\left|T\left(x,\varphi\right)\right| \approx log\left(\frac{Q}{4\pi\rho Ce}\right) - log\ f - x\sqrt{\frac{\pi f}{\alpha}} \tag{6}$$

Drawing $log\left(\left|T\left(x,\varphi\right)\right|\right) + log\ f$ versus $\sqrt{f}$, gives a straight line, coefficient $-x\sqrt{\frac{\pi}{\alpha}}$ (see **Figure 7** for an illustration).

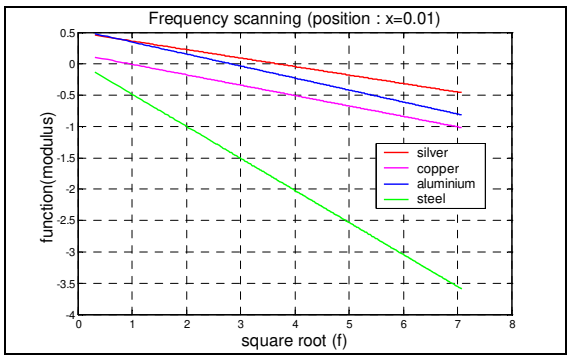

Figure 7 : *Temperature modulus for frequency scanning*

- Phase lag measurements at a given distance to the mask lead for a frequency scanning to a straight line while drawing $\varphi\left(\sqrt{f}\right)$: $Arg\left(T\left(x,\varphi\right)\right) = -x\sqrt{\frac{\pi}{\alpha}}\sqrt{f} - \frac{\pi}{2}$ (see **Figure 8** for an illustration).

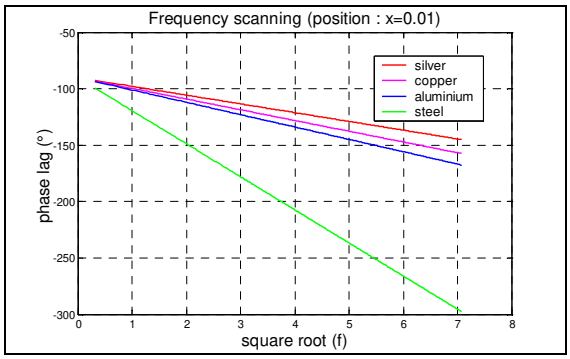

Figure 8 : *Phase lag for frequency scanning*

3.4. Experimentations

Measurements obtained on thin metallic samples are presented in order to verify theoretical results considered above. For well-known materials two experimentations are proposed. Firstly, thermocouple is fixed to the sample and mask is moved for a spatial scanning. Then temperature modulus and phase lag measurements are obtained and results

are compared to **Figures 5** and **6**. Secondly, mask and thermocouple are fixed and a frequency scanning is performed. Modulus and phase lag measurements obtained for several excitation frequencies are compared with theoretical results presented in **Figures 7** and **8**.

4. Sensitivity analysis

4.1. Aims

In this paragraph, thermal system analysis is investigated and sensitivity analysis is proposed in order to estimate the effect of mathematical model input uncertainties. In such a way, it is essential to verify that temperature observations are efficient to identify material diffusivity. Moreover, uncertainties of input parameters which are assumed to be known have not to dramatically affect identification result. Then optimal design of experimental bench can be studied.

4.2. Presentation

Sensitivity analysis is performed in order to estimate the effect of the variation of model input parameter (p_i) on a model output (s_i). In order to ensure that observation $\left(s_i \in \{|T|, \varphi\}\right)$ depends on diffusivity in the studied configuration, it is important to verify that $\frac{\partial s_i}{\partial \alpha}$ is maximum. In such a way, due to uncertainties of well-known parameters, we have to verify that $\frac{\partial s_i}{\partial p_i}$ is minimum ($(p_i \neq f)$ or $(p_i \neq x)$). Then, several situations are presented:

- Spatial scanning
  - Modulus measurement: it is important to verify that $\frac{\partial |T|}{\partial \alpha}$ is great and that (see equation 5) $\left(\frac{\partial |T|}{\partial Q}\right)$, $\left(\frac{\partial |T|}{\partial \rho} = \frac{\partial |T|}{\partial C} = \frac{\partial |T|}{\partial e}\right)$, $\left(\frac{\partial |T|}{\partial f}\right)$ are minimum. Comparisons are proposed on the same figure while $\left(p_i \frac{\partial |T|}{\partial p_i}\right)$ are drawing versus x.
  - Phase lag measurement: $\frac{\partial \varphi}{\partial \alpha}$ has to be maximum and $\left(\frac{\partial \varphi}{\partial f}\right)$ has to be minimum.
- Frequency scanning:
  - Modulus measurement: $\frac{\partial |T|}{\partial \alpha}$ has to be maximum and (see equation 6) $\left(\frac{\partial |T|}{\partial Q}\right)$, $\left(\frac{\partial |T|}{\partial \rho} = \frac{\partial |T|}{\partial C} = \frac{\partial |T|}{\partial e}\right)$, $\left(\frac{\partial |T|}{\partial x}\right)$ have to be minimum. Comparisons are proposed on the same figure while $\left(p_i \frac{\partial |T|}{\partial p_i}\right)$ are drawing versus f.

- Phase lag measurement: $\frac{\partial \varphi}{\partial \alpha}$ has to be maximum and $\left(\frac{\partial \varphi}{\partial x}\right)$ has to be minimum.

Sensitivity functions are derived from equations (3) and (4). Let us consider the following notations $A = \frac{Q}{2\omega\rho Ce}$; $B = \sqrt{\frac{\pi f}{\alpha}}$; $E = \exp\left(-x\sqrt{\frac{\pi f}{\alpha}}\right)$

scanning	observation	Sensitivity functions
spatial	modulus	$\alpha\frac{\partial \lvert T\rvert}{\partial \alpha}$
		$Q\frac{\partial \lvert T\rvert}{\partial Q}$ and $f\frac{\partial \lvert T\rvert}{\partial f}$
		$\rho\frac{\partial \lvert T\rvert}{\partial \rho} = C\frac{\partial \lvert T\rvert}{\partial C} = e\frac{\partial \lvert T\rvert}{\partial e}$
	phase lag	$\alpha\frac{\partial \varphi}{\partial \alpha}$ and $f\frac{\partial \varphi}{\partial f}$
frequency	modulus	$\alpha\frac{\partial \lvert T\rvert}{\partial \alpha}$
		$Q\frac{\partial \lvert T\rvert}{\partial Q}$ and $\rho\frac{\partial \lvert T\rvert}{\partial \rho} = C\frac{\partial \lvert T\rvert}{\partial C} = e\frac{\partial \lvert T\rvert}{\partial e}$
		$x\frac{\partial \lvert T\rvert}{\partial x}$
	phase lag	$\alpha\frac{\partial \varphi}{\partial \alpha}$ and $x\frac{\partial \varphi}{\partial x}$

Table 2: *Sensitivity functions*

Sensitivity functions for a steel sample are presented in **Figures 9, 10, 11** and **12**.

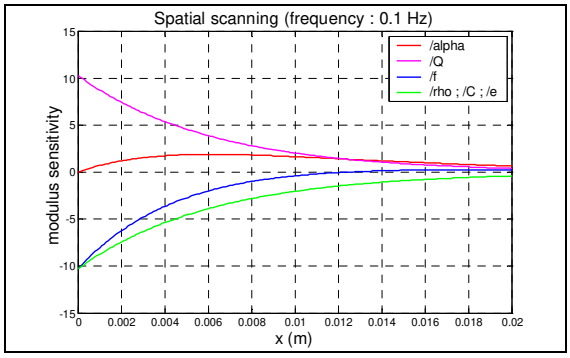

Figure 9: *Modulus sensitivity for spatial scanning*

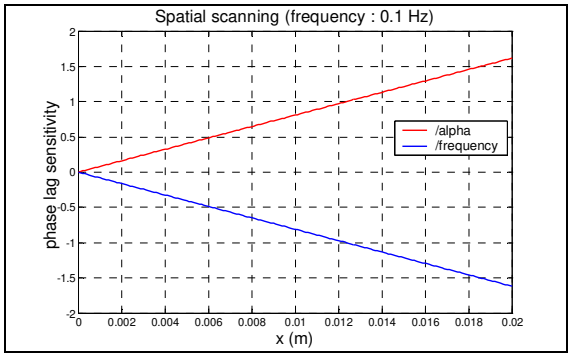

Figure 10: *Phase lag sensitivity for spatial scanning*

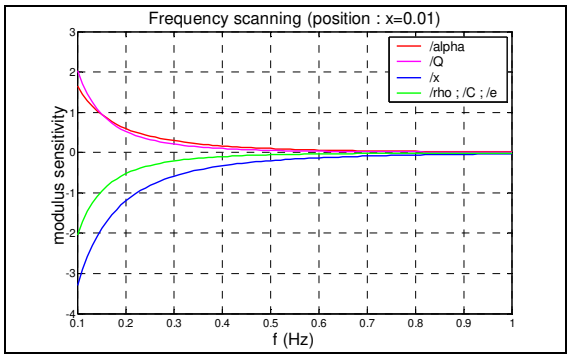

Figure 11: *Modulus sensitivity for frequency scanning*

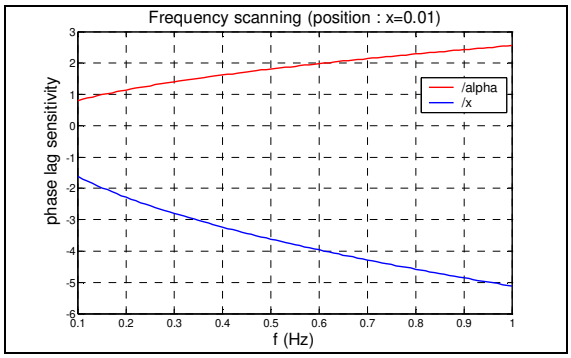

Figure 12: *Phase lag sensitivity for frequency scanning*

Sensitivity functions for a steel sample are analysed as follows:

- **Figure 9**: for temperature modulus observation during a spatial scanning, it is important to not take into account measurements near to the mask or too far. An intermediate distance has to be chosen. Sensitivity to frequency f is low enough but other input parameters Q, ρ, C, e have too be carefully known.
- **Figure 10** and **12**: for phase lag measurements for spatial or frequency scanning it is crucial to well determine the mask position x.
- **Figure 11**: for temperature modulus measured during a frequency scanning, it is better to avoid low or high frequencies. Intermediate frequency range has to be investigated. Sensitivity to position x is important but for the other parameters Q, ρ, C, e sensitivity is low enough.

Thus in the studied configuration several remarks are proposed:

- it is crucial to well determine the mask position in order to minimise the uncertainty on input parameter x,
- if the excitation frequency is not well known then diffusivity can be identified with temperature modulus measurements during a spatial scanning in an intermediate domain,
- If at least one input parameter (Q, ρ, C, e) is not well known then a frequency scanning in an intermediate frequency range can lead to good estimation of the diffusivity.

Several fields of interests can be developed, such as the optimal design for the experimental bench in order to optimise the signal / noise ratio.

5. Diffusivity identification

Once the thermal model has been established, the previous study of sensitivies gives the optimal experimental conditions and allows estimating the error range on identified properties according to measurement errors on experimental parameters. The sample being subjected to a periodic heating (system input), an appropriate sensor is used to measure the modulus and phase lag of the temperature field (system output) at a given location. A thermal transfer model allows the calculation of theses output at any location knowing the heating input and the thermal parameters controlling the system (diffusivity and Biot number). These thermal properties are identified by minimizing the measurement-calculation difference. Various

criteria for this identification can be considered and according to the students' knowledge, several studies based on several cost function determination are proposed; for example [7]:

- Quadratic cost functions which are by far the most commonly used because of their intuitive appeal. Such an estimator is usually called a weighted least square estimator,
- Weighted sum of absolute values of error (weighted least-modulus estimators) are used while very large errors are encountered since penalization is less than for quadratic costs.

Estimator robustness can also be investigated in order to study if its performance does not deteriorate too much when uncertainties are considered on the noise distribution.

6. Implementation of a finite element method

6.1. Aims

In this paragraph the interest of the implementation of a finite element method (FEM) is shown. The aim is to validate hypothesis which have been considered in the second paragraph for the determination of an analytical solution. Previous knowledge about numerical resolution of partial differential equation and FEM software are required.

6.2. Presentation

For large material thickness, heat transfers in the sample are not described by equation (1), and the following partial differential equations system is considered in spatial domain $\Omega = \left\{ (x,y) \in \mathbb{R} \times \left[-\frac{e}{2}, \frac{e}{2} \right] \right\}$, where $\vec{n}$ is the normal vector exterior to boundary $\Gamma = \left\{ \left(x, -\frac{e}{2} \right) \right\} \cup \left\{ \left(x, \frac{e}{2} \right) \right\}$ (see **Figure 13**).

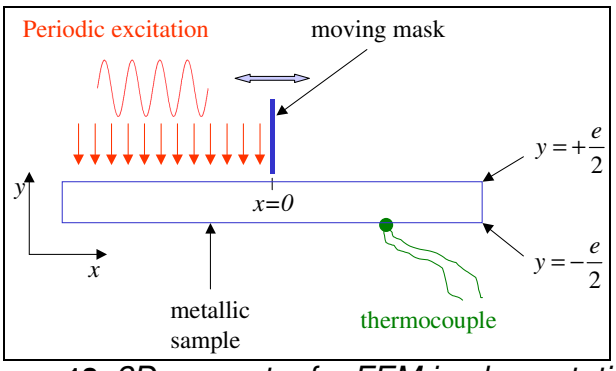

Figure 13*: 2D geometry for FEM implementation*

$$\rho C\frac{\partial T(x,y;t)}{\partial t}-k\Delta T(.,t)=0 \qquad \forall((x,y),t)\in \Omega\times T$$
$$-k\frac{\partial T(x,y,t)}{\partial \vec{n}}=hT(x,y,t)-Q\left(x,\frac{e}{2};t\right) \quad \forall((x,y),t)\in \Gamma\times T$$
$$T(x,y,0)=0 \qquad \forall(x,y)\in \Omega$$

Previous system is solved by a FEM (with an adapted discretization in space and time) in order to estimate for the studied material if the sample thickness e is too large. Limit thickness corresponds to isomodulus and isophaselag which do not correspond to equations (3) and (4).

In such a framework, CPU time can be reduced by introducing complex temperature. According to notations presented in paragraph 2.2 $T(x,y,t)=T(x,y,\varphi)e^{j\omega t}$, the following system has to be solved:

$$\rho Cj\omega T(x,y,\varphi)-k\Delta T(x,y,\varphi)=0 \qquad \forall(x,y)\in \Omega$$
$$-k\frac{\partial T(x,y,\varphi)}{\partial \vec{n}}=hT(x,y,\varphi)-Q\left(x,\frac{e}{2}\right) \quad \forall(x,y)\in \Gamma$$

Resolution of previous system using a FEM leads to the determination of modulus and phase lag of $T(x,y,\varphi)$ which are compared with analytical solutions given in equations (3) and (4).

In such a framework, hypothesis $\omega\tau=\frac{\omega\rho Ce}{h}\gg 1$ can also be investigated.

7. Concluding remarks

In this workshop, periodic methods are exposed in order to identify thermal diffusivity. A experimental bench is developed for educational purposes. Based on this easily understandable configuration, several aspects can be investigated: heat transfer modelling, complex temperature, analytical resolution, sensitivity analysis, optimal design, numerical simulation, parametric identification, finite element method. Gradual difficulties can be proposed to students in order to improve their knowledge about identification by periodic method and thermal characterisation.

8. References

[1] A.J. Angstrom, A.J., Phil. Mag, 25, p.130, 1863.
[2] R.D. Cowan, J. Appl. Phys, 34, p.1363, 1961.
[3] L. Autrique, L. Perez, E. Scheer, « On the use of periodic photothermal methods for material diagnosis », Sensors and Actuators B. Vol. 135 n°2, pp.478-487, 2009.
[4] B. Lascoup, L. Perez, L. Autrique, « Defect localization based on modulated photothermal local approach », Composites Part B engineering, Vol. 65 n°1, pp 109-116, 2014.

[5] J. Martinet, La méthode des températures complexes in Elements de thermocinétique, Tec&Doc, Lavoisier, 1989.
[6] J. Max, Méthodes et techniques de traitement du signal et applications aux mesures physiques, T.1, Masson, 1972.
[7] E. Walter, L. Pronzato, Identification of parametric models from experimental data, Springer, 1997.

Some questions for understanding

Q 1.1 Complex temperature

Assuming that the temperature within the material subjected to sinusoidal excitation satisfies the following system of equations:

$$\begin{cases} \Delta T_s = \dfrac{1}{\alpha_s}\dfrac{\partial T_s}{\partial t} \\ -\lambda \dfrac{\partial T_s}{\partial x} = \Phi \cos(\omega t) \end{cases}$$

Deduce the system of equation satisfied by $\tilde{T}(x)$ from the system of equations satisfied by $\overline{T_s}$. The excitation can be considered in the form $\overline{F} = F\exp(j\omega t)$. What can we say about modulus and phase lag of temperature oscillations?

Q 1.2 Lock-in Amplifier

Express the modulus A_r and the phase lag φ_r according to the data *XXX* and *YYY*.

Q 1.3 Study of a thin metallic sample

Calculate the diffusion lengths (unit?) for the metals whose properties are defined in the following table. What can we say about that?

	ρ $kg.m^{-3}$	C $J.kg^{-1}.K^{-1}$	λ $W.m^{-1}.K^{-1}$	μ for $f = 0.01$ Hz	μ for $f = 10$ Hz
Silver	10500	230	413		
Copper	8940	380	387		
Aluminium	2700	860	200		
Steel	7850	490	46		

Considering the previous materials and the table below, calculate the minimum value of the time constant τ and check that $\omega\tau >> 1$ for $f \geq 0.1\,\text{Hz}$.

Q $W.m^{-2}$	e m	h $W.m^{-2}.K^{-1}$
5.10^3	10^{-4}	10

For $x \geq 0$, assuming that $\omega\tau \gg 1$, simplify $|z|$ and θ in order to express

- $|T(x,\varphi)|$ depending on Q, ω, ρ, C, e, x and μ.
- $Arg(T(x,\varphi)) = \varphi$ depending on x and μ.

Q 1.4 Spatial scanning analysis

Using the results of the previous question, what can be said:

- Of the plot of $log|T(x,\varphi)|$ versus x; give the corresponding equation.

- Of the plot of the phase lag φ versus x ; give the corresponding equation.

Can the diffusivity of the studied material be deduced from these plots?

Q 1.5 Frequency scanning analysis

Using the results of the previous question, what can be said:

- Of the plot of $log\left|T\left(x,\varphi\right)\right|+log\ f$ versus $\sqrt{f}$; give the corresponding equation.
- Of the plot of the phase lag φ versus $\sqrt{f}$; give the corresponding equation.

Can the diffusivity of the studied material be deduced from these plots?

Q 1.6 Sensitivity analysis

Complete the following table by expressing the sensitivity functions considering the following notations $A=\frac{Q}{2\omega\rho Ce}$; $B=\sqrt{\frac{\pi f}{\alpha}}$; $E=\exp\left(-x\sqrt{\frac{\pi f}{\alpha}}\right)$

scanning	observation	Sensitivity functions	Plot
spatial	modulus	$\alpha \dfrac{\partial \lvert T \rvert}{\partial \alpha}$	Versus ?
		$Q \dfrac{\partial \lvert T \rvert}{\partial Q}$	
		$f \dfrac{\partial \lvert T \rvert}{\partial f}$	
		$\rho \dfrac{\partial \lvert T \rvert}{\partial \rho} = C \dfrac{\partial \lvert T \rvert}{\partial C} = e \dfrac{\partial \lvert T \rvert}{\partial e}$	
	phase lag	$\alpha \dfrac{\partial \varphi}{\partial \alpha}$	
		$f \dfrac{\partial \varphi}{\partial f}$	
frequency	modulus	$\alpha \dfrac{\partial \lvert T \rvert}{\partial \alpha}$	Versus ?
		$Q \dfrac{\partial \lvert T \rvert}{\partial Q}$	
		$\rho \dfrac{\partial \lvert T \rvert}{\partial \rho} = C \dfrac{\partial \lvert T \rvert}{\partial C} = e \dfrac{\partial \lvert T \rvert}{\partial e}$	
		$x \dfrac{\partial \lvert T \rvert}{\partial x}$	
	phase lag	$\alpha \dfrac{\partial \varphi}{\partial \alpha}$	
		$x \dfrac{\partial \varphi}{\partial x}$	

The sensitivity functions of the modulus are plotted in the following **Figure** (material: steel; spatial scanning; the excitation frequency is arbitrarily set to $f = 0.1\,\mathrm{Hz}$)

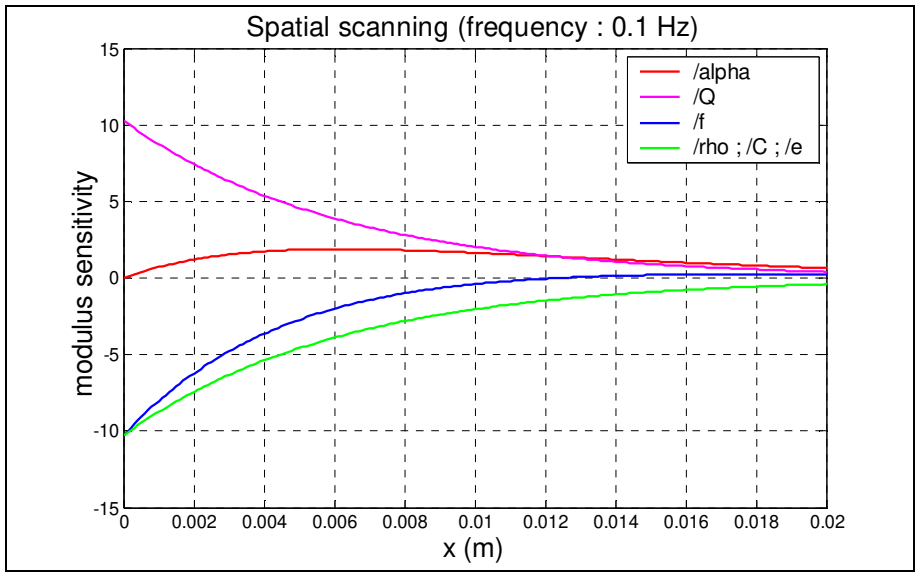

sensitivity functions of the modulus in spatial scanning

For a spatial scanning is it wise to consider measurements close to the origin $x = 0$? Far from the origin? What seems to be the optimal observation area? What can we say about the sensitivity functions represented by the purple and green curves?

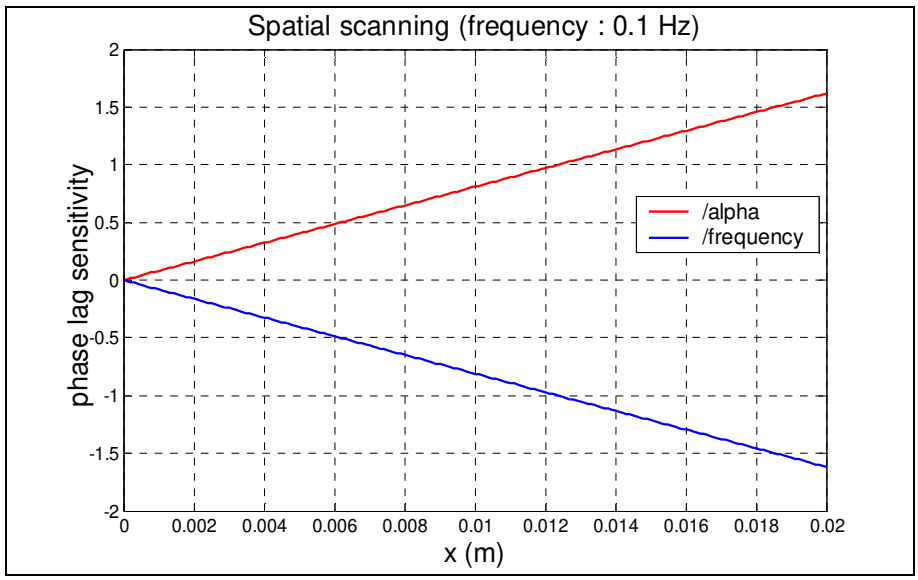

Sensitivity functions of phase lag in spatial scanning

For a spatial scanning, what can we say about the sensitivity functions of the diffusivity and the frequency? If the excitation frequency is poorly controlled, what can be said about identifying diffusivity using phase lag measurements in spatial scanning ?

Using appropriate software, draw curves representing sensitivity functions of the modulus considering a frequency scanning in between 0.1 and 1 Hz at a distance set to 0.01m. Analyse the results as much as possible.

Using appropriate software, draw curves representing sensitivity functions of the phase lag considering a frequency scanning in between 0.1 and 1 Hz at a distance set to 0.01m. Analyse the results as much as possible.

For each of the following questions, choose the best answer:

Question	*Answer*	*Choice*
If, during the experiment, uncontrolled variations of Q or e occur, should we carry out:	*a modulus analysis* *a phase lag analysis*	☐ ☐
If the origin position $x=0$ is not known accurately should we carry out:	*a spatial scanning* *a frequency scanning*	☐ ☐
If the excitation frequency is noisy, a spatial scanning is performed and	*a modulus analysis* *a phase lag analysis*	☐ ☐

Experiments for the identification of the diffusivity considering a spatial scanning.

Experiments for the identification of the diffusivity considering a frequency scanning.

Special features if time and appropriate software…

The purpose here is to implement a finite element method to simulate heat transfers in the material. The validity of certain hypotheses made when solving the direct problem are tested. The first hypothesis concerns the relationship between the diffusion length and the thickness which allows for a sufficiently fine sample to consider a simplified formulation of the heat balance. Particular attention will be paid to visualizing the importance of the ratio e/μ. The second hypothesis allowing expressing by a simple expression the modulus and the phase lag will be validated by checking the concordance between the analytical solution and the numerical solution.
The main pedagogical objective is the use of finite element software to test experimental configurations.

Why for a thick material the following equation does not describe the heat transfer in the studied sample?

$$\rho C e \frac{\partial T(x,t)}{\partial t} + hT(x,t) - ke\frac{\partial^2 T(x,t)}{\partial x^2} = Q(x,t)$$

Considering the sample of thickness e the studied spatial domain is defined by $\Omega = \left\{ (x,y) \in \mathbb{R} \times \left[-\frac{e}{2}, \frac{e}{2} \right] \right\}$, $\vec{n}$ is the normal external vector to $\Gamma = \left\{ \left(x, -\frac{e}{2} \right) \right\} \cup \left\{ \left(x, \frac{e}{2} \right) \right\}$:

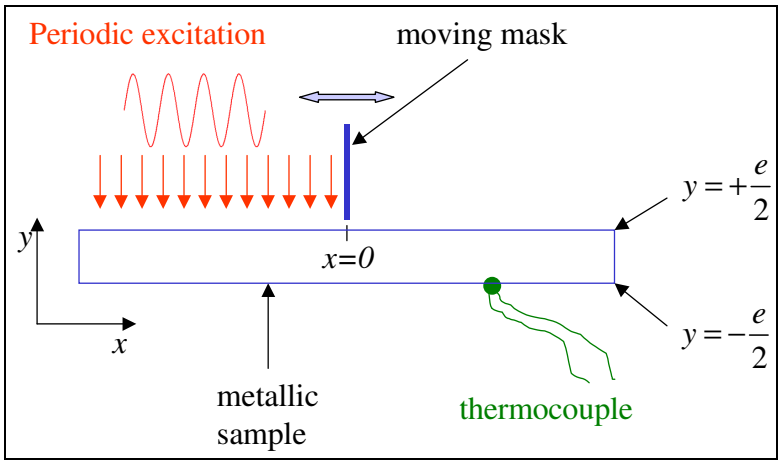

Heat transfers are described by the following system:

$$(S)\begin{cases} \rho C\dfrac{\partial T(x,y;t)}{\partial t}-k\Delta T(.,t)=0 & \forall((x,y),t)\in \Omega\times T \\ -k\dfrac{\partial T(x,y,t)}{\partial \vec{n}}=hT(x,y,t)-Q\left(x,\dfrac{e}{2};t\right) & \forall((x,y),t)\in \Gamma\times T \\ T(x,y,0)=0 & \forall(x,y)\in \Omega \end{cases}$$

With $Q(x,y,t)=\begin{cases} Q\dfrac{1+\cos\omega t}{2} & if \quad x<0 \quad et \quad y=\dfrac{e}{2} \\ 0 & if \quad x\geq 0 \end{cases}$

The objective is to put in evidence that for a larger thickness of the sample, temperature gradients appear in between the upper and the lower surfaces. Which material (silver, copper, aluminium, steel) is the most likely to encounter this situation? Are gradients more susceptible to appear at high frequency or low frequency?

	ρ $kg.m^{-3}$	C $J.kg^{-1}.K^{-1}$	λ $W.m^{-1}.K^{-1}$	μ for $f=0.01$ Hz	μ for $f=10$ Hz
Silver	10500	230	413		
Copper	8940	380	387		
Aluminium	2700	860	200		
Steel	7850	490	46		

Simulate the problem describes by the (S) system considering a steel sample of 6 mm thick subjected to $Q=5000\,W.m^{-2}$ at frequency of $f=0.1\,\text{Hz}$ with a heat transfer coefficient $h=10\,W.m^{-2}.K^{-1}$. Particular attention will be paid to the discretisation in space and time which must be judicious.
What temperature difference is observed under the moving mask (at $x=0$) between the upper and the lower surface after 10 seconds ?

Calculate from the simulated data the phase lag over the first 10 seconds. Compare with the values predicted with the analytical solution at $x = 1\,\text{mm}$.

Same questions with a steel sample of 1 mm thick?

Tutorial 6: Model Reduction by Modal Analysis

F. JolyY.Rouizi, B. Gaume, **O. Quéméner**

Laboratoire de Mécanique et d'Energétique d'Evry,
Univ. Paris-Saclay
40 rue du Pelvoux, Courcouronnes 91020 Evry, France

E-mail: f.joly@iut.univ-evry.fr
yassine.rouizi@univ-evry.fr
o.quemener@iut.univ-evry.fr
b.gaume@iut.univ-evry.fr

Abstract. The aim of this tutorial is to show the interest of using modal reduction to solve inverse problems. The tutorial is structured in two parts. The first one concerns the construction of the modal reduced model from an already known detailed model (finite elements). The Dirichlet-Steklov base, as well as different reduction techniques (temporal truncation, Energetic criteria) will be investigated. The second part deals with solving an inverse problem by using modal reduced models. During this work, we will show the influence of the order of the reduced model on the estimation results and on the calculation times. An example of an estimation of boundary conditions or thermo-physical parameter characterization will be treated. The different algorithms will be coded by participants using Octave software

Scope

1 Decomposition on a Dirichlet-Steklov base **3**
1.1 Position of the problem . . . 3
1.2 Variational formulation . . . 3
1.3 Modal formulation . . . 4
1.3.1 Dirichlet Base . . . 4
1.3.2 Steklov base . . . 5
1.3.3 The Dirichlet-Steklov basis . . . 6
1.3.4 Amplitude equations . . . 6
1.4 Numerical implementation . . . 7
1.4.1 Computation of the Dirichlet base . . . 7
1.4.2 Computation of the Steklov base . . . 7
1.4.3 State equation . . . 7
1.5 Example of application . . . 9
1.5.1 Finite elements model . . . 9
1.5.2 Reduced order model . . . 9
1.5.3 Orthogonality relations . . . 10
1.5.4 Modal model construction . . . 10
1.5.5 To go further... . . . 11

2 Utilization of reduced order model for inverse problem **12**
2.1 Inverse approach . . . 12
2.1.1 Beck method . . . 13
2.1.2 Global method . . . 14
2.2 Numerical results of inversion . . . 17
2.2.1 Beck method . . . 18
2.2.2 Global method . . . 20
2.3 Conclusion . . . 21

Chapter 1

Decomposition on a Dirichlet-Steklov base

1.1 Position of the problem

Let Ω a domain closed by its boundary Γ. The spatio-temporal evolution of temperature is modeled by the heat equation:

$$\forall M \in \Omega, \forall t \in \mathbb{R}^+ \quad \rho c_p \frac{\partial T}{\partial t} = \underline{\nabla} \cdot (k \underline{\nabla} T) + \Pi, \tag{1.1}$$

$$\forall M \in \Gamma, \forall t \in \mathbb{R}^+ \quad k \underline{\nabla} T \cdot \underline{n} = h(T_{ext} - T) + \varphi, \tag{1.2}$$

$$\forall M \in \Omega, t = 0 \quad T = T_i, \tag{1.3}$$

where $\underline{n}$ is the outward facing normal to Γ, T_i is the initial temperature, T_{ext} the surrounding temperature, and φ a received heat flux density.

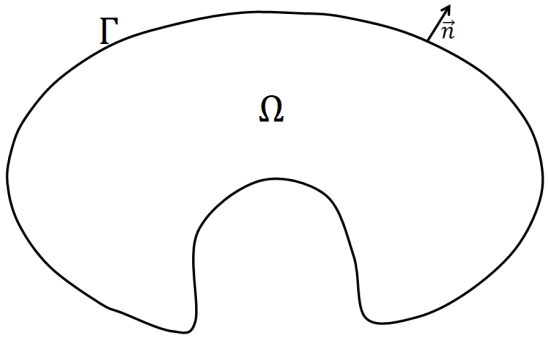

Figure 1.1: Physical domain

1.2 Variational formulation

Let suppose that T is sufficiently regular, for example $T \in H^2(\Omega)$ ($T \in \mathcal{L}^2(\Omega)$, $\partial T \in \mathcal{L}^2(\Omega)$, $\partial^2 T \in \mathcal{L}^2(\Omega)$). Let f a function belonging to the same functional space. The variational

formulation is obtained by multiplying Eq. (1.1) by f and by an integration on Ω.

$$\int_\Omega \rho c_p \frac{\partial T}{\partial t} f d\Omega = \int_\Omega \underline{\nabla} \cdot (k \underline{\nabla} T) f d\Omega + \int_\Omega \Pi f d\Omega. \tag{1.4}$$

Virtually, the solution is searched in $H^1(\Omega)$: with the Green-Ostrogradski theorem, Eq. (1.4) writes:

$$\int_\Omega \rho c_p \frac{\partial T}{\partial t} f d\Omega = -\int_\Omega k \underline{\nabla} T \cdot \underline{\nabla} f d\Omega + \int_\Gamma k \underline{\nabla} T \cdot \underline{n} f d\Gamma + \int_\Omega \Pi f d\Omega. \tag{1.5}$$

Now T only has to be once differentiable (so it can be defined in $H^1(\Omega)$). Boundary conditions appears by replacing $k\underline{\nabla} T.\underline{n}$ thanks to Eq. (1.2). The weak variational formulation is then obtained:

Definition 1.2.1 *Find $T \in H^1(\Omega)$ such that for all $f \in H^1(\Omega)$*

$$\int_\Omega \rho c_p \frac{\partial T}{\partial t} f d\Omega = -\int_\Omega k \underline{\nabla} T \cdot \underline{\nabla} f d\Omega - \int_\Gamma hT\, f d\Gamma + \int_\Gamma (hT_{ext} + \varphi)\, f d\Gamma + \int_\Omega \Pi f d\Omega. \tag{1.6}$$

The following operators are defined:

$$\forall u, v \in H^1(\Omega) \quad \mathcal{C}_\Omega(u,v) = \int_\Omega \rho c_p\, u\, v\, d\Omega;$$

$$\forall u, v \in H^1(\Omega) \quad \mathcal{K}_\Omega(u,v) = \int_\Omega k \underline{\nabla} u \cdot \underline{\nabla} v\, d\Omega;$$

$$\forall u, v \in H^1(\Omega) \quad \mathcal{H}(u,v) = \int_\Gamma h\, u\, v\, d\Gamma;$$

$$\forall u \in H^1, \forall \Pi, T_{ext} \in \mathcal{L}^2(\Omega) \quad L(u) = \int_\Gamma (hT_{ext} + \varphi)\, u\, d\Gamma + \int_\Omega \Pi u\, d\Omega.$$

Equation (1.6) writes on a condensed form:

$$\mathcal{C}_\Omega(\dot{T}, f) = -\mathcal{K}_\Omega(T, f) - \mathcal{H}(T, f) + L(f). \tag{1.7}$$

1.3 Modal formulation

The decomposition of a thermal problem with non homogeneous boundary conditions on a classical base is inconvenient. First, the sliding/dynamic separation is not satisfying, as the resolution of the sliding temperature still involves a large size problem. Second, if the boundary conditions change, the correct reconstruction of the thermal field becomes (theoretically) impossible, as the ratio $h = \frac{k\underline{\nabla} V_i \cdot \underline{n}}{V_i}$ is fixed. For the same reason, it is hopeless to treat properly a problem with a non-linear conductivity with that kind of modes. Another base is thus defined, which is the gathering of two bases.

1.3.1 Dirichlet Base

Dirichlet base is classical. It is defined by the eigenmodes of the Laplace operator with a null value on the boundary:

Definition 1.3.1 *Dirichlet base is defined by the set of pairs $\left(\lambda^D, V^D\right) \in \mathbb{R}^+ \setminus \{0\} \times H_0^1(\Omega)$ solutions of the following eigenvalue problem:*

$$\begin{cases} \Omega & -\underline{\nabla} \cdot \left(k \underline{\nabla} V^D\right) = \lambda^D \rho c_p V^D, \\ \partial\Omega & V^D = 0. \end{cases} \tag{1.8}$$

Eigenvectors V^D are named Dirichlet modes. The eigenvalues λ^D, associated to each vector V^D, have the dimension of frequency, and their inverses are characteristic time of the associated eigenmodes. The weak variational formulation reads then as:

Definition 1.3.2 *Find* $\left(\lambda^D, V^D\right) \in \mathbb{R}^+ \setminus \{0\} \times H_0^1(\Omega)$ *such as* $\forall u \in H_0^1(\Omega)$.

$$\mathcal{K}_\Omega(V^D, v) = \lambda^D \mathcal{C}_\Omega(V^D, v) \tag{1.9}$$

The following orthogonality properties are verified:

$$\begin{aligned} \forall i,\, j \in \mathbb{N}, \quad & \mathcal{K}_\Omega(V_i^D, V_j^D) = \delta_{ij}, \\ & \mathcal{C}_\Omega(V_i^D, V_j^D) = \frac{\delta_{ij}}{\lambda_i^D}, \end{aligned} \tag{1.10}$$

with δ_{ij} the Kronecker delta.
The set of Dirichlet modes $\{V_i^D\}_{i\in\mathbb{N}}$ forms an infinite but countable base of the Hilbert space $H_0^1(\Omega)$.

1.3.2 Steklov base

Definition 1.3.3 *Steklov base is defined by the set of pairs* $\left(\lambda^S, S\right) \in \mathbb{R}^+ \times H^{1/2}(\partial\Omega)$ *solutions of the following eigenvalue problem:*

$$\begin{cases} \Omega & -\underline{\nabla} \cdot \left(k \underline{\nabla} V^S\right) = 0, \\ \partial\Omega & k \underline{\nabla} V^S \cdot \underline{n} = \lambda^S \zeta\left(x\right) S, \qquad V^S|_{\partial\Omega} = S. \end{cases} \tag{1.11}$$

S is the Steklov eigenvector, but by language abuse, we will denote Steklov modes the functions $V^S \in H^1(\Omega)$, which are the harmonic lifting of S in Ω. With the following bilinear operator

$$\forall u,\, v \in H^1(\Omega), \mathcal{C}_{\partial\Omega}(u, v) = \int_{\partial\Omega} \zeta(x) u|_{\partial\Omega} v|_{\partial\Omega}, \tag{1.12}$$

the weak variational form of Eq. (1.11) reads:

Definition 1.3.4 *Find* $(\lambda^S, V^S) \in \mathbb{R}^+ \times H^1(\Omega)$ *such as* $\forall v \in H^1(\Omega)$

$$\mathcal{K}_\Omega(V^S, v) = \lambda^S \mathcal{C}_{\partial\,\Omega}(V^S, v). \tag{1.13}$$

The following orthogonality properties are verified

$$\begin{aligned} \forall i,\, j \in \mathbb{N}, \quad & \mathcal{K}_\Omega(V_i^S, V_j^S) = \delta_{ij} \frac{\lambda_i^S}{h_0 + \lambda_i^S}, \\ & \mathcal{C}_{\partial\Omega}(V_i^S, V_j^S) = \frac{\delta_{ij}}{h_0 + \lambda_i^S}. \end{aligned} \tag{1.14}$$

with $h_0 > 0$ a weighted factor with the dimension of a heat transfer coefficient. Note that Eqs. (1.10) and (1.14) are not standard orthogonality properties as they result from the norm adopted to combine both Dirichlet and Steklov bases. This norm will be explicated in the next section.
The set of Steklov eigenvectors $\{S_i\}_{i\in\mathbb{N}}$ forms an infinite but countable base of the Hilbert space $H^{1/2}(\partial\Omega)$.

1.3.3 The Dirichlet-Steklov basis

Orthogonality properties play a fundamental role in modal methods. They ensure that the decomposition $T = \sum_{i=1}^{N^D} x_i V_i^D + \sum_{i=1}^{N^S} x_i V_i^S$ is unique. The following scalar product is defined:

Definition 1.3.5 *Let u, $v \in H^1(\Omega)$. The scalar product $(u|v)_{H(\Omega)}$ is defined*

$$\begin{aligned}(u|v)_{H(\Omega)} &= \int_\Omega k\underline{\nabla}u \cdot \underline{\nabla}v + h_0 \int_{\partial\Omega} \zeta(x) uv \\ &= \mathcal{K}_\Omega(u,v) + h_0\, \mathcal{C}_{\partial\Omega}(u,v),\end{aligned} \tag{1.15}$$

This scalar product yields a norm:

$$\forall u \in H^1(\Omega), \quad \|u\|_{H(\Omega)} = \sqrt{(u|u)_{H(\Omega)}}. \tag{1.16}$$

This norm is equivalent to the usual norm in $H^1(\Omega)$:

$$\forall u \in H^1(\Omega), \quad \|u\|_{H^1(\Omega)} = \sqrt{\||\underline{\nabla}u|\|^2_{L^2(\Omega)} + \|u\|^2_{L^2(\Omega)}} \tag{1.17}$$

Dirichlet and Steklov bases can thus be normalized with $\|\cdot\|_{H(\Omega)}$[1]. This new scalar product on $H^1(\Omega)$ enables to establish orthogonality relations between Steklov modes and Dirichlet modes:

$$\begin{aligned}\forall i,\, j \in \mathbb{N}, \quad & (V_i^D|V_j^S)_{H(\Omega)} = 0, \\ & \mathcal{K}_\Omega(V_i^D, V_j^S) = 0.\end{aligned} \tag{1.18}$$

Equation (1.18) allows the simultaneous use of Dirichlet and Steklov bases to decompose a thermal field. Thus, the term Dirichlet-Steklov base is legitimate. On a more mathematical point of view, the union of the bases of Dirichlet and Steklov $\{V_i^D\}_{i\in\mathbb{N}} \oplus \{V_j^S\}_{j\in\mathbb{N}}$ forms a Hilbertian base of $H_0^1(\Omega) \bigoplus \mathrm{E}(\Omega) = H^1(\Omega)$, where $\mathrm{E}(\Omega) \subset H^1(\Omega)$ is the space of harmonic lifting. In particular:

$$\exists\, x_i^D,\, x_j^S \text{ such that } \forall u \in H^1(\Omega), \quad u = \sum_{\mathcal{X}\in\{D,S\}} \sum_{i=1}^{\infty} x_i^{\mathcal{X}} V_i^{\mathcal{X}}, \tag{1.19}$$

with $x_i^{\mathcal{X}} = (u|V_i^{\mathcal{X}})_{H(\Omega)}$.

1.3.4 Amplitude equations

The amplitude equations are obtained by replacing temperature by their decomposition on the Dirichlet-Steklov modes in equations (1.7). Dirichlet-Steklov modes are substituted for tests functions v:

$$\begin{aligned}1 \le i \le N_D, \quad & \sum_{\mathcal{X}\in\{D,S\}} \sum_{j=1}^{N_{\mathcal{X}}} x_j^{\mathcal{X}}\, \mathcal{K}_\Omega\left(V_i^D, V_i^{\mathcal{X}}\right) + \\ & \sum_{\mathcal{X}\in\{D,S\}} \sum_{j=1}^{N_{\mathcal{X}}} \dot{x}_j^{\mathcal{X}}\, \mathcal{C}_\Omega\left(V_i^D, V_j^{\mathcal{X}}\right) = \mathcal{L}\left(V_i^D\right)\end{aligned} \tag{1.20a}$$

[1] Hence orthogonality properties (1.10) and (1.14).

$$1 \leq i \leq N_S, \quad \sum_{\mathcal{X}\in\{D,S\}} \sum_{j=1}^{N_\mathcal{X}} x_j^\mathcal{X}\, \mathcal{K}_\Omega\left(V_i^S, V_i^\mathcal{X}\right) + \sum_{\mathcal{X}\in\{D,S\}} \sum_{j=1}^{N_\mathcal{X}} \dot{x}_j^\mathcal{X}\, \mathcal{C}_\Omega\left(V_i^S, V_j^\mathcal{X}\right) + \sum_{j=1}^{N_S} x_j^S\, \mathcal{H}\left(S_i, S_j\right) = \mathcal{L}\left(V_i^S\right) \quad (1.20b)$$

1.4 Numerical implementation

1.4.1 Computation of the Dirichlet base

The correct consideration of Dirichlet boundary conditions is a bit tricky. Discretization of Eq. (1.9) yields the following eigenvalue problem:

$$\mathbf{K}V_i^D = \lambda_i \mathbf{C}V_i^D. \quad (1.21)$$

$\mathbf{K}$ and $\mathbf{C}$ are matrices that corresponds respectively to operators $\mathcal{K}_\Omega(u,v)$ and $\mathcal{C}_\Omega(u,v)$. They are of dimension $[N \times N]$ where N is the number of nodes of the discretized geometry. They can be obtained by classical numerical methods (finite elements, etc.) However, in the variational formulation, it is specified that solution is searched in $H_0^1(\Omega)$. What does that mean concretely? That means that every line and column corresponding to a point which belongs to a boundary is null. The eigenvalue problem is replaced by a smaller one:

$$\mathbf{K}^D V_i^D = \lambda_i \mathbf{C}^D V_i^D, \quad (1.22)$$

where matrix $\mathbf{K}^D$ and $\mathbf{C}^D$ are obtained by removing every line and column corresponding to a point which belongs to a boundary.

1.4.2 Computation of the Steklov base

Discretization of Eq. (1.11) yields the following eigenvalue problem:

$$\mathbf{K}V_i^S = \lambda_i \mathbf{C}_\zeta V_i^S. \quad (1.23)$$

Non-zero elements of matrix $\mathbf{C}_\zeta$ are only on the points which belong to a boundary. Equation (1.23) results in a saddle-node problem.

1.4.3 State equation

The discretization of the weak variational formulation of (1.7) yields the following matrix formulation:

$$\mathbf{C}\dot{T} = -\left(\mathbf{K}+\mathbf{H}\right)T + U. \quad (1.24)$$

The state equation is directly built from Eq. (1.24). First, T is replaced by its modal formulation $\mathbf{V}X$. Matrix $\mathbf{V}$ of dimension $[N \times (N_D + N_S)]$ gathers N_D Dirichlet and N_S Steklov eigenvectors V_i^D and V_i^S. Next step is to project the resulting equation to the reduced base. Concretely, this operation is made by multiplying Eq. (1.24) by ${}^T\mathbf{V}$. It results in:

$${}^T\mathbf{V}^D\mathbf{C}\mathbf{V}^D\dot{X}^D + {}^T\mathbf{V}^D\mathbf{C}\mathbf{V}^S\dot{X}^S = -{}^T\mathbf{V}^D\left(\mathbf{K}+\mathbf{H}\right)\mathbf{V}^D X^D - {}^T\mathbf{V}^D\left(\mathbf{K}+\mathbf{H}\right)\mathbf{V}^S X^S + {}^T\mathbf{V}^D U \quad (1.25a)$$

$$ {}^{T}\mathbf{V}^{S}\mathbf{C}\mathbf{V}^{S}\dot{X}^{S} + {}^{T}\mathbf{V}^{S}\mathbf{C}\mathbf{V}^{D}\dot{X}^{D} = -{}^{T}\mathbf{V}^{S}\left(\mathbf{K}+\mathbf{H}\right)\mathbf{V}^{S}X^{S} - {}^{T}\mathbf{V}^{S}\left(\mathbf{K}+\mathbf{H}\right)\mathbf{V}^{D}X^{D} + {}^{T}\mathbf{V}^{S}U \quad (1.25b) $$

If the conductivity and the heat capacity used in the eigenvalue problems and in the heat equation are the same, then these equations might be simplified thanks to orthogonality properties.

$$ \mathbf{\Lambda}^{D}\dot{X}^{D} + {}^{T}\mathbf{V}^{D}\mathbf{C}\mathbf{V}^{S}\dot{X}^{S} = -X^{D} + {}^{T}\mathbf{V}^{D}U \quad (1.26) $$

$$ {}^{T}\mathbf{V}^{S}\mathbf{C}\mathbf{V}^{S}\dot{X}^{S} + {}^{T}\mathbf{V}^{S}\mathbf{C}\mathbf{V}^{D}\dot{X}^{D} = -{}^{T}\mathbf{V}^{S}\left(\mathbf{K}+\mathbf{H}\right)\mathbf{V}^{S}X^{S} + {}^{T}\mathbf{V}^{S}U \quad (1.27) $$

At the steady-state, Dirichlet states are obtained without any resolution. Furthermore, if the volume solicitation (*i.e.* Π) is null, then at the steady-state, Dirichlet states are also null. Finally, Dirichlet state-equation is diagonal. This property can be used during temporal discretization: the numerical resolution is then reported only on the Steklov modes.

1.5 Example of application

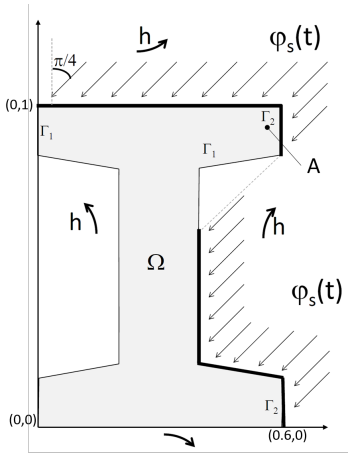

Figure 1.2: A slice of the considered concrete beam

We consider a concrete beam, sufficiently long to be modeled in 2D (see Fig. 1.2). Initially at a temperature $T_0 = 0°C$, the beam is subjected to:

- a global exchange with the outside ($T_{ext} = 0°C$, $h_{ext} = 10\,W.m^{-2}.K^{-1}$);
- a time-dependent solar radiation, estimated by a simple sinus law;

Physical properties of concrete are given in Table 1.1:

$k\ \left(W.m^{-2}.K^{-1}\right)$	$\rho\ \left(kg.m^{-3}\right)$	$c_p\ \left(J.kg^{-1}.K^{-1}\right)$	α_s
1.4	2250	800	0.9

Table 1.1: Physical properties of concrete

1.5.1 Finite elements model

Finite element matrices are given in the working directory, and a broad outline of a finite element code is given `FE_model.m`.. With a backward first order Euler scheme, Eq. (1.24) splits in:

$$\left[\mathbf{C} + dt\left(\mathbf{K} + \mathbf{H}\right)\right] T(t + dt) = \mathbf{C}T(t) + dtU. \tag{1.28}$$

This equation is integrated over a time $\tau = 72h$, with a time-step $dt = 1s$. Thermal field is recorded every 3600 s. The resulting temperature field is recorded in `T_EF`. To visualize a temperature field, just type `Visu(T_EF,i)` with i the hour you want to see.

1.5.2 Reduced order model

Eigenmodes computation

As said above, matrices involved in eigenvalue problem (1.22) are amputated from lines and columns corresponding to boundary nodes. They are given in the working directory under the names `K_dir` and `C_dir`. The command line to compute modes is:

```
[Vec_dir,Val_dir]=eigs(K_dir,C_dir,N,'la');
```

with N the number of desired eigenmodes. Computation of the 937 eigenmodes is quasi immediate. Another step is necessary: these eigenmodes are defined on the 937 interior points. They have to be resized to insert zero at the boundary points. You can find those complete eigenmodes in the working directory under the names `Vectors_Diric`. The Steklov eigenmodes are also given in `Vectors_Stekl`.

Modes visualization

To visualize modes, just type `Visu(Vectors_diric,i)` or `Visu(Vectors_Stekl,i)` with i the number of the mode you want to see.

1.5.3 Orthogonality relations

Please open script `Reduced_model.m`. It contains an outline of the code.

Check that the following orthogonality relations are verified:

$$ {}^{T}V_i^{\mathcal{X}}\mathbf{K}V_j^{\mathcal{Y}} = a_i\delta_{ij}\delta_{\mathcal{X}\mathcal{Y}}, {}^{T}V_i^{D}\mathbf{C}V_j^{D} = b_i\delta_{ij}, {}^{T}V_i^{\mathcal{X}}\mathbf{C}_\zeta V_j^{\mathcal{Y}} = c_i\delta_{ij}\delta_{\mathcal{X}\mathcal{Y}} $$

where a_i, b_j and c_j are real values that depend on the chosen norm.

Write a loop to normalize the modes such that ${}^{T}V_i^{\mathcal{X}}\left[\mathbf{K}+\mathbf{C}_\zeta\right]V_j^{\mathcal{Y}} = a_i\delta_{ij}\delta_{\mathcal{X}\mathcal{Y}}$

1.5.4 Modal model construction

Construction of the modal model is very easy once the modes have been computed and normalized. The simplest way is to first gather Dirichlet and Steklov eigenvectors into one matrix noted $\mathbf{V} = \left\{\mathbf{V}^D|\mathbf{V}^S\right\}$ of dimension $[N \times (N_d + N_s)]$. Reduced matrices are easily computed thanks to:

$$ \mathbf{L} = {}^{T}\mathbf{V}\mathbf{C}\mathbf{V}, \quad \mathbf{M} = {}^{T}\mathbf{V}\left(\mathbf{K}+\mathbf{H}\right)\mathbf{V}, \quad N = {}^{T}\mathbf{V}U \tag{1.29} $$

With a backward first order Euler scheme, Eq. (1.24) splits in:

$$ \left[\mathbf{L}+dt\mathbf{M}\right]X(t+dt) = \mathbf{L}X(t) + dtN \tag{1.30} $$

Compute the reduced matrices and write the program to solve the reduced model. An outline is given in the program `Reduced_model.m`. To recover the temperature just write `T_red=V*X` Note: Finite elements matrix are sparse and of large size. Their inverse, is still of large size, but is not sparse anymore. The preliminary computation of $\left[\mathbf{C}+dt\left(\mathbf{K}+\mathbf{H}\right)\right]^{-1}$ might not be a good idea. On the opposite, reduced matrix are of small size and full, just as their inverse. If dt is fixed, then the preparatory computation of $\left[\mathbf{M}+dt\mathbf{L}\right]^{-1}$ speeds up the temporal resolution.

Selection matrix

In several applications, the knowledge of the whole temperature field is not necessary. The information is only needed in few points, names observables and noted Y. Y is retrieved from the temperature field T by the simple relation:

$$ Y = \mathbf{E}T $$

$\mathbf{E}$ is basically a boolean matrix with ones at the selected points and zeros elsewhere. The modal formulation yields:

$$ Y = \mathbf{E}\mathbf{V}X $$

We want to see the temperature evolution at location $x = 0.55\,m$ and $y = 0.95\,m$. Use function `location(x,y)` to find the point corresponding to this location. Build the reduced selection matrix **EV**.

Reduced model performance

Several criteria are used to evaluate the performance of the reduced model. The first one is the time needed to solve the temporal loop. The other ones concern the error between reduced and finite elements model. Several error are defined:

$$<\varepsilon> = \frac{1}{V}\frac{1}{\tau}\int_0^\tau \int_\Omega |T^{FE} - T^{mod}|\, dt d\Omega \;\; ; \;\; \varepsilon_\infty = \max_\tau \max_\Omega |T^{FE} - T^{mod}| \tag{1.31}$$

The error on the observables are also considered.

$$<\varepsilon>_i = \frac{1}{\tau}\int_0^\tau |Y_i^{FE} - Y_i^{mod}|\, dt \;\; ; \;\; \varepsilon_{\infty,i} = \max_\tau |Y_i^{FE} - Y_i^{mod}| \tag{1.32}$$

Two reductions have to be handled: one on the Steklov modes, and one on the Dirichlet modes.
The number of Dirichlet modes is set to 10, and the number of Steklov modes is increased from 10 to 70, by step of ten. Compute the errors defined above. How do they behave ? Is it useful to retain more Steklov modes ?
Now, the number of Steklov modes is set to 40, and the number of Dirichlet modes is increased from 5 to 40, by step of five. Compute the errors defined above.

New boundary conditions

We consider the same beam, but now the wind has risen, and the heat exchange is now modeled by $h = 100\,W.m^{-2}.K^{-1}$. The finite elements solution is given in the working directory `T_EF_h_100.mat`. Try a reduced model with 20 Dirichlet modes and 40 Steklov modes, and compute the errors. Compare to the case with $h = 10\,W.m^{-2}.K^{-1}$.

1.5.5 To go further...

Matrix shape

Visualize matrices **L** and **M**. Are they really dense matrices ?

Energetic criteria

The criteria used here is the temporal criteria, also called Marshall truncature. It has the advantage if being immediate, but might not be very efficient. Another criteria might be used, based on the temporal response. Assume a known finite element solution T_{EF}. With the orthogonality properties, the projection of that solution on the Dirichlet-Steklov base writes:

$$X = {}^T\mathbf{V}(\mathbf{K} + \mathbf{C}_\zeta)T_{EF}$$

The modal dominance $\mathcal{E}_i$ is defined by:

$$\mathcal{E}_i = \int x_i^2\, dt$$

the program `dominance.m` computes $\mathcal{E}_i$. For a reduced model of order 50, how many Dirichlet modes and Steklov modes would you take following this new criteria ? Compare to the above study.

Chapter 2

Utilization of reduced order model for inverse problem

2.1 Inverse approach

From the knowledge of the temperature field, the aim here is to identify the evolution of the heat flux $\varphi_u(t)$ (figure 2.1) received by the concrete beam. In practice, inverse approach focuses on a part of the temperature field, *i.e.* an observable vector $\boldsymbol{Y}$ that gives the temperature evolution on N_{mes} particular points of interest for the user.
From the measurements $\boldsymbol{Y}$, the real heat flux $\varphi_u(t)$ is estimated by $\hat{\varphi}_u(t)$. From this estimated flux, direct model (detailed or reduced) gives an estimate of the observable, noted $\hat{\boldsymbol{Y}}$, through a selection matrix $\boldsymbol{E}$ such as:

$$\hat{\boldsymbol{Y}} = \boldsymbol{E}\hat{\boldsymbol{T}} = \boldsymbol{E}\boldsymbol{V}\boldsymbol{X} \tag{2.1}$$

To quantify the quality of estimations we introduce two quantities σ_T and σ_{φ_u}. σ_T represents the mean quadratic error on temperatures between the observable (measurements) $\boldsymbol{Y}$ and the output $\hat{\boldsymbol{Y}}$ of numerical model, while σ_{φ_u} represents the mean quadratic error on fluxes. These quantities are computed according to the following equations:

$$\sigma_T = \sqrt{\frac{\sum_{j=1}^{N_{mes}} \sum_{i=1}^{N_t} \left(Y_j(t_i) - \hat{Y}_j(t_i)\right)^2}{N_t \times N_{mes}}} \tag{2.2}$$

$$\sigma_{\varphi_u} = \sqrt{\frac{\sum_{i=1}^{N_t} \left(\varphi_u(t_i) - \hat{\varphi}_u(t_i)\right)^2}{N_t}} \tag{2.3}$$

For this kind of inverse problem, two methods are often used. The first one, known as Beck method, is sequential, and has been the object of many works. The second one, is global, and is based on the minimization of a cost function.
Before implementing this parameter estimation problem, a sensitivity study has been made. The sensitivity is defined by:

$$S = \frac{\partial T}{\partial \varphi_u} \tag{2.4}$$

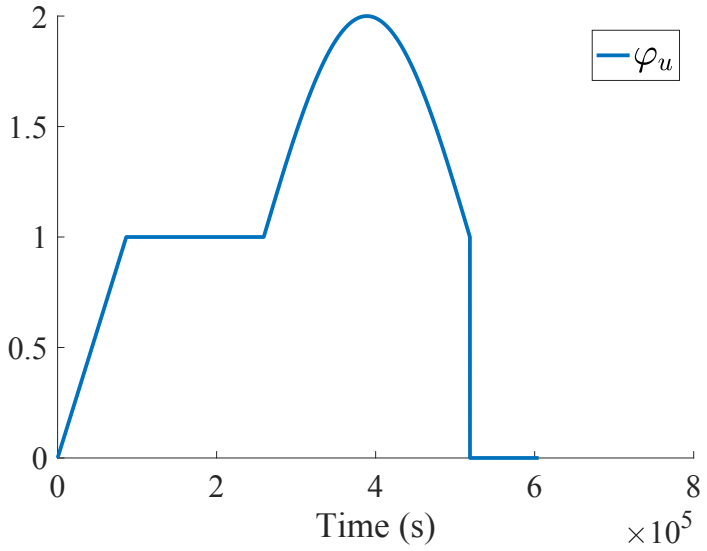

Figure 2.1: Evolution of the heat flux $\varphi_u(t)$.

2.1.1 Beck method

Only a brief description of Beck method is given here. For further information, the reader is encouraged to read [1, 2] for example.
Beck method is a sequential process in which the amplitude of the heat flux at each time step $\hat{\varphi}_u^{k+1}$ is identified from the temperature at time step $k+1$. It consists in minimizing a temperature difference between the measurement and the recalculated temperature. Generally, future time steps are used to regularize the unstable character of inverse problem as well as the lagging and damping effects due to the diffusion process [3, 4, 5]. In that case, unknown heat flux $\hat{\varphi}_u^{k+1}$ is estimated from temperature measurements at time step $k+1$ and at n_f future time steps $k+2, k+3, \ldots, k+1+n_f$ under assumption:

$$\hat{\varphi}_u^{k+1} = \hat{\varphi}_u^{k+1+f} = constant \quad f \in [1, n_f] \tag{2.5}$$

From reduced state representation (2.6):

$$\left\{ \begin{array}{rcl} \boldsymbol{L}\dot{\boldsymbol{X}} & = & \boldsymbol{M}\boldsymbol{X} + \varphi_u(t)\,\boldsymbol{N} \\ \hat{\boldsymbol{Y}} & = & \boldsymbol{E}\boldsymbol{V}\boldsymbol{X} \end{array} \right. \tag{2.6}$$

a temporal discretization with a constant time step is used to obtain the excitation state at each iteration k:

$$\boldsymbol{X}^{k+1} = [\boldsymbol{L} - \Delta t \boldsymbol{M}(t)]^{-1} \left[\boldsymbol{L}\boldsymbol{X}^k + \Delta t \varphi_u^{k+1} \boldsymbol{N} \right] \tag{2.7}$$

The estimated solution is given by a least squares minimization:

$$\hat{\varphi}_u^{k+1} = \left[\boldsymbol{\Theta}^t \boldsymbol{\Theta} \right]^{-1} \boldsymbol{\Theta}^t \boldsymbol{Z}^{k+1} \tag{2.8}$$

where $\boldsymbol{\Theta}$ and $\boldsymbol{Z}$ are defined by:
If $n_f = 0$

$$\boldsymbol{\Theta} = \boldsymbol{E}\boldsymbol{V} [\boldsymbol{L} - \Delta t \boldsymbol{M}(t)]^{-1} [\Delta t \boldsymbol{N}] \tag{2.9a}$$

$$\boldsymbol{Z}^{k+1} = \boldsymbol{Y}^{k+1} - \boldsymbol{E}\boldsymbol{V} [\boldsymbol{L} - \Delta t \boldsymbol{M}(t)]^{-1} \left[\boldsymbol{L}\boldsymbol{X}^k \right] \tag{2.9b}$$

or if $n_f > 0$ by:

$$\Theta = \begin{bmatrix} \boldsymbol{EV}\left[\boldsymbol{L} - \Delta t \boldsymbol{M}\left(t\right)\right]^{-1} \Delta t \boldsymbol{N} \\ \boldsymbol{EV}\left[\left(\boldsymbol{L} - \Delta t \boldsymbol{M}\left(t\right)\right)^{-1} + \left(\boldsymbol{L} - \Delta t \boldsymbol{M}\left(t\right)\right)^{-2}\right] \Delta t \boldsymbol{N} \\ \vdots \\ \vdots \\ \boldsymbol{EV}\left[\sum_{i=1}^{n_f+1} \left(\boldsymbol{L} - \Delta t \boldsymbol{M}\left(t\right)\right)^{-i}\right] \Delta t \boldsymbol{N} \end{bmatrix} \tag{2.10}$$

and

$$\boldsymbol{Z}^{k+1} = \begin{bmatrix} \boldsymbol{Y}^{k+1} - \boldsymbol{EV}\left[\boldsymbol{L} - \Delta t \boldsymbol{M}\left(t\right)\right]^{-1} \boldsymbol{L} \boldsymbol{X}^{k} \\ \boldsymbol{Y}^{k+2} - \boldsymbol{EV}\left[\boldsymbol{L} - \Delta t \boldsymbol{M}\left(t\right)\right]^{-2} \boldsymbol{L} \boldsymbol{X}^{k} \\ \vdots \\ \vdots \\ \boldsymbol{Y}^{k+1+n_f} - \boldsymbol{EV}\left[\boldsymbol{L} - \Delta t \boldsymbol{M}\left(t\right)\right]^{-\left(n_f+1\right)} \boldsymbol{L} \boldsymbol{X}^{k} \end{bmatrix} \tag{2.11}$$

The results of this technique and the difficulties related to regularization through the future time steps method are presented in section (2.2.1).

2.1.2 Global method

As represented in figure 2.2, the global method requests the entirety of the data on the temporal domain. It aims at minimizing a cost function built on the difference between the measured temperatures $\boldsymbol{Y}$ and those resulting from calculation with direct model $\hat{\boldsymbol{Y}}$. The cost function can also be penalized by a regularization term:

$$\mathcal{J}\left(\varphi_u\left(t\right)\right) = \frac{1}{2}\left[\int_0^\tau \left\|\boldsymbol{Y}\left(t\right) - \hat{\boldsymbol{Y}}\left(t\right)\right\|^2 \mathrm{d}t + \epsilon \left\|\varphi_u\left(t\right)\right\|^2\right] \tag{2.12}$$

The penalisation term is pondered by a positive coefficient ϵ named Thikonov parameter.
The identification problem consists in finding the optimal solicitation $\bar{\varphi}_u$ such as $\mathcal{J}$ is minimum:

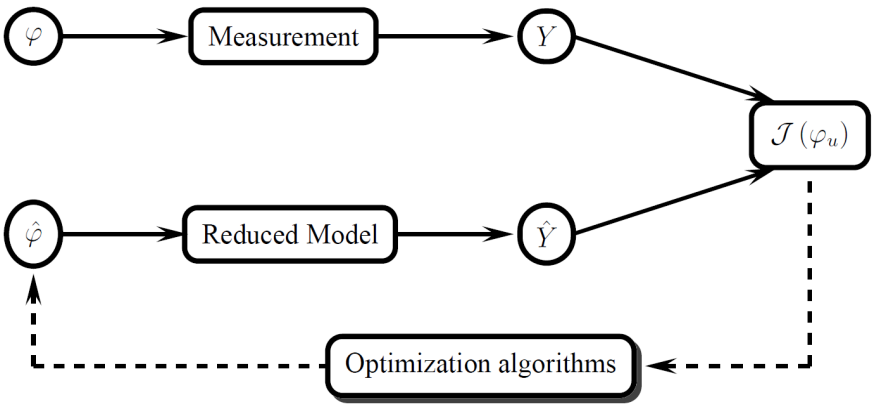

Figure 2.2: General scheme of parameters estimation

$$\bar{\varphi}_u = \arg\left[\min \mathcal{J}\left(\varphi_u\right)\right] \tag{2.13}$$

This problem can be solved with a method of descent, which requires the estimation of the gradient of the cost function $\mathcal{J}\left(\varphi_u\left(t\right)\right)$ with respect to the solicitations $\varphi_u\left(t\right)$. This is performed by the adjoint method [6, 7]. This method allows to implement low-cost algorithms compared to a finite difference method, since only the adjoint problem has to be resolved besides the direct problem. As this iterative procedure may require many runs of direct model, reduced models are perfectly fitted for this method.

The Lagrangian formulation is used to establish the equations of the reduced adjoint problem. From the problem of optimization, described by equation (2.13), we consider the Lagrangian formulation defined by:

$$\mathcal{L}\left(\varphi_u, \boldsymbol{X}, \boldsymbol{\lambda}\right) = \mathcal{J}\left(\varphi_u\right) + \int_0^\tau \boldsymbol{\lambda} \cdot \left(L\left(\varphi_u, \boldsymbol{X}\right)\right) \mathrm{d}t \tag{2.14}$$

where $L\left(\varphi_u, \boldsymbol{X}\right)$ is the constraint equation of the state variable $\boldsymbol{X}$ defined by:

$$L\left(\varphi_u, \boldsymbol{X}\right) = -\boldsymbol{L}\frac{\mathrm{d}\boldsymbol{X}}{\mathrm{d}t} + \boldsymbol{M}\boldsymbol{X} + \boldsymbol{N}\varphi_u \tag{2.15}$$

The constraint equation $L\left(\varphi_u, \boldsymbol{X}\right)$ is by definition always zero (see Eq. (2.6)), which leads to an equality between the Lagrangian $\mathcal{L}$ and the criterion $\mathcal{J}$.
At the point where the criterion is minimal, Lagrangian derivatives with respect to these three variables are zero:

$$\frac{\partial \mathcal{L}}{\partial \boldsymbol{\lambda}} = 0 \tag{2.16a}$$

$$\frac{\partial \mathcal{L}}{\partial \varphi_u} = 0 \tag{2.16b}$$

$$\frac{\partial \mathcal{L}}{\partial \boldsymbol{X}} = 0 \tag{2.16c}$$

The derivative defined by equation (2.16a) retrieves the state equation (2.6).
Both last derivative (Eq. (2.16b) and Eq. (2.16c)) bring two new relations, called equation of the gradient (Eq. (2.17a)) and adjoint equation (Eq. (2.17b)):

$$\boldsymbol{\nabla}\mathcal{J} = \epsilon\varphi_u + \boldsymbol{N}^t\boldsymbol{\lambda} \tag{2.17a}$$

$$-\boldsymbol{L}\dot{\boldsymbol{\lambda}} = \boldsymbol{M}^*\boldsymbol{\lambda} + \boldsymbol{V}^t\boldsymbol{E}^t\left(\boldsymbol{Y}\left(t\right) - \hat{\boldsymbol{Y}}\left(t\right)\right) \tag{2.17b}$$

where $\boldsymbol{M}^*$ is the adjoint matrix of $\boldsymbol{M}$.

Iterative computing of the solicitation φ_u which is based on the computation of first derivatives $\boldsymbol{\nabla}\mathcal{J}$ is called *gradient method*. In these iterative methods, the new estimate of $\hat{\varphi}_u^k$ is computed from an initial guess $\hat{\varphi}_u^0$ by:

$$\hat{\varphi}_u^{k+1} = \hat{\varphi}_u^k + \rho^k w^k \tag{2.18}$$

where ρ^k is a positive scalar that represents the search step size, and w^k is the direction of descent at each iteration k.

Compared to the steepest descent method, the Conjugate Gradient Method (CGM) [6, 4, 8, 9] improves the convergence rate by choosing the descent directions that reach minimum of the cost function faster. In this iterative technique, descent directions are obtained as a linear combination of the negative gradient direction at the current iteration with the direction of descent of the previous iteration:

$$w^k = -\boldsymbol{\nabla} J^k, \quad k = 0 \tag{2.19a}$$

$$w^k = -\boldsymbol{\nabla} J^k + \gamma^k w^{k-1}, \quad k > 0 \tag{2.19b}$$

and where γ^k is the conjugation parameter. Various formula expression of γ^k can be found in the literature [6, 8, 9]. One can cite the Flecher-Reeves formula [4, 10, 11], given by:

$$\gamma^k = \frac{\left\| \boldsymbol{\nabla} J^k \right\|^2}{\left\| \boldsymbol{\nabla} J^{k-1} \right\|^2} \tag{2.20}$$

The line search in the direction w^k of the step ρ^k can be performed by secant method [12]:

$$\rho^k = -\alpha \frac{\left\langle \boldsymbol{\nabla} J\left(\hat{\varphi}_u^k\right), w^k \right\rangle}{\left\langle \boldsymbol{\nabla} J\left(\hat{\varphi}_u^k + \alpha w^k\right), w^k \right\rangle - \left\langle \boldsymbol{\nabla} J\left(\hat{\varphi}_u^k\right), w^k \right\rangle} \tag{2.21}$$

To illustrate this iterative procedure we give the corresponding pseudo-code algorithm.

k=0;
Make initial guess for $\hat{\varphi}_u^0(t)$;
repeat
  $k = k + 1$;
  Solve for $\forall t \in [0:\tau]$: $\boldsymbol{L}\dot{\boldsymbol{X}} = \boldsymbol{M}(t)\boldsymbol{X} + \boldsymbol{N}\hat{\varphi}_u^{k-1}(t)$;
  $\hat{\boldsymbol{Y}}(t) = \boldsymbol{E}\boldsymbol{V}\boldsymbol{X}$;
  Solve for $\forall t \in [\tau:0]$: $-\boldsymbol{L}\dot{\boldsymbol{\lambda}} = \boldsymbol{M}^*\boldsymbol{\lambda} + \boldsymbol{V}^t\boldsymbol{E}^t\left(\boldsymbol{Y}(t) - \hat{\boldsymbol{Y}}(t)\right)$;
  $\boldsymbol{\nabla}\mathcal{J} = \epsilon\hat{\varphi}_u^{k-1}(t) + \boldsymbol{N}^t\boldsymbol{\lambda}$;
  Compute γ^k (Eq. (2.20)) ;
  Compute w^k (Eq. 2.19);
  begin
    Determine ρ^k (Eq. (2.21)) ;
    Solve for $\forall t \in [0:\tau]$: $\boldsymbol{L}\dot{\boldsymbol{X}}_e = \boldsymbol{M}\boldsymbol{X}_e + \boldsymbol{N}\left(\hat{\varphi}_u^{k-1} + \alpha w^k\right)$;
    $\hat{\boldsymbol{Y}}_e(t) = \boldsymbol{E}\boldsymbol{V}\boldsymbol{X}_e$;
    Solve for $\forall t \in [\tau:0]$: $-\boldsymbol{L}\dot{\boldsymbol{\lambda}}_e = \boldsymbol{M}^*\boldsymbol{\lambda}_e + \boldsymbol{V}^t\boldsymbol{E}^t\left(\boldsymbol{Y}(t) - \hat{\boldsymbol{Y}}_e(t)\right)$;
    $\boldsymbol{\nabla}\mathcal{J}\left(\hat{\varphi}_u^{k-1} + \alpha w^k\right) = \epsilon\left(\hat{\varphi}_u^{k-1} + \alpha w^k\right) + \boldsymbol{N}^t\boldsymbol{\lambda}_e$;
    return ρ^k
  end
  $\hat{\varphi}_u^k = \hat{\varphi}_u^{k-1} + \rho^k w^k$;
until Stopping criteria (see below);

Algorithm 1: Iterative procedure for GGM

This iterative calculation ends when one of the following criteria is met:

- The first is based on the evolution of functional $\mathcal{J}$:

$$\frac{\mathcal{J}\left(\hat{\varphi}^{k-50}\right)-\mathcal{J}\left(\hat{\varphi}^{k}\right)}{\mathcal{J}\left(\hat{\varphi}^{k}\right)} \leq 1\% \tag{2.22}$$

- The second is based on Morozov's discrepancy principle [13], stipulating that the mean quadratic residual σ_T (Eq. (2.2)) should be close to the standard deviation of the measurement noise (or added noise in numerical case) σ_B.

$$\sigma_T \approx \sigma_B \tag{2.23}$$

2.2 Numerical results of inversion

In this section we present a numerical validation of inverse approach with reduced model by comparing Beck to global method. This numerical validation consists in recovering the identified flux $\hat{\varphi}(t)$ from data temperature $\boldsymbol{Y}$ at point A located at $(x, y) = (0.55, 0.95)$. The time evolutions of temperature at point A obtained by the complete model $\boldsymbol{Y}_{CM}$ and the reduced one $\boldsymbol{Y}_{RM}$ $(n = 110)$ are presented in figure 2.3.

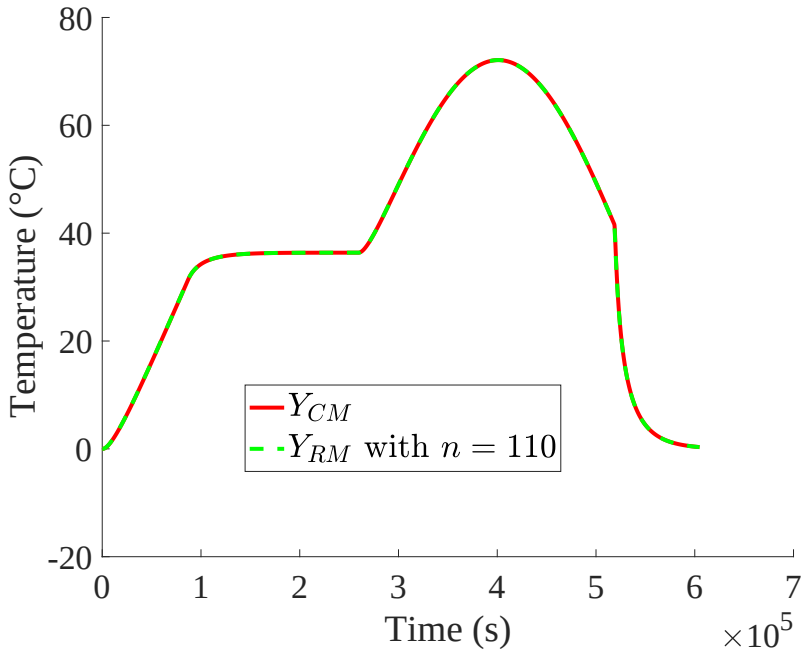

Figure 2.3: Validation of Reduced Model of order $n = 110$.

Both temperature evolutions are in very good agreement.
The reduction errors $(\boldsymbol{Y}_{RM} - \boldsymbol{Y}_{CM})$ for different orders reduction n are plotted in figure 2.4. For $n = 110$, the error is less than 0.08 (°C) except at the sudden change in the flux density. For the other models $n = 30$ and $n = 50$, the errors remain acceptable except, if we except again the peak due to the sudden variation of heat flux. The choice of the order reduction n will depend on the nature of the flux density (frequency) and the physical problem.
It is important to note that for inversion:

- The data $\boldsymbol{Y}$ is obtained by adding a normal and independent noise to the temperature obtained through the complete model $\boldsymbol{Y}_{CM}$. This noise is characterized by a standard deviation $\sigma_B = 0.1$ (°C). Only one point is considered.

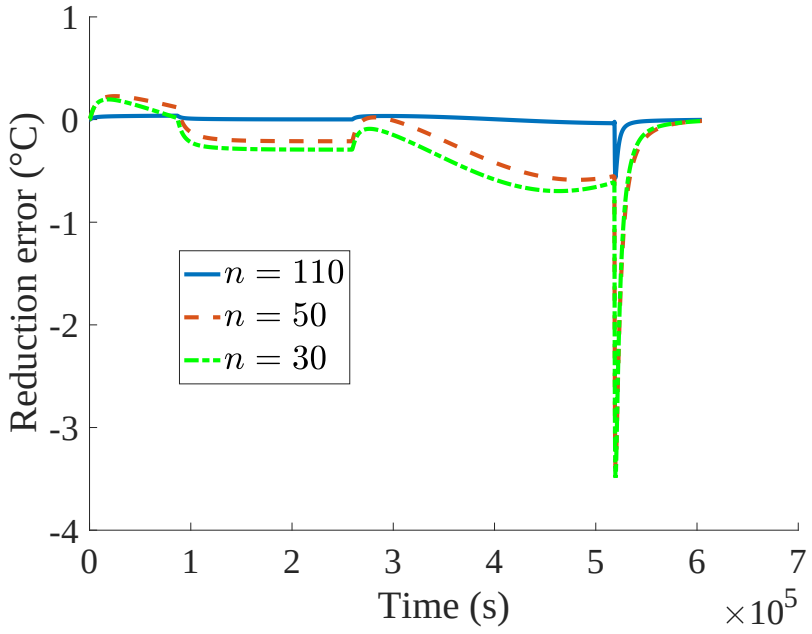

Figure 2.4: Reduction errors for different n.

- Inverse problems (Beck or global method) are solved with the reduced model (Eq. (2.6)) of order $n = 110$. Classically the order is chosen such that the additional error introduced by the reduction is of the same order than the noise. Obviously, the use of a reduced model facilitates and accelerates computation of $[\boldsymbol{L} - \Delta t \boldsymbol{M}(t)]^{-1}$ at each N_t time step (size 110×110 instead of 1139×1139).

2.2.1 Beck method

On-line identification by coupling Beck's method and reduced models has already been done in many works [14, 2, 15, 16]. The difficulty with this method is related to the choice of the n_f future time steps.
As evidenced in figure 2.5, the identified heat flux presents disturbances for $n_f = 0$. The high frequency oscillations do no impact on the temperature evolution at point A as shown

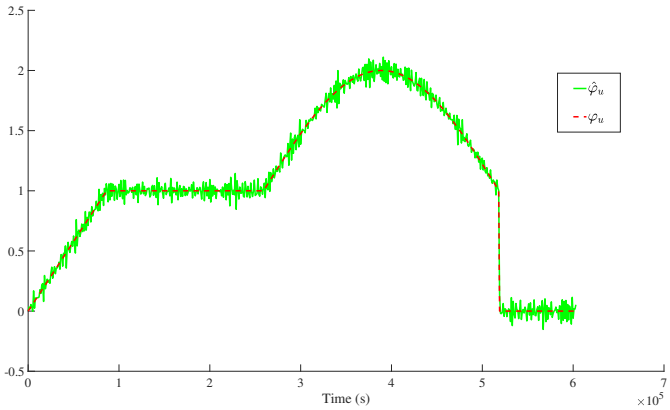

Figure 2.5: Evolution of estimated flux with σ_b=0.1 (°C) and $n = 110$.

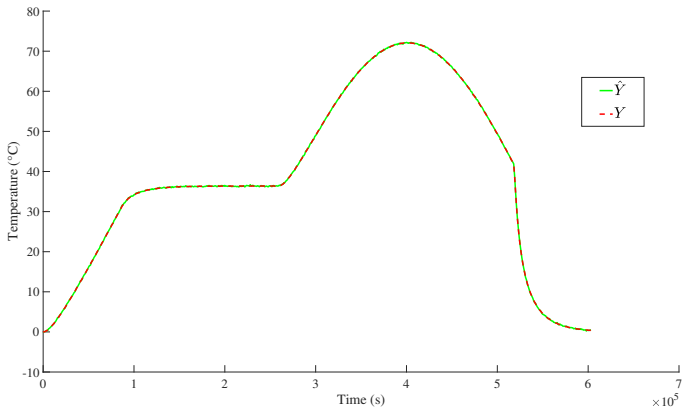

Figure 2.6: Estimated temperature compared to the exact one.

in figure 2.6.
Table 2.1 indicates errors observed on different cases. In case of $n = 110$ and σ_b=0.1 (°C), the mean quadratic error on temperature σ_T is of the same order as the added noise σ_b. When σ_b=0 (°C), we note that the result is more accurate with the model of reduced order $n = 110$ compared to the smaller model, with a calculation time less then 0.5 s.
Now comparing the 1st and the last cases, we observe this time that the smallest model is more accurate. This is due to the fact that the reduced model naturally filters the high frequencies of the signal.

case	σ_T [°C]	σ_{φ_u} [-]	CPU time [s]
$n = 110$ σ_b=0.1	0.095	5.4 E-2	0.53
$n = 110$ σ_b=0	$2.19E-14$	5.0 E-3	0.52
$n = 50$ σ_b=0	$2.85E-14$	2.2 E-2	0.18
$n = 30$ σ_b=0	$1.82E-14$	2.3 E-3	0.11
$n = 30$ σ_b=0.1	0.095	3.5 E-2	0.11

Table 2.1: Inversion results by Beck's method for different cases.

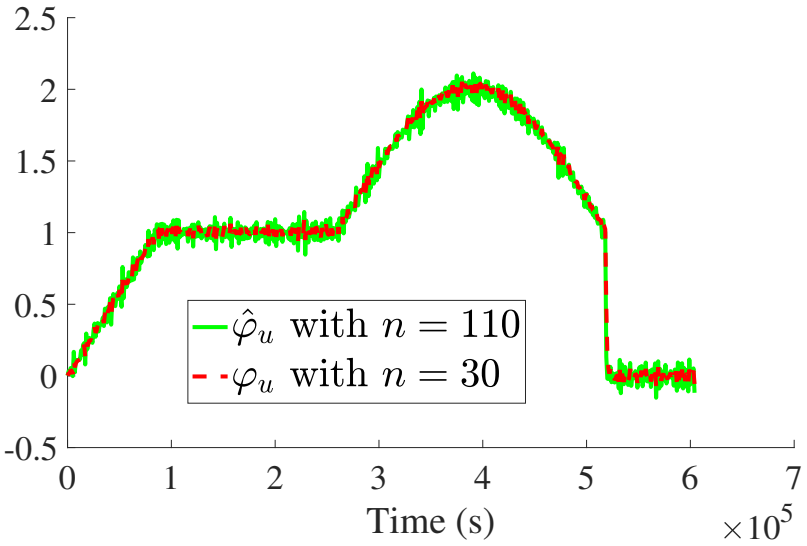

Figure 2.7: Evolution of estimated heat flux with $n = 110$ and $n = 30$.

2.2.2 Global method

The result can be obtained either:

- By implementing algorithm 1.
- Or by using the Matlab optimization toolbox with function *lsqcurvefit*. This function starts from initial guess $\varphi_u^{k=0}(t)$ and finds coefficients $\hat{\varphi}_u(t)$ that fit the best the nonlinear function *myfun*($\hat{\varphi}$,time) to the data $\boldsymbol{Y}$ (in the least-squares sense). *myfun*($\hat{\varphi}_u$,time) is the reduced order model function that takes as input a vector $\hat{\varphi}_u$ and returns a vector $\boldsymbol{Y}_{RM}$.

The obtained estimated heat flux is plotted in figure 2.8, where the exact flux is also represented for a comparison. The results presented here are obtained by keeping the default values of the Matlab function.
Table 2.2 presents the mean quadratic errors on estimated flux σ_{φ_u} and on temperature σ_T, as well as magnitude of computing time, for different cases.
The results clearly prove the efficiency of a reduced model in a global identification procedure : thanks to the reduced model, the identification is done in 30 seconds with a standard laptop.

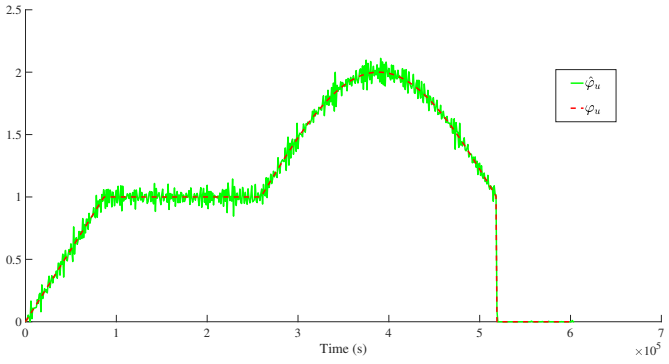

Figure 2.8: Estimated heat flux obtained with a global method.

case	σ_T [°C]	σ_{φ_u} [-]	CPU time [s]
$n = 110$ σ_b=0.1	0.03	4.9 E-2	28
$n = 110$ σ_b=0	$3.5E-7$	5.0 E-3	28
$n = 30$ σ_b=0.1	0.05	3.3 E-2	9

Table 2.2: Inversion results with a global method for different cases.

2.3 Conclusion

This study demonstrated the interest of using a reduced model to identify thermal sources. The obtained reduced model has proven its effectiveness by reducing the number of degrees of freedom of the problem. For the case under study, a reduced model defined by 110 modes runs almost 100 times faster than the classical method of finite elements. Two standard methods were then compared to solve the inverse problem. The Beck method has the advantage of being sequential. Nevertheless, in some other configurations, this method requires the implementation of a delicate regularization in a systematic way. Indeed, the optimum number of future time steps varies according to the respective importance of diffusion and advection phenomena.
The global method is considered robust since it requires the entire time evolution of the observable. It is thus an a posteriori method which is not adapted for a real-time identification. Moreover, it also requires a regularization parameter (the Tikhonov parameter) that has to be determined empirically. In the studied case, this parameter was not necessary, as the reduction naturally filters the high frequency, and acts as a regularization parameter. In addition, the reduced modal model decreases satisfactorily the computational times : it paves the way to implement an almost on-line identification strategy by a variable-sized sliding window approach. This technique was used in [17] to estimate heat flux on a braking system.

Bibliography

[1] J. Beck, B. Blackwell, A. Haji-Sheikh, Comparison of some inverse heat conduction methods using experimental data, International Journal of Heat and Mass Transfer 39 (17) (1996) 3649 – 3657. doi:http://dx.doi.org/10.1016/0017-9310(96)00034-8.
URL http://www.sciencedirect.com/science/article/pii/0017931096000348

[2] M. Girault, E. Videcoq, D. Petit, Estimation of time-varying heat sources through inversion of a low order model built with the modal identification method from in-situ temperature measurements, International Journal of Heat and Mass Transfer 53 (1-3) (2010) 206 – 219. doi:http://dx.doi.org/10.1016/j.ijheatmasstransfer.2009.09.040.
URL http://www.sciencedirect.com/science/article/pii/S0017931009005213

[3] C. R. S. C. J. James V. Beck, Ben Blackwell, Inverse Heat Conduction: Ill-Posed Problems, Wiley-Interscience, 1985.

[4] M. Ozisik, H. Orlande, Inverse Heat Transfer: Fundamentals and Applications, Taylor & Francis, 2000.
URL https://books.google.fr/books?id=D1JbgfxXg5MC

[5] K. Woodbury, Inverse Engineering Handbook, Handbook Series for Mechanical Engineering, CRC Press, 2002.
URL https://books.google.fr/books?id=hyPNBQAAQBAJ

[6] Y. Jarny, H. R. B. Orlande, Thermal Measurements and Inverse Techniques, CRC Press, 2001, Ch. Adjoint Methods, pp. 407–436.

[7] Y. Jarny, M. Ozisik, J. Bardon, A general optimization method using adjoint equation for solving multidimensional inverse heat conduction, International Journal of Heat and Mass Transfer 34 (11) (1991) 2911 – 2919. doi:http://dx.doi.org/10.1016/0017-9310(91)90251-9.
URL http://www.sciencedirect.com/science/article/pii/0017931091902519

[8] M. J. Colaco, G. S. Dulikravich, Thermal Measurements and Inverse Techniques, Heat Transfer, CRC Press, Taylor & Francis Group, 2011, Ch. A Servy of Basic Deterministic, Heuristic, and Hybrid Methods for Single-Objective Optimization and Response Surface Generation, pp. 355–405.

[9] M. J. Colaço, H. R. B. Orlande, G. S. Dulikravich, Inverse and optimization problems in heat transfer, Journal of the Brazilian Society of Mechanical Sciences and Engineering 28 (2006) 1 – 24.
URL https://www.scielo.br/j/jbsmse/a/ZVtPzmfXcq6d67DDkrJf9wf/?lang=en

[10] R. Fletcher, C. M. Reeves, Function minimization by conjugate gradients, The Computer Journal 7 (2) (1964) 149–154.
URL http://comjnl.oxfordjournals.org/content/7/2/149.abstract

[11] R. Fletcher, Practical Methods of Optimization, Wiley, 2013.
URL https://books.google.com.br/books?id=_WuAvIx0EE4C

[12] J. R. Shewchuk, An introduction to the conjugate gradient method without the agonizing pain, Tech. rep., Pittsburgh, PA, USA (1994).

[13] J. Beck, B. Blackwell, C. St-Clair, Inverse Heat Conduction-Ill Posed Problems, Wiley, Chichester, U.K., 1985.

[14] O. Quéméner, F. Joly, A. Neveu, On-line heat flux identification from a rotating disk at variable speed, International Journal of Heat and Mass Transfer 53 (7-8) (2010) 1529 – 1541. doi:http://dx.doi.org/10.1016/j.ijheatmasstransfer.2009.11.032.
URL http://www.sciencedirect.com/science/article/pii/S0017931009006322

[15] M. Girault, D. Petit, Identification methods in nonlinear heat conduction. part ii: inverse problem using a reduced model, International Journal of Heat and Mass Transfer 48 (1) (2005) 119 – 133. doi:http://dx.doi.org/10.1016/j.ijheatmasstransfer.2004.06.033.
URL http://www.sciencedirect.com/science/article/pii/S001793100400273X

[16] E. Videcoq, M. Lazard, O. Quéméner, A. Neveu, Online temperature prediction using a branch eigenmode reduced model applied to cutting process, Numerical Heat Transfer, Part A: Applications 55 (7) (2009) 683–705. http://dx.doi.org/10.1080/10407780902821490, doi:10.1080/10407780902821490.

[17] S. Carmona, Y. Rouizi, O. Quéméner, F. Joly, A. Neveu, Estimation of heat flux by using reduced model and the adjoint method. application to a brake disc rotating, International Journal of Thermal Sciences 131 (2018) 94 – 104. doi:https://doi.org/10.1016/j.ijthermalsci.2018.04.036.
URL http://www.sciencedirect.com/science/article/pii/S1290072917311171

Tutorial 7: Identification of Transfer Functions and of Boundary conditions

B. Rémy, D. Maillet*, A. Barthélémy

LEMTA, University of Lorraine & CNRS, Vandoeuvre-lès-Nancy, France
* E-mail: denis.maillet@univ-lorraine.fr

Abstract.

The objective of this tutorial, composed of two 1h30 sessions, is to construct a virtual sensor, that is a combination of physical sensors, associated with a mathematical model that allows the estimation, by an inverse technique, of quantities (local temperatures or rate of heat lowss) associated to locations where no sensor is present. This applies here to linear time invariant heat transfer, where temperature variation at any point in the system (output) is a convolution product between the intensity of a transient excitation (input) and a corresponding impulse response.The first session of the tutorial is devoted first to the solution of a direct 1D problem in a simulated case where the Laplace transforms of the 3 functions are analytically known, with a corresponding inversion to retrieve a surface temperature or a surface rate of heat flow. The second part of this session is devoted to experiments on a hollow cast-iron cylinder, with 2 thermocouples embedded in the thickness of its wall, with stimulation by a foil electric resistance over a part of its inner (front) face. Either the transient temperature or the rate of heat flow on this face is looked for. So, it requires first the the identification of the impulse response of each thermocouple (a transmittance or an impedance), which corresponds to a deconvolution problem in a calibration/validation experiment, followed by a new experiment for estimating front face temperature and rate of flow by a regularized deconvolution. In a second session of the tutorial, the identification step of the second part is replaced by the estimation of the parameters of a model of ARX structure (AutoRegressive model with eXogenous inputs), for retrieving the above impulse responses in a more parsimonious way.

Keywords: inverse heat conduction problem - virtual temperature sensor - deconvolution - thermal impedance - thermal transmittance – ARX parametric model

Scope

1. Introduction

2. Direct problem in 1D using analytical transfer functions in Laplace domain

3. Direct problem in any dimensions

   3.1 Scalar form of a discrete convolution product in heat transfer
   3.2 Vector/matrix form of a discrete convolution product in heat transfer

4. Different types of inverse deconvolution problems in time in 1D

   4.1 Recap
   4.2 Inverse heat conduction problem and virtual temperature sensor

      4.2.1 Position of the inverse problem (IHCT or VTS)
      4.2.2 Regularization of the IHTC and VTS deconvolution problems

5. Solution of the inverse 1D problem using two outputs

6. Solution of the inverse multidimensional problem using prior model identification

7. Use of an ARX model for IHCP and VTS problems

   7.1 Structure of an ARX model

   7.2 Link between ARX and convolutive models

   7.3 Identification of the ARX parameters and their validation

      7.3.1 Estimation of the ARX parameters for three given orders
      7.3.2 Interest of ARX models and choice of the optimal order for an ARX model and its validation

Appendix A - Laplace transforms and thermal quadrupoles: a reminder

Appendix B - Inversion of the Laplace transform

Appendix C - Singular Value Decomposition of a matrix and SVD version of the ordinary least square estimator

Appendix D - Truncated SVD and Tikhonov regularization of zero order

   D.1 TSVD regularization
   D.2 Tikhonov regularization of zero order

Appendix E - Regularization using future time steps

Appendix F - Construction of models for 2 points VTS and IHCP

Appendix G - Interest of the Singular Value Decomposition in linear parameter estimation

References

1. Introduction

Classical heat flux sensors do not provide really non-intrusive measurements of the transient heat flux at a solid/solid or solid/fluid interface because their presence generates a 3D heat transfer, if their area is small, or add an extra resistance and heat capacity, if their area is large. In some applications, use of temperature sensors at similar interfaces may also be difficult, because of a harsh outside environment (possible sensor destruction) or by presence of radiation (possible different absorptivities between surface sensor and the surrounding surface, with a resulting temperature measurement bias).

Here the alternative consists in considering an inverse input problem: one or two temperatures are measured at different depths with respect to the excitated front face of a wall in a transient configuration in a slab of finite thickness.

These temperatures can be expressed in terms of the unknowns of the inverse problem, which allows the estimation of either the wall heat flux for an Inverse Heat Conduction Problem, or the temperature at location where no temperature sensor is present once a Virtual Temperature Sensor has been designed.

The corresponding direct problems, in a 1D heat transfer configuration, are presented in section 2. They use models based on convolution products with corresponding impulse responses (transmittances and impedances). These transforms, the transfer functions, have explicit analytical expressions in 1D in the Laplace domain (see, the Thermal Quadrupole method [1]), that are detailed in Appendix A. The values of their the impulse responses can be found by numerical inversion of their Laplace transforms (the « operational » transfer functions), see details in Appendix B.

Section 3 is devoted to the general subject of parameterizing a convolution product, either with a scalar expression or in a vector/matrix form, in order to give it a finite dimensional structure in linear algebra. Both expressions make the notion of doses of input and impulse response appear.

The 1D inverse input problem, using 1 temperature output, is presented in section 4, with details on 3 regularization techniques (Tikhonov, TSVD and Future Time Steps) given in Appendices C, D and E.

Section 5 is devoted to the corresponding 1D inverse input problem, using now 2 temperature outputs. Its main advantage is to retrieve estimations of front face temperature and rate of heat flows independent of the boundary conditions. Derivation of the models used is detailed in Appendix F.

If heat transfer is not 1D but still linear, with coefficients of the heat equation and of its associated conditions that do no not depend of time, the temperature and heat flux solution has still a convolutive nature if the thermal stimulation is separable. This is the subject of section 6, where the impulse responses are estimated in an identification experiment for further use in an inverse input problem after an experimental verification. Both steps require a regularized deconvolution, whose performance can be assessed before making the measurements, by the indicators, derived from the Singular Values Decomposition technique, that are presented in Appendix G.

Another type of experimental identification, using a AutoRegressive model with eXogeneous structure (ARX) is presented in section 7. Its main advantage, with respect to a convolutive model is the weak numbers of parameters that can reproduce the experimental output, which is not the case for impulse responses, even if a link exists between them.

Seven appendices complete the text of this tutorial. They are followed by a list of references.

2. Direct problem in 1D using analytical transfer functions in Laplace domain

We consider here the case of a linear 1D heat transfer in a slab of thickness e heated by a surface source $P(t)$ (W) over one of its faces of area S. The analytical solution of this problem, that is the temperature field $\theta(x, t)$ (K) and the rate of heat flow $\Phi(x, t)$ (W) field can be found in Laplace domain by the Quadrupole method, see Appendix 1, as soon as the two boundary conditions at $x_{in}=0$ and $x_{in}=e$ are given. Convective and (linearized) radiative heat losses are also assumed on both front and rear faces, towards the surrounding fluid at temperature θ_∞, through two heat exchange coefficients, h_0 and h_e, see figure 1.

We assume here that θ_∞ is equal to zero, in order to have one single source $P(t)$ only, in the direct problem to be solved. The surface density of the source $q(t)=P(t)/S$ (W/m^2) is absorbed by the front face ($x_{in}=0$).

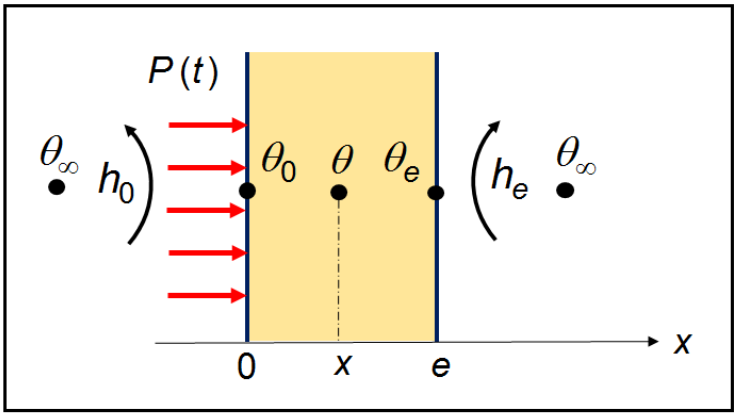

Figure 1 – Heated slab on its front face, with linear heat losses on both faces

It is shown in Appendix 1 that the temperature (θ) / rate of heat flow (Φ) vectors, in the Laplace domain (noted here with an upper bar on temperatures and on the front face source) are given by the following matrix equation:

$$\begin{bmatrix}\bar{\theta}_0\\ \bar{P}\end{bmatrix}=\begin{bmatrix}1 & 0\\ k_0 & 1\end{bmatrix}\begin{bmatrix}A_e & B_e\\ C_e & D_e\end{bmatrix}\begin{bmatrix}1 & 0\\ k_e & 1\end{bmatrix}\begin{bmatrix}\bar{\theta}_e\\ 0\end{bmatrix}=\begin{bmatrix}A_T & B_T\\ C_T & D_T\end{bmatrix}\begin{bmatrix}\bar{\theta}_e\\ 0\end{bmatrix} \quad \text{with} \quad k_0=h_0 S \quad \text{and} \quad k_e=h_e S \qquad (1)$$

where the four coefficients A_e, B_e, C_e and D_e depend on the Laplace variable, on the area S and on the thickness e of the slab, and on the conductivity λ and on the volumetric heat ρc of its constitutive material).

Equations (1), and (A8a,b) in Appendix A, yield the solution of the direct problem, that is finding the temperatures and conductive rates of heat flow on both faces of the slab, that are proportional, in the transformed domain, to the transform of the given stimulation $P(t)$:

$$\bar{\theta}_0 = \bar{z}_0\ \bar{P} \quad \text{with} \quad \bar{z}_0 = A_T / C_T \quad ; \quad \bar{\Phi}_0 = \bar{w}_0^{\Phi}\ \bar{P} \quad \text{with} \quad \bar{w}_0^{\Phi} = (C_e + k_e D_e) / C_T \quad \text{(2a,b)}$$

$$\bar{\theta}_e = \bar{z}_e\ \bar{P} \quad \text{with} \quad \bar{z}_e = 1/C_T \quad ; \quad \bar{\Phi}_e = \bar{w}_e^{\Phi}\ \bar{P} \quad \text{with} \quad \bar{w}_e^{\Phi} = k_e / C_T \quad \text{(2c,d)}$$

A specific notation is usedhere. $L[\,.\,]$ to designate the Laplace transform in time of a function depending on both space (x) and time (t) :

$$\bar{\psi}(x, p) \equiv L[\psi(x, t)] \equiv \int_0^t \psi(x, t) \exp(-p\,t)\, \mathrm{d}t \quad \text{for} \quad \psi = \theta \quad \text{or} \quad \Phi \qquad \text{(2e)}$$

So, in the Laplace domain, temperature responses as well as rate of heat flow responses are proportional to the surface power excitation P, that is the ***cause*** of the corresponding transient heat transfer. Mathematically speaking, $P(t)$ is the unique (power) source which differs from the front face rate of heat flows $\Phi_0(t)$ (proportional to the material conductivity and area and to the local temperature gradient), because of convective and/or radiative losses that are linearized here. So, if $P(t)$ is an incoming radiative rate of heat flow, $\Phi_0(t)$ is the corresponding absorbed conductive flow.

Its consequence, the temperature rise on the front face, can be considered as a "*pseudo source*" and the corresponding temperature/heat flux responses are easily deduced from equations (2):

$$\bar{\theta}_e = \bar{w}_{e0}\ \bar{\theta}_0 \quad \text{with} \quad \bar{w}_{e0} = 1/A_T \qquad \text{(3a)}$$

$$\bar{\Phi}_0 = \bar{y}_{00}\ \bar{\theta}_0 \quad \text{with} \quad \bar{y}_{00} = (C_e + k_e D_e)/(A_e + k_e B_e) \qquad \text{(3b)}$$

$$\bar{\Phi}_e = \bar{y}_{e0}\ \bar{\theta}_0 \quad \text{with} \quad \bar{y}_{e0} = k_e / A_T \qquad \text{(3c)}$$

Equations (2a to d) and (3a to c) have the same generic form:

$$\bar{y}(p) = \bar{h}(p)\ \bar{u}(p) \qquad \text{(4a)}$$

where $\bar{h}(p)$ is called a *transfer function*, the input u being either the real heat source P, or the pseudo sources θ_0 or Φ_0, while the output y is either the temperature θ or the rate of heat flow Φ on one face of the slab or inside of it.

In order to retrieve the solution of the inverse Laplace transform $y(t)$ of $\bar{y}(p)$, two methods are available:

i) The first one consists in calculating the exact Laplace transform of the input $\bar{u}(p)$ of $u(t)$, which is possible if an analytical expression of $u(t)$ is available, and to multiply it by $\bar{h}(p)$. Once the analytical expression of $\bar{y}(p)$ is available, return to its inverse transform can be implemented by various techniques, either analytical or numerical, detailed in Appendix B.

ii) The second method consists in inverting the transfer function $\bar{h}(p)$ first, using one of the techniques described in Appendix B, in order to get its corresponding inverse Laplace transform $h(t)$, which is called the *impulse response*. It can also be considered as a Green's function, for the special case of linear time invariant systems (see section 6 further on). This impulse response can be (see Appendix A for the complete expressions of the corresponding transfer functions) :

- an impedance (in K.W^{-1}.s^{-1}) $z_0(t)$, $z_e(t)$ or $z_x(t)$ (input, the real power source $P(t)$, in watts and output, a local temperature in kelvins), or an other impedance $z_0'(t)$, $z_e'(t)$ or $z_x'(t)$ where a pseudo-source, the front face rate of heat flow Φ_0 replaces P,

- a power transmittance (in s^{-1}) $w_0^{\Phi}(t)$, $w_e^{\Phi}(t)$ or $w_x^{\Phi}(t)$ (input, the real power source $P(t)$, and an output, a local rate of heat flow, both in watts),

- a temperature transmittance (in s^{-1}) $w_{e0}(t)$ or $w_{x0}(t)$ (input, a pseudo-source, the front face temperature $\theta_0(t)$, and output, a local temperature, both in kelvins),

- an admittance (in W.K^{-1}.s^{-1}) $y_{00}(t)$, $y_{e0}(t)$ or $y_{x0}(t)$ (input, a pseudo-source, the front face temperature $\theta_0(t)$, in kelvins, and output a local rate of heat flow, in watts).

The second step in this second method consists in using the return from the Laplace domain of equation (7a) into the original time domain that makes a convolution product appear:

$$y(t) = (h * u)(t) = \int_0^t h(t-t')\,u(t')\,\mathrm{d}t' = \int_0^t u(t-t')\,h(t')\,\mathrm{d}t' \qquad (4b)$$

Remark 1: Equation (4b) shows that the convolution product is commutative, which means that the two functions $h(t)$ and $u(t)$ can be exchanged in the definition and the practical calculation of the output $y(t)$.

Remark 2 (important): The various analytical close form expressions of the transfer functions (operational impedances, transmittances and admittances), in the Laplace domain, are given above for an homogeneous slab in transient 1D transfer, with linear heat losses over both of its faces, see equations (2a) to (6c). However, analogous transfer functions exist in transient 3D linear heat transfer in material systems, if some conditions are met, see [11], even if their corresponding expressions are not available. In these more involved configurations, the inverse Laplace transforms of the transfer function, that is the impulse response, can be found by model reduction, if a detailed numerical solution for the output is available, or by model identification, if experimental measurements of both both input and output have been made, see section 3.2 below.

Three conditions are necessary for an impulse response to exist, in a Single Input/Single Output (SISO) case in a transient 0D, 1D, 2D or 3D heat transfer case: i) Initial steady state temperature field, ii) Space/time separation in the writing of the thermal source for a detailed model of transient diffusion with boundary conditions and iii) This model has to be Linear with Time Independent coefficients (LTI). Forced convection in a porous medium, or in a heat exchanger, with a 3D velocity field that does not vary in time, can meet these conditions [14].

3. Direct problem in any dimensions

3.1 Scalar form of a discrete convolution product in heat transfer

By definition, the 3 functions *y, h* and *u* involved in convolution product (4b) are equal to zero at time $t = 0$ and the source u departs from zero at time $t = 0^+$, that is at a time immediately past zero. This departure from a zero level for u is the definition of the origin of the time scale. This stems from the fact that the output of this model is a forced one and that no relaxation of a past non-zero output levels is considered here. So, one writes here :

$$u(0) = y(0) = h(0) = 0 \quad \text{and} \quad \dot{u}(0^-) = \dot{y}(0^-) = \dot{h}(0^-) = 0$$
$$\text{with } \dot{x}(t) = \frac{\mathrm{d}x}{\mathrm{d}t} \quad \text{for } x = u, h \text{ or } y \tag{5}$$

Equation (5), means that at time 0 the 3 functions, as well as their derivatives, are equal to zero, even if a sudden change, for example to a finite or infinite level can happen at a positive time $t = 0^+$. In that case

In practice, the output is calculated, or measured, on a discrete time grid using a discretizetion or acquisition time step Δt and model (4b) is written at a time $t_k = k\,\Delta t$ for $k \geq 1$and a numerical quadrature has to be made:

$$y_k = y(t_k) \approx \Delta t \sum_{j=1}^{k} \tilde{h}_j \, \tilde{u}_{k-j+1} \quad \text{with } \tilde{x}_j = \frac{1}{\Delta t} \hat{x}_j \quad \text{and } \hat{x}_j = \int_{t_{j-1}}^{t_j} x(t)\,\mathrm{d}t \quad \text{for } x = h \text{ or } u \tag{6}$$

In this notation $\hat{x}_j$ is the dose of function $x(t)$ on interval $\left]t_{j-1},\ t_j\right]$, while $\tilde{x}_j$ is its average value on the same interval. Let us note that the zero value of j corresponds to initial time, where $t_0 = u_0 = h_0 = y_0 = 0$. Of course approximation (6) is valid if Δt is small enough to make the approximation converge.

Remark 3: The numerical quadrature above of the continuous integral consists in replacing the 2 original functions $u(t)$ and $h(t)$ by their averaged values, $\tilde{u}_j$ and $\tilde{h}_j$, that solely depends on their doses $\hat{h}_j$ and $\hat{u}_j$ over a given time interval of duration Δt. The calculation of doses can be made through the use of either the cumulative input, or of the step response. This last one is the response to a Heaviside input of unit level and is also the primitive of the step function. A new notation is introduced here, where a capital letter $X(t)$ designates the primitive of a function $x(t)$ that meets conditions (5) :

$$X(t) = \int_0^t x(t')\,\mathrm{d}t' \quad \Leftrightarrow \quad \bar{X}(p) = \frac{1}{p}\,\bar{x}(p) \qquad \text{for} \quad x = h \ \text{or}\ u \tag{7a,b}$$

An exact expression of this integral, in terms of doses, is available on the time grid:

$$X(t_k) = \sum_{j=1}^{k} \hat{x}_j \quad \text{for} \quad x = h \ \text{or}\ u \tag{7c}$$

So, the dose of the input or of the impulse response is simply the variation of the cumulative input or of the step response between the two bounds of the corresponding time interval :

$$\hat{x}_j \equiv \Delta X_j \quad \text{where} \ \ X_j = X(t_j) \ \ \text{and} \ \ \Delta X_j = X_j - X_{j-1} \ \ \text{for} \ \ x = u \ \text{or}\ h \tag{7d}$$

So, equation (6) takes the following form, sometimes called the Duhamel convolution product:

$$y_k = y(t_k) \approx \sum_{j=1}^{k} \Delta H_j\ \tilde{u}_{k-j+1} \tag{7e}$$

Remark 4: The exact step response $H(t)$ can be found by numerical Laplace inversion of $\bar{H}(p) = \bar{h}(p)/p$ if the explicit analytical expression of the transfer function $\bar{h}(p)$ is available, see (7b).

Remark 5: Because numerical quadrature (6) is just an approximation, valid for small time step, its inversion, for known exact or noisy input and output (model reduction/identification problem), see section 3.2, is not able to bring any information about the point values of $h(t)$ within the $\left]t_{j-1},\ t_j\right]$ interval: only doses, or averaged values, also defined in (6), of this function can be estimated . Let us also note that even if function $h(t)$ is not bounded on a given time interval, its dose

can be calculated. This is the case for the front face time impedance $h(t) = z_0(t)$, whose Laplace impedance is given in (2a). Its short time approximation is $z_0(t) \approx 1/(b\sqrt{\pi t})$, where *b* is the thermal effusivity of the material, see [1, section 1.4.1]). It goes to infinity as time t goes to zero whereas its corresponding step response $H(t) = Z_0(t) \approx 2\sqrt{t}/(b\sqrt{\pi})$ is finite, which yields a dose of impulse response on the $\left]t_{j-1},\ t_j\right]$ interval that this calculated by (7e): $\hat{h}_j = \hat{z}_{0,j}(t) \approx \left(2/(b\sqrt{\pi})\right)\left(\sqrt{t_j} - \sqrt{t_{j-1}}\right)$.

Remark 6 : If the input $u(t)$ is both ***bounded*** and ***continuous***, but only known on the two bounds of the $\left[t_{j-1},\ t_j\right]$ interval, a good approximation of its dose is :

$$\hat{u}_j \approx \frac{\Delta t}{2}\left(u(t_{j-1}) + u(t_j)\right) \tag{7f}$$

Remark 7 : If there is a local discontinuity of the input at time t_j , right and left limit values around this time are used and this approximation becomes:

$$\hat{u}_j \approx \frac{\Delta t}{2}\left(u(t_{j-1}) + u(t_j^-)\right) \text{ and } \hat{u}_{j+1} \approx \frac{\Delta t}{2}\left(u(t_j^+) + u(t_{j+1})\right) \tag{7g}$$

3.2 Vector/matrix form of a discrete convolution product in heat transfer

Equation (7d) can be given the following expression, involving column vectors and matrices:

$$\boldsymbol{y} = \frac{1}{\Delta t}\,\mathbf{N}(\hat{\boldsymbol{u}})\,\hat{\boldsymbol{h}} = \frac{1}{\Delta t}\,\mathbf{N}(\hat{\boldsymbol{h}})\,\hat{\boldsymbol{u}} \quad \text{with} \quad \boldsymbol{y} = \begin{bmatrix} y_1 = y(t_1) \\ y_2 = y(t_2) \\ y_3 = y(t_3) \\ \vdots \\ y_k = y(t_k) \end{bmatrix} \;;\; \hat{\boldsymbol{x}} = \begin{bmatrix} \hat{x}_1 \\ \hat{x}_2 \\ \hat{x}_3 \\ \vdots \\ \hat{x}_k \end{bmatrix} \quad \text{for } x = h \text{ or } u \tag{8a}$$

Here $\mathbf{N}(.)$ is a square matrix of size k x k ,that is a function of a column vector of size k x 1 :

$$\mathbf{N}(\boldsymbol{\psi}) \equiv \begin{bmatrix} \psi_1 & & & & \\ \psi_2 & \psi_1 & & 0 & \\ \psi_3 & \psi_2 & \psi_1 & & \\ \vdots & \vdots & \vdots & \ddots & \\ \psi_k & \psi_{k-1} & \psi_{k-2} & \cdots & \psi_1 \end{bmatrix} \quad \text{where} \quad \boldsymbol{\psi} = \begin{bmatrix} \psi_1 \\ \psi_2 \\ \psi_3 \\ \vdots \\ \psi_k \end{bmatrix} \tag{8b}$$

$\mathbf{N}(\boldsymbol{\psi})$ is a lower triangular Toeplitz matrix of order *k*, whatever the nature of vector $\boldsymbol{\psi}$.

The set of real-valued lower triangular Toeplitz matrices of a given order, associated with the matrix addition and the multiplication by a vector, constitutes a commutative ring [15]. This kind of structure is both commutative and associative, which means :

$$\mathbf{N}(\boldsymbol{\psi}_1)\,\boldsymbol{\psi}_2 = \mathbf{N}(\boldsymbol{\psi}_2)\,\boldsymbol{\psi}_1 \quad \text{and} \quad \mathbf{N}(\boldsymbol{\psi}_1)\,\mathbf{N}(\boldsymbol{\psi}_2)\,\boldsymbol{\psi}_3 = \mathbf{N}\left(\mathbf{N}(\boldsymbol{\psi}_1)\,\boldsymbol{\psi}_2\right)\boldsymbol{\psi}_3 = \mathbf{N}(\boldsymbol{\psi}_1)\left(\mathbf{N}(\boldsymbol{\psi}_2)\,\boldsymbol{\psi}_3\right) \tag{8c}$$

An alternate expression of the vector of doses of input and impulse response is available, using their expressions (7a,b,c,d) in terms of their cumulative doses $\hat{\boldsymbol{x}} = \Delta t\ \tilde{\boldsymbol{x}}$:

$$\boldsymbol{X} = \mathbf{N}(\boldsymbol{g})\,\hat{\boldsymbol{x}} \;\Rightarrow\; \hat{\boldsymbol{x}} = \left(\mathbf{N}(\boldsymbol{g})\right)^{-1}\boldsymbol{X} = \mathbf{N}(\boldsymbol{g}^{+})\,\boldsymbol{X} \quad \text{for} \quad x = u \ \text{ or } \ h \tag{8d}$$

$$\text{where } \boldsymbol{X} = \begin{bmatrix} X_1 \\ X_2 \\ X_3 \\ \vdots \\ X_k \end{bmatrix} \;;\; \boldsymbol{g} = \begin{bmatrix} 1 \\ 1 \\ 1 \\ \vdots \\ 1 \end{bmatrix} \text{ and } \boldsymbol{g}^{+} = \begin{bmatrix} 1 \\ -1 \\ 0 \\ \vdots \\ 0 \end{bmatrix}$$

So, the corresponding alternate expression of the convolutive model becomes, using the properties of Toeplitz matrices and the relationship between doses and internal averages is:

$$\boldsymbol{y} = \mathbf{N}(\boldsymbol{g}^{+})\,\mathbf{N}(\boldsymbol{U})\,\tilde{\boldsymbol{h}} = \mathbf{N}(\boldsymbol{g}^{+})\,\mathbf{N}(\boldsymbol{H})\,\tilde{\boldsymbol{u}} \tag{8e}$$

The interest of this model is to use only cumulative vectors $\boldsymbol{U}$ **and** $\boldsymbol{H}$ and to replace doses by interval averages $\tilde{\boldsymbol{u}}$ and $\tilde{\boldsymbol{h}}$, whose absolute levels can be compared to the corresponding levels of the continuous functions $u(t)$ and $h(t)$, disregarding the magnitude of the time step Δt.

From now on, we restrict the generality of model (8a) to cases where the impulse response and input are both ***bounded*** and ***continuous*** on the $]0,\, t_m]$ time interval, where $t_m = m\Delta t$ is the final time of observation. So approximation (7d) is used and model (8a) becomes:

$$\boldsymbol{y} = \mathbf{M}(\boldsymbol{u})\,\boldsymbol{h} = \mathbf{M}(\boldsymbol{h})\,\boldsymbol{u} \quad \text{where } \mathbf{M}(\boldsymbol{u}) = \Delta t\ \mathbf{N}^2(\boldsymbol{f})\,\mathbf{N}(\boldsymbol{u}) \text{ and } \mathbf{M}(\boldsymbol{h}) = \Delta t\ \mathbf{N}^2(\boldsymbol{f})\,\mathbf{N}(\boldsymbol{h}) \tag{8f}$$

$$\text{with } \boldsymbol{f} = \begin{bmatrix} 1/2 \\ 1/2 \\ 0 \\ \vdots \\ 0 \end{bmatrix};\ \boldsymbol{x} = \begin{bmatrix} x_1 = x(t_1) \\ x_2 = x(t_2) \\ x_3 = x(t_3) \\ \vdots \\ x_k = x(t_k) \end{bmatrix};\ \text{and } \tilde{\boldsymbol{x}} = \mathbf{N}(\boldsymbol{f})\,\boldsymbol{x} \text{ with } \hat{\boldsymbol{x}} = \Delta t\,\tilde{\boldsymbol{x}} \text{ for } x = h \text{ or } u$$

So approximation (8e), in case of **continuous and bounded** functions or possibly (7g), in case of **local discontinuiti(es)**, can be used to solve the direct problem where input and output are known on a discrete grid only.

Let us note that equation (8f) corresponds to the two models that can be used for 3 different inverse problems, numbered 1 to 3 that are detailed below.

If the impulse response $\boldsymbol{h}$ is unknown, it has to be identified by inversion of matrix $\mathbf{M}(\boldsymbol{u})$, for the $\boldsymbol{y} = \mathbf{M}(\boldsymbol{u})\,\boldsymbol{h}$ version of the direct problem. This type of identification problem concerns two applications:

1) The data of the inverse problem can stem from the solution (output) $\boldsymbol{y}$ of a detailed model, that is the solution by finite elements or by any numerical solution of the heat equation with its associated boundary conditions for a given input $\boldsymbol{u}$. This type of inverse problem is called **model reduction**, since the detailed model will be replaced by a reduced model, here $\boldsymbol{y} = \mathbf{M}(\boldsymbol{h})\,\boldsymbol{u}$ the convolutive model, here $\boldsymbol{y} = \mathbf{M}(\boldsymbol{h})\,\boldsymbol{u}$, for future diverse direct or inverse applications. The interest of this reduced model is that its output is simpler and faster to solve, see lectures 7A and B in this school.

2) The data of the inverse problems can stem from a calibration experiment, where the input $\boldsymbol{u}$ and the output $\boldsymbol{y}$ are measured, possibly with noise present in the two experimental signals. This type of inverse problem is called (experimental) **model identification**, where no detailed model is not implemented, with exactly the same type of future use. However Model identification problems require generally the use of a regularized inversion, because of presence of noise in the data, which is not always the case for model reduction.

3) If the impulse response is known, after a model reduction or identification, and an input $\boldsymbol{u}$ (also called a "source") is unknown for a given experiment, where the output $\boldsymbol{y}$ is measured at one location of the system (it can also be extended to several point peasurements, see section 5). So, it is matrix $\mathbf{M}(\boldsymbol{h})$ that has to be inverted in the form $\boldsymbol{y} = \mathbf{M}(\boldsymbol{h})\,\boldsymbol{u}$ of the direct problem (8f). This type of inverse problem is called a **source estimation problem**, which is called, in heat transfer, an **Inverse Heat Conduction Problem** (IHCP) if u is a flux or rate of heat flux, or a **Virtual Temperature Sensor** (VTS) if it is a measured temperature variation.

4. Different types of inverse deconvolution problems in time in 1D

4.1 Recap

The most general form of the discrete convolutive model, is given by equation (6), for a scalar version, or by equation (8a) for its vector/matrix version. These two versions of the same model use a dosal parametrization of both input and impulse response that explain the instantaneous response $y(t)$ at discrete instants of a time grid. The doses of a given function $x(t)$ are just the integral of a this function on a given time step .They are valid if the calculated response do not vary when the time step decreases.

From now on, we'll be using the vector version, which makes writing more compact. Let us also note that in the direct problem, where doses $\hat{\boldsymbol{u}}$ and $\hat{\boldsymbol{h}}$ are known, both quantities commute in (8d).

4.2 Inverse heat conduction problem and virtual temperature sensor

4.2.1 Position of the inverse problem (IHCT or VTS)

In the preceding configuration depicted in Figure 1, we are interested in estimating the front face rate of heat flow $\Phi_0(t) = -\lambda S \left.\dfrac{\partial \theta}{\partial x}\right|_{x=0}$ using the measurement $\theta^{\exp}(t)$ of the rear face temperature $\theta(t)$ on the $[0, t_f]$ time interval at a point P at a depth x $(0 \le x \le e)$ where a temperature sensor is present. This problem is called the *Inverse Heat Condition Problem* (IHCP), see Beck et al. [9] and is based on model (A13b), see Annex A, written with the assumption $h_0 = 0 \Rightarrow \Phi_0(t) = P(t)$ and $z_x = z_x'$.

$$\bar{\theta} = \bar{z}_x \, \bar{\Phi}_0 \qquad \Leftrightarrow \qquad \theta(t) = \left(z_x * \Phi_0\right)(t) \tag{9a, b}$$

Instead of looking for the front face heat flux $\phi_0(t)$, that is a Neumann boundary condition, we can try to recover the Dirichlet boundary condition, that is the front face temperature $\theta_0(t)$, with the same local temperature measurements $\theta^{\exp}(t)$. This corresponds to the use of a *Virtual Temperature Sensor* (VTS), see [10], and is based on model (A13a), see Annex A:

$$\bar{\theta} = \bar{w}_{x0} \, \bar{\theta}_0 \qquad \Leftrightarrow \qquad \theta(t) = \left(w_{x0} * \theta_0\right)(t) \tag{10a,b}$$

In both cases (IHCP or VTS) the discrete inverse problem is an inverse input problem whose direct model can be put under the form (8e), that is :

$$\boldsymbol{y} = \boldsymbol{A}\,\tilde{\boldsymbol{u}} = \mathbf{N}(\boldsymbol{g}^{+})\,\mathbf{N}(\boldsymbol{H})\,\tilde{\boldsymbol{u}} \quad \text{with} \quad \begin{cases} \boldsymbol{A} = \mathbf{N}(\boldsymbol{g}^{+})\,\mathbf{N}(\boldsymbol{Z}_x) \text{ and } \tilde{\boldsymbol{u}} = \tilde{\boldsymbol{\Phi}}_0 \text{ in the IHCP case} \\ \boldsymbol{A} = \mathbf{N}(\boldsymbol{g}^{+})\,\mathbf{N}(\boldsymbol{W}_{x0}) \text{ and } \tilde{\boldsymbol{u}} = \tilde{\boldsymbol{\theta}}_0 \text{ in the VTS case} \end{cases} \tag{11a,b}$$

Here $\boldsymbol{Z}_x$ is the cumulated impedance while $\boldsymbol{W}_{x0}$ is the cumulative transmittance, while of the matrices and vectors present in the above equations are now of order $k = m$.

Let us note that if function $u(t)$ is bounded and continuous, the above model can be given the following form :

$$\boldsymbol{y} = \boldsymbol{B}\,\boldsymbol{u} \quad \text{where} \quad \boldsymbol{B} = \mathbf{N}(\boldsymbol{g}^+)\,\mathbf{N}(\boldsymbol{f})\,\mathbf{N}(\boldsymbol{H}) \quad \text{since} \quad \tilde{\boldsymbol{u}} = \mathbf{N}(\boldsymbol{f})\,\boldsymbol{u} \qquad \text{(12a, b)}$$

However this writing is not really useful for the inverse problem, since inversion of (12b) is:

$$\boldsymbol{u} = \left(\mathbf{N}(\boldsymbol{f})\right)^{-1} \tilde{\boldsymbol{u}} = \mathbf{N}(\boldsymbol{f}^+)\,\tilde{\boldsymbol{u}} \quad \text{where} \quad \boldsymbol{f}^+ = 2\left[1\ \text{-}1\ 1\ \text{-}1 \cdots (\text{-}1)^{m\text{-}1}\right]^T \qquad \text{(12c)}$$

So, because of the oscillatory nature of the coefficients of $\mathbf{N}(\boldsymbol{f}^+)$, it is not possible to retrieve the exact instantaneous values of the input, even if its interval averages are exact.

Each of the two inverse problems (11a,b) is a deconvolution problem, whose solution, the input $\hat{u}(t)$, is very unstable, that is very sensitive to the level of noise in the data, that is in the measured values of the exact output $y(t) = \theta(x, t)$, if the parameters of model (11a,b), that is the cumulative impulse response $H(t) = Z_x(t)$ or $W_{x0}(t)$ is perfectly known. It results from the numerical inversion of the analytical transfer function $\bar{h}\ (p)$, or of its primitive, the Laplace transform $\bar{H}\ (p) = \bar{h}\ (p)/p$ of the step response here, see equation (7c). This ill-posed character derives from two factors:

i) In real physical or in numerical experiments, the output $y(t)$ is not known in a continuous way. It is observed, or calculated, for discrete values of the time variable on the $[0,\ t_f]$ time interval, $t_f = t_m$ being the last time of measurement, and the preceding convolution product becomes:

$$y(t_k) = \int_0^{t_k} h(t_i - t')\,u(t')\,\mathrm{d}t' \quad \text{with} \quad t_k = k\ \Delta t \quad \text{for} \quad k = 1 \text{ to } m \quad \text{and} \quad \Delta t = t_f / m \qquad \text{(13a)}$$

So, in order to have a finite number of unknowns (m at most), the 3 functions present in (11a,b) have been replaced by their parameterized form, their interval averages or doses, which is described in section 3 above.

ii) In experiments, the different measured values y_k^{exp} differ from their exact theoretical counterparts, that are corrupted by some measurement (additive) noise ε_i :

$$y_k^{exp} = y(t_i) + \varepsilon_k \qquad \text{(13b)}$$

where this noise is a random variable, characterized by a given probability law of zero mean (its expectation is equal to zero).

4.2.2 Regularization of the IHTC and VTS deconvolution problems

We now focus on point ii) above. The solution of system (11a,b, or 12a) is not immediate and its exact right member $\boldsymbol{y}$ has to be replaced by its measured noisy version $\boldsymbol{y}^{exp}$, with:

$$\boldsymbol{y}^{exp} = \boldsymbol{y} + \boldsymbol{\varepsilon} \quad \text{with} \quad \boldsymbol{\varepsilon} = \left[\varepsilon_1 \quad \varepsilon_2 \quad \cdots \quad \varepsilon_i \quad \cdots \quad \varepsilon_m \right]^T \tag{14}$$

where exponent T designates the transpose of a matrix.

So, instead of solving one of the equations (11), we have to solve the same equation where $\boldsymbol{y}^{exp}$ replaces $\boldsymbol{y}$, with the following solution:

$$\hat{\tilde{\boldsymbol{u}}} = \tilde{\boldsymbol{u}} + \boldsymbol{e}_{\tilde{u}} = \boldsymbol{A}^{-1}\, \boldsymbol{y}^{\exp} \quad \Rightarrow \quad \boldsymbol{e}_{\tilde{u}} = \boldsymbol{A}^{-1} \boldsymbol{\varepsilon} \tag{15a,b}$$

Here $\hat{\tilde{\boldsymbol{u}}}$ is the estimated input interval average with $\boldsymbol{e}_{\tilde{u}}$ the vector of the corresponding inversion errors. Its euclidian norm (its length) can be huge if the noise is not equal to zero. This stems from the ill-posed character of the system matrix $\boldsymbol{A} = \mathbf{N}(\boldsymbol{g}^+)\, \mathbf{N}(\boldsymbol{H})$, which is also the sensitivity matrix of the output to the parameterized input. Its determinant, equal to $\left(H_1\, \Delta t\right)^m$ (it is a triangular matrix), can become very small in the case of a small time step corresponding to a good resolution of the exact impulse response. So matrix $\boldsymbol{A}$ has generally a very high condition number (see the section about the singular value decomposition of a sensitivity matrix in lecture L3 about the basics of linear inversion) and one shows, see Appendix G:

$$\| \boldsymbol{e}_{\tilde{u}} \| / \| \tilde{\boldsymbol{u}} \| \leq \text{cond}(\boldsymbol{A}) \| \boldsymbol{\varepsilon} \| / \| \boldsymbol{y} \| \quad \text{with} \quad \| \boldsymbol{\Psi} \| = \left(\sum_{i=1}^{m} \psi_i^2 \right)^{1/2} \quad \text{for } \psi = \tilde{u},\, e_{\tilde{u}},\, y \text{ or } \varepsilon \tag{16}$$

This means that a high condition number acts as a multiplier of the noise-to-signal ratio, with a high relative error for the parameter to be estimated.

One shows in the same lecture that the variance/covariance matrix of the estimate of $\tilde{\boldsymbol{u}}$ depends linearly on the variance/covariance matrix of the measurement noise. In case of an i.i.d. (independent and identically distributed) noise of standard deviation σ, one shows that the standard deviation $\sigma_{\tilde{u}_i}$ of each component $\hat{\tilde{u}}_i$ of the estimate of $\tilde{\boldsymbol{u}}$ is proportional to the corresponding square root of the diagonal component of the inverse of the information matrix $\boldsymbol{A}^T \boldsymbol{A}$:

$$\sigma_{u_i} = \sigma \sqrt{C_{ii}} \quad \text{with} \quad \boldsymbol{C} = \left(\boldsymbol{A}^T \boldsymbol{A} \right)^{-1} \tag{17}$$

Since the lower triangular Toeplitz matrix $\boldsymbol{A}$ may be close to singular, the same is true for $\boldsymbol{A}^T\boldsymbol{A}$ and the diagonal components of $\boldsymbol{C}$ may be very large, resulting in high values of the standard deviations of the estimated parameters.

So, model (11a) has to be modified in order to get stable estimates, see lecture L6 about inverse problems and regularized solutions. Many different methods exist, such as *truncated singular value decomposition* (TSVD), see Appendices C and D, or *Tikhonov regularization, see Appendix* D, to give a few examples of *full domain* regularization techniques, where the solution is found in one shot on the $[0,\ t_f]$ time domain. They all require the adjustment, that is the optimization, of a regularization hyperparameter h_p, in order to get a root mean square residual of about the same size, but not lower, than the standard deviation of the i.i.d. noise:

$$\sqrt{J_{OLS}(\hat{\hat{\boldsymbol{u}}}_{reg}(h_p))/m} \approx \sigma \qquad \text{with} \quad J_{OLS}(.) \equiv \left\| \boldsymbol{y} - \boldsymbol{A}(.) \right\|^2 \tag{18}$$

Here $\hat{\hat{\boldsymbol{u}}}_{reg}$ is the regularized (parameterized) solution, which depends on h_p while $J_{OLS}(.)$ is the ordinary least square sum, a scalar function whose argument is any value of the parameter vector. This rule for choosing the optimum regularization hyperparameter is called *Morozov's discrepancy principle* [9].
Let us note that the non-regularized estimate defined by equation (15a) corresponds not only to the minimum of $J_{OLS}(.)$ but to its zero and is in fact the Ordinary Least Square estimator noted as $\hat{\hat{\boldsymbol{u}}}_{OLS}$:

$$J_{OLS}(\hat{\hat{\boldsymbol{u}}}) = 0 \quad \Rightarrow \quad \hat{\hat{\boldsymbol{u}}} = \hat{\hat{\boldsymbol{u}}}_{OLS} \tag{19}$$

This stems from the fact that matrix $\boldsymbol{A}$ is square: the number of unknowns and of data are equal. This type of estimation is called *exact matching*.

Another regularization technique, the *function specification method*, also called *method of future time steps* (FTS) [9] is detailed in Appendix E. It differs from the above mentioned techniques since it is not a whole domain, but a *sequential regularization* technique.

Any of the regularization techniques (such as Tikhonov, TSVD, FTS) can be applied to get a regularized estimation of either the front face rate of heat flow (IHCP solution), see (11a) or the front face temperature (VTS solution), see (11b), once a temperature θ has been measured inside the wall.

However, in the 1D case studied here, the model of the output of the unique sensor used depends on its position x, of the thermal properties (λ, a) of the constitutive material and on the level of the heat exchange coefficient h_e on the rear face and of its area for both the VTS case, see equation (A13a) defining w_{x0}, and for the IHTC case, see equation (A13a) defining z_x. These parameters may not be perfectly known. So, an error on h_e for example, can lead to some bias in the estimated values of θ_0 or Φ_0, if the sensitivity coefficient of one of the two

above transfer functions to this parameter is not negligible. To prevent this for happening, it is possible to use two temperature sensors instead of one.

5. Solution of the inverse 1D problem using two outputs

We consider now two temperature sensors, located at depths x_1 and x_2, with $x_1 < x_2$, and whose exact temperatures are θ_1 and θ_2, see figure 2.

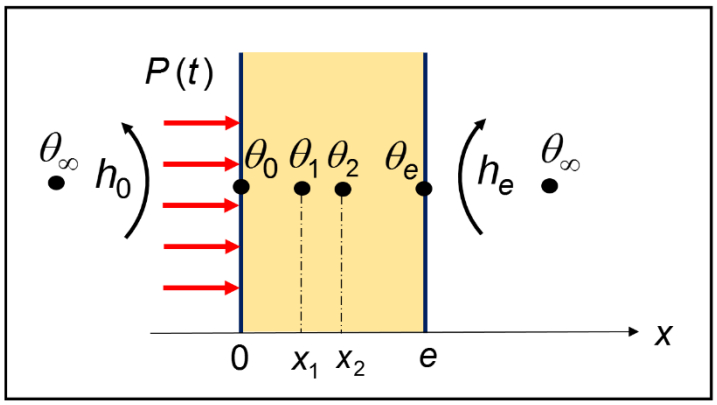

Figure 2 – Heated slab on its front face, with two internal temperature observations

The idea is to get a model that relates θ_1 and θ_2 to the front face temperature θ_0 and to the front face rate of heat flow Φ_0.

So, starting from a quadrupolar relationship between points 0 and x_1 and between 0 and x_2, one shows in Appendix F, that equation (F6a) leads to the following model for the virtual temperature sensor :

$$\bar{\theta}_{VTS} = \bar{w}_{VTS}\ \bar{\theta}_0 \quad \text{with} \quad \bar{\theta}_{VTS} = \bar{\theta}_1 - \frac{\sinh\left(x_1\sqrt{p/a}\right)}{\sinh\left(x_2\sqrt{p/a}\right)}\ \bar{\theta}_2 \quad \text{and} \quad \bar{w}_{VTS} = \frac{\sinh\left((x_2-x_1)\sqrt{p/a}\right)}{\sinh\left(x_2\sqrt{p/a}\right)} \tag{20a}$$

In equation (20a) above, θ_{VTS} is the equivalent output for the 1D model of a virtual temperature sensor. In the Laplace domain, it is a linear combination of two exact temperature observations, θ_1 and θ_2. It depends on both of them through the following relationship :

$$\bar{\theta}_{VTS} = \bar{\theta}_1 - \bar{w}_{12}^{VTS}\ \bar{\theta}_2 \quad \text{with} \quad \bar{w}_{12}^{VTS} = \frac{\sinh\left(x_1\sqrt{p/a}\right)}{\sinh\left(x_2\sqrt{p/a}\right)} \tag{20b}$$

where w_{12}^{VTS} is a correction transmittance used to make the equivalent temperature θ_{VTS} differ from θ_1 by substraction of the convolution product $w_{cor}^{vts} * \theta_2$, which takes the influence of θ_2 into account.

So, this VTS sensor θ_{VTS} , can be expressed as a linear combination of the two physical signals in the time domain too:

$$\theta_{VTS}(t) = \theta_1(t) - \left(w_{VTS} * \theta_1\right)(t) \tag{20c}$$

with a single input single output equivalent model being :

$$\theta_{VTS}(t) = \left(w_{VTS} * \theta_0\right)(t) \tag{20b}$$

In the same way, equation (F6b) in Appendix F leads to the following model for the inverse heat conduction problem :

$$\bar{\theta}_{IHTC} = \bar{z}_{IHCP}\ \bar{\Phi}_0 \text{ with } \bar{z}_{IHCP} = \frac{1}{\lambda\, S\, \sqrt{p/a}}\ \frac{\sinh\left((x_2 - x_1)\sqrt{p/a}\right)}{\cosh\left(x_2\sqrt{p/a}\right)} \text{ and } \bar{\theta}_{IHTC} = \bar{\theta}_1 - \bar{w}_{12}^{IHCP}\ \bar{\theta}_2 \tag{21a}$$

In model (21a) above, $\theta_{IHCP}(t)$ is the equivalent output for the 1D model used for the inverse heat conduction problem using two temperature measurements, θ_1 and θ_2. It depends on both of them through the following relationship :

$$\bar{\theta}_{IHCP} = \bar{\theta}_1 - \bar{w}_{cor}^{IHCP}\ \bar{\theta}_2 \quad \text{with} \quad \bar{w}_{12}^{IHCP} = \frac{\cosh\left(x_1\sqrt{p/a}\right)}{\cosh\left(x_2\sqrt{p/a}\right)} \tag{21b}$$

where $w_{12}^{IHCP}(t)$ is a correction transmittance used to make the equivalent temperature θ_{IHCP} differ from θ_1 by substraction of the convolution product $w_{12}^{IHCP} * \theta_2$ which takes the influence of θ_2 into account.

Remark 8 - Alternate derivation of the 2 temperatures output 1D models for the 2 inverse problems

Let us note that the two models (21a) and (21a) can also be derived, by expressing the conductance k_e as a function of $\bar{w}_{x0} = \bar{\theta} / \bar{\theta}_0$ in equation (A13a) and as a function of $\bar{z}_x = \bar{\theta} / \bar{\Phi}_0$ in equation (A13b):

$$k_e = \frac{A_e\ \bar{\theta} - A_{e-x}\ \bar{\theta}_0}{B_{e-x}\ \bar{\theta}_0 - B_e\ \bar{\theta}} \quad : \quad k_e = \frac{C_e\ \bar{\theta} - A_{e-x}\ \bar{\Phi}_0}{B_{e-x}\ \bar{\Phi}_0 - D_e\ \bar{\theta}} \tag{22a, b}$$

If equations (22a) and (22b) are written for both locations x_1 and x_2, elimination of k_e in both resulting equations yields models (21a) and (21b).

So, the VTS and IHCP problems, in case of 2 temperature measurements correspond to the deconvolution of the following model outputs:

$$\boldsymbol{y} = \boldsymbol{A}\,\tilde{\boldsymbol{u}} = \mathbf{N}(\boldsymbol{g}^{+})\,\mathbf{N}(\boldsymbol{H})\,\tilde{\boldsymbol{u}} \quad \text{with} \quad \begin{cases} \boldsymbol{y} = \boldsymbol{\theta}_{VTS} \;;\; \boldsymbol{H} = \boldsymbol{W}_{VTS} \text{ and } \boldsymbol{u} = \boldsymbol{\theta}_0 & \text{in the VTS case} \\ \boldsymbol{y} = \boldsymbol{\theta}_{IHCP} \;;\; \boldsymbol{H} = \boldsymbol{Z}_{IHCP} \text{ and } \boldsymbol{u} = \boldsymbol{\Phi}_0 & \text{in the IHCP case} \end{cases} \tag{23a,b}$$

The real advantage of this method using the signals of 2 sensors is to be independent of the value of the front and rear face conductances k_0 and k_e and to avoid a possible estimation bias caused by an imperfect knowledge of the external boundary conditions.

6. Solution of the inverse multidimensional problem using prior model identification

The quadrupolar type models presented in sections 2, 4 and 5 can be used for VTS or IHCP applications if heat transfer is 1D in the wall. If it is not the case, a 2 or 3D detailed model, often numerical, has to be constructed. This type of model is useful for studying the internal type of transfer, and to make sensitivity studies of its outputs to its various structural parameters, but it does not guarantee the absence of bias for the solution of the inverse problem, a variation of temperature or of rate of heat flow on the heated area of the front face of the slab, because of errors of these parameters that are only "supposed to be known".

So, the alternate solution is to identify the direct model through a calibration experiment first, (this is called "model identification") before using this model to estimate the front face temperature or rate of heat flow in the experiment of interest. In order to construct a (direct) reduced model through the experimental identification phase, one has to choose its model structure. In this tutorial, this structure is either a convolution product, which is developed below, or an ARX one, which is presented in section 7.

We have focused in [11] on a physical system that is modeled by a *linear* partial differential equation, such as the *heat equation* and of its *associated boundary and interface conditions* whose *coefficients do not depend on time*.

We showed that, *starting from steady state* :

- if at time t = 0 a *unique* heat or temperature source changes from a initial steady state level u_0^{SS} to a transient $u_0^{SS} + u(t)$,

the variation at any point P

- of temperature $y(t) = \theta(t) = T$ (P, t) - T (P, 0),
- or of (Fourier) heat flux $y = \varphi_d$ (P, t) $-\varphi_d$ (P, 0) in any direction *d*,
- or of the rate of heat flow $y = \Phi_S$ (t) $-\Phi_S$ (0) through a given surface S,

is a convolution product between $u\,(t)$ and a corresponding impulse response $h\,(\mathrm{P}, t)$ or $h\,(S, t)$. So even if the transfer is multidimensional, models (4a) and (4b) are still valid:

$$\bar{y} = \bar{h}\ \bar{u} \qquad \Leftrightarrow \qquad y\,(t) = \big(h * u\big)(t) \tag{24a,b}$$

where, depending on the definitions of input u and output y, the impulse response can be an impedance z, a power transmittance w^{Φ}, a temperature transmittance w or an admittance y, according to the definitions given in section 2.

In the same way, the parameterized versions (6) and (8a) of this type of model, under a scalar or a column vector/matrix form, still hold.

$$y_k = \Delta t \sum_{j=1}^{k} \tilde{h}_j\ \tilde{u}_{k-j+1} \quad \Leftrightarrow \quad \boldsymbol{y} = \frac{1}{\Delta t}\ \mathbf{N}(\hat{\boldsymbol{u}})\ \hat{\boldsymbol{h}} \tag{25a,b}$$

Remark 9 - A second condition on the thermal source (either a power change in watts or a temperature change in kelvins) for getting a convolutive model is that it should be a unique one, which means that its support in space should not change with time : the source should be fixed.

Remark 10 – Whatever the dimensionality of the direct problem, one shows [11] the following property for any impulse response, that is the steady state form of equation (4b):

$$y^{SS} = H^{SS}\ u^{SS} \ \text{ with } \quad H^{SS} = \int_0^{\infty} h(t)\ \mathrm{d}t \tag{26a,b}$$

with superscript *ss* designating a steady state value here.

This means that if an asymptotic regime, that is a final steady state, is reached, the output change with respect to the initial steady state, is equal to the simple product between the input change and the time integral of the impulse response.

The only difference with the 1D case is that the analytical expressions of the transfer functions $\bar{h}$ are not available anymore. So, they have to be *identified* on an experimental basis, where both input and output are measured and where the parameterized forms of the convolution product (32b) are written as:

$$y_k = \Delta t \sum_{j=1}^{k} \tilde{h}_j\ \tilde{u}_{k-j+1} \quad \Leftrightarrow \quad \boldsymbol{y} = \frac{1}{\Delta t}\ \mathbf{N}(\hat{\boldsymbol{u}})\ \hat{\boldsymbol{h}} \tag{27a,b}$$

In this tutorial, the material system is composed of a hollow half cylinder made out of cast iron, with a foil electrical resistance stuck to the central part of it inner surface, with a full 180° angular coverage, but with a height smaller than the half cylinder height, which makes 3D effects inside the cast iron wall. A thin thermocouple has been set between the front wall and the foil resistance and two other thermocouples have been inserted inside the wall. Both corresponding temperature rises θ_0 (front face) and θ_1 (internal) are measured, together with

the external ambient temperature through a 3rd thermocouple, as well as the electrical power P dissipated in the foil resistance, and the objective is to reconstruct the power P using the 2 temperature response only.

So, the 2 experiments are the following ones:

i) Calibration experiment

A power step $P(t)$ is imposed and the experimental signals $P^{cal}(t)$, $\theta_0^{cal}(t)$ and $\theta_1^{cal}(t)$ are measured.
The 3 $h(t)$ impulse responses $z_1(t)$, $z_2(t)$ and $w_{10}(t)$ defined by:

$$\theta_0 = (z_0 * P)(t) \quad ; \quad \theta_1 = (z_1 * P)(t) \quad ; \quad \theta_1 = (w_{10} * \theta_0)(t) \qquad (28a,b,c)$$

are estimated using the inversion of the linear model (33a,b), using one of the regularization methods described in Appendices D and E. The corresponding regularized estimates $\hat{h}^{cal}$ are called $\hat{z}_0^{cal}$, $\hat{z}_1^{cal}$ and $\hat{w}_{10}^{cal}$ (the tilda symbol over the 4 quantities has been removed here, for alleviating the notation)

ii) Validation experiment

A second experiment, used for validating the concepts of VTS or IHCP is made, with a different power simulation $P^{val}(t)$ and the same kind of temperature measurements $\theta_0^{val}(t)$ and $\theta_1^{val}(t)$. The corresponding regularized estimates $\hat{u}^{val}$, using (27a,b) with $h = \hat{h}^{val}$ are called:

- $\hat{\theta}_0^{val}$ (case of the VTS, for $y = \theta_1^{val}$ and $h = \hat{W}_{10}^{cal}$),
- $\hat{P}_0^{val}$ (case of the IHCP, for $y = \theta_0^{val}$ and $h = \hat{Z}_0^{cal}$)
- $\hat{P}_1^{val}(t)$ (case of the IHCP, for $y = \theta_1^{val}$ and $h = \hat{Z}_1^{cal}$)

Of course, it is interesting to compare $\hat{\theta}_0^{val}$ and θ_0^{val}, as well as the three thermal powers $\hat{P}_0^{val}$, $\hat{P}_1^{val}(t)$ and P^{val}.

Remark 11 - Contrary to the model used for a temperature estimations with a unique temperature sensor presented in section 4, see equations (9a,b) and (10a,b), the models used in the identification/validation technique do not requires the knowledge of any boundary conditions, here the conductance of the heat losses on the rear face k_e, since they are implicitely taken into account in the phase of calibration of the impedances and transmittance. However, the IHCP presented here differs since it is not the front face rate of heat flow Φ_0 which is estimated, but the dissipated power P. Hence, if Φ_0 looked for too, its estimation would be, *with the only use of the* θ_0^{val} *data* of the validation experiment:

$$\hat{\Phi}_0^{val} = \hat{P}_1^{val} - k_0^{nom}\ \hat{\theta}_0^{val} \tag{29}$$

So, a nominal value k_0^{nom} for the conductance of the heat losses on the front face k_0 is compulsory.

Only the use of a detailed model describing the 3D transfer would allow to reach the estimation of k_0 using surface or internal temperature measurements in the wall.

7. Use of an ARX model for IHCP and VTS problems

7.1 Structure of an ARX model

An AutoRegressive with eXogenous input model (ARX) has the following structure, in the Single Input – Single Output (SISO) case :

$$y_k = -\sum_{\substack{i=1 \\ i<k}}^{n_a} a_i\ y_{k-i} + \sum_{\substack{j=1 \\ j\le k}}^{n_b} b_j\ u_{k-j+1-n_r} + e_k = y_k^{ARX}(\boldsymbol{y}, \boldsymbol{u}; n_a, n_b, n_r) + e_k \tag{30}$$

The output $y_k = y(t_k)$, with $t_k = k\,\Delta t$ and $k > 0$, of the model at time t_k is supposed to be a linear combination of the $n_a > 0$ outputs at the previous times y_{k-i}, the « autoregessive terms », and of the $n_b > 0$ inputs at present and previous times $u(t_{i-j-n_r+1})$, the « eXogeneous terms », with a possible time lag equal to $n_r\,\Delta t$, with $n_r > 0$.

Remark 12: The perturbation term e_k is supposed to be a white noise, that is an independent and identically distributed random variable, with zero mean. This definition of a white noise is valid within the context of study of time series only (in signal analysis, the Gaussian character of this random variable is added). This type of ARX model, which belongs to what is called a "grey box" model, has been extensively studied by Ljung [12]. The "grey" character of this model only concerns cases where the existence of an exact deterministic model linking output to input(s) is not known. This is not the case here, in LTI heat transfer since, in the SISO case, an impulse response exists linking output to input.

Remark 13: Perturbation e_k is also called "equation error" term, since it is an additive term that applies to the right member of equation (30), where the outputs are present on both sides of its equal term. Another model exists, called Output Error model, where this error, noted e_k^{OE} here, that applies to the output only:

$$y_k = x_k + e_k^{OE} \quad \text{where} \quad x_k = y_k^{ARX}(\boldsymbol{y}, \boldsymbol{u}; n_a, n_b, n_r) \tag{31}$$

This error e_k^{OE} is simply the output measurement noise, noted ε_y in equation (14).

Remark 14: Contrary to what can be found in Ljung [12], the right term of model (30) includes a term $a_1\, u_k$ (for a zero delay: $n_r = 0$). This term is useful in cases where input and output occur at the same location. This is for example the case for the front face temperature response to a front face thermal power thermalization, that is for $h = z_0$ in model (9a,b).

The order of the ARX model is determined by the triplet (n_a, n_b, n_k). In the present context (LTI heat transfer with SISO configurations) :

- the output y is an internal or surface temperature variation θ (P, t) = T (P, t) - T (P, 0) at point P in the wall,
- the input u corresponds either to a source or to a pseudo source $u(t)$, with $u = \theta_0$ (VTS case) or $u = \Phi_0$ (IHCP case).

7.2 Link between ARX and convolutive models

We notice that if n_a is null and if n_b is equal to the number m of times of measurement then the ARX model is similar to the parameterized form (6) of the convolutive model presented in section 3.1. This means equation (30) can be recasted to make averaged values of the corresponding input $u(t)$ over the $]t_{k-1}, t_k]$ interval appear.

This property is demonstrated below, where 2 vectors gathering the *a*'s and the *b*'s coefficients are introduced:

$$\boldsymbol{a}_{large} = \left[1 \;\; a_1 \;\; a_2 \;\; \cdots \;\; a_{na} \;\; \underbrace{0 \;\cdots\; 0}_{m-na-1} \right]^T \quad \text{where } \dim(\boldsymbol{a}_{large}) = m\,x1 \;;\; \boldsymbol{a} = \left[a_1 \;\; a_2 \;\; \cdots \;\; a_{na} \right]^T$$

$$\boldsymbol{b}_{large} = \left[\underbrace{0 \;\cdots\; 0}_{nr} \;\; b_1 \;\; b_2 \;\; \cdots \;\; b_{nb} \;\; \underbrace{0 \;\cdots\; 0}_{m-nr-nb} \right]^T \text{ where } \dim(\boldsymbol{b}_{large}) = m\,x1 \;;\; \boldsymbol{b} = \left[b_1 \;\; b_2 \;\; \cdots \;\; b_{nb} \right]^T \tag{32a,b}$$

The matrix function $\mathbf{N}(.)$ defined in equation (8b) is introduced here, with its dimension k being equal here to the number of observation points m and the product $\mathbf{N}(\boldsymbol{y})\,\boldsymbol{a}_{large}$ is calculated using a partition of both matrices:

$$\mathbf{N}(\boldsymbol{y})\boldsymbol{a}_{large} = \left(\left[\boldsymbol{y} \;\; \mathbf{N}_a(\boldsymbol{y}) \;\; \mathbf{N}_a^{comp}(\boldsymbol{y}) \right] \right) \left(\begin{bmatrix} 1 \\ \mathbf{0}_{na\,x\,1} \\ \mathbf{0}_{(m-na-1)\,x\,1} \end{bmatrix} + \begin{bmatrix} 0 \\ \boldsymbol{a} \\ \mathbf{0}_{(m-na-1)\,x\,1} \end{bmatrix} \right) = \boldsymbol{y} + \mathbf{N}_a(\boldsymbol{y})\,\boldsymbol{a} \tag{33c}$$

Here the dimensions of matrix $\mathbf{N}_a(\boldsymbol{y})$ are $m \times n_a$ and this matrix, as well as its right complementary matrix $\mathbf{N}_a^{comp}(\boldsymbol{y})$, are given below, using Matlab© convention for designing the coefficients of a matrix :

$$\mathbf{N}_a(\boldsymbol{y}) = \mathbf{N}_y(m, 2:n_a+1) \text{ and } \mathbf{N}_a^{comp}(\boldsymbol{y}) = \mathbf{N}_y(m, n_a+2:m) \quad \text{with } \mathbf{N}_y = \mathbf{N}(\boldsymbol{y}) \tag{33d}$$

The same kind of partition is made for the product $\mathbf{N}(\boldsymbol{u})\,\boldsymbol{b}_{large}$:

$$\mathbf{N}(\boldsymbol{u})\,\boldsymbol{b}_{large} = \left(\left[\mathbf{0}_{m \times nr} \;\; \mathbf{N}_b(\boldsymbol{u}) \;\; \mathbf{N}_b^{comp}(\boldsymbol{y}) \right] \right) \left(\begin{bmatrix} \mathbf{0}_{nr\,x\,1} \\ \mathbf{0}_{nb\,x\,1} \\ \mathbf{0}_{(m-nr-nb)\,x\,1} \end{bmatrix} + \begin{bmatrix} 0 \\ \boldsymbol{b} \\ \mathbf{0}_{(m-nr-nb)\,x\,1} \end{bmatrix} \right) = \mathbf{N}_b(\boldsymbol{u})\,\boldsymbol{b} \tag{33e}$$

Matrix $\mathbf{N}_b(\boldsymbol{u})$, of dimensions $m \times n_b$, as well as its right complementary part, are defined below:

$$\mathbf{N}_b(\boldsymbol{u}) = \mathbf{N}_u(m, n_r+1:n_r+n_b) \text{ and } \mathbf{N}_b^{comp}(\boldsymbol{u}) = \mathbf{N}_u(m, n_r+n_b+1:m) \quad \text{with } \mathbf{N}_u = \mathbf{N}(\boldsymbol{u}) \tag{33f}$$

One notices that equation (30) is the k^{th} line of vector equality:

$$\boldsymbol{y}^{ARX} = -\mathbf{N}_a(\boldsymbol{y})\,\boldsymbol{a} + \mathbf{N}_b(\boldsymbol{u})\,\boldsymbol{b} \tag{33g}$$

So, ARX model (30) is given the following form :

$$\mathbf{N}(\boldsymbol{y}^{ARX})\,\boldsymbol{a}_{large} = \mathbf{N}(\boldsymbol{u})\,\boldsymbol{b}_{large} \;\Leftrightarrow\; \boldsymbol{A}\,\boldsymbol{y}^{ARX} = \boldsymbol{B}\,\boldsymbol{u} \quad \text{where } \boldsymbol{A} = \mathbf{N}(\boldsymbol{a}_{large}) \text{ and } \boldsymbol{B} = \mathbf{N}(\boldsymbol{b}_{large}) \tag{34a}$$

This gives, in the case without any lag ($n_r = 0$):

$$\boldsymbol{A} = \begin{bmatrix} 1 & 0 & \cdots & \cdots & \cdots & \cdots & 0 \\ a_1 & 1 & & & & & \vdots \\ \vdots & \ddots & \ddots & & & & \vdots \\ a_{n_a} & & \ddots & 1 & & & \vdots \\ 0 & a_{n_a} & & a_1 & \ddots & & \vdots \\ \vdots & & \ddots & & \ddots & \ddots & \vdots \\ 0 & \cdots & 0 & a_{n_a} & \cdots & a_1 & 1 \end{bmatrix} \text{ and } \boldsymbol{B} = \begin{bmatrix} b_1 & 0 & \cdots & \cdots & \cdots & \cdots & 0 \\ b_2 & b_1 & & & & & \vdots \\ \vdots & \ddots & \ddots & & & & \vdots \\ b_{n_b} & & \ddots & b_1 & & & \vdots \\ 0 & b_{n_b} & & b_2 & \ddots & & \vdots \\ \vdots & & \ddots & & \ddots & \ddots & \vdots \\ 0 & \cdots & 0 & b_{n_b} & \cdots & b_2 & b_1 \end{bmatrix} \tag{34b}$$

If a lag is present, a matrix of size n_r x m full of zeros has to be inserted above the lines of matrix $\boldsymbol{B}$ given by equation (34b).

Equation (34a) can be be given the following form, that can be related to form (8f) of the convolutive model, denoted $\boldsymbol{y}^{conv}$ here :

$$\boldsymbol{y}^{ARX} = \boldsymbol{A}^{-1}\,\boldsymbol{B}\,\boldsymbol{u} \quad ; \quad \boldsymbol{y}^{conv} = \Delta t\ \mathbf{N}^2(\boldsymbol{f})\,\mathbf{N}(\boldsymbol{h})\,\boldsymbol{u} \tag{35a,b}$$

Equating (39a) and (39b), for any value of the input $\boldsymbol{u}$ yields:

$$\mathbf{N}(\boldsymbol{h}) = \boldsymbol{C} \ \text{ with } \ \boldsymbol{C} = \frac{1}{\Delta t}\ \mathbf{N}^2(\boldsymbol{f}^+)\ \boldsymbol{A}^{-1}\,\boldsymbol{B} \tag{36c}$$

This means that if the outputs of both models fit noiseless data in a perfect way, the first column of matrix $\boldsymbol{C}$, formed with the *a* and *b* coefficients of the ARX model, should be equal to the vector composed of the sampled form (13) of the impulse response $h(t)$ on the $[\,0\,,\,t_f\,]$ interval, for the same time grid :

$$\boldsymbol{h} = \frac{1}{\Delta t}\ \mathbf{N}^2(\boldsymbol{f}^+)\,\mathbf{N}^{-1}(\boldsymbol{a}_{large})\,\mathbf{N}(\boldsymbol{b}_{large})\,\mathbf{1} \tag{36d}$$

where $\mathbf{1}$ is the vector of size $m\,x\,1$ that is full of ones. Since there is no way to get access to instantaneous values of the impulse response in the general case, see section 4.2.1 above and equation (12c), the vector of interval averages of the impulse response is deduced from the parameters of the ARX thanks to the following equation :

$$\tilde{\boldsymbol{h}} = \frac{1}{\Delta t}\ \mathbf{N}(\boldsymbol{f}^+)\,\mathbf{N}^{-1}(\boldsymbol{a}_{large})\,\mathbf{N}(\boldsymbol{b}_{large})\,\mathbf{1} \tag{37}$$

Remark 15: Equation (37) (40) shows that there is an infinity of ARX models that yield the same parameterized impulse response $\tilde{\boldsymbol{h}}$. In fact, let us assume first that an ARX model of order (n_a, n_b, n_k) has been identified for a calibration experiment, with an estimated set of parameters $\left\{\hat{\boldsymbol{a}}, \hat{\boldsymbol{b}}\right\}$ (see section 7.3 below) with a satisfactory equation error residual (the root mean square of the e_k's in equation (30) and has been validated in another experiment, see section 7.
Let us take next any vector $\boldsymbol{d}$ of size $m\,x\,1$ with a unit first coefficient $d_1 = 1$, which defines a lower triangular Toeplitz matrix $\boldsymbol{D} = \mathbf{N}(\boldsymbol{d})$. A set of two resulting vectors $\left\{\hat{\boldsymbol{a}}'_{large} = \boldsymbol{D}\,\hat{\boldsymbol{a}}_{large}, \hat{\boldsymbol{b}}'_{large} = \boldsymbol{D}\,\hat{\boldsymbol{b}}_{large}\right\}$ is defined, starting from the set $\left\{\hat{\boldsymbol{a}}_{large}, \hat{\boldsymbol{b}}_{large}\right\}$ defined in (32a,b). Extraction of alternate ARX parameter vectors $\left\{\hat{\boldsymbol{a}}', \hat{\boldsymbol{b}}'\right\}$ based on these equations yield exactly the same estimated impulse response vector $\hat{\tilde{\boldsymbol{h}}}$. In this transformation of ARX parameters, the n_a order keeps unchanged, while the n_b and n_k orders do not remain a priori the same.

In the present section, the derivation of the parameterized impulse function, starting from the ARX parameters has been showed. The inverse procedure, the expression of the ARX

parameters for a given impulse function is more difficult, because of their above non-unicity. The interested resder can find such a problematic in reference [16].

7.3 Identification of the ARX parameters and their validation

7.3.1 Estimation of the ARX parameters for three given orders

The parameters a_j and b_j have to be estimated for a given order (n_a, n_b, n_k). We need two different input/output sets.

The first set is called the calibration set and the second one the validation set. The calibration experiment is used to estimate a_i and b_j. The matrix form (33g) of the model is written under the form:

$$\boldsymbol{y} = \boldsymbol{S}_\beta \ \boldsymbol{\beta} \quad \text{with} \ \boldsymbol{S}_\beta = \left[-\mathbf{N}_a(\boldsymbol{y}) \ \mathbf{N}_b(\boldsymbol{u}) \right] \ \text{and} \ \boldsymbol{\beta} = \begin{bmatrix} \boldsymbol{a} \\ \boldsymbol{b} \end{bmatrix} \tag{38a}$$

Matrices $\mathbf{N}_a(\boldsymbol{y})$ and $\mathbf{N}_b(\boldsymbol{u})$ are defined in (33d) and (33f), while the dimensions of the sensitivity matrix $\boldsymbol{S}_\beta$, which results from a concatenation of these matrices, is m x $(n_a + n_b)$ with a parameter vector of length $(n_a + n_b)$.

This sensitivity matrix depends on both input and output, and can have a stochastic nature because of possible presence of noise in these data, see Lectures L3 and L5. However the philosophy of the ARX model is to get a model that fits them in a robust way, whatever their nature, see section 7.3.2 below. So, in spite of the possible non linear nature of this estimation problem, an ordinary least square estimator is used, based on the data of the calibration experiment:

$$\hat{\boldsymbol{\beta}} = \left(\boldsymbol{S}_\beta^T \ \boldsymbol{S}_\beta \right)^{-1} \boldsymbol{S}_\beta^T \ \boldsymbol{y} \quad \Rightarrow \ \hat{\boldsymbol{a}} = \hat{\boldsymbol{\beta}}(1{:}n_a) \ \text{ and } \ \hat{\boldsymbol{b}} = \hat{\boldsymbol{\beta}}(n_a + 1{:}n_a + n_b) \tag{38b}$$

The root mean square of the equation error is calculated next :

$$e^{RMS} = \sqrt{\frac{\boldsymbol{e}^T \boldsymbol{e}}{m}} \quad \text{where} \quad \boldsymbol{e} = \boldsymbol{y} - \boldsymbol{y}^{ARX}(\hat{\boldsymbol{a}}, \hat{\boldsymbol{b}}) \tag{38c}$$

The quality of the fit is characterized in terms of percentage :

$$fit = 100\left[1 - \frac{\sum_{k=1}^{m}\left(y_k - y_k^{ARX}(\hat{\boldsymbol{a}},\hat{\boldsymbol{b}})\right)^2}{\sum_{k=1}^{m}\left(y_k - y^{ave}\right)^2}\right] = 100\left(1 - \left(\frac{e^{RMS}}{s^{shape}}\right)^2\right) \qquad (38d)$$

$$\text{where } y^{ave} = \frac{1}{m}\sum_{k=1}^{m} y_k \text{ and } s^{shape} = \sqrt{\frac{1}{m}\sum_{k=1}^{m}\left(y_k - y^{ave}\right)^2}$$

The quantity s^{shape} above is a statistical standard deviation characterizing the dispersion of the output around their arithmetic average y^{ave}. It is equal to zero in case of a constant output. So, it is related to the shape of the corresponding y versus t plot.

Of course, once the ARX parameters have been found with a satisfactory fit for the calibration experiment, their validation requires comparisons of the output of the identified model with the output of a second experiment with a different input.

7.3.2 Interest of ARX models and Choice of the optimal order of an ARX model and its validation

In experimental identification, or model reduction, the interest of using an ARX model results from its parsimony: it uses a few tenth of parameters at most, even in the non SISO cases where several outputs and/or inputs are present (MISO, SIMO and MIMO) with respect to a convolutive structure based on the identification of a whole function, the impulse response. Estimation of its parameters is fast and easy (linear least squares) and generally provides a very high percentage of fit, see (41d). A useful corresponding reference is [17].

However, there is no way to find the optimal orders (n_a, n_b, n_k), that is the corresponding point in $\mathbb{N}^3$ in a single shot. It requires the implementation of multiple estimations for the same input/output data: so a set P of possible candidates has to be found , with a variation of each order.

For example, one can test 11 integer values for n_a in the [0,10] interval, and similarly the same number of values for n_b and n_r in the same interval, which gives a set P of 11^3 different estimates. Once this set obtained, the following version of Akaike's Information criterium, valid for small samples, that is for small sizes of P, can be minimized. In the SISO case, this criterion is:

$$\text{AIC}_c = m\ \ln\left(\frac{1}{m}\left\|\boldsymbol{y} - \boldsymbol{y}^{ARX}(n_r, \hat{\boldsymbol{a}}, \hat{\boldsymbol{b}})\right\|^2\right) + m\ \left(\ln(2\pi) + 1\ \right) + \frac{2\,m\,(n_a + n_b + 1)}{m - n_a - n_b} \qquad (39)$$

This criterion is based on a compromise, between quality of fit and the complexity of the model, that is its order. It penalizes models with a high number of parameters that tend to over fit, that is to mimic the noise in the data. So it can be regarded as a way to regularize the estimation of the ARX parametres, together as its structure (the level of n_r). The interested reader can

refer to [18], especially for finding applications in cases of multiple inputs or outputs. In a similar way, a modified version of the ARX model, designed for an IHTC problem can be found in [19]

Remark 16: Akaike's information criterion minimizes the Kullback-Leidler information, that is the distance between a model with a given structure and a given number of parameters and the true unknown model that can explain the data. This minimization is made using the maximum likelihood estimator (MLE) of the parameters, here the a and b coefficients, as well as the standard deviation σ of the equation errors vector $\boldsymbol{e}$, see (38c), whose coefficients are thet errors e_k at different times, defined in (30). This stochastic vector is supposed to be independent, identically distributed and of zero expectancy here. Here, in the SISO case, the estimated value of their standard deviation is $\hat{\sigma} = e^{RMS}$, see (38c), the number of MLE estimated parameters being equatl to $n_a + n_b + 1$.

Appendix A - Laplace transforms and thermal quadrupoles: a reminder

We assume that 1D heat transfer occurs in a medium where temperature θ is function of the location x and of time t and are interested by a slice of this medium, corresponding to interval $[x_{in}, x_{out}]$, of thickness Δx. This slice, see figure A1, is composed of a homogeneous material, whose thermal conductivity λ, density ρ and specific heat c are supposed to be constant. There is also no volumetric heat source in the slice and its initial temperature is supposed to be zero. Under these conditions, the heat equation, as well as the initial conditions are:

$$\frac{\partial^2 \theta}{\partial x^2} = \frac{1}{a}\frac{\partial \theta}{\partial t} \quad \text{for} \quad x_{in} < x < x_{out} \quad \text{and} \quad t > 0 \tag{A1}$$

$$\theta = 0 \quad \text{at} \quad t = 0 \quad \text{for} \quad x_{in} \le x \le x_{out} \tag{A2}$$

The local heat flux ϕ (W/m^2) and the rate of heat flow Φ (W), for the area S (m^2) of a plane surface normal to the x axis, are introduced:

$$\phi(x,t) = -\lambda \frac{\partial \theta}{\partial x} \qquad \text{and} \qquad \Phi = S\,\phi \tag{A3}$$

Let us remark that the sign of ϕ and of Φ depends on the orientation chosen for the x axis. The Laplace transforms of temperature and flux are introduced:

$$\bar{\psi}(x,p) \equiv \int_0^t \psi(x,t) \exp(-pt)\, dt \quad \text{for} \quad \psi = \theta \quad \text{or} \quad \phi \quad \text{or} \quad \Phi \tag{A4}$$

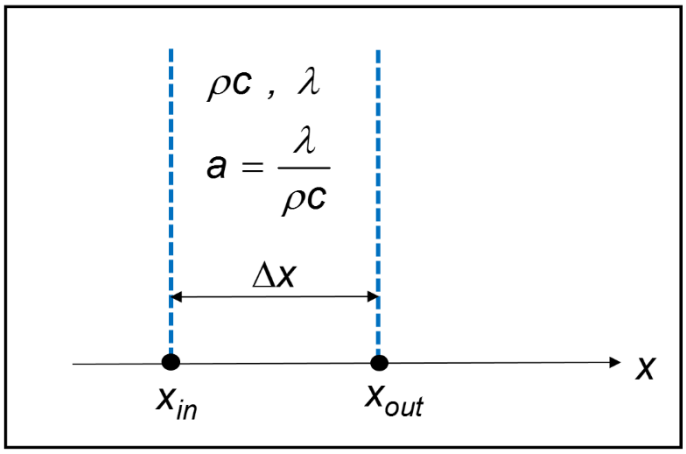

Figure A1 – 1D heat transfer

Under these conditions, the temperature-heat flux vectors in the Laplace domain at the two ends of the considered interval verify the following matrix/vector equation :

$$\begin{bmatrix} \bar{\theta}(x_{in},p) \\ \bar{\Phi}(x_{in},p) \end{bmatrix} = \begin{bmatrix} A(\Delta x,p) & B(\Delta x,p) \\ C(\Delta x,p) & D(\Delta x,p) \end{bmatrix} \begin{bmatrix} \bar{\theta}(x_{out},p) \\ \bar{\Phi}(x_{out},p) \end{bmatrix} \tag{A5a}$$

with:

$$\begin{cases} A = D = \cosh(\Delta x\sqrt{p/a}) \;;\; B = \dfrac{1}{\lambda S\sqrt{p/a}} \sinh(\Delta x\sqrt{p/a}) \\ C = \lambda S\sqrt{p/a}\,\sinh(\Delta x\sqrt{p/a}) \;;\; a = \lambda/\rho c \;\text{ and }\; \Delta x = x_{out} - x_{in} \geq 0 \end{cases} \tag{A5b}$$

Equations (A5a) and (A15b) are strictly equivalent to system (A1) – (A2).

Let us note that quadrupolar equation (A5a) is valid *whatever the boundary conditions in* x_{in} *and* x_{out} , see [1] for more details.

We will know set these 2 boundary conditions, for the specific case of the slab shown in figure A2, where $x_{in} = 0$ and $x_{in} = e$, and for the surface heat source $P(t)$ (W) absorbed by the front face ($x_{in} = 0$).

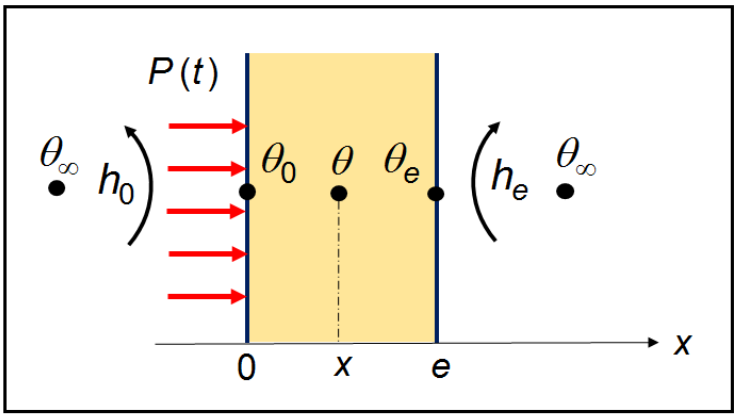

Figure A2 – Heated slab on its front face, with linear heat losses on both faces

The boundary conditions are:

$$\Phi = -\lambda S \frac{\partial \theta}{\partial x} = P(t) - h_0 S(\theta - \theta_0) \quad \text{at } x = 0 \text{ for } t > 0 \tag{A6a}$$

$$\Phi = -\lambda S \frac{\partial \theta}{\partial x} = h_e S(\theta - \theta_0) \quad \text{at } x = 0 \text{ for } t > 0 \tag{A6b}$$

Let us note that, contrary to what seems to mean figure 2, the sign of $q(t)$ does not depend on the orientation of the x axis. Since it is a source, the thermodynamics convention is applied: if heat is added to the front face of the system, which is the case here, $q(t)$ is positive, while $q(t)$ is negative if heat is removed from it (case of a refrigerated front face).

So, equations (A1) and (A2) reduce, if only the front and rear face are observed, to the quadrupolar equation, where the p argument has been omitted in the different functions:

$$\begin{bmatrix} \bar{\theta}_0 \\ \bar{\Phi}_0 \end{bmatrix} = \begin{bmatrix} A_e & B_e \\ C_e & D_e \end{bmatrix} \begin{bmatrix} \bar{\theta}_e \\ \bar{\Phi}_e \end{bmatrix} \quad \text{with} \quad \begin{cases} \bar{\psi}_x = \psi(x,p) & \text{for } \psi = \theta \text{ or } \Phi \text{ and } x = 0 \text{ or } e \\ K_e = K(e,p) & \text{for } K = A, B, C \text{ or } D \end{cases} \tag{A7}$$

In the same way, boundary conditions (A6a) and (A6b) are written as:

$$\begin{bmatrix} \bar{\theta}_0 \\ \bar{P} \end{bmatrix} = \begin{bmatrix} 1 & 0 \\ k_0 & 1 \end{bmatrix} \begin{bmatrix} \bar{\theta}_0 \\ \bar{\Phi}_0 \end{bmatrix} \quad \text{where} \quad k_0 = h_0 S \tag{A8a}$$

$$\begin{bmatrix} \bar{\theta}_e \\ \bar{\Phi}_e \end{bmatrix} = \begin{bmatrix} 1 & 0 \\ k_e & 1 \end{bmatrix} \begin{bmatrix} \bar{\theta}_e \\ 0 \end{bmatrix} \quad \text{where} \quad k_e = h_e S \tag{A8b}$$

Equations (A7), (A8a) and (A8b) reduce to one single equation, by elimination of the temperature/flux vectors at the two faces of the slab:

$$\begin{bmatrix} \bar{\theta}_0 \\ \bar{P} \end{bmatrix} = \begin{bmatrix} 1 & 0 \\ k_0 & 1 \end{bmatrix} \begin{bmatrix} A_e & B_e \\ C_e & D_e \end{bmatrix} \begin{bmatrix} 1 & 0 \\ k_e & 1 \end{bmatrix} \begin{bmatrix} \bar{\theta}_e \\ 0 \end{bmatrix} = \begin{bmatrix} A_T & B_T \\ C_T & D_T \end{bmatrix} \begin{bmatrix} \bar{\theta}_e \\ 0 \end{bmatrix} \tag{A9}$$

The coefficients of the product matrix are:

$$\begin{aligned} A_T &= A_e + k_e B_e \quad ; \quad B_T = B_e \\ C_T &= C_e + k_0 A_e + k_e D_e + k_0 k_e B_e \quad ; \quad D_T = D_e + k_0 B_e \end{aligned} \tag{A10}$$

Let us note that no boundary condition was present in equation (A7), which links the vectors of temperature and of rate of heat flow, while both boundary conditions are taken into account in equation (A9), that relates the temperature/surface heat source vectors, where the surface heat source $P(t)$ is present at the front face, with a corresponding zero surface heat source at the rear face.

The front face flux can be considered as a "pseudo source", with the following responses in the Laplace domain, using equations (2a), (2b) and (2c), in the main part of this text:

$$\bar{\theta}_0 = \bar{z}_0' \, \bar{\Phi}_0 \quad \text{with} \quad \bar{z}_0' = \bar{z}_0 / \bar{w}_0^{\Phi} = A_T / (C_e + k_e D_e) \tag{A11a}$$

$$\bar{\theta}_e = \bar{z}_e' \, \bar{\Phi}_0 \quad \text{with} \quad \bar{z}_e' = \bar{z}_e / \bar{w}_0^{\Phi} = 1 / (C_e + k_e D_e) \tag{A11b}$$

The outputs $\bar{\theta}$ and $\bar{\Phi}$ of the model can also be calculated at any depth x in the slab, see figure 1, using (2c):

$$\begin{bmatrix} \bar{\theta} \\ \bar{\Phi} \end{bmatrix} = \begin{bmatrix} A_{e-x} & B_{e-x} \\ C_{e-x} & D_{e-x} \end{bmatrix} \begin{bmatrix} 1 & 0 \\ k_e & 1 \end{bmatrix} \begin{bmatrix} \bar{\theta}_e \\ 0 \end{bmatrix} \Rightarrow \begin{cases} \bar{\theta} = \bar{z}_x \, \bar{P} \quad \text{with} \quad \bar{z}_x = \dfrac{A_{e-x} + k_e \, B_{e-x}}{C_T} & \text{(A12a)} \\ \bar{\Phi} = \bar{w}_x^{\Phi} \, \bar{P} \quad \text{with} \quad \bar{w}_x^{\Phi} = \dfrac{C_{e-x} + k_e \, D_{e-x}}{C_T} & \text{(A12b)} \end{cases}$$

where A_{e-x}, B_{e-x}, C_{e-x} and D_{e-x} are given by equation (A5b) in Appendix 1, replacing Δx by $e - x$.

Output $\bar{\theta}$ is expressed in terms of the two above pseudo sources, using equations (2a) and (2b) in the main part of the text:

$$\bar{\theta} = \bar{w}_{x0} \, \bar{\theta}_0 \quad \text{with} \quad \bar{w}_{x0} = \frac{A_{e-x} + k_e \, B_{e-x}}{A_T} \tag{A13a}$$

$$\bar{\theta} = \bar{z}_x' \, \bar{\Phi}_0 \quad \text{with} \quad \bar{z}_x' = \frac{A_{e-x} + k_e \, B_{e-x}}{C_e + k_e \, D_e} \tag{A13b}$$

In the same way, output $\bar{\Phi}$ is expressed in terms of the temperature pseudo source, using equation (2a) in the main part of the text:

$$\bar{\Phi} \equiv \bar{y}_{x0}\ \bar{\theta}_0 \quad \text{with} \quad \bar{y}_{x0} = \frac{C_{e-x} + k_e\ D_{e-x}}{A_T} \tag{A13c}$$

Appendix B- Inversion of the Laplace transform

Inversion of an analytically known Laplace transform $\bar{\psi}(p)$, in order to retrieve its original $\psi(t)$, is an ill-posed problem. This original can be constructed for continuous values of the time variable t in 4 cases:

- for very specific expressions of $\bar{\psi}(p)$ given in tables of analytical direct and inverse Laplace transforms;
- use of the usual properties of this transform (derivative, integral, translated function, shift in time, change of scale, long or small times approximation)

- when $\bar{\psi}(p)$ is a rational function of p, where developments in terms of its zeros and poles can be constructed;
- using the Bromwich's (also called Mellin's) contour integral in the complex plane.

In practice, it is more convenient to use a numerical inversion algorithm. Several are available, see Chapter 9 in [1] and [2]:

- Gaver Stehfest's algorithm [3, 4, 5], which is very simple to implement, with possible singularities in t = 0 but not convenient for non monotoneous functions or periodic functions over the [0, +∞] interval,
- Inversion based on Bromwich integral, using either a classical Fourier transform, or an inverse fast Fourier transform, see Appendix 9.2 in [1] and Hsu and Dranoff [6],

In this second class of inversion methods, de Hoog's algorithm [7], which is implemented under the "Invlap" name as a script in Matlab®, provides an acceleration of the convergence, while den Iseger's algorithm [2, 8] provides an improved quadrature of the Bromwich integral.

If none of the above algorithms gives satisfactory results, an hybrid technique can be implemented, using a function $\bar{f}(p)$ whose inverse transform $f(t)$ is known analytically or numerically. If the inverse Laplace transform $g(t)$ of the product $\bar{g}(p) = \bar{f}(p)\,\bar{\Psi}(p)$ can be reached numerically, the parameterized form of the corresponding convolution product is:

$$\boldsymbol{g} = \mathbf{M}(\boldsymbol{f})\,\boldsymbol{\Psi} \quad \Rightarrow \quad \boldsymbol{\Psi} = \left(\mathbf{M}(\boldsymbol{f})\right)^{-1}\boldsymbol{g} \tag{B1}$$

So, this technique consists in transforming the Laplace inversion into a deconvolution problem.

Appendix C – The Singular Value Decomposition of a matrix and the SVD version of the ordinary least square estimator

Any rectangular matrix (called $\boldsymbol{K}$ here) with real or complex coefficients and of dimensions (m, n) with $m \geq n$ (SVD also exists in the case $m < n$, but it won't be dealt with here), can be written under the form :

$$\boldsymbol{K} = \boldsymbol{U}\,\boldsymbol{W}\,\boldsymbol{V}^t \text{ that is } \begin{bmatrix} & \boldsymbol{K} & \end{bmatrix} = \begin{bmatrix} & \boldsymbol{U} & \end{bmatrix} \begin{bmatrix} w_1 & & \boldsymbol{0} \\ & \ddots & \\ \boldsymbol{0} & & w_n \end{bmatrix} \begin{bmatrix} & \boldsymbol{V}^t & \end{bmatrix} \quad \text{(C1)}$$

where superscript t stands for the conjugate transpose of the corresponding matrix. If the coefficients of $\boldsymbol{K}$ are real, it is simply its transpose.

This expression is sometimes called "thin" or “economy size” SVD and involves

- $\boldsymbol{U}$, a unitary matrix (orthogonal if $\boldsymbol{K}$ is real) of dimensions (m, n) : its column vectors (the *left* singular vectors of $\boldsymbol{K}$) have a unit norm and are orthogonal by pairs : $\boldsymbol{U}^t\boldsymbol{U} = \boldsymbol{I}_n$, where $\boldsymbol{I}_n$ is the identity matrix of dimension n. Its columns are composed of the first n eigenvectors $\boldsymbol{U}_k$, ordered according to decreasing values of the eigenvalues of matrix $\boldsymbol{K}\,\boldsymbol{K}^t$. Let us note that, in the general case, $\boldsymbol{U}\boldsymbol{U}^t \neq \boldsymbol{I}_m$.

- $\boldsymbol{V}$, a square unitary matrix (orthogonal if $\boldsymbol{K}$ is real) of dimensions (n, n), : $\boldsymbol{V}\boldsymbol{V}^t = \boldsymbol{V}^t\boldsymbol{V} = \boldsymbol{I}_n$. Its column vectors (the *right* singular vectors of $\boldsymbol{K}$), are the n eigenvectors $\boldsymbol{V}_k$, ordered according to decreasing eigenvalues, of matrix $\boldsymbol{K}^t\boldsymbol{K}$;

- $\boldsymbol{W}$, a square diagonal matrix of dimensions (n x n), that contains the n so-called *singular* values of matrix $\boldsymbol{K}$, ordered according to decreasing values : $w_1 \geq w_2 \geq \cdots \geq w_n$. The singular values of matrix $\boldsymbol{K}$ are defined as the square roots of the eigenvalues of matrix $\boldsymbol{K}^t\boldsymbol{K}$. If matrix $\boldsymbol{K}$ is square and symmetric, its eigenvalues and singular values are the same.

Another SVD form called "Full Singular Value Decomposition" is available for matrix $\boldsymbol{K}$. In this equivalent definition, both matrices $\boldsymbol{U}$ and $\boldsymbol{W}$ are changed: the matrix replacing $\boldsymbol{U}$ is now square (size m x m) and the matrix replacing $\boldsymbol{W}$ is now diagonal but non square (size m x n). In the present case where $m \geq n$, this can be written:

$$\boldsymbol{K} = \boldsymbol{U}_0\,\boldsymbol{W}_0\,\boldsymbol{V}^t \quad \text{with} \quad \boldsymbol{U}_0 = \begin{bmatrix} \boldsymbol{U} & \boldsymbol{U}_{comp} \end{bmatrix};\ \boldsymbol{W}_0 = \begin{bmatrix} \boldsymbol{W} \\ \boldsymbol{0}_{(m-n)\ x\ n} \end{bmatrix} \text{ and } \dim(\boldsymbol{U}_{comp}) = m\ x\ (m - n) \quad \text{(C2a)}$$

or:

$$\begin{bmatrix} \\ \boldsymbol{K} \\ \\ \end{bmatrix} = \begin{bmatrix} \\ \boldsymbol{U} \qquad \boldsymbol{U}_{comp} \\ \\ \end{bmatrix} \begin{bmatrix} w_1 & & 0 \\ & \ddots & \\ 0 & & w_n \\ 0 & \cdots & 0 \\ \vdots & \ddots & \vdots \\ 0 & \cdots & 0 \end{bmatrix} \begin{bmatrix} \\ \boldsymbol{V}^t \\ \\ \end{bmatrix} \qquad \text{(C2b)}$$

Matrix $\boldsymbol{U}_{comp}$ is composed of the (m - n) left singular column vectors not present in $\boldsymbol{U}$. So, the concanated matrix $\boldsymbol{U}_0$ verifies now:

$$\boldsymbol{U}_0^t \boldsymbol{U}_0 = \boldsymbol{U}_0 \boldsymbol{U}_0^t = \boldsymbol{U}\boldsymbol{U}^t + \boldsymbol{U}_{comp}\boldsymbol{U}_{comp}^t = \boldsymbol{I}_m \qquad \text{(C3)}$$

This singular value decomposition (C1) can be implemented for any matrix $\boldsymbol{K}$, with real or complex value coefficients, for $m \geq n$.

We assume now that the model $\boldsymbol{y}_{mo}(\boldsymbol{x}) = \boldsymbol{S}\,\boldsymbol{x}$ is linear and that all the parameters gathered in the parameter vector $\boldsymbol{x}$ have the same unit. We use the SVD of the sensitivity matrix $\boldsymbol{S}$, that is we write the generic equation (C1) for $\boldsymbol{K} = \boldsymbol{S}$ which yields $\boldsymbol{S} = \boldsymbol{U}\,\boldsymbol{W}\,\boldsymbol{V}^t$. Substitution of this expression in the OLS estimate equation, see Lecture 3, gives:

$$\hat{\boldsymbol{x}}_{OLS} = \left(\boldsymbol{S}^t\boldsymbol{S}\right)^{-1}\boldsymbol{S}^t\boldsymbol{y} = \boldsymbol{V}\,\boldsymbol{W}^{-1}\boldsymbol{U}^t\,\boldsymbol{y} \qquad \text{(C4)}$$

This identity is valid only if matrix $\boldsymbol{S}$ is of full rank, which means that its smaller singular value $w_1(\boldsymbol{S})$ should be strictly positive. As a consequence the covariance matrix can be written the following way:

$$\text{cov}(\hat{\boldsymbol{x}}_{OLS}) = \sigma_\varepsilon^2\,\boldsymbol{V}\,\boldsymbol{W}^{-2}\boldsymbol{V}^t \qquad \text{(C5)}$$

This shows that the smallest singular values present in matrix $\boldsymbol{W}^{-2}$ will bring a dominant contribution to the diagonal coefficients of $\text{cov}(\boldsymbol{x})$, that is the variances of the different parameters.

Appendix D – Truncated SVD and Tikhonov regularization of zero order

D.1 TSVD regularization

In any linear inverse input problem, the OLS solution, see equation (C4) in Appendix C, minimizes the following least square criterion:

$$J(\boldsymbol{x}) = \left\| \boldsymbol{y} - \boldsymbol{S}\boldsymbol{x} \right\|^2 = \left(\boldsymbol{y} - \boldsymbol{S}\boldsymbol{x}\right)^t \left(\boldsymbol{y} - \boldsymbol{S}\boldsymbol{x}\right) \qquad \text{(D1)}$$

Ideally, if no noise is present in the data $\boldsymbol{y}$, the best option is to choose a parameterization based on the largest possible number of parameters n, that is n equal to the number of

measurements m. However, because of the presence of noise, the larger n, the larger the condition number of the inversion and the largest the standard deviations of the estimated parameters because of the smallest singular value $w_n(\boldsymbol{S})$.

So, one of the solution is to replace, in the SVD expression of the OLS minimum, the inverse of the matrix $\boldsymbol{W}$ of the singular values by a its truncated inverse $\boldsymbol{W}_\alpha^{-1}$, see equation (C4) in Appendix C,:

$$\boldsymbol{W}_\alpha^{-1} = \begin{bmatrix} 1/w_1 & & & & & \\ & 1/w_2 & & 0 & & \\ & & \ddots & & & \\ & & & 1/w_\alpha & & \\ & 0 & & 0 & & \\ & & & & \ddots & \\ & & & & & 0 \end{bmatrix} \tag{D2}$$

So, the regularized TSVD estimate is:

$$\hat{\boldsymbol{x}}_\alpha^{TSVD} = \boldsymbol{V}\,\boldsymbol{W}_\alpha^{-1}\,\boldsymbol{U}^t\,\boldsymbol{y} \tag{D3}$$

Let us note that $\boldsymbol{W}_\alpha$ cannot be calculated since the $n-\alpha$ smallest singular values of $\boldsymbol{S}$, $w_{\alpha+1}, w_{\alpha+2}, \cdots, w_{n-1}, w_n$, have been given an infinite level.

The TSVD solution (C3) can be rewritten using the left and right singular column vectors $\boldsymbol{U}_k$ and $\boldsymbol{V}_k$:

$$\hat{\boldsymbol{x}}_\alpha^{TSVD} = \begin{bmatrix}\boldsymbol{V}_1 & \boldsymbol{V}_2 & \cdots & \boldsymbol{V}_\alpha\end{bmatrix} \begin{bmatrix} 1/w_1 & & 0 \\ & 1/w_2 & \\ 0 & & 1/w_\alpha \end{bmatrix} \begin{bmatrix} \boldsymbol{U}_1^t \\ \boldsymbol{U}_2^t \\ \\ \boldsymbol{U}_\alpha^t \end{bmatrix} \boldsymbol{y} = \sum_{k=1}^{\alpha} \frac{1}{w_k} \left(\boldsymbol{U}_k^t \boldsymbol{y}\right) \boldsymbol{V}_k \tag{D4}$$

The discrepancy principle can be adopted for the choice of the optimal value for α:

$$J(\hat{\boldsymbol{x}}_\alpha^{TSVD}) < m\sigma_\varepsilon^2 \text{ and } J(\hat{\boldsymbol{x}}_{\alpha+1}^{TSVD}) \geq m\sigma_\varepsilon^2 \tag{D5}$$

D.2 Tikhonov regularization of zero order

Another popular method of regalurization is based on a penalization of the OLS sum (A1) by an additive term that would prevent and explosion of the standard deviations of the different coefficients of $\boldsymbol{x}$. Tikhonov regularization of zero order consists in minimizing the following criterion:

$$J_\mu(\boldsymbol{x}) = \| \boldsymbol{y} - \boldsymbol{S}\boldsymbol{x} \|^2 + \mu \| \boldsymbol{x} \|^2 = (\boldsymbol{y} - \boldsymbol{S}\boldsymbol{x})^t (\boldsymbol{y} - \boldsymbol{S}\boldsymbol{x}) + \mu \boldsymbol{x}^t \boldsymbol{x} \quad \text{(D6)}$$

The solution is explicit:

$$\hat{\boldsymbol{x}}_\mu^{Tik0} = \left(\boldsymbol{S}^t \boldsymbol{S} + \mu \boldsymbol{I}_n \right)^{-1} \boldsymbol{S}^t \boldsymbol{y} \quad \text{(D7)}$$

This can be written using the SVD decomposition of $\boldsymbol{S}$:

$$\left(\boldsymbol{V}\boldsymbol{W}^2\boldsymbol{V}^t + \mu \boldsymbol{I}_n \right) \hat{\boldsymbol{x}}_\mu^{Tik0} = \boldsymbol{V}\boldsymbol{W}\boldsymbol{U}^t \boldsymbol{y} \quad \text{(D8)}$$

Using the fact that $\boldsymbol{V}\boldsymbol{V}^t = \boldsymbol{I}_n$, the preceding equation can be simplified:

$$\hat{\boldsymbol{x}}_\mu^{Tik0} = \boldsymbol{V} \left(\boldsymbol{W}^2 + \mu \boldsymbol{I}_n \right)^{-1} \boldsymbol{W}\boldsymbol{U}^t \boldsymbol{y} = \sum_{k=1}^{n} \frac{w_k}{w_k^2 + \mu} \left(\boldsymbol{U}_k^t \boldsymbol{y} \right) \boldsymbol{V}_k \quad \text{(D9)}$$

Comparison of OLS (equation (C4) in Appendix (C), TSVD (D4) and Tikhonov (D9) estimates show that both OLS and regularized solutions can be written under the common form:

$$\hat{\boldsymbol{x}}_{reg} = \sum_{k=1}^{n} f_k \left(\boldsymbol{U}_k^t \boldsymbol{y} \right) \boldsymbol{V}_k \quad \text{(D10)}$$

where coefficients f_k are called "filter factors, see [13] and are defined by:

- $f_k = 1$ for $k = 1$ to $n \le m$ without any regularization (Ordinary Least Squares)
- $f_k = 1$ for $k = 1$ to $\alpha < n \le m$ and $f_k = 0$ for $k = \alpha + 1$ to $n \le m$ for TSVD regularization
- $f_k = \dfrac{w_k^2}{w_k^2 + \mu}$ for $k = 1$ to $n \le m$ for Tikhonov regularization of zero order

Appendix E – Regularization using future time steps

We recall here one of the regularization technique, the *function specification method*, also called *method of future time steps* (FTS) [9], which is not a *whole domain*, but a *sequential regularization* technique.

So, equation (7e) in section 3.1, that is Duhamel's form of the convolution product model, that uses the variations of the step response on a time grid, as well as the interval averages of the input, is rewritten :

$$y_k = y(t_k) \approx \sum_{j=1}^{k} \Delta H_{k-j+1}\, \tilde{u}_j \tag{E1}$$

A change in the notation introduce in equation (7d), is made here :

$$H_j = H(t_j) \text{ and } \mathrm{D}H_j = H_{j+1} - H_j \;\Rightarrow\; \mathrm{D}H_j = \Delta H_{j+1} = \hat{h}_{j+1}$$

This means that the variation of the step response at time t_j, is not considered in the past time step, that is in interval $\left]t_{j-1},\ t_j\right]$, but in the future time step, that is in the $\left]t_j,\ t_{j+1}\right]$ interval. This means that equation (E1) becomes, for the k^{th} output :

$$y_k \approx \sum_{j=1}^{k} \mathrm{D}H_{k-j}\, u_j \tag{E2}$$

In equation (E2), the tilde symbol has been removed for the input over the $\left]t_{j-1},\ t_j\right]$ interval, in order to simplify the notation. One suppose next that the previous inputs have already been estimated, with values equal to $\hat{u}_j$, for $j = 1$ to $k-1$ and that the current estimate $\hat{u}_k$ is looked for.

One assumes here, on a provisional basis, that the following $(r+1)$ components u_k to u_{k+r+1} are equal to a common value q :

$$u_k = u_{k+1} = u_{k+2} = \cdots = u_{k+r} = q \tag{E3}$$

Equation (E2), is written then, for the $(r+1)$ corresponding times:

$$\begin{aligned}
y_k &= \sum_{j=1}^{k} \mathrm{D}H_{k-j}\, u_j \approx \sum_{j=1}^{k-1} \mathrm{D}H_{k-j}\, \hat{u}_j + \mathrm{D}H_0\, q = y_k\big|_{q=0} + \mathrm{D}H_0\, q \\
y_{k+1} &= \sum_{j=1}^{k+1} \mathrm{D}H_{k+1-j}\, u_j \approx \sum_{j=1}^{k-1} H_{k+1-j}\, \hat{u}_j + (\mathrm{D}H_0 + \mathrm{D}H_1)\, q = y_{k+1}\big|_{q=0} + (\mathrm{D}H_0 + \mathrm{D}H_1)\, q \\
&\vdots \\
y_{k+r} &= \sum_{j=1}^{k+r} \mathrm{D}H_{k+r-j}\, u_j \approx \sum_{j=1}^{k-1} \mathrm{D}H_{k+r-j}\, \hat{u}_j + (\mathrm{D}H_0 + \mathrm{D}H_1 + \cdots + \mathrm{D}H_r)\, q \\
&= y_{k+r}\big|_{q=0} + (\mathrm{D}H_0 + \mathrm{D}H_1 + \cdots + \mathrm{D}H_r)\, q
\end{aligned} \tag{E4}$$

Here the notation $y_j\big|_{q=0}$, for $j = k$ to $k+r$, designates temperature at time $t = t_j$, with $j \geq k$ corresponding to a relaxation of the temperature field reached at time

$t = t_{k-1}$, that is the time at which the last non zero input u_{k-1} ends. So, it is a relaxation temperature which is calculated using the already estimated $(k-1)$ input levels $\hat{u}_j$,for $j = 1$ to $k-1$.

These equations can be put under the following vector/matrix form:

$$\boldsymbol{y}^{future} = \boldsymbol{y}^{relax} + q\,\boldsymbol{S} \quad \text{with} \quad \boldsymbol{y}^{relax} = \boldsymbol{H}^{relax}\,\hat{\boldsymbol{u}}^{past} \tag{E5a,b}$$

with

$$\boldsymbol{y}^{future} = \left[\, y_k \;\; y_{k+1} \cdots y_{k+r} \,\right]^T ; \hat{\boldsymbol{u}}^{past} = \left[\, \hat{u}_1 \;\; \hat{u}_2 \cdots \hat{u}_{k-1} \,\right]^T \tag{E5c,d}$$

and

$$\boldsymbol{S} = \begin{bmatrix} S_1 \\ S_2 \\ \vdots \\ S_{r+1} \end{bmatrix} = \begin{bmatrix} \mathrm{D}H_0 \\ \mathrm{D}H_0 + \mathrm{D}H_1 \\ \vdots \\ \mathrm{D}H_1 + \mathrm{D}H_2 + \cdots \mathrm{D}H_r \end{bmatrix} \;\; ; \;\; \boldsymbol{H}^{relax} = \begin{bmatrix} \mathrm{D}H_{k-1} & \mathrm{D}H_{k-2} & \cdots & \mathrm{D}H_1 \\ \mathrm{D}H_k & \mathrm{D}H_{k-1} & \cdots & \mathrm{D}H_2 \\ \vdots & \vdots & & \vdots \\ \mathrm{D}_{k+r-1} & \mathrm{D}H_{k+r-2} & \cdots & \mathrm{D}H_{r+1} \end{bmatrix} \tag{E5e,f}$$

The dimensions of matrix $\boldsymbol{H}^{relax}$ are $(r+1)$ x $(k-1)$. Let us note that this matrix is just a sub matrix of Toeplitz matrix $\mathbf{M}(\boldsymbol{H})$.

Parameter q, and as a consequence the new value u_k of the input is then estimated in the ordinary least square sense, using the measured values of $\boldsymbol{y}^{\exp}_{future}$:

$$\hat{u}_k = \hat{q} = \left(\boldsymbol{S}^T\boldsymbol{S}\right)^{-1}\boldsymbol{S}^T\left(\boldsymbol{y}^{\exp}_{future} - \boldsymbol{y}^{relax}\right) = \frac{1}{\sum_{j=1}^{r+1} S_j^2}\sum_{j=1}^{r+1} S_k\,(y^{\exp}_{k+j-1} - y^{relax}_{k+j-1}) \tag{E6}$$

Once $\hat{u}_k$ has been calculated, the same procedure is repeated for calculating $\hat{u}_{i+1}$, with a new common parameter q for future inputs u_{k+1} to u_{k+r+1}, and so on.

In this technique, the regularization hyperparameter is the number r of future time steps. If r is equal to one, the future time step estimate is equal to $\hat{\boldsymbol{u}}_{OLS}$.

Appendix F – Construction of models for 2 points VTS and IHCP

The following quadrupolar relationship is written, between points 0 and x_1 and between 0 and x_2:

$$\begin{bmatrix} \bar{\theta}_0 \\ \bar{\Phi}_0 \end{bmatrix} = \begin{bmatrix} A_1 & B_1 \\ C_1 & D_1 \end{bmatrix}\begin{bmatrix} \bar{\theta}_1 \\ \bar{\Phi}_1 \end{bmatrix} = \begin{bmatrix} A_2 & B_2 \\ C_2 & D_2 \end{bmatrix}\begin{bmatrix} \bar{\theta}_2 \\ \bar{\Phi}_2 \end{bmatrix} \tag{F1}$$

where the 4 coefficients of each 2 x 2 matrix are based on the corresponding thickness, see equations (A5a) and (A5b) in Appendix A, that is for example :

$$A_i = \cosh(\alpha x_i) \text{ for } i = 1 \text{ or } 2 \quad \text{and} \quad \alpha = \sqrt{p / a} \tag{F2}$$

Elimination of Φ_2 between the two scalar equations resulting from the equality between the two matrix products of (F1) yields:

$$\bar{\Phi}_1 = \frac{A_\Delta}{B_\Delta}\bar{\theta}_1 - \frac{1}{B_\Delta}\bar{\theta}_2 \text{ with } A_\Delta = \cosh(\alpha\ \Delta x)\ ;\ B_\Delta = \frac{1}{\lambda\ \alpha\ S}\sinh(\alpha\ \Delta x)\ ;\ \Delta x = x_2 - x_1 \tag{F3}$$

Substitution of this expression for Φ_1 into the first and into the second lines of the first matrix equation (F1) yields:

$$\bar{\theta}_0 = \frac{B_2}{B_\Delta}\bar{\theta}_1 - \frac{B_1}{B_\Delta}\bar{\theta}_2 \tag{F4a}$$

$$\bar{\Phi}_0 = \frac{A_2}{B_\Delta}\bar{\theta}_1 - \frac{A_1}{B_\Delta}\bar{\theta}_2 \tag{F4b}$$

Inversion of the system of equations (A4a) and (A4b) yields:

$$\bar{\theta}_1 = A_1\ \bar{\theta}_0 - B_1\ \bar{\Phi}_0 \tag{F5a}$$

$$\bar{\theta}_2 = A_2\ \bar{\theta}_0 - B_2\ \bar{\Phi}_0 \tag{F5b}$$

After elimination of $\bar{\Phi}_0$ between (A5a) and (A5b), one gets the following result, which will be used as the model of a two points virtual temperature sensor of the front face temperature:

$$\bar{\theta}_{VTS} = \bar{w}_{VTS}\ \bar{\theta}_0 \quad \text{with } \bar{\theta}_{VTS} = \bar{\theta}_1 - \frac{B_1}{B_2}\bar{\theta}_2 \quad \text{and} \quad \bar{w}_{VTS} = \frac{B_\Delta}{B_2} \tag{F6a}$$

Elimination of $\bar{\theta}_0$ between the same equations lead to the model for a two points estimation of the fronf face rate of heat flow:

$$\bar{\theta}_{VTS} = \bar{z}_{IHCP}\ \bar{\Phi}_0 \quad \text{with } \bar{\theta}_{IHCP} = \bar{\theta}_1 - \frac{A_1}{A_2}\bar{\theta}_2 \quad \text{and} \quad \bar{z}_{IHCP} = \frac{B_\Delta}{A_2} \tag{F6b}$$

Appendix G - Interest of the Singular Value Decomposition in linear parameter estimation

If all the *n* parameters in a parameter vector $\boldsymbol{x}$ are looked for, for a linear model $\boldsymbol{y}_{mo}(\boldsymbol{x}) = \boldsymbol{S}\,\boldsymbol{x}$, where *m* noised measurements $\boldsymbol{y} = \boldsymbol{S}\,\boldsymbol{x} + \boldsymbol{\varepsilon}$ are available, and if noise $\boldsymbol{\varepsilon}$ is independent and identically distributed (i.i.d.), that is $\mathrm{cov}(\boldsymbol{\varepsilon}) = \sigma_\varepsilon^2\,\boldsymbol{I}_m$, its Ordinary Least Square (OLS) estimator can be written (see Lecture 3 of this Metti school):

$$\hat{\boldsymbol{x}}_{OLS} = \left(\boldsymbol{S}^t\,\boldsymbol{S}\right)^{-1}\boldsymbol{S}^t\,\boldsymbol{y} \quad \text{with} \quad \mathrm{E}(\boldsymbol{\varepsilon}) = \boldsymbol{0} \quad \text{and} \quad \mathrm{cov}(\hat{\boldsymbol{x}}_{OLS}) = \sigma_\varepsilon^2\left(\boldsymbol{S}^t\,\boldsymbol{S}\right)^{-1} \qquad \text{(G1)}$$

Of course, in order for the inverse of the information matrix $\boldsymbol{S}^t\,\boldsymbol{S}$ to exist, matrix $\boldsymbol{S}$ must not be singular, which means that its *n* sensitivity column vectors should form a free system of vectors (see lecture L5 in this series): the rank of $\boldsymbol{S}$ should be equal to *n*.

The potential difficulty in the estimation of $\boldsymbol{x}$ may stem from the possible ill-conditioning of the square information matrix $\boldsymbol{S}^t\,\boldsymbol{S}$ whose inversion makes the standard deviations of its different parameters $\hat{x}_j$ become very large with respect to their exact value. So, a normalized criterion can be constructed in order to assess the quality of the estimation of the *n* parameters.

We assume here that all the coefficients of $\boldsymbol{x}$ have the same unit as all the coefficients of $\boldsymbol{y}$. This is the case for input estimation problems where $\boldsymbol{y}$ is for example the vector of the sampled measured temperatures at *m* times t_i and $\boldsymbol{x}$ the parameterized heat source $x(t)$ using a basis composed of *n* functions $g_j(t)$:

$$\begin{aligned} &x(t) \approx x_{param}(t) = \sum_{j=1}^{n} x_j\; g_j(t) \;\Rightarrow\; x_{param}(t_i) = \boldsymbol{g}(t_i)\;\boldsymbol{x} \\ &\text{with}\quad \boldsymbol{g} = \begin{bmatrix} g(t_i) & g_2(t_i) & \cdots & g_n(t_i) \end{bmatrix} \text{ and } \boldsymbol{x} = \begin{bmatrix} x_1 & x_2 & \cdots & x_n \end{bmatrix}^t \end{aligned} \qquad \text{(G2)}$$

In this parameterization a column-vector $\boldsymbol{x}$ composed of *n* coefficients has replaced a function $x(t)$ of infinite continuous dimensions.

So, it is now possible to write the thin SVD decomposition of $\boldsymbol{S}$, which uses the notion of Euclidian norm of different true vectors, see equation (C1) in Appendix C:

$$\boldsymbol{S} = \boldsymbol{U}\,\boldsymbol{W}\,\boldsymbol{V}^t \qquad \text{(G3)}$$

It is now possible to calculate the amplification coefficient of the relative error k_r :

$$k_r(\boldsymbol{\varepsilon}) = \frac{\left\|\boldsymbol{e}_x\right\| \,/\, \left\|\boldsymbol{x}_{exact}\right\|}{\left\|\boldsymbol{\varepsilon}\right\| \,/\, \left\|\boldsymbol{y}_{mo}\left(\boldsymbol{x}_{exact}\right)\right\|} \quad \text{with} \quad \boldsymbol{e}_x = \hat{\boldsymbol{x}} - \boldsymbol{x}_{exact} \qquad \text{(G4)}$$

Using the properties of matrices $\boldsymbol{U}$ and $\boldsymbol{V}$ described in Appendix C, one can show:

$$\left.\begin{array}{l} \|\boldsymbol{e}_x\| = \|\boldsymbol{V}\,\boldsymbol{W}^{-1}\boldsymbol{U}^t\,\boldsymbol{\varepsilon}\| \le \|\boldsymbol{V}\,\boldsymbol{W}^{-1}\boldsymbol{U}^t\|\,\|\boldsymbol{\varepsilon}\| \\ \|\boldsymbol{y}_{mo}(\boldsymbol{x}_{exact})\| = \|\boldsymbol{S}\,\boldsymbol{x}\| \le \|\boldsymbol{U}\,\boldsymbol{W}\,\boldsymbol{V}^t\|\,\|\boldsymbol{x}\| \end{array}\right\} \Rightarrow k_r(\boldsymbol{\varepsilon}) \le \|\boldsymbol{V}\,\boldsymbol{W}^{-1}\boldsymbol{U}^t\|\,\|\boldsymbol{U}\,\boldsymbol{W}\,\boldsymbol{V}^t\| = \|\boldsymbol{S}^+\|\,\|\boldsymbol{S}\| \quad \text{(G5)}$$

One can recognize in the right-hand term of the last inequality (G5) the product of the norms of two matrices. The second matrix is simply the SVD form of the reduced sensitivity matrix $\boldsymbol{S}^*$ while the first one is just the pseudo inverse of $\boldsymbol{S}^*$, which is noted $\boldsymbol{S}^+$ here.

Let us remind that the norm of any matrix $\boldsymbol{K}$ (which has not to be square) is defined by:

$$\|\boldsymbol{K}\|^2 = \underset{\|\boldsymbol{z}\|=1}{\text{Max}}\left(\boldsymbol{z}^t\,\boldsymbol{K}^t\boldsymbol{K}\,\boldsymbol{z}\right) = w_1^2(\boldsymbol{K}) \quad \text{(G6)}$$

where $w_1(\boldsymbol{K})$ is the largest singular value of $\boldsymbol{K}$. This singular value is simply the square root of the largest (positive) eigenvalue of the reduced information matrix $\lambda_1(\boldsymbol{S}^t\,\boldsymbol{S})$. One can show that:

$$\|\boldsymbol{S}\| = w_1(\boldsymbol{S}) \quad \text{and} \quad \|\boldsymbol{S}^+\| = w_1(\boldsymbol{S}^+) = \frac{1}{w_n(\boldsymbol{S})} \quad \text{(G7)}$$

So, it can be shown, using (G4), (G5) and (G7) that the maximum value of the amplification coefficient of the relative error k_r, that is the criterion that assesses the ill-posed character of the OLS parameter estimation problem is equal to the condition number, noted cond (.) here, of the reduced sensitivity matrix:

$$k_r(\boldsymbol{\varepsilon}) \le \text{cond}(\boldsymbol{S}) = \frac{w_1(\boldsymbol{S})}{w_n(\boldsymbol{S})} \quad \text{(G8)}$$

So, this condition number, defined here with the Euclidian L_2 norm, is the pertinent criterion that can be used to measure the degree of ill-posedness of a linear parameter estimation problem, whatever the value of the noise level (for an i.i.d. noise). If the different parameters defining the parameter vector have not the same physical unit, the reduced sensitivity matrix $\boldsymbol{S}^*$, see Lecture L3, has to replace $\boldsymbol{S}$ in the definition of the condition number. The condition number of $\boldsymbol{S}^*$ depends on the nominal values of the parameters and can vary strongly, depending on the value chosen for normalizing the parameters, even if the problem is linear.

References

[1] D. Maillet, S. André, J.-C. Batsale, A. Degiovanni, C. Moyne, *Thermal quadrupoles – Solving the heat equation through integral transforms*, Wiley, Chichester (2000).

[2] J. Toutain, J.-L. Battaglia, C. Pradère, J. Pailhes, A. Kusiak, W. Aregba, J.-C. Batsale, Numerical inversion of Laplace transform for time resolved thermal characterization experiment, *Journal of Heat Transfer* 133 (April 2011) pp. 044504-1 to 3.

[3] D.P. Gaver, Observing stochastic processes, and approximate transform inversion, *Oper. Res.*14 (1966) pp. 444-459.

[4] H. Stehfest, Algorithm 368. Numerical inversion of Laplace transforms, *Comm. ACM* 13 (1970) pp. 47-49.

[5] H. Stehfest, Remarks on algorithm 368. Numerical inversion of Laplace transforms, *Comm. ACM* 13 (1970) p. 624.

[6] J. Hsu and J.S. Dranoff, Numerical inversion of certain Laplace transforms by the direct application of the fast Fourier transform (fft) algorithm, *Comput. Cham. Eng.* 11 (1987) pp. 101-110.

[7] F.R. de Hoog, J.H. Knight, A.N. Stokes, An improved method for numerical inversion of Laplace transforms, *SIAM J. Sci. Stat. Comput.* 3 (1982) pp. 357-366. http://dx.doi.org/10.1137/0903022.
[8] P. Den Iseger, Numerical transform inversion using Gaussian quadrature, *Probability in the Engineering and Informational Sciences* 20 (2006) 1–44.

[9] J.V. Beck, B. Blackwell, C. St. Clair Jr., *Inverse Heat Conduction*, Wiley, Chichester (1985).

[10] W. Al Hadad, Y. Jannot, D. Maillet, Characterization of a heat exchanger by virtual temperature sensors based on identified transfer functions, *Journal of Physics: Conference Series*, Volume 745, Issue 3, 21 October 2016, Article number 032089, Proceedings of 7th European Thermal Sciences Conference, (Eurotherm, Krakow, 19-23 June 2016).

[11] W. Al Hadad, D. Maillet, Y. Jannot, Modeling unsteady diffusive and advective heat transfer for linear dynamical systems: A transfer function approach, *International Journal of Heat and Mass Transfer* 108 (2017) 115, Part A, December 2017, Pages 304-313, http://dx.doi.org/10.1016/j.ijheatmasstransfer.2017.07.009.

[12] L. Ljung , System identication: theory for the user, 2nd ed., Upper Saddle River NJ: Prentice-Hall PTR (1999).

[13] R.C. Aster, B. Borchers, C.H. Thurber, *Parameter estimation and inverse problems*, 2nd edition, Academic Press, Oxford (2011).

[14] W. Al Hadad , D. Maillet , Y. Jannot , Experimental transfer functions identifica- tion: thermal impedance and transmittance in a channel heated by an up- stream unsteady volumetric heat source, Int. J. Heat Mass Transf. 116 (2018) 931–939 .

[15] H. Dogan, K. A. Khalil, L. R. Suarez, Some results on the ideals of real-valued lower triangular Toeplitz matrices, Turk. J. Math. Comput. Sci.vol. 9, pp. 50–54, 2018.

[16] D. Maillet, V. Zacharie, B. Rémy, Identification of an impulse response through a model of ARX structure, *Journal of Physics: Conference Series*, Volume 2444 (2023) 012002 IOP Publishing, doi:10.1088/1742-6596/2444/1/012002.

[17] K. P. Burnham and D. R. Anderson, Model Selection and Multimodel Inference – A Practical Information – Theoric Approach, 2nd edition, Springer (2002).

[18] Vélien Zacharie, Modélisation des transferts thermiques instationnaires par modèles paramétriques : application à un four industriel de brasage d'échangeur sous vide [Modelling of unsteady heat transfers by parametric models : application to an industrial vacuum furnace for brazed heat exchangers], PhD thesis, Université de Lorraine, Dec. 14, 2020 .

[19] A. V. S. Oliveira, C. Zacharie , B. Rémy , V. Schick, D. Maréchal, J. Teixeira, S. Denis , M. Gradeck, Inverse ARX (IARX) method for boundary specification in heat conduction problems, Int. J. Heat Mass Transf. 180 (2021) 121783.

Tutorial 8: Heat Flux estimation using deconvolution and regularization procedure

J-L. Gardarein[a], J-L. Battaglia[b], J. Gaspar[a]

[a]IUSTI UMR 7343, Aix-Marseille University, Marseille Cedex13, France
[b]I2M UMR , Bordeaux University,

Abstract: This tutorial is especially designed to the beginners in inverse heat conduction techniques. An estimation of a surface heat flux on a material will be done using embedded thermocouples. Through an experimental example, we propose to detail the heat flux estimation procedure associating deconvolution and regularization method (Tikhonov). After a brief presentation of the experimental context, the inversion procedure will be applied using an experimental signal generated during the tutorial. The codes used will be accessible to the participants.

1. Introduction

In many industrial applications or large research facilities, heat flux and temperature control are essential for a better understanding of the process and for the safety of the facilities. There are different possible temperature measurements: at the surface or using embedded sensors. The heat fluxes are generally deduced from these temperatures. On some setups, it is possible to measure temperature within the region of interest. But this is not always the case. In this workshop, we present a method that allows the estimation of heat flux and temperature using embedded measurements.

We will focus on heat flux estimation based on embedded measurements using thermocouples. It is clear that a very small change in the measurement will lead to a large variation of the heat flux estimated. In other words, measurement errors are amplified and could make the results unusable. A solution to such an issue is to use a specific regularization method that would allow a better reliability of the solution. The best-known techniques include Thikonov's penalization regularization [Thikonov, 1977], and spectrum truncature regularization (SVD) [Hansen, 1993]. To solve the inverse problems in heat conduction, many numerical techniques have been developed using different approaches, some analytical or semi-analytical, others based on classical numerical approximations, such as finite differences or finite elements. In this tutorial, a method based on the inversion of the Duhamel integral is used [Osizik, 1980], [Beck, 1985].

This method extends the use of analytical solutions and solves multidimensional problems. The adjoint state method well described in [Jarny, 1990] can also be used to solve boundary condition estimation problems in complex geometries using the direct problem as an observation. However, the iteration process implementing a direct finite element calculation does not make it possible to perform a fast calculation.

In a first part, a very simple direct problem is presented in order to explain the difference between a direct and an inverse procedure. Then, the convolution method allows writing a link between the temperature and the heat flux. The next section deals with the transfer function of

the experimental devices and the different ways to estimate them. Finally, the inversion process and the regularization method are described.

2. Direct Problem, convolution

2.1 Presentation of a simple direct problem

Considering a 1D material with constant thermal properties (λ = 240W/m.K, ρ=1800kg/m^3, C_p=780 J/kg.K, e=0.04m) submitted to a heat flux step of 1W/m^2 between 5 and 10 seconds, we can compute the temperature at different depth values within the material (z=0, 1, 2, 3, 4 cm) with a direct calculation (numerical simulations, thermal quadrupoles [Maillet et al., 2000], analytical solution,…). We assume that the initial temperature distribution in the material (at t = 0) is uniform and equal to T_0.

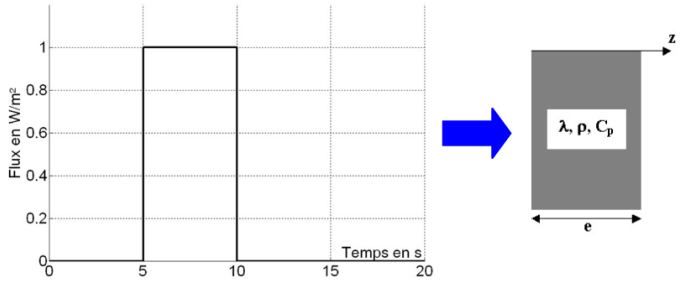

Figure 1. Heat flux applied to the surface of material with thickness e.

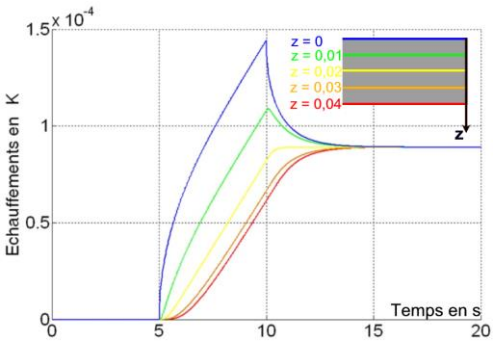

Figure 2. Temperature rise at different thickness: z=0, z=0.01m, z=0.02m, z=0.03m, z=0.04m.

Since the material is insulated, one can note that all the temperature rise is the same for all the sensors location from 15 sec. and is equal to:

$$\Delta T_{stab} = T_{stab} - T_0 = \frac{E}{\rho C_p e} = \frac{5 \times 1}{1800 \times 780 \times 0.04} = 8{,}903.10^{-5} K \quad (1)$$

E is the energy per unit volume absorbed within the bulk in J/m^3.

A noise is added to the calculated values in order to simulate real temperature measurements as:

$$Y = Y_{num} + \varepsilon \quad (2)$$

Y is the noised signal of Y_{num} that is the exact temperature given by (2).

ε is a Gaussian noise with zero mean and constant 10% standard deviation. Using the direct model leads to the temperature field when the thermal properties, the geometry and the heat flux are well known. Let us note however that, in the case of a complex geometry, a finite element method is generally used to obtain a field of temperature.

In this tutorial, we deal with the case when the heat flux is unknown and we have only one or several temperature measurement, not necessarily located on the region of interest. In this case, how can we obtain the heat flux on a boundary of the component? In the particular case presented on the Figure 1 and 2, the problem could be: how to estimate the heat flux deposited at the surface of the material using only the temperature measurement depending on time at 1cm from the surface?

2.2 Convolution procedure description [Carslaw-Jaeger, 1959]

The component is modelled by a linear system subjected to a prescribed heat flux $Q(z=0,t)$ having for effect the temperature $T(z,t)$. Using the linear system, the temperature $T(z,t)$ can be written as the convolution of $Q(z=0,t)$ with the impulse response $h(z,t)$ of the system, (i.e. the tile temperature response after a Dirac function of power applied to the surface). The temperature of the material is assumed to be uniform at t = 0.

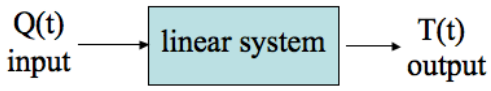

Figure 3. Linear System.

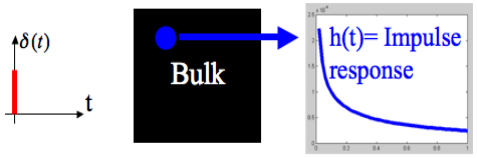

Figure 4. Impulse response of the bulk.

For the temperature T at the time t, the depth z:

$$T(z,t) = T(z,t=0) + Q(z=0,t) \ddot{A}\, h(z,t) = T(z,t=0) + \int_{t_0}^{t} Q(z=0,t)h(z,t-t)dt \quad (3)$$

The impulse response $h(z,t)$ of the system is the first time derivative of its step response $u(z,t)$. So, we approximate (3) by finite differences which leads to the expression of the temperature at each time step F in matrix form: where X is a triangular lower square matrix (of order F) assembled with the components:

$$\begin{bmatrix} \Delta T(z,1) \\ \Delta T(z,2) \\ \vdots \\ \vdots \\ \vdots \\ \Delta T(z,F) \end{bmatrix} = \begin{bmatrix} \Delta u(z,1) & 0 & \square & \square & \square & 0 \\ \Delta u(z,2) & \Delta u(z,1) & \square & \square & \square & 0 \\ \Delta u(z,3) & \Delta u(z,2) & \ddots & . & . & 0 \\ & & \ddots & \ddots & . & \vdots \\ & & . & \ddots & \ddots & \vdots \\ \Delta u(z,F) & \Delta u(z,F-1) & \square & \square & . & \Delta u(z,1) \end{bmatrix} \cdot \begin{bmatrix} Q(z=0,1) \\ Q(z=0,2) \\ \vdots \\ \vdots \\ \vdots \\ Q(z=0,F) \end{bmatrix} \quad (4)$$

with

$$\Delta u(z,F) = u(z,F) - u(z,F-1)$$

Finally, the heating vector ΔT is the multiplication of the X matrix with the heat flux vector Q:

$$\mathbf{\Delta T = X.Q} \quad (5)$$

Since the X matrix is build with the transfer function of the component, this one has to be computed or measured.

3. Determining the transfer function

In this part, several ways to obtain the transfer function of the components are presented. For the case presented previously, an analytical transfer function can be computed using the thermal quadrupoles modelling [Maillet et al., 2000] because the geometry is perfectly known and relatively simple. In the case of a complex geometry, multidimensional, multi-materials, a numerical simulation can be used to compute the transfer function of the experimental device. An example is presented in subsection 3.2. Then, in a case of an experimental device complicated to model with a good level of accuracy (the thermal properties or the dimensions are note perfectly known, old experimental without map), the transfer function can be estimated experimentally directly on the device, using an appropriate methodology presented on the subsection 3.3.

3.1 Analytical transfer function

For a simple case, the thermal transfer function of an experimental device can be computed with the thermal quadrupoles method [Maillet et al., 2000]. With this method, the temperature and the heat flux at the surface of the material can be written respect to the heat flux and the temperature at the back face of the material, the thermal properties and the dimensions of the sample, in the Laplace space. Each layer of the material is represented with a 2x2 matrix containing the thermal properties and the thickness of the layer. For the particular case presented in the subsection 2.1, the transfer is mono dimensional and we want to compute the transfer function of the material at the thickness *z* (corresponding to a TC location) after a step of heat flux of *1 W/m²* imposed at *z=0* (surface of the component). To obtain the step response at the thermocouple location $z=e_1$, the material of width *e* is modelled by a bi-layer material of respectively e_1 and e_2 width:

$$\begin{bmatrix}\theta_{in}(0,p)\\ \phi_{in}(0,p)\end{bmatrix}=\begin{bmatrix}A_1 & B_1\\ C_1 & D_1\end{bmatrix}\begin{bmatrix}\theta_{e_1}(e_1,p)\\ \phi_{e_1}(e_1,p)\end{bmatrix}$$

$$\begin{bmatrix}\theta_{e_1}(\boldsymbol{e_1},\boldsymbol{p})\\ \boldsymbol{\phi}_{e_1}(\boldsymbol{e_1},\boldsymbol{p})\end{bmatrix}=\begin{bmatrix}\boldsymbol{A_2} & \boldsymbol{B_2}\\ \boldsymbol{C_2} & \boldsymbol{D_2}\end{bmatrix}\begin{bmatrix}\theta_{out}(e,p)\\ \phi_{out}(e,p)\end{bmatrix} \quad (6)$$

With $A_i = D_i = cosh(\sigma.e_i)$

$B_i = \frac{1}{\lambda\sigma}.sinh\,(\sigma.e_i)$

$C_i = \lambda\sigma.sinh\,(\sigma.e_i)$ and $\sigma = \sqrt{\frac{p}{a}}$

Since the material is supposed to be insulated in *z=e*, $\phi_{out}(e,p) = 0$. Furthermore, the heat flux imposed at *z=0* is a Heaviside function equal to *1W/m²*, in the Laplace space, this function becomes: $\phi_{in}(0,p) = 1/p$.

With theses assumptions, it is now possible to write in Laplace transform of the step response at $z=e_1$:

$$\theta_{e_1}(e_1,p) = \frac{A_2}{C_1A_2 + A_1C_2}.\frac{1}{p} \quad (7)$$

A numerical inverse Laplace transform [DeHoog, 1982] allows computing this step response in the time domain.

3.2 Transfer function computation with finite element method

When the step response can't be computed with this kind of simple modelling, it is also possible to compute it with a finite element method. In the next case, the experimental device is a pervaporation cell made of PVC matter [Toudji, 2017] with a low thermal conductivity of about *0.16 W/m.K* to limit heat exchanges with the external environment and with the liquid. The liquid is filled in a cylindrical tank above the pervaporative membrane surface. Several thermocouples are located in the fluid. The goal of this experimental device is to estimate the heat flux consumed on the membrane in *z=0m*, using the thermocouples data and the deconvolution method. As in the precedent case, the first problem is the identification of device transfer function. Since, the diffusive time of the ethanol is very important, in a first approximation, it is possible to use an analytical solution assuming the ethanol as a semi-infinite medium. In this case, the step response can be written as follow:

$$T(z,t) - T(z,0) = 2.\frac{Q}{\lambda}\sqrt{at}.ierfc(\frac{z}{\sqrt{4at}}) \quad (8)$$

T(z,t) is the field of temperature depending on time and on the location *z*
T(z,0) is the initial temperature of the device
Q is the heat flux density (W/m^2), equal to $1W/m^2$ for a step response.
λ is the thermal conductivity (*W/mK*)
a is the thermal diffusivity (m^2/s)
t is the time (*s*)

The semi-infinite approximation can be useful for a short experience but this kind of experiments are interesting at long time, typically 2000s. It was essential to compute a step response taking into account the complex geometry of the experimental device. This computation has been done with StarCCM+. The mesh and the results are presented on the following figures for a negative heat flux of $-200W/m^2$. Indeed, a first computation has been done with a value of heat flux density in order to see the order of magnitude of the cooling at the thermocouples locations.

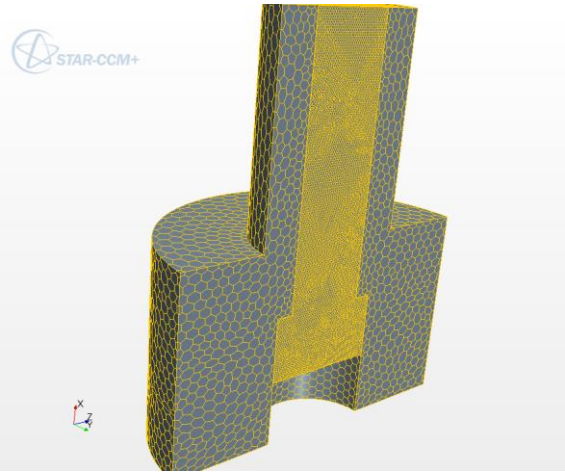

Figure 5. Mesh of the pervaporation experimental cell

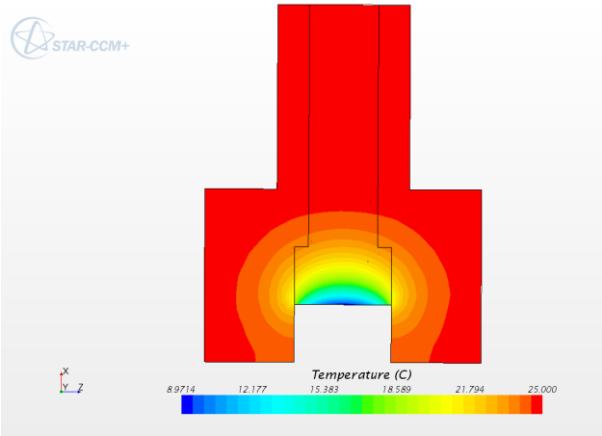

Figure 6. Temperature field obtained with a negative heat flux of 200W/m^2

In a second time, the step responses have been computed at three TC locations with a heat flux of *1W/m^2* imposed at *z=0m*. The computed step response are presented on the following figure:

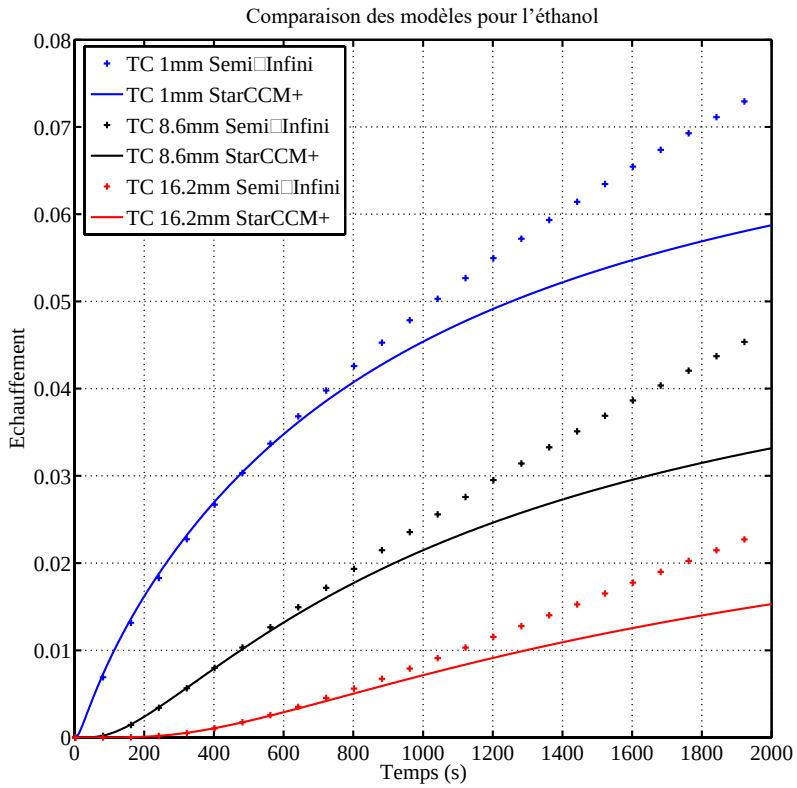

Figure 7. Step response function computed at three TC locations with numerical simulations and semi-infinite approximation

One can see on this figure the comparison for each thermocouple of the numerical simulation and the semi-analytical one. We can see that the semi-infinite solution can be used until 500s, for a longer experiment, the numerical responses are essential.

3.3 Transfer function identification

As said previously, the direct model is generally known, i.e., the thermal properties of the medium as well as the location of the sensors are accurately known. However, many practical configurations do not enter this ideal world and solving the inverse problem with great uncertainty on the direct one would lead to very inaccurate results. Therefore, as proposed in lecture L7, the transfer function that links the heat flux to the temperature at the sensors can be identified. In order to make a comprehensive application of the proposed methods in system identification, only one input (heat flux) and output (temperature measurement) will be considered.
The first approach, know as the non-parametric one, will lead to estimate the transfer function from measured values of the heat flux and the sensor temperature within an experimental configuration where the heat flux can be monitored. The methods that will be used are the spectral technique based on the Welch algorithm.
The second approach will consist in identifying the parameters involved within the expression of the transfer function. The first step will use the ARX technique that is faster but unfortunately biased since it is based on the minimization of the prediction error. The second method is based on the OE (output error) minimization technique that is a bit longer but unbiased.

4. Deconvolution and regularization

After the estimation of the transfer function of the experimental device studied, the matrix X can be built and the direct problem presented on the equation (5) can be easily solved. It is just a multiplication of the matrix *X* (built with the step response computed) with the heat flux vector. When the temperature vector is measured, the heat flux vector can be estimated using a specific methodology. The deconvolution procedure consists in reversing Eq.(5), i.e. expressing surface heat fluxes with measured surface heating as:

$$\mathbf{Q} = \mathbf{X}^{-1}\,\mathrm{D}T \tag{9}$$

In the case of a surface temperature deconvolution ($z = 0m$), the problem is inverse but stable and matrix X inversion doesn't cause any problem. In the case of the deconvolution of the temperature measured with an embedded thermocouple ($z=e$); the inverse problem is now unstable. A low variation of the measurement induces a big variation of the estimated heat flux. Indeed, the matrix *X* is ill conditioned. Clearly, it means that the matrix *X* is difficult to inverse because of very low terms in the diagonal. Consequently, a regularization procedure is needed to stabilize the solution.

4.1 The Thikonov regularization

The solution vector *Q*, is very sensitive to measurement errors contained in vector ΔT. In order to obtain a stable solution, we use a regularization procedure. For example, we can use the Thikonov regularization operator. The regularized solution becomes:

$$\hat{\mathbf{Q}}_{reg} = (\mathbf{X}^t\mathbf{X} + g\mathbf{R}^t\mathbf{R})^{-1}\,\mathbf{X}^t\,\mathrm{D}T \tag{10}$$

- $\hat{Q}_{reg}$ is the regularized solution (an approximation of *Q*)

- γ is the regularization parameter
- R is the regularization operator depending on the type of information that we want to obtain.

In the specific case of heat flux estimation, we want a solution with a minimal norm of the solution (0 order) $\hat{Q}_{reg}$, so we will take $R = Id$. An optimal value of the regularization parameter can be found using the "L curve" technique [Hansen, 1993]. This type of representation allows choosing the best compromise - which is located at the bending point of the 'L-curve' - between a stable solution, with a low value of $\|R.\hat{Q}_{reg}\|$ and an accurate solution, with low residuals $\|X.\hat{Q}_{reg} - \triangle T\|$.

4.2 Application to the case presented in the section 2.1

For lower values of γ (Figure 8), the solution is unstable with low residuals, on the other hand, for strong values of γ (Figure 9), the solution is stable but moves away from the exact solution. The Figure 10 shows the heat flux estimated with the best compromise for γ.

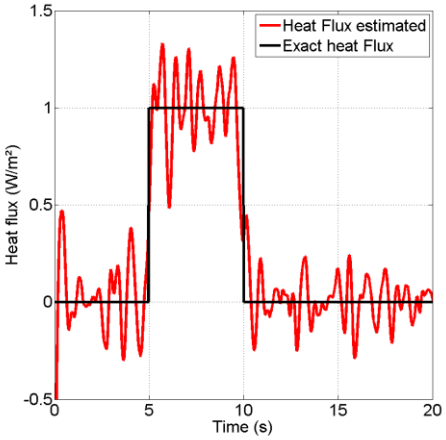

Figure 8. Heat flux estimation with a low γ

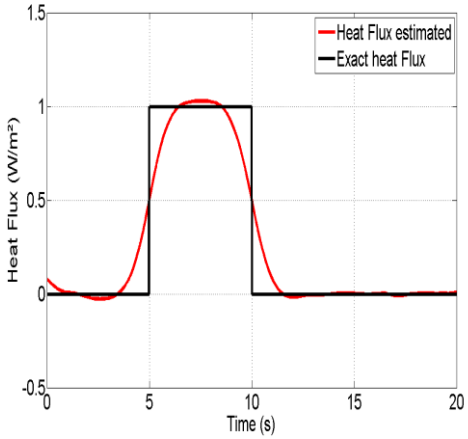

Figure 9. Heat flux estimation with a strong γ.

On Figure 11 is presented an example of L curve with the best γ for heat flux estimation with the embedded measurement. One can note that the value γ depends on the level of the noise, the temporal resolution and the depth of the measurement.

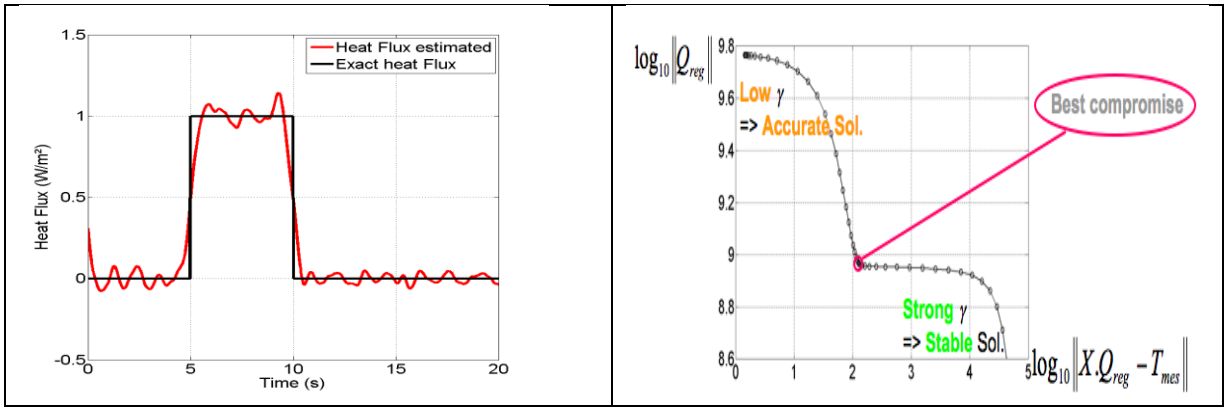

Tutorial 8: Heat Flux estimation using deconvolution and regularization procedure 8/10

Figure 10. Heat flux estimation with the best compromise of γ.	Figure 11. L curve and best γ in the case of an embedded thermocouple located at 3cm of the surface.

4.3 Application to the case presented on section 3.2

In this case, three similar experiments have been performed in laboratory with ethanol. The heat fluxes have been estimated using the step response presented on Figure 7 and the deconvolution and regularization procedure. On Figure 12, the heat fluxes have been estimated with the thermocouple located at 1mm from the surface for three different experiments. On Figure 13, this is the same experiment but the heat fluxes are estimated with the three thermocouples (*z=1mm, z=8.6mm and z=16.2mm*). In the two cases, the values of the heat fluxes are similar. First, one can note that the experiment is reproducible. On Figure 13, one can see that the heat flux estimated with the TC located at 8.6mm and 16.2mm are very smooth. This is because the depth of the thermocouple needs a higher value of the regularization parameter to obtain an exploitable solution. Nevertheless, the obtained values are very similar between the three thermocouples, proving the good level of accuracy of the step responses computed with STARCCM+.

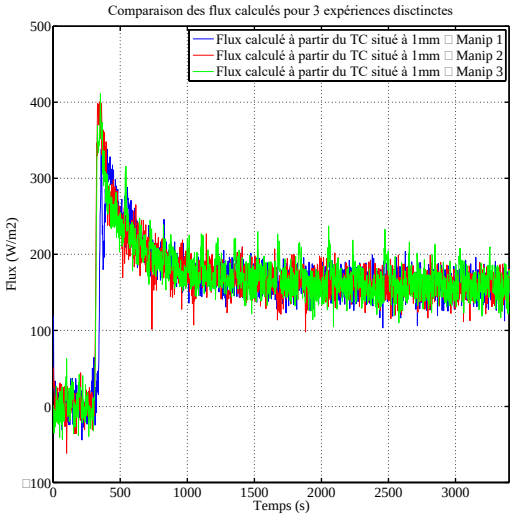

Figure 12. Heat flux estimation with the same thermocouple for three different experiences.

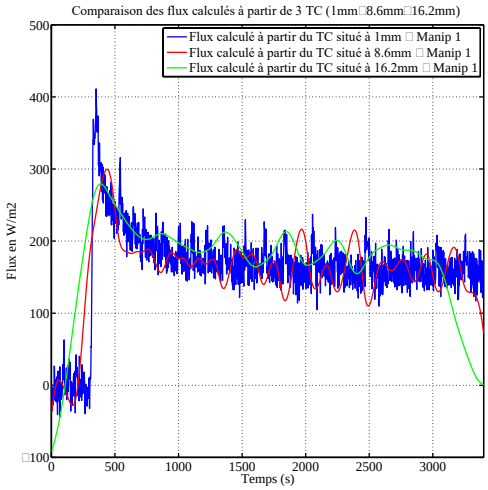

Figure 13. Heat flux estimation for the same experiment with three different thermocouples.

5. During the tutorial…

We propose to apply the methods presented below considering experimental signals measured during the tutorial using a simple experiment. The principle of this experiment is to heat a sample with a lamp and to measure the temperature with thermocouples at several locations within the medium. The transfer function will be either derived analytically or identified. The measured signals will be recorded on a computer and the inverse problem will be solved using the deconvolution technique. All the codes are based on Octave GNU software.

References

J.V. Beck, B. Blackwell, C. R. ST. Clair, JR., "Inverse heat conduction, Ill-posed Problems" Wiley-Interscience Publication - 1985.

H.S. Carslaw, J.C. Jaeger, "Conduction of Heat in Solids", Oxford University Press -1959.

F.R. De Hoog, J. H. Knight, and A. N. Stokes, "An Improved Method for Numerical Inversion of Laplace Transforms", SIAM J. Sci. and Stat. Comput., 3(3), 357–366. (10 pages)-1982.

P. Hansen, D.O'Leary, SIAM, J. Sci. Comput 14 (1993) 1487-1503.

Y. Jarny et al., "A general optimization method using adjoin equation for solving multidimensional inverse heat conduction", Int. Journal Heat and Mass Transfer, Vol. 34 (11) – 1990.

D. Maillet, S. André, J-C. Batsale, A. Degiovanni, C. Moyne, "Thermal Quadrupoles", New-York: Wiley & Sons; 2000.

N. Osizik, "Heat Conduction", John Wiley & Sons – 1980.

A.N. Tikhonov, V.Y. Arsenin, "Solutions of Ill-Posed Problems", V.H. Winston&Sons, Washington, D.C., 1977.

S.A. Toudji, J-P. Bonnet, J-L. Gardarein, E. Carretier, "New experimental setup for continuous mass flux measurement in pervaporation", Chem. Eng. Research and design 124 (2017) 252–259.

Tutorial 9: Bayesian approach for inversion

S. Demeyer[1]
[1] LNE, Laboratoire National de Métrologie et d'Essais, Département Science des Données et Incertitude

E-mail: severine.demeyer@lne.fr

Abstract. The aim of this tutorial is to enable participants to apply Bayesian inversion algorithms to estimate thermal properties of walls (thermal resistance, thermal conductivity, areal heat capacity) and their associated uncertainty from surface measurements of the wall. The Bayesian inversion relies on the setting of prior distributions on the parameters of interest that are combined with the information gained from the measurements to provide the posterior distributions of the thermal parameters. Participants will experiment various prior settings and tuning parameter values as input parameters of a given Bayesian algorithm and see the effect on the convergence of the Bayesian algorithm and the posterior distributions. The required software is R with R Studio user inferface and a R notebook is provided during the tutorial in addition to this document.

List of acronyms:

MCMC: Markov Chain Monte Carlo

1. Introduction

In the ANR RESBATI project[1], a technical solution was developed to allow the in-situ estimation of the thermal resistance of walls with interior wall insulation (IWI) when the thermal resistance is less than 4 m²K/W. A follow-up of this project ANR RESBIOBAT aims at investigating a solution for highly insulated walls and other types of sustainable walls composed of bio-sourced hygroscopic products.

In the RESBATI project, the developed measuring device consisted of an active solicitation of the wall by a local constant heating, to measure its flux and temperature dynamic responses and then to determine its thermal resistance using identification methods (inverse modelling).

The objective of this tutorial is to apply a Bayesian inversion procedure to measurement data collected during the ANR RESBATI project (inner surface temperature denoted TSI and absorbed flux measurements), adapted from [Demeyer, 2021], to estimate the thermal resistance of a multi-layer wall and its associated uncertainty.

Due to the active method applied to produce measurements, thermal resistance cannot be inferred directly and requires the inversion (calibration) of a thermal model being able to produce temperatures as a function of conductivity and heat capacity of unit area (at least) based on observations.

The thermal resistance of a multi-layer wall is given by the sum of the thermal resistance of each layer as $R = \sum_{i=1}^{I} \frac{l_i}{k_i}$ where k_i and l_i are respectively the thermal conductivity and thickness of layer i and I is the number of layers.

[1] The RESBATI project was supported by ANR (Agence Nationale de la Recherche) the French National Research Agency under Grant agreement ANR-16-CE22-0010-02.

2. Description of the studied wall

The following IWI wall is considered in this tutorial, for which measured or tabulated values of the thermal parameters of the constituents are displayed in Table 1. The results of the inversion will be compared with the theoretical or experimental values.

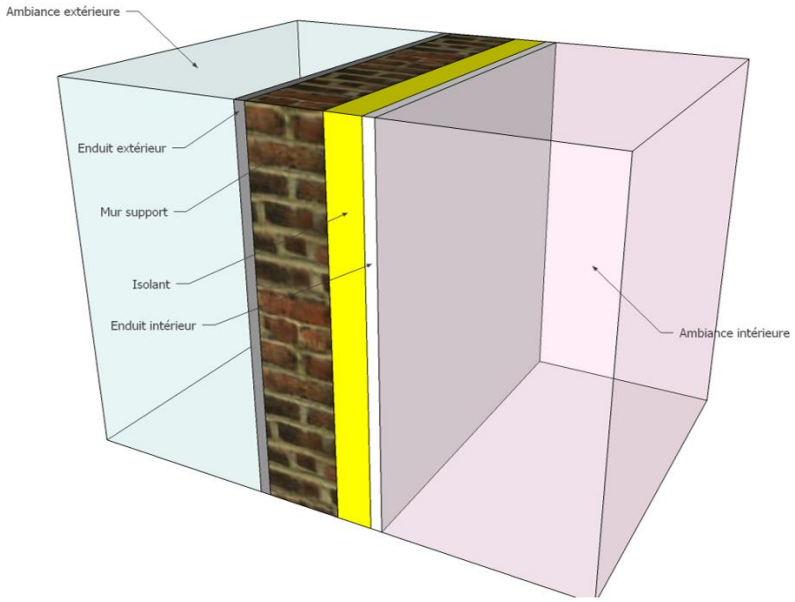

Layer	Thickness (m)	Heat capacity of unit area cw / J/(K.m²)	Thermal conductivity k / $Wm^{-1}K^{-1}$	Thermal resistance R / m^2KW^{-1}	Thermal resistance %
Plasterboard	$e_1 = 0.013$	$cw_1 = 7.44 \times 10^5$	$k_1 = 0.250$	$R_1 = 0.052$	1.2
Insulation	$e_2 = 0.12$	$cw_2 = 3 \times 10^4$	$k_2 = 0.031$	$R_2 = 3.87$	91.5
Cinderblock	$e_3 = 0.15$	$cw_3 = 9.5 \times 10^5$	$k_3 = 0.580$	$R_3 = 0.258$	6.1
Exterior coating	$e_4 = 0.015$	$cw_4 = 1.30 \times 10^6$	$k_4 = 0.3$	$R_4 = 0.05$	1.2
				$R = 4.23$	100

Table 1 Measured or tabulated values of the thermal performance of the constituents of the wall

From Table 1, draw conclusions on the most influential layer

3. Exploration of the direct thermal model

A 1D thermal model is considered. We assume that this simplified model, which does not depict transverse flows in the walls, is well adapted to IWI walls.

3.1. Plot the output TSI curve obtained with the measured or tabulated values of the thermal parameters in Table 1 and the observed TSI.

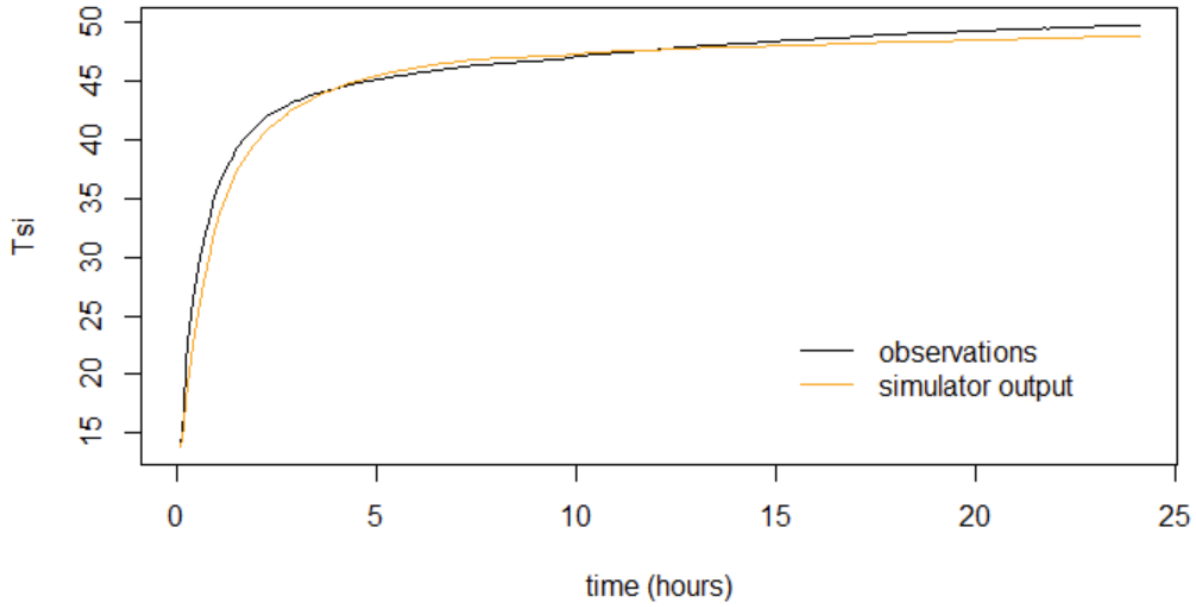

3.2. Observe the effect of departures from these values on the curve, for the parameters of your choice

4. Methodology for Bayesian inversion

4.1. Inversion

Among all the input quantities to a simulator used to represent a physical process, only a fraction of them are usually considered as the quantities of interest (the measurands), called calibration parameters in the inversion terminology, the others being considered as control or nuisance parameters. Some other inputs may be fixed to nominal values.

In this tutorial, the calibration parameters of the thermal model representing the thermal response of the studied wall are the thermal parameters θ of the wall. The control parameters x are observed variables that allow to reproduce numerically the experimental conditions that have produced the observations, see Figure 1.

From the experimental values and the outputs generated by the thermal model, the aim of the identification technique is to find the values of the thermal parameters of the wall entered in the thermal model so that the outputs are as close as possible to the experimental values.

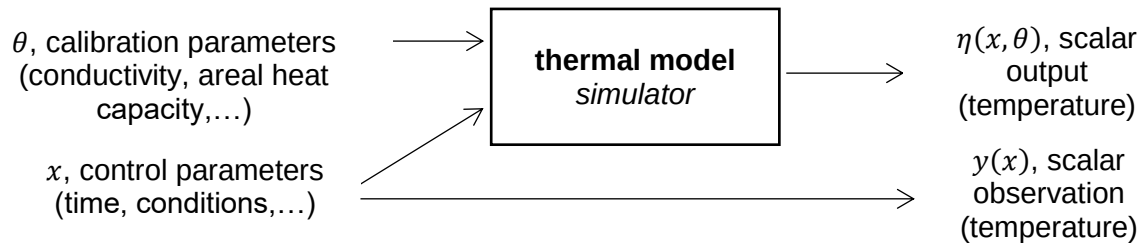

Figure 1 Schema of a physical model used as a simulator and the quantities involved in the calibration of the simulator

Recently, Bayesian inversion procedure has been applied to infer thermo-physical properties of building walls or envelopes from thermal physical models [Iglesias, 2018], [Thebault, 2018], [Demeyer, 2021].

4.2. Steps for a Bayesian inversion

a) Choice of a statistical model for calibration

A model assuming no discrepancy between observations y_i and outputs of the thermal model η for the observed conditions x_i and calibration parameters θ writes

$$y_{\mathrm{i}} = \eta(x_i, \theta) + \varepsilon_i, i = 1, \dots, N$$

where ε_i is the measurement error, assumed to be independently normally distributed with standard deviation u_i the reported measurement uncertainty

$$\varepsilon_{\mathrm{i}} \sim N(0, u_i)$$

The previous model can be extended to take into account potentially underestimated reported uncertainties u_i by introducing an adjustment factor $\sigma > 0$ (the Birge ratio of the model)

$$y_{\mathrm{i}} = \eta(x_i, \theta) + \sigma\varepsilon_i, i = 1, \dots, N$$

Assuming that $\sigma^2 \sim InvChi^2(\nu_0, s_0^2)$, the marginal distribution of the observations integrated out σ^2 is multivariate t-distributed

$$y \sim t_{\nu_0}(\eta(x, \theta), s_0^2 \Sigma_\varepsilon)$$

where $x = (x_1, \dots, x_N)$ and $\Sigma_\varepsilon = diag(u_1^2, \dots, u_N^2)$

Bayesian inversion [Kennedy,2001], [Higdon, 2004], provides the posterior distribution denoted $\pi(\theta|y, x)$ of the calibration parameters θ given observations y, control parameters x and a prior distribution $\pi(\theta)$.

b) Choice of prior distributions

The potential ranges for the thermal parameters of each layer are given in Table 2 and uniform distributions are chosen as prior distributions.

Layer	Heat capacity of unit area cw / J/(K.m²)	Thermal conductivity k / $Wm^{-1}K^{-1}$
Plasterboard	$1 \times 10^5 \leq cw_1 \leq 1.5 \times 10^6$	$0.2 \leq k_1 \leq 0.8$
Insulation	$2 \times 10^4 \leq cw_2 \leq 2 \times 10^5$	$0.02 \leq k_2 \leq 0.06$
Cinderblock	$6.5 \times 10^5 \leq cw_3 \leq 2.5 \times 10^6$	$0.1 \leq k_3 \leq 2.3$
Exterior coating	$5 \times 10^5 \leq cw_4 \leq 2 \times 10^6$	$0.1 \leq k_4 \leq 1.8$

Table 2 Potential values for thermal parameters of the insulation layer

c) Choice of a MCMC algorithm

The Metropolis-Hastings [Chib, 1995] algorithm (see Appendix B) is implemented in the function `MH` which performs the MCMC simulations in the posterior distribution of θ

```
MH<- function(n_sim,pars.init,scale,par_names)
```

`n_sim` number of MCMC simulations
`pars.init` initial value $\theta^{(0)}$
`scale` variance covariance matrix of the multivariate proposal distribution N(θ^((c)),Σ)

Additional functions:

`addMHsimulations` adds MCMC samples to a previously generated samples from the stationary distribution
`traceMH` plots the MCMC simulations
`histMH` plots the histogram of the MCMC simulations
`post_trait` computes the posterior mean and standard deviation of the thermal resistance and plots the posterior density of the thermal resistance

`MH` function returns MCMC samples (also called chain) and the acceptance rate.

d) Analysis of posterior samples from the Markov chains

- autocorrelation function of the chains
- traceplots
- density plots
- burn-in, thinning,…

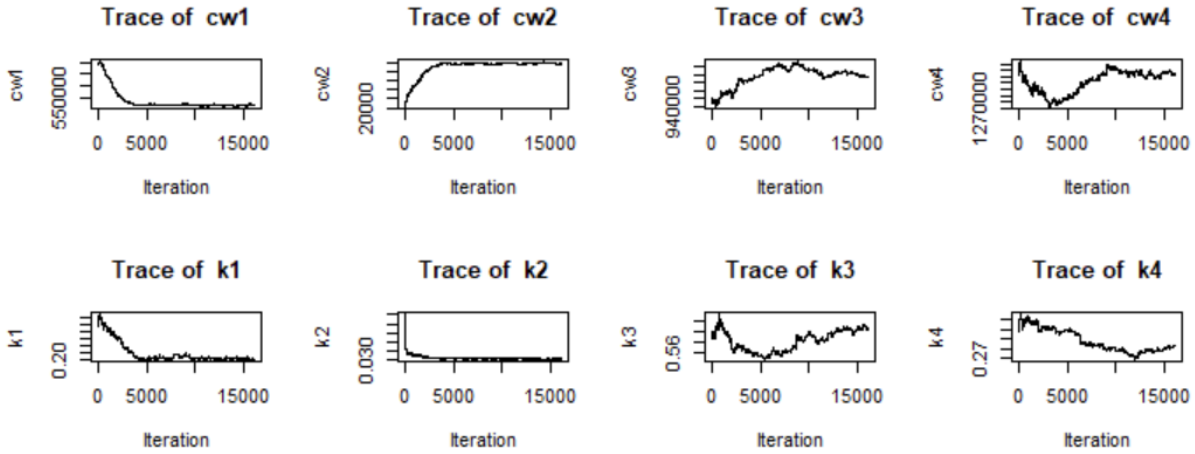

Comment the traceplots

e) Convergence diagnostics

Convergence diagnostics tools are usually employed to check the stationarity of the Markov chain. A review of convergence diagnostics for MCMC is given in [Roy, 2020], among which we will focus on the effective sample size and the Gelman-Rubin diagnostic. In brief, the effective sample size gives the number of independent samples equivalent to a set of correlated Markov chain samples and the output of the Gelman-Rubin diagnostic is the so-called potential scale reduction factor which should be close to 1 and is computed from at least two chains ran with overdispersed starting points w.r.t. the posterior distribution.

f) Summary graph

Complete the plot of Section 3.1 with $\eta(\theta_{post})$ where θ_{post} is the vector of the posterior means

```
> post_mean
          cw1           cw2           cw3           cw4           k1           k2           k3           k4
5.213307e+05 1.169856e+05 9.847284e+05 1.294803e+06 2.020837e-01 3.014809e-02 5.724725e-01 2.811880e-01
```

Comment

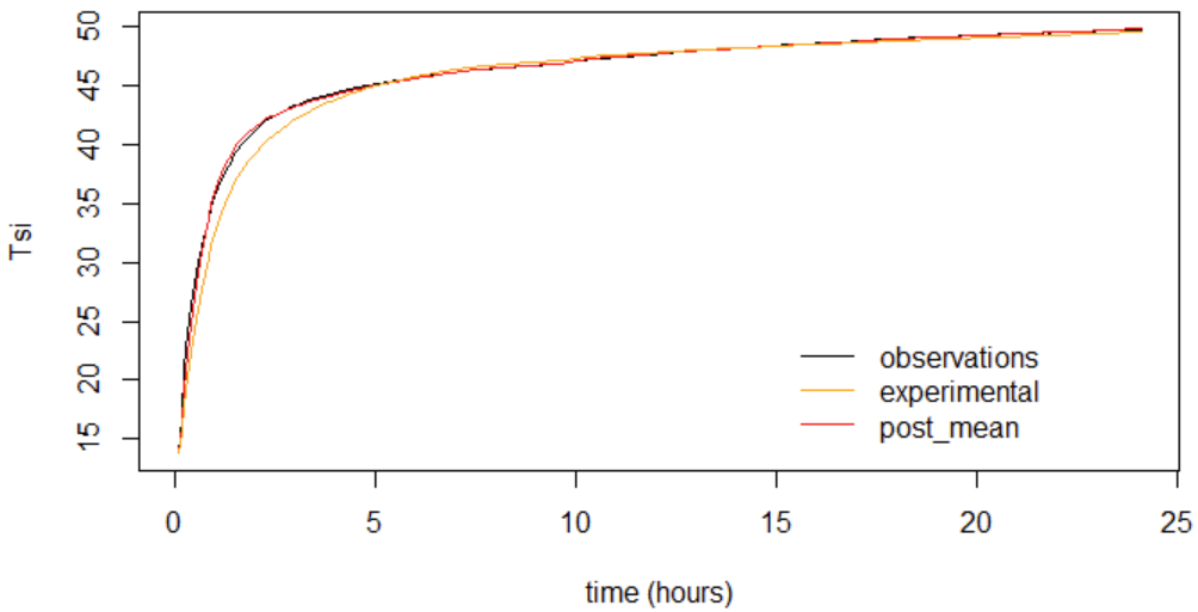

f) Conclusion

For this problem, the traceplot of some of the chains is typical of non identifiability, meaning that various combinations of values of these parameters can yield to the same likelihood of the data.

However, the identified parameters allow to reproduce the observed TSI curve.

Indeed, only the global thermal resistance is identifiable with the experimental setting, not the thermal resistance of the individual constituents.

5. Estimation of the thermal resistance of the wall

After discarding the burn-in period and applying thinning to the chains, plot the posterior density of the thermal resistance. Compare with the theoretical R value.

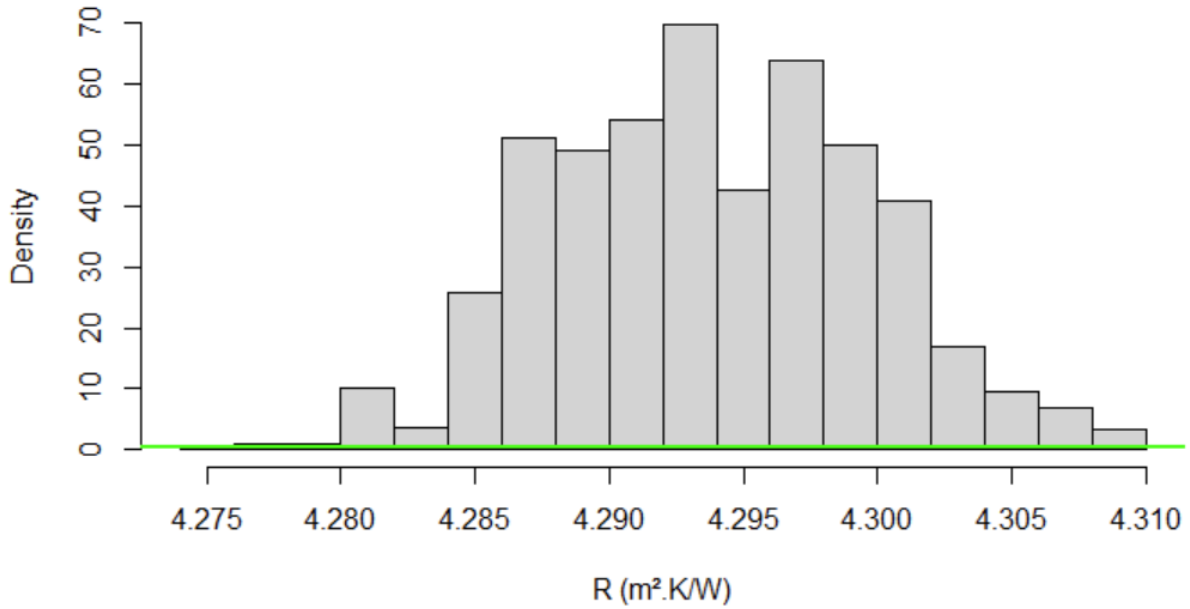

From the resulting posterior simulations, give posterior estimates

R_posterior =…… u(R_posterior)=……

relative uncertainty = (u/R)= ……

Conclusion

References

Chib, S. and Greenberg, E. (1995). Understanding the Metropolis-Hastings algorithm. The American Statistician, 49(4):327-335.

Demeyer, S., Le Sant, V., Koenen, A., Fischer, N., Waeytens, J., Bouchié, R. Bayesian uncertainty analysis of inversion models applied to the inference of thermal properties of walls, Energy & Buildings, 249, 2021, https://doi.org/10.1016/j.enbuild.2021.111188

Higdon, D., Kennedy, M., Cavendish, J., Cafeo, J., and Ryne, R. (2004). Combining field data and computer simulations for calibration and prediction. SIAM Journal on Scientific Computing, 26(2):448-466.

Iglesias, M., Sawlan, Z., Scavino, M., Tempone, R., and Wood, C. (2018). Bayesian inferences of the thermal properties of a wall using temperature and heat flux measurements. International Journal of Heat and Mass Transfer, 116:417-431.

Kennedy, M. and O'Hagan, A. (2001). Bayesian calibration of computer models. J. R. Statist. Soc. B, 63(3):425-464.

Roy, V., Convergence diagnostics for markov chain monte carlo, Annual Review of Statistics and Its Application 7 (2020) 387–412.

Thébault, S. and Bouchié, R. (2018). Refinement of the Isabele method regarding uncertainty quantification and thermal dynamics modelling. Energy and Buildings,78:182- 205.

Appendix

A) Inverse chi-squared distribution for σ^2

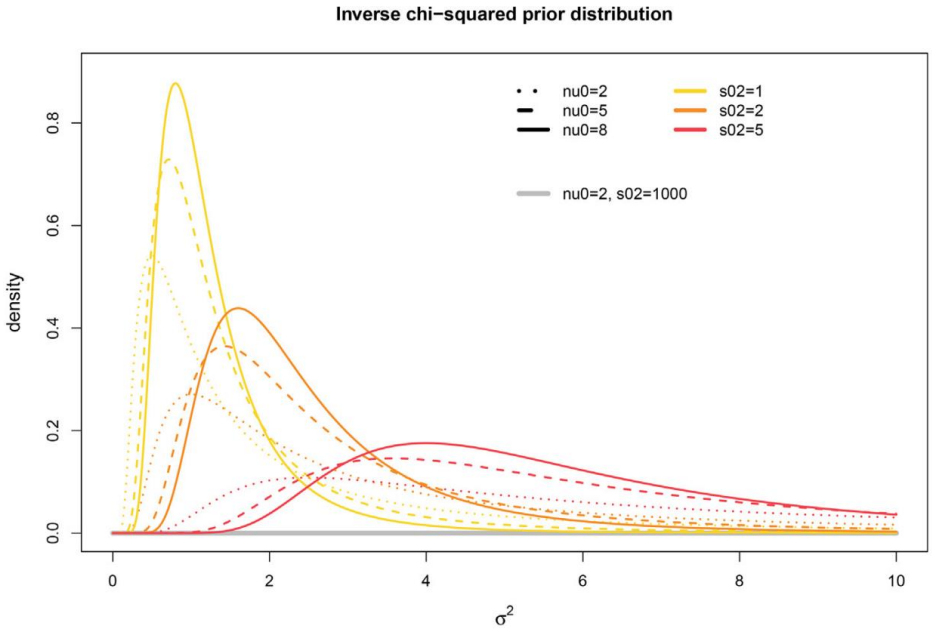

Figure 2 Plots of the density of the inverse chi-squared distribution with ν_0 degrees of freedom and scale parameter s_0^2 for various combinations of these values.

B) Metropolis-Hastings algorithm

Input: observations $(y_1, \ldots, y_N)$
Output: M samples from marginal posterior distribution $\pi(\theta|y,x)$
1: initialize: $\theta^{(1)}, \eta(x,\theta_1)$
2: compute $a = \ln(\pi(\theta^{(1)}) l_{int}(\theta^{(1)}|y,x))$
3: repeat
4: $l \leftarrow l+1$;
5: sample $\theta^{(c)} \sim N(\theta^{(l-1)}, \Sigma)$
6: compute $\eta^{(c)} = \eta(x,\theta^{(c)})$
7: compute $b = \ln(\pi(\theta^{(c)}) l_{int}(\theta^{(c)}|y,x))$
8: let $\alpha = \min(\exp(b-a), 1)$ and $u \sim Unif(0,1)$
9: if $\alpha \geq u$ then $\theta^{(l)} = \theta^{(c)}$
10: else $\theta^{(l)} = \theta^{(l-1)}$
11: $a \leftarrow b$
12: until $l = M$

Tutorial 10: Thermomechanical inversion

J.G. BAUZIN, M.N. NGUYEN, N. LARAQI

LTIE, Université Paris Nanterre, 92410 Ville d'Avray – France

E-mail: jbauzin@parisnanterre.fr
paulminhnhat.nguyen@gmail.com
nlaraqi@parisnanterre.fr

Abstract. The aim of this tutorial is to present an inverse thermomechanical methodology. By means of an analytical approach, we establish a thermoelastic mechanical transfer function between the temperature of a heated surface and the mechanical distortion of a solid at a given abscissa far from the surface. Subsequently, we measure the distortion at discrete time intervals using strain gauge and we apply a deconvolution product for those measurements to identify the temperature of the heated surface. By this way, it is no longer necessary to know the temperature field to solve the thermomechanical problem of our experimental device. We demonstrate that the inversion procedure can be applied successfully even in situations where the measured signal is affected by noise, through using the Tikhonov regularization method. Lastly, the surface temperature identified from the deformation measurements is compared to a temperature measurement.

List of acronyms:

- **NLPE**: Non-Linear Parameter Estimation
- **PEP**: Parameter Estimation Problem
- **SVD**: Singular Value Decomposition
- **IHCP** Inverse Heat conduction Problem
- **OLS**: Ordinary Least Squares

1.Introduction

In most mechanical experiments, we find that temperature plays a major role in the behavior of the system under study. Mechanical constraints, and thus, the displacements resulting from mechanical distortions, do depend on the temperature field present in the system. This is particularly relevant in the case of thermal surface treatment processes that are applied to manufactured objects.

In the context of heat transfer studies, the problem of estimating boundary conditions, such as the heat flux flowing thru the surface, or such as the temperature at the surface, have been the subject of many studies in the literature [1]–[3]. By reviewing the studies related to the IHCP problem, we observe that temperature measurements are being used in almost every case. Experimentally, it is found that determining the evolution of temperatures at certain points of the device is essential to solve the IHCP. Sensitivity analysis makes it possible to analyze and optimize the position of temperature sensors in order to ensure the feasibility of the resolution. However, some studies approach the thermomechanical inverse problem. Wang et al. [4]conducted an experiment to measure temperatures inside solid devices by means of thermocouples, and based on the obtained measurements, they performed a thermal inverse study by the Conjugate Gradient method. As indicated in many studies trying to solve the Inverse Problem [5], [6], sensitivity analysis shows that the location of the thermocouples should be as close as possible to the heated surface. Then, using the experimental data from Wang et al. [4], Chen and Wu [7] had proposed a hybrid technique based on Laplace Transform and on the Finite Difference method, to estimate the temperature of the laser-heated surface. Lee and Huang [8] developed an integral-transform-free methodology for one-dimensional IHCP with time-dependent boundary conditions to estimate the heat flux of the same problem. They approximated the unknown surface temperature using a fourth-degree polynomial function in order to reduce the number of unknowns of the IHCP.

So, it would be interesting to solve the IHCP from mechanical measurements only (displacement measurement) without requiring any temperature sensor. But this novel approach requires to solve a coupled thermoelastic problem. In the literature, only a few investigations [9]–[13] were able to predict the unknown boundary condition on the heated surface via using only displacement sensors. Blanc and Raynaud [10] solved the IHCP by using the thermal strain and temperature measurements instead of the temperature measurements only. Taler and Zborowski [11] used the discrete form of Duhamel's integral and future time steps, in order to control the thermal stress in elements of complex shapes. Chen et al. [12] applied a hybrid numerical algorithm of the Laplace transform technique, the finite-difference method with a sequential-in-time concept, and the least-squares scheme, so as to estimate the surface heat flux from the theory of dynamic thermal stresses. Recently, Tu [13] developed a strain gauge measurement method to measure the thermal strain and performed the thermal inverse analysis of the laser heating process. Bauzin et al proposed a thermoelastic mechanical and heat conduction study through inverse method and transfer functions [14].

Solving the inverse problem in heat transfer through transfer functions has been the subject of several works in the literature. Fernandes et al. [15] solve the IHCP (multidimensional problem) by identifying the analytical transfer function by means of Green's functions. Al Hadad et al. [16] performed an experimental transfer function identification for the thermal impedance and transmittance in a channel heated by an upstream unsteady volumetric heat source.

In this study, we develop a thermoelastic transfer function between the temperature of a heated surface and the mechanical distortion of a solid at a given abscissa far from the surface. This analytical model is validated by comparison with a numerical one. In a first hand, the identification of the linear coefficient of thermal expansion is performed from measurements of temperatures and mechanical distortion.

2. Analytical approach

2.1 Thermoelastic transfer function

To serve as a model for our study, we consider a thin cylinder with constant cross section, made of a material that is both homogeneous and isotropic (Fig. 1). The cylinder is heated on its surface at the point of abscissa $x=0$ and it is fixed at its other end, at $x = L$. We measure the displacement of the rod particles in a point located at abscissa x. In order to solve the thermoelastic problem associated to this model, we assume that no radial nor circumferential expansion occurs. Furthermore, we assume that the particles of the rod will undergo only slow motion, so that the cylinder behaves according to the longitudinal free vibration of a rod model. The large length-to-diameter ratio of the cylinder will be taken into account to ensure the one-dimensional nature of the thermoelastic problem. Under those assumptions, and as it is presented by Tu in [13], the equation for the displacement $u(x,t)$ could be written as follows [14], [17]:

$$\frac{\partial^2 u}{\partial x^2}-\frac{1}{c_0^2}\frac{\partial^2 u}{\partial t^2}=k_0\frac{\partial T}{\partial x},\ 0<x<L,\ t>0 \tag{1}$$

where the parameters k_0 and c_0 are defined as

$$k_0=\frac{1+\nu}{1-\nu}\alpha_t,\ c_0=\sqrt{2G(1-\nu)/\left[\rho(1-2\nu)\right]} \tag{2}$$

In addition, the relationship between the stress $\sigma(x,t)$, the displacement $u(x,t)$, and the temperature $T(x,t)$ can be generated from the one-dimensional Duhamel-Neumann equation in terms of the shear modulus G, the Poisson's ratio ν, and the linear coefficient of thermal expansion α_t as:

$$\sigma(x,t)=\frac{2G}{1-2\nu}\left[(1-\nu)\frac{\partial u(x,t)}{\partial x}-\alpha_t(1+\nu)T(x,t)\right] \tag{3}$$

Using the boundary condition $\sigma(0,t)=0$ on the heated surface, we can write:

$$\frac{\partial u(0,t)}{\partial x}=k_0T_0(t) \tag{4}$$

Because we assume a constant surrounding temperature T_{amb} in the experimental process, the temperature function $T(x,t)$ and $T_0(t)$ are defined as the rise of temperature above the ambient temperature T_{amb}. Moreover, the cylinder is fixed at the unheated end ($x=L$), the other boundary condition is:

$$u(L,t)=0 \tag{5}$$

The cylinder is initially at rest, the initial conditions are thus:

$$u(x,0)=0,\ \frac{\partial u(x,0)}{\partial t}=0 \tag{6}$$

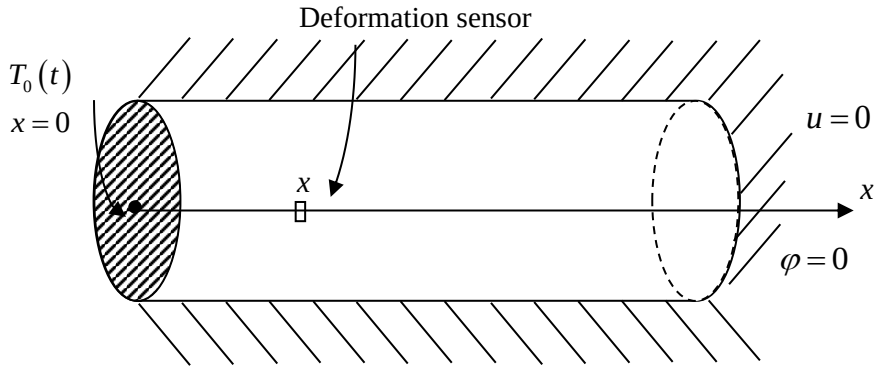

Figure 1 : *Schematic diagram of the problem with a displacement sensor*.

We recall that the Laplace transform of a function *f* is defined as follows:

$$\bar{F}(x)=L\{f(t,x)\}=\int_0^{\infty} f(t,x)e^{-pt}dt \tag{7}$$

Where: *L* is the Laplace operator, *p* the Laplace variable. The inverse Laplace transform, given by equation (8), can be used to obtain back function *f* from its Laplace-transformed form. In this study, in order to compute the inverse Laplace transform if the expression is not explicit, a numerical Euler procedure [18] is used.

$$f(x,t)=L^{-1}\left\{\bar{F}(x)\right\} \tag{8}$$

The Laplace transform is applied to the displacement: $\bar{U}=L\{u(x,t)\}$. The equations (1), (5) and (6) become:

$$\frac{\partial^2\bar{U}}{\partial x^2}-\frac{p^2}{c_0^2}\bar{U}=k_0\frac{\partial\bar{T}}{\partial x} \tag{9}$$

$$\bar{U}(L)=0;\left(\frac{\partial\bar{U}}{\partial x}\right)_{x=0}=k_0\bar{T}_0 \tag{10}$$

In order to take into account the heat, a time-dependent temperature function $T_0(t)$ is imposed on the surface ($x=0$) at the end of the cylinder (Eq. (10)). This function will be unknown and needs to be identified. Moreover, in order to solve the mechanical problem of the equation (9) , it is necessary to know the expression of the Laplace transform of the temperature $\bar{T}$ in the solid. The cylinder is insulated along the longitudinal direction, resulting in the surface of the unheated end to be considered as a zero temperature gradient. Furthermore, the large length-to-diameter ratio of the cylinder permits us to assume one-dimensional heat conduction. The governing partial differential equation, and the boundary and initial conditions of the heat conduction system are thus:

$$\frac{\partial^2 T}{\partial x^2}=\frac{1}{\alpha}\frac{\partial T}{\partial t},\ 0<x<L,\ t>0 \tag{11}$$

$$T(0,t)=T_0(t) \tag{12}$$

$$\frac{\partial T}{\partial x}=0,\ x=L,\ t>0 \tag{13}$$

$$T(x,0)=0,\ 0\le x\le L,\ t=0 \tag{14}$$

The Laplace transform is this time applied to the temperature variable, within equations (11)-(14) and the solution of this system of equations in the Laplace space can be written in the following form:

$$\bar{T}(x) = \frac{ch\left[q(L-x)\right]}{ch(qL)}\bar{T}_0 \tag{15}$$

with $q = \sqrt{\frac{p}{\alpha}}$, and for the heat flux:

$$\bar{\varphi}(x) = -\lambda q \frac{sh\left[q(L-x)\right]}{ch(qL)}\bar{T}_0 \tag{16}$$

By replacing the expression of the temperature in the transformed equations (9) and (10), it comes:

$$\frac{\partial^2 \bar{U}}{\partial x^2} - \frac{p^2}{c_0^2}\bar{U} = -k_0 q \frac{sh\left[q(L-x)\right]}{ch(qL)}\bar{T}_0 \tag{17}$$

$$\bar{U}(L) = 0\,; \left(\frac{\partial \bar{U}}{\partial x}\right)_{x=0} = k_0 \bar{T}_0 \tag{18}$$

For a fixed *x*, the relationship between the displacement and the temperature is written as:

$$\bar{U}(x) = \bar{G}_u(x) \cdot \bar{T}_0 \tag{19}$$

The thermomelastic transfer function $\bar{G}(x)$ is:

$$\bar{G}_u(x) = \frac{k_0}{q\left(1-\beta^2\right)}\left(\beta \frac{sh\left(\beta q(L-x)\right)}{ch(\beta qL)} - \frac{sh\left(q(L-x)\right)}{ch(qL)}\right) \tag{20}$$

With $\beta = \frac{\alpha q}{c_0}$

Similarly, it is possible to calculate the displacement at a given abscissa *x* in the solid from the knowledge of the temperature $\bar{T}(x) = L\{T(x,t)\}$ at this position by the following relation:

$$\bar{U}(x) = \bar{M}_u(x) \cdot \bar{T}(x) \tag{21}$$

with:

$$\bar{M}_u(x) = \frac{k_0}{q\left(1-\beta^2\right)}\left(\beta \frac{sh\left(\beta q(L-x)\right)}{ch(\beta qL)} - \frac{sh\left(q(L-x)\right)}{ch(qL)}\right)\frac{ch(qL)}{ch\left(q(L-x)\right)} \tag{22}$$

The inverse Laplace transform of the transfer function $\bar{G}(x)$ is the impulse response of the problem (equation (23)):

$$g(x,t) = L^{-1}\left\{\bar{G}_u(x)\right\} \tag{23}$$

The deformation ε is related to the displacement u by the following relation (in the Laplace space):

$$\bar{\varepsilon}(x,p) = \frac{\partial \bar{U}(x,p)}{\partial x} \tag{24}$$

So it comes by deriving the expression $\bar{U}(x)$ from with respect to x:

$$\bar{\varepsilon}(x,p)=\frac{k_0}{(1-\beta^2)}\left(\frac{ch(q(L-x))}{ch(qL)}-\beta^2\frac{ch(\beta q(L-x))}{ch(\beta qL)}\right)\cdot\bar{T}_0 \tag{25}$$

The transfer function for de distortion is:

$$\bar{G}(x,p)=\frac{k_0}{(1-\beta^2)}\left(\frac{ch(q(L-x))}{ch(qL)}-\beta^2\frac{ch(\beta q(L-x))}{ch(\beta qL)}\right)$$
$$\bar{\varepsilon}(x,p)=\bar{G}(x,p)\cdot\bar{T}_0 \tag{26}$$

In order to return into the temporal space and calculate the impulse response, a numerical inversion is used (Euler procedure [21]). Indeed, in this general case, the expression of $g(x,t)$ the inverse Laplace transformation $\bar{G}(x,p)$ is not explicit.

2.2 Simplification of the transfer function

If we neglect the vibratory part of the mechanical equation (β very small), it comes:

$$\bar{\varepsilon}(x,p)=k_0\left(\frac{ch(q(L-x))}{ch(qL)}\right)\cdot\bar{T}_0$$
$$\bar{\varepsilon}(x,p)=\bar{G}_s(x,p)\cdot\bar{T}_0 \tag{27}$$

With

$$\bar{G}_s(x,p)=k_0\left(\frac{ch(q(L-x))}{ch(qL)}\right) \tag{28}$$

By replacing hyperbolic cosines with their exponential expressions, the deformation is written:

$$\bar{\varepsilon}(x,p)=k_0\frac{e^{q(L-x)}+e^{-q(L-x)}}{e^{qL}+e^{-qL}}\bar{T}_0 \tag{29}$$

Either

$$\bar{\varepsilon}(x,p)=k_0\frac{e^{-qx}+e^{-q(2L-x)}}{1+e^{-2qL}}\bar{T}_0 \tag{30}$$

And the serial development of the exponential is written:

$$\frac{1}{1+e^{-2qL}}=\sum_{n=0}^{\infty}(-1)^n e^{-2nqL} \tag{31}$$

Which gives the expression of the Laplace transformation distortion :

$$\bar{\varepsilon}(x,p)=k_0\sum_{n=0}^{\infty}(-1)^n\left(e^{-q(2nL+x)}+e^{-q(2L(n+1)-x)}\right)\cdot\bar{T}_0 \tag{32}$$

The reverse Laplace transformation of e^{-qX} is known:

$$L^{-1}\left\{e^{-qX}\right\}=\frac{X}{2\sqrt{\pi\alpha t^3}}e^{\frac{-X^2}{4\alpha t}} \tag{33}$$

The explicit expression in this case simplified for the deformation is written:

$$\varepsilon(x,t)=k_0\sum_{n=0}^{\infty}(-1)^n\left(\frac{(2nL+x)}{2\sqrt{\pi\alpha t^3}}e^{\frac{-(2nL+x)^2}{4\alpha t}}+\frac{(2L(n+1)-x)}{2\sqrt{\pi\alpha t^3}}e^{\frac{-(2L(n+1)-x)^2}{4\alpha t}}\right)*T_0(t) \quad (34)$$

The simplified impulse response is:

$$g_s(x,t)=k_0\sum_{n=0}^{\infty}(-1)^n\left(\frac{(2nL+x)}{2\sqrt{\pi\alpha t^3}}e^{\frac{-(2nL+x)^2}{4\alpha t}}+\frac{(2L(n+1)-x)}{2\sqrt{\pi\alpha t^3}}e^{\frac{-(2L(n+1)-x)^2}{4\alpha t}}\right) \quad (35)$$

For the rest of the study, the hypothesis that $g(x,t)=g_s(x,t)$ will be made.

2.3 Impulse response

The inverse Laplace transform of the transfer function $\bar{G}_S(x)$ is the impulse response of the problem (equation (35)). An example of the impulse response for the displacement is presented in **Figure 2**.on a Cartesian scale and on a semi logarithmic scale for different abscissae in the solid.

$$g(x,t)=L^{-1}\left\{\bar{G}(x)\right\} \quad (36)$$

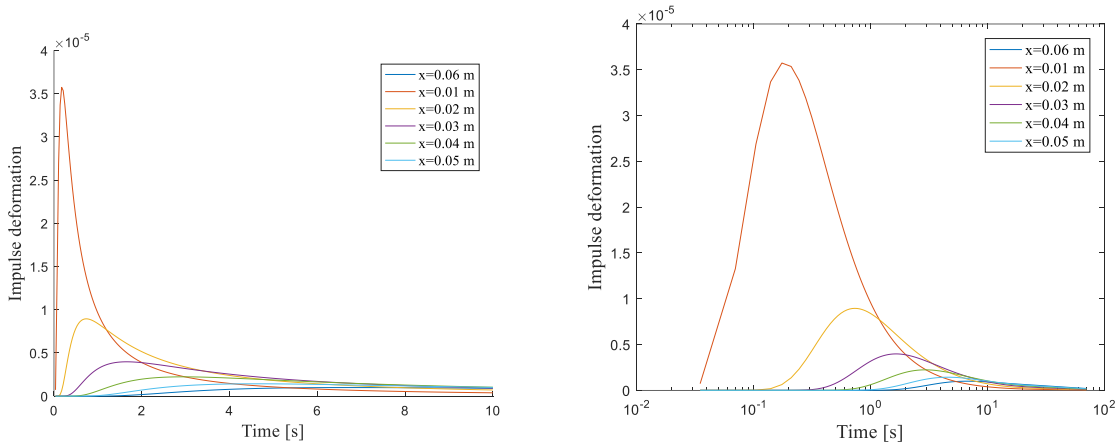

Figure 2 : *Impulse response for different positions x for AA1100***.**

These impulse responses are calculated with the thermo-physical properties of AA1100 aluminum alloy. The thermo-physical properties and material properties of the AA1100 aluminum alloy are:

$\rho=2710\,kg\cdot m^{-3}$, $\lambda=222W\cdot m^{-1}\cdot K^{-1}$, $C_p=904\,J\cdot kg^{-1}K^{-1}$, $G=2.69\cdot10^{10}N\cdot m^{-2}$, $\nu=0.3$, and $\alpha_t=23\cdot10^{-6}\mathrm{K}^{-1}$. The length *L* of the sample cylinder is 10 cm.

2.4 Response calculation of displacements by means of the convolution product

It is shown that the output could be calculated by the convolution product [16], [19], [20] between the input (excitation or cause) $T_0(t)$ and a corresponding thermoelastic transfer function $g(x,t)$ (impulse response of the system given by equation (23)):

$$\varepsilon(x,t) = g(x,t) * T_0(t) \tag{37}$$

where $*$ denotes the convolution product. For any input $T_0(t)$ the output $\varepsilon(x,t)$ is given by the convolution integral, as expressed in Eq. (38) represented in terms of Temperature (input) and deformation (response) [15]. Thus, we have:

$$\varepsilon(x,t) = \int_0^t g(x,t-\xi) T_0(\xi) d\xi \tag{38}$$

Parameterization of the excitation $T_0(t)$, over a base of piecewise constant functions defined on a constant time step Δt allows to exhibit a sampling $\varepsilon_k = \varepsilon(x,t_k)$ of the response. The convolution product can then be expressed in the following matrix form [16]:

$$\underline{\varepsilon} = \underline{\underline{C}}\,\underline{T} \tag{39}$$

where:

$$\underline{\varepsilon} = \begin{bmatrix} \varepsilon_1 \\ \varepsilon_2 \\ \vdots \\ \varepsilon_{N_{f-1}} \\ \varepsilon_{N_f} \end{bmatrix}, \quad \underline{\underline{C}} = \begin{bmatrix} g_1 & 0 & \cdots & \cdots & 0 \\ g_2 & g_1 & \ddots & & \vdots \\ \vdots & g_2 & \ddots & \ddots & \vdots \\ g_{N_{f-1}} & & \ddots & \ddots & 0 \\ g_{N_f} & g_{N_{f-1}} & \cdots & g_2 & g_1 \end{bmatrix}, \quad \underline{T} = \begin{bmatrix} T_1 \\ T_2 \\ \vdots \\ T_{N_{f-1}} \\ T_{N_f} \end{bmatrix} \tag{40}$$

with:

$$g_i = \int_{t_{i-1}}^{t_i} g(x,t) dt \tag{41}$$

$\underline{\underline{C}}$ is a square matrix of size $N_f \times N_f$ where each element g_i is given by equation (41) . It is important to note that equation (39) is valid, it is necessary that the time step be small enough with respect to the characteristic times of the input $T_0(t)$ and transfer function $g(x,t)$. In a first approach, the temporal discretization being sufficiently fine, the hypothesis of a linear variation on the time step Δt can be made and it comes:

$$g_i = \left(\frac{g(x,t_i) + g(x,t_{i-1})}{2} \right) (t_i - t_{i-1}) \tag{42}$$

2.5 Validation of the analytical solution with numerical simulations

The analytical solution developed is compared to a numerical solution computed by finite element software. The mesh resolution chosen is sufficiently fine to ensure that discretization has no significant impact on the results. The applied temperature $T_0(t)$ on the surface in $x = 0\ m$ is a door function (**Figure 3**). The temporal deformation calculated by a numerical method (finite elements) is compared in **Figure 3** to the deformation values resulting from our analytical approach using the convolution product presented previously.

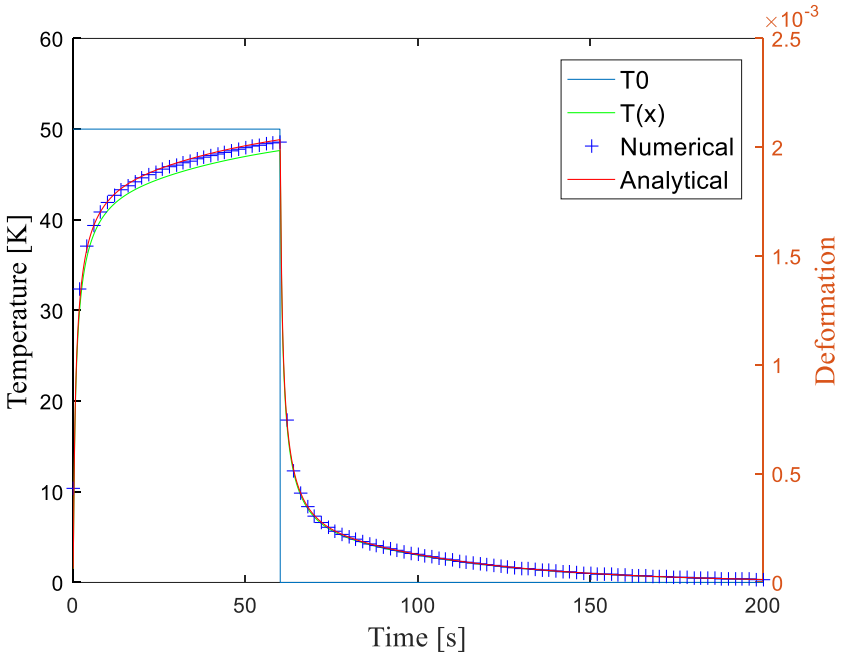

Figure 3 : *Input surface temperature and comparison of the numerical solution (FEM) with analytical method for the deformation in* $x = 0.01m$

It can be seen that the analytical solution and the numerical solution give very similar results. The analytical approach is thus validated. Consequently, the proposed analytical approach can also be used in a reverse approach to identify the surface temperature from the measurement of deformation.

2. Experimental device

The experimental setup consists of a steel bar, heated at its end by a heating element. On the other side, the bar is fixed in a clamp, the displacement is zero. Temperature measurement is performed (in) different positions by type K thermocouples directly welded to the material (**Figure 4** (a)). A strain gauge is fixed to the bar to measure the deformation (**Figure 4** (a)). The positions of the sensors are measured by image analysis. The solid is isolated to be placed in similar conditions (in) the model presented (**Figure 4** (b)).

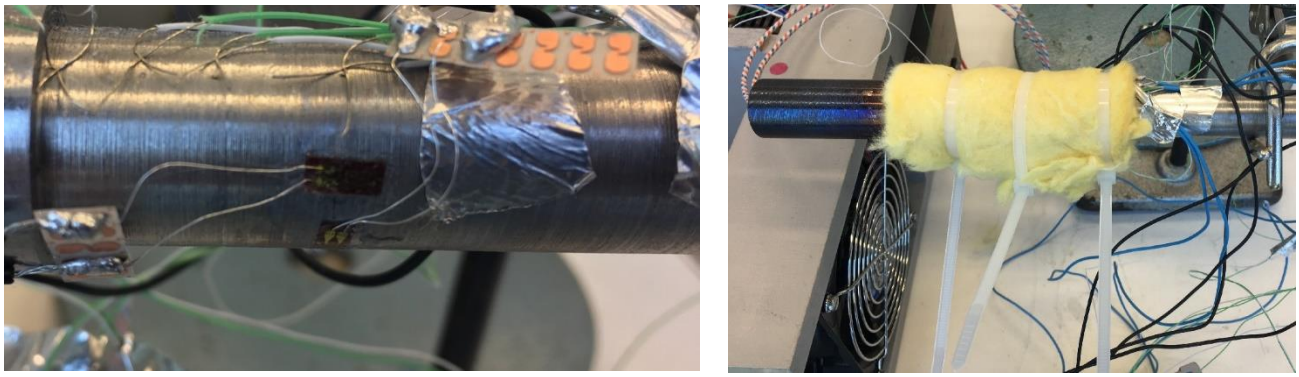

(a) *(b)*

Figure 4 : *Experimental device*

The temperature of the strain gauge is closed to the sample one. Then, the sensor also expands according to the temperature evolution. Therefore, the measurement represents the differential of deformation between the sensor and the solid:

$$\varepsilon_{mes} = \varepsilon_{steel} - \varepsilon_{sensor} \quad \textbf{(43)}$$

Taking a relative expansion coefficient in the analytical model, we represent the experimental measurements:

$$\alpha_{T\,mes} = \alpha_{T\,steel} - \alpha_{T\,sensor} \quad \textbf{(44)}$$

If the expansion coefficient of the steel of the bar is lower than that of the strain gauge coefficient, then a negative deformation will be measured (the gauge being in compression). The thermal properties of the steel are: $\rho = 8000\,kg\cdot m^{-3}$, $\lambda = 41.7 W\cdot m^{-1}\cdot K^{-1}$, $C_p = 474.6\,J\cdot kg^{-1}K^{-1}$. The expansion coefficient of the sensor is given by the manufacturer and is $\alpha_{T\,sensor} = 11.7\cdot 10^{-6}\ K^{-1}$.

Examples of measurements for the temperatures and the deformation are presented in **Figure 5**. The positions of the strain gauge from the imposed temperature position is *17.83mm.* The temperature evolutions are defined as the rise of temperature, above the ambient temperature (or initial temperature).

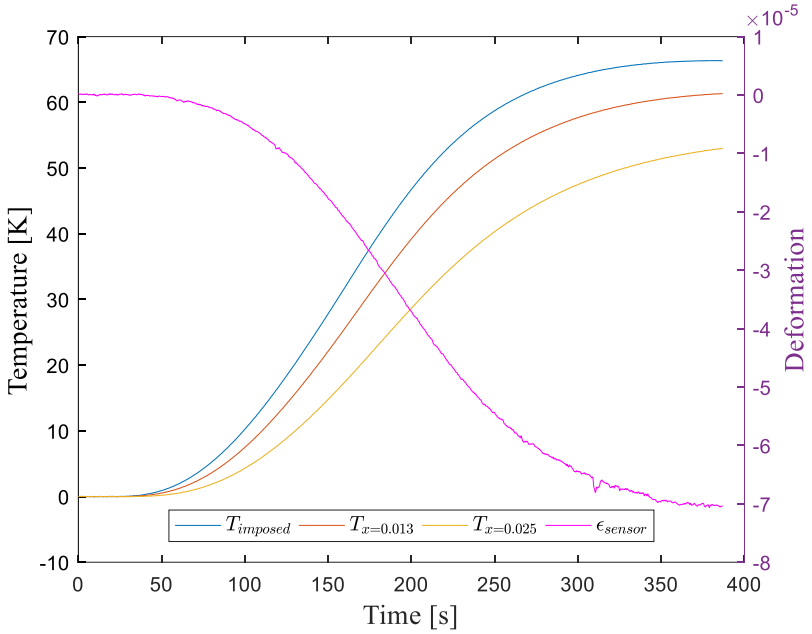

Figure 5 : *Experimental measurements (temperature and deformation).*

The linear coefficient of thermal expansion will be estimated in part 3. The experimental bench and the analytical model do not take into account the same radial mechanical boundary conditions. Then, the Poisson's ratio is fixed to zero. in this case, the deformations of the analytical model (taking into account an imposed zero radial displacement) and the deformations calculated by a numerical model with free radial displacement are similar (**Figure 6**)

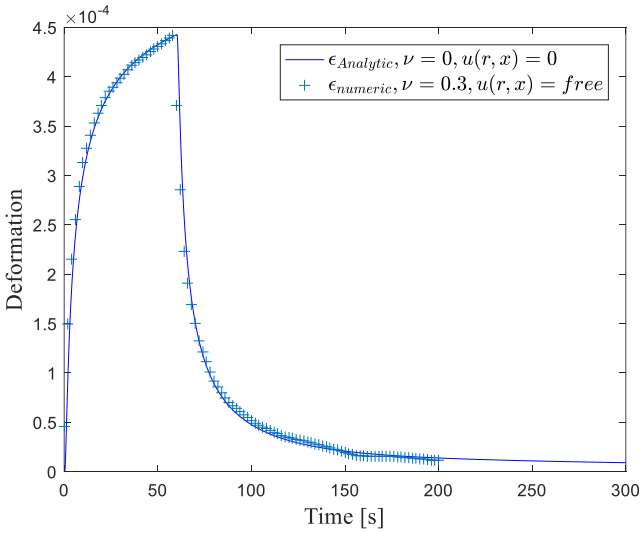

Figure 6 : *Comparison of the deformation between the analytical solution (imposed radial displacement and a numerical solution (with representative experimental boundary condition).*

3. Identification of the linear coefficient of thermal expansion

In order to identify the linear coefficient of thermal expansion α_T (**PEP)**, we use a method of minimisation criterion (**OLS**) which is represented by the functional F_N , such:

$$F_N = \sum_{j=1}^{j=N} \left(\varepsilon_j - \varepsilon_j \right)^2 \tag{45}$$

For each time step *j* (i.e. time t_j), the calculated temperature ε_j by the direct model is compared to the measured temperature ε_j . The minimization procedure of F_N with respect to the unknown linear coefficient of thermal expansion consists to solve the equation:

$$\sum_{j=1}^{j=N} \frac{\partial \varepsilon_j}{\partial \alpha_T} \left(\varepsilon_j - \varepsilon_j \right) = 0 \tag{46}$$

The system is non-linear (**NLPE**) but does not pose any problem of resolution. It is solved by an algorithm of Levenberg Marquardt [21], [22]. The identified value is $\hat{\alpha}_{T\,mes} = -7.58 \cdot 10^{-7}\ K^{-1}$. Then the estimated value of the material is $\alpha_{T\,steel} = 10.94 \cdot 10^{-6}\ K^{-1}$ which is in agreement with the values that can be found in the literature. The comparison of the strain gauge measurement and the calculated deformation with the identified value is presented in Figure 7.

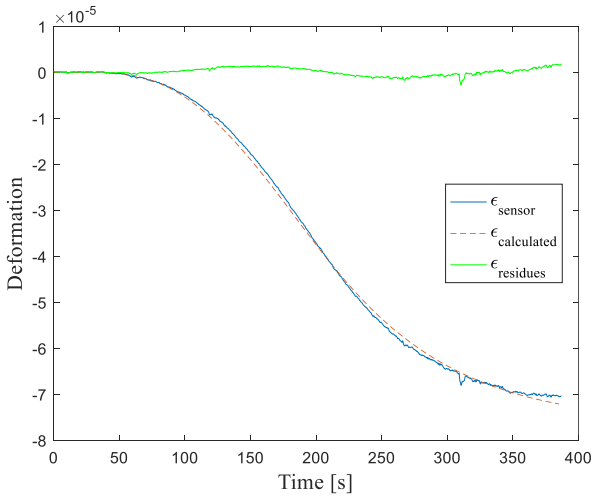

Figure 7 : *Measurement, calculation with the identified α_T and residues of the deformation*

4. Identification of the surface temperature from deformation

4.1 Identification Procedure

For any dynamic system, the relation between input and output in the complex variable *p* domain is given by the multiplication expressed in Eq. (19) or in the time domain by the convolution (Eq. (37)). Thus, in terms of the temperature/deformation we can write the deconvolution product:

$$T_0(t) = \frac{1}{g(x,t)} * \varepsilon(x,t) \tag{47}$$

Therefore, observing Eq.(47), it results that an inversion occurred between the input/output pair. The solution of this problem is the surface temperature $T_0(t)$, the input being the deformation. The new transfer function of this system is $1/g(x,t)$. By discretizing the linear problem on a constant time step Δt, according to equation (8) the matrix system becomes:

$$\underline{\hat{T}} = \underline{\underline{C}}^{-1}\underline{\varepsilon} \tag{48}$$

In order to invert the system, a singular value decomposition of the matrix $\underline{\underline{C}}$ is carried out:

$$\underline{\underline{C}} = \underline{\underline{U}}\,\underline{\underline{D}}\,\underline{\underline{V}}^T \tag{49}$$

with:

$$\begin{gathered}\underline{\underline{U}}^T\underline{\underline{U}} = \underline{\underline{U}}\,\underline{\underline{U}}^T = \underline{\underline{V}}\,\underline{\underline{V}}^T = \underline{\underline{V}}^T\underline{\underline{V}} = \underline{\underline{I}}_{Nf} \\ \underline{\underline{D}} = diag\left(D_1, D_2, \ldots, D_{Nf}\right) \text{ where } D_1 \geq D_2 \geq \ldots \geq D_{Nf}\end{gathered} \tag{50}$$

Equation (48) is then written in the following form:

$$\underline{\hat{T}} = \underline{\underline{V}} \cdot \underline{\underline{D}}^{-1}\underline{\underline{U}}^T\underline{u} \tag{51}$$

with:

$$\underline{\underline{D}}^{-1} = diag\left(D_1^{-1}, D_2^{-1}, \ldots, D_{Nf}^{-1}\right) \tag{52}$$

According to equation (47), it is then possible to calculate the temporal evolution of the surface temperature $T_0(t)$ (which we will name "identified surface temperature" in the sequel of this

article) from the knowledge of the deformation at a certain depth and the thermomechanical characteristics of the material. This identification of the surface temperature from the deformation data will be validated on experimental case.

4.2 Sensitivity analysis to the known parameters

It is important to present how the performance of the reconstruction of the surface temperature can be biased when some confidence bounds of the parameters are considered. The length of the cylinder *L* has no impact on the deformation calculation until the heat front has reached the end of the specimen. Similarly, an error in this parameter would have very little impact on the result. For the configuration presented and for the numerical values used in this study, the shear modulus does not affect significantly the calculation on the deformation. For the other physical parameters, **Figure 8** presents the error made on the identification of the surface temperature with regard to the error made on each parameter (α_T, ν, α). The calculation is performed from perfect deformation data, without noise.

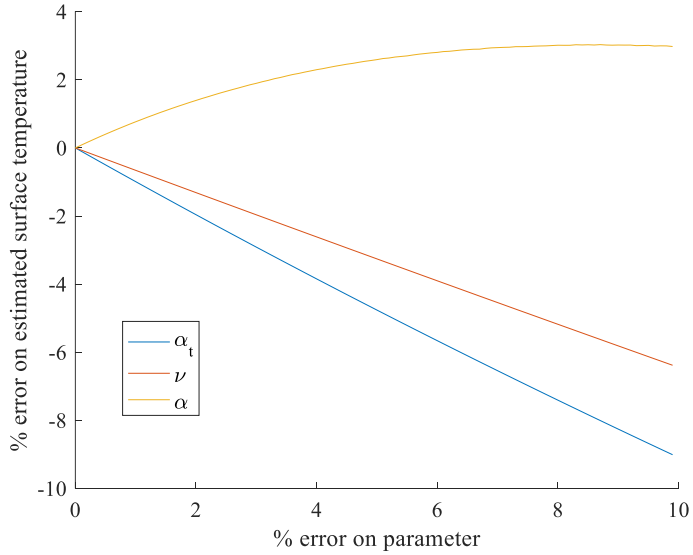

Figure 8 : *Impact of the error of the known parameters on the estimation of the surface temperature.*

The imposed surface temperature is constant T_0. The error on the estimated temperature is $\left(\hat{T}_0 - T_0\right)/T_0$. It can be seen that the sensitivities of the model to the thermal and mechanical characteristics are in the same order of magnitude. The calculation has been performed with the numerical values given in section 2.3. Thus, from the knowledge of the accuracy of the thermomechanical characteristics, it is possible to predict the error made in the estimation of the surface temperature. We can notice that if the characteristics are perfectly known, we find perfectly the input temperature. In addition, identification from a noised data representative of a real measurements cannot be carried out without regularization of the problem (cf. part 4.3)

4.3 Regularized identification of the surface temperature

So far, we have achieved that the estimation procedure using the deconvolution product can be used without prior knowledge of the form of the surface temperature function. In the previous examples, the signals being used were interpolated curves (i.e. signal was not affected by noise). However, the use of a noisy deformation signal in the procedure causes instability in the inversion of the system of equations (51). It is therefore essential to regularize the procedure. Indeed, the matrix to be inverted is ill-conditioned: the ratio of the largest to the smallest singular value is large. In the literature two techniques are proposed to treat this undesirable situation: either by filtering the noise or by regularizing the matrix to be inverted, so as to make it well-conditioned [23]. It is usually preferable to use the matrix regularization approach. Hence, in this work, we will regularize the matrix to be inverted, in order to get a stable identification. We present in this study the Tikhonov regularization method [24], [25].

The estimation of parameters is performed by minimizing the square of the norm of the difference between measured and calculated deformations. The functional $F(\underline{T})$ of the least-squares method is given by the following equation:

$$F(\underline{T}) = \left\| \underline{\underline{C}}\,\underline{T} - \underline{u}_{mes} \right\|^2 + \mu \left\| \underline{T} \right\|^2 \qquad \textbf{(53)}$$

Where μ is the Tikhonov regularization parameter which varies from 0 to ∞. If $\mu = 0$, this corresponds to the case without regularization. The Tikhonov estimate can be given an inverse SVD-like form:

$$\underline{\hat{T}}_{\mu} = \underline{\underline{V}} \cdot \underline{\underline{D}}_{\mu}^{-1} \underline{\underline{U}}^{T} \underline{u} \qquad \textbf{(54)}$$

with :

$$\underline{\underline{D}}_{\mu}^{-1} = diag\left(\frac{D_1}{D_1^{\,2} + \mu^2}, \frac{D_2}{D_2^{\,2} + \mu^2}, \ldots, \frac{D_{Nf}}{D_{Nf}^{\,2} + \mu^2} \right) \qquad \textbf{(55)}$$

The choice of the regularization parameter is important. If the standard deviation of the measurement noise σ_m is known, the optimal hyper-parameter (μ_{DP}) value can be found by Morozov's discrepancy principle. The regularization hyper-parameter value can be set according to Morozov's discrepancy principle as the value which proscribes the inversion process to go beyond a minimization making residuals lower than the measurement noise [23]. This can be expressed as:

$$RMSR \geq \sigma_m$$
$$RMSR = \sqrt{\frac{\sum_{i=1}^{i=N_f} \left(u_i^{rec} - u_i \right)^2}{N_f - 1}} \qquad \textbf{(56)}$$

RMSR is the Root Mean Square Residual, σ_m is the standard deviation of the noise and u_i^{rec} the deformation signal recalculated using estimation approach. In the rest of this study, we will take the numerical cases studied previously by noisily randomizing the data.

4.4 Numerical case

The deformation is simulated from the door temperature imposed on the surface. The data are now corrupted by noise, such as $\varepsilon(t)=\varepsilon(t)^{exact}+e$. e is a uniformly distributed random number with $-e_{\max}\le e\le e_{\max}$. The standard deviation is $\sigma_{\mathrm{m}}=1.116\cdot10^{-7}\,m$, which is representative of the experimental noise. **Figure 9** shows this randomly noisy deformation that will be used for the identification of the door function of temperature that has been imposed in part 2.5.

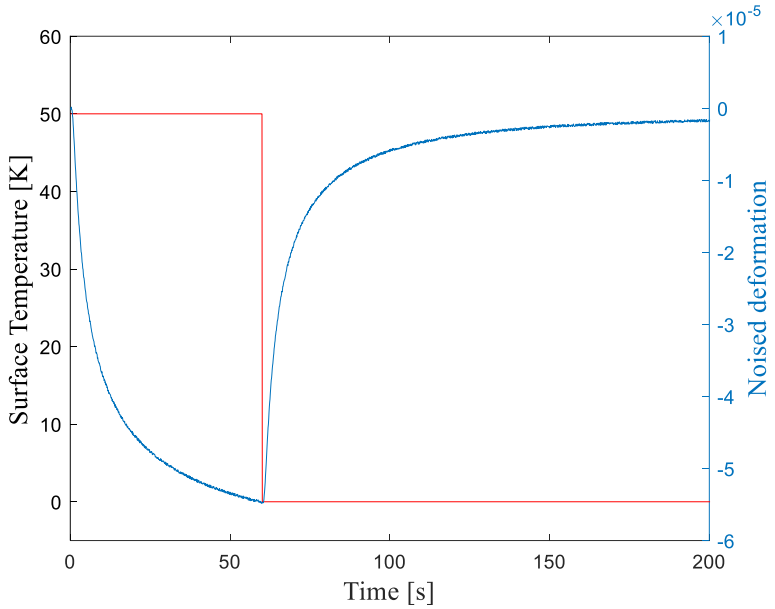

Figure 9 : *Noised relative deformation in* $x=0.01m$.

If the inversion procedure based on a deconvolution product is not regularized, then we obtain an unstable, divergent system. A Tikhonov regularization is applied. Figure 10 presents the evolution of RMSR as a function of the hyper-parameter. The equality $RMSR=\sigma_m$ is calculated by using the function *fsolve* in Matlab. The optimum hyper-parameter for the inversion procedure is $\mu_{optim}=3.8782\cdot10^{-8}$.

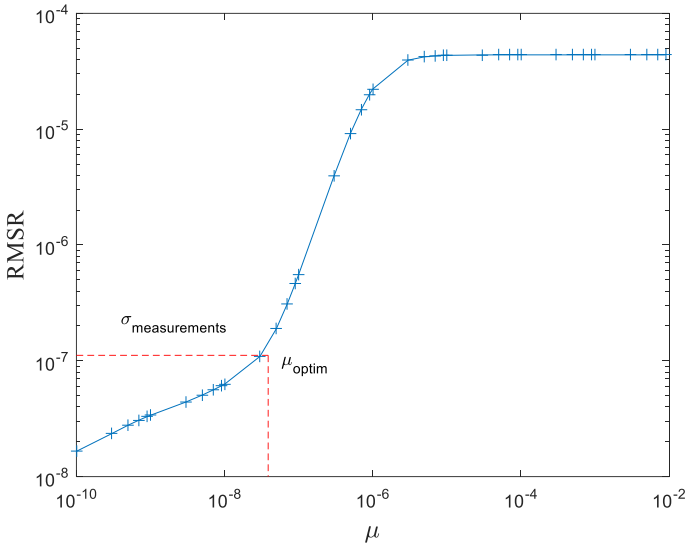

Figure 10 : *RMSR for Tikhonov surface temperature estimation.*

Then, the result of the identification of the surface temperature is presented in **Figure 11** for three values of Tikhonov regularization parameter (μ_{optim}, $\mu_{optim}/2$, $2\mu_{optim}$). We thus visualize the sensitivity of the estimates with respect to some deviations in the regularization parameter value from the Morozov principle. It is noted that the temperature identified is representative of the temperature entered in the model.

We find that the standard deviation of the residues is the standard deviation of the added noise to the deformation. The identification performed is therefore coherent. The inversion procedure is thus validated by the residuals recalculated after identification.

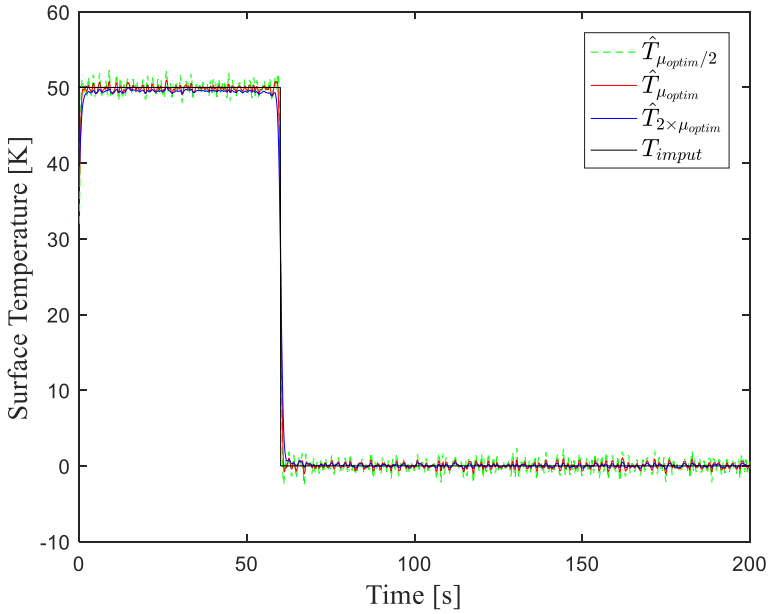

Figure 11 : *Comparison of the input surface temperature and the identified surface temperature using noised deformation for different* Tikhonov regularization parameter.

4.5 Experimental Results

The experimental measurements of the strain gauge are used to identify the real imposed temperature (which is measured to verify the inversion) (**Figure 5**). Then, the result of the identification of the surface temperature is presented in **Figure 12** for three values of Tikhonov regularization parameter (μ_{optim}, $\mu_{optim}/2$, $2\mu_{optim}$). We thus visualize the sensitivity of the estimates with respect to some deviations in the regularization parameter value from the Morozov principle. It is noted that the temperature identified is representative of the temperature entered in the model.
Then, it is thus possible to reconstruct the temperature signal applied to the surface. The residues on the deformation ($\sigma_{residues} = 1.31 \cdot 10^{-7}\, m$) (**Figure 13**) are in agreement with the noise measured on the experimental setup ($\sigma_{\mathrm{m}} = 1.116 \cdot 10^{-7}\, m$).

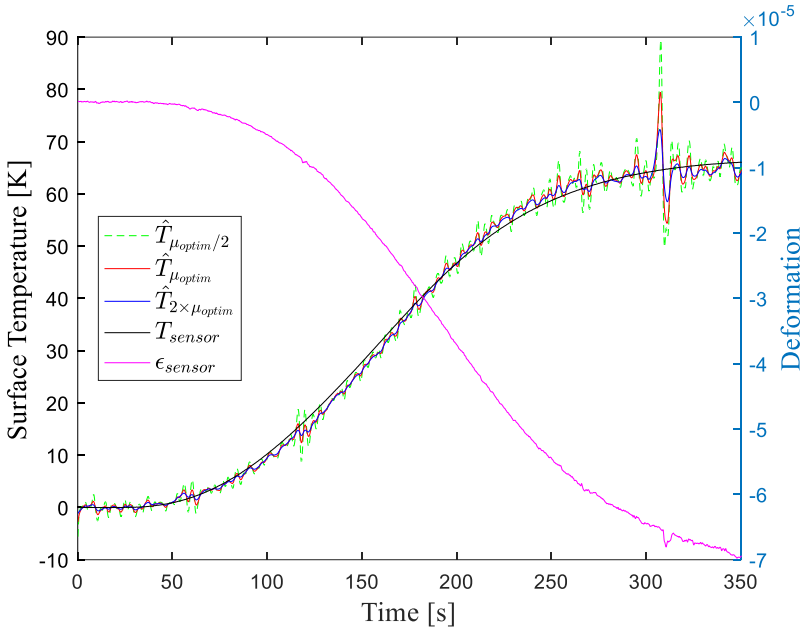

Figure 12 : *Comparison of the real input surface temperature and the identified surface temperature using gauge strain measurements for different Tikhonov regularization parameter.*

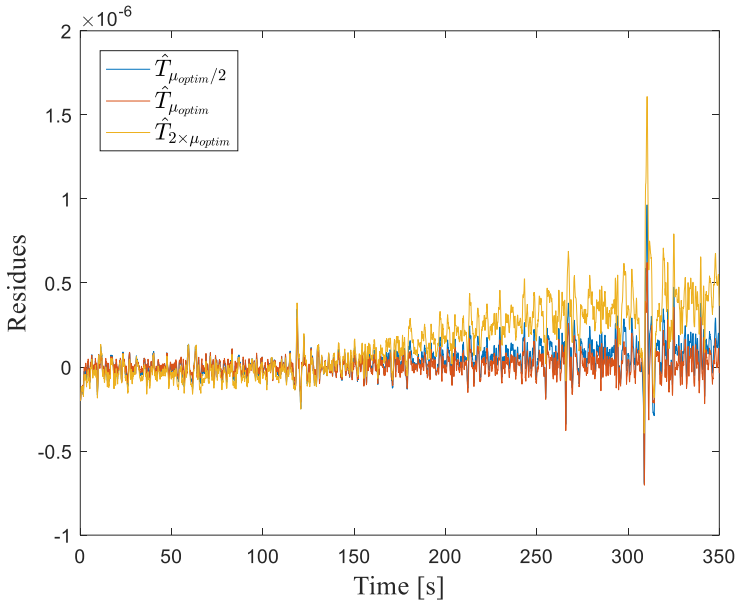

Figure 13 : *Residues for different Tikhonov regularization parameter.*

5. Conclusion

This work proposes an inverse methodology to define the temperature evolution of a heated surface through the deformation measurements. The approach presented is based on mechanical and thermal equations, applied to the measurement of deformation resulting from mechanical distortions due to heating. Indeed, no temperature measurement is required. The inversion procedure developed in this work is based on the convolution product of the impulse response of the thermoelastic problem, by the deformation signal. This work provides a novel approach that is easy to use. An inverse identification method for the linear coefficient of thermal expansion is presented. The results obtained from experimental measurements are consistent. In addition, our procedure enables identification of the evolution governing the temperature on the surface of a heated solid, whatever the form of the temperature function.

References

[1] J. V. Beck, B. Blackwell, and C. R. S. C. Jr, *Inverse Heat Conduction: Ill-Posed Problems*. James Beck, 1985.
[2] O. M. Alifanov, E. A. Artiukhin, and S. V. Rumiantsev, *Extreme Methods for Solving Ill-Posed Problems With Applications to Inverse Heat Transfer Problems*. New York: Begell House, 1995.
[3] M. N. Ozisik, *Inverse Heat Transfer: Fundamentals and Applications*. CRC Press, 2000.
[4] J.-T. Wang, C.-I. Weng, J.-G. Chang, and C.-C. Hwang, "The influence of temperature and surface conditions on surface absorptivity in laser surface treatment," *J. Appl. Phys.*, vol. 87, no. 7, pp. 3245–3253, Mar. 2000.
[5] D. Maillet and D. Petit, "Techniques inverses et estimation de paramètres. Partie 1," *Tech. Ing. Phys. Stat. Mathématique*, vol. base documentaire : 42619210., no. ref. article : af4515, 2008.

[6] D. Maillet, T. Metzger, and S. Didierjean, "Integrating the Error in the Independent Variable for Optimal Parameter Estimation Part I: Different Estimation Strategies on Academic Cases," *Inverse Probl. Sci. Eng.*, vol. 11, no. 3, pp. 175–186, Jun. 2003.
[7] H.-T. Chen and X.-Y. Wu, "Estimation of surface absorptivity in laser surface heating process with experimental data," *J. Phys. Appl. Phys.*, vol. 39, no. 6, p. 1141, 2006.
[8] S.-Y. Lee and T.-W. Huang, "A method for inverse analysis of laser surface heating with experimental data," *Int. J. Heat Mass Transf.*, vol. 72, pp. 299–307, May 2014.
[9] K. Grysa, MichałJ. Ciałkowski, and H. Kamiński, "An inverse temperature field problem of the theory of thermal stresses," *Nucl. Eng. Des.*, vol. 64, no. 2, pp. 169–184, Apr. 1981.
[10] G. Blanc and M. Raynaud, "Solution of the Inverse Heat Conduction Problem From Thermal Strain Measurements," *J. Heat Transf.*, vol. 118, no. 4, p. 842, 1996.
[11] J. Taler and M. Zborowski, "Solution of the Inverse Problems in Heat Transfer and Thermal Stress Analysis," *J. Therm. Stress.*, vol. 21, no. 5, pp. 563–579, Jul. 1998.
[12] H.-T. Chen, X.-Y. Wu, and Y.-S. Hsiao, "Estimation of surface condition from the theory of dynamic thermal stresses," *Int. J. Therm. Sci.*, vol. 43, no. 1, pp. 95–104, Jan. 2004.
[13] T. W. Tu, "Inverse analysis of laser surface heating from thermal strain measurements," *Int. J. Heat Mass Transf.*, vol. 116, pp. 1213–1224, Jan. 2018.
[14] J.-G. Bauzin, M.-N. Nguyen, N. Laraqi, A. Vaca Hernández, and A. Dehmani, "Thermoelastic mechanical and heat conduction study through inverse method and transfer functions," *Int. J. Heat Mass Transf.*, vol. 135, pp. 1260–1268, Jun. 2019.
[15] A. P. Fernandes, M. B. dos Santos, and G. Guimarães, "An analytical transfer function method to solve inverse heat conduction problems," *Appl. Math. Model.*, vol. 39, no. 22, pp. 6897–6914, Nov. 2015.
[16] W. Al Hadad, D. Maillet, and Y. Jannot, "Experimental transfer functions identification: Thermal impedance and transmittance in a channel heated by an upstream unsteady volumetric heat source," *Int. J. Heat Mass Transf.*, vol. 116, pp. 931–939, Jan. 2018.
[17] W. A. Day, *Heat Conduction Within Linear Thermoelasticity*. New York, NY: Springer New York, 1985.
[18] J. Abate and W. Whitt, "A Unified Framework for Numerically Inverting Laplace Transforms," *Inf. J. Comput.*, vol. 18, no. 4, pp. 408–421, Nov. 2006.
[19] K. B. Howell, *Principles of Fourier Analysis*. CRC Press, 2001.
[20] J. Peyrière, *Convolution, séries et intégrales de Fourier*. Ellipses, 2012.
[21] K. Levenberg, "A method for the solution of certain non-linear problems in least squares," *Q. Appl. Math.*, vol. 2, no. 2, pp. 164–168, Jul. 1944.
[22] D. W. Marquardt, "An Algorithm for Least-Squares Estimation of Nonlinear Parameters," *J. Soc. Ind. Appl. Math.*, vol. 11, no. 2, pp. 431–441, Jun. 1963.
[23] R. C. Aster, B. Borchers, and C. H. Thurber, *Parameter Estimation and Inverse Problems*. Academic Press, 2011.
[24] A. N. Tikhonov and V. I. Arsenin, *Solutions of ill-posed problems*. Washington; New York: Winston ; Distributed solely by Halsted Press, 1977.
[25] A. N. Tikhonov, A. Goncharsky, V. V. Stepanov, and A. G. Yagola, *Numerical Methods for the Solution of Ill-Posed Problems*. Springer Science & Business Media, 2013.

Tutorial 11:

Thermal imaging in semi-transparent media

S. Chevalier[1,2], **C. Bourgès**[1,2], **J. Maire**[1,2], **A. Sommier**[1,2], **C. Pradère**[3], **S. Dilhaire**[4]

1. ENSAM, CNRS, Bordeaux INP, I2M, UMR 5295, F-33400 Talence, France
2. Univ. Bordeaux, CNRS, Bordeaux INP, I2M, UMR 5295, F-33400, Talence, France
3. EPSILON-ALCEN, F-33400 Talence, France
4. Univ. Bordeaux, CNRS, LOMA, UMR 5798, F-33400 Talence, France

E-mail: stephane.chevalier@u-bordeaux.fr
coline.bourges@u-bordeaux.fr
jeremie.maire@u-bordeaux.fr

Abstract. Modulated thermotransmittance infrared imaging is a non-destructive method for measuring thermal properties and temperature fields in semi-transparent media. It differs from IR thermography as it does not require knowledge of the material's emissivity and can achieve spatial resolutions down to 10 µm/px. Through this experimental tutorial, we propose to measure the heat diffusivity and the thermal field in a glass wafer. After a brief description of the setup and the demodulation technique, the analytical model of the temperature will be derived and used in an inverse method to measure the borofloat thermal diffusivity.

Scope

1 Introduction **3**

2 Thermotransmittance working principle and modeling **4**

3 Modulated thermotransmittance imaging experimental setup **5**

4 Double-demodulation method applied on images **8**
4.1 Proper emission subtraction: the two-image method 8
4.2 Demodulation of the transmitted signal 9

5 Heat transfer modeling of a thin wafer in cylindrical coordinates **10**
5.1 Solving the heat transfer equation 10

6 Inverse methods **12**
6.1 Minimization and objective function 12
6.2 Standard deviation 13

7 Measurements **13**
7.1 Experimental setting 13
7.2 Image processing 13
7.3 Results 14

8 Conclusions **16**

1 Introduction

In this tutorial work, the semitransparent materials under study are non-scattering at their surface as their roughness is much lower than the illumination wavelength $\lambda \in [2-6]$ µm, and the reflectance at their surface is considered specular. All our samples are double-side polished to remain in this working hypothesis. In addition, we use homogeneous materials, whose scattering in the volume is negligible compared to the absorbance. We develop the experiment mainly using a double-side polished glass wafer. In addition, these materials can reflect or absorb a part of the incident light, as shown in Figure 1.

We present some contactless methods to measure temperature of semitransparent materials, without coating them. First, we introduce the IRT applied to semitransparent media and the associated issue to measure the temperature field. Second, we detail the principle of thermo-transmittance.

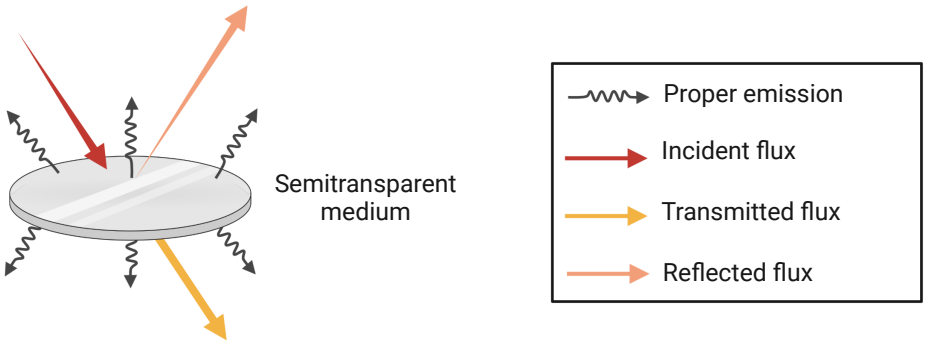

Figure 1: IR radiations interactions with a semitransparent medium.

IRT applied to semitransparent materials

Measuring temperature in semitransparent media using IRT is much more challenging than in opaque ones. The proper emission comes from the two material surfaces, but also from its volume. The emissivity is no longer defined for these materials: one uses the apparent emissivity [1] or emittance [2]. In addition, it is essential to consider the radiations from the environment, which are reflected, absorbed, and transmitted through the material [3].

Because of these challenges, IRT in semitransparent media is not yet widely used, although several groups are interested in it and develop specific calibration processes. For instance, some works measured the emittance, such as [3, 4, 5, 6], but the definition may vary from one study to another, and not always take into account the direction of radiations. Other works focused on thermal properties measurements of these materials, such as the thermal diffusivity [7]. In this thesis work, we propose an alternative method that does not require the knowledge of the emittance of the medium and allows to discriminate the signal of interest from the radiation coming from the environment.

Thermotransmittance

We introduce the thermotransmittance phenomenon, by establishing the link between temperature dependence of the transmitted light in non-opaque materials [8]. As a consequence, to measure temperature using thermotransmittance, we need the proportionality factor: the

thermotransmittance coefficient κ (K^{-1}). Unfortunately, there is no database on the coefficient κ. This property is often measured but mostly in the visible or NIR range [9].

Preliminary studies reported promising results in calibrating the thermotransmittance coefficient for various materials across different spectral ranges, including mid-infrared [10] and terahertz [11]. Additionally, works demonstrated the temperature dependency of absorbance in water-ethanol mixtures within the near-infrared spectrum [12]. As the thermotransmittance signal is affected by both absorbance and reflectance variations (see section 2), it has potential applications for diverse semitransparent media, providing either a measurement of thermoreflectance, thermo-absorbance, or a combination of both. Finally, these studies showed that the thermal dependency of absorbance/transmittance varies with the illumination wavelength. As a result, it should be possible to differentiate several components of a semitransparent media depending on their thermotransmittance coefficient behavior as a function of the wavelength, provided the initial spectrum of each component is known.

However, the thermotransmittance coefficient in the mid-IR is usually weak, about 10^{-4} K^{-1}. Therefore, it is essential to heat the sample sufficiently and use sensitive detectors (in the work [10] $\Delta T = 120$ K and detector with a dynamic range of 2^{16}).

The objectives of this tutorial are as follows:

1. to measure the thermotransmittance in a semi-transparent media from an IR beam;
2. to estimate the heat diffusivity in the bulk of the semi-transparent media.

2 Thermotransmittance working principle and modeling

This section describes the working principle of thermotransmittance. First, the transmitted signal through a non-scattering media is detailed. Second, we introduce the thermal dependence of this signal and present the working hypotheses.

Transmittance of a semitransparent material

When a monochromatic incident flux Φ_0 illuminates a semitransparent material, a part of the flux is reflected at the material surface, and a part is transmitted through the sample [13] depending on the reflectance coefficient R_0, as illustrated in Figure 2. As it passes through the medium, the flux is attenuated by the attenuation coefficient α_0 (m^{-1}) within the thickness L_z (m) of the material. At ambient temperature, the transmitted flux is written $\Phi_\Gamma = \Phi_0 \Gamma_0$, with Γ_0 the transmittance of the material which is expressed in the following equation.

$$\Gamma_0 = [1 - R_0]^2 e^{-\int_0^{L_z} \alpha_0(z) dz} \tag{1}$$

Expression of the thermotransmittance

Since the optical properties of a material vary with temperature, we express the equation 1 as a function of temperature in the general case, where both surfaces of the sample are not necessarily at the same temperature.

$$\Gamma(T) = \underbrace{[1 - R(T_1)]}_{\text{Surface 1}} \underbrace{[1 - R(T_2)]}_{\text{Surface 2}} \underbrace{e^{-\int_0^{L_z} \alpha(z, T_z) dz}}_{\text{Volume}} \tag{2}$$

The thermal dependency of transmittance comes from both the reflectance and the attenuation coefficient. At the first order, their temperature variations are expressed in the equations 3

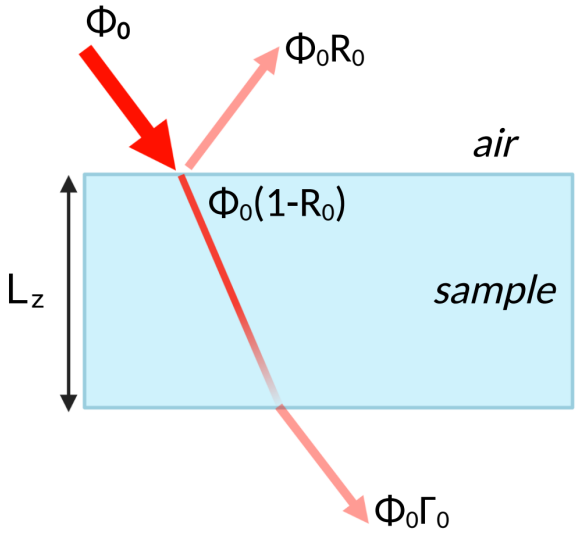

Figure 2: Illustration of a light beam path in a semitransparent medium.

and 4, with $\Delta T = T - T_0$ the temperature variation, κ_R the thermoreflectance coefficient (K^{-1}), and κ_α the thermo-absorbance coefficient (K^{-1}).

$$R(T) = R_0[1 + \kappa_R \Delta T] \tag{3}$$
$$\alpha(T) = \alpha_0[1 + \kappa_\alpha \Delta T] \tag{4}$$

By injecting 3 and 4 in the expression 2 and linearizing the exponential term, the thermo-transmittance relation at first order is given in the following expression.

$$\frac{\Delta\Gamma(T)}{\Gamma_0} \approx \underbrace{-\frac{R_0\kappa_R}{1-R_0}\left[\Delta T_1 + \Delta T_2\right]}_{\text{reflectance}} \underbrace{-\alpha_0\kappa_\alpha \int_0^{L_z} \Delta T(z)dz}_{\text{absorbance}} \tag{5}$$

As a result, the reflectance part gives information about the temperature variations at the surfaces of the sample, whereas the absorbance provides information on the temperature gradient through the thickness. In this tutorial we limit the study to uniform temperature along the material thickness ($\Delta T_1 = \Delta T_2 = \langle \Delta T \rangle_z = \Delta T$). The thermotransmittance has therefore a simple expression:

$$\frac{\Delta\Gamma(T)}{\Gamma_0} = \kappa \Delta T \tag{6}$$

κ is the thermotransmittance coefficient (K^{-1}) which contains both absorbance and reflectance thermal dependencies.

3 Modulated thermotransmittance imaging experimental setup

Figure 3 illustrates the experimental setup for modulated thermotransmittance imaging. The thermal modulation of the sample has great advantage to increase the signal to noise ratio by filtering the noise from images in order to detect the weak thermotransmittance signal.

In the experimental setup, we use the IR source, the mechanical chopper for modulating the source, the annular Peltier module for heating the sample, and an infrared camera as detector. The double-demodulation is post-processed, and the operations are detailed in section 4.

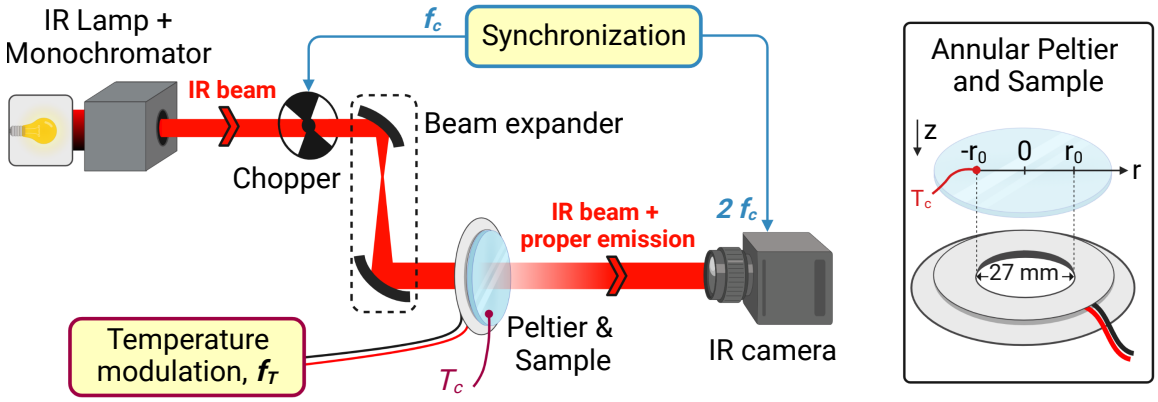

Figure 3: Experimental setup for modulated thermotransmittance imaging measurement. The insert illustrates the Peltier module with its dimensions.

Heating of the sample

The sample is heated using a ring-shaped Peltier module. The temperature at the edges of the wafer is modulated at $T(t) = T_0 + \Delta T \cos(2\pi f_T t)$, with $T_0 \sim 20°C$, $\Delta T \sim 10°C$. We will choose the modulation frequency f_T in the order of tens mHz for Borofloat wafer.

Infrared camera properties

We use an infrared camera as detector (FLIR SC7000). The camera has an Indium-antimonide sensor composed of 256 x 320 pixels with a pitch of 30 μm. The focal length of the objective is 50 mm, and the spatial resolution of the images recorded by the camera around 200 μm/pixel. In addition, the camera spectral sensitivity range is $\lambda \in [2.5 - 5.5]\ \mu m$. Figure 4 plots the normalized spectral sensitivity of the acquisition system, which includes the spectral responses of the camera, the lens objective, the air absorption, and the IR lamp emission. We are not able to differentiate the different contributions with the available equipment. However, the absorption peak at $\lambda = 4300$ nm is the signature of the CO_2 in the air [14]. In this tutorial, polychromatic light integrated over the spectral range of the camera is used to increase the SNR.

The signal measured by each pixel, $U_{\text{pix}}(t)$, is directly proportional to the total flux $\Phi_{\text{tot}}(t)$ it receives. Depending on the received flux, each pixel generates an electrical signal: $U_{\text{pix}} = \rho_{\text{pix}}\Phi_{\text{tot}}$, with ρ_{pix} a proportionality factor specific to each pixel since they are all slightly different (size, noise, offset, ...). To compensate for these differences, we perform a non-uniformity correction (NUC) before starting the measurements [15]. The method consists in taking several images of a black body covering the entire field of view of the camera. After calculating the temporal and spatial average of the signal, a correction coefficient is applied to each pixel. This operation is performed by the software of the camera (Altair).

In addition, the IR camera converts the voltage signal of each pixel in digital levels (DL). Since the camera has a dynamic range of 14 bits, the pixel value is in the range [0 ; 2^{14}-1] DL. If the incident flux is too intense, the pixel is saturated, and its value is theoretically 16 383

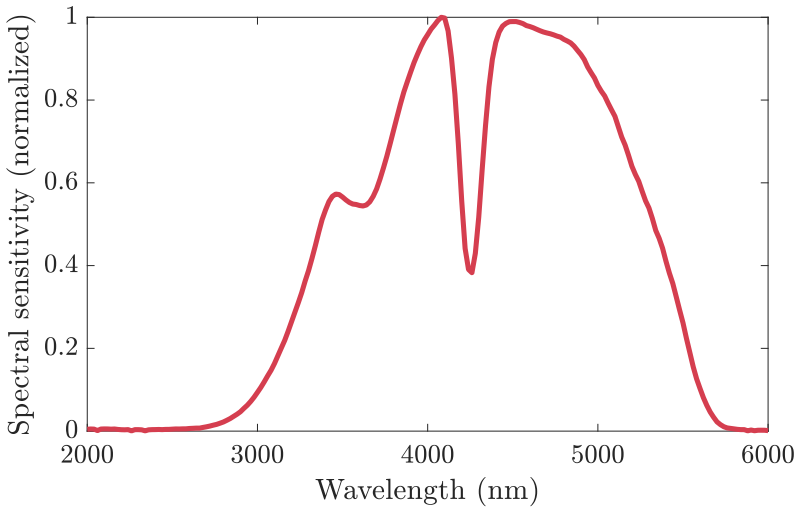

Figure 4: Spectral sensitivity of the acquisition chain, measured by scanning the wavelength with the monochromator. The peak around $\lambda = 4300$ nm corresponds to the CO_2 absorption.

DL. However, the upper limit of the camera operating range is 14 000 DL. Beyond that, the incident flux and pixel value are no longer proportional, and the signal should be saturated. In addition, below 2 000 DL, the camera does not operate optimally either. Therefore, always be sure to work in the [2 000 - 14 000] DL range.

Finally, a Stirling cools the camera to a temperature of $T_{\mathrm{CAM}} \approx 79$ K. As long as the camera is not properly cooled, the recorded signal is not stable enough. Figure 5 shows the drift of the measured signal over time. We propose to determine this drift by placing an ambient black body at 30 cm in front of the camera and regularly recording the measured signal. The sensor is only stable after two hours of operation: the measured signal at $t = 200$ min varies by more than 5% compared to the beginning of the measurement. That shows the importance of letting the camera cool down for at least two hours before making the measurements. Working with modulated signals reduces the impact of the camera drift on the results.

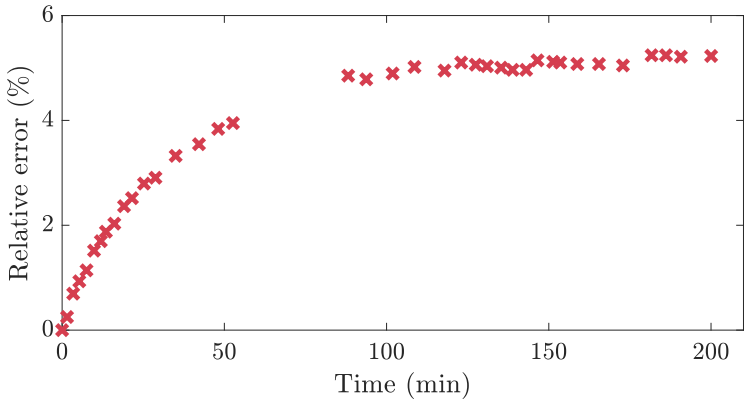

Figure 5: Drift of the signal recorded by the camera over time, measured on a ROI of 50x50 pixels.

Mechanical chopper settings

In this setup, the camera is synchronized with the mechanical chopper to record one frame when the chopper cuts the IR beam, and another when the light passes through the sample [16]. The only requirement for the chopper frequency f_c is $f_c \gg f_T$ to properly remove the proper emission of the sample. We choose $f_c = 11$ Hz, and the camera acquisition frame rate is $f_{\text{cam}} = 22$ Hz. The output signal of each pixel of the camera is given in the equation 7: the IR transmitted signal is only measured every other frame, at the frequency f_c. $\mathcal{C}(t)$ is the chopper rectangular wave function equals to 1 when the IR beam passes through the sample, and 0 when it is cut. The next section presents the double-demodulation method, applied on the images recorded by the camera.

$$U_{\text{pix}}(t) = \rho_{\text{pix}} \left[\Phi_0 \Gamma_0 (1 + \kappa \Delta T \cos(2\pi f_T t)) \mathcal{C}(t) + E(T,t)\right] \tag{7}$$

$$\begin{cases} \mathcal{C}(t) = 0, \text{ when the chopper cuts the IR beam} & (8) \\ \mathcal{C}(t) = 1, \text{ when the IR beam passes through the sample} & (9) \end{cases}$$

4 Double-demodulation method applied on images

As mentioned in the introduction, we use the two-image method, subtracting the proper emission thanks to the synchronization of the camera with the chopper.
The presented methods allow us to demodulate simultaneously the signal recorded by all the pixels of the camera. We do not work in real time but post process the films recorded during the experiment.

4.1 Proper emission subtraction: the two-image method

As mentioned, the camera is synchronized with the mechanical chopper to discriminate the transmitted flux $\Phi_0\Gamma(t)$ from the parasitic signal $E(t)$. The camera successively records one frame when the chopper lets the light passing through the sample (U_{on}) and another when it cuts the light beam (U_{off}). The frequency of the camera is $f_{\text{cam}} = 2f_c$ with f_c the chopper frequency, we define $\tau_c = 1/f_c$. The difference between two consecutive frames results in equation 10.

$$U_{\text{on}}(t) - U_{\text{off}}(t + \frac{\tau_c}{2}) = \rho_{\text{pix}} \Phi_0 \Gamma_0 [1 + \kappa \Delta T \cos(2\pi f_T t)] + \Delta_{\text{res}} \tag{10}$$

The term Δ_{res} is the residuals of the parasitic radiations and noise measurement after the subtraction: $\Delta_{\text{res}} = E(t) - E(t + \frac{\tau_c}{2})$. These residuals are negligible compared to the thermotransmittance signal, providing some conditions: the proper emission must be constant between two consecutive frames, otherwise the residual Δ_{res} depends on the temperature, and the source demodulation is not correctly performed. This is why the chopper frequency, f_c, is set much higher than the thermal frequency, f_T. The first experimental measurement is to check if the proper emission is correctly removed with the chosen frequencies (f_T, f_c).
Figure 6 shows the two-image method on two consecutive images recorded by the IR camera, when the IR flux passes through the sample (a) and when it is cut by the chopper (b). The subtraction of the two images results in frame (c). As mentioned in section 3, the camera has a limited dynamic range of 14 bits. Since all the parasitic radiations are added to the useful IR transmitted flux, the remaining signal after two-image subtraction may be weak. So, we understand the interest of maximizing the IR flux compared to the unwanted radiations. Several strategies are possible:

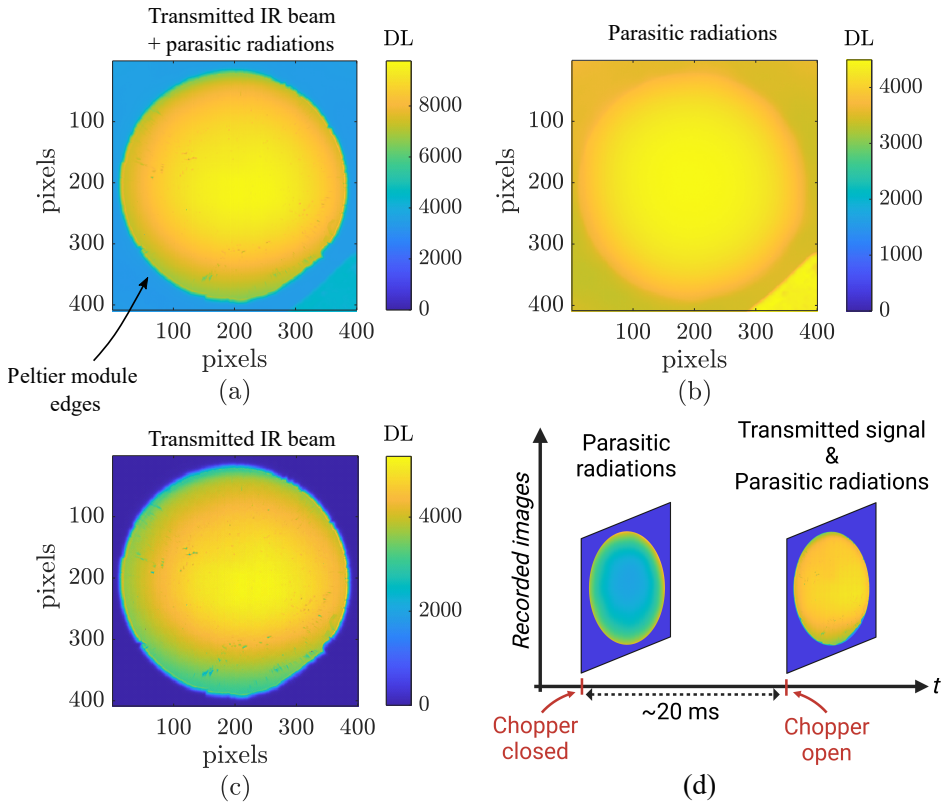

Figure 6: Images of (a) IR transmitted beam with proper emission, $U_{\text{on}}(t)$, (b) proper emission and parasitic radiations, $U_{\text{off}}(t + \frac{\tau_c}{2})$, and (c) IR beam after proper emission subtraction, $U_{\text{on}}(t) - U_{\text{off}}(t + \frac{\tau_c}{2})$. (d) Illustration of the two-image process.

- As we cannot influence the proper emission of the sample, we must operate on the IR incident beam. One possibility is to concentrate its power. The higher the intensity of the transmitted beam, the more we can decrease the integration time of the camera and, thus, the component of the proper emission.
- The wavelength of the IR beam is chosen where the measured IR transmitted beam is maximal. This wavelength depends on the camera sensitivity and the transmittance of the sample.
- We can use an IR bandpass filter between the sample and the camera. That eliminates the components of the proper emission outside the filter. The filter must be adapted to the wavelength of the IR beam.

Using a filter generates parasitic reflections, attenuates the transmitted IR beam, and must be changed according to the wavelength. As a consequence, we will focus on the first two points for the following. Finally, after the two-image subtraction, we get the signal $U_{\text{pix,IR}}(t)$ at the chopper frequency f_c.

$$U_{\text{pix,IR}}(t) = \rho_{\text{pix}} \Phi_0 \Gamma_0 [1 + \kappa \Delta T \cos(2\pi f_T t)] + \Delta_{\text{res}} \tag{11}$$

4.2 Demodulation of the transmitted signal

A numerical demodulation is used to obtain the module and phase from the thermotransmittance. A Fast Fourier Transform (FFT) algorithm in Matlab is employed to process the

image. These, in each pixel of the image we obtain the module:

$$\|\Delta U_{\text{pix,IR}}(\omega = 2\pi f_T)\| = \rho_{\text{pix}}\Phi_0\Gamma_0\kappa\Delta T, \tag{12}$$

and the thermotransmittance phase

$$\arg(\Delta U_{\text{pix,IR}}(\omega = 2\pi f_T)) = \hat{\phi} \tag{13}$$

These two quantities can be used to estimate the heat diffusivity, convective coefficient, or to calibrate the thermotransmittance coefficient κ over the spectral range of the camera. The demodulation based on FFT requires to record at least 10 periods to ensure a sufficient spectral resolution in the process data. The longer the experiments lasts, the better the precision of the algorithm is.

5 Heat transfer modeling of a thin wafer in cylindrical coordinates

This section studies the heat transfer in a thin silicon wafer heated at its edges by a ring-shaped Peltier module. We calculate the temperature variation ΔT in the sample, and determine the operating modulation frequency f_T.

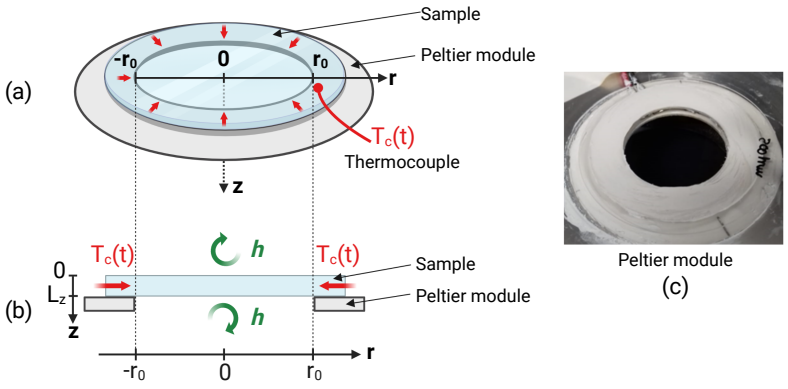

Figure 7: Illustration of the heat transfer problem. (a) 3D view of the Peltier module and the sample heated to a modulated temperature $T_c(t)$. (b) Cross-sectional view with boundary conditions. (c) Image of the Peltier module.

5.1 Solving the heat transfer equation

The shape of the heating system is important to let the incident flux Φ_0 passing through the sample. The sample and the Peltier module are positioned vertically. Figure 7 illustrates the geometry of the problem with the boundary conditions. Let's consider a sample of radius r_0 (m) and thickness L_z (m), of thermal diffusivity a (m^2/s) and thermal conductivity k (W/m/K). Due to the geometry of the wafer and the heating system, we use the cylindrical coordinate system (r, ϑ, z). As the sample is homogeneously heated at its edges, we do not consider the azimuth coordinate ϑ: the temperature does not depend on the angle ϑ. The final coordinate system is (r, z).

Boundary conditions

The temperature is set to the modulated temperature $T(t) = T_0 + \Delta T \cos(\omega_T t)$ at the edges of the sample ($r = r_0$ and $r = -r_0$), with T_0 the ambient temperature and $\omega_T = 2\pi f_T$ the angular frequency (rad/s). For symmetry reasons, at the position $r = 0$, the radial flux is assumed to be equal to zero. We impose convection losses at the surfaces $z = 0$ and $z = L_z$, with h being the convection coefficient (W/m^2/K). The system of equations [14 to 19] expresses the heat transfer problem in cylindrical coordinates with boundary conditions over time t.

$$\begin{cases} \dfrac{\partial^2 T(r,z,t)}{\partial r^2} + \dfrac{1}{r}\dfrac{\partial T(r,z,t)}{\partial r} + \dfrac{\partial^2 T(r,z,t)}{\partial z^2} = \dfrac{1}{a}\dfrac{\partial T(r,z,t)}{\partial t} & (14) \\ -k \left.\dfrac{\partial T(r,z,t)}{\partial z}\right|_{z=0} = -h(T(r,z=0,t) - T_0) & (15) \\ -k \left.\dfrac{\partial T(r,z,t)}{\partial z}\right|_{z=L_z} = h(T(r,z=L_z,t) - T_0) & (16) \\ \left.\dfrac{\partial T(r,z,t)}{\partial r}\right|_{r=0} = 0 & (17) \\ T(r=r_0,z,t) = T(r=-r_0,z,t) = T_0 + \Delta T(r_0)\cos(\omega_T t) & (18) \\ T(r,z,t=0) = T_0 & (19) \end{cases}$$

Linearization of convective losses

The borofloat thermal conductivity is about $k \approx 1$ W/m/K, its thickness is 500 µm and the convection coefficient is approximately $h \approx 15$ W/m^2/K for the vertical configuration used in the experimental setup. This leads to a Biot number $B_i \approx 2.10^{-2} \ll 1$, which means that the temperature is homogeneous in the sample thickness. As a result, the partial derivative with respect to z can be linearized, as expressed in equation 21. We substitute this result in the previous system of equations.

$$\frac{\partial^2 T(r,z,t)}{\partial z^2} \approx \frac{\left.\frac{\partial T(r,z,t)}{\partial z}\right|_{z=L_z} - \left.\frac{\partial T(r,z,t)}{\partial z}\right|_{z=0}}{L_z} \quad (20)$$

$$\approx -\frac{2h}{kL_z}(T(r,z=L_z,t) - T_0) \quad (21)$$

Temperature decomposition as periodic function

To solve the system, the temperature is decomposed into a constant and a term depending on the angular frequency ω_T:

$$\underline{T}(r,t) = T_0 + \Delta\underline{T}(r,\omega_T)e^{i\omega_T t} \quad (22)$$

With $\Delta\underline{T}(r,\omega_T)$ the complex temperature amplitude at the frequency f_T. After substituting the partial derivative with respect to z and the expression of $\underline{T}(r,t)$, the previous system of equations [14 to 19] becomes:

$$\begin{cases} \dfrac{d^2\Delta\underline{T}(r,\omega_T)}{dr^2} + \dfrac{1}{r}\dfrac{d\Delta\underline{T}(r,\omega_T)}{dr} - \dfrac{2h}{kL_z}\Delta\underline{T}(r,\omega_T) = \dfrac{i\omega_T}{a}\Delta\underline{T}(r,\omega_T) & (23) \\ \left.\dfrac{d\Delta\underline{T}(r,\omega_T)}{dr}\right|_{r=0} = 0 & (24) \\ |\Delta\underline{T}(r=r_0,\omega_T)| = |\Delta\underline{T}(r=-r_0,\omega_T)| = \Delta T(r_0) & (25) \end{cases}$$

Solution of the system

The solution of the system is given in equation 26, with $H = 2h/kL_z$ the loss factor (m^{-2}), $\mathcal{I}_0$ and $\mathcal{K}_0$ the modified Bessel functions of first and second kind.

$$\Delta\underline{T}(r,\omega_T) = A\mathcal{I}_0\left(r\sqrt{H + i\frac{\omega_T}{a}}\right) + B\mathcal{K}_0\left(r\sqrt{H + i\frac{\omega_T}{a}}\right) \quad (26)$$

A and B are determined with the boundary conditions:

- At the center of the wafer, an adiabatic condition is assumed. As the function $\mathcal{K}_1(r)$ tends towards ∞ at $r = 0$, B must be equal to zero to satisfy equation 24.
- At the edge $r = r_0$, the boundary condition gives: $A = \Delta T(r_0)/\mathcal{I}_0\left(r_0\sqrt{H + i\frac{\omega_T}{a}}\right)$.

Finally, the complex temperature field as a function of the position r and the frequency f_T is expressed in equation 27.

$$\Delta\underline{T}(r,\omega_T) = \Delta T(r_0)\frac{\mathcal{I}_0\left(r\sqrt{H + i\frac{\omega_T}{a}}\right)}{\mathcal{I}_0\left(r_0\sqrt{H + i\frac{\omega_T}{a}}\right)} \quad (27)$$

Two quantities are then extracted from this model, the phase $\phi = \arg(\Delta\underline{T}(r,\omega_T))$ and the normalized modulus $\|\Delta\underline{T}(r,\omega_T)\|/\|\Delta\underline{T}(R,\omega_T)\|$.

6 Inverse methods

6.1 Minimization and objective function

The inverse method to estimated a is based here on the minimization between the calculated phase from the model and the measured thermotransmittrance phase. The cost function to be minimised takes into account the error bar on the phase measurements, and writes as

$$\mathcal{J}(a) = (\hat{\boldsymbol{\phi}} - \boldsymbol{\phi}(a))^T \boldsymbol{W}(\hat{\boldsymbol{\phi}} - \boldsymbol{\phi}(a)) \quad (28)$$

where $\boldsymbol{W}$ is a diagonal weight matrix containing the standard deviation of the measurements $\hat{\boldsymbol{\phi}}$. Each element of the diagonal of the matrix is computed as $1/\sigma^2_{\hat{\phi}}$.

A simple gradient method can be used to estimate a. Algorithms such as Levenberg-Marquardt are recommended in Matlab. But here we propose to use the Gauss-Newton algorithm such as

$$a^{k+1} = a^k + [(\boldsymbol{S}^k)^T \boldsymbol{W} \boldsymbol{S}^k]^{-1}(\boldsymbol{S}^k)^T \boldsymbol{W}(\hat{\boldsymbol{\phi}} - \boldsymbol{\phi}(a^k)), \quad (29)$$

where the S is the sensitivity of the parameter a on the phase. It is expressed as

$$S = \frac{\partial\phi(a)}{\partial a}. \quad (30)$$

This quantity can be computed numerically using a finite difference scheme and by assuming a small variation of the diffusivity, i.e. 1%.
The algorithm can be initiated with a heat diffusivity of 1 mm^2/s as it is the order of magnitude for glass wafer.

6.2 Standard deviation

Once the diffusivity estimated, one can compute the associated standard deviation. From the standard deviation on the heat diffusivity is straightforward as

$$\sigma_a = \sigma_r \sqrt{[(\boldsymbol{S})^T \boldsymbol{W} \boldsymbol{S}]^{-1}} \tag{31}$$

with $\sigma_r = \sqrt{\mathcal{J}(a)/(N-1)}$ where N is the number of data points used to fit a. It is important to note that this standard deviation takes only into account the deviation between the measurement and the model, and the standard deviation on the measurements. However, several others bias in the measurement (position of the wafer, non linearity in the Peltier module during the heating...) can increase significantly this value.

7 Measurements

7.1 Experimental setting

Instructions to realise the thermal imaging in semi transparent media, and an estimate of the thermal diffusivity of a Borofloat sample are as follows:

1. Turn on all the instruments and set the chopper chopping frequency to $f_c \sim 10 - 12$ Hz. This value can be checked on the oscilloscope.

2. Set the waveform generator to trigger the camera. Two triggers need to be sent to the camera: one when the chopper is close, one when the chopper is open. The camera trigger needs therefore to be set at $2f_c \sim 20 - 24$ Hz.

3. Set the thermal modulation at 20 mHz with a voltage peak-peak value of 4 V. The electronic card powering the Peltier module converts this signal in current at the rate of 1 A/V. Use the second channel of the waveform generator to do so.

4. Once the periodic regime is established (after 10 min), record at least 10 thermal modulations to perform an accurate Fourier transform with at least a spectral resolution of 2 mHz.

7.2 Image processing

Once the set of a data is recorded, the data processing consists in two successive steps. First, the proper emission and transmitted signal needs to be separated. The images when the chopper is open and close are subtracted. A example of this signal are presented in Figure 8(a) and (b).

The variations of the transmitted signal over the recorded time is presented in Figure 8(c) for two pixels. Pixel 1, close to the edge where the wafer is heated, clearly shows a peak to peak modulation of 5×10^{-3}. Pixel 2, taken farther from the wafer edge, shows the same modulation but attenuated and shifted. This behaviour is expected. It is important to note here that a signal variation of only 1% is recorded at the maximum (pixel 1), corresponding to a variation of 80 DL over 8000 DL. This illustrates the weakness of the signal and justified the advanced metrology that needs to be used to be able to measure it properly.

The modulus of these signals, obtained by FFT, are presented in Figure 8(d). Two clear peaks at 20 mHz can be observed, validating the good result of the method. Such demodulation processing is extended to all the pixels of the images, and the fields at 20 mHz are extracted

for the parameter estimation.

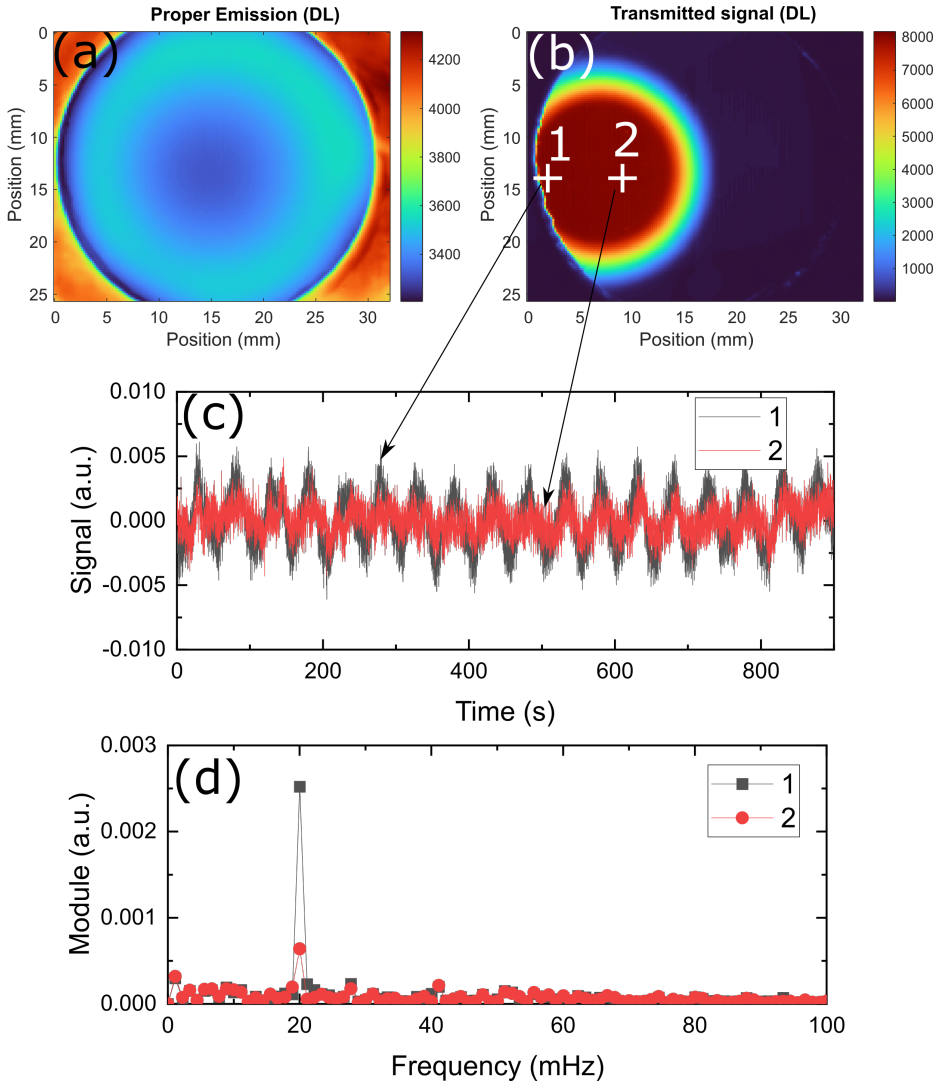

Figure 8: Image processing. (a) proper emission. (b) transmitted signal. (c) transmitted signal recorded during the experiment and divided by its mean. The location of the two pixels is indicated in (b). (d) associated fourier transform of the signal shown in (c).

7.3 Results

The modulus and phase fields obtained at 20 mHz are presented in Figure 9(a) and (b), respectively. Only the part of the image containing the IR beam (see Figure 8(b) for comparison) can be exploited. The rest of the image is only noise.

Both the modulus and the phase decrease from the edge of the wafer toward the center (between 2 and 15 mm in the image). Several artefacts are visible in the images. They are associated with the IR sensor itself, where small variations in the pixel reading by the camera electronics can be seen here. Usually, such artefacts are not visible when measurements with high SNR are performed.

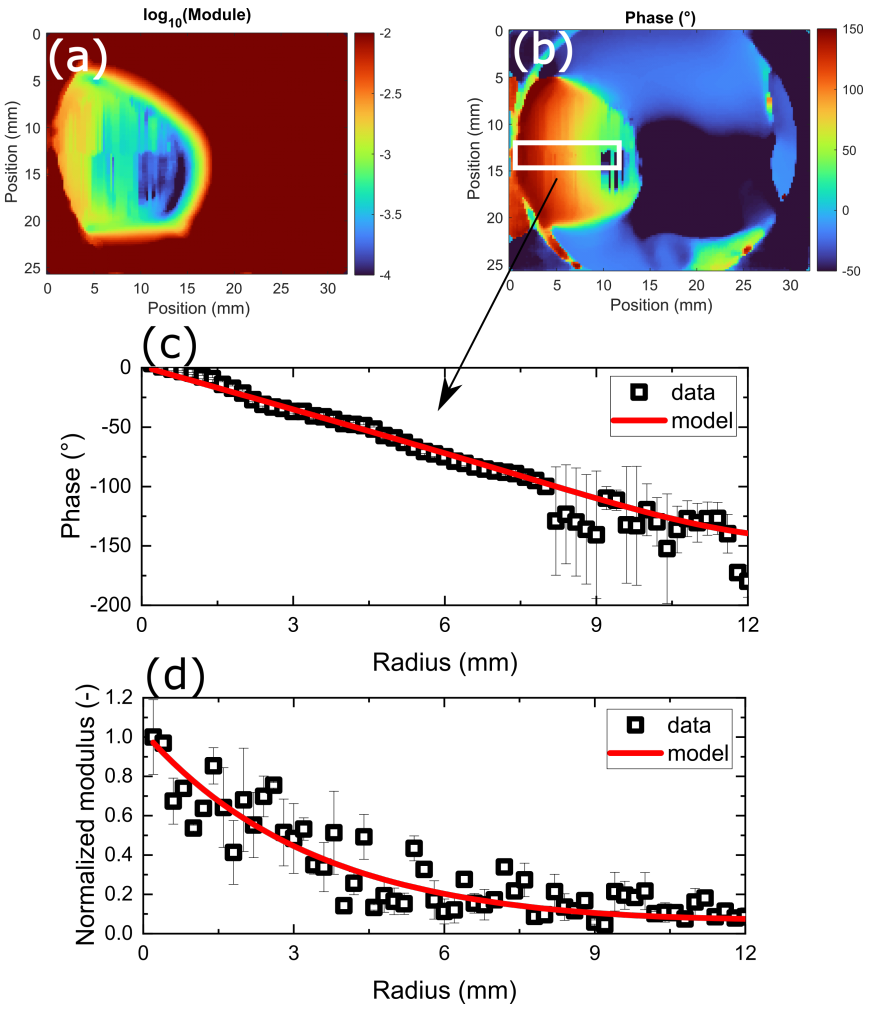

Figure 9: Image demodulation. (a) modulus of the thermotransmittance at 20 mHz. (b) the corresponding phase shift. (c) phase shift along a wafer radius average in the white rectangle in (b). (d) the corresponding modulus for the same location. A comparison with the model is done in (c) and (d).

In order to fit the thermal diffusivity, the data in the white rectangle are extracted and averaged along the vertical position (20 pixels) to obtain the phase versus the wafer radius. The error bar in the experimental data are related to the standard deviation over the average 20 pixels. Equation 29 is used to estimate the thermal diffusivity. The convection coefficient is taken to be 15 $W/m^2/K$, the wafer has a thickness of 500 µm, and the thermal conductivity of Borofloat is 1 W/m/K. The algorithm was able to converge in less than 10 iterations (see Figure 10). The tolerance limits was set to 10^{-6}.

The result of the fit can be seen in Figure 9(c). Overall a good agreement between the model and the data is observed, except when $r > 8$ mm where the IR sensor artefacts are visible. The estimated diffusivity is $a = (0.93 \pm 0.2)$ mm^2/s which is typically in the expected range for such glass wafer. A check on the modulus distribution is done through Figure 9, and here again, a excellent agreement between the model and data is obtained.

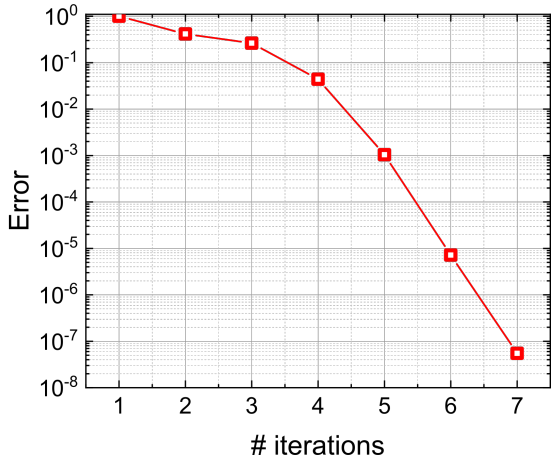

Figure 10: Convergence of the Gauss-Newton algorithm during the diffusivity estimation.

8 Conclusions

In this tutorial a new method to measure the temperature fields in semi-transparent media was introduced. Thermotransmittance enabled a contactless measurement of the mean temperature in semi-transparent media with the downside to be a very weak signal. Therefore, an advanced metrology was carried out, based on a double modulation of the signal recorded by the camera. Image processing in Matlab enabled to extract the thermotransmittance phase and modulus which were successfully used for parametric estimation. More detailed on the techniques can be found in the following publication [17].

Such technique can be extended to many other measurements ranging from optical properties characterisation, thermal microscopy, thermal characterization of heterogeneous materials, to 3D temperature fields measurements.

References

[1] J. Gieseler, A. Adibekyan, C. Monte, J. Hollandt, Apparent emissivity measurement of semi-transparent materials part 2: Theoretical concept, Journal of Quantitative Spectroscopy and Radiative Transfer 258 (2021) 107317. doi:10.1016/j.jqsrt.2020.107317. URL https://doi.org/10.1016/j.jqsrt.2020.107317

[2] S. Jeon, S.-N. Park, Y. S. Yoo, J. Hwang, C.-W. Park, G. W. Lee, Simultaneous measurement of emittance, transmittance, and reflectance of semitransparent materials at elevated temperature, Optics Letters 35 (23) (2010) 4015. doi:10.1364/ol.35.004015. URL https://doi.org/10.1364/ol.35.004015

[3] J. Gieseler, A. Adibekyan, C. Monte, J. Hollandt, Apparent emissivity measurement of semi-transparent materials part 1: Experimental realization, Journal of Quantitative Spectroscopy and Radiative Transfer 257 (2020) 107316. doi:10.1016/j.jqsrt.2020.107316. URL https://doi.org/10.1016/j.jqsrt.2020.107316

[4] O. Rozenbaum, D. D. S. Meneses, Y. Auger, S. Chermanne, P. Echegut, A spectroscopic method to measure the spectral emissivity of semi-transparent materials up to high temperature, Review of Scientific Instruments 70 (10) (1999) 4020–4025.

doi:10.1063/1.1150028.
URL https://doi.org/10.1063/1.1150028

[5] D. D. S. Meneses, P. Melin, L. del Campo, L. Cosson, P. Echegut, Apparatus for measuring the emittance of materials from far infrared to visible wavelengths in extreme conditions of temperature, Infrared Physics andTechnology 69 (2015) 96–101. doi:10.1016/j.infrared.2015.01.011.
URL https://doi.org/10.1016/j.infrared.2015.01.011

[6] A. Adibekyan, E. Kononogova, C. Monte, J. Hollandt, Review of PTB measurements on emissivity, reflectivity and transmissivity of semitransparent fiber-reinforced plastic composites, International Journal of Thermophysics 40 (4) (Mar. 2019). doi:10.1007/s10765-019-2498-0.
URL https://doi.org/10.1007/s10765-019-2498-0

[7] A. Philipp, N. W. Pech-May, B. A. F. Kopera, A. M. Lechner, S. Rosenfeldt, M. Retsch, Direct measurement of the in-plane thermal diffusivity of semitransparent thin films by lock-in thermography: An extension of the slopes method, Analytical Chemistry 91 (13) (2019) 8476–8483. doi:10.1021/acs.analchem.9b01583.
URL https://doi.org/10.1021/acs.analchem.9b01583

[8] E. A. A. Pogna, X. Jia, A. Principi, A. Block, L. Banszerus, J. Zhang, X. Liu, T. Sohier, S. Forti, K. Soundarapandian, B. Terrés, J. D. Mehew, C. Trovatello, C. Coletti, F. H. L. Koppens, M. Bonn, H. I. Wang, N. van Hulst, M. J. Verstraete, H. Peng, Z. Liu, C. Stampfer, G. Cerullo, K.-J. Tielrooij, Hot-carrier cooling in high-quality graphene is intrinsically limited by optical phonons, ACS Nano 15 (7) (2021) 11285–11295. doi:10.1021/acsnano.0c10864.
URL https://doi.org/10.1021/acsnano.0c10864

[9] M. Polyanskiy, Refractiveindex.info.
URL https://refractiveindex.info/

[10] C. Pradere, M. Ryu, A. Sommier, M. Romano, A. Kusiak, J. L. Battaglia, J. C. Batsale, J. Morikawa, Non-contact temperature field measurement of solids by infrared multispectral thermotransmittance, Journal of Applied Physics 121 (8) (2017) 085102. doi:10.1063/1.4976209.
URL https://doi.org/10.1063/1.4976209

[11] M. Bensalem, A. Sommier, J. C. Mindeguia, J. C. Batsale, L.-D. Patino-Lope, C. Pradere, Contactless transient THz temperature imaging by thermo-transmittance technique on semi-transparent materials, Journal of Infrared, Millimeter, and Terahertz Waves 39 (11) (2018) 1112–1126. doi:10.1007/s10762-018-0521-3.
URL https://doi.org/10.1007/s10762-018-0521-3

[12] N. Kakuta, Y. Fukuhara, K. Kondo, H. Arimoto, Y. Yamada, Temperature imaging of water in a microchannel using thermal sensitivity of near-infrared absorption, Lab on a Chip 11 (20) (2011) 3479. doi:10.1039/c1lc20261h.
URL https://doi.org/10.1039/c1lc20261h

[13] E. Hecht, Optics, 4th Edition, Addison Wesley, 2002.

[14] P. Linstrom, Nist chemistry webbook, nist standard reference database 69 (1997). doi:10.18434/T4D303.
URL http://webbook.nist.gov/chemistry/

[15] Y. Souhar, Caractérisation thermique de matériaux anisotropes à hautes températures, Theses, Institut National Polytechnique de Lorraine (May 2011).
URL https://hal.univ-lorraine.fr/tel-01749289

[16] M. Romano, M. Ryu, J. Morikawa, J. Batsale, C. Pradere, Simultaneous microscopic measurements of thermal and spectroscopic fields of a phase change material, Infrared Physics and Technology 76 (2016) 65–71. doi:10.1016/j.infrared.2016.01.010.
URL https://doi.org/10.1016/j.infrared.2016.01.010

[17] C. Bourges, S. Chevalier, J. Maire, A. Sommier, C. Pradere, S. Dilhaire, Infrared thermotransmittance-based temperature field measurements in semitransparent media, Review of Scientific Instruments 94 (3) (2023) 034905. doi:10.1063/5.0131422.
URL https://doi.org/10.1063/5.0131422

Tutorial 12 : Optimal Wavelengths Selection Criteria for Multispectral Pyrometry

Christophe RODIET[1]

[1] ITheMM (EA 7548), Université de Reims Champagne-Ardenne, 51100 Reims, France.
E-mail: Christophe.Rodiet@univ-reims.fr

Abstract. In this tutorial, it's shown that for mono-spectral and bi-spectral methods used for temperature measurement of opaque surfaces exhibiting non-uniform emissivity, optimal wavelengths minimizing the standard deviation on the estimated temperature can be obtained from similar laws to that of the Wien's law, and for multi-spectral methods, a more general methodology (based on the ordinary least squares method) to obtain the optimal wavelengths selection is presented. The goal consists in minimizing the standard deviation of the estimated temperature (optimal design experiment). Two methods for wavelengths selection are presented, sequential and global with or without constraints on the spectral range. Then, the estimated temperature results obtained by a model considering up to a second-order polynomial global spectral transfer function of the overall system (including the emissivity) and for different number of parameters and wavelengths are compared. The model is based on the fluxes (Planck's law and without fluxes ratio). Different selection criteria are presented. These points are treated from theoretical, numerical, and experimental points of view.

Keywords: Multispectral, thermometry, pyrometry, temperature measurement, multi-band, optical measurement, emissivity, optimal wavelengths, infrared thermography.

Nomenclature

φ	Flux, $W.m^{-2}$
M°	Irradiance $W.m^{-3}$ (or $W.m^{-3}.sr^{-1}$)
C_1	Constant Planck's law, $W.m^2$
C_2	Constant Planck's law, $m.K$
T	Temperature, K or $°C$
T_{ij}	Temperature calculated from the wavelengths filters λ_i, λ_j
$\propto$	Proportional

Greek letters

ε	Emissivity
λ	Wavelength, m
χ	Sensitivity

Indices and subscripts

λ	Spectral, or wavelength
m	Mean
i,j,k	Number of filter

Table of Contents

1. Introduction 3

2. mono-spectral method: Analogous Wien's law for optimal wavelengths selection minimizing the relative error on the estimated temperature 3

3. The multispectral method 5

3.1. Selection of the optimal wavelengths for minimum error on the estimated temperature 5

3.1.1. Some measurement criteria 6

3.1.2. Determination of best sequential wavelengths 7

3.1.3. Determination of global optimal wavelengths: Analogous Wien's law for optimal wavelengths selection in mono-spectral and bi-spectral methods 9

3.1.4. Global optimal wavelengths selection for multispectral measurements 10

4. Numerical validation of models for temperature measurement in the infrared wavelength range 11

4.1. Simulations without noise 12

4.2. Simulations with noise 13

5. Application to experimental thermography 13

5.1. Description of the experimental bench 13

5.2. Measurement methodology, data processing and results 14

6. Conclusion 16

1. Introduction

The thermal characterization of weakly reflective opaque materials at high temperatures often uses optical methods for measuring space and/or time distributions of temperature [4]. It is usually done by infrared cameras, quantum detectors or photomultipliers (in the case of measurements at shorter wavelengths [5]). The difficulty with this type of measurement is the spatial and time variation of the emissivity of the material making it non-uniform over the sample surface, especially at high temperature where significant oxidation phenomena can occur. One solution is to make a measurement by the multispectral method [5-10] (a non-exhaustive state-of-the-art has been made in [8], or in [2]). Even if the idea is interesting, its implementation is tricky because of the difficulty to choose the adapted wavelengths λ_i. Indeed, they must be chosen "close enough" to overcome emissivity variations of the material (and more generally, the global transfer spectral function of the overall system, including the emissivity), but not "too close" to obtain an uncertainty on the measured temperature lowest as possible. Note that in this paper we speak indifferently of emissivity or global transfer function (of the overall system, including the emissivity), because each transfer function taking values in the range [0;1], so their product is bounded by 0 and 1.
After a presentation of an analogous Wien's laws allowing to find the "optimal" wavelengths for mono-spectral and bi-spectral measurements, the theoretical principle of the multi-spectral methods is presented and validated through numerical simulations and experiments. Several models are validated numerically through Monte-Carlo simulations for different spectral emissivity variations and compared experimentally. The facility is presented in section 5 and the considered typical variations of emissivity (or more generally, global transfer function) shown in section 4. These simulated variations of emissivity (or global transfer function) versus wavelength are used to validate our theoretical model for estimating temperature through an inverse technique based on an Ordinary Least Squares (OLS) method. The cost function (3.2) is used in order to estimate this temperature by inverse method. Based on the minimization of the standard deviation of the estimated temperature *T*, sequential and global selection methods are presented to determine the optimal wavelengths to choose for optimizing the temperature measurement.

2. mono-spectral method: Analogous Wien's law for optimal wavelengths selection minimizing the relative error on the estimated temperature

Calling $f(\lambda)$ the global spectral transfer function including all unknowns (emissivity $\varepsilon(\lambda)$, sample area, quantum efficiency…), the flux emitted by an object is defined by the Planck's law (1) which can take a simpler form (named Wien's approximation) if $\lambda T << C_2 \approx 14400\mu m.K$:

$$\varphi(\lambda,T) = f(\lambda)M^o(\lambda,T) = f(\lambda)\frac{C_1\lambda^{-5}}{\exp\left(\frac{C_2}{\lambda T}\right)-1} \underset{\text{approximation}}{\simeq} f(\lambda)C_1\lambda^{-5}\exp\left(\frac{-C_2}{\lambda T}\right), \forall \lambda T << C_2 \approx 14400\mu m.K \quad (1)$$

Considering λ as a parameter, by differentiating the Planck's law (1) with respect to temperature and equating the differential terms to errors, it can be shown that the relative error on the temperature is:

$$\frac{e_T}{T} = \frac{e_\varphi}{\varphi}\frac{\lambda T}{C_2}\left(1-\exp\left(\frac{-C_2}{\lambda T}\right)\right) \underset{\text{approximation}}{\simeq} \frac{e_\varphi}{\varphi}\frac{\lambda T}{C_2} \quad (2)$$

Furthermore, if it is assumed that $e_\varphi/f(\lambda) = k$ (with *k* a constant), find the wavelength that minimizes (2) under the Wien's approximation, leads to:

$$\min_{\lambda}\left(\frac{e_T}{T}\right) \Rightarrow \frac{\partial}{\partial\lambda}\left(\frac{e_T}{T}\right) = 0 \Rightarrow \frac{\partial}{\partial\lambda}\left(\frac{kT}{C_2}\frac{\lambda}{M^o}\right) = 0 \Leftrightarrow \lambda_{opt}^{Wien}T = \frac{C_2}{6} \approx 2400\mu mK = C_{MW}^R \quad (3)$$

Accordingly, (3) shows that under the Wien's approximation and for the mono-spectral measurements, the wavelength that minimizes the relative error on the temperature is defined from an analogous to Wien's law: $\lambda_{opt}^{Wien}T = C_{MW}^R \approx 2400\mu mK$. Note that, equating the errors to the standard deviation (to the least squares sense), minimizing (2) is equivalent to minimize the standard deviation σ_T of the temperature for a constant standard deviation σ_φ of the flux (cf. section 3.1.3).

It seems legitimate to wish extend this law, but for a flux defined by Planck's law. The equation to solve being nonlinear (cf. (2) and (3)), the method consists in search numerically for several temperatures T_i the wavelengths λ_i^{opt} that minimize e_{T_i}/T_i (cf. figure 1), then to determine the constant $C_{MP}^R = \lambda_{opt}^{Planck}T$ by a least squares method, such as:

$$\hat{C}_{MP}^R = \underset{C_{MP}^R}{\operatorname{argmin}} \sum_i \left(\lambda_i^{opt} - \frac{C_{MP}^R}{T_i}\right)^2 \Rightarrow \lambda_{opt}^{Planck}T = \hat{C}_{MP}^R \approx 2410.3\mu mK \quad (4)$$

The residues defined by $r(T_i) = \lambda_i^{opt} - 2410.3/T_i$ are plotted in figure 2. Low residue values (cf. figure 2) corroborate a good fit of the law $\lambda_{opt}^{Planck}T = \hat{C}_{MP}^R \approx 2410.3\mu mK$ to find the optimal wavelengths for mono-spectral measurements (with Planck's law).

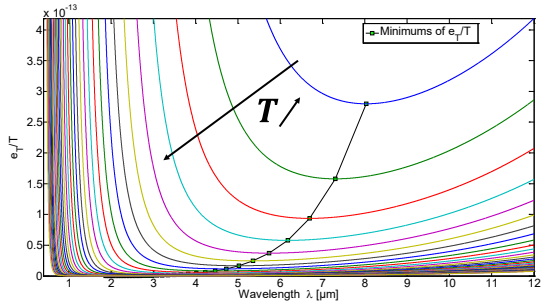

Figure 1. Minimums of $e_T/T \propto \lambda/M^o$ for $T \in [300K\ ;\ 1300K]$ (1 curve out of 30).

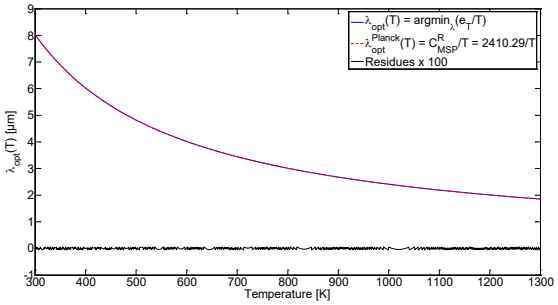

Figure 2. Optimal wavelengths obtained numerically and by the law $\lambda_{opt}^{Planck} = \hat{C}_{MP}^R/T$ for $T \in [300K\ ;\ 1300K]$. The maximum residue is of about 5.10^{-4}µm.

Note that, minimizing (2) is equivalent to maximizing (with respect to λ) the sensitivity $\chi_T = \frac{\partial\varphi(\lambda,T)}{\partial T}$, with $f(\lambda)$ assumed to be constant. Indeed:

$$\chi_T = \frac{\partial\varphi(\lambda,T)}{\partial T} = \frac{C_2}{\lambda T^2}\left(1 - \exp\left(\frac{-C_2}{\lambda T}\right)\right)^{-1}\varphi(\lambda,T) \underset{\text{approximation}}{\overset{\text{Wien's}}{\simeq}} \frac{C_2}{\lambda T^2}\varphi(\lambda,T) \quad (5)$$

Thus, using the Wien's approximation, maximizing (5) with respect to λ, leads to (cf. figure 3 for an illustration):

$$\frac{\partial^2\varphi(\lambda,T)}{\partial\lambda\partial T} = 0 \Leftrightarrow \lambda_{opt}^{Wien}T = \frac{C_2}{6} \approx 2400\mu mK = C_{MW}^R \quad (6)$$

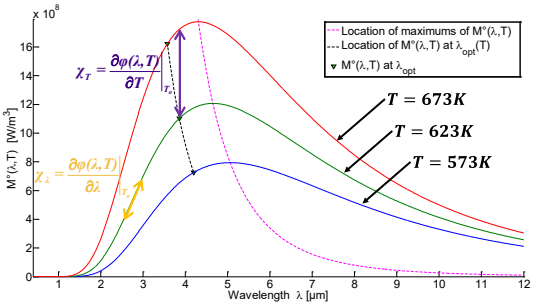

Figure 3. Graphical illustration of the sensitivities.

Note that, the optimal wavelengths are slightly shifted to the left of the maxima of the Planck's curves (figure 3) and can be interpreted as a compromise between sensitivity and signal over noise ratio (cf. section 3.1.3).

3. The multispectral method

The principle of multispectral method which is based on the use of multiple wavelengths to obtain the value of different physical quantities have been presented in the associated lecture of this METTI-8 School. Here, we focus our attention on a method using direct radiative heat fluxes in order to estimate the temperature of an opaque material with a spectral emissivity varying spatially and/or temporally.

The estimation model used in this tutorial is an unbiased model (called *TNL.Tabc* model) based on the Planck law (3.1). This model considers a second-order polynomial model for modeling the overall spectral transfer function (including the emissivity) $f(\lambda)$ through three unknown parameters *(a, b ,c)* to estimate. In (3.2), $\varphi_i^{\exp}$ represents the flux measured at the experimental wavelength λ_i, and N_f the total wavelengths number.

$$\varphi_i(T,a,b,c) = \underbrace{(a+b\lambda_i+c\lambda_i^2)}_{=f(\lambda)\text{ or }\varepsilon(\lambda)} \frac{C_1\lambda_i^{-5}}{\exp\left(\frac{C_2}{\lambda_i T}\right)-1} \underset{\text{approx.}}{\simeq}_{\text{Wien}} \underbrace{(a+b\lambda_i+c\lambda_i^2)}_{f(\lambda)\text{ or }\varepsilon(\lambda)} C_1\lambda_i^{-5}\exp\left(\frac{-C_2}{\lambda_i T}\right) \quad ,\forall i \in [\![1\,;\,N_f]\!] \qquad (3.1)$$

The objective is to find the values of *(T,a,b,c)* that minimize the following cost function:

$$J(T,a,b,c) = \sum_{i=1}^{N_f}\left(\varphi_i^{\exp} - \varphi_i(T,a,b,c)\right)^2 = \left(\varphi_1^{\exp} - \varphi_1(T,a,b,c)\right)^2 + \ldots\ldots\ldots + \left(\varphi_4^{\exp} - \varphi_4(T,a,b,c)\right)^2 \qquad (3.2)$$

3.1. Selection of the optimal wavelengths for minimum error on the estimated temperature

In this section, criteria allowing to define a methodology to follow to perform measurements without amplifying the uncertainties will be first established (section 3.1.1). Then, a method to determine sequentially the best wavelengths is presented in section 3.1.2. Even if this method is not optimal, it has an educational interest in showing what happens when the number of wavelengths is increasing. Next, it's shown (section 3.1.3) for bispectral measurements that optimal wavelengths, minimizing the standard deviation on the estimated temperature, can be obtained by an analogous Wien's law.To finish, the results of a global optimization (with and without constraints), which gives the "optimal global wavelengths" is shown (section 3.1.4). Even if the methods can be applied for any spectral emissivity variation, in order to simplify the

interpretation of the results, a unitary emissivity (or global spectral transfer function) is assumed for the simulation of the "experimental" fluxes used both for the sequential and global methods (Section 3.1). Note that each theoretical optimal wavelength represents experimentally the central wavelength of the narrow filter, which is used with the infrared camera. To conclude, a link between the temperature relative error, the flux sensitivity to the temperature, and the temperature standard deviation is established [9].

3.1.1. Some measurement criteria

First, for monospectral measurements the increasing part of the Planck law is preferred since the relative sensitivities of flux to the temperature $\chi_T^r = \chi_T/\varphi_\lambda$ and to the wavelength $\chi_\lambda^r = \chi_\lambda/\varphi_\lambda$ are greater at short wavelengths (3.3) [10]. Secondly, for bispectral measurements, a flux ratio as large as possible is chosen to minimize the measurement uncertainty on the flux (3.4) (assuming that $e_{\varphi_{\lambda_i}} \approx e_{\varphi_{\lambda_j}}$) [1]. In addition, the filters must be chosen distant enough $\Delta\lambda$ (3.5) to avoid amplification of measurement uncertainties but also close enough to minimize measurement uncertainty due spectral emissivity (or more generally spectral global transfer function including emissivity) variation. More precisely, it can be shown that optimal bispectral wavelengths must be spaced from $1.9\Delta\lambda$ [9]. However, at very short wavelengths (UV), relation (3.5) can be linearized and therefore it becomes possible to choose a constant distance between two successive wavelengths [1, 10]. Furthermore, note that the relative uncertainty on the temperature e_T/T [1] (under assumption $e_{\varphi_\lambda}/f(\lambda)$ = constant) is increasing with temperature (3.6). Even if relations (3.4) and (3.5) have been obtained by differentiating a flux ratio [8] (classical bispectral method based on the Wien approximation), they are also valid for the proposed method based on (3.1) with $b = c = 0$.

Finally, note that relations (3.3) and (3.6) obtained by differentiating (3.1) under Wien approximation with $b = c = 0$ show that it is equivalent to maximize the sensitivity of the flux to the temperature X_T or to minimize the relative uncertainty on the temperature e_T/T [3, 9, 10].

$$\begin{aligned} &\varphi_\lambda \cdot \chi_T^r = \chi_T = \frac{d\varphi_\lambda(T)}{dT} \simeq \frac{C_2}{T^2}\frac{\varphi_\lambda(T)}{\lambda} \qquad \varphi_\lambda \cdot \chi_\lambda^r = \chi_\lambda = \frac{d\varphi_\lambda(T)}{d\lambda} \simeq \left(\frac{C_2}{\lambda T} - 5\right)\frac{\varphi_\lambda(T)}{\lambda} \\ &\Rightarrow \Delta T_{ij} = T_j - T_i \approx \frac{1}{\chi_T^r}\left(\frac{\varphi_\lambda(T_j)}{\varphi_\lambda(T_i)} - 1\right); \quad \Rightarrow \Delta T_{ij} = T_j - T_i \approx \frac{1}{\chi_\lambda^r}\left(\frac{\varphi_\lambda(T_j)}{\varphi_\lambda(T_i)} - 1\right) \end{aligned} \tag{3.3}$$

$$\frac{e_{\varphi_{\lambda_i}}}{\varphi_{\lambda_i}} + \frac{e_{\varphi_{\lambda_j}}}{\varphi_{\lambda_j}} = \frac{e_{\varphi_{\lambda_i}}}{\varphi_{\lambda_i}}\left(1 + \frac{\varphi_{\lambda_i}}{\varphi_{\lambda_j}}\frac{e_{\varphi\lambda_j}}{e_{\varphi_{\lambda_i}}}\right) \simeq \frac{e_{\varphi_{\lambda_i}}}{\varphi_{\lambda_i}}\left(\forall(\varphi_{\lambda_i}, \varphi_{\lambda_j})/\frac{\varphi_{\lambda_i}}{\varphi_{\lambda_j}} << 1\right) \tag{3.4}$$

$$\Delta\lambda = \left|\lambda_j - \lambda_i\right| > \left.\frac{T{\lambda_j}^2}{C_2}\right|_{\lambda_i<\lambda_j} \tag{3.5}$$

$$\frac{e_T}{T} \underset{\text{under Wien's approx.}}{\propto} \frac{T}{C_2}\frac{\lambda}{\varphi_\lambda(T)} = \frac{1}{T.\chi_T}, \text{for } e_{\varphi_\lambda} \propto \left(f(\lambda) \text{ or } \varepsilon(\lambda)\right) \tag{3.6}$$

3.1.2. Determination of best sequential wavelengths

The previously established criteria allow to set up a wavelengths selection methodology. Nevertheless, as they are given in term of inequalities, it is not possible to know if the wavelengths choice is optimal or not. As the method used for the temperature estimation is based on the functional minimization through an OLS method, the idea is to select optimal wavelengths by minimizing the standard deviation of the estimated temperature. In the OLS method, the statistical properties of the parameters (3.2) are given by the variance-covariance matrix, from which the standard deviations σ_{β_i} of the estimated parameters and particularly of the temperature σ_T can be determined. The model (3.1) being non-linear, the approximate expression of the variance-covariance matrix of the OLS method is used, which is given for a parameter vector $\boldsymbol{\beta}$ = (*T*, *a*, *b*, *c*), under assumptions of an additive noise, non-correlated, identically distributed (zero mean and constant variance), by:

$$\mathbf{cov}(b) = \begin{bmatrix} \sigma_T^2 & \mathrm{cov}(T,a) & \mathrm{cov}(T,b) & \mathrm{cov}(T,c) \\ \mathrm{cov}(T,a) & \sigma_a^2 & \mathrm{cov}(a,b) & \mathrm{cov}(a,c) \\ \mathrm{cov}(T,b) & \mathrm{cov}(a,b) & \sigma_b^2 & \mathrm{cov}(b,c) \\ \mathrm{cov}(T,c) & \mathrm{cov}(a,c) & \mathrm{cov}(b,c) & \sigma_c^2 \end{bmatrix} = (\boldsymbol{X^t X})^{-1}\sigma_{noise}^2 \qquad (3.7)$$

$$\boldsymbol{X} = \frac{\partial \varphi_i}{\partial \beta_j} = \begin{bmatrix} \frac{\partial \varphi_1}{\partial T} & \frac{\partial \varphi_1}{\partial a} & \frac{\partial \varphi_1}{\partial b} & \frac{\partial \varphi_1}{\partial c} \\ \vdots & \vdots & \vdots & \vdots \\ \frac{\partial \varphi_N}{\partial T} & \frac{\partial \varphi_N}{\partial a} & \frac{\partial \varphi_N}{\partial b} & \frac{\partial \varphi_N}{\partial c} \end{bmatrix}$$

The sequential method consists in choosing the first optimal wavelength λ_{opt1} minimizing the standard deviation of the temperature, assuming that we perform only a monospectral measurement (thus with the only one unknown parameter *T*) (Figures 4 and 5). Note that this value does not correspond to the maximum of the Planck law. It can be shown that $\lambda_{opt1}T \approx 2\,410$ µm·K and compared with the Wien law $\lambda_{max}T \approx 2\,898$ µm·K [9].

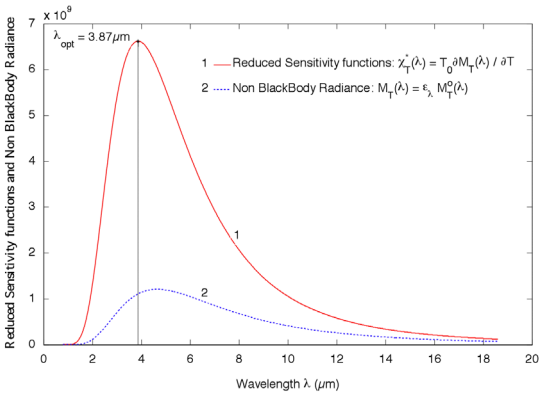

Figure 4. Reduced sensitivity curves for unitary emissivity with $M_T(\lambda)=\varphi_T(\lambda)$ given by (3.1) and for T_0 = 623 K.

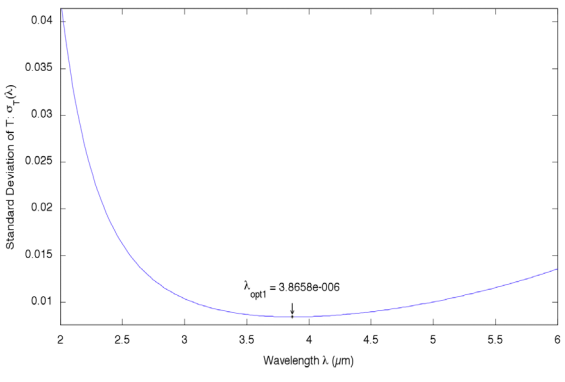

Figure 5. Standard deviation of T for unitary emissivity with σ_T given by (3.7) and β = 623 (just one wavelength and the parameter *T*).

The value is slightly shifted on the left and appears as a compromise solution between a large sensitivity and a good signal over noise ratio. This result shows the interest of the OLS method allowing to define an optimal wavelength for the temperature measurement, contrary to expression (3.1) that only takes into account the sensitivity aspect and gives for optimal wavelength $\lambda = 0$ because the relative uncertainty on the temperature is null for this value. Figure 5 shows that there is a unique wavelength, $\lambda_{opt1} = 3.87$ µm, that minimizes the standard deviation $\sigma_T(\lambda)$ (for monospectral measurements). The increasing of the standard deviation when the wavelength is decreasing for $\lambda < \lambda_{opt1}$ can be explained by the fact that the signal over noise ratio is decreasing for $\lambda \to 0$. The increasing of the standard deviation for $\lambda > \lambda_{opt1}$ is due to the fact that the sensitivities of flux to the temperature X_T (3.3) are decreasing with the wavelength (Figure 4). Indeed, for a monospectral measurement $\sigma_T(\lambda) = \chi_T^{-1}$, which is similar to the relative uncertainty on the temperature e_T/T (3.6).
Then, to choose the value of the second filter λ_1 is fixed to λ_{opt1}, and the shortest wavelength is sought ($\lambda_{opt21} \approx 2.64$ µm in Figure 6) that minimizes the local temperature standard deviation in the model *TNL.Ta*. The notation (cf. Section 4 for more details) *TNL.Ta* means that in (3.1) and (3.2) only the parameters *T* and *a* are considered (i.e. *b* = *c* = *0*). λ_{opt21} has been preferred to λ_{opt22} since the latter is not in the detector spectral range and allows to reduce the working spectral range. Furthermore, note that at $\lambda_2 = \lambda_{opt1}$, there is a vertical asymptote ($\sigma_T \to \infty$) due to the fact that the numeric system to solve is ill-conditioned and leads to infinite uncertainties. There are two unknowns (*T* and *a*) but only one equation. For $\lambda_2 < \lambda_{opt21}$ and $\lambda_2 > \lambda_{opt22}$, the standard deviation $\sigma_T(\lambda_2)$ is increasing because the signal over noise ratio and the sensitivity to the temperature are decreasing, and for $\lambda_{opt21} < \lambda_2 < \lambda_{opt22}$, $\sigma_T(\lambda_2)$ is increasing because the criteria (3.5) is less and less respected.

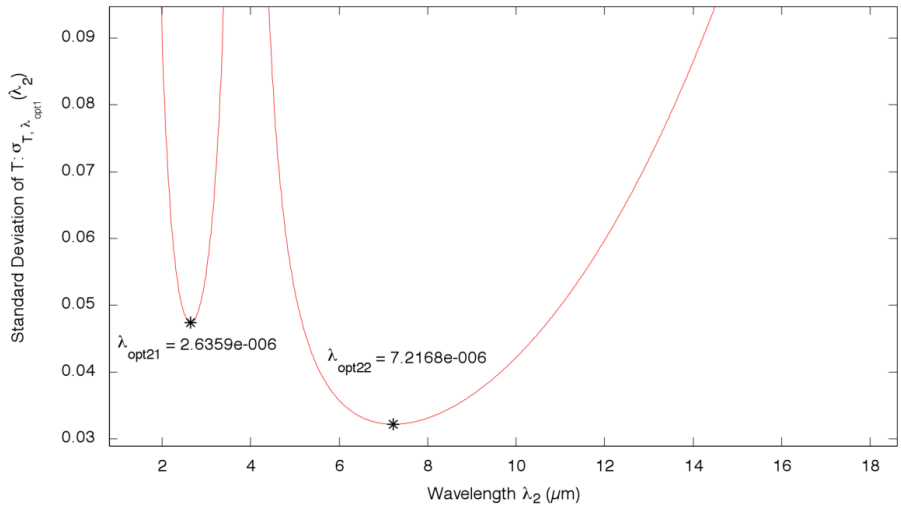

Figure 6. Standard deviation of *T* for unitary emissivity with $\lambda_1 = \lambda_{opt1}$ fixed and λ_2 free; σ_T given by (3.7) and β= (623; 1) (just one wavelength: λ_2, and two parameters: *T* and *a*): Model (*T*;*a*).

The same procedure is followed to get the third and the fourth wavelengths, which minimize the standard deviation of the temperature in the model (*T,a,b,c)*. With this process, we finally obtain the following wavelengths set: $\boldsymbol{\lambda_{opt_seq}}$ = {1.67µm; 2.05 µm; 2.64 µm; 3.87 µm} with $\sigma_T \approx 4.0$ K. Because of experimental constraints (availability of filters), the selected wavelengths filters are the following: $\boldsymbol{\lambda_{opt_seq}}$ = {2.00 µm; 2.35 µm; 2.85 µm; 4.00 µm} with

$\sigma_T \approx 2.6$ K. These two wavelengths set shows that the sequential process is not optimal but presents the advantage of illustrating that it is important to carefully choose the different wavelengths for multispectral measurements.

3.1.3. Determination of global optimal wavelengths: Analogous Wien's law for optimal wavelengths selection in mono-spectral and bi-spectral methods

The optimal wavelengths determination can be done using a global optimization algorithm such as "Nelder Mead" (NM), "Levenberg-Marquardt" (LM) or "Trust-Region" (TR)...

For monospectral and bispectral (under assumption of grey body) measurements, it can be shown that the optimal wavelengths are defined by an analogous Wien law [9].

First, note that for the mono-spectral measurements the minimization of the relative error of the temperature can be linked to the minimization of the standard deviation of the temperature. Indeed, for mono-spectral measurements (one wavelength and one unknown parameter "T" (assumed constant and known emissivity)) from (3.7) and (6), we have:

$$\min_{\lambda_1}\left(\sigma_T(\lambda_1)\right) \Leftrightarrow \min_{\lambda_1}\left(\left(\frac{\partial\varphi_1}{\partial T}\right)^{-1}\sigma_{noise}\right) \Rightarrow \frac{\partial^2\varphi(\lambda,T)}{\partial\lambda\partial T} = 0 \Rightarrow \lambda_{opt}^{Wien}T = \frac{C_2}{6} \approx 2400\mu m.K = C_M^W \quad (7)$$

Thus, we see from (3), (6) and (7), that there is equivalence between minimizing the relative error on the temperature, maximize the flux sensitivity to the temperature, or minimize the standard deviation of the temperature. This last observation will allow us to generalize the method for determining the optimal wavelengths for bi-spectral and multi-spectral measurements.

For bi-spectral measurements through Wien's approximation but without flux ratio (i.e. two wavelengths and two unknown parameters "{T,a}" in (3.1) and (3.7) but with Wien's approximation), it is possible to show analytically that the optimal wavelengths which minimize the standard deviation of the temperature(3.7), are defined by two laws (one for each wavelength) analogous to the Wien's law, such as:

$$\min_{\lambda_1,\lambda_2}\left(\sigma_T(\lambda_1,\lambda_2)\right) \Rightarrow \begin{cases}\lambda_{opt1}^{bi-Wien}T = C_{BW}^{R1}\\ \lambda_{opt2}^{bi-Wien}T = C_{BW}^{R2}\end{cases} \quad (8)$$

As in the case of mono-spectral measurements, it seems legitimate to extend these laws for fluxes defined by Planck's law. The equations to minimize being once again non-linear, then the approach will be similar as for (4), we will seek numerically the set of pairs of wavelengths $\left(\lambda_{1,i}^{opt}, \lambda_{2,i}^{opt}\right)$ that minimize the standard deviation $\sigma_{T_i}(\lambda_1,\lambda_2)$ of the temperature (calculated from (3.7) with sensitivities$\boldsymbol{X}$evaluated at$\boldsymbol{\beta}_0 = (T_i, 1)$), then we will determine the law constants $\left(\hat{C}_{BP}^{R1}, \hat{C}_{BP}^{R2}\right)$ using a least squares method, such that:

$$\left(\hat{C}_{BP}^{R1}, \hat{C}_{BP}^{R2}\right) = \arg\min_{\hat{C}_{BP}^{R1},\hat{C}_{BP}^{R2}} \sum_i \left(\left(\lambda_{1,i}^{opt} - \frac{\hat{C}_{BP}^{R1}}{T_i}\right)^2 + \left(\lambda_{2,i}^{opt} - \frac{\hat{C}_{BP}^{R2}}{T_i}\right)^2\right) \Rightarrow \begin{cases}\lambda_{opt1}^{bi-Planck}T = C_{BP}^{R1} \approx 1830.8\mu m.K\\ \lambda_{opt2}^{bi-Planck}T = C_{BP}^{R2} \approx 4465.8\mu m.K\end{cases} \quad (9)$$

A graphical representation of wavelengths minimizing standard deviation of the temperature (obtained numerically and for the Planck's law) and those obtained with the laws (9) is given figure 7.

The residues are not shown, but as in the mono-spectral case, the maximum error is of about 10^{-4}µm. An illustration of optimal wavelengths for mono-spectral and bi-spectral measurements is shown in figure 8.

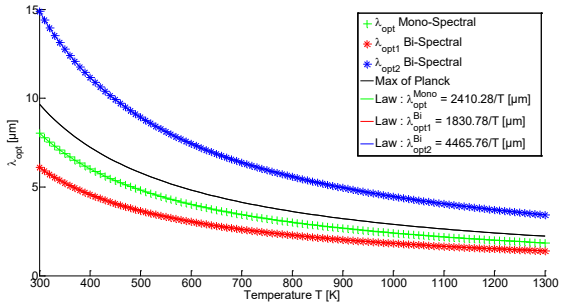

Figure 7. Optimal wavelengths for bi-spectral measurements. Comparisons between wavelengths obtained numerically and from the laws (9) : $\lambda_{opt,k}^{bi-Planck} = \hat{C}_{BP}^{R,k}/T$.

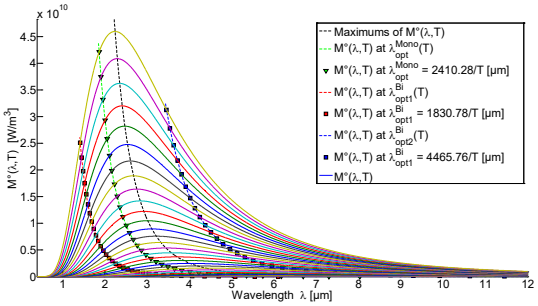

Figure 8. Illustration on Planck's curves of optimal wavelengths for mono-spectral and bi-spectral measurements.

Note that the optimal wavelengths for bi-spectral measurements satisfy:

$$\Delta\lambda_{opt}^{bi-Planck} = \lambda_{opt2}^{bi-Planck} - \lambda_{opt1}^{bi-Planck} = 1.9\underbrace{\frac{\left(\lambda_{opt2}^{bi-Planck}\right)^2 T}{C_2}}_{\Delta\lambda_{\min}} = 1.9\Delta\lambda_{\min} \qquad (10)$$

We can show [6, 9] that $\Delta\lambda_{\min} = \left.\frac{\lambda_j^2 T}{C_2}\right|_{\lambda_j>\lambda_i}$ is the minimum distance between two wavelengths to avoid amplification of measurement errors on the temperature.

3.1.4. Global optimal wavelengths selection for multispectral measurements

- Optimal wavelengths for monospectral measurements: $\lambda_{opt}^{Planck} T = \hat{C}_{MP}^{R} \approx 2\,410\ \mu m \cdot K$
- Optimal wavelengths for bispectral measurements: $\begin{cases} \lambda_{opt1}^{bi-Planck} T = C_{BP}^{R1} \approx 1\,831\ \mu m \cdot K \\ \lambda_{opt2}^{bi-Planck} T = C_{BP}^{R2} \approx 4\,466\ \mu m \cdot K \end{cases}$

Otherwise, for "general" multispectral measurements, the minimization calculus of the standard deviation gives for the determination of optimal wavelengths by an unconstrained estimation, with $\sigma_{noise} \approx 9 \times 10^4 W = 7 \times 10^{-6}$ % of the Planck law maximum (equivalent to the value of the experimental noise), and $\boldsymbol{\beta}$ = (623;1;0;0) as nominal parameters vector:

- For $\boldsymbol{\beta}$ = (*T*,*a*,*b*,*c*), we find: $\boldsymbol{\lambda_{opt_global}} = \{2.53\ ;\ 4.7\,0\ ;\ 8.87\ ;\ 26.18\}\ \mu m$ and $\sigma_T \approx 0.07\ K$
- For $\boldsymbol{\beta}$ = (*T*,*a*,*b*), we find: $\boldsymbol{\lambda_{opt_global}} = \{2.67\ ;\ 5.24\ ;\ 12.57\}\ \mu m$ and $\sigma_T \approx 0.05\ K$
- For $\boldsymbol{\beta}$ = (*T*,*a*), we find: $\boldsymbol{\lambda_{opt_global}} = \{2.94\ ;\ 7.17\}\ \mu m$ and $\sigma_T \approx 0.02\ K$

For $\boldsymbol{\lambda_{opt_global}} = \{2.94\ ;\ 7.17\}\ \mu m$, Figure 9 shows that the minimum is unique (two symmetric solutions $\{\lambda_1\ ;\ \lambda_2\} \approx \{2.94\mu m\ ;\ 7.17\mu m\}$), and that these solutions are different but lead to better results than those obtain by sequential method $\{\lambda_{opt1}\ ;\ \lambda_{opt22}\} \approx \{3.87\mu m\ ;\ 7.22\mu m\}$.

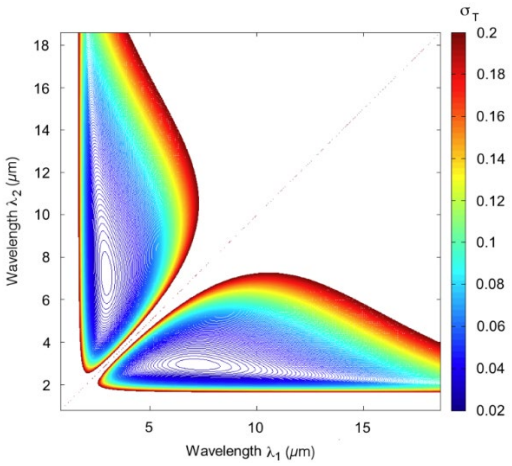

Figure 9. Isovalues of standard deviation of *T*.

Although this set of values are the best in terms of minimization of the standard deviation, performing measurements at these different wavelengths is difficult in practice because such a detector with a so wide spectral range does not exist. For this reason, we decide to choose the wavelengths only in the spectral range of the detector [1.5 µm - 5.5 µm]. If the global optimization with this constraint is performed, the results obtained are:

- For $\boldsymbol{\beta} = (T, a, b, c)$, it comes: $\boldsymbol{\lambda_{opt_cam_spec-range}} = \{2.14\ ;\ 3.39\ ;\ 4.76\ ;\ 5.50\}\ \mu m$ and $\sigma_T \approx 0.32\ K$
- For $\boldsymbol{\beta} = (T, a, b)$, it comes: $\boldsymbol{\lambda_{opt_cam_spec-range}} = \{2.43\ ;\ 4.21\ ;\ 5.50\}\ \mu m$ and $\sigma_T \approx 0.09\ K$
- For $\boldsymbol{\beta} = (T, a)$, it comes: $\boldsymbol{\lambda_{opt_cam_spec-range}} = \{2.93\ ;\ 5.50\}\ \mu m$ and $\sigma_T \approx 0.03\ K$

But the Wien approximation being better at short wavelengths, we will force ourselves to choose our wavelengths only in the spectral range corresponding to the increasing part of the Planck curve. In this context, the global estimation with constraint $\lambda \in [1.5\mu m\ ;\ 2898/T\ \mu m]$ gives:

- For $\boldsymbol{\beta} = (T, a, b, c)$, it comes: $\boldsymbol{\lambda_{opt_\lambda_{max}_spec-range}} = \{2.03\ ;\ 3.11\ ;\ 4.15\ ;\ 4.65\}\ \mu m$ and $\sigma_T \approx 0.52\ K$
- For $\boldsymbol{\beta} = (T, a, b)$, it comes: $\boldsymbol{\lambda_{opt_\lambda_{max}_spec-range}} = \{2.32\ ;\ 3.79\ ;\ 4.65\}\ \mu m$ and $\sigma_T \approx 0.14\ K$
- For $\boldsymbol{\beta} = (T, a)$, it comes: $\boldsymbol{\lambda_{opt_\lambda_{max}_spec-range}} = \{2.82\ ;\ 4.65\}\ \mu m$ and $\sigma_T \approx 0.03\ K$

Note that in both global estimation with constraints, the last wavelength is always the upper bound, which means that the best wavelength is probably out of the interval.

4. Numerical validation of models for temperature measurement in the infrared wavelength range

To validate the model, thousand noised fluxes are simulated through the Monte Carlo method (normal noise exhibiting the same level as standard deviation measured on the experimental thermographic images under the same conditions) (Tables 1 and 2) from four different variations/values of emissivity (or global spectral transfer function) (Figure 10): constant, linear, order 2 and Drude. We took care that the variations of order 2 and Drude models are significant on the IR spectral range of the study (and in agreement with the experimental behavior of different materials). Tables 1 and 2 show the results for the four filters chosen experimentally. The notation *TNL* means that the temperature is obtained from a "nonlinear least squares"

estimation using the regularized LM algorithm. *TNL.Tabc* (respectively *TNL.Tab*), means that we use (3.2) and the unknown parameters are (*T,a,b,c*) (resp. (*T,a,b*)). For *TNL.Tab,* the three shorter wavelengths are used.

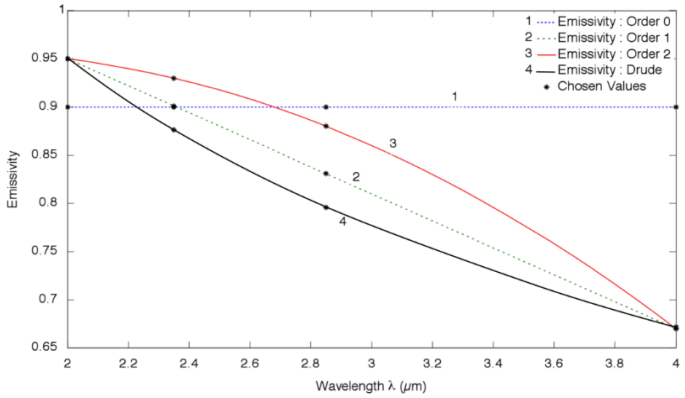

Figure 10. Emissivity variation/values used for numerical validation. The "chosen values" are the fixed or calculated values of simulated emissivity at the experimental wavelengths to have significant variations of emissivity compared with the linear variation.

4.1. Simulations without noise

λ_i (μm) = {2; 2.35; 2.85; 4} T^{exp} = 623 K ; Radiance law: Planck							
Noise	Emissivity	Model	T [K]	Absolute Error [K]	Relative Error [%]	Sigma [K]	Sigma [%]
Without	Constant	TNL.Tabc (4 bands)	623.00	0.00	0.00	-	-
		TNL.Tab (3 bands)	623.00	0.00	0.00	-	-
	Linear	TNL.Tabc (4 bands)	623.00	0.00	0.00	-	-
		TNL.Tab (3 bands)	623.00	0.00	0.00	-	-
	Order 2	TNL.Tabc (4 bands)	623.00	0.00	0.00	-	-
		TNL.Tab (3 bands)	608.52	14.48	2.32	-	-
	Drude	TNL.Tabc (4 bands)	636.91	13.91	2.23	-	-
		TNL.Tab (3 bands)	641.01	18.01	2.89	-	-

Table 1. Simulations for estimating the temperature (without noise).

As models *TNL.Tabc* and *TNL.Tab* do not use Wien approximation, no bias appears on estimated temperature except for emissivity variation of order 2 for *TNL.Tab,* and Drude for the models *TNL.Tabc* and *TNL.Tab*. The results in table 1 show that the model *TNL.Tabc* seems to be the better (lowest uncertainties).

4.2. Simulations with noise

AVERAGE TEMPERATURE OF 1 000 ESTIMATES: λ_i (µm) = {2; 2.35; 2.85; 4} T^{exp} = 623 K; Radiance law: Planck; Noise: constant; Sigma Noise: 7.43*10^{-3} % (max of Planck law)							
Noise	Emissivity	Model	T [K]	Absolute Error [K]	Relative Error [%]	Sigma [K]	Sigma [%]
With	Constant	TNL.Tabc (4 bands)	623.02	0.02	0.00	1.13	0.18
		TNL.Tab (3 bands)	623.00	0.00	0.00	0.52	0.08
	Linear	TNL.Tabc (4 bands)	623.01	0.01	0.00	0.70	0.11
		TNL.Tab (3 bands)	623.00	0.00	0.00	0.32	0.05
	Order 2	TNL.Tabc (4 bands)	623.02	0.02	0.00	1.05	0.17
		TNL.Tab (3 bands)	608.52	14.48	2.32	0.30	0.05
	Drude	TNL.Tabc (4 bands)	636.91	13.91	2.23	0.74	0.12
		TNL.Tab (3 bands)	641.01	18.01	2.89	0.38	0.06

Table 2. Monte Carlo simulations for estimating the temperature (with noise).

Table 2 shows that it is impossible by the method *TNL.Tabc* to accurately estimate the temperature because the problem seems ill-posed. This observation is confirmed by the best results given by *TNL.Tab* in the case of emissivities ranging up to order 2, which shows that it is possible to regularize the problem by reducing the number of parameters. Nevertheless, it is important to note that the standard deviations of the estimations are significant, suggesting that it will be necessary to have lot of points (high spatial resolution allowing a local averaging) or to use larger integration times to increase the measurement accuracy. From these results, the *TNL.Tabc* model is retained for the estimation model for the experiments.

5. Application to experimental thermography

5.1. Description of the experimental bench

The schematic diagram of the facility is shown in Figure 11. An oxidized cast iron sample on which "FT 25" is carved (its surface being varied, so it is for the emissivity) is placed in a tube furnace at a temperature of 623 K controlled by a PID with a great stability (negligible oscillations in temperature recording due to furnace regulation). The sample temperature is obtained using a thermocouple placed on its rear face. The spatial radiative flux emitted by the sample is measured through a high sensitive broadband InSb infrared matrix camera working in the spectral range [1.5 µm - 5.5 µm]. Four monochromatic filters: $\boldsymbol{\lambda_{exp}} = \{2\ ;\ 2.35\ ;\ 2.85\ ;\ 4\}\ \mu m$ are mounted in the filters wheel of this camera to measure the emitted flux coming from the sample at four different wavelengths. The signal is digitized through a 14 bits Analog/Digital card. Each pixel is associated to a DL corresponding to the spectral radiance of a surface area of the sample. The camera has previously been calibrated in the temperature range [573 K – 673 K] using a 4' x 4' extended area blackbody.

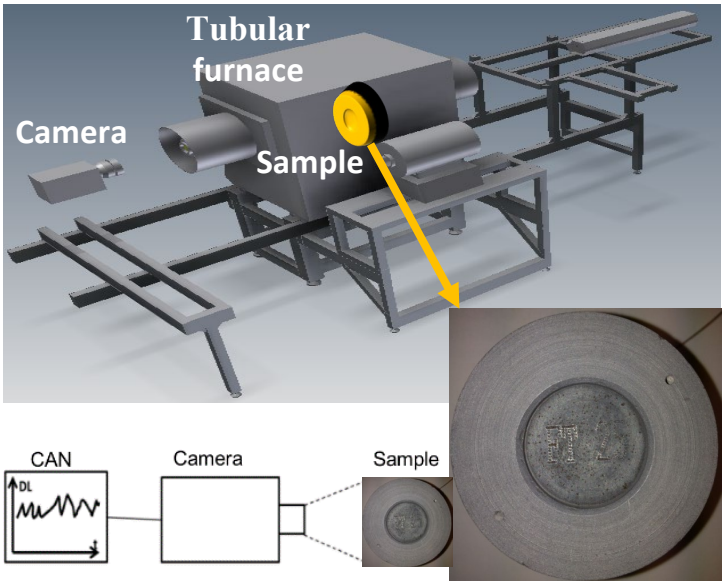

Figure 11. Facility for IR measurements.

5.2. Measurement methodology, data processing and results

Using a tubular furnace, the sample is heated at three different temperatures levels {T_1 = 573 K; T_2 = 623 K; T_3 = 673 K}. For each temperature, a recording of 1 000 images for each filter is performed. Before each acquisition, great care is taken to check whether thermal equilibrium is reached. To get free of the reflection through the non-blackbody sample that is not negligible at this level of temperature due to presence of the hot furnace walls in this vicinity, we use the average image made with 4 filters at 573 K and 673 K to correct the existing offset between our measurements at these two temperatures and the flux that a blackbody at these same temperatures would emit. Calling $M_{\lambda_i}^{\exp}(T_j)$ the experimental heat flux measured for each pixel at the wavelengths λ_i and at the temperature T_j, and K_i a variable to correct the offset between the measured flux and the blackbody flux, we have a set of 8 equations with 8 unknowns (the four couples $(\varepsilon_i \ ; \ K_i)$) to solve. The system is as follows:

$$M_{\lambda_i}^{\exp}(T_j) = \varepsilon_i M_{\lambda_i}^{o} + K_i, \forall i \in [\![1 \ ; \ 4]\!] \quad and \quad \forall j \in \{1 \ ; \ 3\}$$

$$\Leftrightarrow \begin{cases} M_{\lambda_1}^{\exp}(T_1) = \varepsilon_1 M_{\lambda_1}^{o} + K_1 \\ \vdots \\ M_{\lambda_4}^{\exp}(T_1) = \varepsilon_4 M_{\lambda_4}^{o} + K_4 \\ M_{\lambda_1}^{\exp}(T_3) = \varepsilon_1 M_{\lambda_1}^{o} + K_1 \\ \vdots \\ M_{\lambda_4}^{\exp}(T_3) = \varepsilon_4 M_{\lambda_4}^{o} + K_4 \end{cases} \tag{3.8}$$

The 8 unknowns $(\varepsilon_i \ ; \ K_i)$ (for each pixel) are estimated by a regularized LM ordinary least square method. Using the K_i (assuming the reflected part of the heat flux as constant in the

temperature range 573 K - 673 K), our experimental flux can be corrected to get rid of the reflection. Finally, the experimental flux is corrected for each pixel through the following relation:

$$\varphi_{\lambda_i}^{\exp}(T_j) = M_{\lambda_i}^{\exp}(T_j) - K_i, \ \forall i \in [\![1 \ ; \ 4]\!] \quad and \quad \forall j \in [\![1 \ ; \ 3]\!] \tag{3.9}$$

The aim is now to estimate the temperature field of the sample when the furnace is at T_2 = 623 K using adjusted flux emitted by each pixel. For this, we will find for each pixel the value of temperature *T* that minimizes the cost function.
Figures 12-15 show the averaged (1 000 Images) thermographic images recorded by the camera through the four monochromatic filters $\boldsymbol{\lambda_{exp}} = \{2 \ ; \ 2.35 \ ; \ 2.85 \ ; \ 4\} \, \mu m$. The inscription "FT25" is indistinguishable at 2 µm due to the low flux emitted but appears more and more clearly up to 4 µm. The result of the temperature estimation by inversion of Planck law (assuming unit emissivity) is given in Figure 16 for 4 µm wavelength. As expected, we note that this simple estimation assuming a uniform emissivity does not correct the emissivity field because the pattern "FT25" is still visible on the calculated temperature field. Moreover, the estimation uncertainty of temperature is large (experimental temperature is about 623 K), while the estimated temperature is about 587 K (approximately 6 % uncertainty or 40 K) with a standard deviation of about 1.5 K. Finally, Figure 17 shows the result of the estimated temperature (of about 625 K) field given by the *TNL.Tabc* model (minimization of the cost function). We note that the pattern has totally disappeared and that the temperature uncertainty is about 2 K (0.3 %) with a standard deviation of 4 K. We have tried different models but the best results are given by the model *TNL.Tabc*, which allows us to take into account the emissivity variation over the wavelength range [2 µm – 4 µm].

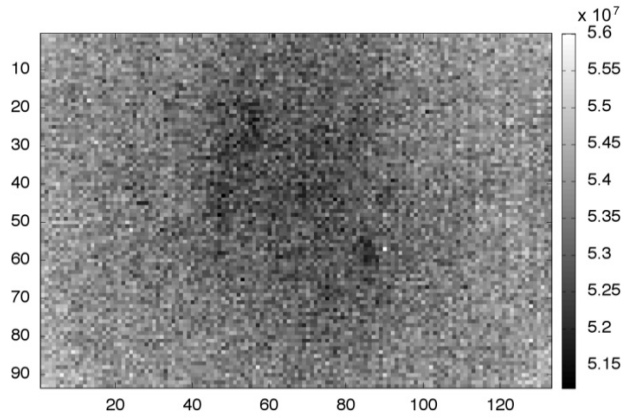

Figure 12. Flux 2 µm.

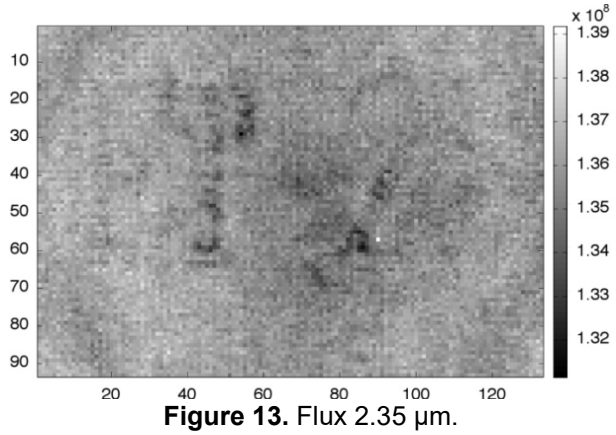

Figure 13. Flux 2.35 µm.

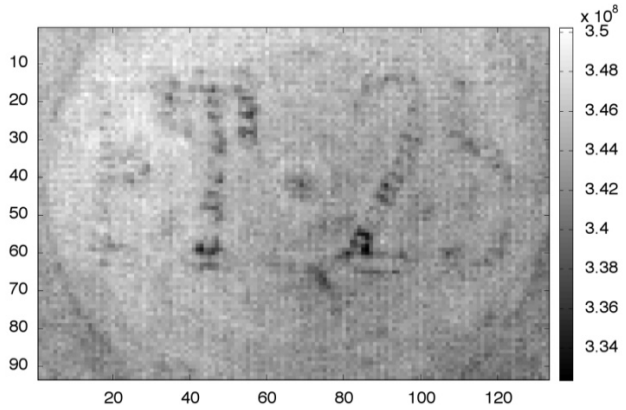

Figure 14. Flux 2.85 µm.

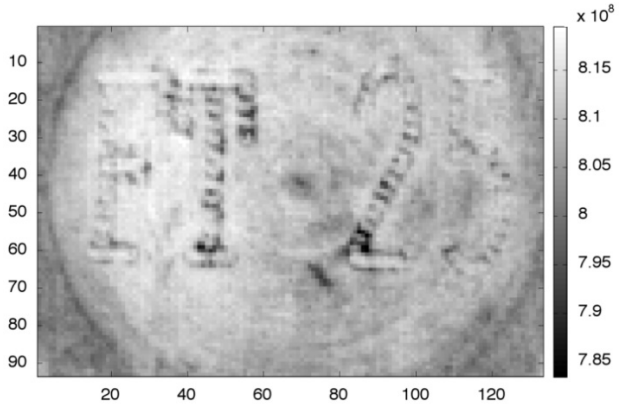

Figure 15. Flux 4 µm.

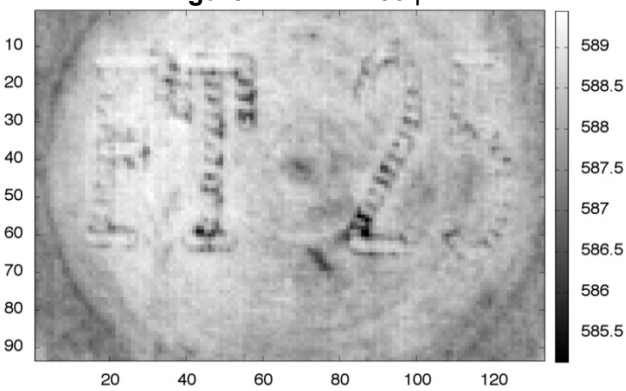

Figure 16. Estimated temperature: *TCN* 4 µm.

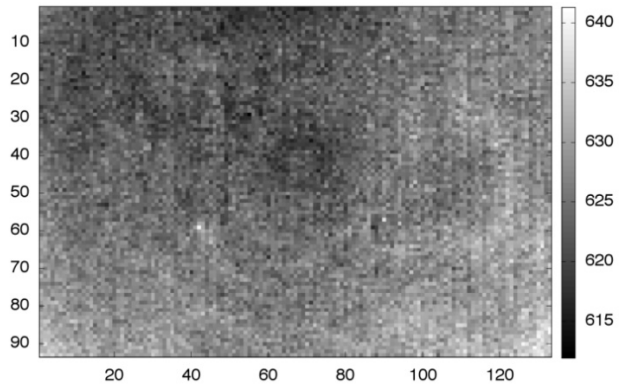

Figure 17. Estimated temperature: *Tabc*.

6. Conclusion

First, the results given by the unbiased model *TNL.Tabc* (using fluxes without Wien approximation and without fluxes ratio) and summarized in Table 2 are very satisfactory for emissivity variations of order between 0 and 2 (Drude model is a more difficult case). The inverse problem being numerically ill-conditioned, if the relative variation of the emissivity (or global spectral transfer function, including the emissivity) is known, it is preferable to use the lowest number of parameters allowing to model emissivity variations. However, in the absence of *a priori* knowledge about the emissivity, the *TNL.Tabc* model seems to be the best compromise.

Next, two different methods for selecting "optimal" wavelengths have been proposed: one through a sequential procedure (not optimal) and the other based on a global minimization with constraints which gives the best results. Although the iterative procedure is less efficient than the global minimization in term of temperature standard deviation, it presents the advantage to show the important of the choice of the different wavelengths.

Furthermore, the experimental results obtained using the *TNL.Tabc* model from the filters available experimentally $\boldsymbol{\lambda_{exp}} = \{2\ ;\ 2.35\ ;\ 2.85\ ;\ 4\}\ \mu m$ (close to theoretical optimal filters $\boldsymbol{\lambda_{opt}} = \{2.03\ ;\ 3.11\ ;\ 4.15\ ;\ 4.65\}\ \mu m$) are also very encouraging with an uncertainty of about 2K (0.3 %) and a standard deviation of 4 K.

To finish, some criteria allowing to not amplify the uncertainty on the measurements have been presented, it has also been shown that there is equivalence between minimizing the relative error on the temperature, maximizing the flux sensitivity to the temperature, or minimizing the standard deviation of the temperature. Furthermore, it has been shown that the wavelengths that minimize the standard deviation of the estimated temperature in monospectral and bispectral methods (without the Wien approximation, *i.e.,* for a Planck law) can be determined by an analogous displacement Wien's law.

References

[1] T. Pierre, B. Rémy, and A. Degiovanni, *Microscale temperature measurement by the multispectral and statistic method in the ultraviolet-visible wavelengths*, J. Appl. Phys., 103, 034904, 2008.

[2] J.-C. Krapez, H. Pron, *Lecture 5: Measurements without contact in heat transfer: principles, implementation and pitfalls*, Metti 6 Advanced School: Thermal Measurements and Inverse Techniques, volume 1, Biarritz, March 1-6, 2014.

[3] C. Rodiet, B. Remy, A. Degiovanni, F. Deumerie, *Optimisation of wavelengths selection used for the multi-spectral temperature measurement by ordinary least squares method of surfaces exhibiting non-uniform emissivity*, *Quantitative InfraRed Thermography Journal*, 2013, vol. 10, n°2, pp. 222-236.

[4] Y. Souhar, B. Rémy, A. Degiovanni, *Thermal Characterization of Anisotropic Materials at High Temperature through Integral Methods and Localized Pulsed Technique*, International Journal of Thermophysics,34, p. 322–340, 2013.

[5] J.L. Gardner, T.P. Jones, M.R. Davies, *A six wavelength radiation pyrometer*, High Temperatures – High Pressures, 13, p. 459-466, 1981.

[6] F. Meriaudeau, *Real time multispectral high temperature measurement: application to control in industry*, Image and Vision Computing, 25(7), p. 1124–1133, 2007.

[7] P. Hervé, J. Cedelle, I. Negreanu, *Infrared technique for simultaneous determination of temperature and emissivity*, Infrared Physics & Technology, 55(1), p. 1-10, 2012.

[8] J.-C. Krapez, *Radiative measurements of temperature*, In: H.R.B. Orlande, O. Fudym, D. Maillet, R. M. Cotta, editors. Thermal measurements and inverse techniques. Boca Raton: CRC Press, Taylor & Francis Group, pp. 185-230, 2011.

[9] C. Rodiet, B. Remy, A. Degiovanni. *Optimal wavelengths obtained from laws analogous to the Wien's law for monospectral and bispectral methods, and general methodology for multispectral temperature measurements taking into account global transfer function including non-uniform emissivity of surfaces*, Infrared Physics and Technology, 76, p. 444-454, 2016.

[10] C. Rodiet, B. Remy, T. Pierre, A. Degiovanni, *Influence of measurement noise and number of wavelengths on the temperature measurement of opaque surface with variable emissivity by a multi-spectral method based on the flux ratio in the infrared-ultraviolet range*. High Temperatures - High Pressures, 44(3), p. 211-226, 2015.

Tutorial 13: Optimal Experiment Design for inverse heat conduction problem

J. Berger[a], **S. Gasparin**[b], **A. Jumabekova**[a]

[a] Laboratoire des Sciences de l'Ingénieur pour l'Environnement (LaSIE), UMR 7356 CNRS, La Rochelle Université, CNRS, 17000, La Rochelle, France
[b] Cerema, French Ministry of Ecological Transition, BPE Research team, 44200 Nantes, France

E-mail: julien.berger@univ-lr.fr

Abstract. The estimation of model unknown parameters in a model through an inverse problem procedure enables an increase in the reliability of the model predictions. Such approach requires defining an experimental campaign to obtain observations of the physical phenomena. However, the accuracy of the estimated parameters strongly depends on the quality of the experimental data. The design of experiments enables the search for the optimal measurement plan that ensures the highest degree of accuracy in parameter estimation. The objective of this tutorial is to introduce some tools for searching the optimal experiment design. It enables answering practical questions such as: what type of measurement techniques to apply? what are the positions and numbers of sensors? What is the starting day and duration of the experimental campaign?

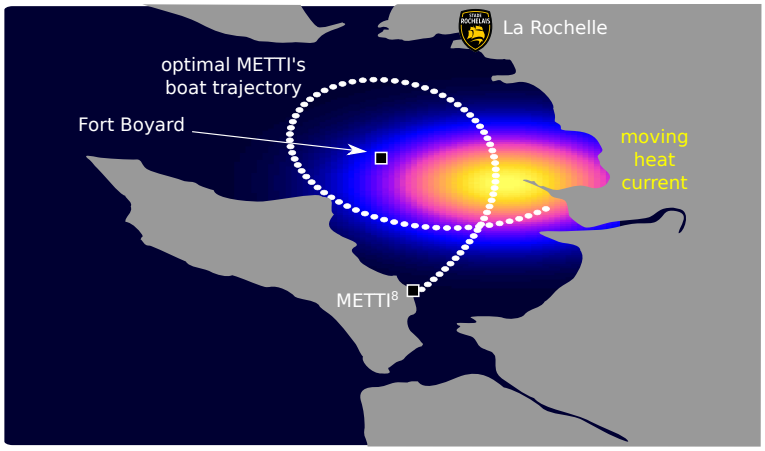

Introductory example: It is well known that Fort Boyard creates a temperature gradient in the sea between La Rochelle and Ile d'Oléron, France. This current moves around the castle according to the sea tides. The METTI [8] scientific committee aims at estimating the magnitude of this temperature gradient. To accomplish this, they sail with a boat equipped with sensors capable of measuring the sea temperature. Starting from Ile d'Oléron's harbor, the question is: why is the trajectory of the boat, illustrated in white dots, the optimal route to estimate the magnitude of the temperature gradient with the highest precision? (this story is purely invented but the scientific question is real.)

This tutorial is dedicated to Prof. James W. "Jim" Beck who was called to his eternal resting place on the 28^{th} of July 2022. He was this unique constructive person who wanted to spread research and encourage everyone to progress in the field of inverse heat conduction problem.

Scope

1 Introduction **3**

2 Searching the Optimal Experiment Design **3**
2.1 Experiment Design 3
2.2 Brief recall on parameter estimation problem 5
2.3 Optimal experiment design 6

3 Practical applications **8**
3.1 Example 1. Steady state model, measurement plan: sensors positions 8
3.2 Example 2. Time dependent model, measurement plan: control variables . . . 9
3.3 Example 3. Heat diffusion equation, measurement plan: sensor position . . . 11
3.4 Example 4. Time dependent model, measurement plan: sensor position and time horizon 14
3.5 Example 5. Lumped capacitance model, measurement plan: control variables 15

4 Coming back to the abstract example: time dependent model, one parameter, moving sensor **17**

5 To go further **19**

6 Conclusion **21**

1 Introduction

Unknown parameters of a model can be determined by solving a parameter estimation problem. The general procedure is illustrated in Figure 1. Such procedure requires an observation, *i.e.* a measurement of a physical phenomena (temperature, heat flux, moisture content, etc.). It also needs a model which depends on the unknown parameters. Given a value of such parameters, the model can predict the physical phenomena. The unknown parameter are retrieved by minimizing the differences, denoted as cost function, between model predictions and observations.
As noted in Figure 1, an experimental design is defined to obtain observations of the physical phenomena. The measurements are obtained by a numbers of sensors, placed at given locations, that monitored the phenomena during a certain time horizon. Some examples of measurement are given in [**?**, **?**, **?**]. In these articles, the experimental observations used to solve the parameter estimation problem are provided without any justification for the chosen design. In [**?**], it can be remarked that authors discuss the influence of the number and location of sensors on the accuracy of the estimated properties of a wood fiber material.
Therefore, an interesting question follows: How to define the experimental design? And more precisely, how to define the experimental design to ensure the maximum accuracy of the estimated parameters? Such design is denoted by Optimal Experiment Design (OED). The word "optimal" is used in the sense that it maximizes the accuracy of the estimates. The objective of this tutorial is to introduce some tools to search OED and discuss the quality of measurements. It enables to answer practical questions such as: what type of measurement techniques to apply? what are the positions and numbers of sensors? what is the starting day and duration of the experimental campaign?
This tutorial is mostly based on three references:

- the early and pedagogical work from Beck *Parameter Estimation in Engineering and Science* [**?**],
- the work from Ucinski *Optimal Measurement Methods for Distributed Parameter System Identification* with a more statistical and partial derivative point of view [**?**],
- the work from Pronzato and Pázman having a state-space representation point of view [**?**],

The knowledge on inverse problem framework and particularly the computation of sensitivity coefficients is an important prerequisite.
The structure of the tutorial is the following. The methodology to search the OED is introduced in Section 2. Then, simple examples are introduced in Section 3 for practical applications. Some complementary remarks to go further on the subjects and general conclusion are provided in Sections 5 and 6.

2 Searching the Optimal Experiment Design

2.1 Experiment Design

First, the experimental design is defined. An example of experimental design is illustrated in Figure 2. Assume a slab which temperature varies according to space, time and some unknown parameters. To retrieve the latter, the slab is submitted to a heat flux density on one side. The rear face is maintained at a certain temperature. The temperature can be recorded by sensors positioned in the slab. The physical phenomenon of transfer occurs through a spatial domain (like a porous media) denoted as $\Omega_x \subset \mathbb{R}^3$ and the temporal one, denoted as $\Omega_t \subset \mathbb{R}_+$.

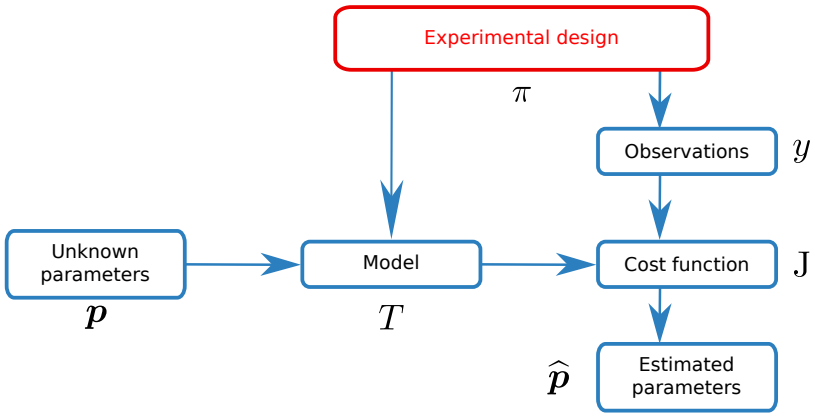

Figure 1: Classical procedure to solve parameter estimation problem.

The experimental design includes M sensors where χ_n is the position of sensor n. We denote by Ω_χ the set of possible sensor positions, which element is:

$$\boldsymbol{\chi} = (\chi_1, \dots, \chi_M) \in \Omega_\chi. \tag{1}$$

Note that $\Omega_\chi \subset \mathbb{R}_+^M$.
Depending on the defined time acquisition, the measurement are obtained for a discrete time grid. The set of time observations is written as Ω_τ, which element is:

$$\boldsymbol{\tau} = (\tau_1, \dots, \tau_I) \in \Omega_\tau, \tag{2}$$

where τ_k is the time when measurement k is obtained. We have $\Omega_\tau \subset \mathbb{R}_+^I$.
In the experimental design, several conditions can be controlled or forced by the investigator. As illustrated in Figure 2, the control (also called command or input) variables can be the forcing conditions (ambient air temperature on the rear face, the incident heat flux density, etc.) and their time variations (signal shape, frequency, amplitude, etc.). In some cases, it is possible to control some physical parameters such as thermophysical properties, surface transfer coefficients, etc. Thus, we define the set of controllable parameters of the measurement plan by Ω_u, which element is:

$$\boldsymbol{u} = (u_1, \dots, u_U) \in \Omega_u, \tag{3}$$

where u_ℓ is one of the U variables which is possible to control and modify in the experiment. In the end, the measurement plan or experimental design π includes *(i)* the number of sensors and their positions, *(ii)* the observation time grids for each sensor and *(iii)* the control variables of the experiments. Thus, the measurement plan is defined by the following set:

$$\Omega_\pi = \Omega_\chi \cup \Omega_\tau \cup \Omega_u \subset \mathbb{R}^{M+I+U}, \tag{4}$$

which one element is given by:

$$\pi = (\boldsymbol{\chi}, \boldsymbol{\tau}, \boldsymbol{u}) \in \Omega_\pi. \tag{5}$$

Once the experiment is done, we obtain by measurement an observable y defined as:.

$$y : \quad \Omega_\pi \longrightarrow \Omega_{\text{obs}} \tag{6a}$$

$$(\boldsymbol{\chi}, \boldsymbol{\tau}, \boldsymbol{u}) \longmapsto y(\boldsymbol{\chi}, \boldsymbol{\tau}, \boldsymbol{u}), \tag{6b}$$

where $\Omega_{\text{obs}} \subset \mathbb{R}^{M+I}$ is the co-domain of the observable data y. In the end, the measurement plan provides a total of $D = M + I$ discrete experimental measurements. For heat conduction problems, the observable field corresponds for instance to temperature, water mass content or heat flux. The interested reader may refer to Figure 3 for the representation of the mathematical mapping diagrams involved in the experimental campaign.

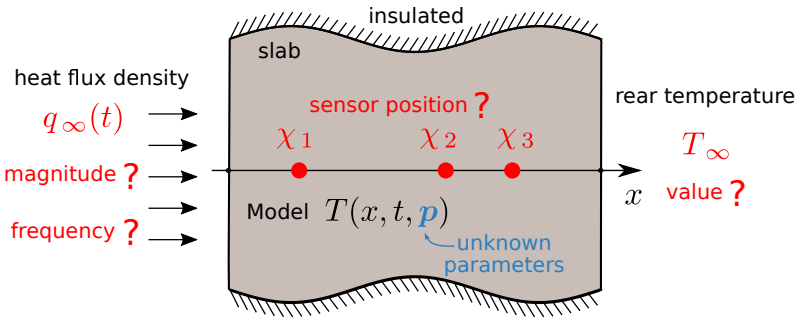

Figure 2: Example of a measurement plan for the estimation of unknown parameters in a material. The parameters that can be included in the measurement plan are highlighted in red color.

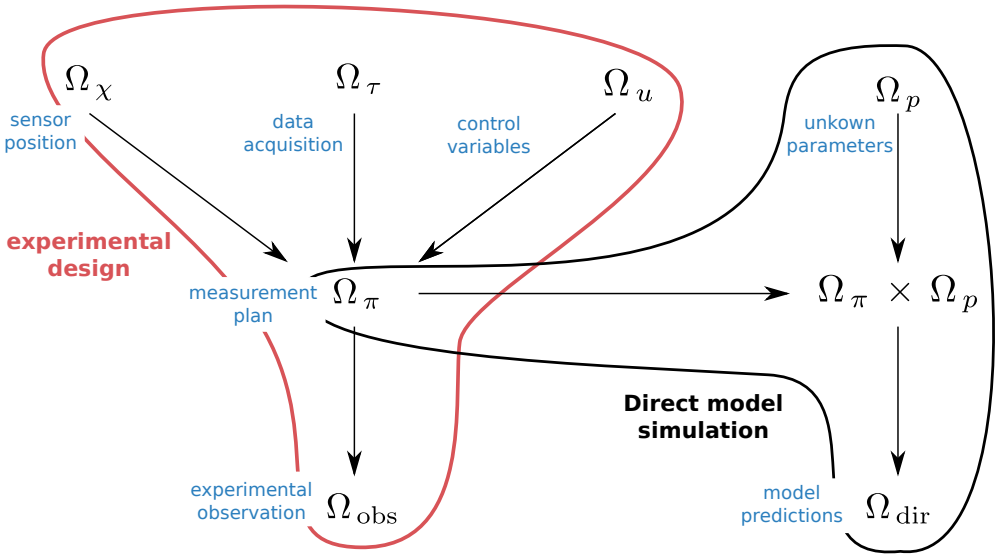

Figure 3: Diagram of the mapping involved in the experimental campaign and the direct problem simulation.

2.2 Brief recall on parameter estimation problem

Once the observable y is hold, the parameter estimation problem can be solved. The unknown parameters are denoted by $\boldsymbol{p}$. A total of N parameters are unknown so that the parameter domain is $\Omega_p \in \mathbb{R}^N$. One may have *a priori* knowledge on the unknown parameters. The confidence in this *a priori* value can be important. These values are generally used as first guesses in the algorithm employed to solve the inverse problem and in the search of OED. The estimates of the unknown parameters $\widehat{\boldsymbol{p}}$ are determined by solving the following minimization

problem:

$$\widehat{\boldsymbol{p}} \;=\; \arg \min_{\boldsymbol{p}\in\Omega_p} \mathrm{J}(\,\boldsymbol{p}\,)\,, \tag{7}$$

where J is the so-called cost function. It corresponds to the difference between the direct problem solution T and the experimental observation of the phenomenon y. Considering the *Least Square Estimator*, it is mathematically defined by:

$$\mathrm{J}(\,\boldsymbol{p}\,) \;=\; \sum_{n=1}^{M}\sum_{k=1}^{I}\left(T\left(\chi_n\,,\tau^k\,,\boldsymbol{u}\,,\boldsymbol{p}\right) \;-\; y\left(\chi_n\,,\tau^k\,,\boldsymbol{u}\right)\right)^2, \tag{8}$$

where T is the prediction of the physical phenomena computed using a model. It is mathematically defined by:

$$T\;:\qquad \Omega_\pi \,\times\, \Omega_p \longrightarrow \Omega_{\mathrm{dir}} \tag{9}$$

$$\left(\boldsymbol{\chi}\,,\boldsymbol{\tau}\,,\boldsymbol{u}\,,\boldsymbol{p}\right) \longmapsto T\big(\boldsymbol{\chi}\,,\boldsymbol{\tau}\,,\boldsymbol{u}\,,\boldsymbol{p}\big)\,. \tag{10}$$

The prediction T can be obtained as a solution of any model. It can be formulated using partial or ordinary differential equations, as well as very simple approach such as polynomials. The solution of the model can be obtained by numerical or analytical approaches, depending on the nature of the equations.
Last, the sensitivity coefficients can be computed to evaluate how the variation in the model parameters affects the model predictions. The sensitivity related to an individual parameter p is defined as the partial derivative of the model output and called the sensitivity coefficient X_p [**?**]:

$$X_p\;:\qquad \Omega_\pi \,\times\, \Omega_p \longrightarrow \Omega_{\mathrm{dir}} \tag{11a}$$

$$\left(\boldsymbol{\chi}\,,\boldsymbol{\tau}\,,\boldsymbol{u}\,,\boldsymbol{p}\right) \longmapsto \frac{\partial T}{\partial p}\,. \tag{11b}$$

High values of X_p indicate that T is more sensitive to p, *i.e.*, small changes in p cause large changes in the model output. The computation of X_p can be performed either through the direct differentiation of model–governing equations [**?**], using the finite difference approximations or complex step differentiation [**?**]. Note that a scaled version of the sensitivity coefficient can be defined as $\dfrac{\sigma_p}{\sigma}\dfrac{\partial T}{\partial p}$ with σ_p the uncertainty on *a priori* parameter and σ the measurement uncertainty. Last, a diagram of the mathematical mapping corresponding to the direct problem simulation is given in Figure 3.

2.3 Optimal experiment design

By analyzing the diagram in Figure 3, it can be noted that the direct problem solution is influenced by the experimental design π. It means that the choice of the experimental configuration directly impacts the parameter estimation. Thus, one may ask the following question: is it possible to define an optimal experiment design ensuring the estimation of the unknown parameters with maximum accuracy? The answer to this question corresponds to search for the optimal experiment design (OED).
In the analysis of optimal experiments for the estimation of unknown parameters, we define the normalized Fisher information matrix:

$$\boldsymbol{\mathcal{F}}\;:\,\Omega_{\mathrm{dir}}\times\Omega_{\mathrm{dir}} \longrightarrow \mathcal{M}\Big(\mathbb{R}\,,\;N\,,\,N\Big)\,, \tag{12a}$$

$$\left(X_{p_i}\,,X_{p_j}\right) \longmapsto \Big[F_{ij}\Big]\,,\qquad\qquad \forall\left(i\,,j\right)\,\in\,\big\{1,\ldots,N\big\}^2\,, \tag{12b}$$

where

$$F_{ij} = \frac{1}{M\,I} \sum_{n=1}^{M} \sum_{k=1}^{I} \frac{\sigma_p^2}{\sigma\left(\chi_n, \tau^k\right)^2} X_{p_i}\left(\chi_n, \tau^k, \boldsymbol{u}, \boldsymbol{p}\right) X_{p_j}\left(\chi_n, \tau^k, \boldsymbol{u}, \boldsymbol{p}\right), \quad (13)$$

where σ is the observations uncertainty related to sensor χ_n and measurement obtained at time τ^k. The matrix $\boldsymbol{\mathcal{F}}$ characterizes the total sensitivity of the system. If the accuracy of the measurement is low, then the term of the matrix is high, indicating a good sensitivity of the problem. The term $\frac{1}{M\,I}$ is introduced to scale each term of the matrix. If this term is not introduced, then the more sensors and the longer is the time measurement, the better will be the sensitivity of the problem.
The quality index, so-called D–optimum criterion Ψ, is used to assess the accuracy of the estimated unknown parameters:

$$\Psi : \mathcal{M}\Big(\mathbb{R},\ N,\ N\Big) \longrightarrow \mathbb{R}_+, \quad (14a)$$

$$\boldsymbol{\mathcal{F}} \longmapsto \det\left(\boldsymbol{\mathcal{F}}\right). \quad (14b)$$

Note that a theoretical justification as well as interesting discussions on the choice of the quality index (14a) are provided in [**?**, **?**].
The Optimal Experiment Design, which is the experimental configuration ensuring maximum accuracy when estimating the unknown parameters, can be defined by the measurement plan verifying π°:

$$\pi^\circ = \arg \max_{\pi \in \Omega_\pi} \Psi(\pi). \quad (15)$$

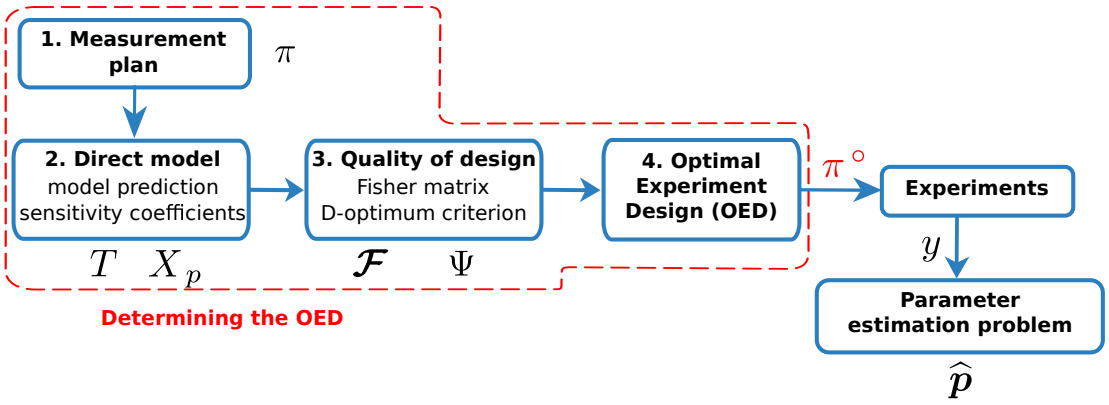

Figure 4: Illustration of the procedure to search for the optimal experiment design.

The different steps to determine the OED are illustrated in Figure 4. The first one is to define the measurement plan by setting the control variables, the number of sensors and the data acquisition. The second step is to define a numerical strategy to compute the direct model prediction and the sensitivity coefficients, given a value of the unknown parameter. Third step aims at computing the FISHER MATRIX and D-optimum criterion, used to evaluate the quality of the experiment design. Finally, the issue is to find the optimal plan. From a practical point of view, there is generally no analytical solution to Eq. (15). Thus, two strategies can be employed. The first one, is the so-called exhaustive search (or brutal force) which may lead to a local maximum. We define a set for the measurement plan Ω_π, *i.e.* a domain of variation for the sensor positions $\boldsymbol{\chi}$, the time grid of observation $\boldsymbol{\tau}$ for the controllable parameters $\boldsymbol{u}$. Then, we compute the criterion Ψ for each element of the given set of measurement plan Ω_π to

find its maximum. The alternative strategy is to consider Eq. (15) as an optimization problem and use suitable algorithm to find the maximum. In the end, when the OED is determined, the experimental campaign can be carried to generate the measurement and solve the parameter estimation problem.
An important remark concerns the dependency of the criterion Ψ according to the unknown parameters. One understands that the computations require an *a priori* value of parameter p^{apr}, since the inverse problem is not solved and the unknown parameter is not determined yet.

3 Practical applications

In the followings, practical and simple examples are proposed to search for optimal experiment design.

3.1 Example 1. Steady state model, measurement plan: sensors positions

A simple model is considered to introduce the search of the OED. In steady state condition the temperature in a slab is approximated by a first order polynomial. The model can be written as:

$$T\left(x\,,\,p_1\,,\,p_2\right) \;=\; p_1 \;+\; p_2 \cdot x\,, \qquad x \;\in\; \left[\,0\,,\,1\,\right], \qquad \left\{\,p_1\,,\,p_2\,\right\} \in \mathbb{R}^2\,, \tag{16}$$

where $x \in \left[\,0\,,\,1\,\right]$ is the space domain where sensors can be placed and $\left\{\,p_1\,,\,p_2\,\right\} \in \mathbb{R}^2$ are the $N \;=\; 2$ unknown parameters. Several observations can obtained by placing temperature sensors at different positions in the space domain, to solve the parameter estimation problem. The issue is to search the OED in terms of two sensor positions.
step 1. We assume $M \;=\; 2$ sensors at the positions χ_1 and χ_2 respectively. The measurement plan is defined by:

$$\Omega_\pi \;=\; \left\{\,\chi_1\,,\,\chi_2\,\right\}, \qquad\qquad \forall\left(\,\chi_1\,,\,\chi_2\,\right) \;\in\; \left[\,0\,,\,1\,\right]^2, \tag{17}$$

so each sensor can be placed in any part of the slab. It is assumed that there is no controllable parameters $\Omega_u \;=\; \emptyset$ and that the measurement is performed for one unique time ($I \;=\; 1$).
step 2. We compute the sensitivity coefficients of the two parameters p_1 and p_2 (for all spatial variable x):

$$X_{p_1}\left(\,x\,,\,p_1\,,\,p_2\,\right) \;=\; \frac{\partial T}{\partial p_1} \;=\; 1\,, \qquad\qquad X_{p_2}\left(\,x\,,\,p_1\,,\,p_2\,\right) \;=\; \frac{\partial T}{\partial p_2} \;=\; x\,. \tag{18}$$

On one hand, the sensitivity of the model to the parameter p_1 is invariant with the sensor position. In other words, the estimation of this parameter is independent to the measurement plan. On the other hand, the sensitivity function for parameter p_2 increases with the sensor position. The sensitivity is maximum at the maximum value of x.
step 3. We compute the D-optimum criterion. Considering $\sigma \;=\; \sigma_p \;=\; 1$, the Fisher matrix is given by:

$$\boldsymbol{\mathcal{F}} \;=\; \frac{1}{2}\begin{pmatrix} 2 & \chi_1 \;+\; \chi_2 \\ \chi_1 \;+\; \chi_2 & \chi_1^2 \;+\; \chi_2^2 \end{pmatrix},$$

and the criterion:

$$\Psi \;=\; \det\,\boldsymbol{\mathcal{F}} \;=\; \left(\,\chi_1 \;-\; \chi_2\,\right)^2.$$

Here, the Fisher matrix $\boldsymbol{\mathcal{F}}$ and the criterion Ψ do not depend on the parameter p_1 and p_2. Thus, the determination of the OED is independent of the *a priori* knowledge on the unknown parameters.

step 4. Figure 5 gives the variation of the criterion with the position of the two sensors. It is maximum for the two following measurement plan:

$$\pi^\circ = \left\{ \chi_1^\circ = 0\,,\, \chi_2^\circ = 1 \right\},$$
$$\pi^\circ = \left\{ \chi_1^\circ = 1\,,\, \chi_2^\circ = 0 \right\}.$$

Therefore, to estimate parameters p_1 and p_2 with maximum accuracy, the sensor has to be positioned at each extremity of the space domain $\left[0\,,\,1\right]$.

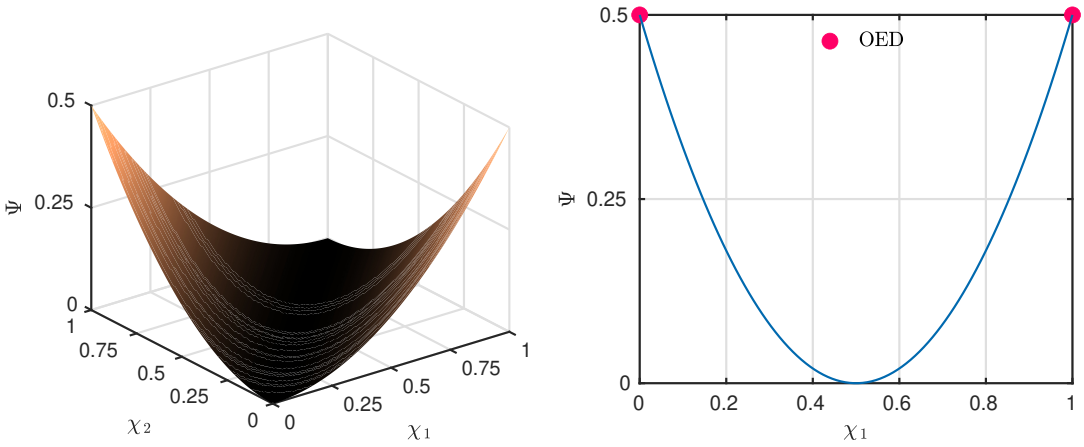

Figure 5: Variation of the D-optimum criterion according to the two sensors positions χ_1 and χ_2 *(a)* and for the particular case $\chi_2 = 1 - \chi_1$ *(b)*.

3.2 Example 2. Time dependent model, measurement plan: control variables

The following transient model is considered to represent the temperature in a slab according to time:

$$T\left(t\,,\,p_1\right) = T_0 + p_1\left(u_1\,\sin\!\left(2\,\pi\,u_2\,t\right) - 1\right), \qquad t \in \left[0\,,\,1\right], \qquad p_1 \in \mathbb{R},$$

where p_1 is the unknown parameter ($N = 1$). $u_1 \in \left[0.5\,,\,4\right]$ and $u_2 \in \left[0.1\,,\,2\right]$ are the control variables, corresponding to the amplitude and frequency of the imposed signal. The objective is to determine the optimal signal to determine p_1 with maximum accuracy. It is assumed that $I = 101$ measurements are performed with a time step $\Delta\tau = 0.01$ with $M = 1$ sensor.

step 1. The measurement plan is defined by:

$$\Omega_\pi = \left\{ u_1\,,\, u_2 \right\}, \qquad \forall\left(u_1\,,\,u_2\right) \in \left[0.5\,,\,4\right] \times \left[0.1\,,\,2\right],$$

so the amplitude of the signal can be controlled between 0.5 and 4 while the frequency between 0.1 and 2. The model does not vary with space, so the sensor position design is null $\Omega_\chi = \emptyset$. The time acquisition is not part of the OED investigations.

step 2. We compute the sensitivity coefficients of the parameter p_1:

$$X_{p_1}\left(t\right) = \left(u_1\,\sin\!\left(2\,\pi\,u_2\,t\right) - 1\right),$$

which is independent on the unknown parameter.

step 3. We compute the D-optimum criterion. Considering $\sigma = \sigma_p = 1$, the FISHER matrix is given by:

$$\mathcal{F} = \frac{1}{I} \sum_{k=1}^{I} \Big(u_1 \sin\big(2\pi u_2 k \Delta\tau\big) - 1 \Big)^2 .$$

Since there is only one parameter, the criterion is given directly by the FISHER matrix:

$$\Psi = \frac{1}{I} \sum_{k=1}^{I} \Big(u_1 \sin\big(2\pi u_2 k \Delta\tau\big) - 1 \Big)^2 .$$

step 4. The OED is searched using the exhaustive strategy with 100 values of both variables u_1 and u_2 in their respective domain of definition $[0.5, 4]$ and $[0.1, 2]$. Figure 6 gives the variation of the criterion with two control variables. It is maximum for the two following measurement plan:

$$\pi^\circ = \{ u_1^\circ = 4, u_2^\circ = 0.89 \} .$$

In this example, the determination of the OED is independent of the *a priori* knowledge on the unknown parameter p_1. It is also interesting to note that the amplitude of the signal u_1 has to be maximal to determine p_1 with accuracy.

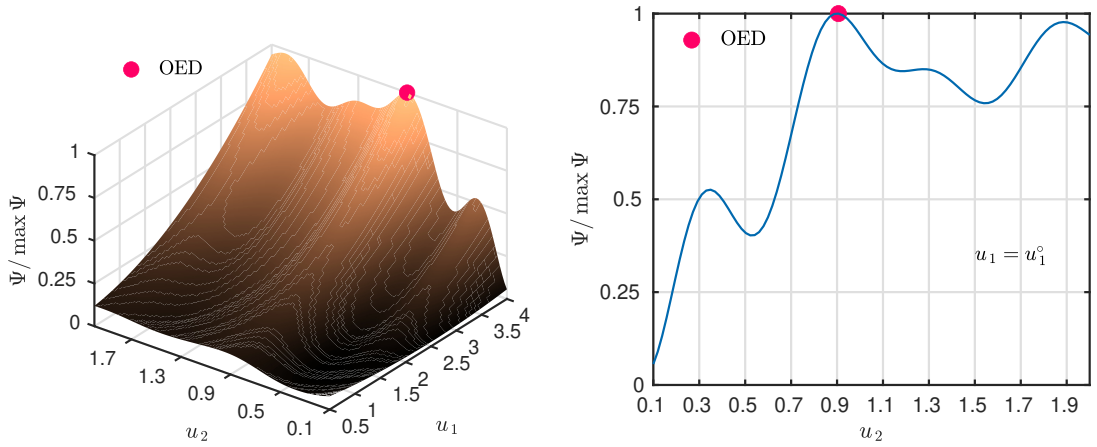

Figure 6: Variation of the D-optimum criterion according to the two control variables u_1 and u_2 *(a)* and for the particular case where u_1 is set to the OED value *(b)*.

Remark 1: *Continuous approach*

When measurements are carried out continuously over time, *i.e.* with a constant (small) time step acquisition, it is possible to formulate the D-optimum criterion as:

$$\Psi = \int_0^1 X_{p_1}^2 \, \mathrm{d}t ,$$

which gives:

$$\Psi = \frac{-1}{4\pi u_2} \Big(-2u_1^2 \pi u_2 + u_1^2 \cos\big(2\pi u_2\big) \sin\big(2\pi u_2\big) - 4\pi u_2 - 4u_1 \cos\big(2\pi u_2\big) + 4u_1 \Big) .$$

Such equation can be solved analytically (by looking at the first and second derivatives) according to the control variables to find the optimal value of u_1° and u_2°.

■

Remark 2: *Verification of the accuracy of the estimates according to the measurement plan*

The impact of the measurement plan on the accuracy of the estimates can be evaluated by generating synthetic experimental data. For this, the following procedure is adopted: *(i)* we numerically generate 10^6 observations y using the direct problem model and adding a noise of 0.1 magnitude, generated with a normal distribution. The measurements are produced for two measurement plans, *i.e* two values of the control variables u_1 and u_2. The first one is the OED $\pi = \pi^\circ$ while the second has a D-optimum criterion equals to 5% of the OED one. For the latter, the control variables are $\pi = \{u_1 = 4, u_2 = 0.1\}$. Then *(ii)* the parameter p_1 is estimated using the synthetic observations. The accuracy of the estimated parameters with the real ones is analyzed as a function of the measurement plans. Figure 7 presents the probability distribution of the estimates. It can be remarked that the standard deviation in the estimation of the parameter is smaller by one order for the OED measurement plan.

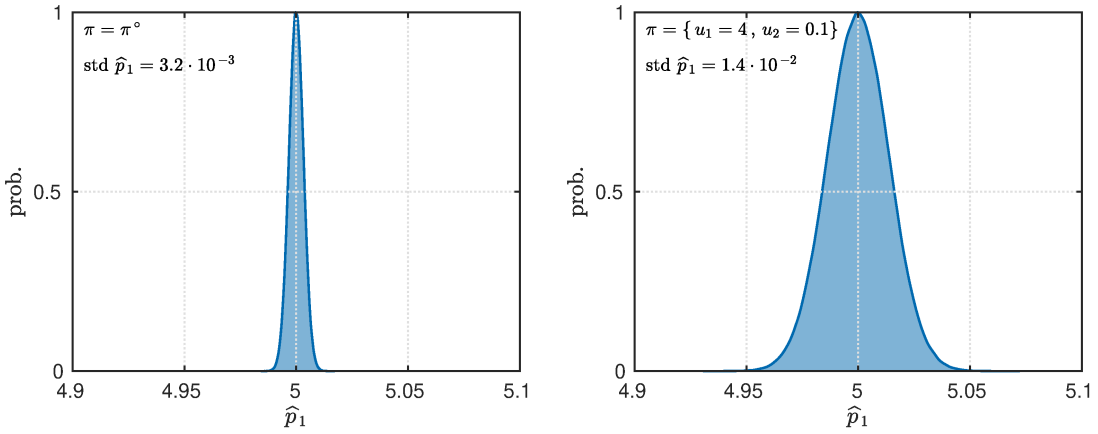

Figure 7: Probability distribution of the estimate $\widehat{p}_1$ for 10^6 synthetic observations sampled for OED measurement plan *(a)* and for a plan where the D-optimum criterion equals 5% of the OED one *(b)*.

■

3.3 Example 3. Heat diffusion equation, measurement plan: sensor position

Considering the following model of heat transfer in a slab:

$$\frac{\partial T}{\partial t} - p_1 \frac{\partial^2 T}{\partial x^2} = 0,$$

where p_1 is the unknown diffusivity. The following boundary and initial conditions are defined:

$$T = \bar{T}, \quad x = \{0, L\},$$
$$T = \bar{T} + T_0 \sin(\lambda x), \quad t = 0, \quad \lambda = \frac{\pi}{L}.$$

For this specific case, an analytical solution exists:

$$T\left(x\,,\,t\,,\,p_1\right) \;=\; \bar{T} \;+\; T_0\,\exp\Big(-p_1\,\lambda^2\,t\Big)\,\sin\big(\lambda\,x\big)\,,$$

defined for $x \in \left[0\,,\,L\right]$ and $t \in \left[0\,,\,t_{\rm f}\right]$. The optimal experiment design is searched in terms of sensor position. The number of measurements is set with a time step $\Delta\tau$.
step 1. The measurement plan is defined by the position of the sensor:

$$\Omega_\pi \;=\; \big\{\,\chi\,\big\}\,, \qquad\qquad \forall\,\chi \;\in\; \left[0\,,\,L\right].$$

The time acquisition is not part of the OED investigations.
step 2. We compute the sensitivity coefficients of the parameter p_1:

$$X_{p_1}\big(x\,,\,t\,,\,p_1\big) \;=\; -\,T_0\,\lambda^2\,t\,\exp\Big(-p_1\,\lambda^2\,t\Big)\,\sin\big(\lambda\,x\big)\,.$$

step 3. We compute the D-optimum criterion. Considering $\sigma \;=\; \sigma_p \;=\; 1$, the FISHER matrix is given by:

$$\boldsymbol{\mathcal{F}} \;=\; \frac{1}{I}\;\sum_{k=1}^{I} T_0^2\,\lambda^4\,k^2\,\Delta\tau^{\,2}\,\exp\Big(-2\;p_1\,\lambda^2\,k\,\Delta\tau\Big)\,\sin^2\big(\lambda\,\chi\big)\,.$$

After analytical computations, the D-optimum criterion is:

$$\Psi \;=f(\,I\,)\Big(\cos^2\big(\lambda\,\chi\big)\;-\;1\Big)\,, \tag{19a}$$

$$f(\,I\,) \;=\; \exp(2\,p1\,\lambda^2\,\Delta\tau)\,T_0^2\,\lambda^4\,\Delta\tau^2\,\Bigg(\,I^2\,\exp(-2\,p1\,\lambda^2\,\Delta\tau\,(I-1))+2\,I\,\exp(-2\,p1\,\lambda^2\,\Delta\tau\,(I-1)) \tag{19b}$$

$$-\,2\,I^2\,\exp(-2\,p1\,\lambda^2\,\Delta\tau\,I)+\exp(-2\,p1\,\lambda^2\,\Delta\tau\,(I-1))-\exp(2\,p1\,\lambda^2\,\Delta\tau) \tag{19c}$$

$$-\,2\,I\,\exp(-2\,p1\,\lambda^2\,\Delta\tau\,I)+I^2\,\exp(-2\,p1\,\lambda^2\,(I+1)\,\Delta\tau)+\exp(-2\,p1\,\lambda^2\,\Delta\tau\,I)-1\,\Bigg) \tag{19d}$$

$$\cdot\,\Bigg(\,I\,\Big(\,\exp(2\,p1\,\lambda^2\,\Delta\tau)-1\,\Big)^3\,\Bigg)^{-1} \tag{19e}$$

step 4. In this particular case, the OED problem has an analytical solution. In the interval $\chi \in \left[0\,,\,L\right]$, the criterion is maximum for:

$$\chi^\circ \;=\; \frac{\pi}{2\,\lambda} \;=\; \frac{L}{2}\,. \tag{20}$$

This results is independent on the *a priori* value of the unknown parameter p_1. The readers are invited to verify this results using an exhaustive (or maximization) strategy. For numerical applications, the following values are used $p_1 \;=\; 2\cdot 10^{-3}$, $\bar{T} \;=\; 10$, $T_0 \;=\; 5$, $\Delta\tau \;=\; 10^{-2}$ and $L \;=\; 0.1$. Figure 8(a) presents the exhaustive search of the OED for 100 values of the sensor position in $\left[0\,,\,L\right]$. Figure 8(b) shows that the optimal position corresponds to the points of higher magnitude of temperature.

Remark 3: *Considering the number of time acquisition in the measurement plan*

The measurement plan can be defined by the number of time acquisition of the observation:

$$\Omega_\pi \;=\; \big\{\,I\,\big\}\,, \qquad\qquad \forall\,I \;\in\; \mathbb{N}\,, \tag{21}$$

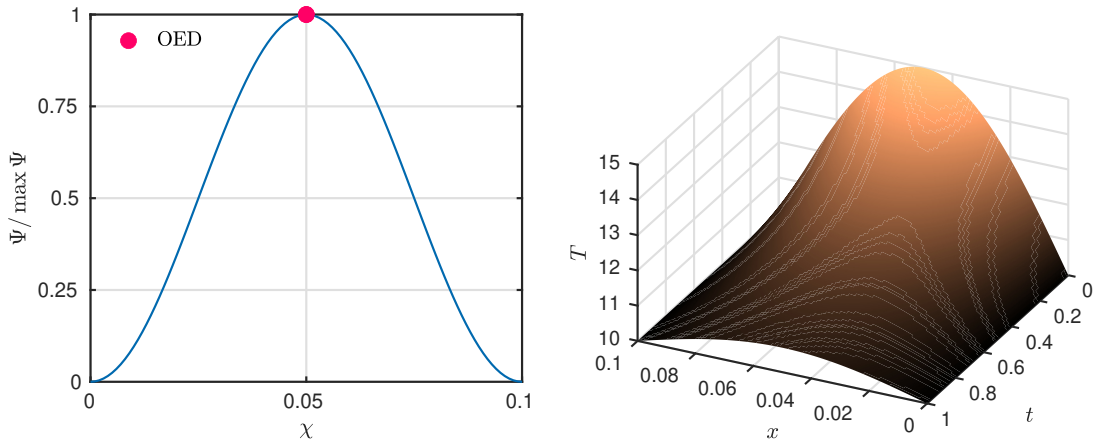

(a) (b)

Figure 8: Variation of the D-optimum criterion according to the sensor position χ *(a)* and variation of the model prediction according to space and time *(b)*.

for a sensor placed at the optimal location $\chi = \frac{L}{2}$. Results from Eq. (19a) are true for this measurement plan. The maximization of the D-optimum criterion can be investigated using the brutal force strategy for 10^3 values of I in the interval $\left[1, 10^3\right]$. Results are illustrated in Figure 9(a) and the optimal number of data acquisition is $I^\circ = 86$. An important point is that function $f(I)$ in Eq. (19a) varies with the the parameter p_1. Thus, the OED depends on the *a priori* value as shown in Figure 9(b).

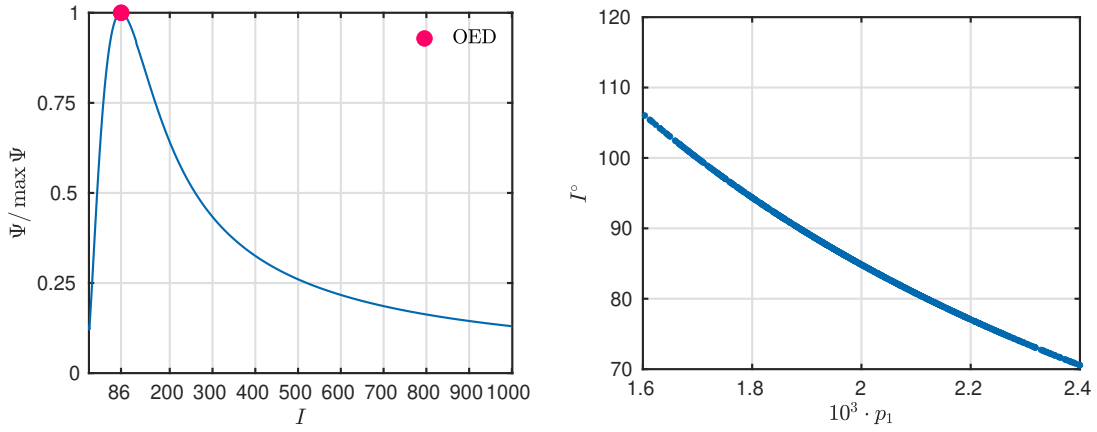

(a) (b)

Figure 9: Variation of the D-optimum criterion according to the number of time acquisition I *(a)* and optimal number of acquisition with the *a priori* value of the unknown parameter *(b)*.

■

3.4 Example 4. Time dependent model, measurement plan: sensor position and time horizon

The following transient model is considered to represent the temperature in a slab according to time:

$$T\left(x\,,\,t\,,\,p_1\,,\,p_2\right) \;=\; p_1\,\frac{x^{\,2}}{H^{\,2}}\left(1\;-\;\frac{x}{H}\right)\exp\!\left(-\,p_2\,t\right), \tag{22}$$

$$t\;\in\;\left[\,0\,,\,\tau_{\rm f}\,\right],\quad x\;\in\;\left[\,0\,,\,H\,\right],\quad \left(p_1\,,\,p_2\right)\;\in\;\mathbb{R}^{\,2}_{*}, \tag{23}$$

where $\left(p_1\,,\,p_2\right)$ are the unknown parameters ($N\;=\;2$). Consider $M\;=\;1$ sensor to be placed in the slab. The objective is to determine the optimal sensor position χ and the time horizon $\tau_{\rm f}$ of the experiments. It is assumed that measurements are monitored with a constant time step $\Delta\tau$ so that $\tau_{\rm f}\;=\;\Delta\tau\cdot(\,I-1\,)$.

step 1. The measurement plan is defined by:

$$\Omega_{\,\pi}\;=\;\left\{\,\chi\,,\,\tau_{\rm f}\,\right\},\qquad\qquad \forall\left(\,\chi\,,\,I\,\right)\;\in\;\left[\,0\,,\,H\,\right]\;\times\;\left\{\,1\,,\,\ldots\,,\,100\,\right\}, \tag{24}$$

so that the sensor position and number of measurement I can be chosen in the experimental design.

step 2. We compute the sensitivity coefficients for both parameters:

$$X_{p_1}\left(\,x\,,\,t\,,\,p_2\,\right)\;=\;\frac{x^{\,2}}{H^{\,2}}\left(1\;-\;\frac{x}{H}\right)\exp\!\left(-\,p_2\,t\right), \tag{25}$$

$$X_{p_2}\left(\,x\,,\,t\,,\,p_1\,,\,p_2\,\right)\;=\;-\,p_1\,\frac{x^{\,2}}{H^{\,2}}\left(1\;-\;\frac{x}{H}\right)t\,\exp\!\left(-\,p_2\,t\right). \tag{26}$$

step 3. We compute the D-optimum criterion. Assuming $\sigma\;=\;\sigma_p\;=\;1$, the terms of the Fisher matrix are:

$$F_{1\,1}\;=\;\frac{1}{I}\sum_{k=0}^{I-1}X^{\,2}_{p_1}\left(\,\chi\,,\,k\cdot\Delta\tau\,,\,p_2\,\right), \tag{27}$$

$$F_{1\,2}\;=\;\frac{1}{I}\sum_{k=0}^{I-1}X_{p_1}\left(\,\chi\,,\,k\cdot\Delta\tau\,,\,p_2\,\right)\cdot X_{p_2}\left(\,\chi\,,\,k\cdot\Delta\tau\,,\,,p_1\,,\,p_2\,\right), \tag{28}$$

$$F_{2\,2}\;=\;\frac{1}{I}\sum_{k=0}^{I-1}X^{\,2}_{p_2}\left(\,\chi\,,\,k\cdot\Delta\tau\,,\,p_1\,,\,p_2\,\right). \tag{29}$$

Note that the complete analytical expressions can be obtained. Then, with linear algebra computations, the D-optimum criterion can be obtained:

$$\Psi\;=\;f(\,\chi\,)\cdot g(\,I\,) \tag{30}$$

with

$$f(\,\chi\,)\;=\;-\chi^{\,8}\cdot(\,H\;-\;\chi\,)^{\,4}\cdot p_1^{\,2}\,\Delta\tau^{\,2}, \tag{31a}$$

$$g(\,I\,)\;=\left(-2\,I^{\,2}\,\exp\Big(-\beta\,(I-3)\Big)+I^{\,2}\,\exp\Big(-\beta\,(I-4)\Big)+I^{\,2}\,\exp\Big(-\beta\,(I-2)\Big)\right. \tag{31b}$$

$$\left.+\,2\,\exp\Big(-\beta\,(I-3)\Big)-\exp\Big(-\beta\,(2\,I-3)\Big)-\exp\Big(3\,\beta\Big)\right) \tag{31c}$$

$$\left(H^{\,12}\left(\exp(\beta)-1\right)^{\,4}I^{\,2}\right)^{\,-1},\quad \beta\;=\;2\,p_2\,\Delta\tau\,. \tag{31d}$$

step 4. The interesting point is that the D-optimum criterion is a product of two functions, one for each parameter of the design plan. Thus, considering function $f(\chi)$ the OED can be computed analytically and is given by:

$$\chi^\circ = \frac{2}{3} H \,. \tag{32}$$

Regarding function $g(I)$, the maximum can be computed using a numerical approach with maximization or brutal force strategy. Following values are considered for the numerical applications: $H = 3$, $p_1 = 20$, $\Delta\tau = 10^{-1}$ and $p_2 = 0.5$. Results are shown in Figure 10(a). As remarked in Eq. (30), the OED depends on the *a priori* value of p_1 and p_2. To investigate such influence, for each parameters we assume a normal probability with 10% of standard deviation:

$$p_1 = \mathcal{N}(20, 2), \qquad p_2 = \mathcal{N}(0.5, 0.05). \tag{33}$$

For 10^6 values samples according to such probabilities, the optimal number of data acquisition I° is computed using the maximization strategy of Eq. (30). Figure 10(b) presents the resulting probability of I°. Such results provide an idea of variation of the optimal number of data acquisition to perform the experimental campaign.

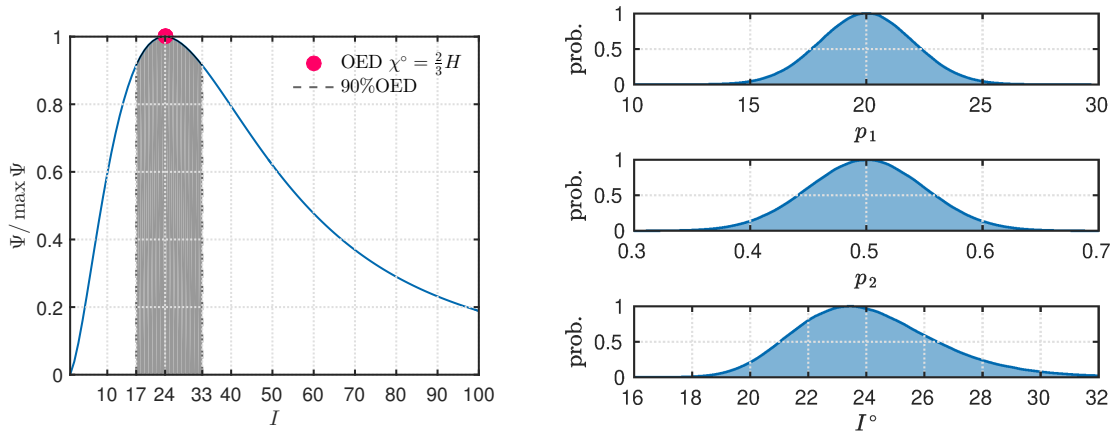

(a) (b)

Figure 10: Variation of the D-optimum criterion according to the number of time acquisition I *(a)* and optimal number of acquisition with the *a priori* value of the unknown parameter *(b)*.

3.5 Example 5. Lumped capacitance model, measurement plan: control variables

The temperature in a slab is modeled by the following ordinary differential equation:

$$\frac{\mathrm{d}T}{\mathrm{d}t} = p_1 \left(T_\infty - T \right) + q(t), \qquad \forall t \in \left[0, 1 \right], \tag{34}$$

with p_1 the unknown parameter ($N = 1$) playing the role of a Biot number, T_∞ the temperature of the air surrounding the slab and q a heat source term that can be controlled according to:

$$q(t) = q_0 \Big(1 - \exp\big(-u_1 t\big) \Big) \exp\big(-u_1 t\big) \sin\big(\pi u_2 t\big), \tag{35}$$

where u_1 and u_2 are the control variables of the experiment, corresponding to the frequency of the signal and fluctuation of the heat source. One sensor enables to measure the temperature according to time. Measurement are obtained with a constant time step $\Delta\tau$ and a fixed number of measurements $I = 101$. The objective is to determine the optimal control variables u_1 and u_2 of the experiment.

step 1. The measurement plan is defined by:

$$\Omega_\pi \;=\; \{u_1\,,\,u_2\}\,, \qquad\qquad \forall\,(u_1\,,\,u_2) \;\in\; [0\,,\,10] \;\times\; [0.1\,,\,5]\,. \tag{36}$$

step 2. The governing equation can be solved to obtain the solution:

$$T\,(t\,,\,p_1) \;=\; T_\infty \;+\; \exp(-p_1\,t) \int_0^t \exp(p_1\,z)\,q(z)\,\mathrm{d}z\,, \tag{37}$$

and the sensitivity coefficient for the parameter is given by:

$$X_{p_1}\,(t\,,\,p_1) \;=\; -\;t\,\exp(-p_1\,t) \int_0^t \exp(p_1\,z)\,q(z)\,\mathrm{d}z \tag{38a}$$

$$+\;\exp(-p_1\,t) \int_0^t z\,\exp(p_1\,z)\,q(z)\,\mathrm{d}z\,. \tag{38b}$$

step 3. We compute the D-optimum criterion. For the sake of compactness, the complete analytical expressions is not detailed.

step 4. An exhaustive search is carried out using the following numerical values: $p_1 = 1$, $T_\infty = 20$ and $q_0 = 500$. Figure 11(a) is obtained considering 100 values of u_1 and u_2. The optimal design is defined for:

$$u_1^\circ \;=\; 1.81\,, \qquad u_2^\circ \;=\; 1.09\,. \tag{39}$$

The corresponding flux and temperature according to time are presented in Figure 11(b).

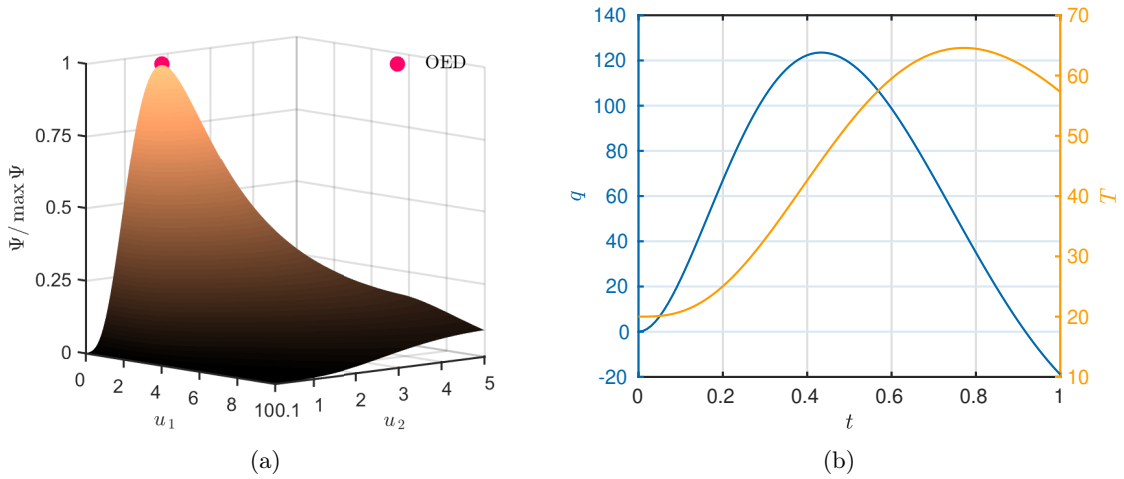

(a) (b)

Figure 11: Variation of the D-optimum criterion according to the two control variables u_1 and u_2 *(a)* and time variation of the heat source and model prediction for the OED case *(b)*.

4 Coming back to the abstract example: time dependent model, one parameter, moving sensor

It is well known that Fort Boyard creates a temperature gradient in the sea between La Rochelle and île d'Oléron, France[1]. This current moves around the castle according to the sea tides as illustrated in Figure 12(a). During the METTI 8 school, the scientific committee aims to estimate the magnitude of this temperature gradient. To accomplish this, they have a boat equipped with sensors capable of measuring the sea temperature. Starting from Île d'Oléron's harbor, the committee can sail over the day to monitor the temperature. The question is: what is the optimal trajectory of the boat to estimate the magnitude of the current temperature with the highest precision?
The model of the moving heat current is given by:

$$T\left(x\,,\,y\,,\,t\,,\,p_1\right) \;=\; T_0 \;+\; p_1\,\exp\!\left(\frac{1}{s}\left(x \;-\; x_0(t)\right)^2\right)\,\exp\!\left(\frac{1}{s}\left(y \;-\; y_0(t)\right)^2\right), \quad (40)$$

$$x_0(t) \;=\; x_c \;+\; R\,\cos\!\big(2\,\pi\,t\big)\,, \quad (41)$$

$$y_0(t) \;=\; y_c \;+\; R\,\sin\!\big(2\,\pi\,t\big)\,, \quad (42)$$

where $\left(x_c\,,\,y_c\right)$ are the center of the moving current (Fort Boyard), R is the radius of movement, T_0 is the sea water temperature and p_1 is the unknown parameter corresponding to the magnitude of the temperature gradient implied by the current. The time and space domains are given by $(x\,,\,y) \in \big[\,0\,,\,1\,\big]^2$ and $t \in \big[\,0\,,\,1\,\big]$.
The starting position of the boat is denoted χ_0. It is sailing with a velocity vector field is defined by:

$$\boldsymbol{v}(t) \;=\; \Big(v_x(\tau)\,,\,v_y(\tau)\Big)\,, \quad (43)$$

which is driven by the motor velocity $v_0 \in \big[\,0\,,\,v_\infty\,\big]$ and the sailing direction angle $\theta \in \big[\,0\,,\,2\,\pi\,\big]$, which both vary with time:

$$v_x(\tau) \;=\; v_0(\tau)\cdot\cos\big(\theta(\tau)\big)\,, \qquad v_y(\tau) \;=\; v_0(\tau)\cdot\sin\big(\theta(\tau)\big)\,, \quad (44)$$

where v_∞ is the maximal velocity. A number of I measurement are recorded over the time interval of investigations with a time step $\Delta\tau$. One sensor ($M \;=\; 1$) is placed on the boat that is sailing over time.
step 1. The sensor position is varying in time and is defined by:

$$\boldsymbol{\chi}(\tau) \;=\; \big(\chi_x(\tau)\,,\,\chi_y(\tau)\big)\,, \quad (45)$$

where χ_x and χ_y are the position on x and y coordinates at a time of acquisition τ. Thus, the measurement plan is defined by the positions of the sensor (the boat) at each time τ^k during the monitoring:

$$\Omega_\pi \;=\; \Big\{\,\boldsymbol{\chi}^k\,\big|\,k \in \big\{\,1\,,\,\ldots\,,\,I\,\big\}\,\Big\}, \quad \boldsymbol{\chi}^k \;=\; \boldsymbol{\chi}(\tau^k)\,, \qquad \forall\boldsymbol{\chi} \in \big[\,0\,,\,1\,\big]^2, \quad \forall\tau^k \in \big[\,0\,,\,1\,\big]\,. \quad (46)$$

Since the sensor is moving at velocity $\boldsymbol{v}$, the sensor position at time τ^k is given by:

$$\boldsymbol{\chi}^k \;=\; \boldsymbol{\chi}^{k-1} + \boldsymbol{v}(\tau^k)\,\Delta\tau\,, \qquad \forall\,k \in \big\{\,1\,,\,\ldots\,,\,I\,\big\}\,. \quad (47)$$

[1] Again, this story is not based on any scientific proofs

Therefore, the measurement plan is equivalent to:

$$\Omega_\pi \;=\; \bigcup_{k=1}^{I} \Omega_\pi^k\,, \tag{48}$$

$$\Omega_\pi^k \;=\; \left\{\, v_0^k\,,\, \theta^k \,\right\}, \qquad \forall\, k \,\in\, \left\{\, 1\,,\,\ldots\,,\, I \,\right\}, \tag{49}$$

where $v_0^k \;=\; v_0(\,\tau^k\,)$. In other words, starting from the sensor position $\boldsymbol{\chi_0}$ at $\tau \;=\; 0$, the measurement plan consist in determining the boat velocity v_0^k and direction angle θ^k at each time of the monitoring.

step 2. We compute the sensitivity coefficient related to the unknown parameter p_1:

$$X_{p_1}\left(\,x\,,\,y\,,\,t\,\right) \;=\; \exp\!\left(\frac{1}{s}\Big(\,x \;-\; x_0(\,t\,)\Big)^2\right)\exp\!\left(\frac{1}{s}\Big(\,y \;-\; y_0(\,t\,)\Big)^2\right). \tag{50}$$

The sensitivity is invariant to the parameter p_1 so will be the optimal experiment design.

step 3. We compute the D-optimum criterion between two time acquisition τ^k and τ^{k+1}. Since we have only one parameter, the criterion is equal to the unique element of the FISHER matrix. Assuming $\sigma \;=\; \sigma_p \;=\; 1$, we have:

$$\Psi^k \;=\; \frac{1}{2}\left(\, X_{p_1}\left(\,\boldsymbol{\chi}^k\,,\,\tau^k\,\right) \;+\; X_{p_1}\left(\,\boldsymbol{\chi}^{k+1}\,,\,\tau^{k+1}\,\right)\right). \tag{51}$$

Introducing the velocity of the sensor at time acquisition τ^k, we obtain:

$$\Psi^k \;=\; \exp\!\left(\frac{1}{s}\Big(\,\chi_x^k \;-\; x_0(\,\tau^k\,)\Big)^2\right)\exp\!\left(\frac{1}{s}\Big(\,\chi_y^k \;-\; y_0(\,\tau^k\,)\Big)^2\right) \tag{52a}$$

$$+\;\exp\!\left(\frac{1}{s}\Big(\,\chi_x^k \;+\; v_x^k\,\Delta\tau \;-\; x_0(\,t^k \;+\; \Delta\tau\,)\Big)^2\right) \tag{52b}$$

$$\cdot\;\exp\!\left(\frac{1}{s}\Big(\,\chi_y^k \;+\; v_y^k\,\Delta\tau \;-\; y_0(\,t^k \;+\; \Delta\tau\,)\Big)^2\right). \tag{52c}$$

The OED is given by finding the optimal velocities v_x^k and v_y^k at each measurement time τ^k that maximizes the D-optimum criterion:

$$\left(\,v_x^{k\,\circ}\,,\,v_y^{k\,\circ}\,\right) \;=\; \arg\max_{(\,v_0\,,\,\theta)\,\in\,[\,0\,,\,\boldsymbol{v}_\infty\,]\,\times\,[\,0\,,\,2\pi\,]} \Psi^k\!\left(\,v_0^k\,,\,\theta^k\,\right), \qquad \forall\, k \,\in\, \left\{\, 1\,,\,\ldots\,,\, I\,\right\}. \tag{53}$$

step 4. For the numerical application, the following values are considered: $T_0 \;=\; 10$, $x_c \;=\; y_c \;=\; 0.5$, $s \;=\; 0.05$, $R \;=\; 0.3$, $I \;=\; 101$ and $p_1 \;=\; 3.5$. The OED is determined using the exhaustive search strategy, considering a grid of 501 values of velocity in their respective interval, for each time step.

The optimal sensor position and velocity are shown in Figure 13(a) and 13(a). The optimal trajectory of the boat is presented in Figure 14(a) combined with the spatial variation of the sensitivity coefficient. From the starting point (Oleron island), the boat goes in the direction of maximal sensitivity. Then, at $t \;=\; 0.4$ when it reaches the point of higher sensitivity, it follows the trajectory of the current. Such trajectory can be compared in Figure 14(b) with an *a priori* one, which consists in doing a round trip until Fort Boyard, starting from Oleron island. This trajectory has a lower sensitivity coefficient as presented in Figure 12(b). Note that the OED determination does not depends on the *a priori* value of the unknown parameter.

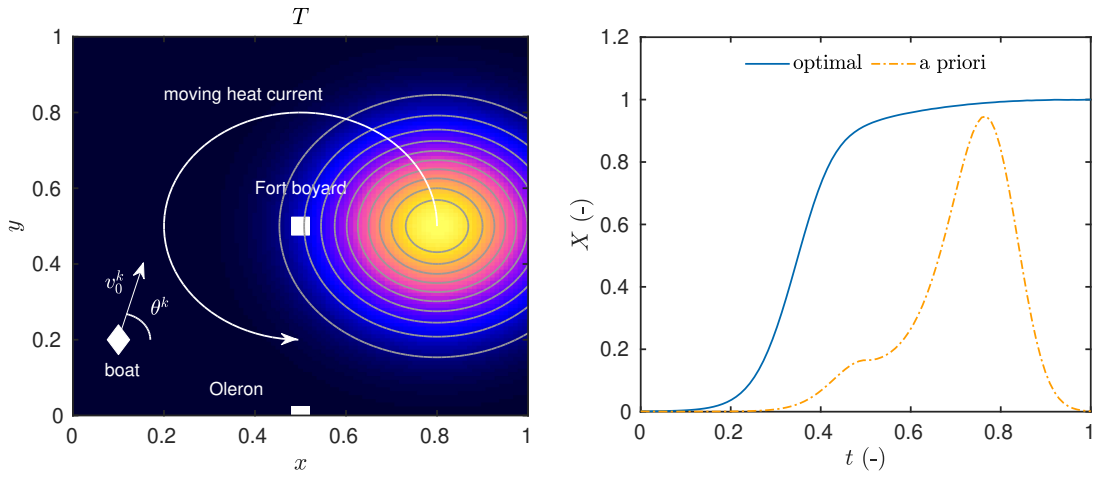

(a) (b)

Figure 12: Illustration of the case study with the spatial distribution of temperature at $t = 0$ *(a)*. Variation of the sensitivity coefficient related to p_1 for two sensor trajectories *(b)*.

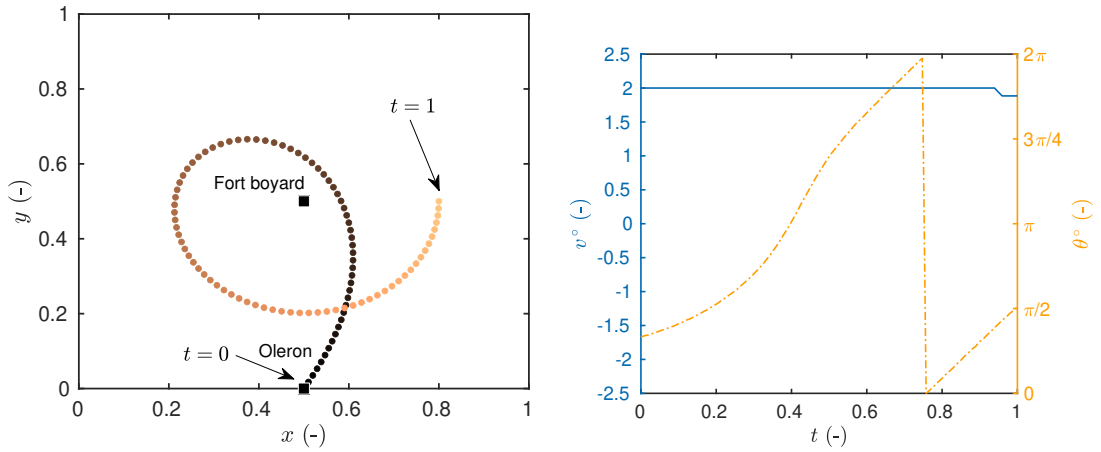

(a) (b)

Figure 13: Position *(a)* and velocity *(b)* of the sensor for the optimal measurement plan.

5 To go further

Readers are invited to consult the following works that focus in determining the OED for inverse problems related to transfer in wall materials. It provides additional examples of use of the OED methodology. In [?], the best experimental plan in terms of quantity and position of sensors and boundary conditions imposed to the material are investigated for purely heat transfer and for strongly coupled heat and mass transfer in porous building material. The investigations remains theoretical, *i.e.* no experimental campaign was performed. In [?], the optimal sensor positions and boundary conditions out of 20 possible designs are searched. The experimental campaign is then performed to identify the sorption curve parameters of a porous material. In [?], the work concerns *in situ* measurement in existing building wall materials. The D-optimum criterion is used to select the optimal experiment duration to collect the temperature measurements inside a wall. The methodology is applied to estimate the thermal conductivity of the three-layer wall of a historical building in France. Last, in [?], the parameter estimation problem considers a two-dimensional heat transfer in a building

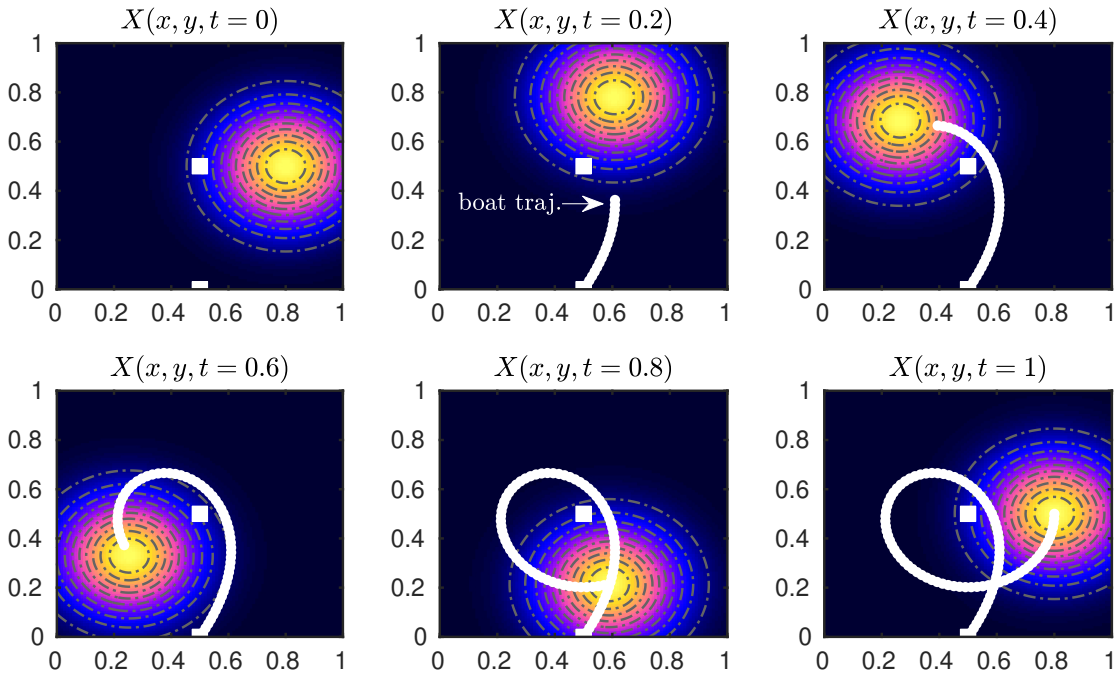

(a) OED trajectory

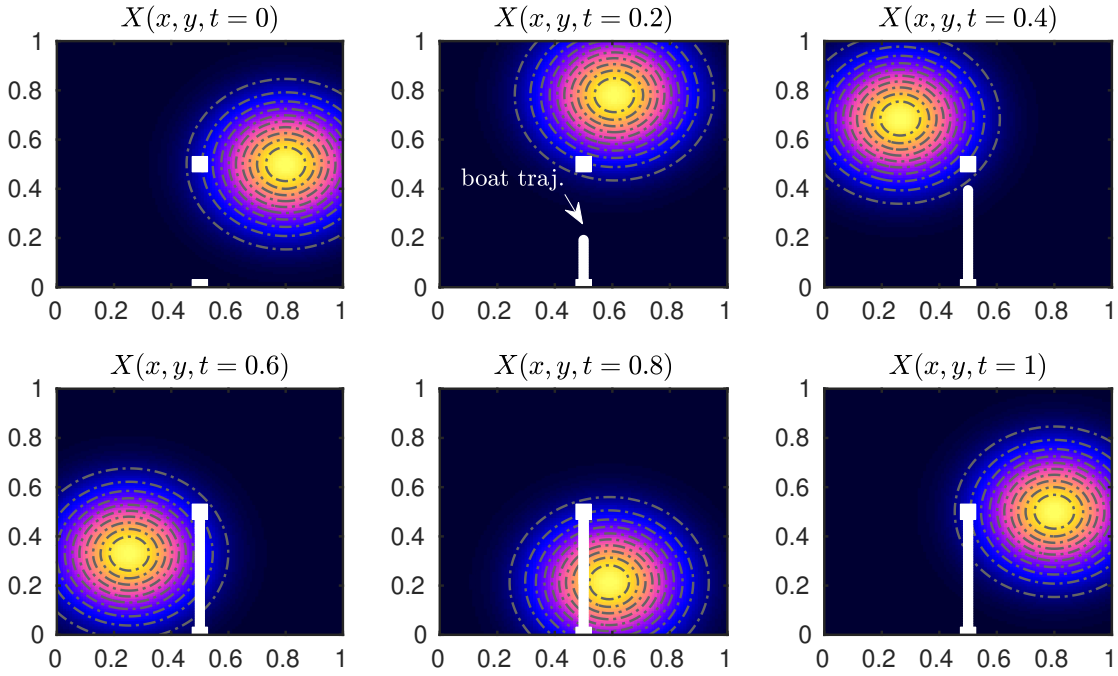

(b) *a priori* trajectory

Figure 14: Spatial distribution of the sensitivitiy coefficient related to p_1 combined with the sensor position at different times (the color of the marker become lighter with time) for two measurement plans.

facade. The OED methodology is applied to determine the optimal number and positions of sensors to determine the thermal conductivity. In [**?**], an optimal design of a three-layer experimental apparatus where a thin heater is placed between two identical samples is proposed. Three experimental variables (experiment duration, heating duration and sensor location) are

investigated. Last, in [**?**], the D-optimum criterion is applied to the three-layer apparatus used for simultaneously estimating thermal properties through the plane source method. A comparison between uniform heating and piecewise-uniform heating of high-conductivity solid samples is performed.

6 Conclusion

This tutorial focused on introducing the OED methodology for practical examples of inverse heat conduction problems. The optimal experiment design guarantees that the solution of the parameter estimation problem will be obtain with maximum accuracy compared to the other experimental configurations. The determination of the OED has two main advantages. First, the approach is half way of the proof of practical identifiability, *i.e.* the analysis of the linear dependency of the sensitivity coefficients, since one needs to compute the sensitivity coefficients. The second advantage is the possibility to define an experiment to estimate with the maximum accuracy the unknown parameters *before* performing the experiments as shown in Figure 4. Nevertheless, it is important to recall that it requires an *a priori* knowledge on the unknown parameters. In some cases, the optimal design can depend on the reliability of this knowledge. To handle this issue, it is possible to use Bayesian inferences as in [**?**].

Nomenclature and symbols

Latin letters		
$\boldsymbol{\mathcal{F}}$	Fisher matrix	*n.a.*
I	number of time measurements	*n.a.*
J	cost function	$[\,]$
M	number of sensors	*n.a.*
$\mathcal{M}$	matrix set	*n.a.*
$\boldsymbol{p}$	unknown parameter of the inverse problem	$[\,]$
T	prediction of the model (output)	$[\,]$
t	time variable	(T)
U	number of control variables	*n.a.*
u	control (or input) variable of experiment design	$[\,]$
X	model sensitivity to the unknown parameter	$[\,]$
x	space variable	(L)
y	observable	$[\,]$
Greek letters		
χ	sensor position	(L)
τ	time of measurements	(T)
π	experimental design	*n.a.*
σ	measurement uncertainty	$[\,]$
σ_p	unknown parameter uncertainty	$[\,]$
Ψ	D-optimum criterion	$(-)$
Ω	set (mathematical sense)	*n.a.*
Subscripts and superscript		
χ	related to sensor position	
τ	related time of measurements	
p	related to unknown parameter	
u	related to control variables	
dir	related to model prediction (direct problem)	
obs	related to measurement (observation of the phenomena)	

$\widehat{}$	estimated parameter
$^{\circ}$	optimal experiment design

Tutorial 14: On the use of the Approximation Error Model Approach in Inverse Problems

Cesar C. Pacheco[1], Helcio R. B. Orlande[2]

[1] Department of Mechanical Engineering, Federal Fluminense University – PGMEC/UFF, Brazil
[2] Department of Mechanical Engineering, Federal University of Rio de Janeiro – COPPE/UFRJ, Brazil

E-mail: cesarp@id.uff.br
helcio@mecanica.coppe.ufrj.br

Abstract. The Approximation Error Model (AEM) Approach is presented in this tutorial in order to account for errors resulting from the use of low-fidelity models, instead of high-fidelity models, for the solution of inverse problems within the Bayesian framework of statistics. In the AEM approach, a statistical representation of the errors between the solutions of the high-fidelity and low-fidelity models is developed, by sampling from the prior distribution of the model parameters. Therefore, AEM requires priors with limited variances, from which samples of the approximation errors can be generated by an offline Monte Carlo simulation. The approximation errors are then represented as additional noise in the measurement error model, thus resulting in a modified likelihood function.

List of acronyms:

- **AE:** Approximation Error
- **AEM**: Approximation Error Model
- **CEM**: Complete Error Model
- **EEM**: Enhanced Error Model
- **KF**: Kalman Filter
- **MCMC**: Markov Chain Monte Carlo
- **MH**: Metropolis-Hastings
- **PF**: Particle Filtering
- **SIR**: Sampling Importance Resampling

Scope

1. Introduction
2. Mathematical background
    2.1. Preliminaries
    2.2. Gaussian Measurement Errors
    2.3. Statistics of the Approximation Error
    2.4. The Approximation Error Model (AEM) Approach
    2.5. AEM in Bayesian Estimation Methods
        2.5.1. Markov Chain Monte Carlo (MCMC)
        2.5.2. Kalman Filter
        2.5.3. Particle Filter
3. Applications
    3.1. A Simple Example
    3.2. Estimation of Heat Fluxes of Large Magnitudes
References

1. Introduction

Mathematical models of natural phenomena are in general based on balance laws, such as those for mass, momentum and energy, which require additional constitutive equations formulated from empirical evidence in order to relate dependent variables. With the scientific advancement through the ages, more complex mathematical models have been proposed as physical, chemical and biological phenomena, among others, were better studied and comprehended. Nevertheless, complex models commonly involve a large number of parameters that need to be known with small uncertainties, so that computational simulations can provide valuable information about the aimed phenomena. Moreover, mathematical models require hypotheses that influence the formulation in terms of the phenomena accounted for, number of dimensions, time dependence, scales, linearity, model parameters, etc. These hypotheses should be carefully selected by following the Principle of Parsimony (Occam's razor or Ockham's razor) in order to obtain simple models, with a small number of parameters, which can represent the phenomena under analysis within a desired amount of uncertainty [1]. In the practice of scientific computation, such philosophical principle [2] can be associated to Verification & Validation [3].

Validation is defined as "the process of determining the degree to which a model is an accurate representation of the real world from the perspective of the intended uses of the model" [3]. The word "model" means the mathematical formulation and its computational solution. The words "real world" mean that validation necessarily involves the comparison between computational and experimental results. Uncertainties in the measured data and in the computational results thus need to be taken into account for the validation process [3,4]. Verification must be performed before validation [3]. The verification procedure includes code verification and solution verification. In the verification of the computational code, an analysis is made to establish if it actually solves the mathematical model that it is intended for. The objective of solution verification is the estimation of the accuracy of the computational solution [3,4].

Beck [5] has clearly evidenced that the use of inverse problems represents a research paradigm that is complementary to that established in Verification & Validation procedures [3]. In the inverse problems paradigm, the results obtained from numerical simulations and from experiments are not compared *a posteriori*, but a close synergism exists between experimental and theoretical researchers during the course of the study, in order to obtain the maximum of information regarding the phenomena under analysis. The solution of an inverse problem relies on the computational solution of the direct (forward) problem, which is used, together with the available experimental data, for the estimation of parameters and/or functions appearing in the mathematical formulation of the phenomena of interest. Therefore, the solution of inverse problems requires code verification and solution verification. On the other hand, the validation of the code comes out as part of the inverse problem solution, for example, through the analysis of the residuals [1]. The residuals are given by the differences between the measurements and the dependent variables that are obtained from the solution of the direct problem. The residuals are expected to be small (of the order of magnitude of the measurement errors) and uncorrelated (without any deterministic behavior), if the mathematical formulation and the solution of the direct problem with the estimated parameters and/or functions appropriately model the phenomena under analysis.

Based on the above discussion, the mathematical model that represents the natural phenomena under analysis with the supposed least amount of uncertainty is denoted here as the *high-fidelity model*. Any other model is referred to as a *low-fidelity model*.

The use of low-fidelity models instead of high-fidelity models is attractive for the reduction of the computational time and implementation of inverse analysis methods. For example, low-fidelity models can be obtained by reducing the physical phenomena accounted for in the formulation, use of variables in a transformed domain, modal analysis, truncation of the computational domain and use of numerical coarse meshes, or even metamodels not related to any of the phenomena in the direct problem formulation, such as the nowadays quite popular machine learning models. The reader is referred to Lecture 7 and Tutorial 6 of this METTI School for techniques to formally obtain low-fidelity models.

A description of the errors inherent to heat transfer measurements and to the solution of inverse problems can be found in Chapter 16 of reference [6], as well as in different Lectures and Tutorials of this METTI School. In particular, the present tutorial is focused on the analysis and quantification of the errors resulting from the replacement of a high-fidelity model by a low-fidelity model for the solution of an inverse problem. Such approximation errors are then taken into account for the solution of the inverse problem by applying the so-called Approximation Error Model (AEM) advanced by Kaipio and his group [7–12].

In general, uncertainty refers to a statistical model for the errors in the form of a probability distribution function, while the error is itself a realization of this probability distribution function [4]. For the implementation of the AEM approach, the statistics of the approximation errors are computed before the solution of the inverse problem, by solving the high-fidelity model and the low-fidelity model with samples of the model parameters obtained from their prior distributions. After computing enough samples of the approximation error to obtain its converged mean and covariance matrix, this random variable is modeled in terms of an analytical probability distribution. A simple but very effective approach is to consider that the approximation errors follow a Gaussian distribution and that they can be directly added to the measurement errors. Basics of the AEM approach will be introduced in this tutorial and computational examples will be presented, by solving the inverse problem within the Bayesian framework of statistics with whole-domain or sequential state-estimation techniques [1,7,13].

2. Mathematical background

2.1. Preliminaries

Consider the forward problem formulated as:

$$\mathbf{y} = \mathbf{T}(\boldsymbol{\beta}, \boldsymbol{\varepsilon}) \tag{1}$$

where $\mathbf{T}(\boldsymbol{\beta}, \boldsymbol{\varepsilon})$ is the mathematical representation of the high-fidelity model and $\boldsymbol{\beta}$ is the vector of model parameters, while $\boldsymbol{\varepsilon}$ is a random vector representing errors in this model with respect to the measurements of the dependent variable $\mathbf{y}$. Hence, $\boldsymbol{\varepsilon}$ are the measurement errors.

As discussed above, solving the inverse problem by using the high-fidelity model may prove to be an impractical task due to its elevated computational cost, even though it represents the phenomena under analysis with small uncertainties. Therefore, we consider for the solution of

the inverse problem the use of a low-fidelity model instead of the computationally expensive high-fidelity model given by Eq. (1). The low-fidelity model is written as:

$$\mathbf{y}_{app} = \mathbf{T}_{app}\left(\boldsymbol{\beta}_{app}, \boldsymbol{\varepsilon}_{app}\right) \tag{2}$$

where $\boldsymbol{\beta}_{app}$ is the vector of parameters of the low-fidelity model, the elements of which might be a subset of the parameters of the high-fidelity model. In Eq. (2), $\boldsymbol{\varepsilon}_{app}$ represents errors of the low-fidelity model. Therefore, we can write:

$$\mathbf{y} = \mathbf{T}_{app}\left(\boldsymbol{\beta}_{app}, \boldsymbol{\varepsilon}_{app}\right) + \left[\mathbf{T}(\boldsymbol{\beta}, \boldsymbol{\varepsilon}) - \mathbf{T}_{app}\left(\boldsymbol{\beta}_{app}, \boldsymbol{\varepsilon}_{app}\right)\right] \tag{3a}$$

or

$$\mathbf{y} = \mathbf{T}_{app}\left(\boldsymbol{\beta}_{app}, \boldsymbol{\varepsilon}_{app}\right) + \mathbf{e}\left(\boldsymbol{\beta}, \boldsymbol{\beta}_{app}, \boldsymbol{\varepsilon}, \boldsymbol{\varepsilon}_{app}\right) \tag{3b}$$

where

$$\mathbf{e}\left(\boldsymbol{\beta}, \boldsymbol{\beta}_{app}, \boldsymbol{\varepsilon}, \boldsymbol{\varepsilon}_{app}\right) = \mathbf{T}(\boldsymbol{\beta}, \boldsymbol{\varepsilon}) - \mathbf{T}_{app}\left(\boldsymbol{\beta}_{app}, \boldsymbol{\varepsilon}_{app}\right) \tag{4}$$

is the approximation error between the solutions of the low-fidelity and the of high-fidelity models.

With the hypotheses that the measurement errors are additive and independent of the parameters $\boldsymbol{\beta}$, Eq. (1) can be written as [1,7,13]:

$$\mathbf{y} = \mathbf{T}(\boldsymbol{\beta}) + \boldsymbol{\varepsilon} \tag{5}$$

Thus, we obtain from Eq. (3a):

$$\mathbf{y} = \mathbf{T}_{app}\left(\boldsymbol{\beta}_{app}, \boldsymbol{\varepsilon}_{app}\right) + \left[\mathbf{T}(\boldsymbol{\beta}) - \mathbf{T}_{app}\left(\boldsymbol{\beta}_{app}, \boldsymbol{\varepsilon}_{app}\right)\right] + \boldsymbol{\varepsilon} \tag{6}$$

which is re-written as:

$$\mathbf{y} = \mathbf{T}_{app}\left(\boldsymbol{\beta}_{app}\right) + \boldsymbol{\eta}(\boldsymbol{\beta}) \tag{7}$$

where

$$\boldsymbol{\eta}(\boldsymbol{\beta}) = \mathbf{e}(\boldsymbol{\beta}) + \boldsymbol{\varepsilon} \tag{8}$$

In Eq. (8), $\boldsymbol{\eta}(\boldsymbol{\beta})$ is the total error that includes the approximation error, $\mathbf{e}(\boldsymbol{\beta})$, as well as the experimental error, $\boldsymbol{\varepsilon}$. By re-writing Eq. (6) as Eq. (7), it is assumed that the effects from $\boldsymbol{\varepsilon}_{app}$ and from the selection of $\boldsymbol{\beta}_{app}$ as a subset of $\boldsymbol{\beta}$ are all accounted for in the statistical representation of the approximation error, which then simplifies from Eq. (4) to $\mathbf{e}\left(\boldsymbol{\beta}, \boldsymbol{\beta}_{app}, \boldsymbol{\varepsilon}, \boldsymbol{\varepsilon}_{app}\right) \equiv \mathbf{e}(\boldsymbol{\beta})$.

2.2. Gaussian Measurement Errors

It is assumed here that the vector of measurement errors, $\boldsymbol{\varepsilon}$, is Gaussian, with zero mean ($\overline{\boldsymbol{\varepsilon}} = \mathbf{0}$) and known covariance matrix $\mathbf{W}$. Thus, the probability density of $\boldsymbol{\varepsilon}$ is given by [1,7,13]:

$$p(\boldsymbol{\varepsilon}) = (2\pi)^{-\frac{D}{2}}|\mathbf{W}|^{-\frac{1}{2}}\exp\left\{-\frac{1}{2}\boldsymbol{\varepsilon}^T\mathbf{W}^{-1}\boldsymbol{\varepsilon}\right\} \tag{9}$$

where D is the total number of measurements. By replacing $\boldsymbol{\varepsilon}$ from Eq. (5) into Eq. (9), we obtain

$$p(\boldsymbol{\varepsilon}) = (2\pi)^{-\frac{D}{2}}|\mathbf{W}|^{-\frac{1}{2}}\exp\left\{-\frac{1}{2}[\mathbf{y}-\mathbf{T}(\boldsymbol{\beta})]^T\mathbf{W}^{-1}[\mathbf{y}-\mathbf{T}(\boldsymbol{\beta})]\right\} \tag{10}$$

Therefore, $p(\boldsymbol{\varepsilon})$ also represents the conditional probability of the measurements $\mathbf{y}$ given the model parameters $\boldsymbol{\beta}$, that is, $p(\boldsymbol{\varepsilon}) = p(\mathbf{y}|\boldsymbol{\beta})$, which is denoted as the likelihood function.

2.3. Statistics of the Approximation Error

Similarly to the measurement errors that appear in Eq. (5), which are used for the definition of likelihood function given by Eq. (10) in terms of the high-fidelity model, the total error $\boldsymbol{\eta}(\boldsymbol{\beta})$ needs to be statistically modeled to obtain a modified likelihood based on the low-fidelity model (see Eqs. 7 and 8). Since the measurement errors can be independently modeled based on the calibration procedure of sensors and data acquisition systems, such as the Gaussian distribution given by Eq. (9), a statistical model for the total errors in fact demands the calculation of the approximation errors between the solutions of the high-fidelity and low-fidelity models, that is,

$$\mathbf{e}(\boldsymbol{\beta}) = \mathbf{T}(\boldsymbol{\beta}) - \mathbf{T}_{app}(\boldsymbol{\beta}_{app}) \tag{11}$$

The solution of the inverse problem within the Bayesian framework of statistics conveniently allows that samples of the approximation error $\mathbf{e}(\boldsymbol{\beta})$ be computed based on the prior information available for the parameters $\boldsymbol{\beta}$, as well as other possible sources of uncertainties. The computation of these samples would not be possible with classical techniques for the solution of the inverse problem because they are limited to the analysis of the likelihood function, which means that the information available for the model parameters before the experiments is not formally taken into account through Bayes' theorem [7,13].

The statistics of the approximation error $\mathbf{e}(\boldsymbol{\beta})$ are computed before the solution of the inverse problem, as follows:

1. Let k = 1. Obtain samples $\boldsymbol{\beta}^{(k)}$ and $\boldsymbol{\beta}_{app}^{(k)}$ from the prior distributions for the parameters.
2. Solve the complete model with the parameter vector $\boldsymbol{\beta}^{(k)}$ and the approximate model with the parameter vector $\boldsymbol{\beta}_{app}^{(k)}$.
3. Compute the sample of the approximation error:

$$\mathbf{e}^{(k)}(\boldsymbol{\beta}) = \left[\mathbf{T}\left(\boldsymbol{\beta}^{(k)}\right) - \mathbf{T}_{app}\left(\boldsymbol{\beta}_{app}^{(k)}\right)\right] \tag{12}$$

4. Make $k = k + 1$.

5. Repeat the steps above until the statistics of $\mathbf{e}(\boldsymbol{\beta})$, obtained with the samples $\mathbf{e}^{(k)} = (\boldsymbol{\beta})$, converge.

As it will be apparent below, the statistics of $\mathbf{e}^{(k)}(\boldsymbol{\beta})$ that are of interest for the Approximation Error Model approach are the mean and the covariance matrix. They can be respectively calculated as follows:

$$\overline{\mathbf{e}} = \frac{1}{N_s}\sum_{k=1}^{N_s}\mathbf{e}^{(k)}(\boldsymbol{\beta}) \tag{13a}$$

$$\mathbf{W}_e = \frac{1}{N_s-1}\sum_{k=1}^{N_s}\left[\mathbf{e}^{(k)}(\boldsymbol{\beta}) - \overline{\mathbf{e}}\right]\left[\mathbf{e}^{(k)}(\boldsymbol{\beta}) - \overline{\mathbf{e}}\right]^T \tag{13b}$$

where N_s is the number of samples of the approximation error.

We note that the mean $\overline{\mathbf{e}}$ usually converges faster than the variances and covariances in $\mathbf{W}_e$. The convergence of $\mathbf{W}_e$ can be verified in terms of the convergence of its trace or its largest eigenvalues. Also, note that the AEM cannot be applied with improper priors, since they have unbounded variances and the samples $\boldsymbol{\beta}^{(k)}$ and $\boldsymbol{\beta}_{app}^{(k)}$ cannot be obtained.

2.4. Approximation Error Model (AEM) Approach

After obtaining the samples $\mathbf{e}^{(k)}(\boldsymbol{\beta})$ in a sufficient number N_s for which $\overline{\mathbf{e}}$ and $\mathbf{W}_e$ are converged, these random variables are modeled in terms of an analytical distribution. A simple but very effective approach is to consider that they follow a Gaussian distribution [7–12], that is,

$$p(\mathbf{e}) \propto \exp\left\{-\frac{1}{2}[\mathbf{e}-\overline{\mathbf{e}}]^T\mathbf{W}_e^{-1}[\mathbf{e}-\overline{\mathbf{e}}]\right\} \tag{14}$$

Then, the likelihood with the error model of equation (7), $\boldsymbol{\eta}(\boldsymbol{\beta})$ given by equation (8) and $\mathbf{e}(\boldsymbol{\beta})$ modeled as a Gaussian variable, is given by:

$$p(\mathbf{y}|\boldsymbol{\beta}) \propto \exp\left\{-\frac{1}{2}\left[\mathbf{y}-\mathbf{T}_{app}(\boldsymbol{\beta}_{app})-\overline{\boldsymbol{\eta}}\right]^T\widetilde{\mathbf{W}}^{-1}\left[\mathbf{y}-\mathbf{T}_{app}(\boldsymbol{\beta}_{app})-\overline{\boldsymbol{\eta}}\right]\right\} \tag{15}$$

For a Gaussian prior with mean $\boldsymbol{\mu}$ and covariance matrix $\mathbf{V}$, that is,

$$p(\boldsymbol{\beta}) \propto \exp\left\{-\frac{1}{2}(\boldsymbol{\beta}-\boldsymbol{\mu})^T\mathbf{V}^{-1}(\boldsymbol{\beta}-\boldsymbol{\mu})\right\} \tag{16}$$

the posterior distribution obtained with the likelihood given by Eq. (15) and the prior given by Eq. (16) is:

$$p(\boldsymbol{\beta}|\mathbf{y}) \propto \exp\left\{-\frac{1}{2}\left[\mathbf{y}-\mathbf{T}_{app}(\boldsymbol{\beta}_{app})-\overline{\boldsymbol{\eta}}\right]^T\widetilde{\mathbf{W}}^{-1}\left[\mathbf{y}-\mathbf{T}_{app}(\boldsymbol{\beta}_{app})-\overline{\boldsymbol{\eta}}\right]-\frac{1}{2}(\boldsymbol{\beta}-\boldsymbol{\mu})^T\mathbf{V}^{-1}(\boldsymbol{\beta}-\boldsymbol{\mu})\right\} \tag{17}$$

The mean and the covariance matrix of the total error $\boldsymbol{\eta}(\boldsymbol{\beta})$ are respectively obtained from [8]:

$$\overline{\boldsymbol{\eta}} = \overline{\boldsymbol{\varepsilon}} + \overline{\mathbf{e}} + \boldsymbol{\Gamma}_{\boldsymbol{\eta\beta}}\mathbf{V}^{-1}(\boldsymbol{\beta} - \boldsymbol{\mu}) \tag{18a}$$

$$\widetilde{\mathbf{W}} = \mathbf{W}_e + \mathbf{W} - \boldsymbol{\Gamma}_{\boldsymbol{\eta\beta}}\mathbf{V}^{-1}\boldsymbol{\Gamma}_{\boldsymbol{\eta\beta}}^{T} \tag{18b}$$

where $\boldsymbol{\Gamma}_{\boldsymbol{\eta\beta}}$ is the covariance of $\boldsymbol{\eta}$ and $\boldsymbol{\beta}$. Equations (18a,b) give the *Complete Error Model* [8].

We note that, with the standard hypotheses regarding the measurement errors made above, $\overline{\boldsymbol{\varepsilon}} = \mathbf{0}$. By further neglecting the linear dependency between $\boldsymbol{\eta}$ and $\boldsymbol{\beta}$, that is, $\boldsymbol{\Gamma}_{\boldsymbol{\eta\beta}} = \mathbf{0}$, equations (18a,b) simplify to the so-called *Enhanced Error Model*:

$$\overline{\boldsymbol{\eta}} \simeq \overline{\mathbf{e}} \tag{19a}$$

$$\widetilde{\mathbf{W}} = \mathbf{W}_e + \mathbf{W} \tag{19b}$$

Therefore, in the *Approximation Error Model* (*AEM*) Approach, the solution of the inverse problem within the Bayesian framework can be readily applied with the posterior given by equation (17), where the original likelihood was modified by the mean and covariance matrix of the total error $\boldsymbol{\eta}(\boldsymbol{\beta})$, that is, $\overline{\boldsymbol{\eta}}$ and $\widetilde{\mathbf{W}}$, respectively (see Eq. 15). These two quantities are usually quite well approximated by equations (19a,b), respectively, and application of the more complicated complete error model given by equations (18a,b) is not needed.

2.5. AEM in Bayesian Estimation Methods

2.5.1. Markov Chain Monte Carlo (MCMC)

Herein we present the application of the AEM in the context of the Metropolis-Hastings (MH) sampling algorithm for solution of inverse problems via Markov Chain Monte Carlo (MCMC). The objective is to draw an ensemble of $\boldsymbol{N}$ samples $\boldsymbol{\beta}^{(\boldsymbol{k})}, \boldsymbol{k} = \mathbf{1}, \dots, \boldsymbol{N}$ from the posterior pdf $\boldsymbol{p}(\boldsymbol{\beta}|\mathbf{y})$ wherefrom the statistics can be calculated. The MH algorithm requires defining a proposal distribution $\boldsymbol{p}\left(\boldsymbol{\beta}^{*}, \boldsymbol{\beta}^{(\boldsymbol{k-1})}\right)$ and is originally applied as follows

(i) Sample a candidate $\boldsymbol{\beta}^{*}$ from $\boldsymbol{p}\left(\boldsymbol{\beta}^{*}, \boldsymbol{\beta}^{\boldsymbol{k-1}}\right)$;
(ii) Calculate the acceptance factor using Eq. (20);

$$\boldsymbol{\alpha} = \mathbf{min}\left[\mathbf{1}, \frac{\boldsymbol{p}(\boldsymbol{\beta}^{*}|\mathbf{y})\boldsymbol{p}\left(\boldsymbol{\beta}^{(\boldsymbol{k-1})}, \boldsymbol{\beta}^{*}\right)}{\boldsymbol{p}(\boldsymbol{\beta}^{(\boldsymbol{k-1})}|\mathbf{y})\boldsymbol{p}(\boldsymbol{\beta}^{*}, \boldsymbol{\beta}^{(\boldsymbol{k-1})})}\right] \tag{20}$$

(iii) Generate a random uniformly distributed number $\boldsymbol{u} \sim \boldsymbol{U}[\mathbf{0}, \mathbf{1}]$;
(iv) If $\boldsymbol{u} \leq \boldsymbol{\alpha}$, set $\boldsymbol{\beta}^{(\boldsymbol{k})} = \boldsymbol{\beta}^{*}$; otherwise, $\boldsymbol{\beta}^{(\boldsymbol{k})} = \boldsymbol{\beta}^{(\boldsymbol{k-1})}$;
(v) Set $\boldsymbol{k} = \boldsymbol{k} + \mathbf{1}$ and return to step (i) until the desired number of states has been achieved.

Applying the AEM in the MH algorithms comprises of making the appropriate modifications in the posterior $\boldsymbol{p}(\boldsymbol{\beta}|\mathbf{y})$. Should one use the high-fidelity model to solve the inverse problem (that is, not use the AEM), the Gaussian prior given in Eq. (16) could be combined with the likelihood given in Eq. (10), yielding the posterior given in Eq. (21).

$$\boldsymbol{p}(\boldsymbol{\beta}|\mathbf{y}) \propto \mathbf{exp}\left\{-\frac{\mathbf{1}}{\mathbf{2}}[\mathbf{y} - \mathbf{T}(\boldsymbol{\beta})]^{T}\mathbf{W}^{-1}[\mathbf{y} - \mathbf{T}(\boldsymbol{\beta})] - \frac{\mathbf{1}}{\mathbf{2}}(\boldsymbol{\beta} - \boldsymbol{\mu})^{T}\mathbf{V}^{-1}(\boldsymbol{\beta} - \boldsymbol{\mu})\right\} \tag{21}$$

On the other hand, if we are to attempt solving the inverse problem using solely the low-fidelity model, a similar posterior would arise, as shown in Eq. (22).

$$\boldsymbol{p}(\boldsymbol{\beta}|\mathbf{y}) \propto \mathbf{exp}\left\{-\frac{\mathbf{1}}{\mathbf{2}}\left[\mathbf{y}-\mathbf{T}_{\boldsymbol{app}}\left(\boldsymbol{\beta}_{\boldsymbol{app}}\right)\right]^{\boldsymbol{T}}\mathbf{W}^{-\mathbf{1}}\left[\mathbf{y}-\mathbf{T}_{\boldsymbol{app}}\left(\boldsymbol{\beta}_{\boldsymbol{app}}\right)\right]-\frac{\mathbf{1}}{\mathbf{2}}\left(\boldsymbol{\beta}_{\boldsymbol{app}}-\boldsymbol{\mu}\right)^{\boldsymbol{T}}\mathbf{V}^{-\mathbf{1}}\left(\boldsymbol{\beta}_{\boldsymbol{app}}-\boldsymbol{\mu}\right)\right\} \quad (22)$$

Now, combining the low-fidelity model with the AEM in MH algorithm would require only to use Eq. (17) in Eq. (20). This goes to show that, in the particular case of MH algorithm, implementing the AEM is minimally invasive, in terms of coding, solely requiring modifications on functions or subroutines involving calculation of the posterior pdf.

2.5.2. Kalman Filter

The recursive solution of inverse problems within the Bayesian approach can benefit from the AEM as well. Particularly, we refer here to state estimation problems, also known as nonstationary inverse problems [7]. In such problems, we are interested in reconstructing information on the state vector $\mathbf{x}$ using the observation vector $\mathbf{y}$, containing the experimental measurements. It bears mentioning that the state vector contains, but is not limited to, the sought variables $\boldsymbol{\beta}$.

The dynamics of the forward problem is mathematically described according to an evolution-observation model (EOM). In this section we focus on linear, Gaussian EOMs, for the purposes of applying the AEM to the classical Kalman Filter [7,14,15]. This EOM is given by Eqs. (23a,b), where $\mathbf{w}_k$ and $\mathbf{v}_k$ are random vectors following a Gaussian distribution with zero mean and covariance matrices $\mathbf{Q}_k$ and $\mathbf{R}_k$, respectively. This model also contains the evolution and observations matrices $\mathbf{F}_k$ and $\mathbf{H}_k$, respectively, and the control matrix and vector $\mathbf{G}_k$ and $\mathbf{u}_k$, respectively.

$$\mathbf{x}_{k+1} = \mathbf{F}_k\mathbf{x}_k + \mathbf{G}_k\mathbf{u}_k + \mathbf{w}_{k+1} \quad (23a)$$
$$\mathbf{y}_k = \mathbf{H}_k\mathbf{x}_k + \mathbf{v}_k \quad (23b)$$

The solution to this state estimation problem is given by Eqs. (24a-e), where $\hat{\mathbf{x}}_k^-$ and $\hat{\mathbf{x}}_k^+$ are the prior and posterior estimated of the state vector $\mathbf{x}_k$; $\mathbf{P}_k^-$ and $\mathbf{P}_k^+$ are the prior and posterior estimation error covariance matrices and $\mathbf{K}_k$ is the Kalman gain matrix.

$$\hat{\mathbf{x}}_{k+1}^- = \mathbf{F}_k\hat{\mathbf{x}}_k^+ + \mathbf{G}_k\mathbf{u}_k \quad (24a)$$
$$\mathbf{P}_{k+1}^- = \mathbf{F}_k\mathbf{P}_k^+\mathbf{F}_k^T + \mathbf{Q}_k \quad (24b)$$
$$\mathbf{K}_k = \mathbf{P}_k^-\mathbf{H}_k^T\left(\mathbf{H}_k\mathbf{P}_k^-\mathbf{H}_k^T + \mathbf{R}_k\right)^{-1} \quad (24c)$$
$$\hat{\mathbf{x}}_{k+1}^+ = \hat{\mathbf{x}}_{k+1}^- + \mathbf{K}_k(\mathbf{y}_k - \mathbf{H}_k\hat{\mathbf{x}}_{k+1}^-) \quad (24d)$$
$$\mathbf{P}_{k+1}^+ = (\mathbf{I} - \mathbf{K}_k\mathbf{H}_k)\mathbf{P}_{k+1}^- \quad (24e)$$

Accounting for AEs in the context of nonstationary inverse problems requires the accounting thereof in the EOM itself, as shown in [16,17]. This means that the AEs appear in both evolution and observation models, as shown in Eqs. (25a,b). In this modified EOM, are included the state evolution approximation error $\boldsymbol{\gamma}_k$ and the observation approximation error $\boldsymbol{\delta}_k$.

$$\mathbf{x}_{k+1} = \mathbf{F}_k\mathbf{x}_k + \mathbf{G}_k\mathbf{u}_k + \boldsymbol{\gamma}_k + \mathbf{w}_{k+1} \quad (25a)$$

$$\mathbf{y}_k = \mathbf{H}_k\mathbf{x}_k + \boldsymbol{\delta}_k + \mathbf{v}_k \tag{25b}$$

In the case of the Enhanced Error Model described above, the modified KF equations are much similar to the original ones, being given in Eqs. (26a-e). To employ the EEM, it is required only to calculate the mean and covariance of the state and observation AEs.

$$\hat{\mathbf{x}}_{k+1}^{-} = \mathbf{F}_k\hat{\mathbf{x}}_k^{+} + \mathbf{G}_k\mathbf{u}_k + \mathbb{E}[\boldsymbol{\gamma}_k] \tag{26a}$$
$$\mathbf{P}_{k+1}^{-} = \mathbf{F}_k\mathbf{P}_k^{+}\mathbf{F}_k^{T} + \mathbf{var}(\boldsymbol{\gamma}_k) + \mathbf{Q}_k \tag{26b}$$
$$\mathbf{K}_k = \mathbf{P}_k^{-}\mathbf{H}_k^{T}\left(\mathbf{H}_k\mathbf{P}_k^{-}\mathbf{H}_k^{T} + \mathbf{var}(\boldsymbol{\delta}_k) + \mathbf{R}_k\right)^{-1} \tag{26c}$$
$$\hat{\mathbf{x}}_{k+1}^{+} = \hat{\mathbf{x}}_{k+1}^{-} + \mathbf{K}_k(\mathbf{y}_k - \mathbf{H}_k\hat{\mathbf{x}}_{k+1}^{-} - \mathbb{E}[\boldsymbol{\delta}_k]) \tag{26d}$$
$$\mathbf{P}_{k+1}^{+} = (\mathbf{I} - \mathbf{K}_k\mathbf{H}_k)\mathbf{P}_{k+1}^{-} \tag{26e}$$

2.5.3. Particle Filter

Like MCMC, Particle Filtering (PF) refers to a class of methods rather than a single one. For this reason, our focus in this section will be the SIR algorithm for particle filtering for the purposes of illustrating the inclusion of the AEM in such methods. The original SIR algorithm can be implemented following the algorithm below [18–20], for each recursive step. Similarly to the KF described above, in the PF we seek to identify the state vector $\mathbf{x}$ which contains – but it is not limited to – the sought variables $\boldsymbol{\beta}$.

(i) For $\boldsymbol{i} = \mathbf{1}, \dots, \boldsymbol{N}$ draw new particles $\mathbf{x}_k^i$ from the prior $\boldsymbol{p}(\mathbf{x}_k|\mathbf{x}_{k-1}^i)$ and calculate their corresponding weights $\boldsymbol{w}_k^i = \boldsymbol{p}(\mathbf{y}_k|\mathbf{x}_k^i)$;
(ii) Normalize the weights, that is, let $\boldsymbol{w}_k^i = \boldsymbol{T}_w^{-1}\boldsymbol{w}_k^i,\ \boldsymbol{i} = \mathbf{1}, \dots, \boldsymbol{N}$ where $\boldsymbol{T}_w = \sum_{i=1}^{N}\boldsymbol{w}_i^k$;
(iii) Resample as follows
   a. Construct the cumulative sum of weights (CSW) $\boldsymbol{c}_i = \boldsymbol{c}_{i-1} + \boldsymbol{w}_k^i,\ \boldsymbol{i} = \mathbf{1}, \dots, \boldsymbol{N}$, with $\boldsymbol{c}_0 = \mathbf{0}$;
   b. Let $\boldsymbol{i} = \mathbf{1}$ and draw a random variable $\boldsymbol{u}_1 \sim \boldsymbol{U}[\mathbf{0}, \boldsymbol{N}^{-1}]$;
   c. For $\boldsymbol{j} = \mathbf{1}, \dots, \boldsymbol{N}$, move along the CSW with $\boldsymbol{u}_j = \boldsymbol{u}_1 + \boldsymbol{N}^{-1}(\boldsymbol{j} - \mathbf{1})$;
   d. While $\boldsymbol{u}_j > \boldsymbol{c}_i$, let $\boldsymbol{i} = \boldsymbol{i} + \mathbf{1}$;
   e. Assign $\mathbf{x}_k^j = \mathbf{x}_k^i$ and $\boldsymbol{w}_k^j = \boldsymbol{N}^{-1}$.

As can be seen, the mathematical model (be it high- or low-fidelity) comes into play in step (i), where the likelihood $\boldsymbol{p}(\mathbf{y}|\mathbf{x})$ is evaluated. That is, should one carry the inverse analysis through using the high-fidelity model, the likelihood would be given by Eq. (27a). On the other hand, it the low-fidelity model is to be used, then Eq. (27b) must be employed. At last, to include the AEM and combine it with the low-fidelity model, Eq. (27c) is the likelihood of choice.

$$p(\mathbf{y}|\mathbf{x}) = (2\pi)^{-\frac{D}{2}}|\mathbf{W}|^{-\frac{1}{2}}\exp\left\{-\frac{1}{2}[\mathbf{y} - \mathbf{T}(\mathbf{x})]^T\mathbf{W}^{-1}[\mathbf{y} - \mathbf{T}(\mathbf{x})]\right\} \tag{27a}$$
$$p(\mathbf{y}|\mathbf{x}) = (2\pi)^{-\frac{D}{2}}|\mathbf{W}|^{-\frac{1}{2}}\exp\left\{-\frac{1}{2}\left[\mathbf{y} - \mathbf{T}_{app}(\mathbf{x})\right]^T\mathbf{W}^{-1}\left[\mathbf{y} - \mathbf{T}_{app}(\mathbf{x})\right]\right\} \tag{27b}$$
$$p(\mathbf{y}|\mathbf{x}) = (2\pi)^{-\frac{D}{2}}|\mathbf{W}|^{-\frac{1}{2}}\exp\left\{-\frac{1}{2}\left[\mathbf{y} - \mathbf{T}_{app}(\boldsymbol{\beta}_{app}) - \overline{\boldsymbol{\eta}}\right]^T\widetilde{\mathbf{W}}^{-1}\left[\mathbf{y} - \mathbf{T}_{app}(\boldsymbol{\beta}_{app}) - \overline{\boldsymbol{\eta}}\right]\right\} \tag{27c}$$

3. Applications

3.1. A Simple Example

A simple heat conduction problem is used here for illustration of the AEM approach. Consider transient linear heat conduction in a slab of thickness L, initially at the temperature T_0. The boundary at $x = 0$ is thermally insulated. For times $t > 0$, the slab exchanges heat by convection with a surrounding fluid at the temperature T_∞ with a heat transfer coefficient h. There are no energy sources inside the slab. The mathematical formulation of this problem is given by:

$$\frac{1}{\alpha}\frac{\partial T(x,t)}{\partial t} = \frac{\partial^2 T}{\partial x^2}, \qquad \text{in } 0 < x < L, t > 0 \tag{28a}$$

$$-k\frac{\partial T}{\partial x} = 0, \qquad \text{at } x = 0, t > 0 \tag{28b}$$

$$k\frac{\partial T}{\partial x} + hT = hT_\infty, \qquad \text{at } x = L, t > 0 \tag{28c}$$

$$T = T_0, \qquad \text{in } 0 < x < L, t = 0 \tag{28d}$$

where k is the thermal conductivity and α is the thermal diffusivity.

By defining the following dimensionless variables:

$$X = \frac{x}{L}, \qquad \tau = \frac{\alpha t}{L^2}, \qquad \theta(X,\tau) = \frac{T(x,t) - T_\infty}{T_0 - T_\infty}, \qquad Bi = \frac{hL}{k} \tag{29}$$

equations (28a-d) are re-written as:

$$\frac{\partial \theta(X,\tau)}{\partial \tau} = \frac{\partial^2 \theta}{\partial X^2}, \qquad \text{in } 0 < X < 1, \tau > 0 \tag{30a}$$

$$\frac{\partial \theta}{\partial X} = 0, \qquad \text{at } X = 0, \tau > 0 \tag{30b}$$

$$\frac{\partial \theta}{\partial X} + Bi\theta = 0, \qquad \text{at } X = 1, \tau > 0 \tag{30c}$$

$$\theta = 1, \qquad \text{in } 0 < X < 1, \tau = 0 \tag{30d}$$

The analytical solution of this problem is given by [21]:

$$\theta(X,\tau) = \sum_{m=1}^{\infty} \frac{e^{-\gamma_m^2 \tau}}{N(\gamma_m)} \psi(\gamma_m, X) \int_{X'=0}^{1} \psi(\gamma_m, X') dX' \tag{31}$$

where

$$\psi(\gamma_n, X) = \cos(\gamma_m X) \tag{32a}$$

$$\frac{1}{N(\gamma_m)} = 2\frac{\gamma_m^2 + Bi^2}{(\gamma_m^2 + Bi^2) + Bi} \tag{32b}$$

and the eigenvalues γ_m are the positive roots of:

$$\gamma \tan \gamma_m = Bi \tag{32c}$$

The dimensionless heat conduction problem (30a-d) is considered as the high-fidelity model in this example. The solution of problem (30a-d) can be obtained from Eq. (31) by truncating the summation with sufficient terms to reach convergence within the desired tolerance.

A lumped formulation is considered as the low-fidelity model in this example. The lumped model is given by:

$$\rho c L \frac{dT_{app}(t)}{dt} = h\left(T_\infty - T_{app}\right), \qquad t > 0 \tag{33a}$$

$$T_{app} = T_0, \qquad t = 0 \tag{33b}$$

Where ρ and c are the density and specific heat.

The solution of the lumped model in dimensionless form is given by:

$$\theta_{app}(\tau) = e^{-Bi\tau} \tag{34}$$

Therefore, the only parameter of both the high-fidelity model and the low-fidelity model is the Biot number, that is,

$$\boldsymbol{\beta} = \boldsymbol{\beta}_{app} = [Bi] \tag{35}$$

As it is well-known from basic heat transfer, the approximation error between the solutions of the high-fidelity model (Eq. 31) and of the low-fidelity model (Eq. 34) in this example is small for small Biot numbers, where usually $Bi = 0.01$ is used as a threshold value for the validity of the lumped model [21]. In fact, the analytical solution for $Bi = 0.01$ presented in Figure 1a shows that temperature gradients are quite small along the plate for different times, thus resulting in maximum errors around 2% at large times tending to steady-state (see Figure 1b). Such behavior is quite different from that observed for large Biot numbers. Figure 2a shows the analytical solution for $Bi = 10$, where large temperature gradients can be observed in the plate, thus resulting in the large approximation errors presented in Figure 2b.

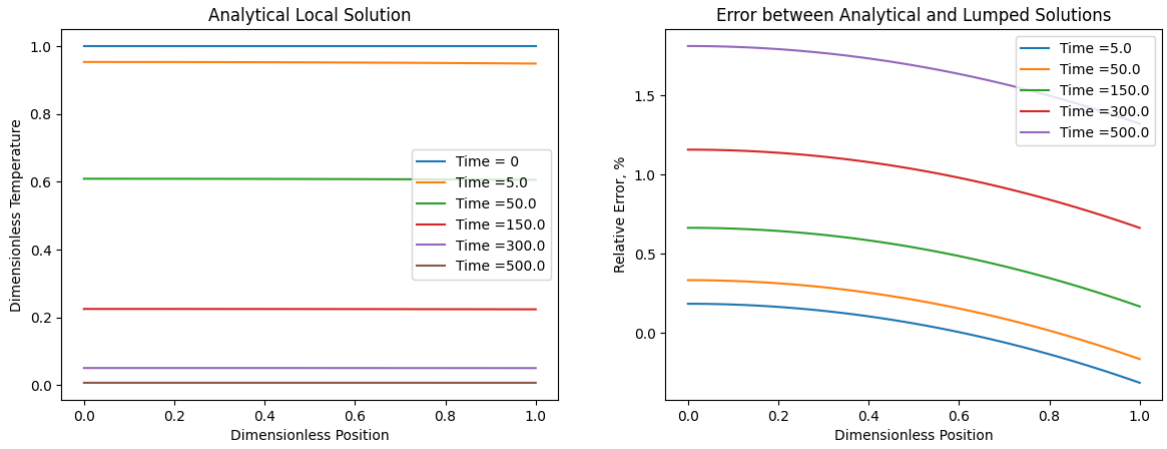

(a) (b)

Figure 1. (a) Analytical solution for $Bi = 0.01$; (b) Relative approximation error for $Bi = 0.01$.

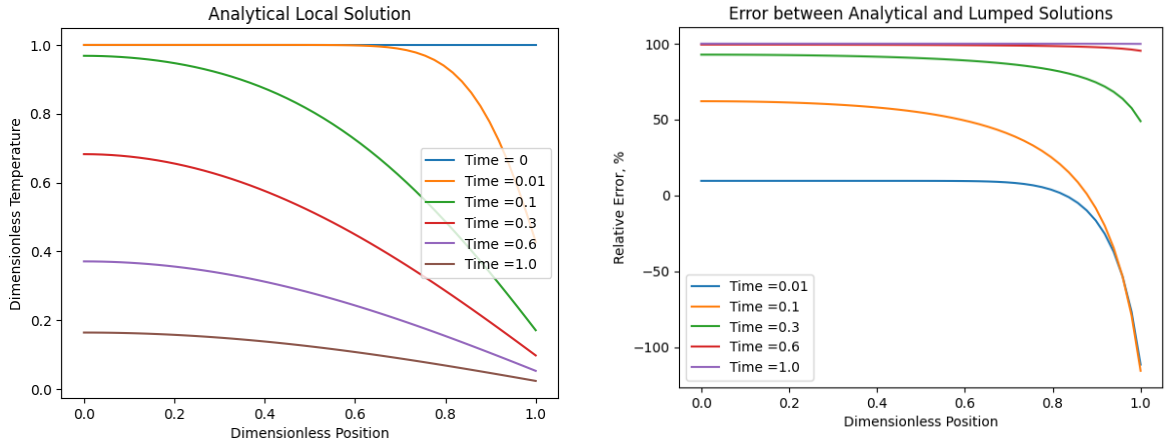

(a) (b)

Figure 2. (a) Analytical solution for $Bi = 10$; (b) Relative approximation error for $Bi = 10$.

Since the approximation errors are larger for large values of the Biot number, a Gaussian prior with mean 10 and standard deviation 2 is considered for the solution of the inverse problem in this example. Three thousand samples of the Biot number obtained from this distribution are presented in Figure 3. The inverse problem of interest involves the estimation of the single parameter appearing in either the high-fidelity model or the low-fidelity model, that is, the Biot number. Nonintrusive transient measurements taken at the insulated boundary ($X = 0$) every $\Delta\tau = 0.02$ are used for the inverse analysis. The measurements were simulated by solving the high-fidelity model with $Bi = 10$ and adding uncorrelated Gaussian errors with zero mean and standard deviation of 0.01. Figure 4 presents the simulated measurements.

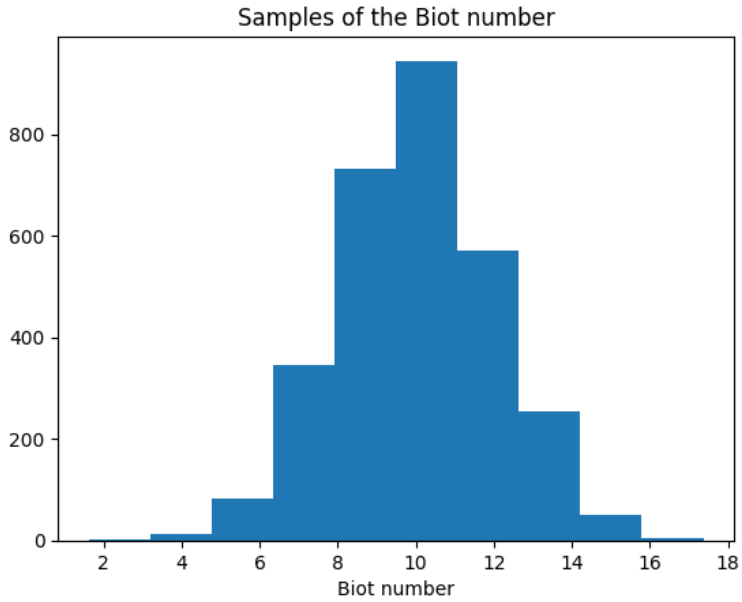

Figure 3. Samples of the Biot number used for the calculation of the approximate error statistics

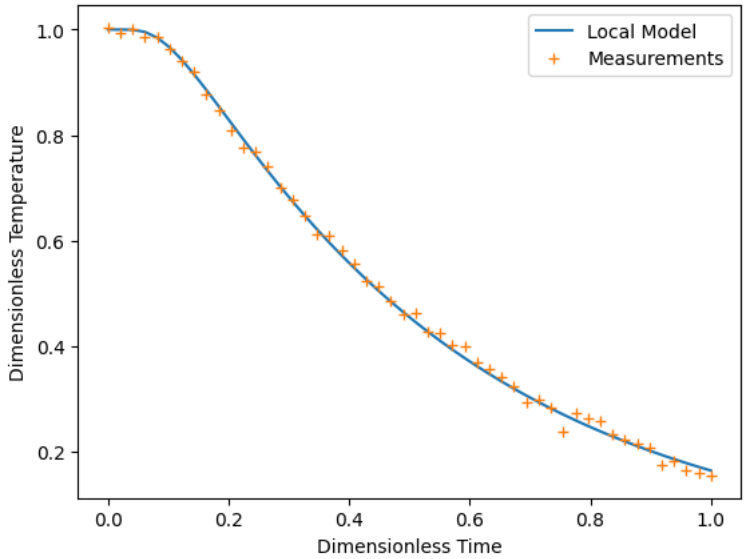

Figure 4. Simulated measurements taken at $X = 0$ with $Bi = 10$

In this example, we consider $N_s = 3000$ samples of the Biot number (see Figure 3) for the calculation of the statistics of the approximation error with Eqs. (13a,b). The means of the approximation errors, as well as the trace and the first 5 eigenvalues of their covariance matrix calculated with different numbers of samples are presented in Figures 5a-c, respectively. Figure 5a shows that the means of the approximation errors reached convergence with a small number of samples. On the other hand, the convergence of the covariance matrix was slow and required more samples as shown by Figures 5b,c. The calculation of the samples of the approximation error and their respective statistics took 731 s with a Python code running as a Google Colab notebook.

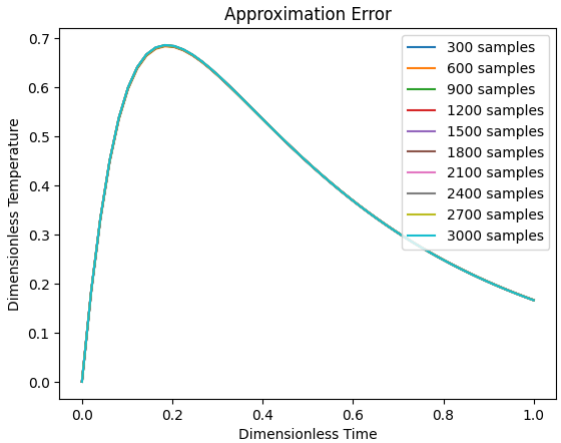

(a)

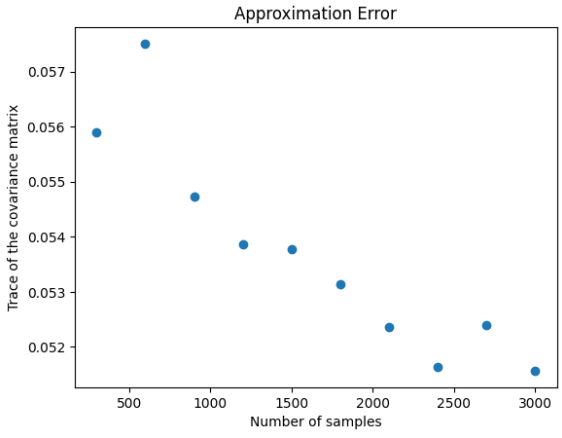

(b)

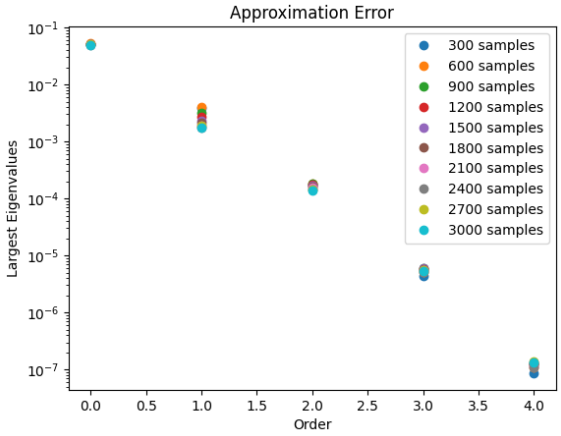

(c)

Figure 5. Convergence of the approximation error statistics: (a) Mean; (b) Trace of the covariance matrix; (c) First five eigenvalues of the covariance matrix

The samples of the solution of the high-fidelity (local) and low-fidelity (lumped) models used for the calculation of the approximation error are illustrated in Figure 6. This figure presents the mean values, as well as the 95% Gaussian confidence intervals ($\pm 1.96\sigma_{sol}$, where σ_{sol} is the respective standard deviation of the solution samples) and the 95% credible intervals (obtained from the 2.5% and 97.5% quantiles of the solution samples). Similar quantities are presented in Figure 7 for the approximation error. We note in Figure 6 that the Gaussian model provided a good representation for the statistics of the high-fidelity (local) model, but such was not the case for the low-fidelity (lumped) model. Thus, the confidence and credible intervals of the approximation error shown in Figure 7 did not coincide in the region of large errors around $\tau = 0.2$ in this example.

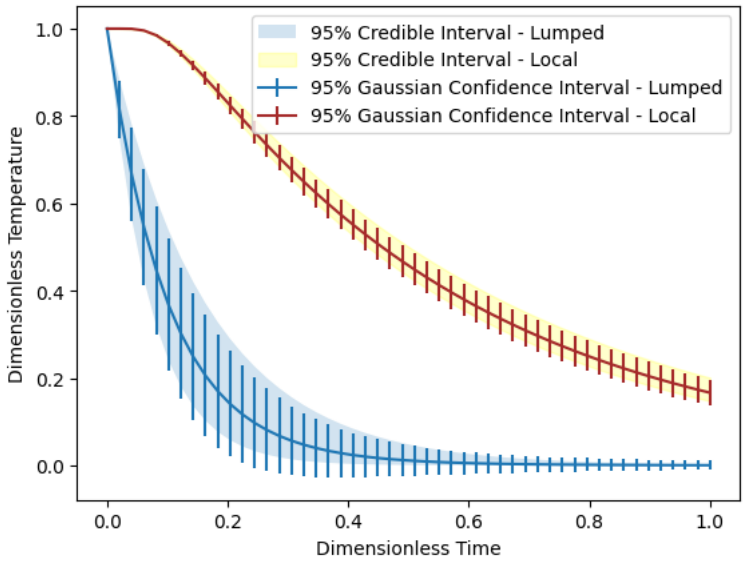

Figure 6. Samples of the solutions of the high-fidelity and low-fidelity models

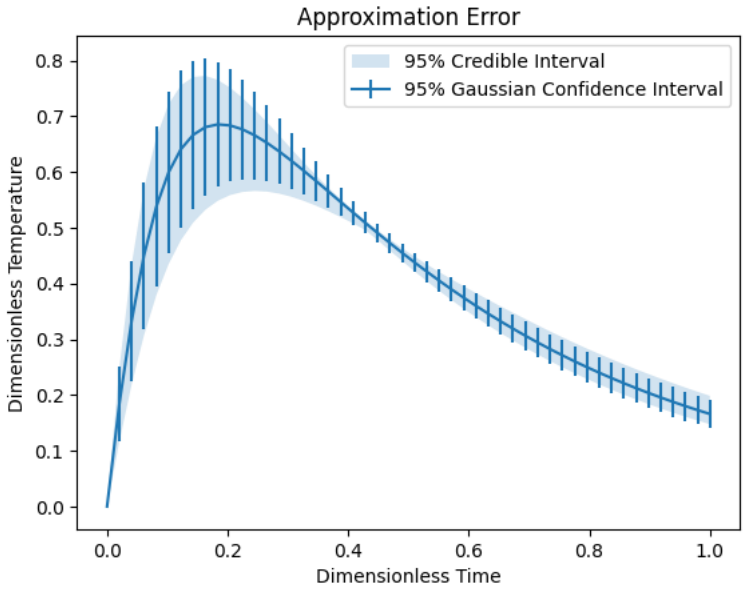

Figure 7. Samples of the approximation error statistics

The solution of the inverse problem with the Metropolis-Hastings algorithm of the Markov Chain Monte Carlo method [6,13] is now considered for this example. Three different test-cases are examined, namely:

(i) The high-fidelity model given by Eq. (31) is used for the calculation of the estimated temperature and the likelihood is calculated with Eq. (10);

(ii) The low-fidelity model given by Eq. (34) is used for the calculation of the estimated temperature and the likelihood is calculated with Eq. (10), that is, the AEM approach is not applied to correct for approximation errors;

(iii) The low-fidelity model given by Eq. (34) is used for the calculation of the estimated temperature and the likelihood is calculated with Eq. (16), that is, the AEM approach is applied to correct for approximation errors.

For all cases, the Markov chains for the Biot number were started at $Bi = 5$, while the simulated measurements were simulated with $Bi = 10$, as shown in Figure 4. The Markov chains were simulated with 20000 states, and the first 5000 states were considered as the burn-in period. The proposal distribution in the Metropolis-Hastings algorithm was given by a Gaussian random-walk process [6,13], with a standard deviation of 5% of the value of the sample at the current state of the Markov chain.

Let´s first analyze test-case (i), where the high-fidelity model was used for the solution of the inverse problem. In fact, an inverse crime [7] is committed in this case, since the same model was used to generate the simulated measurements and for the solution of the inverse problem. The Markov chain for the Biot number is presented in Figure 8. This figure shows that the chain reached equilibrium in about 1000 states. Thus, the assumed burn-in period could be safely used for the calculation of the posterior distribution statistics, with the samples between states 5000 and 20000. Figure 9 shows the histogram of the samples of the Biot number after the burn-in period. This figure reveals that the posterior distribution resembles a Gaussian distribution, centered around the exact value of the Biot number that was used to generate the simulated measurements. The estimated temperatures at the measurement location are in excellent agreement with the measurements, as shown by Figure 10. In fact, the absolute

value of the logarithm of the Posterior distribution was significantly minimized by the Metropolis-Hastings algorithm as the Markov chain evolved, as shown by Figure 11.

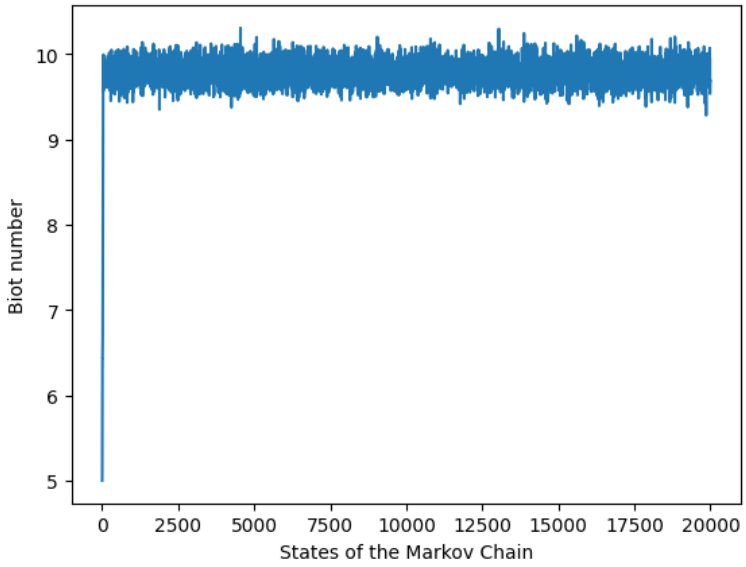

Figure 8. Test-case (i): Markov chain for the Biot number

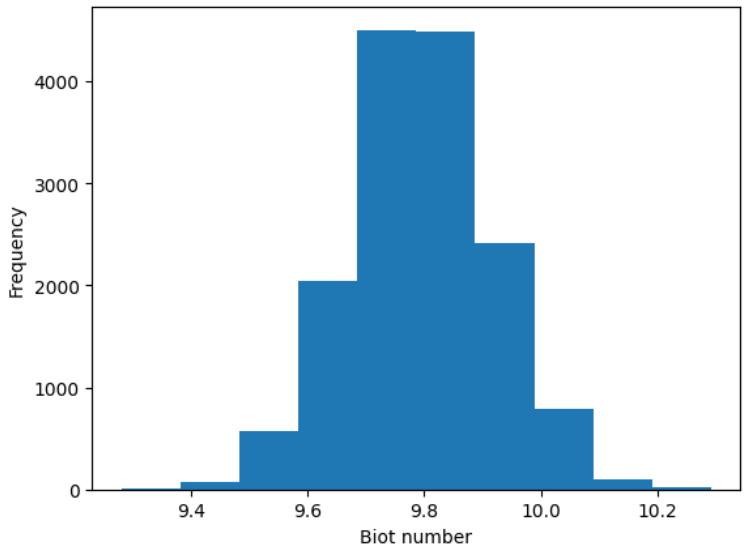

Figure 9. Test-case (i): Histogram of the Biot number samples after the burn-in period

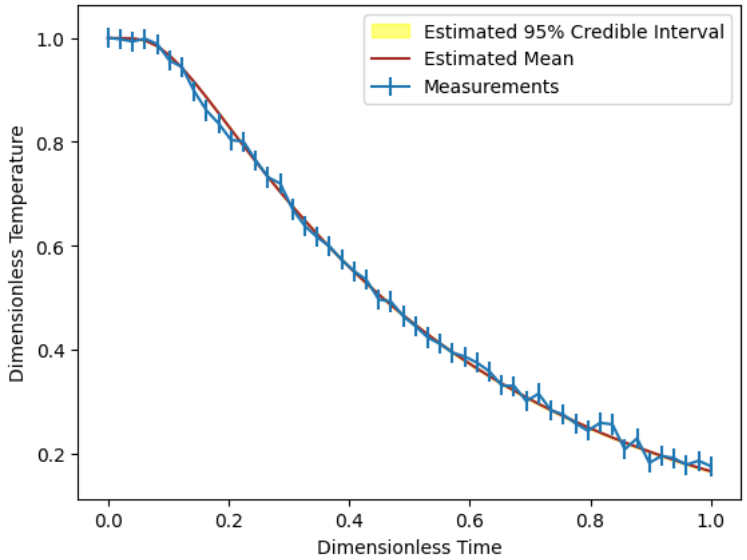

Figure 10. Test-case (i): Comparison between estimated and measured temperatures

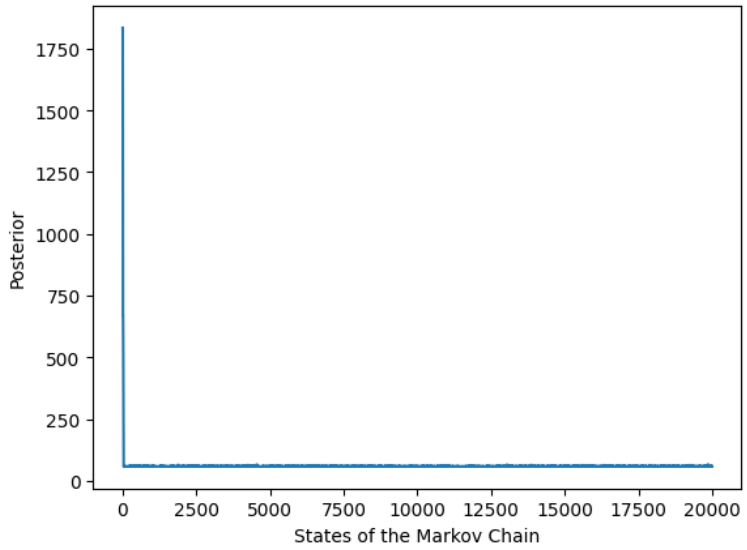

Figure 11. Test-case (i): Markov chain of the absolute value of the logarithm of the Posterior distribution

Test-case (ii) is now analyzed, where the high-fidelity model was replaced by the low-fidelity model for the solution of the inverse problem, without accounting for the approximation errors. The Markov chain and the histogram of the samples (after the burn-in period) of the Biot number are presented in Figures 12 and 13, respectively. These figures show that the equilibrium distribution of the Biot number samples was around a value completely different from the exact one (that was used to generate the simulated measurements). This behavior resulted from the fact that the low-fidelity model used for the solution of the inverse problem was not compatible with the high-fidelity model, as shown by Figure 6, and the AEM approach was not applied in this test-case. Besides reaching the wrong equilibrium posterior distribution for the Biot number, Figure 14 shows that the use of the low-fidelity model resulted in a poor agreement between estimated and measured temperatures. Hence, the temperature residuals

were correlated, clearly demonstrating that the applied low-fidelity model with the estimated parameter was not capable of appropriately reproducing the experimental data. In addition, Figure 15 shows that the minimum absolute value of the logarithm of the Posterior distribution reached in this test-case was significantly larger than that for test-case (i).

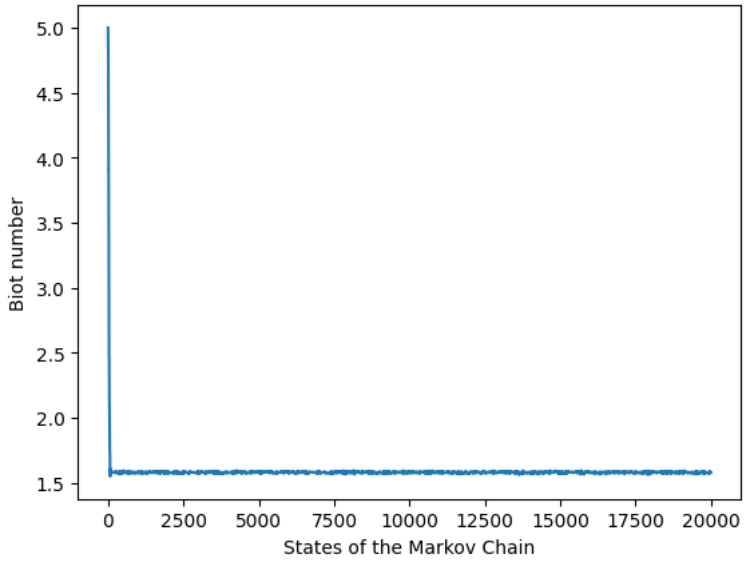

Figure 12. Test-case (ii): Markov chain for the Biot number

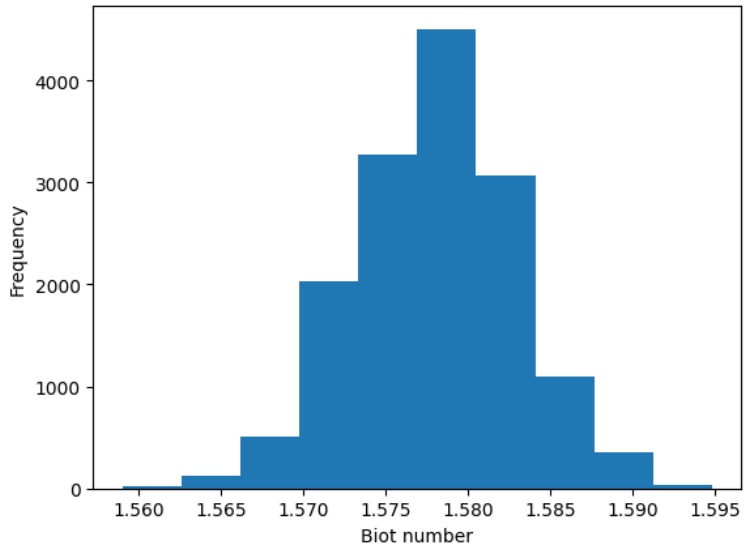

Figure 13. Test-case (ii): Histogram of the Biot number samples after the burn-in period

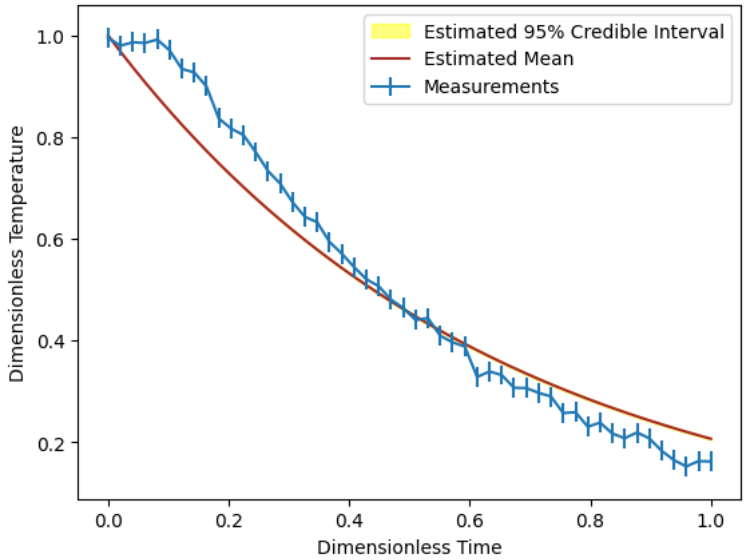

Figure 14. Test-case (ii): Comparison between estimated and measured temperatures

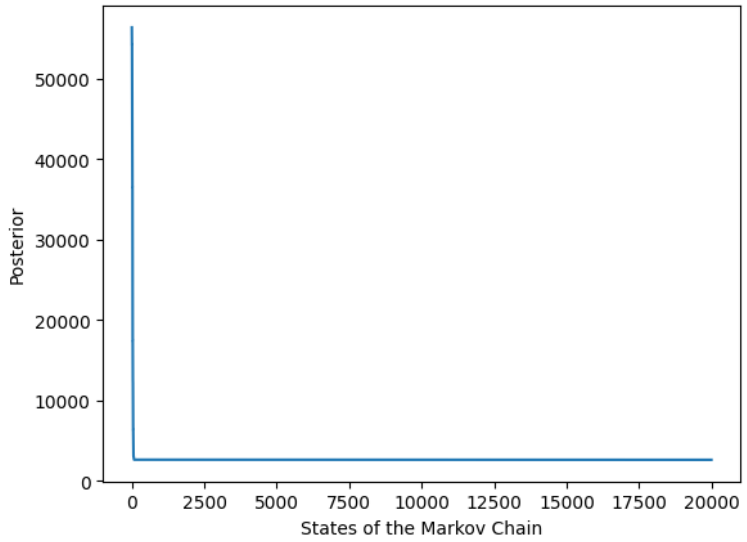

Figure 15. Test-case (ii): Markov chain of the absolute value of the logarithm of the Posterior distribution

The problems evidenced by test-case (ii), resulting from the simple replacement of the high-fidelity model by the low-fidelity model in the solution of the inverse problem, can be overcome if the approximation errors are accounted for in the inverse problem solution with the application of the AEM approach. Test-case (iii) thus considers the approximation error statistics calculated above, for the simulation of the posterior distribution given by Eq. (17) with the Metropolis-Hastings algorithm of the Markov Chain Monte Carlo method. Figure 16 presents the Markov chain of the Biot number for test-case (iii), while Figure 17 shows the histogram of the samples of the Markov chain after the burn-in period. Differently from the results shown by Figures 12 and 13 for test-case (ii), Figures 16 and 17 reveal that the equilibrium distribution of the Biot number obtained with test-case (iii) is indeed around the

exact value of the Biot number, similarly to test-case (i) where the high-fidelity model was used. In addition, the agreement between estimated and measured temperatures for test-case (iii) shown by Figure 18 was analogous to that obtained with the high-fidelity model (see Figure 10), that is, the temperature residuals were not correlated. Therefore, the use of the low-fidelity model with approximation errors accounted for by the AEM approach was capable of accurately representing the experimental data. The behavior of the posterior distribution of test-case (iii) presented by Figure 19 was also quite similar to that observed in Figure 11 for test-case (i).

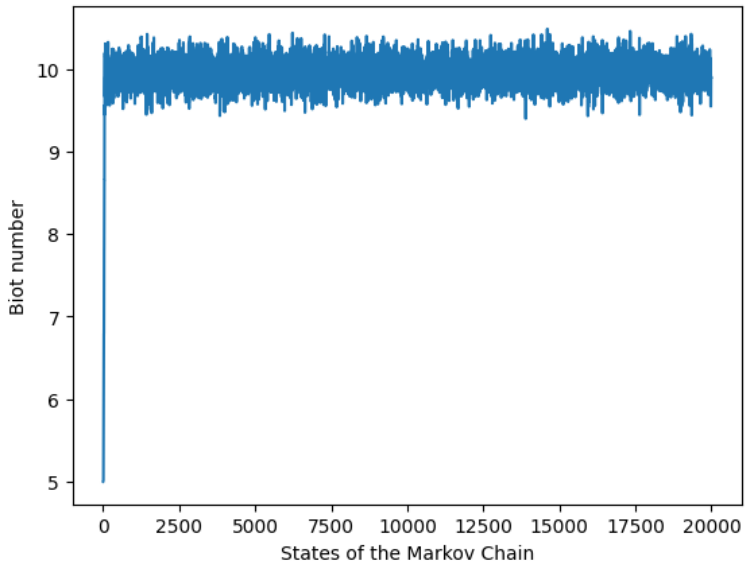

Figure 16. Test-case (iii): Markov chain for the Biot number

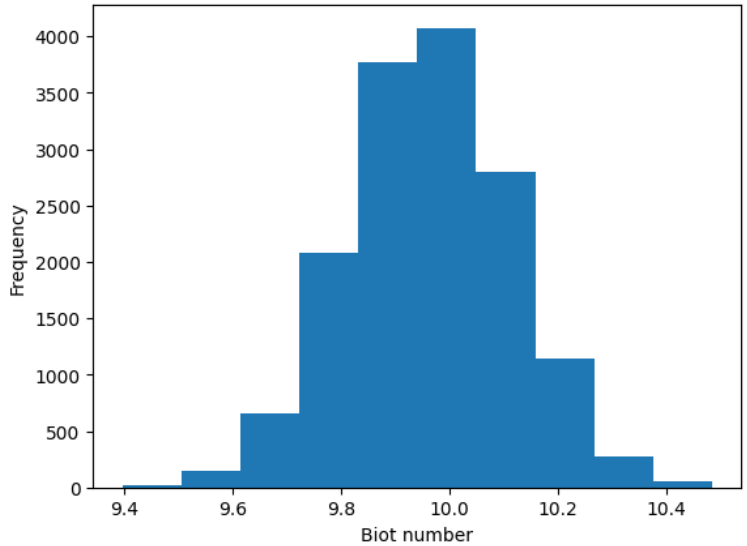

Figure 17. Test-case (iii): Histogram of the Biot number samples after the burn-in period

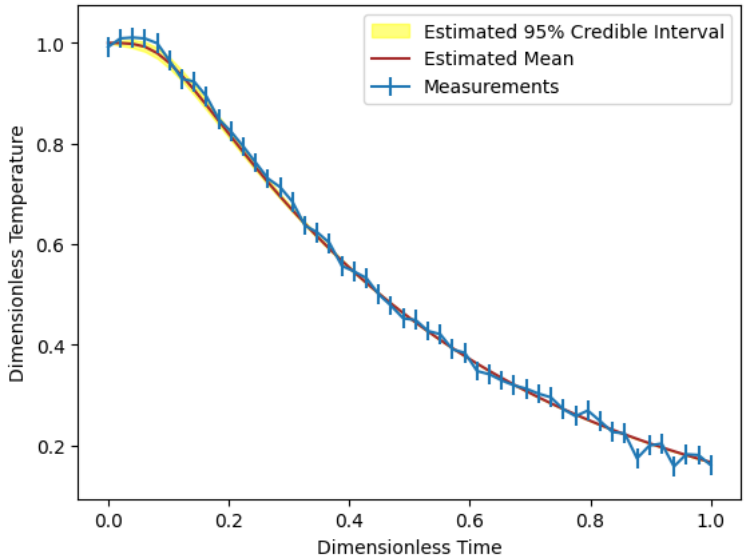

Figure 18. Test-case (iii): Comparison between estimated and measured temperatures

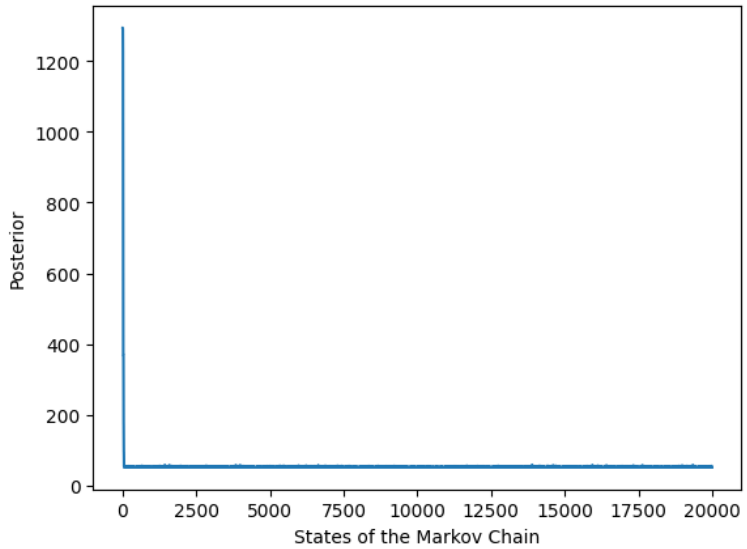

Figure 19. Test-case (iii): Markov chain of the absolute value of the logarithm of the Posterior distribution

Some statistics of the posterior distributions for the Biot number obtained with each of the test-cases presented above are shown by Table 1. The CPU times for the generation of the Markov chains are also presented in this table, which were obtained with a Python code run as a Google Colab notebook. Such as discussed above, the statistics depicted in Table 1 reveal that the use of the low-fidelity model with the AEM approach resulted in a posterior distribution similar to that obtained with the high-fidelity model, but in a much shorter computational time. Even if we take into account the CPU time required for the calculation of the approximation error statistics (731 s), the speed-up was of 6.2 times for using the low-fidelity model with the AEM approach instead of the high-fidelity model in the solution of the inverse problem. On the other hand, the use of the low-fidelity model without accounting for the approximation errors resulted in a totally distinct posterior distribution in test-case (ii), as also evidenced from the

bad agreement between estimated and measured temperatures (see also Figure 14), despite the fact that the Markov chain was generated quite fast. Unfortunately, the application of the AEM approach requires proper priors (with limited variances), for the calculation of the approximation error statistics.

Table 1. Statistics of the estimated Biot number and CPU times of the inverse problem solution

Test-case	Mean	Standard Deviation	2.5% Quantile	97.5% Quantile	CPU Time
(i)	9.794	0.123	9.555	10.041	1.25 h
(ii)	1.578	0.005	1.569	1.588	0.8 s
(iii)	9.962	0.151	9.667	10.253	0.8 s

It is instructive to note that the original uncertainties related to the Biot number before the solution of the inverse problem (represented by the prior information, the samples of which are shown in Figure 3), were significantly reduced when the information provided by measurements was taken into account through the likelihood function, thus resulting in the posterior distribution with samples shown by Figure 9 or Figure 17, and with the statistics presented in Table 1.

3.2. Estimation of Heat Fluxes of Large Magnitudes [22–24]

The physical model considered in this case study draws its foundation from the work of Orlande [22], which formulated both the forward and inverse problems and proposed employing the AEM within a Markov Chain Monte Carlo sampler based on the Metropolis-Hastings algorithm. Next, the AEM was employed as well in the context of the classical and Steady-State Kalman filter by Pacheco et al. [23,24]. Their findings are the subject of this section.

The physical model comprises the flat plate shown in Figure 20. The objective of the forward problem is to evaluate the temperature $T(\mathbf{r}, t)$ in the domain Ω, where $\mathbf{r} = [x \quad y \quad z]^T$ is the position vector and t is the time. The plate has dimensions $a \times b \times c$ such that $0 < x < a, 0 < y < b, 0 < z < c$. The top surface of the place – herein defined as $\partial\Omega_1 = \{\mathbf{r} \in \Omega \mid z = c\}$ – is subjected to a high-magnitude, focused heat flux $q(x, y, t)$, while the remaining boundaries – defined as $\partial\Omega_2$ – are thermally insulated. At last, the initial temperature is assumed uniform and equal to $T_0 = 300$ K. The mathematical model is thus given by Eqs. (36a-d).

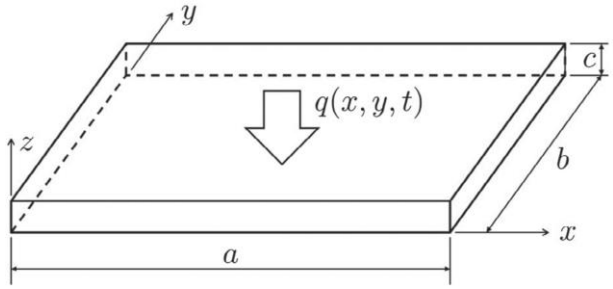

Figure 20. Physical model considered in [22–24]

$$C(T)\frac{\partial T}{\partial t} = \nabla \cdot [k(T)\nabla T], \qquad \mathbf{r} \in \Omega, t > 0 \tag{36a}$$

$$k(T)\frac{\partial T}{\partial \mathbf{n}} = q(\mathbf{r},t), \qquad \mathbf{r} \in \partial\Omega_1, t > 0 \tag{36b}$$
$$\frac{\partial T}{\partial \mathbf{n}} = 0, \qquad \mathbf{r} \in \partial\Omega_2, t > 0 \tag{36c}$$
$$T(\mathbf{r},t) = T_0, \qquad \mathbf{r} \in \Omega, t = 0 \tag{36d}$$

A major challenge in both forward and inverse problems is that a large temperature range unfolds, such that the temperature effect on the thermal properties must not be disregarded. Indeed, the plate thermal properties are given in Eqs. (37a,b).

$$k(T) = 12.45 + 0.014T + 2.517 \times 10^{-6}T^2 \ [\mathrm{W\,m^{-1}\,K^{-1}}] \tag{37a}$$
$$C(T) = 1324.75T + 3557900 \qquad [\mathrm{J\,m^{-3}\,K^{-1}}] \tag{37b}$$

In this context, solving the forward problem comprises bestowing the function $q(\mathbf{r},t)$ in order to evaluate $T(\mathbf{r},t)$. The inverse problem involves thus employing experimentally measured values of $T(\mathbf{r},t)$ to estimate an unknown $q(\mathbf{r},t)$. Particularly in this problem, temperature measurements are assumed available whenever at the $z = 0$ surface – that is the face opposite to where the heat flux is imposed.

The numerical intricacies and high-dimensionality of this complete model compels the deployment of reduced order models to render the inverse problem computationally tractable. The complete derivation of this reduced model is herein suppressed for the sake of brevity and can be found in references [22–24]. Yet, it bears mentioning that its foundation lays in averaging the temperature in the z direction, thus arising the average temperature $\overline{T}(\overline{\mathbf{r}},t)$, where $\overline{\mathbf{r}} = [x \quad y]^T$ is the position vector. The domain $\overline{\Omega}$ is thus the xy plane, with $0 < x < a$ and $0 < y < b$, while $\partial\overline{\Omega} = \{\overline{\mathbf{r}} \in \overline{\Omega} \mid x = 0 \text{ or } x = a \text{ or } y = 0 \text{ or } y = b\}$. The mathematical model is shown in Eqs. (38a-c), where the constant thermal properties k^* and C^* are drawn from Eqs. (37a,b) being evaluated at a reference temperature $T^* = 600$ K.

$$C^*\frac{\partial \overline{T}}{\partial t} = k^*\nabla^2\overline{T} + \frac{q(\overline{\mathbf{r}},t)}{c}, \qquad \overline{\mathbf{r}} \in \overline{\Omega}, t > 0 \tag{38a}$$
$$\frac{\partial \overline{T}}{\partial \mathbf{n}} = 0, \qquad \overline{\mathbf{r}} \in \partial\overline{\Omega}, t > 0 \tag{38b}$$
$$\overline{T} = T_0, \qquad \overline{\mathbf{r}} \in \overline{\Omega}, t = 0 \tag{38c}$$

At last, it bears mentioning that the reduced model provides only the value of the average temperature, while the temperature measurements are taken at the $z = 0$ surface. To relate these quantities, approximations based on both the classical and improved lumped methodologies [25] were proposed in [22] and are presented in Eqs. (39a,b). An equation similar to Eq. (39b) was also derived in [22] to approximate the temperature at $z = c$, shown in Eq. (39c).

$$\text{Classical Lumped: } T(x,y,z=0,t) = \overline{T}(x,y,t) \tag{39a}$$
$$\text{Improved Lumped: } T(x,y,z=0,t) = \overline{T}(x,y,t) - \frac{c}{6k^*}q(x,y,t) \tag{39b}$$
$$T(x,y,z=c,t) = \overline{T}(x,y,t) + \frac{c}{3k^*}q(x,y,t) \tag{39c}$$

Before presenting the numerical results, it bears mentioning that in both reference papers [22,23], the complete model was solved considering reference profiles for $q(\mathbf{r},t)$ with the

objective of providing synthetic measurements with added Gaussian noise with zero mean and standard deviation of 1.25 K. Furthermore, in [22] the sought heat flux is a function of position only, while in [23] the time dependency is accounted for. For the sake of brevity, we will only discuss the latter here, focusing on calculating the approximation errors and the resulting estimates.

Assuming time dependency on the heat flux brings a severe increase in complexity, for the number of unknowns is largely increased. Such complexity renders batch estimation approaches (such as MCMC) computationally intractable. The best alternative is thus resorting to recursive estimation. Therefore, the Kalman Filter [14,15] rises as a powerful candidate. Yet, calculating the approximation errors is not without its challenges, as will be discussed henceforth. The crux of such challenge lies in the need for consistency between the temperature fields of the complete and reduced models at each time step. Although the reader is referred to [23] for a thorough explanation thereof, we will next briefly present the rationale behind it.

As mentioned above, a major challenge lies in maintaining consistency between the high- and low-fidelity models, so the calculated AEs bring meaningful information. Thus, at the beginning of each recursive step, it bears ensuring that the complete model be in the same state of the reduced model. In other words, the average temperature in the complete model must be made equal to $\overline{T}(x, y, t)$. This is clearly an underdetermined problem – the number of volumes in the complete model grid is n_z times larger than in the reduced model, where n_z is the number of control volumes (CVs) in the z-direction. To address this problem, we consider a grid with $n_z = 3$ (cf. Figure 21) with T_1, T_2 and T_3 as the temperatures at the center of the CVs. We approximate $\overline{T}$ as the arithmetic mean of these values and write finite-difference approximations for the temperatures at the boundaries $z = 0$ and $z = c$ in terms thereof. Thereafter, we employ Eqs. (39b,c), thus closing a system of three equations and three unknowns for each CV in the grid. Solving this system yields the approximations for T_1, T_2 and T_3 given in Eqs. (40a-c). These ensure consistency between high- and low- fidelity models, allowing for appropriate calculation of the AEs. With these in hand, we are ready to apply the Kalman Filter with the EEM.

$$T_1 = \frac{1}{99}\left[80T_b + 27\overline{T} - 8T_t + \frac{3q\Delta z}{k(T_{top})}\right] \tag{40a}$$

$$T_2 = \frac{1}{11}\left[-8T_b + 27\overline{T} - 8T_t + \frac{3q\Delta z}{k(T_{top})}\right] \tag{40b}$$

$$T_3 = \frac{1}{99}\left[-8T_b + 27\overline{T} + 80\,T_t - \frac{30q\Delta z}{k(T_{top})}\right] \tag{40c}$$

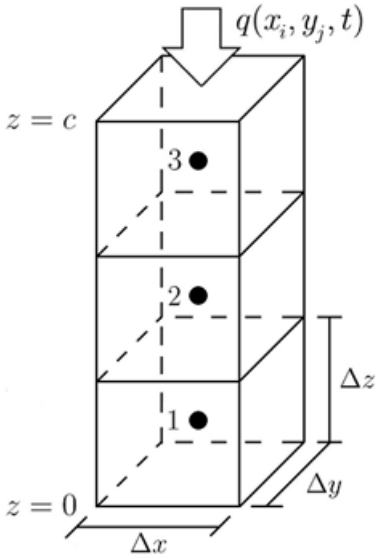

Figure 21. Schematic of three-node mesh in z-direction for calculating AEs

The reference heat flux in this study is shown in Figure 22, with a small region being subjected to a heat flux of $10^7\ \mathrm{W/m^2}$. The synthetic measurements were obtained by solving the complete model with a converged grid and controlled time-stepping, thus ensuring that the present analysis is devoid of inverse crime. In Figure 23 one can observe the resulting temperature field and the respective synthetic measurements. For the sake of brevity, the results presented herein focus on the spatial distribution at the end of the numerical experiment (i.e. at $t = 2.0\ \mathrm{s}$) and the time evolution at the center of the heated region, which we will henceforth refer to as the probed region.

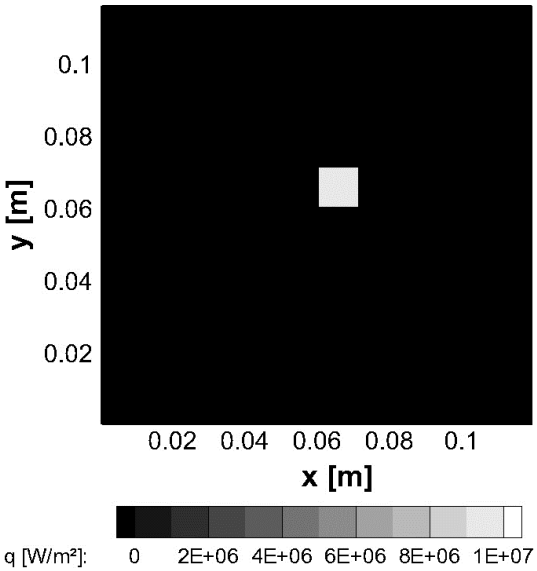

Figure 22. Exact heat flux to be estimated in this case study.

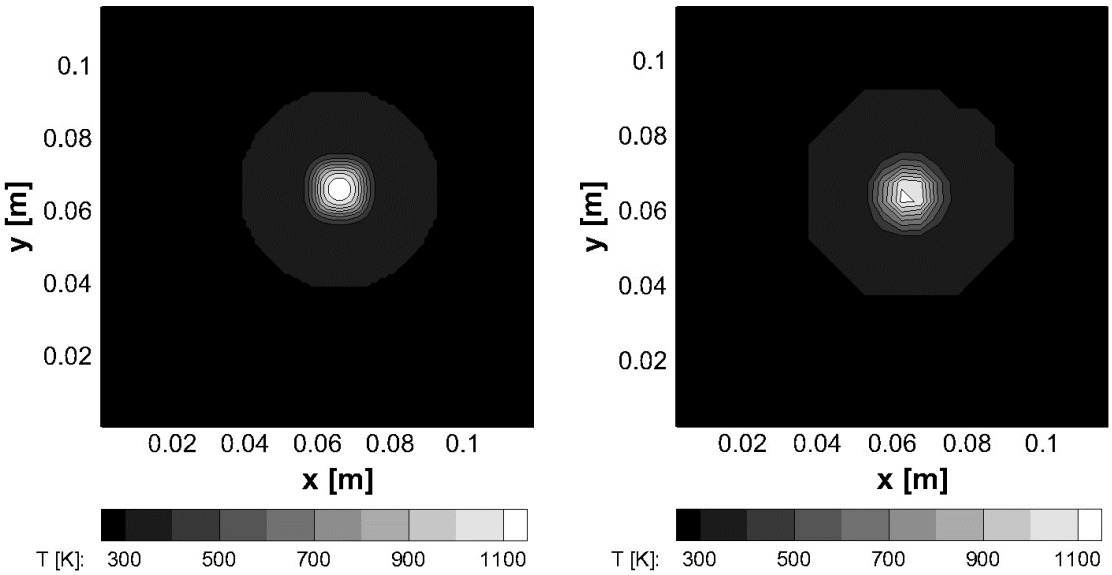

Figure 23. Temperature fields at $z = 0$ and $t = 2.0$ s in the complete model: a) exact values; and b) synthetic measurements.

We first address the results obtained using the Classical Lumped Formulation. Figure 24 presents the estimated heat flux at the probed region without and with the EEM. It is clearly shown that, in the absence of the EEM, the onset of nonlinearities takes its tool in the heat flux estimation. The estimates never arrive at the exact value and the 99% confidence intervals barely encompasses it. On the other hand, including the EEM in the estimation process yields significantly better estimates, meaning that the calculated AEs are indeed providing important corrections to the reduced model. It bears noticing also that despite the improvement in performance, the obtained estimated are somewhat unstable, with noticeable oscillation being observed.

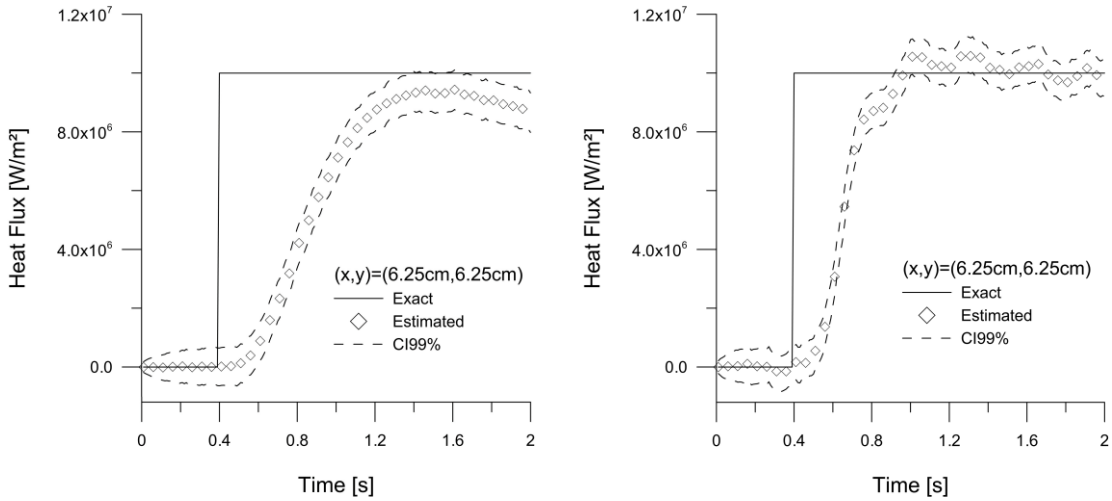

Figure 24. Time evolution of heat flux at the probed region with the Classical Lumped Formulation: (a) without; and (b) with EEM.

Next, we evaluate the results for the temperature at the probed region. It is shown in Figure 25 that the temperature is accurately estimated, within the envelope of the 99% confidence interval throughout the numerical experiment. Taking a closer look at the respective residuals, however, a slight correlation is present, meaning that despite the progress made, there is still information not being fully recovered in the measurements. This is an expected result since this numerical experiment is devoid of inverse crime. Finally, analyzing the estimated temperature and heat flux maps at $t = 2.0\ s$ in Figure 26 and comparing them with Figures 22 and 23 evidences that the performance observed in the probed region is similar throughout the entire domain.

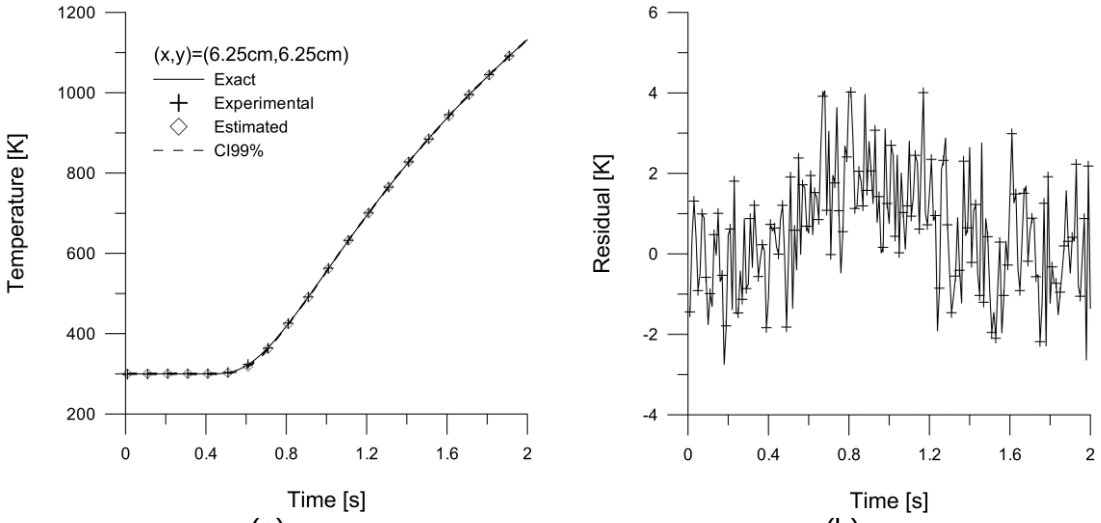

(a) (b)

Figure 25. Time evolution at the probed region with the Classical Lumped Formulation and EEM: (a) exact, synthetic and estimated temperatures; and (b) residuals.

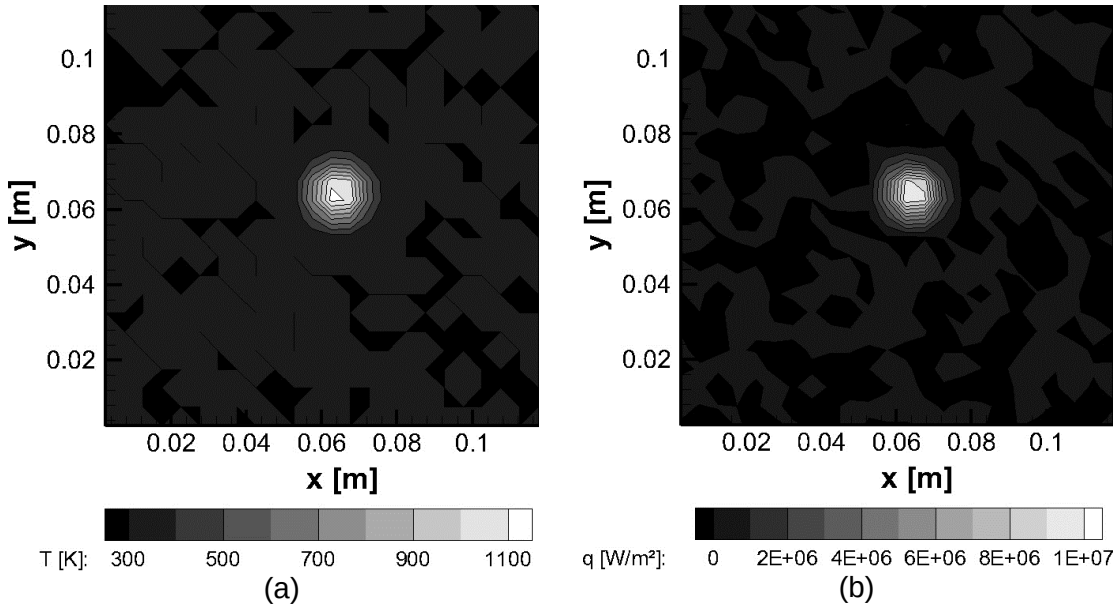

(a) (b)

Figure 26. Results obtained using the Classical Lumped Formulation and EEM at $t = 2.0\ s$: (a) temperature; and (b) heat flux.

Next, we analyze the results obtained using the Improved Lumped Formulation. Similar to what was observed for the Classical Lumped Formulation, the effect of including the EEM in the estimation process is clearly shown in Figure 27, with some particularities to be pointed out. In the absence of the EEM, the estimated heat flux once again falls short of the exact values, although the confidence interval succeeds in encompassing them. This increase in the envelope width is purely due to the Improved Lumped Formulation, though. Nevertheless, as the EEM is included, we notice that the estimated values find the exact values with great accuracy. Furthermore, the results here lack the unstable behavior seen before, which is a noteworthy improvement.

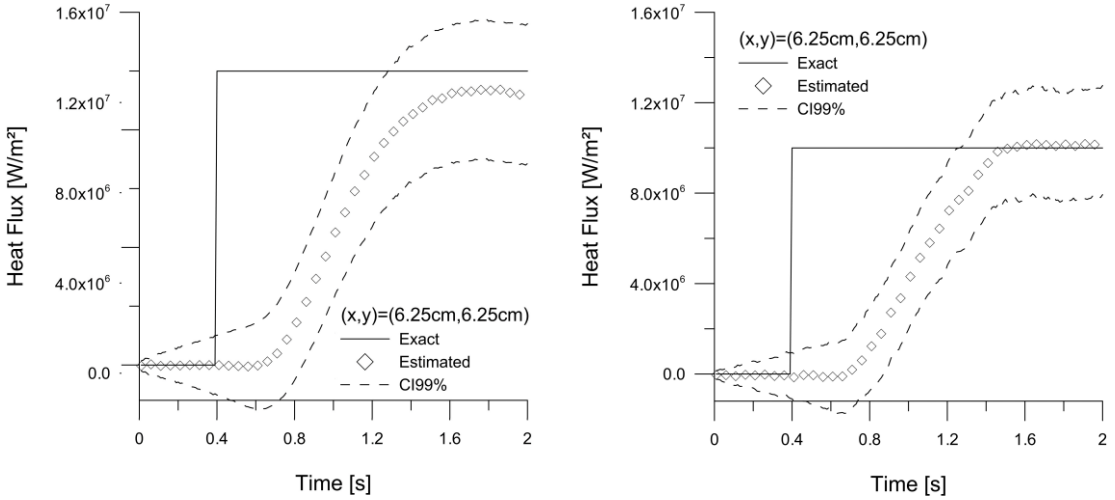

Figure 27. Time evolution of heat flux at the probed region with the Improved Lumped Formulation: (a) without; and (b) with EEM.

More improvements in performance can be seen for the temperature estimation, as shown in Figure 28. We not only observe that the estimated temperatures follow the exact temperatures closely, but also that the residuals stay uncorrelated throughout the entirety of the numerical experiment. This means that the combination of the Improved Lumped Formulation and the EEM yields a framework where we can accurately estimate the sought heat flux, obtaining stable solutions and extracting all information possible from the temperature measurements. In Figure 29 it can be observed the estimated temperature and heat flux maps at $t = 2.0s$ where once again we can infer a likewise performance in the remainder of the domain.

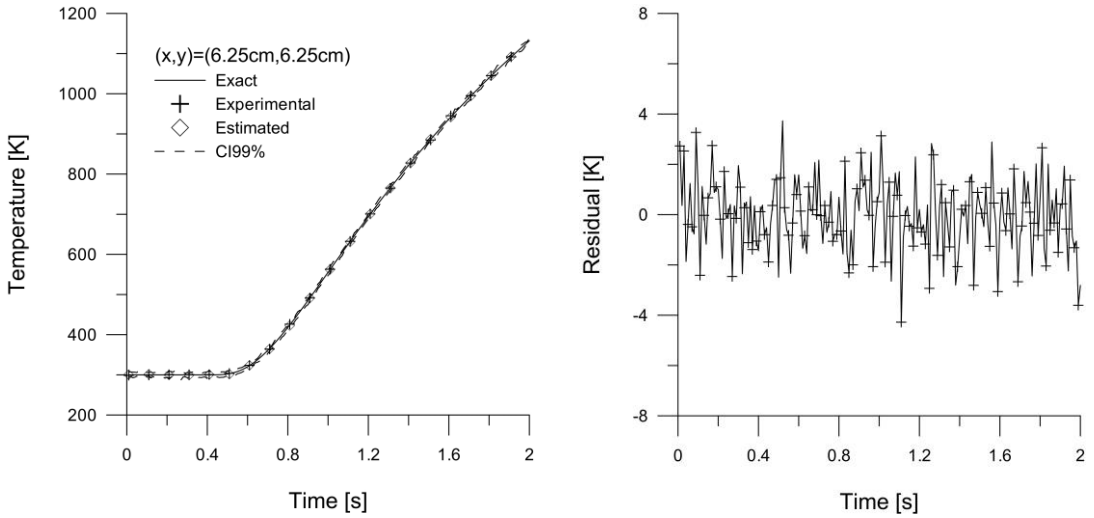

(a) (b)

Figure 28. Time evolution at the probed region with the Improved Lumped Formulation and EEM: (a) exact, synthetic and estimated temperatures; and (b) residuals.

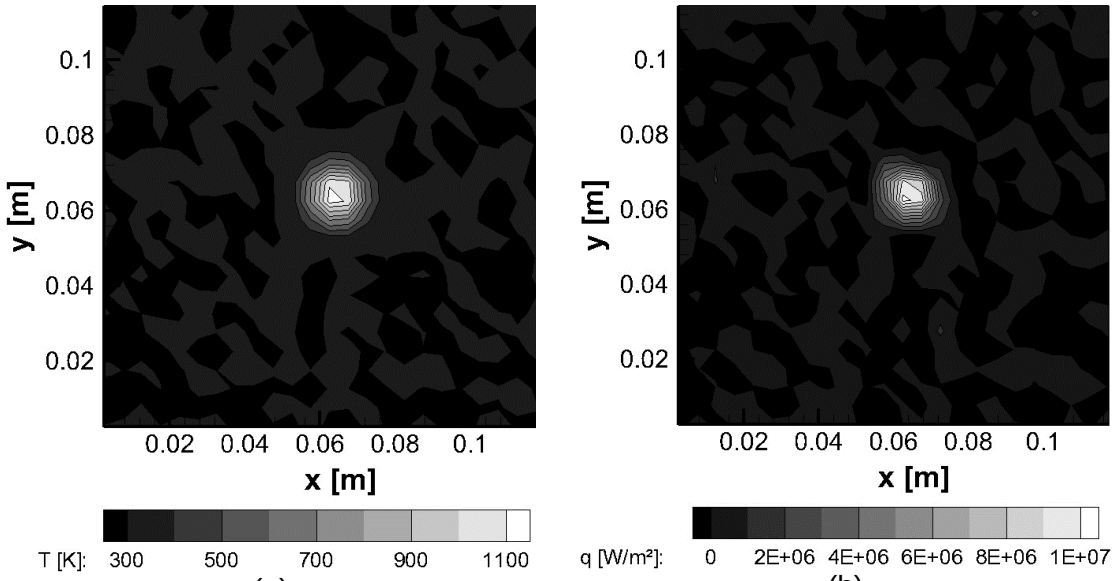

(a) (b)

Figure 29. Results obtained using the Improved Lumped Formulation and EEM at $t = 2.0$ s: (a) temperature; and (b) heat flux.

References

[1] J.V. Beck, K.J. Arnold, Parameter estimation in engineering and science, John Wiley & Sons Australia, Limited, 1977.
[2] Occam's razor, Simple Engl. Wikipedia Free Encycl. (2023). https://simple.wikipedia.org/w/index.php?title=Occam%27s_razor&oldid=8946531 (accessed July 31, 2023).

[3] ASME, Standard for Verification and Validation in Computational Fluid Dynamics and Heat Transfer, Standard No. ASME V&V 20-2009, New York, 2009.
[4] M.N. Ozisik, H.R.B. Orlande, M. Colaço, R.M. Cotta, Finite Difference Methods in Heat Transfer, 2nd ed., CRC Press, Boca Raton, USA, 2017.
[5] J.V. Beck, Sequential Methods in Parameter Estimation, Tutorial Session, in: 3rd Int. Conf. Inverse Probl. Eng., Port Ludlow, WA, 1999.
[6] H.R.B. Orlande, O. Fudym, D. Maillet, R.M. Cotta, Thermal measurements and inverse techniques, CRC Press, Inc., Boca Raton, USA, 2011.
[7] J.P. Kaipio, E. Somersalo, Statistical and Computational Inverse Problems, Springer Science+Business Media, Inc, 2004.
[8] A. Nissinen, Modelling errors in electrical impedance tomography, Dissertation in Forestry and Natural Sciences, University of Eastern Finland, 2011.
[9] A. Nissinen, L.M. Heikkinen, J.P. Kaipio, The Bayesian approximation error approach for electrical impedance tomography—experimental results, Meas. Sci. Technol. 19 (2007) 015501. https://doi.org/10.1088/0957-0233/19/1/015501.
[10] A. Nissinen, L.M. Heikkinen, V. Kolehmainen, J.P. Kaipio, Compensation of errors due to discretization, domain truncation and unknown contact impedances in electrical impedance tomography, Meas. Sci. Technol. 20 (2009) 105504. https://doi.org/10.1088/0957-0233/20/10/105504.
[11] A. Nissinen, V.P. Kolehmainen, J.P. Kaipio, Compensation of modelling errors due to unknown domain boundary in electrical impedance tomography, IEEE Trans. Med. Imaging. 30 (2011) 231–242. https://doi.org/10.1109/TMI.2010.2073716.
[12] A. Nissinen, V. Kolehmainen, J.P. Kaipio, Reconstruction Of Domain Boundary And Conductivity In Electrical Impedance Tomography Using The Approximation Error Approach, Int. J. Uncertain. Quantif. 1 (2011). https://doi.org/10.1615/Int.J.UncertaintyQuantification.v1.i3.20.
[13] M.N. Ozisik, H.R.B. Orlande, Inverse Heat Transfer: Fundamentals and Applications, 2nd ed., CRC Press, Inc., Boca Raton, USA, 2021.
[14] R.E. Kalman, A new approach to linear filtering and prediction problems, Trans. ASME--J. Basic Eng. 82 (1960) 35–45. https://doi.org/10.1115/1.3662552.
[15] D. Simon, Optimal State Estimation: Kalman, H Infinity, and Nonlinear Approaches, John Wiley & Sons, Inc., 2006.
[16] J.M.J. Huttunen, J.P. Kaipio, Approximation errors in nonstationary inverse problems, Inverse Probl. Imaging. 1 (2007) 77–93. https://doi.org/10.3934/ipi.2007.1.77.
[17] J. Huttunen, J. Kaipio, Approximation error analysis in nonlinear state estimation with an application to state-space identification, Inverse Probl. 23 (2007) 2141.
[18] M.S. Arulampalam, S. Maskell, N. Gordon, T. Clapp, A tutorial on particle filters for online nonlinear/non-Gaussian Bayesian tracking, IEEE Trans. Signal Process. 50 (2002) 174–188. https://doi.org/10.1109/78.978374.
[19] B. Ristic, S. Arulampalam, N. Gordon, Beyond the Kalman Filter: Particle Filters for Tracking Applications, Artech House, 2003. https://books.google.com.br/books?id=zABIY--qk2AC.
[20] H.R.B. Orlande, M.J. Colaço, G.S. Dulikravich, F.L.V. Vianna, W.B. da Silva, H.M. Fonseca, O. Fudym, State Estimation Problems in Heat Transfer, Int. J. Uncertain. Quantif. 2 (2012) 239–258. https://doi.org/10.1615/Int.J.UncertaintyQuantification.2012003582.
[21] M.N. Ozisik, Heat Conduction, 2nd ed., John Wiley & Sons, Inc., 1993.
[22] H.R.B. Orlande, G.S. Dulikravich, M. Neumayer, D. Watzenig, M.J. Colaço, Accelerated Bayesian Inference for the Estimation of Spatially Varying Heat Flux in a Heat Conduction Problem, Numer. Heat Transf. Part Appl. 65 (2013) 1–25.

[23] C.C. Pacheco, H.R.B. Orlande, M.J. Colaço, G.S. Dulikravich, Estimation of a location-and-time dependent high magnitude heat flux in a heat conduction problem using the Kalman filter and the approximation error model, Numer. Heat Transf. Part A. 68 (2015) 1198–1219.
[24] C.C. Pacheco, H.R.B. Orlande, M.J. Colaço, G.S. Dulikravich, Real-time identification of a high-magnitude boundary heat flux on a plate, Inverse Probl. Sci. Eng. 24 (2016) 1–1679. https://doi.org/10.1080/17415977.2016.1195829.
[25] R.Machado. Cotta, M.D. Mikhailov, Heat conduction : lumped analysis, integral transforms, symbolic computation, Wiley, Chichester; New York, 1997.

Tutorial 15: Experimental identification of mobile heat sources

MB Cherikh , JG Bauzin, A. Hocine, Najib LARAQI[1]

[1] LTIE, Université Paris Nanterre, Ville d'Avray - France

E-mail: mb.cherikh@parisnanterre.fr
jbauzin@parisnanterre.fr
ahocine@parisnanterre.fr
nlaraqi@parisnanterre.fr

Abstract. This workshop deals with the study of detecting a mobile heat source on a plate using temperatures measured on the rear face. Initially, a numerical approach to the system is carried out to demonstrate the feasibility of the method. In order to identify the trajectory, shape, and intensity of a mobile heat source, a 3D finite volume model is developed. A parameterization of the unknowns is then performed in the model to identify the characteristics of the mobile heat source without making assumptions about its trajectory shape or spatial distribution and temporal evolution. The sensitivity analysis conducted helps define the identifiability of the model parameters. In this numerical approach, temperature data from the rear face is generated from another 3D finite element model different from the direct model used in the inverse procedure. An inverse heat conduction procedure (IHCP) is applied to these simulated measurements. A conjugate gradient method is implemented to identify the parameters of the problem, namely the different heat sources. The study examines the impact of measurement noise as well as the impact of the characteristics of the mobile source on the quality and accuracy of the identification. Thus, the trajectory and shape of the mobile source are identified and compared to the input data without making any assumptions about the characteristics of the mobile source. Subsequently, the identification process is implemented using real measurements obtained from an experimental setup specifically developed for this study. A continuous laser is used to heat the surface of a sample with dimensions of (50x50x4 mm). The laser position control is achieved through a fully controlled system, allowing the movement of a hot spot on the sample surface. Two rails are used in this experimental setup to enable 2D movement of the mobile heat source. On the rear face of the sample, an infrared camera measures the temperature field. Based on the temperature measurements, using a reduced 3D numerical model of the system, the trajectory, shape, and intensity of the heat source are identified over time.

List of acronyms:

- **IHCT**: Inverse Heat Conduction Procedure
- **RMSR**: Root Mean Square Residual
- **FVM**: Finite Volume Method
- **MOR**: Model Order Reduction
- **CGM**: Conjugate Gradient Method

Scope

1. Introduction
2. Presentation of the moving heat source direct model
   2.1. Physical model
   2.2. Description of the finite volume method
   2.3. MOR definition
   2.4. MOR analysis and validation
3. Inversion procedure using conjugate gradient method
   3.1. Sensitivity problem
   3.2. Adjoint problem
   3.3. Conjugate gradient algorithm
4. Numerical inversion result
5. Experimental study
   5.1. Experimental setup
   5.2. Experimental results
6. Conclusion

1. Introduction

Heat transfer in a solid subjected to a moving heat source constitutes a pivotal aspect within various engineering disciplines, encompassing tribology, laser processing, machining, braking systems, and fire detection [1–4]. It is imperative to develop theoretical tools that can facilitate the design, control, and comprehension of the medium's behavior. Numerous studies have been published on this subject matter, all centered around the concept of mobile heat sources. The identification of mobile heat sources holds the potential for detecting material defects or anomalies in electronic component design. Several analytical models have been proposed for mobile source detection [5–9]. Beddiaf et al. [10] examine the iterative regularization method based on Alifanov's iterative regularization method for resolving the inverse problem of heat conduction in a three-dimensional plate. The objective is to ascertain the time-dependent intensity of a planar heat source by employing temperature measurements on the central region of the upper face of a small, thin steel plate. Two different configurations are investigated: the first involves a fixed heat source on the central region of the lower face, while the second entails a mobile heat source with a predetermined trajectory. The study evaluates the robustness of the approach in both scenarios, while accounting for measurements affected by noise. This fully numerical study allows the position and power of a moving heat source to be determined but requires knowledge of the shape of the source and its starting point. The detection of mobile heat sources commonly involves the utilization of inverse techniques, commonly known as Inverse Heat Conduction Problems (IHCPs). Inversion techniques are increasingly prevalent in the field of IHCP, primarily for parameter identification, characterization of convective exchange, material or friction interface, and boundary condition identification [11–14]. Numerous researchers have employed either analytical or numerical modeling to solve inverse heat conduction problems, whether for stationary or moving heat sources [15–17]. Inverse heat conduction problems are well known to be ill-posed in the Hadamard sense. Regularization methods provide a means to obtain accurate solutions for ill-posed problems by introducing an admissible bias. Several studies [18–21] present diverse approaches to increasing IHCP stability. Mohammadi et al. [22] present a heat source detection in medical field. Due to the highly vascular nature and increased perfusion and metabolism rates, tumors present elevated temperatures relative to their adjacent tissues. Building upon this observation, the authors proposed a method based on an analytical solution and temperatures measurement by infrared (IR) cameras in order to deduce crucial tumor parameters, including its depth and its radius. To validate the efficiency of their analytical approach, the researchers conducted a laboratory experiment employing Nobel Agar solution as a tissue phantom. As numerical models are complex, necessitating substantial computational resources and time, the utilization of model reduction techniques and novel machine learning methods in inversion processes is becoming increasingly prevalent [23,24].

The purpose of this work is to estimate the intensity and spatial evolution of a mobile heat source on a plate, using temperature measurements at the rear face which is visible and accessible. No assumptions about the position, trajectory, shape and intensity of the source are made. The effects of the velocity of the source, measurement errors, and the error of parameters assumed to be known, such as thermal properties, are investigated. The developed model is based on the finite volume method. In order to solve the IHCP problem, the conjugate gradient method is used to compute the conjugate descent directions while considering an adjoint problem. The use of an adjoint method with a conjugate gradient

algorithm to minimize the LS-criterion has been discussed in several studies [25–28] both numerical and experimental [29–33]. This method requires a large number of iterations to converge. Thus, in order to reduce the calculation time, a reduced order model is used for the inversion process [34]. After a numerical study on the feasibility of mobile heat source identification, experimental results are presented. A moving laser is used to heat a steel plate. Using temperature measurements made by IR camera on the backside of the plate, the trajectory, the velocity, the shape and the intensity of the heat source produced by the laser are traced.

2. Presentation of the moving heat source direct model

2.1. Physical model

The three-dimensional transient heat conduction of a parallelepiped body with dimensions $L \times W \times H$ subjected to a surface heat source on one of its surfaces is investigated. The plate's dimensions are L=W=50mm, and its thickness is H = 4mm. A Gaussian mobile heat source is applied on the upper face of the plate. Convection heat transfer is applied to all the faces but with different heat transfer coefficients. The studied model is presented in Figure 1. Equation (1) provides the solution to the heat equation, while equation (2) specifies the corresponding boundary and initial conditions.

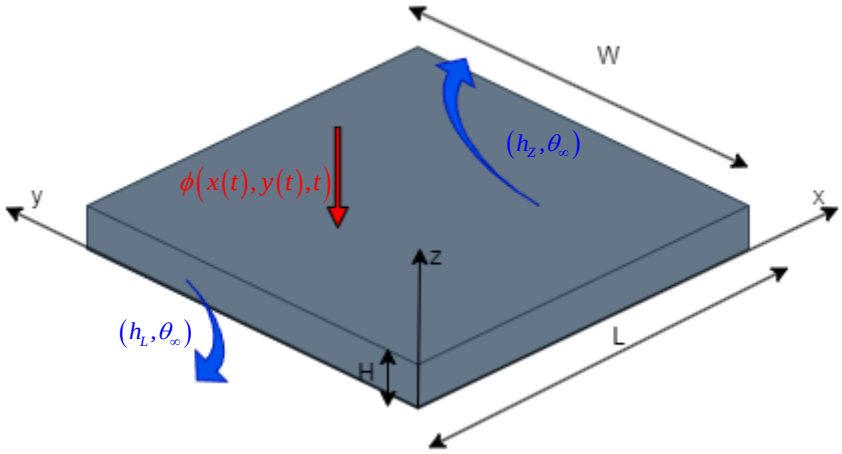

Figure 1: *Geometry and boundary conditions of the studied problem*

The ambient temperature (θ_∞) is assuming to be constant, and the material to be homogeneous and isotropic. The Table 1 gives the thermal properties and the two convective heat transfer coefficients, on the lateral surfaces and on lower and upper surfaces. We assume that $T = \theta - \theta_\infty$, then $T_\infty = 0$.

Table 1: *The known parameters*

λ (W.m^{-1}.K^{-1})	α(m².s^{-1})	h_L(W.m^{-2}.K^{-1})	h_Z (W.m^{-2}.K^{-1})
70	10x10^{-6}	5	10

$$\rho \cdot cp \cdot \frac{\partial T(M,t)}{\partial t} - k \cdot \nabla^2 T(M,t) = 0 \,;\forall M \in \Omega \tag{1}$$

With the boundaries and initial conditions:

$$\begin{aligned} &k \cdot \nabla T(M,t) \cdot \vec{n} + h_z \cdot \left(T(M,t)\right) - \phi\left(x,y,H;t\right) = 0 \,;\forall M \in S_T \\ &k \cdot \nabla T(M,t) \cdot \vec{n} + h_z \cdot \left(T(M,t)\right) = 0 \,;\forall M \in S_B \\ &k \cdot \nabla T(M,t) \cdot \vec{n} + h_L \cdot \left(T(M,t)\right) = 0 \,;\forall M \in S_L \\ &T(M,0) = 0; \forall M \in \Omega \end{aligned} \tag{2}$$

Where S is the surface of the domain Ω. This 3D transient problem is solved by the finite volume method (FVM).

2.2. Description of the finite volume method

The FVM is used to solve the direct problem. The system is divided into regularly parallelepipeds. The number of elements along the x, y, and z axes are denoted as Nx, Ny, and Nz respectively. The total number of volumes is $N_V = N_x \cdot N_y \cdot N_z$. By integration of the equation (1), then using the divergence theorem we get the result given in equation (3)

$$\begin{aligned} &\int_\Omega \left(\rho \cdot cp \cdot \frac{\partial T}{\partial t} - \nabla\left(k \cdot \nabla T\right) \right) \cdot dv = 0 \\ &\int_\Omega \left(\rho \cdot cp \cdot \frac{\partial T}{\partial t} \right) \cdot dv - \int_\Omega \nabla\left(k \cdot \nabla T\right) \cdot dv = 0 \\ &\int_\Omega \left(\rho \cdot cp \cdot \frac{\partial T}{\partial t} \right) \cdot dv - \int_S k \cdot \nabla T \cdot ds = 0 \end{aligned} \tag{3}$$

The surface S is divided into S_{int} (internal domain) and S_{ext} (external domain) such that $S = S_{int} + S_{ext}$. Thus, equation (3) becomes:

$$\begin{aligned} &\int_\Omega \left(\rho \cdot cp \cdot \frac{\partial T}{\partial t} \right) \cdot dv - \int_{S_{\text{int}}} k \cdot \nabla T \cdot ds - \int_{S_{ext}} k \cdot \nabla T \cdot ds = 0 \\ &\int_\Omega \left(\rho \cdot cp \cdot \frac{\partial T}{\partial t} \right) \cdot dv - \int_{S_{\text{int}}} k \cdot \nabla T \cdot ds + \int_{S_{ext}} h \cdot \left(T - T_\infty\right) \cdot ds - \int_{S_{ext}} \phi \cdot ds = 0 \end{aligned} \tag{4}$$

We obtain the discrete equation(5).

$$\rho_i \cdot cp_i \cdot v_i \cdot \frac{\partial T_i}{\partial t} - \sum_{S_{\text{int}}} k_i \cdot S_i \cdot \nabla T_i + \sum_{S_{ext}} h_i \cdot S_i \cdot \left(T_i\right) - \sum_{S_{ext}} \phi_i \cdot S_i = 0 \tag{5}$$

Which can be expressed in matrix form as shown in equation(6).

$$Cap \cdot \dot{T} = K \cdot T + B_f \cdot \phi \tag{6}$$

Where Cap is the capacity matrix. K represents the conductivity matrix, which also includes the convective coefficient in the boundary terms. B_f is a detailed surface model control matrix. *T* is the temperature vector of all the nodes in the system and $\dot{T}$ its derivative. ϕ is the vector of imposed fluxes on each of the nodes on the upper face (*z=H*). An implicit scheme has been utilized to solve the numerical problem using a step time of $\Delta t = 0.1s$.

2.3. Modal order reduction (MOR)

The linear time-invariant system generated is given by equation (7). A state-space system is the mathematical representation of a physical model. It consist in an ODE linking input, output and space state variable.

$$\begin{cases} Cap\dot{T}(t) = K\,T(t) + B_f \cdot \phi(t) \\ Y(t) = C\,T(t) \end{cases} \tag{7}$$

Where C is the observation matrix, $Y(t)$ is the output temperature vector, $\phi(t)$ is the input vector and B_f is a detailed upper surface model control matrix. In our configuration, the output vector represents the surface temperatures at *z=0*. $\phi(t)$ represents the input of the system. We write the system given by equation (7) in the modal base:

$$\begin{cases} \dot{\tau}(t) = \Lambda\,\tau(t) + \Gamma\phi(t) \\ Y(t) = \Omega\,\tau(t) \end{cases} \tag{8}$$

With $\tau = M^{-1} \cdot T$, then $\Lambda = M^{-1} \cdot Cap^{-1} \cdot K \cdot M$, $\Gamma = M^{-1} \cdot Cap^{-1} \cdot B_f$ and $\Omega = MC$.

The matrix M is the matrix of N_V linearly independent eigenvectors (Modal Matrix). The eigenvalues λ_{n_v} are the values that satisfy the expression given in equation (9).

$$\det(A - \lambda I) = 0 \tag{9}$$

The matrix Λ is diagonal and formed by these eigenvalues:

$$\Lambda = diag\left(\lambda_{n_v}\right) \tag{10}$$

Subsequently, the model reduction technique is based on modal reduction through Amalgam Reduction Order Modal Model (AROMM) [34,35]. The temperature, solution of this model is noted $\bar{Y}(x, y, t)$.

2.3.1. MOR analysis and validation

The choice of the right order of reduction is defined in order to maintain the model error lower than the measurement noise. The noise distribution follows a normal distribution with a mean value $\mu_N = 0\,°C$ and a standard deviation $\sigma_N = 0.1°C$ at the sampling frequency $f_s = 10\,Hz$. This standard deviation value is the smallest considered in this article, guaranteeing the utilization of the most precise reduced model. Figure 2 presents the distribution of this noise signal.

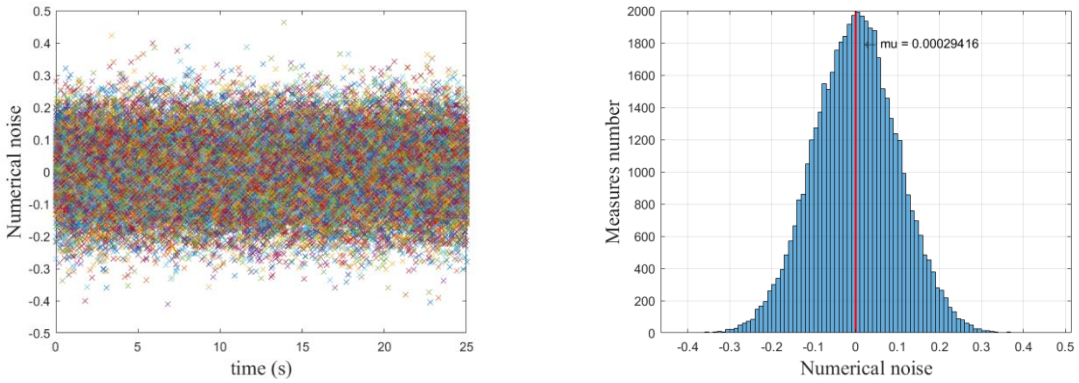

Figure 2: *Values and repartition of the numerical noise*

The subsequent approach is used to estimate the error related to the utilization of a reduced-order model. We sequentially computed the error caused by the input heat flux ϕ_i on each node. While one heat flux is active, the others are equal to zero. The resultant error is denoted as e_i Thus, the subsequent matrix of error is defined by equation (11).

$$e = \left[e_1, e_2, ..., e_i, ..., e_p \right] \tag{11}$$

With each value error e_i calculated by the difference between the reduced model and the complete one:

$$e_i = \sum_{m=1}^{M} \sum_{n=1}^{N_t} \left(\bar{Y}_n^m - Y_n^m \right)^2 \tag{12}$$

We use the RMSR (Root Mean Square Residual) as an error estimator (Eq. (13)). The RMSR should be equal to or less than σ_N. It indicates the square root of the average difference between the temperatures calculated using the complete model Y and those calculated using the reduced model $\bar{Y}$ for various modes.

$$RMSR_i = \sqrt{\frac{e_i}{N_t \times M}} \; ; \; RMSR = \frac{1}{p} \sum_{i=1}^{p} RMSR_i \tag{13}$$

Figure 3 presents the variation of the RMSR as a function of modes number. When additional modes are considered, the temperature field computed from the reduced model becomes more similar to the one calculated using the full model. However, the calculation time of the reduced model increases with the number of modes considered. This evolution is plotted in Figure 3. Therefore, we select the first order of reduction that satisfies the following inequality:

$$RMSR \leq \sigma_N \tag{14}$$

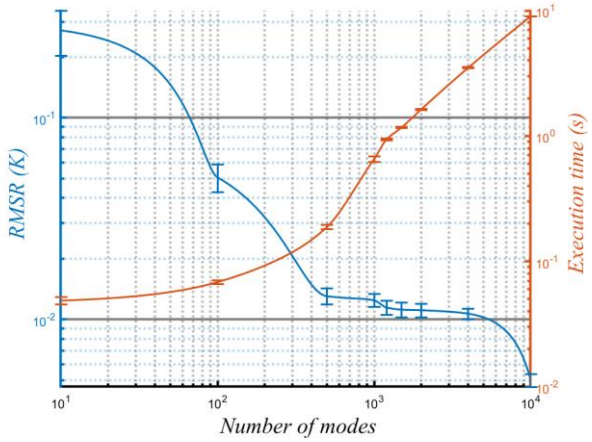

Figure 3: *Evolution of the RMSR for different modes*

Based on this error analysis, the reduction order is defined as $Ro = 1200$. In fact, the highest RMSR value for this reduced order mode is lower than the standard deviation of the imposed numerical noise $\sigma_N = 0.1°C$. The computation time is significantly reduced. Table 2 summarizes the reductions in computational time of the reduced model compared to the full model. We can notice that the computation time is also reduced only by calculating into the modal basis.

Table 2: *Characteristics of the reduced model*

	Complete model	*Complete model in the modal basis*	*Reduced model (R_o=1200)*
Execution time (s)	80	50	0.9
RMSR (K)	-	-	0.012

The choice of a reduced model possessing an RSMR 10 times smaller than the imposed noise is defined by a computation time that, despite this restrictive constraint, remains less than one second.

3. Inversion procedure

The objective of the IHCP is to identify the shape, the intensity, the trajectory and the velocity of the moving heat source using the thermal temperature of the rear surface. This problem can be formulated as a conventional IHCP, with the objective of minimizing a quadratic criterion ***J(ϕ)***. To solve this ill-posed problem, the conjugate gradient method (CGM) algorithm is used, with the sensitivity and adjoint problems. The CGM is a widely used iterative optimization method for solving large-scale linear systems. In each iteration, the algorithm calculates the residual of the current approximation and determines conjugate search directions to update the solution. The residual is then minimized along the conjugate directions through a descend direction. This process continues until the desired accuracy is achieved or the maximum number of iterations is reached. The algorithm is especially efficient for systems with sparse matrices and can provide quicker convergence compared to alternative methods. To ensure convergence, it is important to carefully select appropriate termination criteria and the choice of the descend direction. The associated objective function ***J(ϕ)*** of the inverse problem is given by the following equation:

$$J(\phi) = \int_{S_{mes}} \int (Y - \tilde{Y})^2 \cdot ds \cdot dt \tag{15}$$

Where $\tilde{Y}$ are the measured or simulated temperatures at the rear surface.

3.1. Sensitivity problem

The problem's formulation is beneficial in determining the descent depth estimation in the descent direction. The temperature variation induced by an alteration of the unknown parameters $\delta\phi(t)$ is denoted $\delta T(x,y,z;t)$, for partial differential equations (PDE) satisfied by the temperature $T_\varepsilon^+ = T(x,y,z;t) + \varepsilon\delta T(x,y,z;t)$ with heat source $\phi_\varepsilon = \phi(t) + \varepsilon\delta\phi(t)$ with ε→0. The sensitive function is defined by equation (16).

$$\delta T = \lim_{\varepsilon \to 0} \frac{T_\varepsilon^+ - T}{\varepsilon} \tag{16}$$

The temperature T is substituted by δT, the impulse response to a heat flux in equations (1) and (2), in order to calculate the descent depth:

$$\begin{aligned}
&\rho \cdot Cp \cdot \frac{\partial \delta T(M,t)}{\partial t} - k\left(\Delta \delta T(M,t)\right) = 0\,; \quad \forall M \in \Omega, t > 0 \\
&k \cdot \nabla \delta T(M,t) \cdot n - \delta\phi = 0\,; \quad \forall M \in \partial\Delta_T \\
&k \cdot \nabla \delta T(M,t) \cdot n = 0; \quad \forall M \in \partial\Delta - \partial\Delta_T \\
&\delta T(M,0) = 0; \forall M \in \Omega
\end{aligned} \tag{17}$$

3.2. Adjoint problem

The task involves calculating the cost function's gradient during each iteration of the CGM algorithm through the utilization of an adjoint function $\psi(x,y,z;t)$. The Lagrangian $L(T,\phi,\psi)$ associated with the direct problem is defined by:

$$L(T,\phi,\psi) = J(\phi) + \int_{\Omega}\int \psi(\phi,t)\cdot\left(\rho\cdot cp\cdot\frac{\partial T(\phi,t)}{\partial t} - \nabla\left(k\cdot\nabla T(\phi,t)\right)\right)\cdot dv\cdot dt \tag{18}$$

Assuming that the variables T, ϕ and ψ are independent of one another:

$$L = \int (C\cdot T - \tilde{Y})^2\cdot dt + \int \psi^T\cdot\left(Cap\cdot\dot{T} - K\cdot T - B_f\cdot\phi\right)\cdot dt \tag{19}$$

The development of this method is much more documented in the literature [25–28,36,37].The adjoint system is given by equation (20).

$$\begin{cases} Cap^T\cdot\dot{\psi} + K^T\cdot\psi = -2\cdot C^T\cdot(C\cdot T - \tilde{Y}) \\ \left(\nabla J\right) = -{B_f}^T\cdot\psi \end{cases} \tag{20}$$

3.3. Conjugate gradient algorithm

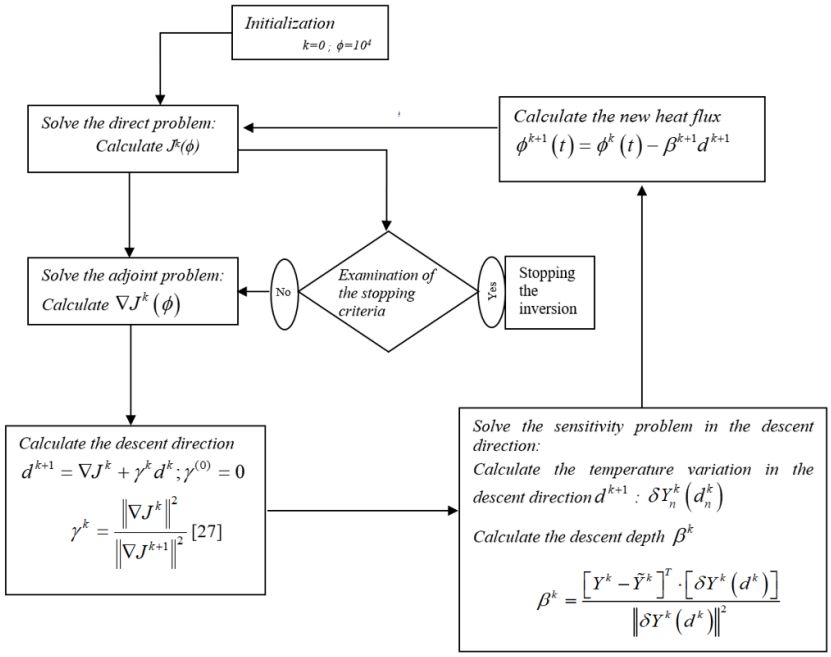

Figure 4 : *Conjugate gradient algorithm with adjoint variable calculation.*

The algorithm for solving the inverse problem by the conjugate gradient method with the calculation of the adjoint variable is presented in Figure 4.

The stopping criteria of the algorithm are:

a) The Morozov's criteria (Discrepancy criteria)

This condition impose to the inversion procedure to perform a solution with an error higher or equal to the standard deviation of the noise σ_N .

$$\sqrt{\frac{\sum_{m=1}^{M}\sum_{n=1}^{N_t}\left(Y_n^m-\tilde{Y}_n^m\right)^2}{M(N_t-1)}}\geq\sigma_N \tag{21}$$

b) The maximum iteration

For the CGM, the maximum number of iteration is given in most of the works as a number of parameter to identify [27].

4. Numerical study

This technique gives also the possibility to identify a multi mobile heat source. In order to validate this technique of identification for multi moving heat source, a case with three different moving sources is simulated. The total power of each source is presented in Figure 5.

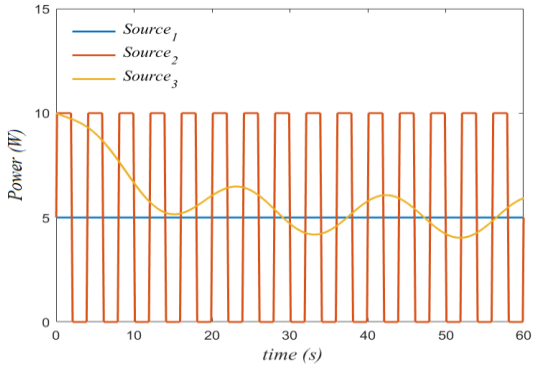

Figure 5: *Evolution of the power of the three sources*

The first source follows a circular path centered in the middle of the upper face. The second source follows the trajectory given in the Figure 6. The third one is fixed in the middle of the plate.

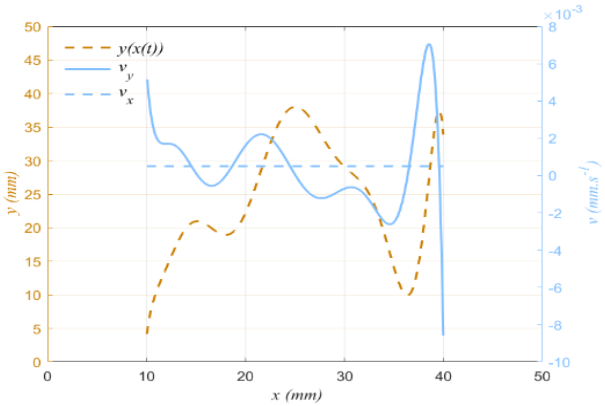

Figure 6: *Trajectory and speed of the second source*

On the basis of heat flux maps given in **Figure 7**, it is possible to identify a large number of sources, even if the intensity of the sources is varying. The same remark could be made about the spreading of the identified heat flux which is more important than the real one.

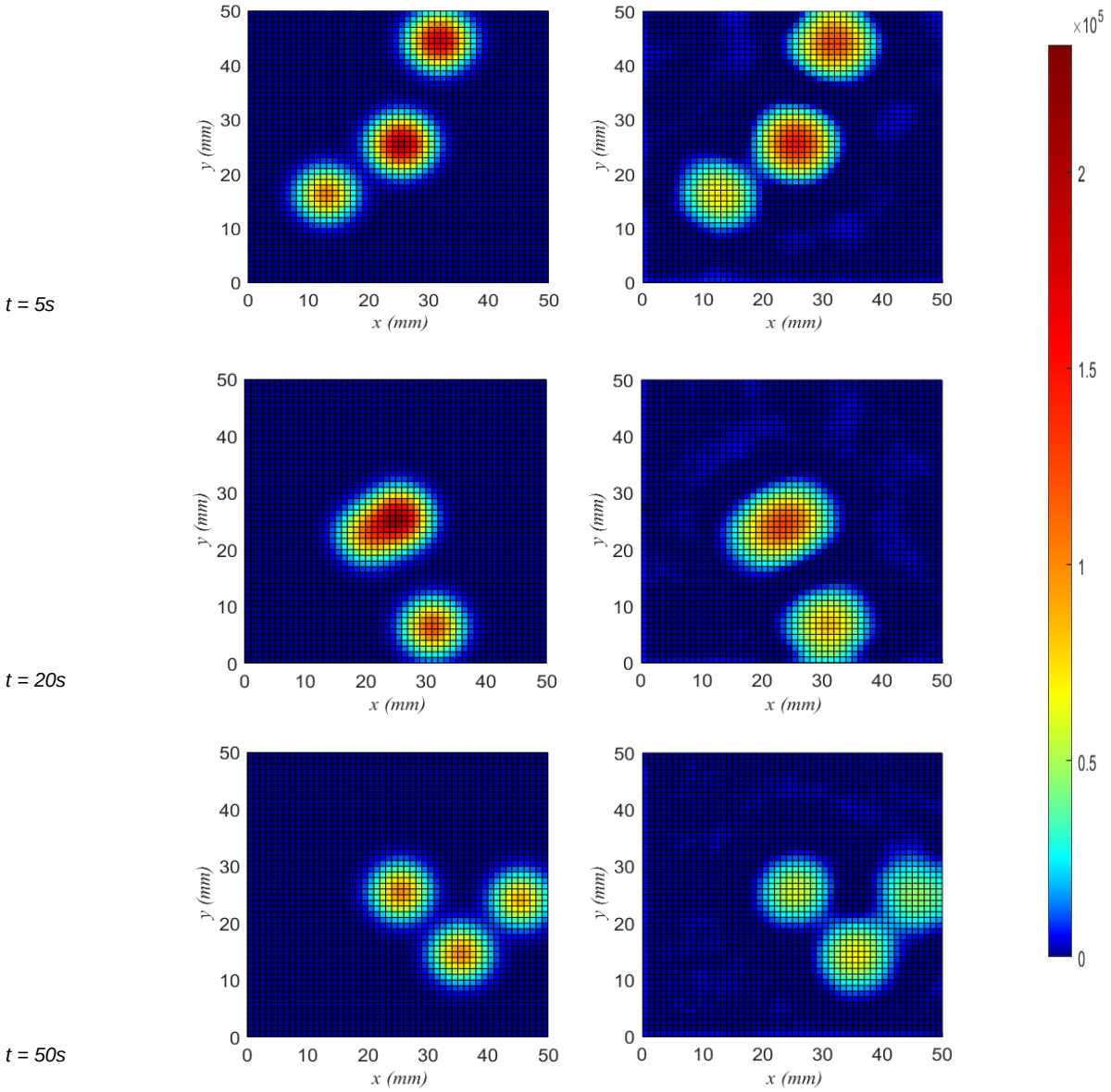

Figure 7: *Heat flux map at surface (z=H) of the solid at (t=5s, 20s, 50s). a) Impose flux; b) Identified flux*

There are no hypotheses about the number or of sources and their trajectories. From Figure 8 (a), it is clear that the identified total power is in good agreement with the total injected

power. The residual temperature (Figure 8 (b)) are as expected: a cloud of points centered on zero, normally distributed according to a standard deviation $\sigma \approx 0.1K$.

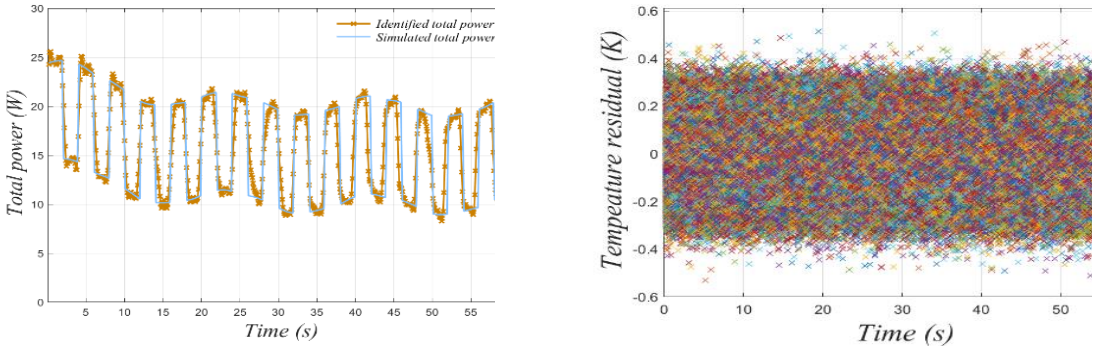

(a) (b)

Figure 8: *Identification results: (a) Total power identified in the multiple heat mobile source case, (b) Temperature residual*

5. Experimental study

In this section, we will observe the feasibility of detecting a mobile heat source based on experimental data. Firstly, we will provide a comprehensive overview of the experimental setup employed for this study. Subsequently, we will present the identification results achieved for different configurations.

5.1. Experimental setup

Figure 12 shows a diagram of the experimental setup used in this study. Figure 13 provides a picture of the experimental test bench. We use a continuous laser to heat one side of a sample that measures (50x50x4mm). The laser moves across the sample's surface using a displacement system with two rails, allowing motion in two dimensions. Specifically, a 690mm rail is attached to a second one (length 1300mm). The rails are controlled precisely using an automation system (ISEL-Automation C-142/4, which works with the Kynon Pro software). The software allows us to control the movement and speed of the rails using a set of instructions. On the opposite side of the sample, an infrared camera (INFRATEC IR-9400) is placed to capture thermal measurements of that particular side. The temperatures measured by the high-resolution IR camera are interpolated onto the nodes of the mesh of the reduced model used for the estimation procedure. Furthermore, thermocouples are placed on the heated surface to verify the obtained results by the inverse method.

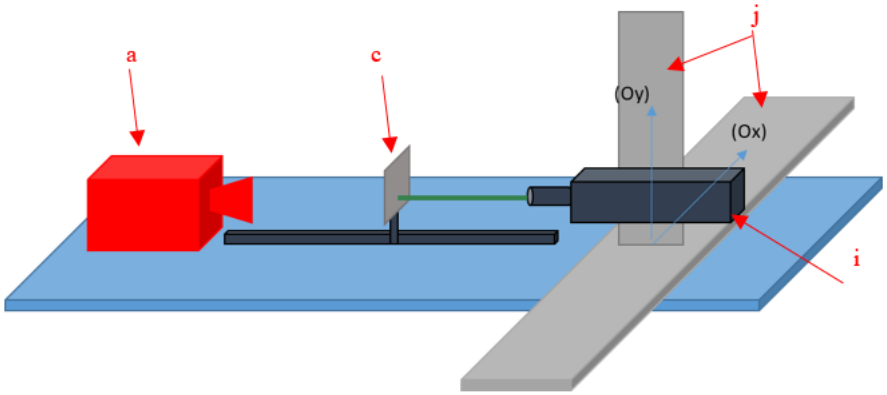

Figure 9 : *Layout of the experimental bench*

a) IR camera (INFRATEC 9400) – b) Sample holder – c) Sample – d) Temperature data acquisition device from thermocouple – e) IR camera software (IRBIS3.1) – f) Shutter – g) rail control software – h) Laser's generator – i) Laser – j) rails

5.2. Experimental results

The laser is moving at a linear velocity of $v=5mm.s^{-1}$, following a circular trajectory with a radius of $R_c=10mm$, whose center is identical to that of the sample. The starting point is located at position $p_i=[15,25]mm$. The identified and the experimental laser's trajectory are compared in the Figure 10.a. On this figure are plotted the location of thermocouples. Indeed, to validate the accuracy of the method, thermocouples are attached to the heated surface. The temperatures calculated from the identified fluxes are compared to these measurements in Figure 10.b.

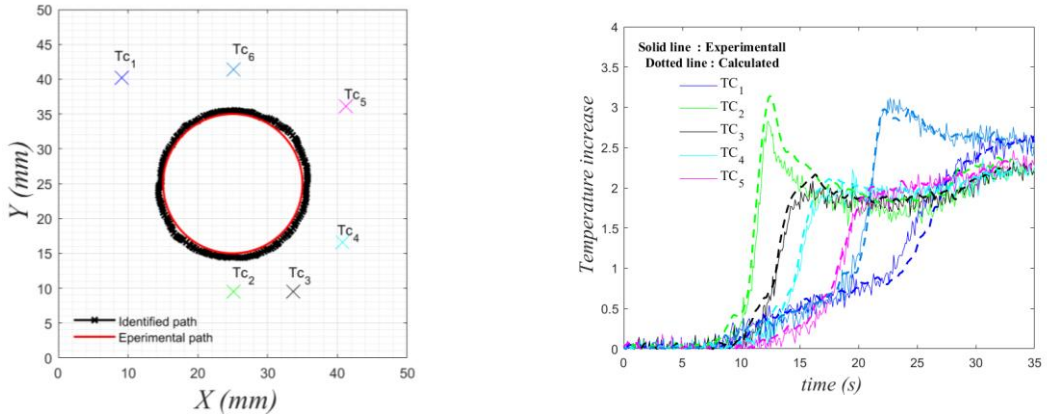

a) b)

Figure 10 *: Identification results. a) Path of the laser and thermocouple positions. b) Measured temperature of the heated face compared to the calculated temperature using identified heat source.*

First of all, the identified path is accurate (Figure 10.a); the circularity is well shown with a small gap between the input trajectory and the identified one. The difference is less than *1mm*. Regarding the temperatures of the thermocouples, two trends can be distinguished. The first concerns the thermocouples closest to the heating zone, with the largest difference observed for thermocouple 2. The other thermocouples provide good accuracy with the calculation, assumed the errors associated with determining their exact position through image analysis. Based on these experimental results and validation, it can be concluded that the method accurately identified the characteristics of the moving heat source. Moreover, the temperature residuals (Figure 11) have the form of a zero-centered scatterplot with a standard deviation equivalent to the standard deviation of the experimental blank noise. The mean power identified from this experimental technique represents 70% of the laser's power. The losses may represent the reflected flux by the sample.

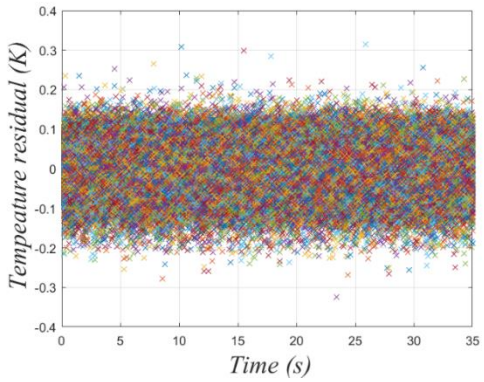

Figure 11 : *Temperature residual*

Figure 12.a illustrates the thermal maps captured on the rear face at different step time. These measurements correspond to the original data obtained from the infrared camera. The reduced model is constructed with a spatial discretization of (51x51) on the (Ox, Oy) plane. The thermal signature generated by the movement of the source is clearly visible. In Figure 12.b is plotted the mapping of the identified surface heat fluxes. It is notable that the power distribution of the source exhibits a Gaussian shape, consistent with the laser beam profile specified by the supplier (Dantech). No significant numerical signature arising from the interplay between transport and diffusion phenomena is observed at this velocity, which confirms the results obtained during the numerical investigation.

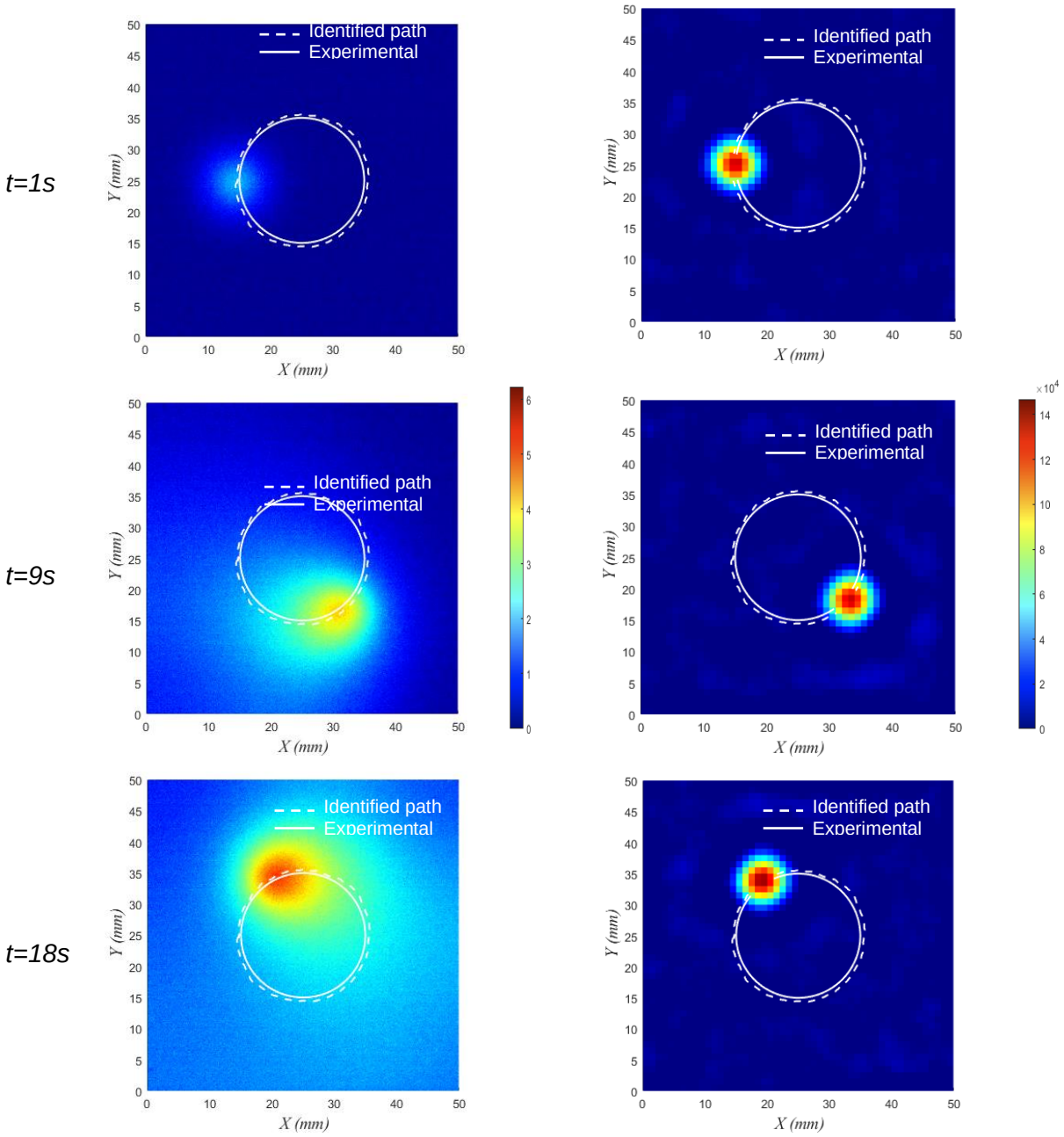

Figure 12 : *Representation of the measured temperatures and the identified heat fluxes at different times for circular path. a) Thermal measurement of the rear face. b) Identified heat flux on the front side*

6. Conclusion

This study presents the identification by inverse method of a moving heat source. A reduced model, based on the model reduction using modal base reduction method with the amalgamation method, has resulted in a significant gain in computation time. The inversion process is performed using the conjugate gradient method and the reduced model. This tool has been applied to the detection of surface moving heat sources. A dedicated experimental setup has been designed and implemented to validate this technique. One side of the sample is excited by a moving laser, and temperatures on the opposite side are measured using an infrared camera. A circular trajectory test has been performed and the results have been validated by comparing the thermal measurements obtained from thermocouples on the upper surface with the recalculated temperatures at the same positions. In this tutorial, participants will manipulate raw experimental data, process them, implement them into the measurement inversion code, and analyze the results. Future prospects are to create a quasi-real-time monitoring of moving heat sources for diverse industrial applications such as welding or machining processes.

[1] H. Bordbar, F. Alinejad, K. Conley, T. Ala-Nissila, S. Hostikka, Fire Saf. J. 133 (2022) 103673.
[2] C. Serra, A. Tadeu, N. Simões, Appl. Math. Model. 40 (2016) 1576–1587.
[3] T. Arafa-Hamed, M. Abdel Zaher, G. El-Qady, H. Marzouk, S. Elbarbary, Y. Fujimitsu, Geothermics 109 (2023) 102648.
[4] X. Wang, L. Liu, R. Duan, Y. Liu, Z. Wei, X. Yang, X. Liu, Z. Li, Int. Commun. Heat Mass Transf. 135 (2022) 106123.
[5] Y. Wang, P.F. Mendez, Int. J. Therm. Sci. 172 (2022) 107334.
[6] B. Çetin, Y.F. Kuşcu, B. Çetin, Ö. Tümüklü, K.D. Cole, Int. J. Heat Mass Transf. 165 (2021) 120692.
[7] Y. Xu, X. Zhang, J. Shen, T. Shi, J. Laser Appl. 32 (2020) 042014.
[8] G. Araya, G. Gutierrez, Int. J. Heat Mass Transf. 49 (2006) 4124–4131.
[9] N. Aderghal, T. Loulou, A. Bouchoucha, P. Rogeon, Appl. Therm. Eng. 31 (2011) 1527–1535.
[10] S. Beddiaf, L. Perez, L. Autrique, J.-C. Jolly, Inverse Probl. Sci. Eng. 23 (2015) 93–111.
[11] J.-G. Bauzin, A. Hocine, M.-B. Cherikh, M.-N. Nguyen, Z.A. Peter, N. Laraqi, Int. J. Therm. Sci. 184 (2023) 107924.
[12] M.-B. Cherikh, J.-G. Bauzin, N. Laraqi, Int. J. Heat Mass Transf. 169 (2021) 120986.
[13] J.-G. Bauzin, M.-B. Cherikh, N. Laraqi, Int. J. Therm. Sci. 164 (2021) 106868.
[14] C. Meunier, J.-G. Bauzin, N. Laraqi, A. Gapin, J.-F. Diebold, Int. J. Heat Mass Transf. 196 (2022) 123277.
[15] J.-G. Bauzin, S. Vintrou, N. Laraqi, Int. J. Therm. Sci. 148 (2020) 106115.
[16] V.-T. Than, C.-C. Wang, T.-T. Ngo, J.H. Huang, Int. J. Therm. Sci. 111 (2017) 50–65.
[17] C. Lv, G. Wang, H. Chen, S. Wan, Int. J. Therm. Sci. 138 (2019) 576–585.
[18] J.V. Beck, B. Blackwell, C.R.S.C. Jr, Inverse Heat Conduction: Ill-Posed Problems, James Beck, 1985.
[19] O.M. Alifanov, Inverse Heat Transfer Problems, Springer Science & Business Media, 2012.
[20] M.N. Ozisik, Inverse Heat Transfer: Fundamentals and Applications, CRC Press, New York, 2000.

[21] A.N. Tikhonov, A. Goncharsky, V.V. Stepanov, A.G. Yagola, Numerical Methods for the Solution of Ill-Posed Problems, 1995th edition, Springer, Dordrecht ; Boston, 1995.
[22] F. Mohammadi, M. Rastgar-Jazi, J. Med. Biol. Eng. 38 (2018) 316–324.
[23] A.G.C. Castillo, B. Gaume, Y. Rouizi, O. Quéméner, P. Glouannec, Int. J. Heat Mass Transf. 166 (2021) 120683.
[24] G. Ren, A. Chuttar, D. Banerjee, Int. J. Heat Mass Transf. 189 (2022) 122628.
[25] Y. Jarny, M.N. Ozisik, J.P. Bardon, Int. J. Heat Mass Transf. 34 (1991) 2911–2919.
[26] H.R.B.O. Marcelo J. Colaco, Numer. Heat Transf. Part Appl. 36 (1999) 229–249.
[27] R. Fletcher, C.M. Reeves, Comput. J. 7 (1964) 149–154.
[28] K.A. Woodbury, ed., in: Inverse Eng. Handb., CRC Press, 2002.
[29] S.D. Farahani, F. Kowsary, M. Ashjaee, Exp. Heat Transf. 29 (2016) 657–672.
[30] H.Y. Li, M.N. Ozisik, J. Quant. Spectrosc. Radiat. Transf. 48 (1992) 237–244.
[31] M. Prud'homme, T. Hung Nguyen, Int. J. Heat Mass Transf. 44 (2001) 2011–2027.
[32] A.J.S. Neto, M.N. Özişik, Numer. Heat Transf. Part Appl. 24 (1993) 467–477.
[33] M. Mohammadiun, A.B. Rahimi, I. Khazaee, Int. J. Therm. Sci. 50 (2011) 2443–2450.
[34] A. Oulefki, A. Neveu, J. Phys. III 3 (1993) 303–320.
[35] J.-P. Lombard, (n.d.) 155.
[36] S. Beddiaf, L. Autrique, L. Perez, J.-C. Jolly, Int. J. Appl. Math. Comput. Sci. 26 (2015).
[37] R. Abou khachfe, Y. Jarny, Int. J. Heat Mass Transf. 44 (2001) 1309–1322.

https://metti8.sciencesconf.org/

The 8th edition of the Advanced Autumn school 'Thermal Measurement and Inverse Techniques' is run by the METTI Group (**ME**sures en **T**hermique et **T**echniques **I**nverses) that constitutes a division of the Société Française de Thermique (SFT, French Heat Transfer Society).

* * *

Finding 'causes' from measured 'consequences' using a mathematical model linking the two is an inverse problem. This is met in different areas of physical sciences, especially in Heat Transfer. Techniques for solving inverse problems as well as their applications may seem quite obscure for newcomers to the field. Experimentalists desiring to go beyond traditional data processing techniques for estimating the parameters of a model with the maximum accuracy feel often ill prepared in front of inverse techniques. In order to avoid biases at different levels of this kind of involved task, it seems compulsory that specialists of measurement inversion techniques, modelling techniques and experimental techniques share a wide common culture and language. These exchanges are necessary to take into account the difficulties associated to all these fields. It is in this state of mind that this school is proposed. The METTI Group (Thermal Measurements and Inverse Techniques), which is a division of the French Heat Transfer Society (SFT), has already run or co- organized seven similar schools, in the Alps (Aussois, 1995 and 2005), in the Pyrenees (Bolquère-Odeillo, 1999), in Brasil (Rio de Janeiro, 2009), in Bretagne (Roscoff, 2011), in Pays Basque (Biarritz, 2015) and in Porquerolles island (Porquerolles 2019). For this eighth edition the school is again open to participants from the European Community with the support of the Eurotherm Committee.

* * *

Two books are distributed at the beginning of the school. Volume 1 contains the texts used as supports for the lectures and Volume 2 contains the texts used as supports for the tutorials.